



University
of Glasgow

<https://theses.gla.ac.uk/>

Theses Digitisation:

<https://www.gla.ac.uk/myglasgow/research/enlighten/theses/digitisation/>

This is a digitised version of the original print thesis.

Copyright and moral rights for this work are retained by the author

A copy can be downloaded for personal non-commercial research or study, without prior permission or charge

This work cannot be reproduced or quoted extensively from without first obtaining permission in writing from the author

The content must not be changed in any way or sold commercially in any format or medium without the formal permission of the author

When referring to this work, full bibliographic details including the author, title, awarding institution and date of the thesis must be given

Enlighten: Theses

<https://theses.gla.ac.uk/>
research-enlighten@glasgow.ac.uk



UNIVERSITY
of
GLASGOW

**Cyclic Analysis
of
Laterally Loaded Pile Foundations**

Yoke Poh LEE

*A thesis submitted for the degree of
Doctor of Philosophy at the University of Glasgow*

Department of Civil Engineering

University of Glasgow

December 1997

© Yoke Poh LEE

ProQuest Number: 10992083

All rights reserved

INFORMATION TO ALL USERS

The quality of this reproduction is dependent upon the quality of the copy submitted.

In the unlikely event that the author did not send a complete manuscript and there are missing pages, these will be noted. Also, if material had to be removed, a note will indicate the deletion.



ProQuest 10992083

Published by ProQuest LLC (2018). Copyright of the Dissertation is held by the Author.

All rights reserved.

This work is protected against unauthorized copying under Title 17, United States Code
Microform Edition © ProQuest LLC.

ProQuest LLC.
789 East Eisenhower Parkway
P.O. Box 1346
Ann Arbor, MI 48106 – 1346

Thesis 11026
copy 1



**To
my family
&
Arthur Nicol**

To God be the Glory



On account of the fact that there is no glory in the foundations, and that the sources of success or failure are hidden deep in the ground, building foundations have always been treated as stepchildren; and their acts of revenge for lack of attention can be very embarrassing.

... Terzaghi

Therefore,

According to the grace of God which is given unto me, as a wise masterbuilder, I have laid the foundation.

... I Corinthians 3 : 10

ACKNOWLEDGEMENTS

I wish to express my sincere gratitude to my supervisor, Dr T.G. Davies for his continued guidance, invaluable advice, encouragement, patience and interest throughout this project.

I would like to thank Dr. J.G. Herbertson and Prof. N. Bicanic, former Head and present Head of the Civil Engineering Department, respectively, for providing good environment and facilities to carry out this research.

I would also like to express my thanks to Prof. D.R. Green, Vice Principal of the University of Glasgow, for his initial help and advice. Appreciation also goes to Prof. D. Muir Wood for his teaching and fruitful discussions, and to Dr. A.H.C. Chan for the use of his finite element program and helpful suggestions.

Grateful thanks are due also to Prof. S.J. Wheeler for the value in his discussions.

My thanks also goes to K. McColl, E. Davies and B. Grant for their kind help and support in everyday matters.

My gratitude is extended to my friends and colleagues, especially B. Scott, M. McKechnie, Dr. B. Zhang, Dr. A. Winnicki, Dr. S. Bu, Dr. G.V. Kumar, Dr. B.T. Lim, C.W. Khong, V. Peloutier, F. Basile, D. Gallipoli, X.W. Gao, H. Chen and A. Al-Muzahmi for their friendship and interesting discussions.

I gratefully acknowledge the financial support given by the Committee of Vice-Chancellors and Principals of the Universities of the United Kingdom and the University of Glasgow throughout the duration of this project.

My heartfelt thanks to A.M. Nicol for his continuous encouragement, concern and support, and in the checking of this dissertation, thus contributing to the completion of this thesis.

Finally, my special thanks are directed to my family, in particular my parents, for their support and understanding in my extended studies.

ABSTRACT

A three-dimensional numerical analysis, based on the indirect boundary element method, is developed to model the cyclic behaviour of laterally loaded pile foundations embedded in cohesive soils. Phenomena observed in cyclic pile-load tests, such as gapping, backsliding and soil strength degradation effects are accounted for in the analysis. The analysis is capable of solving one-way and two-way cyclic loading problems subjected to load-controlled and displacement-controlled conditions.

Two-dimensional plane-strain finite element analyses using a 'bubble' model and Mohr-Coulomb model are carried out, to examine the details of the interaction between the pile and soil when subjected to cyclic loading. These analyses were used to guide the development of the full three-dimensional analysis. A detailed study of the bubble model, including a parametric study is conducted.

The three-dimensional non-linear elasto-plastic analysis uses an elastic-perfectly plastic model for soils, which are assumed to behave linearly elastically at small strain levels, but yield, when the limiting stresses of the surrounding soil are exceeded. After the soil yields, its strength may degrade depending on the magnitude of the plastic displacement (i.e. strain softening). The mechanisms involved in the degradation are investigated, and methods to determine the strength degradation parameters using experimental data and correlations with soil index properties are presented.

Using the foregoing analysis, an extensive parametric study on the principal pile and soil variables is undertaken and presented in dimensionless form, to provide data for design purposes. The economy and generality of the analysis, together with good agreement between its predictions and published case histories, assures confidence in its use in engineering practice.

CONTENTS

DEDICATION	
ACKNOWLEDGEMENTS	i
ABSTRACT	ii
CONTENTS	iii
NOTATION	x
LIST OF TABLES	xv
LIST OF FIGURES	xvi

CHAPTER 1: INTRODUCTION

1.1 General remarks	1
1.1.1 Behaviour of static laterally loaded piles	2
1.1.2 Behaviour of cyclic laterally loaded piles	3
1.2 Analyses of static laterally loaded piles	6
1.2.1 Linear analysis	6
1.2.2 Non-linear analysis	7
1.3 Analyses of cyclic laterally loaded piles	9
1.3.1 Empirical approach	9
1.3.2 Modified p - y analysis	10
1.3.3 Cycle-by-cycle analysis	12
1.3.4 Bilinear-elasto-plastic analysis	13
1.3.5 Discrete element analysis	14
1.3.6 Finite element analysis	16
1.3.7 Modified boundary element analysis	18
1.4 Discussion	20
1.5 Scope of the research	21

CHAPTER 2: CYCLIC SOIL MODELS

2.1 Summary	32
2.2 Introduction	32
2.3 Soil behaviour under cyclic loading	32
2.3.1 Introduction	32
2.3.2 Development of permanent strain	33
2.3.3 Changes in soil stiffness and dissipation of energy	33

2.3.4 Development of excess pore water pressure	34
2.3.5 Strength reduction	34
2.4 Soil models for cyclic loading	35
2.4.1 Equivalent linear models	35
2.4.2 Cyclic non-linear models	36
2.4.3 Advanced constitutive models	37
2.4.3.1 Kinematic hardening models	37
2.4.3.2 Bounding surface plasticity models	38
2.5 The 'bubble' model	40
2.5.1 Introduction	40
2.5.2 Modified Cam clay model	40
2.5.3 Bubble yield surface	42
2.5.4 Translation rule	43
2.5.5 Hardening rule	44
2.5.6 Numerical tests	46
2.5.7 Comparisons with experimental data	47
2.5.8 Parameters required for the bubble model	48
2.5.9 Strengths and weaknesses of the bubble model	48
2.6 Concluding remarks	49

CHAPTER 3: PLANE-STRAIN FINITE ELEMENT ANALYSES

3.1 Summary	63
3.2 Introduction	63
3.3 Finite element packages	64
3.3.1 SWANDYNE	64
3.3.2 OASYS	64
3.4 Idealised model	65
3.4.1 Boundary conditions	65
3.4.2 Cyclic loading conditions	65
3.5 Maximum load and undrained shear strength	65
3.6 Mesh details	67
3.6.1 Mesh discretisation	67
3.7 Convergence study	68
3.7.1 SWANDYNE analysis	68
3.7.2 OASYS analysis	69
3.8 Parametric studies	69
3.8.1 The effect of soil strength parameter M	70
3.8.2 The effect of soil parameter R	71

3.8.3 The effect of soil parameter ψ	71
3.8.4 The effect of soil Poisson's ratio (ν)	71
3.8.5 The effect of soil parameters λ^* and κ^*	72
3.8.6 The effect of load level	72
3.8.7 The effect of overconsolidation ratio	73
3.9 SWANDYNE analysis and results	73
3.9.1 Fully bonded case	74
3.9.1.1 Comparisons of models' predictions	75
3.9.2 Half-debonded case	76
3.9.2.1 Comparisons of models' predictions	77
3.10 OASYS analysis and results	78
3.11 Boundary conditions review	78
3.12 Discussion of results	79
3.13 Concluding remarks	81

CHAPTER 4: SOIL STRENGTH DEGRADATION

4.1 Summary	101
4.2 Introduction	101
4.3 Degradation of shear strength	102
4.3.1 Causes of shear strength degradation	103
4.3.2 Plastic displacement	104
4.4 Correlations of shear strength degradation with soil index properties	105
4.4.1 Correlations of residual angle of shearing resistance (ϕ'_r) with soil index properties	106
4.4.2 Correlations of residual/peak shear strength ratio (R_s) with soil index properties	107
4.4.2.1 Modifications of R_s for low normal effective stress	108
4.5 Rate of degradation of shear strength	110
4.5.1 Shear degradation rate factor (C_s) determination	111
4.6 Correlation of rate of shear strength degradation with soil index properties	112
4.7 Degradation of bearing strength	113
4.7.1 Experimental observations	114
4.8 Rate of degradation of bearing strength	116
4.8.1 Bearing degradation rate factor (C_b) determination	116
4.9 Application to cyclic analysis	117
4.10 Discussion	120
4.11 Concluding remarks	120

CHAPTER 5: BOUNDARY ELEMENT ANALYSIS

5.1 Summary	152
-------------	-----

5.2 Introduction	152
5.3 Soil model	153
5.3.1 Clay types	154
5.3.2 Limit stresses	155
5.3.3 Gap formation	156
5.3.4 Backsliding	157
5.3.5 Soil strength degradation	158
5.4 Boundary element formulation	160
5.4.1 Pile flexure	160
5.4.2 Soil deformation	161
5.4.3 Pile-soil system interaction	162
5.4.4 Pile-head stiffness matrix and compliance matrix	166
5.4.5 Pile tractions and displacements	168
5.4.6 Elastic unloading	171
5.4.7 Gap formation	172
5.4.8 Pile-head reactions	173
5.4.9 Shear strength degradation	175
5.4.10 Bearing strength degradation	176
5.4.11 Modified soil segment stiffness matrix	177
5.4.12 Unloading and reloading	178
5.5 Discussion	178
5.6 Concluding remarks	179
Appendix 5.1 Bernoulli-Euler Beam Theory	180
Appendix 5.2 Mindlin's Solution	181

CHAPTER 6: NUMERICAL IMPLEMENTATION OF CYCLIC LOADING ALGORITHM

6.1 Summary	187
6.2 Introduction	187
6.3 Computational procedure for cyclic analysis	187
6.3.1 Pile-soil system interaction	189
6.3.2 Pile-head stiffness matrix and compliance matrix	191
6.3.3 Pile traction and displacement due to unit boundary conditions	193
6.3.4 Elastic unloading	194
6.3.5 Yield factor	195
6.3.6 Pile traction and displacement	196
6.3.7 Gap formation	197
6.3.8 Pile-head reactions	198
6.3.9 Shear strength degradation	200

6.3.10 Bearing strength degradation	202
6.3.11 Modified soil segment stiffness matrix	204
6.3.12 At specified loads and displacements	205
6.3.13 Unloading and reloading	207
6.4 Description of the program	208
6.5 Typical illustrative results	210
6.5.1 Load-controlled conditions	211
6.5.2 Displacement-controlled conditions	212
6.5.3 Gap formation	212
6.5.4 Backsliding	214
6.5.5 Shear strength degradation	214
6.5.6 Bearing strength degradation	214
6.6 Investigation of cyclic degradation	215
6.6.1 Beam-On-Spring model	215
6.6.1.1 Beam-On-Spring model results	216
6.6.2 Beam-On-Interactive-Spring model	217
6.6.2.1 Beam-On-Interactive-Spring model results	218
6.7 Discussion of results	220
6.8 Concluding remarks	221

CHAPTER 7: PARAMETRIC STUDIES

7.1 Summary	252
7.2 Introduction	252
7.3 Pile discretisation	253
7.4 Standard parameters	254
7.5 Stiff clay	255
7.5.1 The effect of load levels	256
7.5.2 The effect of pile Young's modulus (E_p)	258
7.5.3 The effect of backsliding factor (β)	259
7.5.4 The effect of residual/peak bearing strength ratio (R_b)	260
7.5.5 The effect of bearing degradation rate factor (C_b)	261
7.5.6 The effect of residual/peak shear strength ratio (R_s)	262
7.5.7 The effect of shear strength degradation rate factor (C_s)	263
7.5.8 The effect of adhesion factor (α)	264
7.5.9 The effect of eccentric loading (e)	265
7.6 Soft clay	266
7.6.1 The effect of load levels	266
7.6.2 The effect of pile Young's modulus (E_p)	267

7.6.3 The effect of backsliding factor (β)	269
7.6.4 The effect of residual/peak bearing strength ratio (R_b)	269
7.6.5 The effect of bearing degradation rate factor (C_b)	270
7.6.6 The effect of residual/peak shear strength ratio (R_s)	271
7.6.7 The effect of shear strength degradation rate factor (C_s)	272
7.6.8 The effect of adhesion factor (α)	272
7.6.9 The effect of eccentric loading (e)	273
7.7 Discussion of results	273
7.8 Concluding remarks	276

CHAPTER 8: ANALYSES OF PUBLISHED FIELD TEST DATA

8.1 Summary	317
8.2 Introduction	317
8.3 Selection of soil parameters	318
8.4 Field tests reported by Matlock	319
8.4.1 Field tests at Lake Austin	320
8.4.1.1 Soil conditions	320
8.4.1.2 Predictions by previous workers	321
8.4.1.3 Current analysis	322
8.4.1.4 Discussion	322
8.4.2 Field tests at Sabine	323
8.4.2.1 Soil conditions	323
8.4.2.2 Predictions by previous workers	324
8.4.2.3 Current analysis	325
8.4.2.4 Discussion	326
8.5 Field tests reported by Reese <i>et al.</i>	326
8.5.1 Soil conditions	327
8.5.2 Predictions by previous workers	328
8.5.3 Current analysis	329
8.5.4 Discussion	330
8.6 Field tests reported by Tassios and Levendis	330
8.6.1 Soil conditions	331
8.6.2 Field test observations	331
8.6.3 Current analysis	333
8.6.4 Discussion	334
8.7 Field tests reported by Hamilton and Dunnivant	335
8.7.1 Soil conditions	335
8.7.2 Predictions by previous workers	337

8.7.3 Current analysis	338
8.7.4 Discussion	340
8.8 Discussion of results	341
8.9 Concluding remarks	343
Appendix 8.1 Equivalent Pile Young's Modulus	345

CHAPTER 9: CONCLUSIONS

9.1 Summary and general conclusions	367
9.2 Recommendations for future work	369

REFERENCES	371
-------------------	------------

NOTATION

A_p	pile segment cross sectional area
B_p	pile segment displacement due to unit boundary conditions
B_p^e	pile segment displacement due to unit boundary conditions, corresponding to elastic soil segment
B_p^n	pile segment displacement due to unit boundary conditions, corresponding to plastic soil segment
B_p^u	pile segment displacement due to unit lateral translation of the pile
B_p^θ	pile segment displacement due to unit rotation of the pile about its head
B_p^{eu}	pile segment displacement due to unit lateral translation of the pile, corresponding to the elastic soil segment
$B_p^{e\theta}$	pile segment displacement due to unit rotation of the pile about its head, corresponding to the elastic soil segment
B_p^{nu}	pile segment displacement due to unit lateral translation of the pile, corresponding to the plastic soil segment
$B_p^{n\theta}$	pile segment displacement due to unit rotation of the pile about its head, corresponding to the plastic soil segment
C_b	bearing degradation rate factor
C_{gl}	gap closing factor for the left pile face
C_{gr}	gap closing factor for the right pile face
C_s	shear degradation rate factor
C_u	undrained shear strength
D	pile diameter or width
E_p	pile Young's modulus
E_s	soil Young's modulus
$F_{\theta H}$	coefficient of the pile-head compliance matrix
$F_{\theta M}$	coefficient of the pile-head compliance matrix
F_{uH}	coefficient of the pile-head compliance matrix
F_{uM}	coefficient of the pile-head compliance matrix
H	function of the separation of the bubble and MCC yield surfaces (bubble model only)
H	pile-head lateral load
H_*	pile-head lateral load at the specified load or displacement
H_F	specified pile-head lateral load
H_{max}	maximum lateral load
H_θ	pile-head lateral load due to unit rotation of the pile about its head
H_r	pile-head lateral load (end of previous increment)
H_s	shear force for the pile segment
H_u	pile-head lateral load due to unit lateral translation of the pile
H_y	yield load
I_c	interactive constant
I_p	plasticity index
I_r	interactive term
K_{sp}	spring segment stiffness
K_l	lateral earth pressure coefficient
L	pile length

M	pile-head moment
M	slope of the critical state line (bubble model only)
M_*	pile-head moment at the specified load or displacement
M_{max}	maximum bending moment
M_p	bending moment for the pile segment
M_0	moment at the pile-head due to unit rotation of the pile about its head
M_r	pile-head moment (end of previous increment)
M_u	moment at the pile-head due to unit lateral translation of the pile
M_y	yield moment
N	number of cycles
N_c	bearing capacity factor
N_p	overconsolidation ratio
R	ratio of the sizes of the bubble yield surface and the MCC yield surface
R_b	residual/peak bearing strength ratio
R_{br}	residual bearing ratio
R_s	residual/peak shear strength ratio
R_{sr}	residual shear ratio
V	specific volume
$[G_p]$	pile coefficients obtained by integration of the Bernoulli-Euler kernel
$[G_p^{ee}]$	pile coefficients corresponding to the elastic soil segments
$[G_p^{ne}]$	pile coefficients corresponding to the elastic soil segments
$[G_p^{en}]$	pile coefficients corresponding to the plastic soil segments
$[G_p^{nn}]$	pile coefficients corresponding to the plastic soil segments
$[G_s]$	soil segment coefficients obtained from Mindlin's solution
$[G_{se}]$	soil coefficients obtained from Mindlin's solution
$[G_s^{ee}]$	soil coefficients corresponding to the elastic soil segments
$[G_s^{ne}]$	soil coefficients corresponding to the elastic soil segments
$[G_s^{ee}]$	soil coefficients after modification for soil yielding, corresponding to the elastic soil segments
$[G_{s*}^{ne}]$	undetermined terms corresponding to the elastic soil segments
$[G_{s*}^{nn}]$	undetermined terms corresponding to the elastic soil segments
$[K]$	pile-soil stiffness matrix
$[K_s]$	soil segment stiffness matrix
$[K_s^o]$	original soil segment stiffness matrix
$[K_s^{ee}]$	soil stiffness coefficients corresponding to the elastic soil segments
$[K_s^{ne}]$	soil stiffness coefficients corresponding to the elastic soil segments
$[K_s^{en}]$	soil stiffness coefficients corresponding to the plastic soil segments
$[K_s^{nn}]$	soil stiffness coefficients corresponding to the plastic soil segments
c	rate of increase in undrained shear strength with depth
c'	cohesion intercept
c'_r	residual cohesion intercept
d_b	plastic bearing displacement
d_{gl}	left gap distance
d_{gr}	right gap distance

d_s	plastic shear displacement
d_{sr}	plastic shear displacements (end of previous increment)
e	eccentricity of loading
f	influence factor to modify the soil segment stiffness matrix
f_g	largest gap closing factor
f_y	largest yield factor
h	hardening function
m	rate of increase in soil Young's modulus with depth
n_e	number of elastic soil elements within the segment
n_p	number of yielded soil elements within the segment
p'	mean effective stress
p_f	yield factor for the elastic soil elements
p_m	preconsolidation pressure which defines the size of the yield surface
$2p_o$	defines size of the MCC yield surface
q	deviator stress
t	current bearing strength
t_f	peak bearing strength
t_p	pile segment traction
t_r	residual bearing strength
t_s	soil segment traction
t_{sc}	limit bearing stress
t_{scd}	reduced limit bearing stress
t_{scr}	residual limit bearing stress
t_{ss}	limit shear stress
t_{ssd}	reduced limit shear stress
t_{ssr}	residual limit shear stress
t_{st}	soil element traction
t_{st*}	soil element traction at the specified load or displacement
t_{stb}	limit adhesive stress
t_{str}	soil element traction (end of previous increment)
t_{sy}	yield stress for the soil element
t_{sysc}	yield stress for bearing
t_{sys}	yield stress for shear
t_{syt}	yield stress for tension
u	pile-head lateral displacement
u_*	pile-head lateral displacement at the specified load or displacement
u_F	specified pile-head lateral displacement
u_{gl}	pile displacement when soil element yield in tension at the left faces of the pile
u_{gr}	pile displacement when soil element yield in tension at the right faces of the pile
u_p	pile segment displacement
u_{p*}	pile segment displacement at the specified load or displacement
u_{pr}	pile displacement (end of previous increment)
u_s	soil segment displacement
z	depth
α	empirical adhesion factor
β	backsliding factor

Δ	value obtained by applying unit boundary conditions in each increment
Δt_p	pile segment traction
Δt_p^e	pile segment traction corresponding to the elastic soil segment
Δt_p^n	pile segment traction corresponding to the plastic soil segment
Δt_p^{eu}	pile segment traction due to unit lateral translation of the pile, corresponding to the elastic soil segment
$\Delta t_p^{e\theta}$	pile segment traction due to unit rotation of the pile about its head, corresponding to the elastic soil segment
Δt_s^e	elastic soil segment traction
Δt_s^n	plastic soil segment traction
Δt_{st}^e	elastic soil element traction
Δu_p^e	pile segment displacement corresponding to the elastic soil segment
Δu_p^n	pile segment displacement corresponding to the plastic soil segment
Δu_s^e	elastic soil segment displacement
Δu_s^n	plastic soil segment displacement
δd_s	incremental plastic shear displacement
$\delta \varepsilon_p$	volumetric strain increment
$\delta \varepsilon_p^p$	plastic volumetric strain increment
$\delta \varepsilon_q$	shear strain increment
$\delta \varepsilon_q^p$	plastic shear strain increment
δH	incremental pile-head lateral load
δM	incremental pile-head moment
δ_{\max}	maximum pile-head displacement
$\delta \theta$	incremental lateral pile-head rotation
δt_{st}	soil element traction increment
δu	incremental pile-head lateral displacement
δu_p	pile segment displacement increment
ε_a	axial strain
ε_r	radial strain
ϕ'	angle of shearing resistance
ϕ'_r	residual angle of shearing resistance
γ	effective unit weight of the soil
κ^*	initial slope of the unloading lines in the $\ln V$ - $\ln p'$ compression plane
λ^*	slope of the normal compression lines in the $\ln V$ - $\ln p'$ compression plane
ν	Poisson's ratio for soil
ν_p	Poisson's ratio for pile
θ	pile-head rotation
θ_*	pile-head rotation at the specified load or displacement
θ_r	pile-head rotation (end of previous increment)
σ'_a	effective axial stress
σ'_n	normal effective stress
σ'_r	effective radial stress
σ'_z	vertical effective stress
σ_y	yield stress of the material
τ	current shear strength
τ_{50}	shear strength at $\sigma'_n = 50$ kPa

τ_f	peak shear strength
τ_r	residual shear strength
ψ	exponent in the hardening function

superscripts

e, ee, ne	corresponding to the elastic soil segment
n, nn, en	corresponding to the plastic soil segment
u	due to unit lateral tranlastion of the pile
θ	due to unit rotation of the pile about its head

LIST OF TABLES

Table 3.1	Relative errors based on <i>tolerance</i> = 0.05
Table 3.2	Relative errors based on <i>tolerance</i> = 0.005
Table 4.1	Index properties of clays, after Skempton (1964).
Table 4.2	Soil index properties and strength parameters determined from shear box tests.
Table 4.3	Index properties of clays, from shear box tests.
Table 4.4	Index properties of clays, from ring shear tests.
Table 4.5	Index properties of clays, from triaxial tests.
Table 4.6	Shear degradation rate factors (C_s).
Table 4.7	Residual/peak bearing strength ratios (R_r) and bearing degradation rate factors (C_b).
Table 6.1	Input data for the program APILEC.
Table 7.1	Effect of pile discretisation on the initial stiffnesses of the pile-soil system.
Table 7.2	Effect of pile discretisation on the relative errors in pile-head displacements.
Table 7.3	Effect of pile discretisation on the relative errors in maximum bending moments.
Table 8.1	Displacement increment sequences for laterally loaded pile test at Tilbrook Grange.

LIST OF FIGURES

- Figure 1.1 Increase in pile-head displacements with cycling for (a) one-way and (b) two-way load-controlled cyclic pile-load tests (Tassios and Levendis, 1974).
- Figure 1.2 Increase in pile bending moment for one-way load-controlled cyclic pile-load test (after Matlock, 1970).
- Figure 1.3 Two-way displacement-controlled cyclic laboratory model pile tests (Matlock, 1970).
- Figure 1.4 Phenomena observed and soil zones developed during cyclic pile-load test.
- Figure 1.5 Short vertical pile under lateral load for (a) free-head pile and (b) fixed-head pile.
- Figure 1.6 Long vertical pile under lateral load for (a) free-head pile and (b) fixed-head pile.
- Figure 1.7 Deflections, slopes, bending moments, shearing forces and soil reactions for elastic conditions (Reese and Matlock, 1956).
- Figure 1.8 Cyclic responses for a laterally loaded pile experiencing (a) purely elastic response, (b) shakedown, (c) alternating plasticity and (d) incremental collapse (Swane and Poulos, 1982).
- Figure 1.9 Criteria for predicting p - y curves for (a) short-time static loading, (b) equilibrium under initial cyclic loading and (c) reloading after cycling (Matlock, 1970).
- Figure 1.10 Model developed by Matlock *et al.* (1978).
- Figure 1.11 Model developed by Swane and Poulos (1985).
- Figure 1.12 (a) Discrete element pile model, (b) dry friction element and (c) pile-soil interaction elements (Bijnagte *et al.*, 1991).
- Figure 1.13 Layer system for the quasi three-dimensional model (Bijnagte *et al.*, 1991).
- Figure 1.14 Three-dimensional finite element mesh; backside shown from above with half the pile shown in the background (Bijnagte *et al.*, 1991).
- Figure 1.15 (a) Idealisation of pile (Poulos, 1982) and (b) degradation parameter t (Poulos, 1982 after Idriss *et al.*, 1978a).
-
- Figure 2.1 Typical development of shear strain during a cyclic load test (O'Reilly and Brown, 1991).
- Figure 2.2 The effect of stress reversals on soil stiffness (O'Reilly and Brown, 1991).
- Figure 2.3 (a) Undrained cyclic loading at low stress levels and (b) associated pore pressure response (Sangrey and France, 1980).
- Figure 2.4 Undrained cyclic loading resulting in failure (Sangrey *et al.*, 1969).
- Figure 2.5 The effect of cyclic loading on undrained shear strength and secant shear modulus (Andersen *et al.*, 1982).
- Figure 2.6 The effect of cyclic loading on cyclic strength ratio (Lee and Focht, 1976).
- Figure 2.7 Typical stress-strain behaviour of a clay subjected to symmetric cyclic loading (Kramer, 1996).
- Figure 2.8 Backbone curve showing effect of shear strain on secant modulus G_{sec} (Kramer, 1996).
- Figure 2.9 (a) Shear stress variations and (b) resulting stress-strain behaviour (Kramer, 1996).
- Figure 2.10 (a) Chain of parallel springs and slider elements, (b) load-displacement response of slider and (c) load-displacement response of chain of parallel springs and slider elements (Wood, 1994).
- Figure 2.11 (a) Initial position of nested yield surfaces, (b) position of yield surfaces after stress path AB , (c) position of yield surfaces after stress path ABC and (d) stress-strain response in triaxial compression CB and extension CD (Wood, 1994).
- Figure 2.12 Yield and bounding surfaces in stress space.

- Figure 2.13 The Modified Cam clay model in (a) q - p' stress plane and (b) $\ln V$ - $\ln p'$ space.
- Figure 2.14 General layout of the bubble model.
- Figure 2.15 Assumed motion of the bubble yield surface within the Modified Cam clay (MCC) yield surface along the vector β .
- Figure 2.16 Diagram showing singularity points, stable and unstable regions on the bubble yield surface.
- Figure 2.17 Definition of the vector β and the distance b .
- Figure 2.18 Predicted relative motion of bubble and MCC yield surfaces for (a) normally consolidated clay and (b) overconsolidated clay, subjected to an undrained test.
- Figure 2.19 Failure points: ∇ isotropic undrained; \bullet isotropic drained; ∇ one-dimensional undrained; \circ one-dimensional drained (Al-Tabbaa and Wood, 1989).
- Figure 2.20 Constant q cycles: experimental observations of (a) volumetric strains and (b) shear strains; model predictions of (c) volumetric strains and (d) shear strains (Al-Tabbaa and Wood, 1989).
-
- Figure 3.1 Idealised model under plane-strain conditions.
- Figure 3.2 Two-dimensional half-layer systems.
- Figure 3.3 Mesh boundary conditions.
- Figure 3.4 (a) One-way and (b) two-way cyclic loading.
- Figure 3.5 Stages of loading to simulate cyclic loading for OASYS analysis.
- Figure 3.6 Modified Cam clay yield surface with tension cut-off line.
- Figure 3.7 Mesh used for (a) SWANDYNE analysis and (b) OASYS analysis (not to scale).
- Figure 3.8 Comparisons of mesh sizes.
- Figure 3.9 Typical pile load-displacement response for fully bonded case based on SWANDYNE analysis.
- Figure 3.10 Convergence study based on maximum displacements at the fifth cycle.
- Figure 3.11 Effect of number of load increments per cycle on computational time.
- Figure 3.12 Relative error based on number of load increments.
- Figure 3.13 The effect of soil strength parameter M on maximum and residual displacements.
- Figure 3.14 The effect of soil parameter R on maximum and residual displacements.
- Figure 3.15 The effect of soil parameter ψ on maximum and residual displacements.
- Figure 3.16 The effect of soil Poisson's ratio (ν) on maximum and residual displacements.
- Figure 3.17 The effect of soil parameters λ^* and κ^* on maximum and residual displacements.
- Figure 3.18 The effect of load level on maximum and residual displacements.
- Figure 3.19 The effect of overconsolidation ratio (OCR) on maximum and residual displacements.
- Figure 3.20 (a) Pile and soil elements at initial position. (b) Pile and soil element displacements for the fully bonded case. (c) Gap formation at the debonded interface for the half-debonded case.
- Figure 3.21 Bubble model predictions for the fully bonded case.
- Figure 3.22 Bubble model predictions for the fully bonded case with maximum load reduced by 50%.
- Figure 3.23 Mohr-Coulomb model predictions for the fully bonded case.
- Figure 3.24 Bubble model predictions for the half-debonded case.
- Figure 3.25 Bubble model predictions for the half-debonded case with maximum load reduced by 50%.
- Figure 3.26 SWANDYNE analysis (Mohr-Coulomb model) for the half-debonded case.
- Figure 3.27 OASYS analysis (Mohr-Coulomb model) for the half-debonded case with (a) 10 load increments and 10 iterations and (b) 10 load increments and 5 iterations.

- Figure 3.28 SWANDYNE and OASYS results (a) using 10 load increments and 10 iterations and (b) using 10 load increments and 5 iterations.
- Figure 3.29 SWANDYNE analyses for *case (i)* and initial case using Mohr-Coulomb model.
- Figure 3.30 SWANDYNE analysis for *case (ii)* using Mohr-Coulomb model.
- Figure 3.31 SWANDYNE analysis for *case (iii)* using Mohr-Coulomb model.
-
- Figure 4.1 Soil displacement vectors from a finite element analysis for a pile subjected to lateral load.
- Figure 4.2 Peak and residual strengths of normally consolidated and overconsolidated clays (Skempton, 1964).
- Figure 4.3 Stress-displacement curves at constant normal effective stress (σ'_n) (Skempton, 1985).
- Figure 4.4 Stress-displacement curves for intact clay using multiple-reversal shear box test (Calabresi and Manfredini, 1973).
- Figure 4.5 Peak and residual strengths of overconsolidated clays (Skempton, 1964).
- Figure 4.6 Decrease in residual angle of shearing resistance (ϕ'_r) with increasing clay fraction (Skempton, 1964).
- Figure 4.7 Summary of post-failure structure from Happisburgh-London clay mixtures. (Lupini *et al.*, 1981).
- Figure 4.8 Correlation of residual friction angle (ϕ'_r) with plasticity index (Lupini *et al.*, 1981).
- Figure 4.9 Correlation of residual friction angle (ϕ'_r) with clay fraction for natural soils (Lupini *et al.*, 1981).
- Figure 4.10 Correlation of residual friction angle (ϕ'_r) with plasticity index for natural soils (Lupini *et al.*, 1981).
- Figure 4.11 Correlation of residual friction angle (ϕ'_r) with liquid limit (Mersi and Cepeda-Diaz, 1986).
- Figure 4.12 Correlation of residual/peak shear strength ratio (R_s) with (a) liquid limit and (b) clay fraction.
- Figure 4.13 Correlation of residual/peak shear strength ratio (R_s) with (a) liquid limit and (b) clay fraction (with residual cohesion intercept c' , set to zero).
- Figure 4.14 Failure envelope for compacted London clay; (a) investigated stress range with detail and (b) in the low stress range (Maksimovic, 1989a).
- Figure 4.15 Shear strength failure envelope using bilinear approach.
- Figure 4.16 Correlation of residual/peak shear strength ratio (R_s) with (a) liquid limit and (b) clay fraction (with residual cohesion intercept c' , set to zero and modification for low stress range).
- Figure 4.17 Shear test results on (a) Walton's Wood clay, (b) Jackfield clay and (c) London clay (Skempton, 1964).
- Figure 4.18 Post-peak shear strength degradation after Skempton (1964).
- Figure 4.19 Identification of shear strength degradation rate factor (C_s).
- Figure 4.20 Determination of shear degradation rate factor (C_s) from post-peak shear strength degradation results.
- Figure 4.21 Rate of shear strength degradation from shear box tests.
- Figure 4.22 Determination of shear degradation rate factor (C_s) from post-peak shear strength degradation results using shear box tests.
- Figure 4.23 Determination of shear degradation rate factor (C_s) from post-peak shear strength degradation results using ring shear tests.
- Figure 4.24 Determination of shear degradation rate factor (C_s) from post-peak shear strength degradation results using triaxial tests.

- Figure 4.25 Correlation of shear degradation rate factor (C_s) with (a) liquid limit, (b) clay fraction and (c) plasticity index.
- Figure 4.26 Correlation of shear degradation rate factor (C_s) with (a) liquid limit, (b) clay fraction, and (c) plasticity index, discarding triaxial test results.
- Figure 4.27 Typical load-settlement curves from plate loading tests (Ward *et al.*, 1965).
- Figure 4.28 Shear zones beneath a shallow foundation according to Terzaghi. *A*, zone of elastic equilibrium; *B*, zones of radial shear; *C*, zones of passive shear; *D*, depth of foundation (Whitaker, 1970).
- Figure 4.29 Failure mechanism for soil around laterally loaded pile. (Fleming *et al.*, 1985).
- Figure 4.30 Shear zones around the base of a pile (Whitaker, 1970).
- Figure 4.31 Failure mechanism of soil when a pile is loaded laterally.
- Figure 4.32 Undrained triaxial compression tests on block specimens (Ward *et al.*, 1965).
- Figure 4.33 Measured load-displacement curve from plate loading tests for Test 1 (Andersen and Stenhamar, 1983).
- Figure 4.34 Measured load-displacement curve from plate loading tests for Tests 1 and 3 (Andersen and Stenhamar, 1983).
- Figure 4.35 Identification of bearing strength degradation rate factor (C_b).
- Figure 4.36 Determination of bearing degradation rate factor (C_b) from post-peak bearing strength degradation results using plate loading tests.
- Figure 4.37 (a) Determination of plastic shear displacement (d_s) and reduced limit shear stress (t_{ssd}), and (b) shear strength degradation based on plastic shear displacement.
- Figure 4.38 (a) Determination of plastic bearing displacement (d_b) and reduced limit bearing stress (t_{scd}), and (b) bearing strength degradation based on plastic bearing displacement.
-
- Figure 5.1 Phenomena observed and soil zones developed during cyclic pile-load tests.
- Figure 5.2 (a) Shear test results on Jackfield clay (Skempton, 1964) and (b) typical load-settlement curves for plate loading tests (Ward *et al.*, 1965).
- Figure 5.3 (a) Pile discretisation and (b) four faces of a pile segment.
- Figure 5.4 Unit boundary conditions; (a) unit lateral translation of the pile and (b) unit rotation of the pile about its head.
- Figure 5.5 (a) Four soil elements on the faces of a pile segment treated as one soil segment and (b) full soil stiffness matrix $[F]$ condensed into a soil segment stiffness matrix $[K_s]$.
- Figure 5.6 Determination of yield factors (p_f) for soil elements.
- Figure 5.7 (a) Gap terminology and (b) determination of gap closing factor for soil element.
-
- Figure 6.1 (a) Response of a laterally loaded pile, (b) sign conventions for a pile segment and (c) zones encountered when load direction changes.
- Figure 6.2 (a) Pile discretisation and (b) four faces of a pile segment.
- Figure 6.3 (a) Four soil elements on the faces of a pile segment treated as one soil segment and (b) full soil matrix $[F]$ condensed into a soil segment stiffness matrix $[K_s]$.
- Figure 6.4 (a) Phenomena observed and soil zones developed during cyclic pile load test and (b) pile faces and gaps terminology.
- Figure 6.5 Determination of gap closing factor for soil element.
- Figure 6.6 Soil elements elastic and plastic identification at different increments and elements numbering system.

- Figure 6.7 (a) Progressive yielding of side face soil elements and (b) determination of yield stress for shear.
- Figure 6.8 Flow chart for the determination of incremental and current plastic shear displacements.
- Figure 6.9 Flow chart for the determination of yield stress for shear.
- Figure 6.10 (a) Progressive yielding of bearing soil element, (b) determination of yield stress for bearing and (c) bearing strength degradation as a function of the residual limit bearing stress and the plastic bearing displacement.
- Figure 6.11 Flow chart for the determination of incremental and current plastic bearing displacements.
- Figure 6.12 Flow chart for the determination of yield stress for bearing.
- Figure 6.13 Gap formation; (a) at the beginning of unloading and (b) end of first cycle of one-way cyclic loading.
- Figure 6.14 Structure of APILEC program with its subroutine.
- Figure 6.15 Pile-head load-displacement responses for (a) one-way and (b) two-way cyclic loading under load-controlled conditions.
- Figure 6.16 Pile bending moment distributions for (a) one-way and (b) two-way cyclic loading under load-controlled conditions.
- Figure 6.17 Pile displacement, soil profiles and gap distances at the end of first cycle of one-way cyclic loading.
- Figure 6.18 Pile-head load-displacement responses for (a) one-way and (b) two-way cyclic loading under displacement-controlled conditions.
- Figure 6.19 Pile-head load-displacement responses for one-way cyclic loading with and without gap formation.
- Figure 6.20 Pile-head load-displacement responses for one-way cyclic loading at high load level with and without gap formation.
- Figure 6.21 Pile-head load-displacement responses for two-way cyclic loading with and without gap formation.
- Figure 6.22 Pile-head load-displacement responses for one-way cyclic loading with and without backsliding.
- Figure 6.23 Pile-head load-displacement responses for one-way cyclic loading with and without shear strength degradation.
- Figure 6.24 Pile-head load-displacement responses for one-way cyclic loading with and without shear strength degradation at low limit shear stress.
- Figure 6.25 Pile-head load-displacement responses for one-way cyclic loading with and without bearing strength degradation.
- Figure 6.26 Beam-On-Spring (BOS) model.
- Figure 6.27 Elastic-perfectly plastic soil behaviour.
- Figure 6.28 Pile-head load-displacement responses for one-way cyclic loading with and without gap formation using BOS model.
- Figure 6.29 Pile-head load-displacement responses for one-way cyclic loading with gap formation and bearing strength degradation using BOS model.
- Figure 6.30 Pile-head load-displacement responses for one-way cyclic loading with gap formation and shear strength degradation using BOS model.
- Figure 6.31 Distance between neighbouring spring segments for Beam-On-Interactive-Spring (BOIS) model.
- Figure 6.32 Pile-head load-displacement responses for one-way cyclic loading with gap formation using BOIS model.
- Figure 6.33 Pile-head load-displacement responses for one-way cyclic loading with and without gap formation using BOS and BOIS models.

- Figure 6.34 Pile-head load-displacement responses for one-way cyclic loading without gap formation at high load level using BOIS model.
- Figure 6.35 Comparison on the magnitude and rate of cyclic degradation with different interactive constant (I_c) for BOIS model.
- Figure 6.36 Pile-head load-displacement responses for one-way cyclic loading with gap formation and bearing strength degradation using BOIS model.
- Figure 6.37 Pile-head load-displacement responses for one-way cyclic loading with gap formation and shear strength degradation using BOIS model.
- Figure 6.38 Comparison on the magnitude and rate of cyclic degradation with interactive constant $I_c = 0$ using BOIS model.
-
- Figure 7.1 The effect of pile discretisation on pile-head load-displacement responses.
- Figure 7.2 The effect of pile discretisation on soil segments yielding.
- Figure 7.3 The effect of pile discretisation on (a) pile-head displacements and (b) maximum bending moments.
- Figure 7.4 The effect of pile discretisation on time required for analysis.
- Figure 7.5 The effect of load levels on (a) pile-head displacements and (b) maximum bending moments, for free-head piles in stiff clay.
- Figure 7.6 The effect of load levels on (a) pile-head displacements and (b) maximum bending moments, for fixed-head piles in stiff clay.
- Figure 7.7 The effect of pile Young's modulus (E_p) on (a) pile-head displacements and (b) maximum bending moments, for free-head piles in stiff clay.
- Figure 7.8 The effect of pile Young's modulus (E_p) on (a) pile-head displacements and (b) maximum bending moments, for fixed-head piles in stiff clay.
- Figure 7.9 The effect of backsliding factor (β) on (a) pile-head displacements and (b) maximum bending moments, for free-head piles in stiff clay.
- Figure 7.10 The effect of backsliding factor (β) on (a) pile-head displacements and (b) maximum bending moments, for fixed-head piles in stiff clay.
- Figure 7.11 The effect of residual/peak bearing strength ratio (R_b) on (a) pile-head displacements and (b) maximum bending moments, for free-head piles in stiff clay.
- Figure 7.12 The effect of residual/peak bearing strength ratio (R_b) on (a) pile-head displacements and (b) maximum bending moments, for fixed-head piles in stiff clay.
- Figure 7.13 The effect of bearing degradation rate factor (C_b) on (a) pile-head displacements and (b) maximum bending moments, for free-head piles in stiff clay.
- Figure 7.14 The effect of bearing degradation rate factor (C_b) on (a) pile-head displacements and (b) maximum bending moments, for fixed-head piles in stiff clay.
- Figure 7.15 The effect of residual/peak shear strength ratio (R_s) on (a) pile-head displacements, (b) maximum bending moments and (c) pile-head load-displacement responses for R_s of 0.1 and 0.2, for free-head piles in stiff clay.
- Figure 7.16 The effect of residual/peak shear strength ratio (R_s) on (a) pile-head displacements and (b) maximum bending moments, for fixed-head piles in stiff clay.
- Figure 7.17 The effect of shear strength degradation rate factor (C_s) on (a) pile-head displacements and (b) maximum bending moments, for free-head piles in stiff clay.
- Figure 7.18 The effect of shear strength degradation rate factor (C_s) on (a) pile-head displacements and (b) maximum bending moments, for fixed-head piles in stiff clay.

- Figure 7.19 The effect of adhesion factor (α) on (a) pile-head displacements, (b) maximum bending moments and (c) pile-head load-displacement responses for α of 0.1 and 0.2, for free-head piles in stiff clay.
- Figure 7.20 The effect of adhesion factor (α) on (a) pile-head displacements and (b) maximum bending moments, for fixed-head piles in stiff clay.
- Figure 7.21 The effect of eccentric loading (e) on (a) pile-head displacements and (b) maximum bending moments, for free-head piles in stiff clay.
- Figure 7.22 The effect of load levels on (a) pile-head displacements and (b) maximum bending moments, for free-head piles in soft clay.
- Figure 7.23 The effect of load levels on (a) pile-head displacements and (b) maximum bending moments, for fixed-head piles in soft clay.
- Figure 7.24 The effect of pile Young's modulus (E_p) on (a) pile-head displacements and (b) maximum bending moments, for free-head piles in soft clay.
- Figure 7.25 The effect of pile Young's modulus (E_p) on (a) pile-head displacements and (b) maximum bending moments, for fixed-head piles in soft clay.
- Figure 7.26 The effect of backsliding factor (β) on (a) pile-head displacements and (b) maximum bending moments, for free-head piles in soft clay.
- Figure 7.27 The effect of backsliding factor (β) on (a) pile-head displacements and (b) maximum bending moments, for fixed-head piles in soft clay.
- Figure 7.28 The effect of residual/peak bearing strength ratio (R_b) on (a) pile-head displacements and (b) maximum bending moments, for free-head piles in soft clay.
- Figure 7.29 The effect of residual/peak bearing strength ratio (R_b) on (a) pile-head displacements and (b) maximum bending moments, for fixed-head piles in soft clay.
- Figure 7.30 The effect of bearing degradation rate factor (C_b) on (a) pile-head displacements and (b) maximum bending moments, for free-head piles in soft clay.
- Figure 7.31 The effect of bearing degradation rate factor (C_b) on (a) pile-head displacements and (b) maximum bending moments, for fixed-head piles in soft clay.
- Figure 7.32 The effect of residual/peak shear strength ratio (R_s) on (a) pile-head displacements and (b) maximum bending moments, for free-head piles in soft clay.
- Figure 7.33 The effect of residual/peak shear strength ratio (R_s) on (a) pile-head displacements and (b) maximum bending moments, for fixed-head piles in soft clay.
- Figure 7.34 The effect of shear strength degradation rate factor (C_s) on (a) pile-head displacements and (b) maximum bending moments, for free-head piles in soft clay.
- Figure 7.35 The effect of shear strength degradation rate factor (C_s) on (a) pile-head displacements and (b) maximum bending moments, for fixed-head piles in soft clay.
- Figure 7.36 The effect of adhesion factor (α) on (a) pile-head displacements and (b) maximum bending moments, for free-head piles in soft clay.
- Figure 7.37 The effect of adhesion factor (α) on (a) pile-head displacements and (b) maximum bending moments, for fixed-head piles in soft clay.
- Figure 7.38 The effect of eccentric loading (e) on (a) pile-head displacements and (b) maximum bending moments, for free-head piles in soft clay.
- Figure 8.1 Arrangement of field tests at Sabine for fixed-head pile (Matlock, 1970).
- Figure 8.2 Comparisons with maximum bending moment data for static loading at Lake Austin. After Matlock (1970).
- Figure 8.3 Comparisons with maximum bending moment data for cyclic loading at Lake Austin. After Matlock (1970).

- Figure 8.4 Comparisons with bending moment distributions for cyclic loading at Lake Austin. After Matlock (1970).
- Figure 8.5 Comparisons with maximum bending moment data for static loading at Sabine with free-head pile. After Matlock (1970).
- Figure 8.6 Comparisons with maximum bending moment data for cyclic loading at Sabine with free-head pile. After Matlock (1970).
- Figure 8.7 Comparisons with maximum restraining moment data for static loading at Sabine with fixed-head pile. After Matlock (1970).
- Figure 8.8 Comparisons with maximum restraining moment data for cyclic loading at Sabine with fixed-head pile. After Matlock (1970).
- Figure 8.9 Comparisons with bending moment distributions for cyclic loading at Sabine with free-head pile. After Matlock (1970).
- Figure 8.10 Comparisons with maximum restraining moment data for static loading at Sabine with fixed-head pile (with strength data modifications). After Matlock (1970).
- Figure 8.11 Comparisons with maximum restraining moment data for cyclic loading at Sabine with fixed-head pile (with strength data modifications). After Matlock (1970).
- Figure 8.12 Comparisons with bending moment distributions for cyclic loading at Sabine with fixed-head pile (with strength data modifications). After Matlock (1970).
- Figure 8.13 Pile test set up as described by Reese *et al.* (1975).
- Figure 8.14 Soil profiles as described by Reese *et al.* (1975).
- Figure 8.15 Comparisons with load-displacement responses for static loading. After Reese *et al.* (1975).
- Figure 8.16 Comparisons with load-moment responses for static loading. After Reese *et al.* (1975).
- Figure 8.17 Comparisons with load-displacement responses for cyclic loading. After Reese *et al.* (1975).
- Figure 8.18 Comparisons with load-moment responses for cyclic loading. After Reese *et al.* (1975).
- Figure 8.19 Comparisons with bending moment distributions for cyclic loading. After Reese *et al.* (1975).
- Figure 8.20 Pile test set up as described by Tassios and Levendis (1974).
- Figure 8.21 Soil profiles as described by Tassios and Levendis (1974).
- Figure 8.22 Comparisons with load-displacement responses for static loading. After Tassios and Levendis (1974).
- Figure 8.23 Comparisons with pile-head displacements for one-way cyclic loading. After Tassios and Levendis (1974).
- Figure 8.24 Comparisons with pile-head displacements for two-way cyclic loading. After Tassios and Levendis (1974).
- Figure 8.25 Pile test set up as described by Long *et al.* (1993).
- Figure 8.26 (a) Undrained shear strength profile for axial loaded pile analyses. (b) Detailed revised profile for undrained shear strength for laterally loaded pile analyses (Long *et al.*, 1993).
- Figure 8.27 Comparisons with load-displacement responses for static loading using p - y methods. After Hamilton and Dunnavant (1993).
- Figure 8.28 Comparisons with load-displacement responses for cyclic loading using p - y methods. After Hamilton and Dunnavant (1993).
- Figure 8.29 Comparisons with moment-displacement responses for cyclic loading using p - y methods. After Hamilton and Dunnavant (1993).
- Figure 8.30 Comparisons with load-displacement responses for static loading using APILEC analysis. After Hamilton and Dunnavant (1993).
- Figure 8.31 Comparisons with bending moment distributions for static loading. After Hamilton and Dunnavant (1993).

- Figure 8.32 Comparisons with load-displacement responses for static loading using p - y methods and APILEC analysis. After Hamilton and Dunnavant (1993).
- Figure 8.33 Comparisons with load-displacement responses for static and cyclic loadings using APILEC analysis. After Hamilton and Dunnavant (1993).
- Figure 8.34 Comparisons with moment-displacement responses for cyclic loading using APILEC analysis. After Hamilton and Dunnavant (1993).
- Figure 8.35 Comparisons with bending moment distributions for cyclic loading at displacement increment 8. After Hamilton and Dunnavant (1993).
- Figure 8.36 Comparisons with bending moment distributions for cyclic loading at displacement increment 9. After Hamilton and Dunnavant (1993).
- Figure 8.37 Comparisons with load-displacement responses for cyclic loading using p - y methods and APILEC analysis. After Hamilton and Dunnavant (1993).
- Figure 8.38 Comparisons with moment-displacement responses for cyclic loading using p - y methods and APILEC analysis. After Hamilton and Dunnavant (1993).

CHAPTER 1

Introduction

1.1 General remarks

1.1.1 Behaviour of static laterally loaded piles

1.1.2 Behaviour of cyclic laterally loaded piles

1.2 Analyses of static laterally loaded piles

1.2.1 Linear analysis

1.2.2 Non-linear analysis

1.3 Analyses of cyclic laterally loaded piles

1.3.1 Empirical approach

1.3.2 Modified p - y analysis

1.3.3 Cycle-by-cycle analysis

1.3.4 Bilinear-elasto-plastic analysis

1.3.5 Discrete element analysis

1.3.6 Finite element analysis

1.3.7 Modified boundary element analysis

1.4 Discussion

1.5 Scope of the research

CHAPTER 1

Introduction

1.1 General remarks

Piles are columnar elements, used in foundations, which have the function of transferring load from the superstructure through weak compressible strata to stiffer soils. They may be required to carry uplift loads when used to support structures subjected to overturning forces from winds or waves. Piles used in marine structures are subjected to lateral loads from the impact of berthing ships and from wind and wave action. Combinations of vertical and horizontal loads are carried where piles are used to support retaining walls, bridge piers and abutments, and machinery foundations. A full descriptive account of pile foundations is beyond the scope of this project; details may be found in the comprehensive texts by Poulos and Davis (1980) and Tomlinson (1994).

For pile subjected to static lateral loading, the general characteristics of pile response are reasonably well understood, and a number of methods of analysis have received acceptance. However, the cyclic response characteristics of laterally loaded piles are not so well understood, and suitable methods of analysis are still being developed. Because of the difficulties which are encountered in conducting full-scale pile-load tests, there exists a need for analytical methods that are capable of simulating the cyclic behaviour of laterally loaded piles, as depicted in Figures 1.1 and 1.2. The typical pile response as revealed from the cyclic tests based on the load-controlled conditions (Tassios and Levendis, 1974; Matlock, 1970), showed an increase in the pile-head displacements (maximum and residual) with the increase in the number of cycles (see Figure 1.1), and likewise the bending moments of the pile as shown in Figure 1.2. For the displacement-controlled laboratory model pile tests illustrated in Figure 1.3, a reduction in pile load with cycling is reported by Matlock (1970).

The main aim of this project is to provide a simple and realistic numerical method for the design and analysis of cyclic laterally loaded piles embedded in cohesive soils. The secondary objective is to develop a simple soil model that is capable of describing the gap formation, backsliding and soil strength degradation effects, which are based on the

phenomena observed in the cyclic pile-load tests shown in Figure 1.4. Dynamic effects will not be considered in this project.

To understand the complex behaviour of piles subjected to cyclic loading, some knowledge of the behaviour and analyses of static laterally loaded piles is necessary. This will be reviewed in the following sections, together with the cyclic analysis.

1.1.1 Behaviour of static laterally loaded piles

The ultimate resistance of a vertical pile to a lateral load and the displacement of the pile as the load builds up to its ultimate value are complex matters involving the interaction between a pile and the soil, which deforms partly elastically and partly plastically. Taking the case of a vertical pile unrestrained at the head, the lateral loading on the pile-head is initially carried by the soil close to the ground surface. At low loading levels, the soil deforms elastically. At a further stage of loading, the soil yields plastically and transfers its load to greater depths.

In practical applications, few piles deform over their whole length under lateral loading. The pile displacements and bending moments tend to reduce to negligible proportions within a few (typically less than ten) pile diameters from the ground surface. Broms (1964), Poulos (1971), Poulos and Davis (1980), Randolph (1981), Davies and Budhu (1986) and Budhu and Davies (1988) mentioned that there is a critical or effective length of pile beyond which the pile behaves as it is infinitely long. As such, it is reasonable to assume that piles which are longer than their effective length behave identically. The detailed determination of effective length under elastic and yielding conditions have been described by Davies and Budhu (1986) and Budhu and Davies (1988) for piles embedded in stiff and soft clays, respectively.

A short rigid pile (having a length shorter than its effective length) unrestrained at the top (free-head) shown in Figure 1.5a, tends to rotate and passive resistance develops above the toe on the opposite face to add to the resistance of the soil near the ground surface (Broms, 1964; Tomlinson, 1994). Eventually, the rigid pile will fail by rotation when the passive resistance of the soil at the head and toe are exceeded. The short rigid pile restrained at the head (fixed-head) by a cap or bracing will fail by translation as shown in Figure 1.5b when the lateral soil reactions exceed the passive resistance of the soil.

The failure mechanism of a long free-head pile (having a length longer than its effective length) is different from that of a short pile as described by Broms (1964) and Tomlinson (1994). The passive resistance of the lower part of the pile prevents rotation of the pile, the lower part remaining vertical while the upper part deforms as shown in Figure 1.6a. Failure takes place when the pile fractures at the point of maximum bending moment. For the purpose of analysis, a plastic hinge capable of transmitting shear is assumed to develop at the point of fracture. In the case of a long fixed-head pile, high bending stresses develop at the point of restraint, e.g. just beneath the pile cap, and the pile may fracture at this point (Figure 1.6b).

The typical deformed shape of the pile and the corresponding bending moments, shearing forces and soil reactions under elastic condition are illustrated in Figure 1.7 (Reese and Matlock, 1956). With increasing loading, soil yielding will take place. The deformed patterns and reactions of the pile and soil are similar to those shown in Figure 1.7, but with a greater magnitude.

1.1.2 Behaviour of cyclic laterally loaded piles

Cyclic lateral loading on piles will result in an increase in pile-head displacements and bending moments as compared with a corresponding static lateral loading; see Figures 1.1 and 1.2.

For piles embedded in cohesive soils or clays, there are basically five major factors which may influence the pile behaviour. They are described as:

- 1.) Gap formation around the pile.
- 2.) Backsliding of the soil into the gap.
- 3.) Reduction in soil strength.
- 4.) Cyclic shakedown.
- 5.) Rate of loading.

Gap formation

A principal effect of cyclic loading is the cause of permanent physical separation (gap) of the soil away from the pile in the direction of loading, resulting in the reduction of pile capacity (Matlock, 1970; Dunnavant and O'Neill, 1989; Bijnagte *et al.*, 1991; Long *et al.*, 1993). This is due to the fact that the soil has limited ability to take tension, and it is likely

that separation will occur near the top of the pile, where compressive stress in front of the pile and tensile stress behind the pile, are developed.

The permanent displacement of the soil creates a gap zone such that the soil resistance will be reduced, and the effect is manifested by much greater bending moments and displacements than obtained with similar loading during the initial cycle; see Figures 1.1 and 1.2. This was reported by Matlock (1970) where cyclic pile-load tests were carried out at Lake Austin and confirmed at Sabine river. Bijmagne *et al.* (1991) conducted cyclic pile-load tests and concluded that gaps are evident during the tests, and that the gap formation is restricted to a depth in the range of four pile diameters with gap widths of about 30 mm (5% of the pile diameter) at ground level. Swane and Poulos (1982) pointed out that pile response to cyclic load is dependent, not only on the pile-soil characteristics, but also on the geometry of the gap.

Backsliding

The effects of backsliding of the soil into the gap (i.e. partially closing it; see Figure 1.4a), is due to the tensile or adhesive properties of cohesive soil. During cyclic loading, the soil is first pushed forward by the pile. After the pile has reached its maximum displacement and starts to move back, tensile stresses between the pile-soil contact zone may occur. The adhesive strength of cohesive soil will result in backsliding of the soil into the gap, resulting in the reduction in gap size. This phenomenon has been observed by Matlock (1970) using laboratory model pile tests.

Soil strength degradation

Soil will degrade in strength when subjected to cyclic loading. This is due to the increase in pore water pressures (for undrained condition), changes in soil density and reorientation of the soil particles.

Cyclic loading on piles may cause a considerable loss in shear strength of the soil at its side (slip zone) due to continuous sliding action at the pile-soil interface when the soil has become plastic (i.e. reaches its shear strength); see Figure 1.4c. Shear strength degradation can be observed by conducting reversal shear box tests on clays as reported by Skempton (1964, 1985). The bearing strength of soil in the compression zone, will degrade due to continuous shearing of the soil when the soil has become plastic after reaching its bearing

strength. This phenomenon is observed experimentally using plate loading tests described by Ward *et al.* (1965). Detailed coverage on soil strength degradation is deferred to Chapter 4.

Shakedown and related effects

Load paths which initially cause plastic strains in the soil but stabilise to an elastic response after a finite number of load cycles are said to 'shakedown'. At shakedown, the soil develops a residual stress distribution such that stresses due to an elastic response of the pile to subsequent loads lying within the prescribed load path may be superimposed without causing further yield of the soil. A state of permanent strain and residual stress remains in the soil.

The shakedown limit represents the maximum load at which shakedown can take place along a given load path. For loads which cause shakedown, the increments of pile displacement and plastic work of the soil produced after each cycle tend to decrease, becoming zero after a finite number of cycles as depicted in Figure 1.8b.

When the load path produces no plastic strain in the soil, the pile is said to be experiencing a purely elastic response as depicted in Figure 1.8a. However, if the pile displacement stabilises after a finite number of cycles, while plastic deformation continues within the soil, the pile is said to have experienced alternating plasticity as illustrated in Figure 1.8c, with the load-deflection curve forming a hysteretic loop. The amount of plastic work within the soil increases for load paths undergoing alternating plasticity and may eventually result in failure. If the pile does not stabilise to an elastic or inelastic response, the plastic work done and the pile displacements will continue to increase with each load cycle. After a number of load cycles, the pile may become unserviceable due to progressive deformation, and is said to have failed by incremental collapse or ratchetting as shown in Figure 1.8d.

Although shakedown and the three factors described above are interlinked, the present project will only concentrate on the first three phenomena. The shakedown limit will not be determined, and only pile loading below the 'collapse' load levels described by Davies and Budhu (1986) and Budhu and Davies (1988) will be dealt with. At these levels, although significant changes occurred during load cycling, the behaviour of pile-soil systems tend to stabilise, unless total pile collapse is imminent. Such stabilisation response is usually attained

to a practical degree in less than 100 cycles (Matlock, 1970; Reese *et al.*, 1975; Hamilton and Dunnavant, 1993; Long *et al.*, 1993), depending on loading levels.

Rate of loading

To date, there are no reports of rate of loading effects on cyclic pile-load tests. The only reported case was based on static pile-load tests described by Tassios and Levendis (1974). Their results indicated that substantially lower pile displacement (by a factor between 2 to 4) was measured for rapid rate of loading of 500 kN/h as compared with slower rate application of 5 kN/h. An alternative and economic way to determine the loading rate effect was reported by Andersen and Stenhamar (1983). They conducted plate loading tests on Haga clay and reported that a rapid loading test will give a 10% higher bearing strength as compared with a rate 32 times slower.

The loading rate effect will not be considered in the present method of analysis since there are insufficient data to characterise its influence on cyclic pile behaviour. It is assumed that conventional rates of loading apply.

1.2 Analyses of static laterally loaded piles

Increased interest in the behaviour of lateral loaded piles has resulted in a variety of methods being developed to analyse their response. The earliest and simplest representation of the problem was that of a transversely loaded thin elastic beam, supported by a series of linear springs acting along the length of the beam (Hetenyi, 1946). The analytical simplicity of this representation has resulted in its widespread use in foundation engineering, but at the same time, it is recognised that it has several shortcomings. In particular, the response of a real soil is far from elastic, and non-linear soil response is a key factor in the behaviour of laterally loaded piles. Moreover, group effects cannot be analysed in a rational manner by this approach, and such factors as cyclic loading cannot be accommodated by such simple analyses. Accordingly, more refined methods of analyses have been developed, using more realistic representations of soil behaviour, categorised as linear and non-linear analyses. The following sections contain a brief summary of developments in the analyses of static laterally loaded piles.

1.2.1 Linear analysis

There are essentially three approaches to the analysis of a laterally loaded pile in a linear soil mass:

- 1.) The subgrade reaction or Winkler analysis, in which the pile is idealised as an elastic transversely loaded beam supported by a series of unconnected linear springs representing the soil (Hetenyi, 1946).
- 2.) Finite element analysis, either using two-dimensional or three-dimensional soil and pile elements (Desai and Appel, 1976; Verrujit and Kooijman, 1989), or more economically, by means of expansion of the displacement field in terms of a Fourier series (Kuhlemeyer, 1979; Randolph, 1981).
- 3.) The boundary element (or integral equation) analysis, in which the soil is modelled as an elastic continuum (Poulos, 1971; Banerjee and Davies, 1978).

In all cases, it is possible to incorporate non-homogeneity of the soil, although certain approximations are usually necessary in the boundary element analysis. One major advantage of the finite element or boundary element analysis over the subgrade reaction analysis is that an elastic continuum soil model is adopted, hence a more rational calculation of the displacements and rotations of piles can be made.

1.2.2 Non-linear analysis

The importance of incorporating non-linear response into the analysis of laterally loaded piles is well recognised, and some of the methods employed for static analysis have been extended to allow non-linear load-displacement analysis. These methods may be classified into three categories:

- 1.) Non-linear subgrade reaction analysis.
- 2.) Non-linear finite element analysis.
- 3.) Modified boundary element analysis.

Non-linear subgrade reaction analysis

The most widely used approach is that of Matlock (1970) and Reese *et al.* (1975), who utilise the concept of p - y curves, i.e. relationships between pile-soil pressure (p) and soil displacement (y). Such curves represent, in effect, non-linear soil spring characteristics and have been derived from field measurements on instrumented piles. By making measurements

of bending moments and displacements along the pile at different applied load levels, the relationship between soil pressure and displacement may be inferred for various points along the pile. On the assumption that these relationships apply to piles of all proportions, shapes and relative flexibilities, they may be used in an interaction analysis to determine pile response to applied load. Recommendations for determining p - y curves for different soil types have been summarised by Matlock (1970), Reese *et al.* (1975), Reese and Desai (1977), while Sullivan *et al.* (1980) have generalised procedures to develop a 'unified method' for piles in clay, covering both soft and stiff clays. A somewhat simpler approach has been adopted by Kishida and Nakai (1977) who adopt a bilinear p - y relationship.

Non-linear finite element analysis

In this type of analysis, elasto-plastic constitutive models of the soil continuum are used, usually conducted in either two-dimensions or three-dimensions (Yegian and Wright, 1973; Desai and Appel, 1976; Faruque and Desai, 1982; Kooijman, 1989a, 1989b; Brown and Shie, 1990, 1991; Bhowmik and Long, 1991; Trochanis *et al.*, 1991).

The main advantages of the finite element analysis are: i) the various geometry and boundary conditions for the pile and soil system can be considered, ii) different forms of constitutive models for soils and pile-soil interfaces can be used, and, iii) systematic investigation of various aspects of pile behaviour can be conducted, since several parameters can be varied and their influences studied within the same analytical framework.

A combination of finite and infinite element methods have been adopted by Chen and Poulos (1993). The infinite element is used to simulate the (elastic) far-field behaviour of the soil medium, while standard finite elements are used to model the pile and soil immediately surrounding it (near-field). The incorporation of the infinite element into a standard finite element program can not only approximate the stress distribution in the far-field, but can also save much computational effort and time.

Modified boundary element analysis

The extension of the boundary element method to incorporate an elasto-plastic soil model has been outlined by Banerjee and Davies (1980). Incremental and iterative initial stress or initial strain procedures are employed in which the effects of yielding and slipping are introduced by distributing initial stresses over volume cells and distributing initial surface

tractions over slip surfaces, respectively. A simpler method of treating local soil failure was adopted by Poulos (1971, 1973), in which a limiting lateral pressure p_y (pile-soil yield pressure) is specified for each element of the pile and the analysis ensures that the computed pile-soil pressure does not exceed this limiting value. This approach is analogous to the Kishida and Nakai (1977) analysis except that inter-element interaction is still allowed for, according to the elastic Mindlin's equations (Mindlin, 1936).

A similar approach to the Poulos method was described by Davies and Budhu (1986) and Budhu and Davies (1988) to deal with piles embedded in stiff and soft clay problems, respectively. Unlike Poulos' method, where only the front and back face of the pile are dealt with, they considered the complete three-dimensional nature of the pile-soil interface problem. In their analysis, the soil is assumed to behave linearly elastically but yields when the limiting stresses in the compression, slip and tensile zones are reached. As such, bearing failure at the front face of an advancing pile, shear failure along the sides and tensile failure at the back face of the pile are taken into consideration. Good agreement with the results from published case histories, lended confidence in the application of this method of analysis to deal with practical problems.

1.3 Analyses of cyclic laterally loaded piles

With the increasing use of piles to support offshore structures, the response of piles to lateral cyclic loading has assumed great importance. Over the past years, various methods have been employed to determine the cyclic pile behaviour. To date, the approaches used to determine the cyclic response of laterally loaded piles are as follows:

- 1.) Empirical approach.
- 2.) Modified p - y analysis.
- 3.) Cycle-by-cycle analysis.
- 4.) Bilinear-elasto-plastic analysis.
- 5.) Discrete element analysis.
- 6.) Finite element analysis.
- 7.) Modified boundary element analysis.

1.3.1 Empirical approach

Hettler and Gudehus (1980) developed an empirical expression for the cyclic displacement of piles, based on the results of published pile-load test data. For load levels low enough not to cause failure, they found that the following relationship was applicable to both shallow foundations and laterally loaded piles in sand:

$$\frac{u}{D} = A \left[\frac{H}{\gamma DL^2} \right]^B (1 + C \ln N) \quad (1.1)$$

where u is the pile-head displacement,

D is the pile diameter or width,

H is the cyclic load,

L is the pile length,

γ is the effective unit weight of the soil,

N is the number of cycles, and

A, B, C are empirical parameters.

The shape factor A accounts for the shape of the foundations, while the empirical exponent B is used to adjust the rate of increase in loading in relation to the displacement. The empirical constant C helps to define the increase of displacement with increasing cycles. These three empirical parameters were based on observations from the pile-load test data, and no suggestions were made on the appropriate values to be adopted in the absence of data from the pile-load tests. The effect of soil strength degradation was not included in the analysis, and no indication was given to extend the analysis to deal with cohesive soils. Apparently, no comparisons with field results were carried out. The values of B and C appeared to be independent of the type of pile, but the generality of this finding must be questioned as the relative flexibility of the pile and the pile-head conditions would be expected to be a significant factor. The maximum bending moment subjected onto the pile, which is an important factor in pile design, cannot be determined using this approach. Nevertheless, Equation (1.1) is useful in indicating the form of cycle dependence of lateral displacement.

1.3.2 Modified p - y analysis

A procedure of predicting the load-displacement and bending moment responses of cyclic laterally loaded piles was suggested by Matlock (1970) and Reese *et al.* (1975), involving modifications to the p - y curves for static analysis. Modified p - y curves were employed which took account of the main observed effects of cyclic loading on lateral pile response as observed in model and field tests. For a pile in clay, a 'strain softening' type of behaviour was observed and gaps between the pile and soil were formed, thus leading to the suggested criteria for development of p - y curves as shown in Figure 1.9. Modifications to these criteria have been suggested by Reese and Desai (1977) in which both clays and sands are treated, and a unified approach to p - y curve development for piles in clay has been suggested by Sullivan *et al.* (1980).

These approaches require the determination of a series of p - y curves, coupled with numerical solutions to evaluate the pile response, in terms of pile displacements and bending moments. These p - y curves are often difficult to select in the absence of data from instrumented lateral pile-load tests, though detailed procedures are specified by Tomlinson (1994) and the above mentioned authors, in the selection of required parameters.

The analysis gives an envelope to the behaviour of a pile under cyclic loading and does not consider the change in pile behaviour as the number of load cycles is increased. The resulting load-displacement curve thus represents the behaviour of the pile under an infinitely large number of loading cycles. Furthermore, soil continuity is neglected as the soil pressures on the pile are modelled as independent non-linear springs, allowing no soil interaction with neighbouring soil elements. There is also the question of how the p - y relationships are affected by the pile-head restraint conditions and the relative stiffness of the pile and the soil.

The method, based as it is upon measured field data, reflects the main characteristics of cyclic response. However, there appears to be only fair agreement between predicted and measured behaviour (Long *et al.*, 1993; Hamilton and Dunnavant, 1993) other than those used in the derivation of the p - y curves, and relatively few instances of comparisons were described. Also, there remains uncertainty in the adequacy of a given criterion for a particular soil application and the selection of the required soil parameters (Randolph, 1981; Ruiz, 1986; Dunnavant and O'Neill, 1989). Because of the uncertainty in obtaining the various parameters required, and the method of constructing the p - y curves, many modifications have been suggested by Ruiz (1986), Dunnavant and O'Neill (1989), Long *et al.* (1993), Hamilton and Dunnavant (1993), Rajashree and Sundaravadivelu (1996), among others. However,

although many modifications had been suggested, there remains no change to the established methods first proposed by Matlock (1970) for soft clay, and Reese *et al.* (1975) for stiff clay, which are currently used in API RP 2A(1986) recommended practice.

1.3.3 Cycle-by-cycle analysis

A modification to the p - y analysis, which allows for progressive degradation of soil resistance, has been described by Matlock *et al.* (1978). The soil is represented as a series of non-linear springs, as in the usual p - y analysis, but to allow for the near-surface behaviour of clays, a gap element has been developed. Such elements are attached to the pile in one direction, but are detached as the pile moves away. Only when the pile returns to the point where it left the element previously will its resistance be re-activated (see Figure 1.10a). The number of gap elements can be specified in the analysis program by the user.

The degradation of soil resistance with cycling is modelled by assuming that some proportion of the ultimate resistance is lost after a full reversal of displacement. A factor (λ) is applied to the ultimate resistance of each element after the occurrence of a full reversal of direction of plastic deformation. A lower limit of the ultimate resistance (Q_{min}) is specified, as well as the initial value (Q_u), and whenever the reduction is applied, the existing ultimate resistance (Q_1) is degraded to a new value (Q_2) according to the expression:

$$Q_2 = (1 - \lambda) (Q_1 - Q_{min}) + Q_{min} \quad (1.2)$$

The features of this degradation model are demonstrated in Figure 1.10b. It should also be noted that hardening could be simulated by setting Q_{min} greater than Q_u .

The above method of analysis, although a very useful development, has some disadvantages. Problems can be anticipated when the users are required to specify the number of gap elements, because, to begin with, they do not have a priori knowledge of the gap zones. This raises a question about the appropriate number of gap elements to be used, and the effects of varying the number of these elements. Also, there is no mention of how gap closure is to be dealt with during unloading and subsequent reloading, since care must be taken to ensure that each element does not 'overclose' gaps that have been previously formed. The factors λ and Q_{min} for degradation of soil resistance are ill-defined, and the authors themselves admit that more experimental research in this area of degradation is needed. No

comparison with field results were carried out to prove the validity of the proposed method and Matlock *et al.* state that this method is presently intended to serve primarily as a research tool.

1.3.4 Bilinear-elasto-plastic analysis

The analysis is based on the subgrade reaction theory. The pile is treated as a thin elastic beam and the soil is modelled as a series of independent springs with friction-slider blocks as described by Swane and Poulos (1985). The response of each spring-block system is elasto-plastic as illustrated in Figure 1.11.

The method can be used to describe the shakedown and alternating plasticity responses of cyclic laterally loaded pile. The analysis simulates soil degradation by allowing the soil stiffness and yield pressure to deteriorate during cyclic loading. The contribution of mechanical degradation to the cyclic response of the pile-soil system is included by using a cycle-by-cycle approach. This allows for the effects of soil yielding and pile-soil separation to be considered, when the soil stress exceeds the yield pressure and soil failing in tension respectively.

The degradation functions for soil stiffnesses and yield pressures are of the same basic form as given by Matlock *et al.* (1978); see Equation (1.2). The functions allow both the soil stiffness and yield pressure to degrade, according to the following equations:

$$k_{h2} = (1 - \lambda_k) (k_{h1} - k_{hmin}) + k_{hmin} \quad (1.3)$$

$$p_{y2} = (1 - \lambda_p) (p_{y1} - p_{ymin}) + p_{ymin} \quad (1.4)$$

where k_{h2} is the new spring stiffness,

k_{h1} is the existing spring stiffness,

k_{hmin} is the minimum spring stiffness,

λ_k is the degradation parameter for stiffness,

p_{y2} is the new yield pressure,

p_{y1} is the existing yield pressure,

p_{ymin} is the minimum yield pressure, and

λ_p is the degradation parameter for yield pressure.

For the case where the soil resistance increases during cyclic loading, the term k_{hmin} and p_{ymin} in Equations (1.3) and (1.4), are replaced by k_{hmax} and p_{ymax} , respectively. The degradation functions are applied to plastic soil elements when the soil elements are about to be reloaded. This simulates the deterioration in soil resistance due to repeated passive failure of clay at the front face of an advancing pile as illustrated in Figure 1.11b.

Good agreement was obtained between predictions and the published case history of Reese *et al.* (1975). It was demonstrated that the proposed method of analysis is capable of simulating both the static and cyclic behaviour of cyclic pile-load tests. However, some drawbacks are evident in this method. The use of independent springs to represent the soil resistance ignores the continuous nature of soil. The soil resistance at the side face of the pile is not taken into consideration; an important element in pile-soil interaction as observed in the cyclic pile-load tests. The use of the degradation functions for both stiffness and yield pressure, which have the same basic form employed by Matlock *et al.* (1978), means that at least four soil parameters have to be determined or assumed. No correlations or methods were proposed to obtain these parameters. The determination of the shakedown limit is not of great value, since it is either equivalent to, or represents an upper limit to, the ultimate lateral capacity of the pile. This is because in most cases, failure of the 'long' piles take place at loads far less than the shakedown limit (i.e. bending moment exceeds the yield moment of the pile section before the pile response stabilises). As such, the determination of shakedown limit is not significant in practice.

1.3.5 Discrete element analysis

A one-dimensional discrete element model for laterally loaded piles under cyclic loading conditions was presented by Grashuis *et al.* (1990) and Bijmagne *et al.* (1991). The pile was modelled by rigid body elements, interconnected by elasto-plastic rotational springs, represented by two parallel springs and a hinge, as shown in Figure 1.12a.

The elasto-plastic soil behaviour, gap formation, soil strength degradation and backsliding effects are modelled by a spring and a massless dry friction element in series, as depicted in Figure 1.12b. This element reacts as a linear spring until the force (compression or tension) reaches the threshold force specified for the friction element, after which, the force in the spring remains constant. Gaps originate when the tensile threshold of the friction element is exceeded. Both the stiffness of the spring and the threshold force of the friction

element, which vary with soil types and depths, can be determined from the p - y curve approach derived by Matlock (1970) and Sullivan *et al.* (1980). To model the non-linearity of a p - y curve, a model with two serial friction elements parallel at each hinge can be chosen; see Figure 1.12c.

The cyclic strength of the soil is represented by using an exponential function that models the decreasing soil strength as a function of the number of loading cycles. The degradation function, characterised by two parameters A and B , is given by:

$$F_N = F_0 [1 - B (1 - \exp^{(-A.N)})] \quad (1.5)$$

where F_N is the new soil strength after cycling,

F_0 is the soil strength in the first cycle,

A is the parameter for the rate of degradation; $A \geq 0$,

B is the parameter for the residual soil strength; $0 \leq B \leq 1$, and

N is the number of cycles.

The phenomenon of backsliding in the gap is modelled by a reduction in the gap size, i.e.

$$Gap_i = Gap_{i-1} \frac{F_N}{F_0} C \quad (1.6)$$

where Gap_i is the size of gap in the i -th cycle, and

C is the parameter for the size of backsliding; $0 \leq C \leq 1$.

The backsliding expression is an empirical approach derived from experiments reported by Matlock (1970).

This model is capable of including several phenomena, like gap formation, soil strength degradation and backsliding which have been observed during cyclic pile-load tests. In comparison with measured test results, Bijmagne *et al.* (1991) reported that the model overestimates pile displacements and maximum bending moments. The cause of these conservative prediction may be due to the neglect of soil resistance at the sides of the pile and the continuous nature of the soil. In this analysis, great difficulties can be anticipated in obtaining values for the parameters A , B and C , in addition to those required for p - y curve

method. No suggestions or correlations were offered for determining values for these parameters (A , B and C).

In a later publication by Grashuis and Bijnagte (1992), the non-linearity of the p - y curve is described by three serial friction elements parallel at each hinge to give a tri-linear approximation to the p - y curves. With such adjustments and variations in the parameters A , B and C , better agreement with field results in terms of pile displacements were obtained. However, no concrete justification for curve fitting the p - y curves and varying the three parameters were intimated. This suggests that the 'better' agreement is achieved basically by trial-and-error.

1.3.6 Finite element analysis

Quasi three-dimensional model

In this approach, the three-dimensional analysis was decomposed into a series of two-dimensional analyses, as adopted by Bijnagte *et al.* (1991). For the case of cyclic laterally loaded piles, the horizontal displacements are assumed to dominate the displacement field of the soil around the pile. Further assuming that the vertical stresses in the soil are not influenced by the horizontal load, a quasi three-dimensional model was proposed, where the soil was modelled by a system of continuous layers; see Figure 1.13. These layers are coupled in the vertical direction by an iterative process involving the finite element method. The only stress components that can be transferred from one layer to another are shear stresses in a horizontal plane; such processes have been described by Verrujit and Kooijman (1989). To model plasticity in each layer, Bijnagte *et al.* assumed a Tresca yield criterion (Tresca, 1868).

The local contact between the pile and the soil was modelled by an interface element. This element allows separation of the pile surface and the soil when the soil reaches a limit tensile stress, simulating the formation of a gap.

This method of analysis adopts a continuum approach and includes gap formation via the interface elements. However, the comparisons with experimental results showed that the model overestimated the pile displacements by a factor of between two and three, and also overestimated the maximum bending moments. This seems to be strange as one would anticipate an underestimation rather than an overestimation in prediction, as the model neglects soil strength degradation; an important factor in cyclic pile behaviour.

Three-dimensional model

A three-dimensional elasto-plastic finite element model was employed by Bijnage *et al.* (1991). They used eight-noded quadratic Serendipity, degenerated shell elements to model the pile and twenty-noded quadrilateral hexahedral isoparametric elements to model the soil. The mesh details are depicted in Figure 1.14.

The constitutive behaviour of both granular and cohesive soils and the pile were described by a 'perfect elastic-perfect plastic' (or simply elastic-perfectly plastic) material model, where no hardening or softening was taken into account. The undrained plastic behaviour of the clay was modelled by the Tresca material model (Tresca, 1868). The yield surface for the drained behaviour of the sand layers was modelled by a combination of the Mohr Coulomb model (1776) and the tension cut-off criterion according to Rankine (1857). A non-associated flow rule is used. The yield surface for the pile was modelled using the Von Mises criterion.

The interface element was not available in the three-dimensional configuration; therefore only two extreme cases were analysed, i.e. the fully-bonded and completely smooth cases. For the fully bonded case, no relative displacements between the pile and the soil were allowed at the pile-soil interface. For the completely smooth case, the displacement of the pile and the soil are radially linked in the loading direction. There was no contact between the soil at the back of the pile, characterising the gap formation when tensile stresses occur. In the vertical direction and parallel to the pile-circumference, shear stress cannot be transferred from pile to soil.

The use of a three-dimensional model in the finite element analysis requires enormous pre-processing and post-processing effort and very substantial amounts of computational time. As such, only three different cases were analysed. The difference in results analysed using the fully-bonded and the completely smooth cases for the pile-head load-displacement response is a factor of between two and three, depending on the load level. This suggests that it is important to model the pile-soil interface behaviour properly.

The fully-bonded predictions gave a 'too soft' pile response compared to that measured in the field, although soil strength degradation was not employed in the analysis. Bijnage *et al.* reported that the model overestimated pile displacement by a factor of between two and three, and also overestimated both the depth and the magnitude of the maximum bending moment by about 30%. Such results have also been reported for the quasi

three-dimensional model, despite the large differences in modelling the interface behaviour for the three-dimensional and quasi three-dimensional cases. One would expect the three-dimensional predictions (fully-bonded case) to be significantly stiffer than the quasi three-dimensional predictions, since the former case considers full bonding between the pile and the soil is present along the whole pile circumference. This difference may be due to the differences in the undrained shear strengths and shear modulus adopted in the two models. It might also be due to the fact that in the three-dimensional model, the vertical displacement (as well as the increase of the vertical stress due to horizontal loading) is incorporated, unlike the quasi three-dimensional model where these vertical displacement and stress are not taken into account, thus giving a softer pile response.

Based on the three-dimensional analysis, it is noted that gap formation is restricted to a depth of a few pile diameters and the plastic soil region is limited to a radius of two pile diameters at the surface. Vertical soil stresses and deformations due to horizontal loading occur only in a small zone around the pile top.

1.3.7 Modified boundary element analysis

An approach which might be considered as intermediate between the cyclic p - y analysis and the cycle-by-cycle analysis of Matlock *et al.* (1978) has been suggested by Poulos (1982). This method aims to determine the behaviour of the pile after a specified number of load cycles (N), considering degradation of both the soil modulus and ultimate lateral pile-soil pressure. By progressively increasing N , the relationship between displacement and number of cycles may be determined for a given magnitude of cyclic loading.

The analysis is based upon the simplified boundary element method used for static pile analysis (Poulos, 1971, 1973). The pile is assumed to be a thin rectangular vertical strip of width (D) and length (L) with constant flexibility; the idealisation of the pile is depicted in Figure 1.15a. The soil is essentially modelled as an elastic continuum via Mindlin's solution (Mindlin, 1936) having properties which are unaffected by the presence of the pile. The ultimate pile-soil pressures are specified for each element along the pile to allow for the possibility of soil yielding. It is also assumed that complete adherence is maintained between the pile and the soil.

The effects of cyclic loading on the soil modulus and the ultimate pile-soil pressures are defined by means of degradation factors D_E and D_p respectively, defined as:

$$D_E = \frac{E_c}{E_s} \quad (1.7)$$

and

$$D_p = \frac{p_{yc}}{p_{ys}} \quad (1.8)$$

where E_c is the soil modulus after cyclic loading,

E_s is the soil modulus for static loading,

p_{yc} is the limiting pile-soil interaction stress (yield pressure) after cyclic loading, and

p_{ys} is the yield pressure for static loading.

Based on the data summarised by Idriss *et al.* (1978a), both the soil modulus degradation factor D_E and the ultimate pressure degradation factor D_p are expressed as:

$$D_E = D_p = N^t \quad (1.9)$$

where t is the degradation parameter dependent on cyclic strain.

Figure 1.15b shows a plot of the degradation parameter t against cyclic strain ratio ϵ_c/ϵ_{cr} , derived from the data presented by Idriss *et al.* (1978a) for San Francisco Bay mud; ϵ_c is the cyclic strain and ϵ_{cr} is a reference value of cyclic strain which characterises the response of the soil to cyclic loading. The smaller the value of ϵ_{cr} , the more susceptible is the soil to cyclic degradation.

To allow for the effect of rate of loading, the degradation functions D_E and D_p can be multiplied by a rate factor D_R , in which:

$$D_R = 1 - F_p \log \left(\frac{\zeta_r}{\zeta} \right) \quad (1.10)$$

where F_p is the rate coefficient,

ζ_r is the reference loading rate, and

ζ is the loading rate.

The major weakness of this continuum approach, is the determination of the degradation parameter t , which is based on the estimation of the cyclic strain in the soil at each element of the pile. It appears that there is currently little or no information on the order of values which might be expected for ϵ_{cr} , which is a key parameter in the analysis. Also, the determination of F_p and ζ_r poses problems.

In comparison with published case histories, satisfactory agreement between the predictions and the measured results were obtained, despite the fact that the soil resistance at the side of the pile and the formation of gaps between the pile and the soil at the interface were not taken into consideration.

1.4 Discussion

From the review of the numerical methods used in the analysis of cyclic laterally loaded piles described in Section 1.3, it is clear that there are three major shortcomings in these methods. Firstly, the idealisation of the soil resistance or pressure by discrete springs, is not an appropriate approach, since soil continuity is being neglected. This leads to the choice of continuum approaches, in which the distribution of the stresses and deformations in the soil can be represented in a more rigorous manner. Another advantage of the continuum model is the direct use of physical quantities for the soil properties, such as undrained shear strength, Young's modulus and Poisson's ratio, *etc.* Also, there is the possibility of modelling the detailed pile-soil interaction behaviour. The disadvantages of such models, are the computer memory requirements and the relatively long program 'run times'. However, with the advancement in computer technology, these disadvantages are inconsequential if better representations and accuracy can be attained. In this thesis, the finite element method and a numerical algorithm, termed the indirect boundary element method, based on a continuum approach will be employed for the analyses.

It is evident from the established methods of analyses, except for finite element analysis, that the shear stresses developed between the soil and the sides of the pile have not been taken into account. Some methods, like the empirical approach and p - y method, have ignored pile-head fixity and the relative stiffness of the pile and the soil. Others (e.g. cycle-by-cycle, bilinear-elasto-plastic, finite element and modified boundary element methods) have excluded at least one or more of the phenomena like gap formation,

backsliding, and soil strength degradation, which are vital elements in the mechanism of cyclic pile behaviour. Hence, a numerical analysis is needed which incorporates all these aforementioned features.

Finally, most methods of analyses have involved the use of empirical assumptions to obtain the parameters required. Most often, the manner in which these parameters are acquired cannot be justified, and from the physical point of view cannot be explained. These add to greater uncertainty, particularly if no standard laboratory tests can be used to determine these parameters. To overcome this problem, numerical analyses should involve a minimum of empirical assumptions and parameters should be easily attained via simple standard laboratory tests. Only by this means is it possible to obtain proper predictions of field behaviour.

In this research, a two-dimensional finite element plane-strain analysis will be employed to give insight into the pile-soil interface behaviour. Then, the modified boundary element analysis described by Davies and Budhu (1986) and Budhu and Davies (1988) will be explored and extended for cyclic analysis. This method has been chosen primarily because it takes into consideration the three-dimensional nature of laterally loaded pile problems, and has shown to give very good agreement with published case histories under static lateral loading conditions.

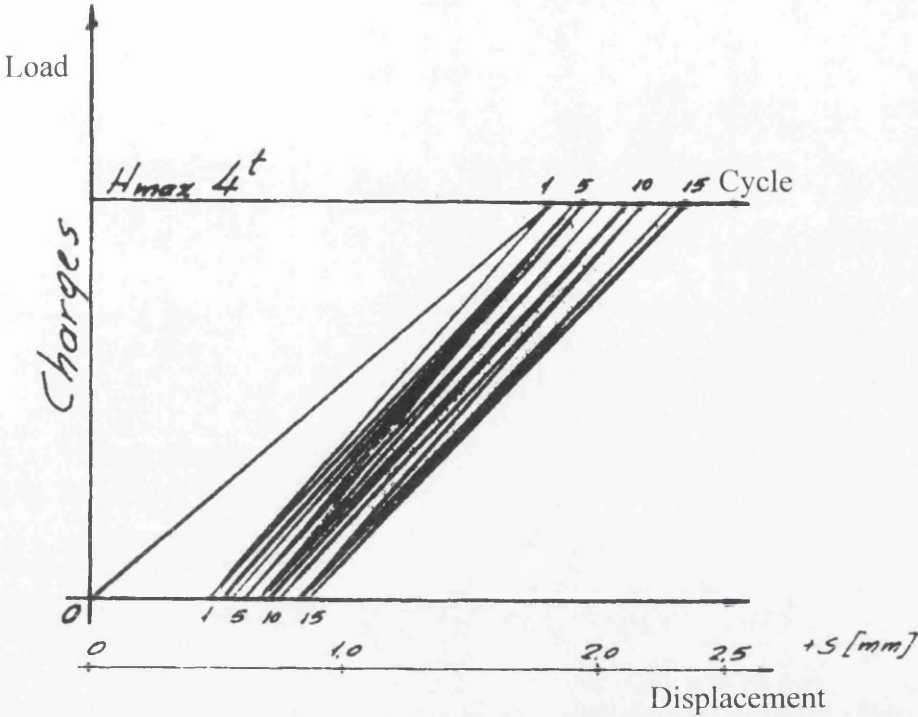
1.5 Scope of the research

The primary objective of this work is the development of a numerical analysis based on the indirect boundary element method framework, to model the cyclic behaviour of laterally loaded piles embedded in cohesive soils. The analysis is capable of simulating most of the phenomena observed in cyclic pile-load tests, such as gapping, backsliding and soil strength degradation effects. The method of analysis is described in detail in Chapter 5, with its implementation into a computer program known as APILEC presented in Chapter 6. The soil strength degradation which is essential for the analysis will be investigated in Chapter 4, together with correlations between strength degradation parameters and soil index properties.

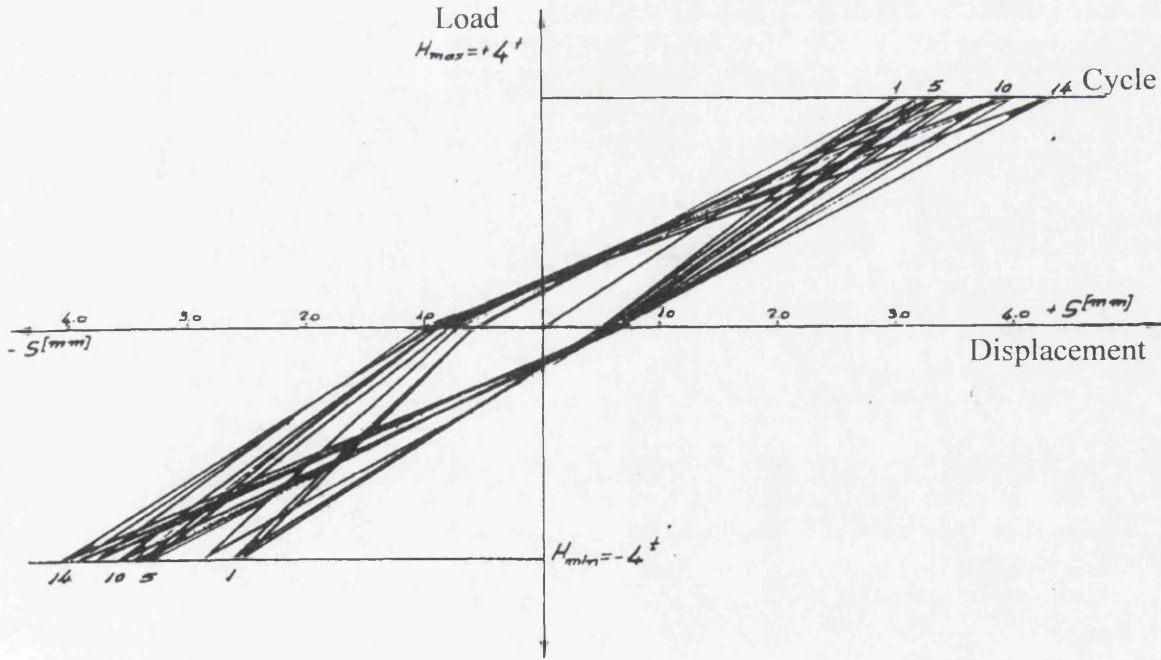
The finite element analysis is described in Chapter 3, where it is employed to gain insight into the details of pile-soil interface behaviour during cyclic loading. This is intended to guide the development of the simplified boundary element analysis in the following

Chapter. The constitutive cyclic soil models employed in the finite element analysis are described in Chapter 2.

The main results of this study are presented in Chapter 7, and illustrate the influence of the major relevant parameters. The validity of the analysis is demonstrated in Chapter 8 via comparisons with published field test results. Based on the work completed during this project, some general conclusions and recommendations for further research complete this thesis.



(a)



(b)

Figure 1.1 Increase in pile-head displacements with cycling for (a) one-way and (b) two-way load-controlled cyclic pile-load tests (Tassios and Levendis, 1974).

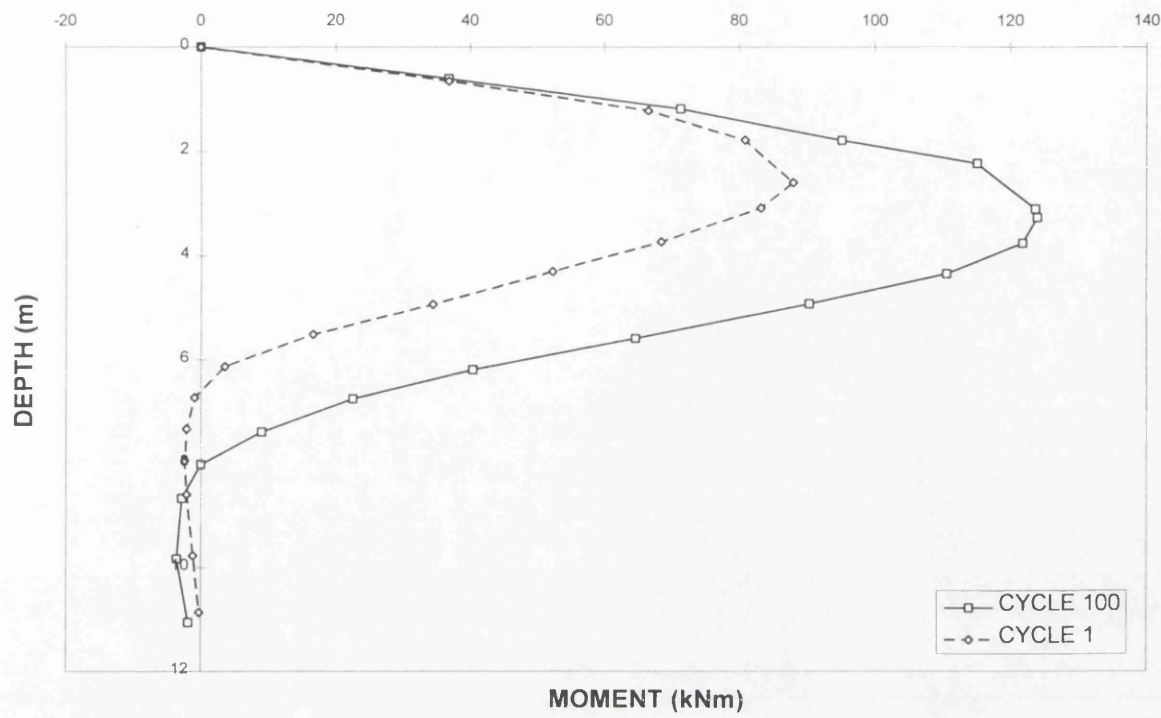


Figure 1.2 Increase in pile bending moment for one-way load-controlled cyclic pile-load test (after Matlock, 1970).

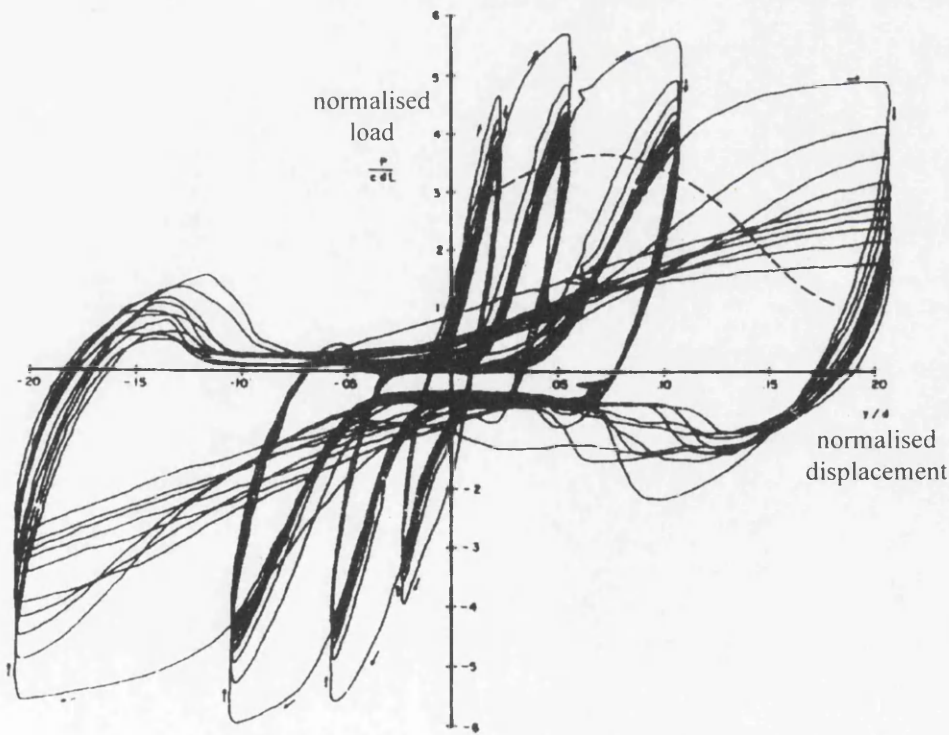


Figure 1.3 Two-way displacement-controlled cyclic laboratory model pile tests (Matlock, 1970).

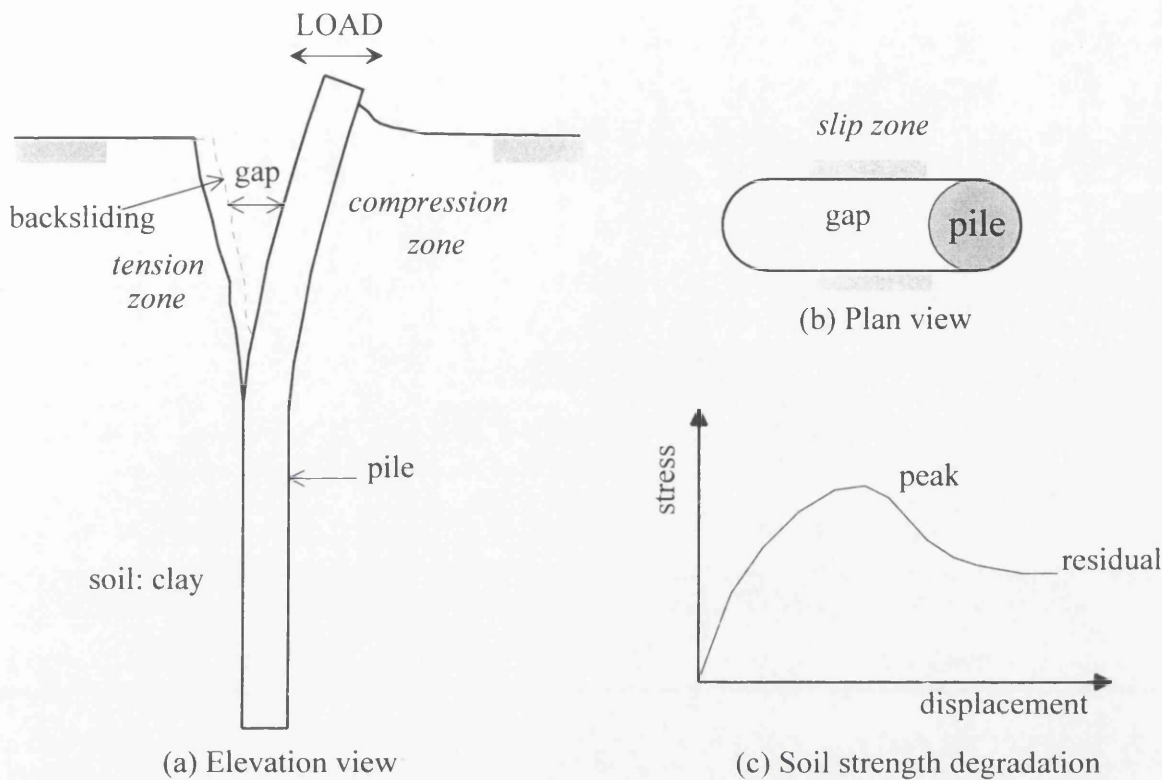


Figure 1.4 Phenomena observed and soil zones developed during cyclic pile-load test.

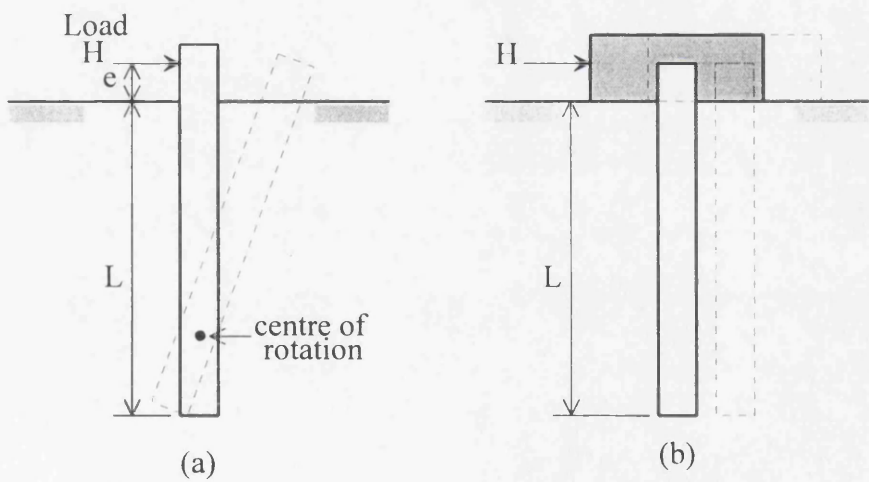


Figure 1.5 Short vertical pile under lateral load for (a) free-head pile and (b) fixed-head pile.

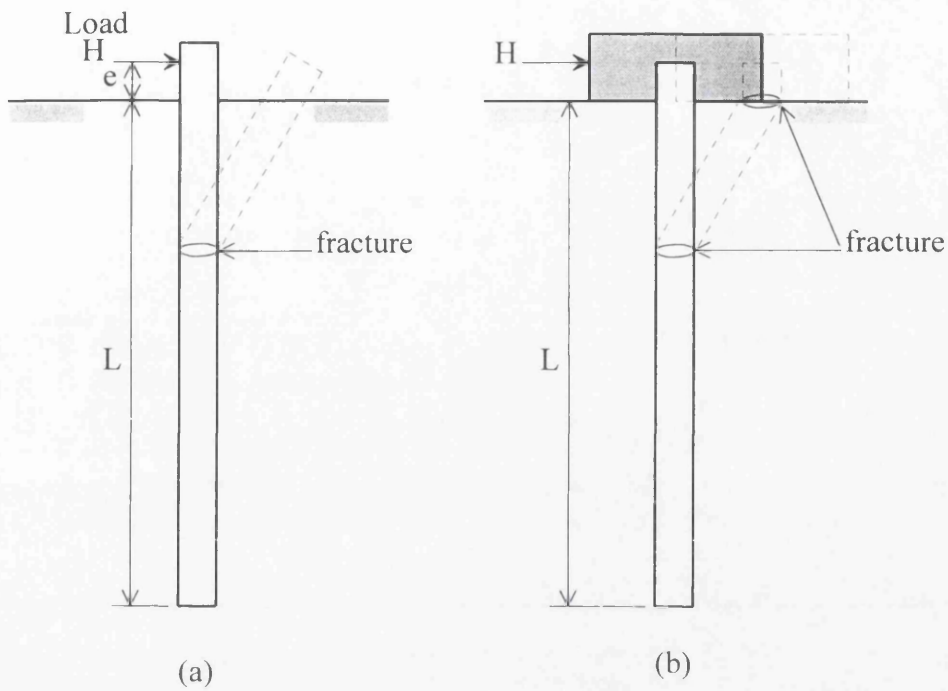


Figure 1.6 Long vertical pile under lateral load for (a) free-head pile and (b) fixed-head pile.

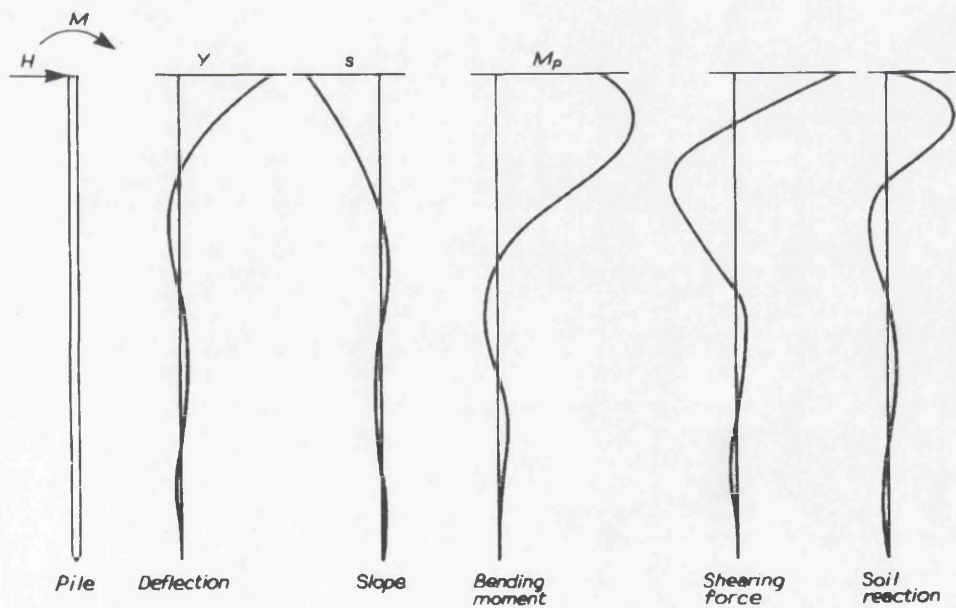


Figure 1.7 Deflections, slopes, bending moments, shearing forces and soil reactions for elastic conditions (Reese and Matlock, 1956).

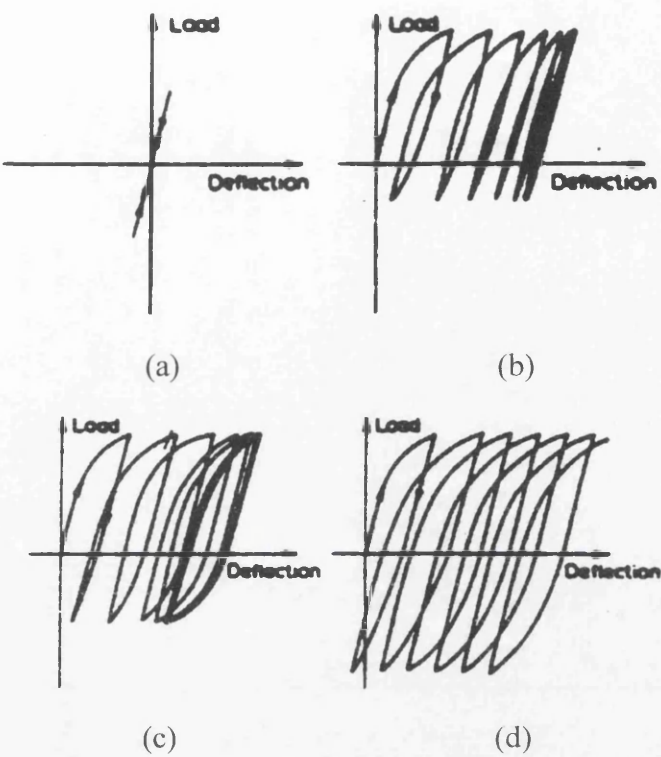


Figure 1.8 Cyclic responses for a laterally loaded pile experiencing (a) purely elastic response, (b) shakedown, (c) alternating plasticity and (d) incremental collapse (Swane and Poulos, 1982)

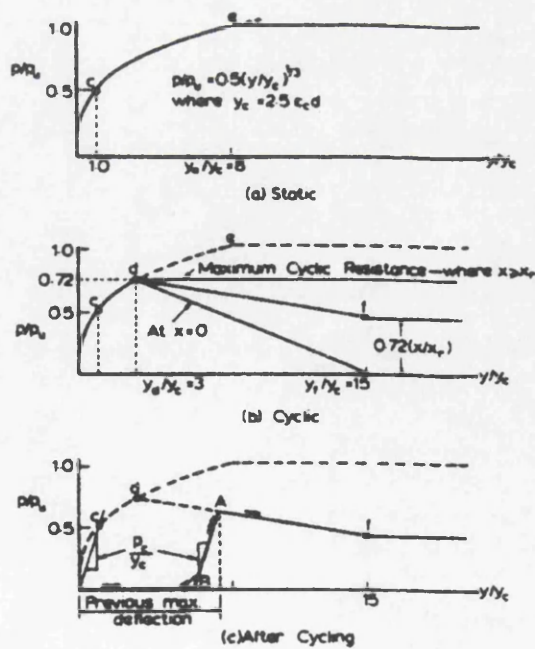


Figure 1.9 Criteria for predicting p - y curves for (a) short-time static loading, (b) equilibrium under initial cyclic loading and (c) reloading after cycling (Matlock, 1970).

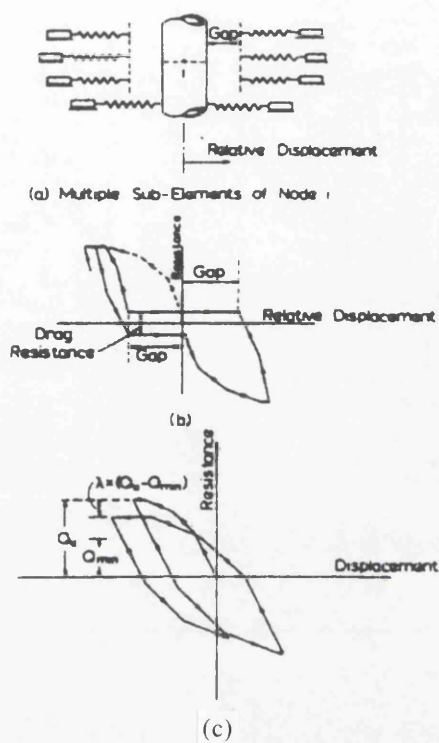


Figure 1.10 Model developed by Matlock *et al.* (1978).

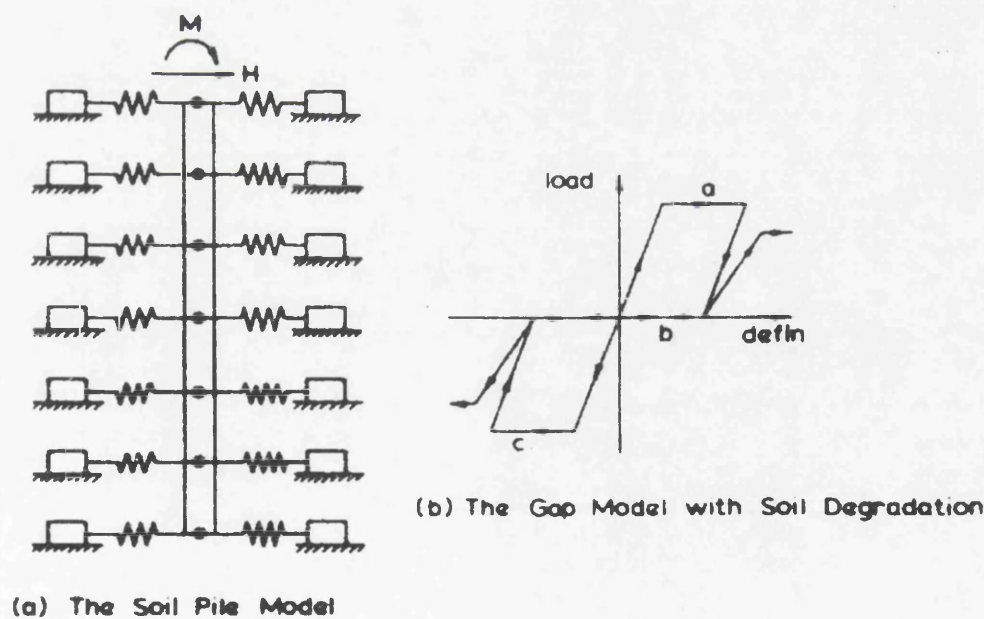


Figure 1.11 Model developed by Swane and Poulos (1985).

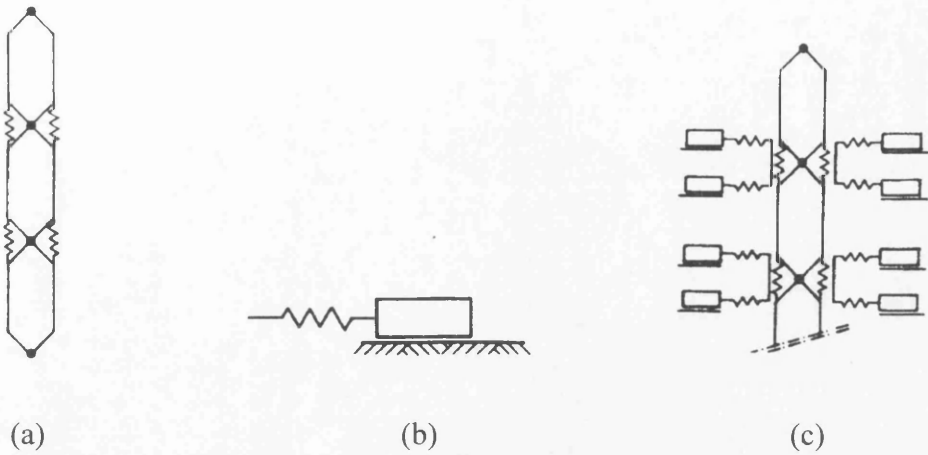


Figure 1.12 (a) Discrete element pile model, (b) dry friction element and (c) pile-soil interaction elements (Bij nagte *et al.*, 1991).

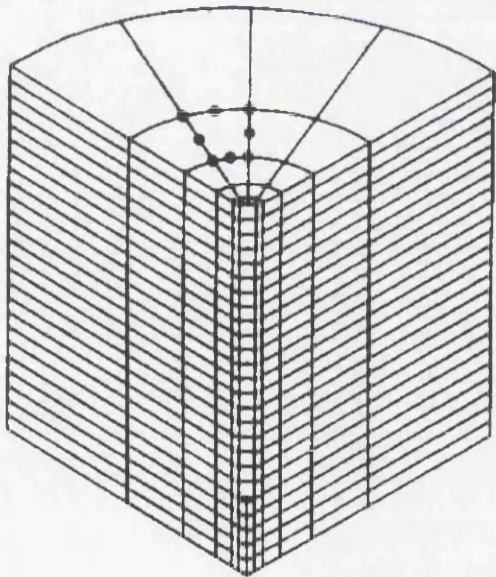


Figure 1.13 Layer system for the quasi three-dimensional model (Bij nagte *et al.*, 1991).

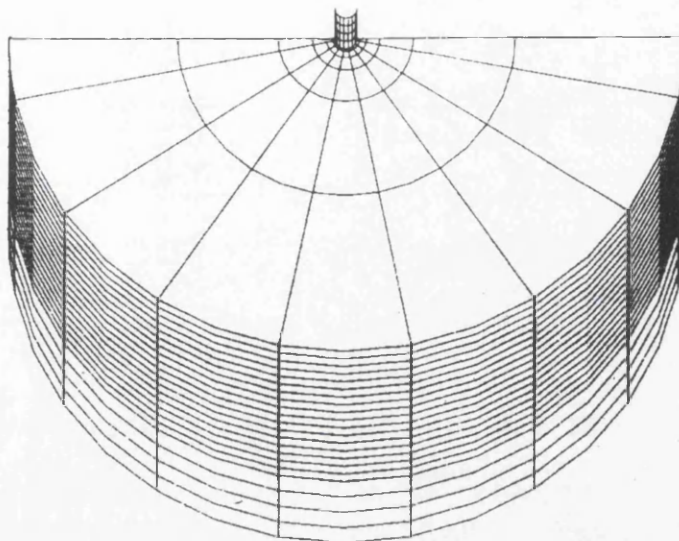


Figure 1.14 Three-dimensional finite element mesh; backside shown from above with half the pile shown in the background (Bijnagte *et al.*, 1991).

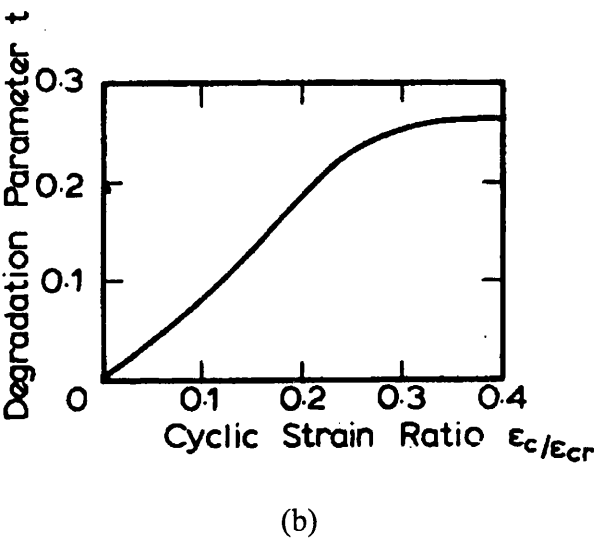
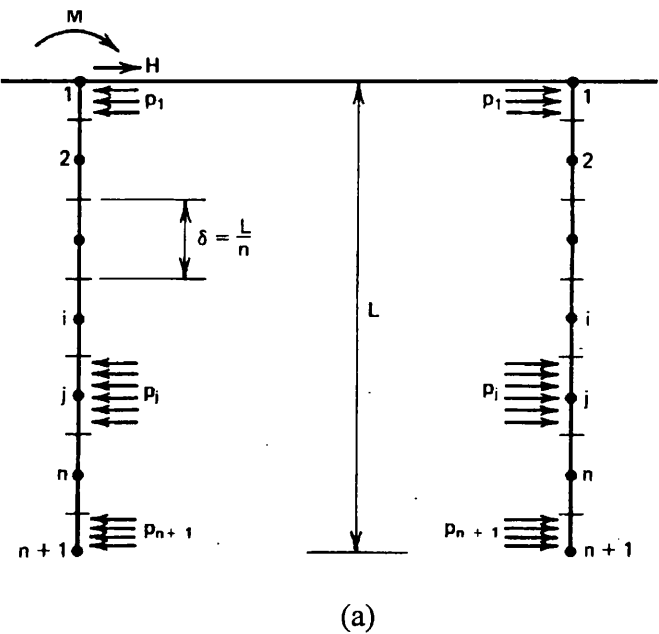


Figure 1.15 (a) Idealisation of pile (Poulos, 1982) and (b) degradation parameter t (Poulos, 1982 after Idriss *et al.*, 1978a).

CHAPTER 2

Cyclic Soil Models

2.1 Summary

2.2 Introduction

2.3 Soil behaviour under cyclic loading

2.3.1 Introduction

2.3.2 Development of permanent strain

2.3.3 Changes in soil stiffness and dissipation of energy

2.3.4 Development of excess pore water pressure

2.3.5 Strength reduction

2.4 Soil models for cyclic loading

2.4.1 Equivalent linear models

2.4.2 Cyclic non-linear models

2.4.3 Advanced constitutive models

2.4.3.1 Kinematic hardening models

2.4.3.2 Bounding surface plasticity models

2.5 The 'bubble' model

2.5.1 Introduction

2.5.2 Modified Cam clay model

2.5.3 Bubble yield surface

2.5.4 Translation rule

2.5.5 Hardening rule

2.5.6 Numerical tests

2.5.7 Comparisons with experimental data

2.5.8 Parameters required for the bubble model

2.5.9 Strengths and weaknesses of the bubble model

2.6 Concluding remarks

CHAPTER 2

Cyclic Soil Models

2.1 Summary

This chapter contains a brief description of some soil models which have been developed to predict the behaviour of soils under cyclic loading, including (in more detail) an elasto-plastic two-surface model, formulated within the framework of critical state soil mechanics. In addition, a brief review of the salient behaviour of clays under cyclic loading, including the development of permanent strains, accumulation of excess pore water pressure, changes in soil stiffnesses, reduction in strength (etc.), is presented.

2.2 Introduction

Successful numerical modelling of soil behaviour, requires the identification of the important characteristics while leaving the model as simple as possible. It is clear that the more sophisticated a model becomes (and the more soil parameters needed to describe it), the more extensive will be the physical tests required to define it. A careful balance, therefore, has to be maintained between cost of soil testing and analysis on the one hand and accuracy on the other. A brief description of some cyclic soil models will be reviewed in this chapter, including a model that will be employed in a subsequent finite element analysis. Before advancing directly into the soil modelling, a brief review of the behaviour of soils when subjected to cyclic loading, is presented. This will help in the selection of the appropriate soil model to be employed in the finite element plane-strain analysis of cyclic laterally loaded piles.

2.3 Soil behaviour under cyclic loading

2.3.1 Introduction

The behaviour of soils under cyclic loading is complex, and to date, even the most sophisticated models fail to provide accurate predictions under generalised cyclic stress conditions. It is nonetheless possible to identify a number of strands of behaviour which

appear to be exhibited in varying degrees by all soils. These can be categorised into four distinct responses:

- 1.) Development of permanent strain.
- 2.) Changes in soil stiffness and dissipation of energy.
- 3.) Development of excess pore water pressure.
- 4.) Strength reduction.

2.3.2 Development of permanent strain

Idealised behaviour of soil subjected to drained cycling during stress-controlled loading between two general stress states, S_1 and S_2 , is depicted in Figure 2.1. Each cycle is accompanied by a change in shear strain, some of which is recoverable and some of which is not. The magnitude of the recoverable strain remains fairly constant during each cycle. On the other hand, the irrecoverable or plastic strain developed during each successive cycle tends to reduce with the increasing number of cycles. Eventually, the soil attains a form of equilibrium for this loading pattern, and the behaviour can be described as quasi-elastic or 'resilient'. It is well established that the resilient stiffness of the soil is stress-level dependent and is also dependent on the magnitude of resilient shear strain.

While experiencing cyclic loading, the permanent strain developed during each individual cycle will usually be small but, over a large number of load cycles, the magnitude of accumulated permanent strains may be significant (Figure 2.1). Where the accumulated strains are high (e.g. cyclic shear strain of 3%) and the soil does not reach an equilibrium condition, failure must occur.

2.3.3 Changes in soil stiffness and dissipation of energy

Two closely interrelated phenomena are manifested during cycling: changes in soil stiffness and dissipation of energy. In Figure 2.2 the changes in stiffness which occur during cyclic loading are illustrated. It can be seen that immediately after each stress reversal, the stiffness increases and subsequently decreases. Such behaviour applies only to soils subjected to stresses that are below the critical level of repeated loading (CLRL as defined by Sangrey *et al.*, 1978), where a state of non-failure equilibrium will ultimately be reached (Sangrey *et al.*, 1980; Houston and Herrmann, 1980; Kramer, 1996); see Figures 2.1 and 2.3. If the soil is subjected to a load level higher than CLRL, the stiffness of the soil immediately after each

stress reversal will drop (as depicted in Figure 2.4) and failure of the soil may eventually be reached after a finite number of cycles. Such results were reported by Sangrey *et al.* (1969), Andersen (1976), Ishihara and Yashuda (1980) Andersen *et al.* (1980) and Ansal and Erken (1989).

Regarding energy dissipation, it is observed in Figure 2.1, that during any stress cycle, the stress sustained at any strain level of the unloading phase is lower than that for the corresponding strain during loading/reloading. This indicates that the soil has failed to return all of the strain energy stored during loading/reloading and some energy has been dissipated, i.e. an hysteretic response.

2.3.4 Development of excess pore water pressure

The failure of soils under undrained cyclic loading is partly a consequence of accumulated excess pore water pressure and partly due to the breakdown of interparticle contacts. When cycled at low load levels (below CLRL), most soils will tend to reach a non-failure equilibrium condition, as illustrated in Figure 2.3a. At this state, there is no further accumulation of either strain or excess pore water pressure with additional stress cycles (Sangrey *et al.*, 1969, 1980; Ansal and Erken, 1989) as depicted in Figure 2.3b. However, if the stress level is increased to a higher level, as shown in Figure 2.4, sufficient excess pore water pressure will develop to reach the effective stress failure condition (Sangrey *et al.*, 1969, 1978). At point *e*, the sample was unable to carry the stress of 47.1 psi and the non-recoverable deformation increased markedly. Figure 2.4 also illustrates that the stress level to cause failure of soil under cyclic loading is lower than that under monotonic loading (dotted line in Figure 2.4).

The accumulation of plastic strain and excess pore water pressure are two of the principal features which distinguish cyclic behaviour from that exhibited during monotonic loading.

2.3.5 Strength reduction

One of the dramatic effects of repeated loading on saturated soils is a loss of strength or failure (defined in terms of specific levels of cyclic shear strain) after a finite number of loading cycles. The potential for strength loss and failure increases as the level of cycled stress increases has been reported by Sangrey and France (1980), Andersen *et al.* (1980),

Ishihara and Yasuda (1980), Ansal and Erken (1989), Kramer (1996), among others. Andersen *et al.* (1982) described direct simple-shear tests on Drammen clay and reported that undrained cyclic loading caused a reduction in the undrained shear strength, which could be related to the overconsolidation ratio (OCR) and the number of load cycles; see Figure 2.5. Andersen *et al.* (1982) also illustrated the dependency of secant shear modulus on the level of cyclic shear stress, number of load cycles and OCR, as shown in Figure 2.5. The results presented by Lee and Focht (1976), showed that the cyclic strength ratio decreases with the increasing number of cycles, refer to Figure 2.6.

2.4 Soil models for cyclic loading

Three classes of soil models are briefly described in this section. They are: i) the equivalent linear models, ii) cyclic non-linear models, and, iii) advanced constitutive models. These models, with varying degrees of success, aim to encapsulate the experimentally observed cyclic behaviour of soils described earlier.

2.4.1 Equivalent linear models

These simple models represent few aspects of soil behaviour under cyclic loading conditions. For a typical soil, subjected to symmetric cyclic loading, the stress-strain plot forms an hysteresis loop, as shown in Figure 2.7. Two important characteristics of the hysteresis loop are its inclination and breadth. The inclination of the loop depends on the stiffness of the soil, and its average value over the entire loop can be approximated by the secant modulus G_{sec} (ratio of shear stress to the corresponding shear strain); see Figure 2.7. The breadth of the hysteresis loop is related to the area of the loop, which is a measure of the energy dissipation and can be expressed in terms of a damping ratio (ξ). The parameters G_{sec} and ξ are often referred to as the equivalent linear material parameters, and have been used in the analysis of soil response under (earthquake) cyclic loading (Idriss and Seed, 1968; Kramer, 1996).

The locus of the points corresponding to the apices of hysteresis loops with various cyclic strains is called a backbone curve (see Figure 2.8). Its slope at the origin (at zero cyclic strain) is equal to the maximum shear modulus, G_{max} . At greater cyclic strain amplitudes, the modulus ratio (G_{sec}/G_{max}) reduces. The modulus ratio can be used to characterise the stiffness of soils as a function of shear strain amplitudes.

The equivalent linear models can provide only a first approximation to the cyclic non-linear behaviour of the soil. Obviously, they cannot be used directly for problems involving permanent deformation (or failure).

2.4.2 Cyclic non-linear models

The non-linear stress-strain behaviour of soils can be represented more accurately by cyclic non-linear models that follow the actual stress-strain path of the soil during cyclic loading. A variety of such models has been described by Idriss *et al.* (1978a, 1978b), Richart (1975), Streeter *et al.* (1974), among others. These models are characterised by a backbone curve and a series of 'rules' that govern unloading and reloading behaviour and other effects.

The most widely accepted rule for generating the hysteresis loops from a backbone curve is to assume that the soil behaviour satisfies the Masing rule (Masing, 1926). This rule states that the unloading and reloading branches of the loop are comprised of the same backbone curve, with both stress and strain scales expanded by a factor of two, and that the origin is translated. At the apices of the loop and after stress reversal, the tangent modulus is equal to G_{max} (see Figure 2.8). Additional rules (extended Masing rules) are needed to describe the soil response under general cyclic loading. For the case when the unloading or reloading curve exceeds the maximum past strain and intersects the backbone curve, it follows the backbone curve until the next stress reversal. When an unloading or reloading curve crosses an unloading or reloading curve from the previous cycle, the stress-strain curve follows that of the previous cycle. An example of a model that follows the above rules is depicted in Figure 2.9.

Cyclic non-linear models do not assume that shear strains are zero when the shear stress is zero. Their ability to represent permanent strains is one of their most important advantages over the equivalent linear models. However, the cyclic non-linear models do not allow for the determination of shear induced volumetric strains, which can lead to hardening under drained conditions (or pore pressure development with stiffness degradation under undrained conditions). Further development in these models has included such factors (Finn *et al.*, 1977; Idriss *et al.*, 1978a; Pyke, 1979), but requires many more parameters to characterise the soil behaviour.

The above rules for generating the hysteresis loops, are not fundamentally accurate. This is because experimentally results for soils loaded under a variety of stress configurations

show no perfect symmetry on an unloading and reloading cycle. Additionally, one must question whether soils really have the capacity to 'memorise' selected prior reversal points, as is required by the extended Masing rules. Note that the Masing rule is not adequate beyond certain strain limits as mentioned by Idriss *et al.* (1978a) and Pyke (1979). Besides these, there remains the uncertainty in determining the backbone curve, and the unloading and reloading curves, involving many complex mathematical functions and parameters to describe them (Finn *et al.*, 1977; Idriss *et al.*, 1978a; Pyke, 1979).

2.4.3 Advanced constitutive models

The most accurate and general models make use of the basic principles of plasticity in order to describe observed soil behaviour for quite general initial stress conditions and stress paths, strain rates and drainage conditions. Such models generally involve a yield surface (which describes the yield stress conditions), a hardening rule (which describes the changes in the size and shape of the yield surface as plastic deformation occurs), and a flow rule (which relates the direction of plastic strain to the stress state). Soil models of this nature, which account for the cyclic behaviour of soils, include the kinematic hardening models and the bounding surface plasticity models.

2.4.3.1 Kinematic hardening models

In an isotropic hardening model such as Modified Cam clay (Roscoe and Burland, 1968; Wood, 1994; see Section 2.5.2), the yield surface expands uniformly with plastic deformation. Yield surfaces can also translate without change in size, described as kinematic hardening. One particular form of kinematic hardening incorporates a series (nest) of yield surfaces of different sizes, which translate in stress space, allowing them to touch and translate together during hardening, but never to intersect (Mróz, 1967; Iwan, 1967; Prévost, 1977; Prévost and Griffiths, 1988 among others). The stiffness associated with any particular change in stress depends on how many of these nested yield surfaces translate during the stress increment.

The concept of these nested kinematic hardening models can be explained with the aid of a one-dimensional model consisting of a series of parallel spring and slider elements; see Figure 2.10a. Each of the springs has the same stiffness, but the sliders have a rigid perfectly plastic response (Figure 2.10b) with different yield loads Y (where $Y_2 = y$, $Y_3 = 2y$, $Y_4 = 3y$).

The load-displacement response of this model subjected to a load of $3y$ is illustrated in Figure 2.10c; a detailed descriptions can be found in O'Reilly and Brown (1991) and Wood (1994).

The generalisation of a one-dimensional slider is a yield surface, and in the kinematic hardening soil model, the sliders of progressively higher yield loads are replaced by yield surfaces of progressively larger sizes. For example, a series of yield surfaces is shown in the q - p' stress plane in Figure 2.11. A stress path will meet successive members of this series of yield surfaces, and drag them with it as it traverses stress space as shown in Figures 2.11a, 2.11b and 2.11c. As more yield surfaces are dragged along by the stress path, the incremental stiffness falls. The effect is shown schematically in Figure 2.11c and 2.11d, where the stress-strain responses to triaxial compression CB and triaxial extension CD (after a stress history ABC) are compared. Path CD activates yield surfaces 1, 2 and 3 and is associated with a low stiffness. A retreat into triaxial compression, path CB translates initially across yield surface 1 and is associated with high stiffness (Figure 2.11d). It can be observed from Figures 2.11c and 2.11d that the stiffness increases when the stress path changes direction. Further, the current distribution of yield surfaces stores information concerning the history of the loading of the soil. A disadvantage of these kinematic hardening models, is that during numerical analysis of boundary value problems, it is necessary to store a large volume of data: this can result in significant computational overhead.

2.4.3.2 Bounding surface plasticity models

In these models, the sudden change of stiffness associated with the passage of the stress state through a yield surface is effected by making the stiffness fall steadily from a high (elastic) value at a point in the interior of the yield surface to a low (plastic) value when the stress state reaches the yield surface. Thus, the response to stress changes inside the yield surface is no longer elastic, and the yield surface is now termed the bounding surface.

The application of bounding surface plasticity to the generation of constitutive models for soils was presented by Dafalias and Herrmann (1980). They used a bounding surface formulation to describe the behaviour of clays under cyclic loading. No explicit yield surface was postulated within the bounding surface. The associated flow rule was utilised for the bounding surface, and the variation of the hardening modulus within the boundary surface was defined on the basis of radial mapping rule. For each stress point within the bounding surface, a corresponding 'image' point on the surface was specified at the intersection of the

surface with the radial line connecting the origin with the current stress point (the origin was assumed to be always within the bounding surface). The hardening modulus is then assumed to be a function of the 'image point' hardening modulus (on the bounding surface) and the distance between the stress point and its image. Some improvements to this model were described by Dafalias and Herrmann (1982). The major shortcomings of such models are the use of complex mathematical formulations to define the bounding surface and the various 'rules' to characterise the soil responses. Furthermore, the parameters involve great uncertainty in defining them. The fact that no yield surface is explicitly introduced in these models, assuming that the soil has zero elastic range. This obviously neglects the initial elastic response of soils observed in the experimental tests as illustrated in Figures 2.3 and 2.4.

A form of bounding surface model is the two-surface model proposed by Mróz *et al.* (1978, 1979) for clays. The two surfaces are a bounding surface (representing the consolidation history of the soil), and a yield surface (defining the elastic domain within the bounding surface); see Figure 2.12. The bounding surface is assumed to expand or contract isotropically, but the yield surface is allowed to translate, expand or contract within the domain enclosed by the bounding surface. The translation of the yield surface is governed by the same rule as the nested yield surfaces described in Section 2.4.3.1 (i.e. the yield surface translates towards the bounding surface along the path PR in Figure 2.12). The hardening modulus of the yield surface is assumed to be a function of the distance b (Figure 2.12) between the stress point P on the yield surface and its conjugate (image) point R on the bounding surface. A detailed discussion of this model and its application to clays under monotonic and cyclic triaxial test conditions has been given by Mróz *et al.* (1979). Further extensions of the model to account for soil stiffness degradation have been presented by Mróz *et al.* (1981). It must be emphasised that these models have employed extremely complex mathematical formulations and involve many ill-defined parameters to predict the cyclic soil behaviour.

A simplified form of two-surface model, which combines features of isotropic hardening, kinematic hardening and bounding surface plasticity, has been developed by Al-Tabbaa (1987) and Al-Tabbaa and Wood (1989). It is known as the 'bubble' model, and is capable of analysing the general stress-strain behaviour of clays under cyclic loading. This model will be described in detail in the next Section.

2.5 The 'bubble' model

2.5.1 Introduction

Although the Modified Cam clay (MCC) model has been successfully used for numerical modelling of the monotonic behaviour of clays, it cannot be used to model the behaviour of clays subjected to cyclic loading. In order to improve the model predictions without making the model too complicated, a single inner kinematic hardening yield surface, a 'bubble' (Al-Tabbaa and Wood, 1989) has been introduced inside the MCC yield surface (acting as a bounding surface).

The bubble encloses the stress space in which only elastic deformations occur. When the current stress state lies on the bubble, the soil behaviour is elasto-plastic, and when the bubble reaches the MCC yield surface, the model degenerates to the MCC model. The bubble model was developed to match experimentally observed phenomena such as accumulation of permanent strains, hysteresis, changing stiffness, etc., during cyclic loading as described in Section 2.3.

Since the bubble model is based on the MCC model developed by Roscoe and Burland (1968), for completeness, the MCC model is briefly reviewed.

2.5.2 Modified Cam clay model

The MCC model is an elasto-plastic model which provides a coherent, if simplified, description of the mechanical behaviour of unstructured cohesive soils. This model was developed by Roscoe and Burland (1968) as a modification of the original Cam clay model developed by Roscoe and Schofield (1963). The MCC model was based mainly on the results of triaxial tests. The stress invariants adopted in the model are the mean effective stress:

$$p' = \frac{1}{3} (\sigma'_a + 2\sigma'_r) \quad (2.1)$$

and the deviator stress:

$$q = \sigma'_a - \sigma'_r \quad (2.2)$$

where σ'_a is the effective axial stress, and

σ'_r is the effective radial stress.

The corresponding, work conjugated, strain increments are the volumetric strain increment:

$$\delta\epsilon_p = \delta\epsilon_a + 2\delta\epsilon_r \quad (2.3)$$

and the shear strain increment:

$$\delta\epsilon_q = \frac{2}{3} (\delta\epsilon_a - \delta\epsilon_r) \quad (2.4)$$

where ϵ_a is the axial strain, and

ϵ_r is the radial strain.

Compressive stresses and strains are taken to be positive.

The MCC theory is based on the concept of the critical state which assumes that soils reach a failure (critical) state at which unlimited shear strains take place without further change in effective stress or volume. It is assumed that the yield surfaces (f) and plastic potentials (g) are identical (associated plasticity) and elliptical in the q - p' stress plane. The yield surface (see Figure 2.13a) is defined by the equation:

$$f = (p' - p_o)^2 + \frac{q^2}{M^2} - p_o^2 = 0 \quad (2.5)$$

where $p_o = \frac{p_m}{2}$,

p_m defines the size of the current yield surface (Figure 2.13), and

M is a function of the angle of shearing resistance.

When the soil yields (i.e. stress point remains on the yield surface), the consistency condition holds (obtained from differentiating Equation (2.5)):

$$(p' - p_o)\delta p' + \frac{q}{M^2} \delta q = p_o \delta p_o \quad (2.6)$$

The normality rule is assumed to apply. In other words, in q - p' stress plane, the plastic strain increment vector $(\delta\epsilon_p^p : \delta\epsilon_q^p)$ is in the direction of the outward normal to the yield surface, at the given stress point, i.e.

$$\frac{\delta\epsilon_p^p}{\delta\epsilon_q^p} = \frac{\partial f / \partial p'}{\partial f / \partial q} = \frac{\partial g / \partial p'}{\partial g / \partial q} \quad (2.7)$$

This relationship defines the relative magnitude of plastic volumetric and shear strains.

An isotropic hardening function is chosen so that the change in size of the yield surface is related to the plastic volumetric strain increment of the soil by the relationship:

$$\delta\epsilon_p^p = (\lambda^* - \kappa^*) \frac{\delta p_m}{p_m} \quad (2.8)$$

where λ^* is the slope of the normal compression lines in the $\ln V$ - $\ln p'$ compression plane, and, V is the specific volume, and

κ^* is the initial slope of the unloading lines in the $\ln V$ - $\ln p'$ compression plane.

Combining Equations (2.6) with (2.7) and (2.8), the soil compliance matrix (for plastic strain increments only) is obtained as:

$$\begin{bmatrix} \delta\epsilon_p^p \\ \delta\epsilon_q^p \end{bmatrix} = \frac{(\lambda^* - \kappa^*)}{p_o p' (p' - p_o)} \begin{bmatrix} (p' - p_o)^2 & (p' - p_o) \frac{q}{M^2} \\ (p' - p_o) \frac{q}{M^2} & \left(\frac{q}{M^2}\right)^2 \end{bmatrix} \begin{bmatrix} \delta p' \\ \delta q \end{bmatrix} \quad (2.9)$$

The elasto-plastic compliance matrix can then be readily determined by assuming that the elasto-plastic strains can be decomposed into elastic and plastic parts (e.g. $\delta\epsilon_p = \delta\epsilon_p^e + \delta\epsilon_p^p$).

The above expression shows that if $p' < p_o$ (i.e. 'dry' of critical, see Figure 2.13b), the soil becomes unstable in the sense that the plastic shear strain increment has an opposite sign to the shear stress increment. That means the yield surface contracts rather than expands, and hence, the soil softens to failure. Further details can be found in Wood (1994).

2.5.3 Bubble yield surface

The bubble model assumes that soils have elliptical yield surfaces in the q - p' stress plane. The inner bubble, introduced as shown in Figure 2.14, has the same shape as the MCC

yield surface. The ratio of their dimensions is R and the bubble is centred at (p'_α, q_α) . The equation of the bubble yield surface is:

$$(p' - p'_\alpha)^2 + \frac{(q - q_\alpha)^2}{M^2} = R^2 p_o^2 \quad (2.10)$$

When the soil yields, the consistency condition (generated by differentiating Equation (2.10), in order to ensure that the changes in p' , p'_α , q , q_α and p_o are consistent with the stress state remaining on the bubble yield surface) gives:

$$(p' - p'_\alpha)(\delta p' - \delta p'_\alpha) + \frac{(q - q_\alpha)}{M^2}(\delta q - \delta q_\alpha) = R^2 p_o \delta p_o \quad (2.11)$$

This consistency equation, valid only for soil yielding, ensures that any stress point always lies on or within the bubble yield surface.

2.5.4 Translation rule

The translation rule of the bubble yield surface which defines $\delta p'_\alpha$ and δq_α as functions of $\delta p'$, δq and δp_o , guarantees that the bubble and MCC yield surfaces can touch each other at a common normal, but never intersect. A conjugate point D on the MCC yield surface can be associated with each point C on the bubble yield surface (Figure 2.15), such that the points C and D have the same outward normal. The translation of the bubble yield surface that occurs when plastic strains are being generated can be separated into two components, namely:

$$\begin{bmatrix} \delta p'_\alpha \\ \delta q_\alpha \end{bmatrix} = \frac{\delta p_o}{p_o} \begin{bmatrix} p'_\alpha \\ q_\alpha \end{bmatrix} + S \begin{bmatrix} \frac{p' - p'_\alpha}{R} - (p' - p_o) \\ \frac{q - q_\alpha}{R} - q \end{bmatrix} \quad (2.12)$$

where S is:

$$S = \frac{(p' - p'_\alpha) \left[\delta p' - \frac{\delta p_o}{p_o} p' \right] + \frac{(q - q_\alpha)}{M^2} \left[\delta q - \frac{\delta p_o}{p_o} q \right]}{(p' - p'_\alpha) \left[\frac{p' - p'_\alpha}{R} - (p' - p_o) \right] + \frac{q - q_\alpha}{M^2} \left[\frac{q - q_\alpha}{R} - q \right]} \quad (2.13)$$

The first part of Equation (2.12) is associated with changes in size of the bubble and MCC yield surfaces (due to change in p_o). The second part is associated with translation of the bubble yield surface along the vector $\underline{\beta}$ (which joins C and D) towards the MCC yield surface (Figure 2.15). The evolution of $\delta p'_\alpha$ and δq_α , as defined in Equation (2.12) satisfies the consistency condition in Equation (2.11). Translation in the direction of the vector $\underline{\beta}$ guarantees that when the bubble yield surface reaches the MCC yield surface, they will have a common normal and will never intersect.

2.5.5 Hardening rule

It is assumed, as in the MCC model, that the vector of plastic strain increments $(\delta \epsilon_p^p : \delta \epsilon_q^p)$ is in the direction of the normal to the bubble yield surface according to Equation (2.7). The hardening rule links the change in size of both the bubble and MCC yield surfaces with the plastic volumetric strain. For the particular situation where the bubble and MCC yield surfaces are in contact at the current stress state, it is assumed that Equation (2.8) is valid. Then, combining Equations (2.11) with (2.7) and (2.8), the plastic strain increments are:

$$\begin{bmatrix} \delta \epsilon_p^p \\ \delta \epsilon_q^p \end{bmatrix} = \frac{(\lambda^* - \kappa^*)}{(p' - p'_\alpha) \left[p' (p' - p'_\alpha) + \frac{q(q - q_\alpha)}{M^2} \right]} \begin{bmatrix} (p' - p'_\alpha)^2 & (p' - p'_\alpha) \frac{(q - q_\alpha)}{M^2} \\ (p' - p'_\alpha) \frac{(q - q_\alpha)}{M^2} & \left(\frac{q - q_\alpha}{M^2} \right)^2 \end{bmatrix} \begin{bmatrix} \delta p' \\ \delta q \end{bmatrix} \quad (2.14)$$

The above expression is then used in a 'modified form' to calculate plastic strains whenever they occur, whether or not the bubble and MCC yield surfaces are in contact:

$$\begin{bmatrix} \delta \epsilon_p^p \\ \delta \epsilon_q^p \end{bmatrix} = \frac{1}{h} \begin{bmatrix} (p' - p'_\alpha)^2 & (p' - p'_\alpha) \frac{(q - q_\alpha)}{M^2} \\ (p' - p'_\alpha) \frac{(q - q_\alpha)}{M^2} & \left(\frac{q - q_\alpha}{M^2} \right)^2 \end{bmatrix} \begin{bmatrix} \delta p' \\ \delta q \end{bmatrix} \quad (2.15)$$

N.B. Please note that the above equation which appeared as Equation (14) in Al-Tabbaa and Wood (1989) contains a minor error, namely:

$$\begin{bmatrix} \delta \epsilon_p^p \\ \delta \epsilon_q^p \end{bmatrix} = \frac{1}{h} \begin{bmatrix} (p' - p'_\alpha)^2 & (p' - p'_\alpha) \frac{(q - q_\alpha)}{M^2} \\ (p' - p'_\alpha) \frac{(q - q_\alpha)}{M^2} & \left(\frac{q - q_\alpha}{M^2} \right)^2 \end{bmatrix} \begin{bmatrix} \delta p' \\ \delta q \end{bmatrix} \quad (14)$$

where h is a hardening function consisting of two parts:

$$h = h_o + H \quad (2.16)$$

where H is a function of the separation of the bubble and MCC yield surfaces (which falls to zero when the two surfaces are in contact at the current stress state), and, h_o (by comparison with Equation (2.14)) is defined as:

$$h_o = \frac{(p' - p'_\alpha)}{(\lambda^* - \kappa^*)} \left[p' (p' - p'_\alpha) + \frac{q(q - q_\alpha)}{M^2} \right] \quad (2.17)$$

Consideration of stability shows that it would not be satisfactory to set $H = 0$ in Equation (2.16) for the stress state inside the MCC yield surface, because unlimited plastic strains could occur at four singularity points, where $h = 0$ in Equation (2.15); see Figure 2.16. Two singularity points, g_1 and g_2 , in Figure 2.16, lie at the top and bottom of the bubble yield surface with $p' = p'_\alpha$; the other two singularity points are g_3 and g_4 where straight lines from the origin touch the bubble yield surface. The vector (p', q) is then perpendicular to the normal of the bubble yield surface which has the direction $[(p' - p'_\alpha), (q - q_\alpha)/M^2]$. The dot product of these two vectors is zero leading to unlimited plastic strains in Equation (2.15) assuming that the numerator is not equal to zero. With $H = 0$, the bubble yield surface would be divided into four regions as marked in Figure 2.16: two stable regions (g_1g_4 and g_2g_3) in which increase of shear strain ($\delta\epsilon_q^p > 0$) is associated with increase in shear stress ($\delta q > 0$), and two unstable regions (g_1g_3 and g_4g_2) in which increase of shear strain ($\delta\epsilon_q^p > 0$) is associated with decrease in shear stress ($\delta q < 0$). Experimental results show typically that behaviour is everywhere stable for $q/p' < M$, and the addition of the extra term H helps to ensure this.

Hashiguchi (1985) suggested that H should be a monotonic function of the degree of approach of the bubble and the MCC surfaces. From a study of experimental data, Al-Tabbaa (1987) proposed that the function H should be written in the form:

$$H = \frac{1}{(\lambda^* - \kappa^*)} \left[\frac{b}{b_{\max}} \right]^\Psi p_o^3 \quad (2.18)$$

where ψ is an experimentally determined positive real exponent,

b is the component of the vector $\underline{\beta}$ in the direction of the normal to the bubble yield surfaces at the current stress point; see Figure 2.17, and,
 b_{max} is taken to be $2p_o(1 - R)$.

The function H is not unique and different functions might be adopted for different soils.

N.B. Please note that the equation in defining b in Al-Tabbaa and Wood (1989) as Equation (17) has a minor error:

$$b = \frac{1}{Rp_o} \left[(p' - p'_\alpha) \left[\frac{p' - p'_\alpha}{R} - (p' - p_o) \right] + \frac{(q - q_\alpha)}{M^2} \left[\frac{q - q_\alpha}{M^2} - q \right] \right] \quad (17)$$

The corrected equation should be:

$$b = \frac{1}{Rp_o} \left[(p' - p'_\alpha) \left[\frac{p' - p'_\alpha}{R} - (p' - p_o) \right] + \frac{(q - q_\alpha)}{M^2} \left[\frac{q - q_\alpha}{R} - q \right] \right] \quad (2.19)$$

2.5.6 Numerical tests

To observe the behaviour of the bubble model, several clays subjected to undrained loading conditions were analysed using the SWANDYNE (Chan, 1990) soil model tester program.

The predicted translations of the bubble and the MCC yield surfaces are illustrated in Figure 2.18. In Figure 2.18a, a normally consolidated clay is tested under undrained loading conditions up to the critical state. The stress path from point A to B in q - p' stress plane, shows that the bubble and the MCC yield surfaces remain in contact at the current stress point. The plastic strains calculated from the bubble model will therefore be identical to those determined using the MCC model. The normality rule in this case predicts compressive volumetric strains which causes the MCC yield surface to expand monotonically. The bubble yield surface also expands and translates so as to remain in contact with the MCC yield surface while remaining a constant size ratio (R) in proportion of it.

In Figure 2.18b, an overconsolidated clay is subjected to an undrained test, illustrating plastic volumetric expansion and strain softening response (and corresponding decrease in the

excess pore water pressure), until it ultimately reaches its critical state. It can be seen that as the stress state moves from C to D (i.e. within the bubble yield surface), only elastic strains occur and hence there is no change in size of the MCC and bubble yield surfaces. As the stress state moves from D to E , it drags the bubble yield surface with it. The dilatant plastic volumetric strains (which result from the application of the normality rule to the bubble yield surface and the hardening function) causes the MCC yield surface to shrink. The bubble yield surface also reduces in size and, in addition, translates within the MCC yield surface. The new stress state always lies on the bubble yield surface, which retains a constant size ratio R in proportion to the MCC yield surface.

2.5.7 Comparisons with experimental data

The effective stresses and specific volume at peak deviator stress in drained tests on overconsolidated clays lie on a so-called Hvorslev surface (Atkinson and Bransby, 1978). Thus, the MCC model tends to overestimate the strengths of such clays.

The hardening function introduced in the previous section inhibits strain softening for stress states lying on the unstable part of the bubble yield surface, when it is not in contact with the MCC yield surface. However, the influence of H in Equation (2.18) reduces as the bubble yield surface approaches the MCC yield surface. Failure conditions may develop for $b > 0$ when $H = -h_o$.

There is an infinite number of yield surfaces that can pass through any particular stress state lying inside the MCC yield surface and consequently the failure points will depend on the previous stress history of the soil. Some typical failure points observed in drained and undrained tests using the present bubble model are shown in Figure 2.19, and it is evident that these define a failure region rather than a failure line. Nevertheless, it is an attractive by-product of this kinematic hardening extension of the MCC model that reasonable strengths are now predicted for overconsolidated clays.

A typical example of the form of cyclic response observed, and analysed using the model is shown in Figure 2.20, taken from Al-Tabbaa and Wood (1989). The model successfully matches many of the important observed aspects of the response. Hysteresis is included in cycles of reloading and unloading. The volumetric response is well matched and the drift of shear strain is correctly reproduced.

2.5.8 Parameters required for the bubble model

The six soil parameters necessary for the bubble model are as follows:

- λ^* : the slope of normal compression lines in the $\ln V - \ln p'$ compression plane,
- κ^* : the initial slope of unloading lines in the $\ln V - \ln p'$ compression plane,
- M : the slope of the critical state line representing ultimate failure conditions in the $q - p'$ stress plane,
- ν : Poisson's ratio,
- ψ : the exponent in the hardening function H , and
- R : the ratio of the sizes of the bubble yield surface and the MCC yield surface.

In addition, a reference point (Γ), on the normal compression line or the critical state line is required. Note that only the first four soil parameters, namely λ^* , κ^* , M and ν , are required for the MCC model, for the predictions of stress-strain behaviour of clays subjected to monotonic loading.

The parameters required for the model can be obtained from simple standard tests. They can also be obtained from one multi-stage test using the triaxial apparatus. An example of such a test involves isotropic compression to determine λ^* followed by isotropic unloading. The initial part of the unloading path will give a value for κ^* and R . The later part of this path will give the value of ψ . The sample can then be isotropically reloaded, and subsequently tested to failure either in an undrained test or a drained test. This will enable the value of M and ν to be obtained.

2.5.9 Strengths and weaknesses of the bubble model

Strengths

The strengths of the bubble model can be summarised by the following:

- 1.) Simple elliptical expression (Equation (2.5)) to define the bounding surface (MCC yield surface) unlike models developed by Dafalias and Herrmann (1980, 1982).
- 2.) The yield surface (bubble) which has the same shape as the MCC surface but R times smaller is explicitly defined in Equation (2.10).
- 3.) The use of the bubble yield surface to define the small elastic region reflects the elastic soil response subjected to initial loadings.

- 4.) The formulations employed to determine the plastic strain increments are easily understandable.
- 5.) Parameters required for the model can be easily obtained from simple laboratory tests.
- 6.) The model is able to predict the experimentally observed cyclic soil behaviour described in Section 2.3. For example the accumulation of permanent strains, changes in stiffness, energy dissipation, etc., except the soil strength reduction.
- 7.) The model can account for the normally and overconsolidated clays, subjected to drained and undrained conditions, which are commonly encountered in many site situations.
- 8.) The model has shown good agreement with experimental results as illustrated in Figure 2.20.
- 9.) The model can be more easily implemented into the finite element program (Chan, 1990) than other models (Mróz *et al.*, 1981; Dafalias and Herrmann, 1982 among others) described in Section 2.4.3.

Weaknesses

The bubble model, like all other models has limitations. They are:

- 1.) The bubble has constant size ratio R , and there is no reason why R should not be a variable (Al-Tabbaa and O'Reilly, 1990). For instance, R can be taken as a function of the bubble proximity to the MCC yield surface or the number of load cycles. Experimental results depicted in Figures 2.3 and 2.4, have shown that the elastic region of the soil varies according to the number of load cycles and the load levels.
- 2.) The assumption of rate independency suggests that the model is only appropriate to the loading rate from which the model parameters were derived, which may pose problems to rate sensitive soils.
- 3.) The model does not take into account soil strength reductions which are evident in cyclic soil tests described in Section 2.3.4.

2.6 Concluding remarks

The dominant factors that influence the behaviour of soils under cyclic loading have been described. The effects of cyclic loading include the loss of strength, changes in soil stiffness and the accumulation of permanent strain.

The review of cyclic models for soils has inevitably been incomplete and partial. Evidently, the model selected should be sufficiently complex to capture the phenomena described above. However, complexity implies an increasing number of soil parameters as is evident in the models that have been discussed.

The advanced constitutive models, in particular, the bubble model, will be employed for the finite element analysis of cyclic laterally loaded pile foundations described in Chapter 3. This model is chosen due to its strength (see Section 2.5.9) and availability in the finite element program. Furthermore, it can account for the behaviour of soils under general initial stress and cyclic loading conditions, subjected to drained and undrained conditions, which the equivalent linear and cyclic non-linear models do not possess.

The concepts of critical state soil mechanics underpin the bubble model which is capable of predicting many aspects of clays under cyclic loading. The model was developed directly from experimental observations using the MCC isotropically hardening yield surface as a bounding surface, within which a kinematically hardening bubble yield surface is introduced. A translation rule for the yield surface is assumed which ensures that the bubble and MCC yield surfaces never intersect. A hardening rule is assumed to predict plastic strains on the yield surface. Comparison between the predictions of the model and the experimental results in Al-Tabbaa (1987) and Al-Tabbaa and Wood (1989) shows overall good agreement. The bubble model has been implemented by Chan (1990) into a finite element program - SWANDYNE. The results of its predictions will be presented in the next Chapter.

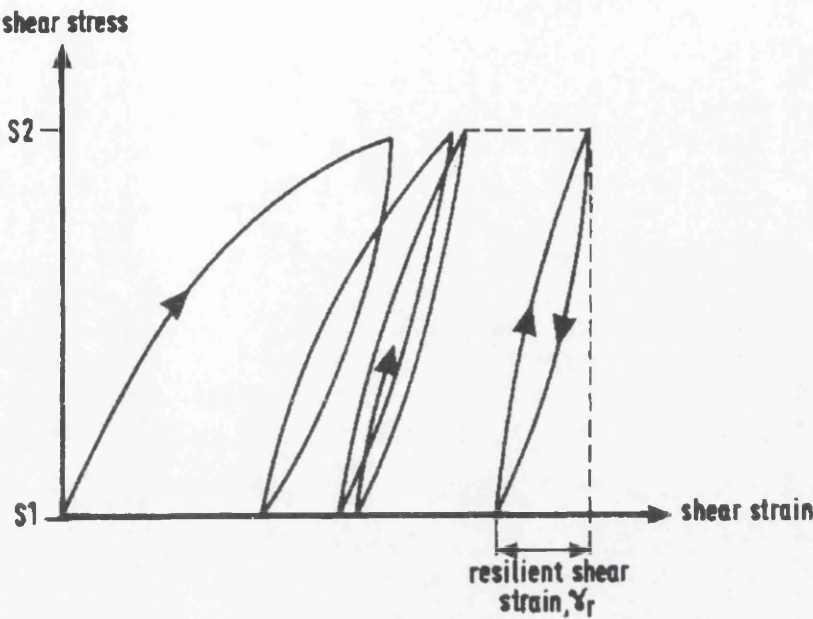


Figure 2.1 Typical development of shear strain during a cyclic load test (O'Reilly and Brown, 1991).

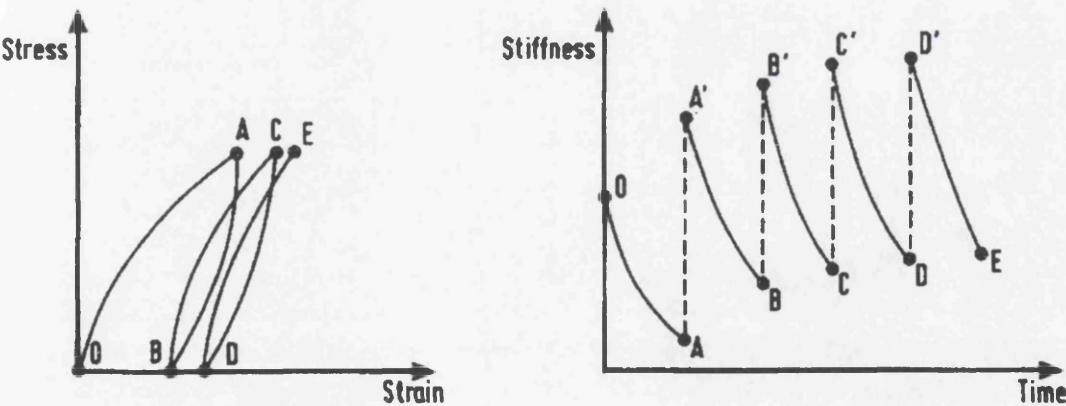


Figure 2.2 The effect of stress reversals on soil stiffness (O'Reilly and Brown, 1991).

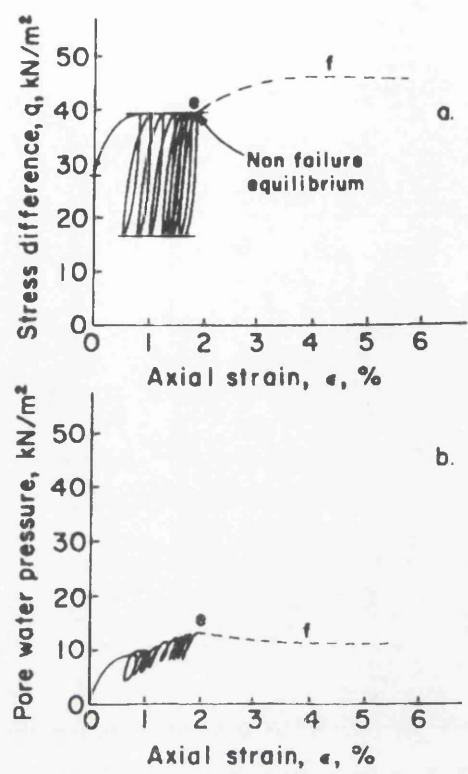


Figure 2.3 (a) Undrained cyclic loading at low stress levels and (b) associated pore pressure response (Sangrey and France, 1980).

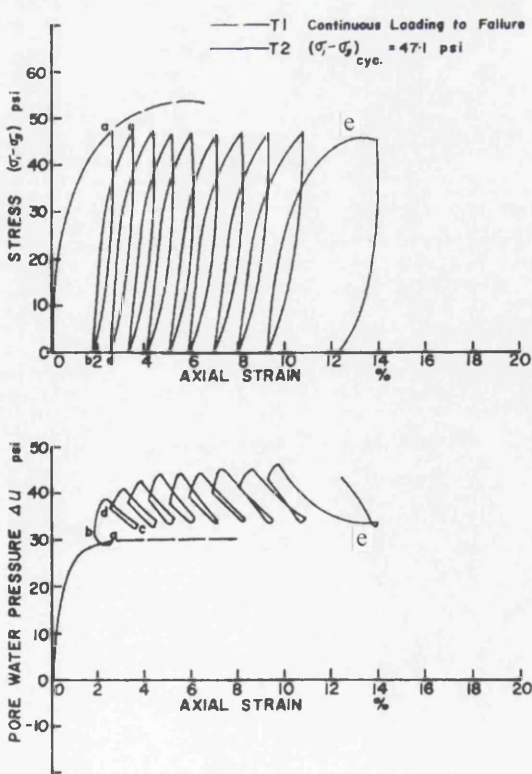


Figure 2.4 Undrained cyclic loading resulting in failure (Sangrey *et al.*, 1969).

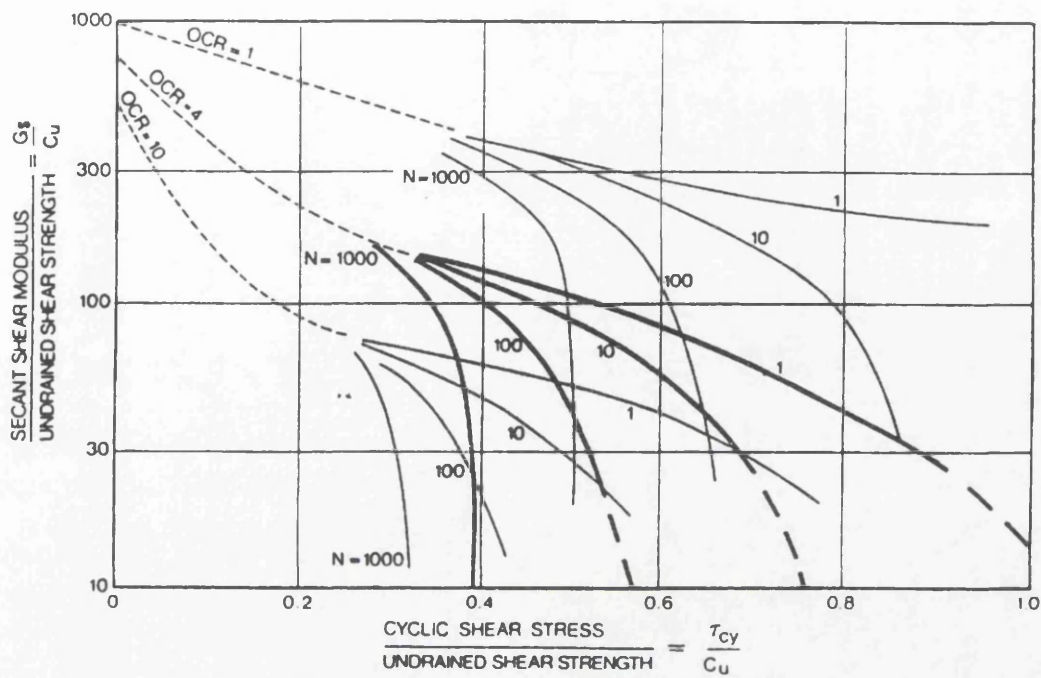


Figure 2.5 The effect of cyclic loading on undrained shear strength and secant shear modulus (Andersen *et al.*, 1982).

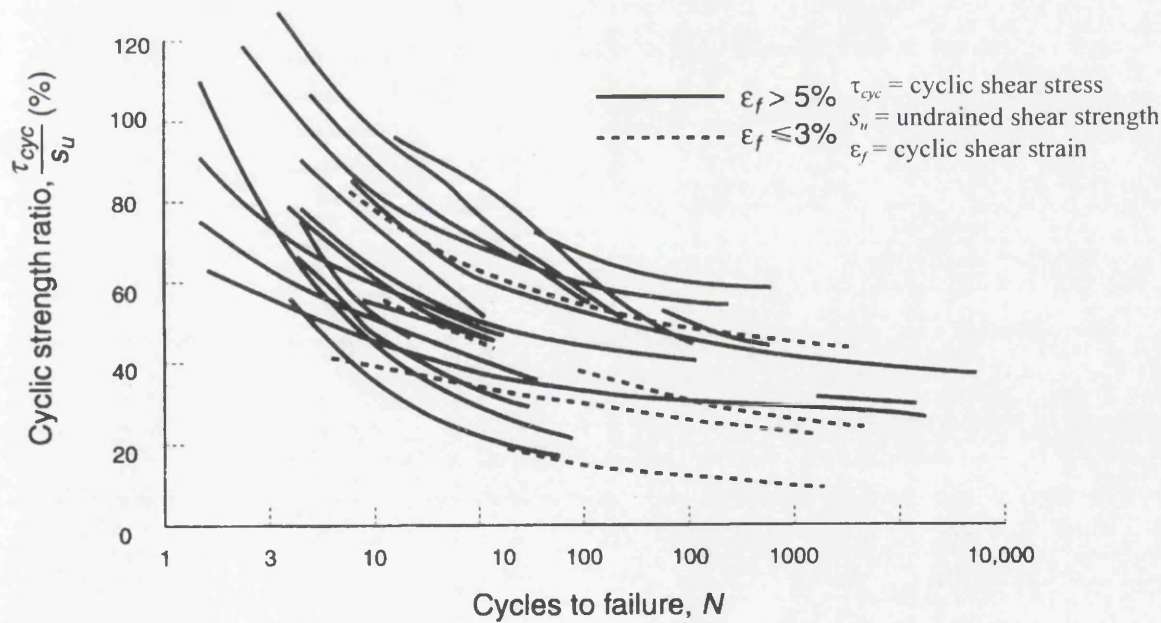


Figure 2.6 The effect of cyclic loading on cyclic strength ratio (Lee and Focht, 1976).

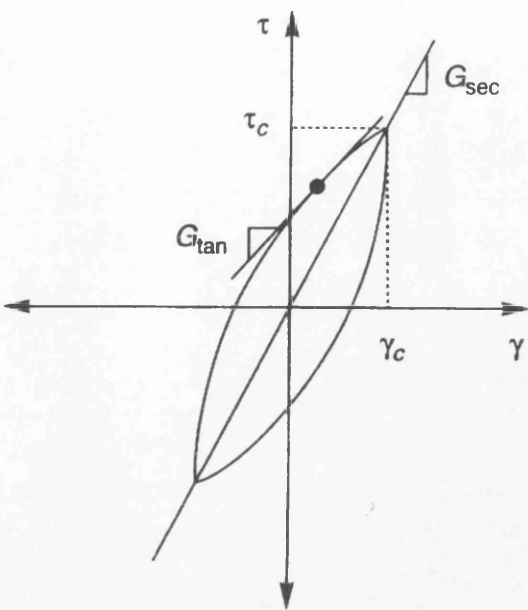


Figure 2.7 Typical stress-strain behaviour of a clay subjected to symmetric cyclic loading (Kramer, 1996).

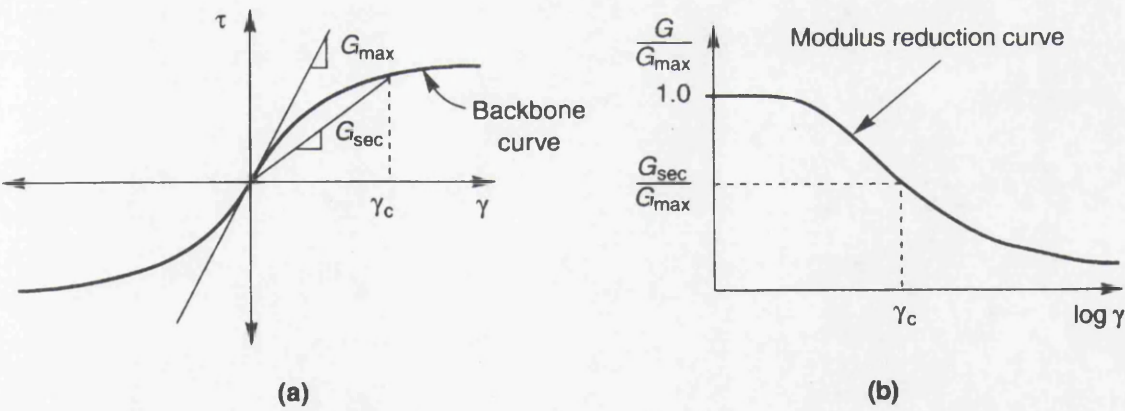


Figure 2.8 Backbone curve showing effect of shear strain on secant modulus G_{sec} (Kramer, 1996).

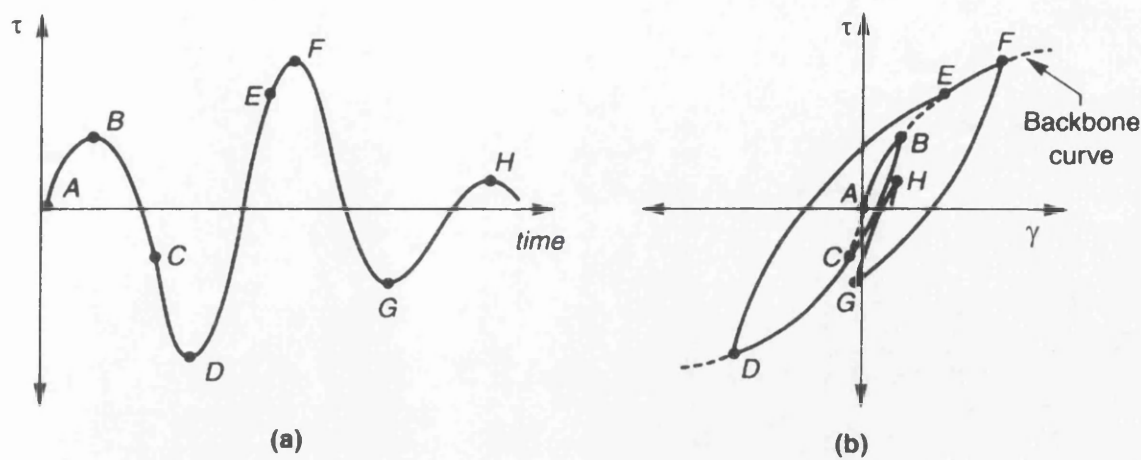


Figure 2.9 (a) Shear stress variations and (b) resulting stress-strain behaviour (Kramer, 1996).

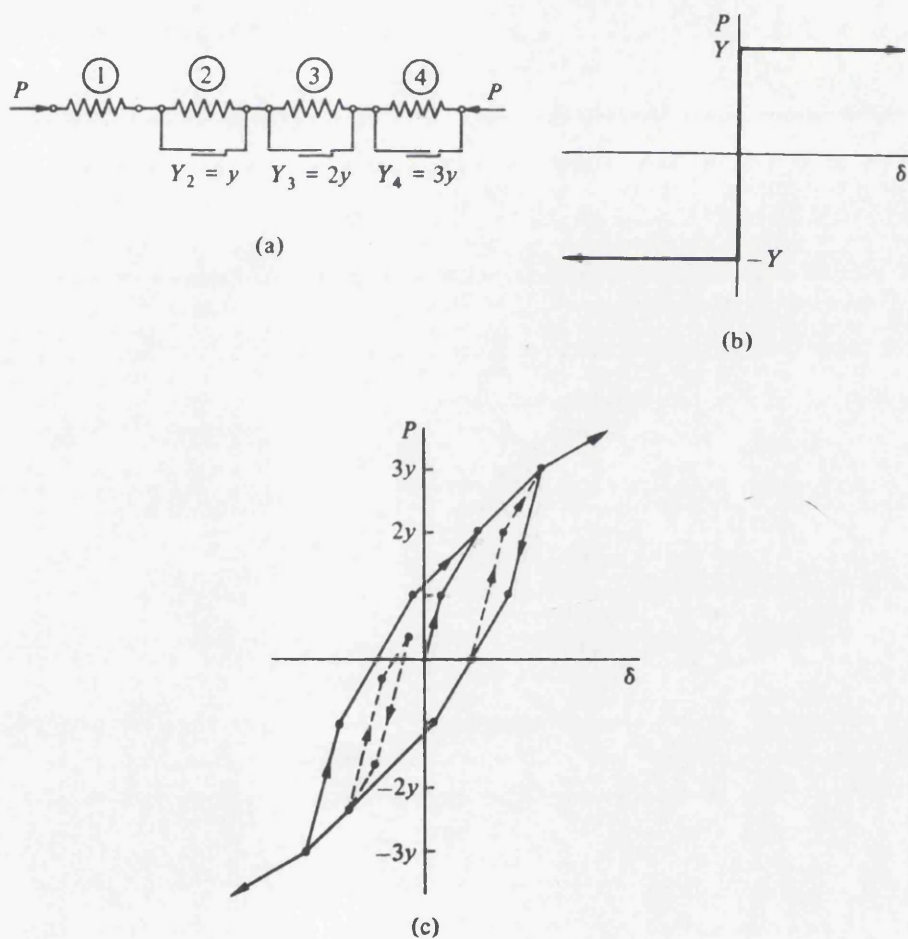


Figure 2.10 (a) Chain of parallel springs and slider elements, (b) load-displacement response of slider and (c) load-displacement response of chain of parallel springs and slider elements (Wood, 1994).

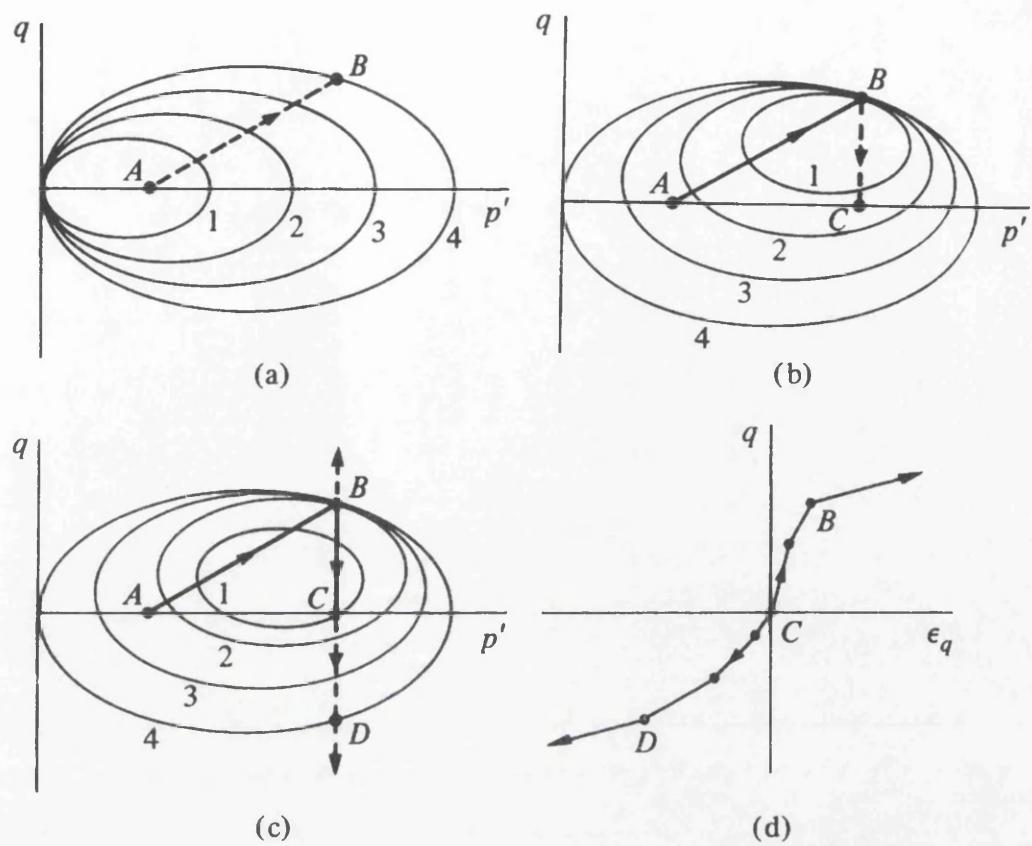


Figure 2.11(a) Initial position of nested yield surfaces, (b) position of yield surfaces after stress path AB , (c) position of yield surfaces after stress path ABC and (d) stress-strain response in triaxial compression CB and extension CD (Wood, 1994).

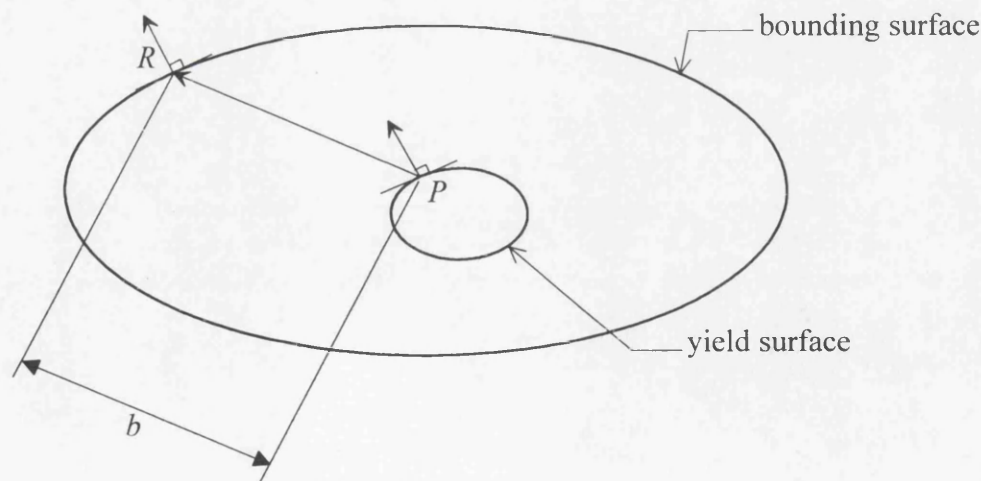


Figure 2.12 Yield and bounding surfaces in stress space.

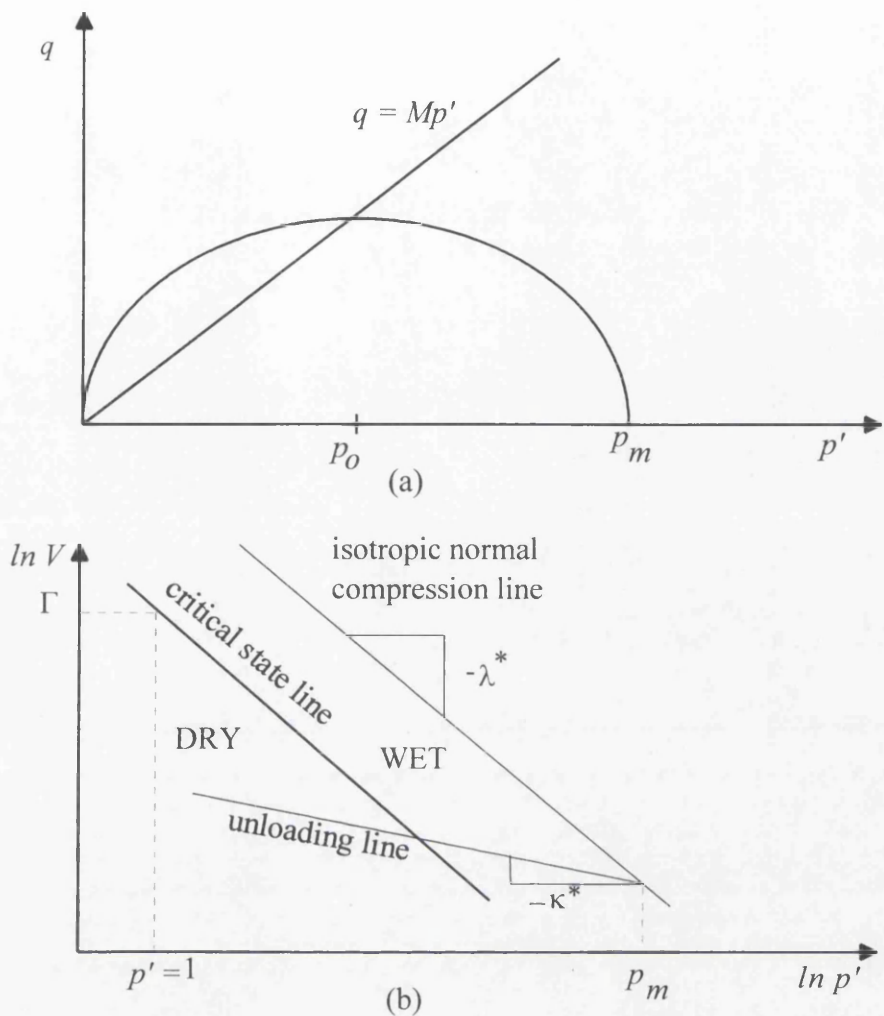


Figure 2.13 The Modified Cam clay model in (a) q - p' stress plane and (b) $\ln V$ - $\ln p'$ space.

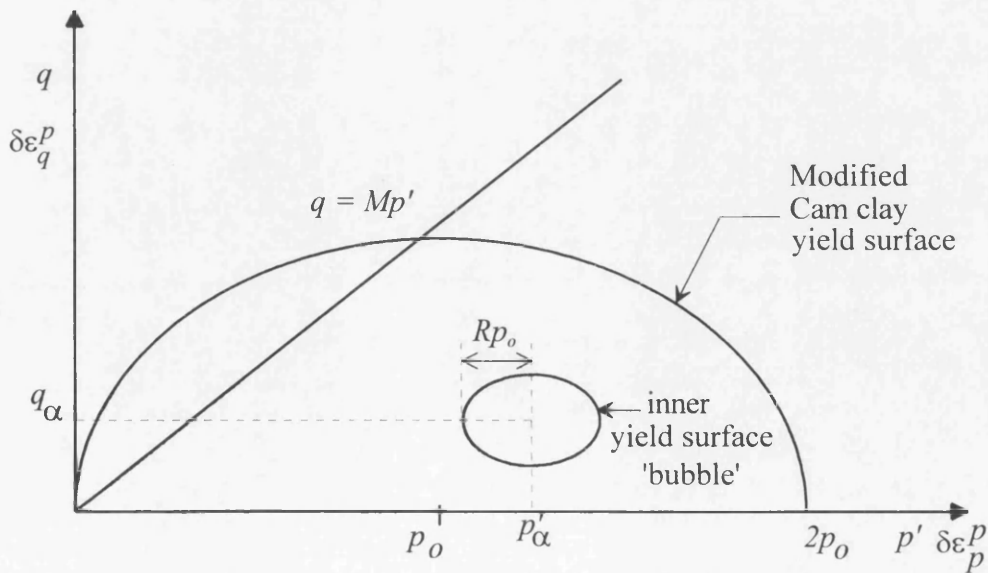


Figure 2.14 General layout of the bubble model.

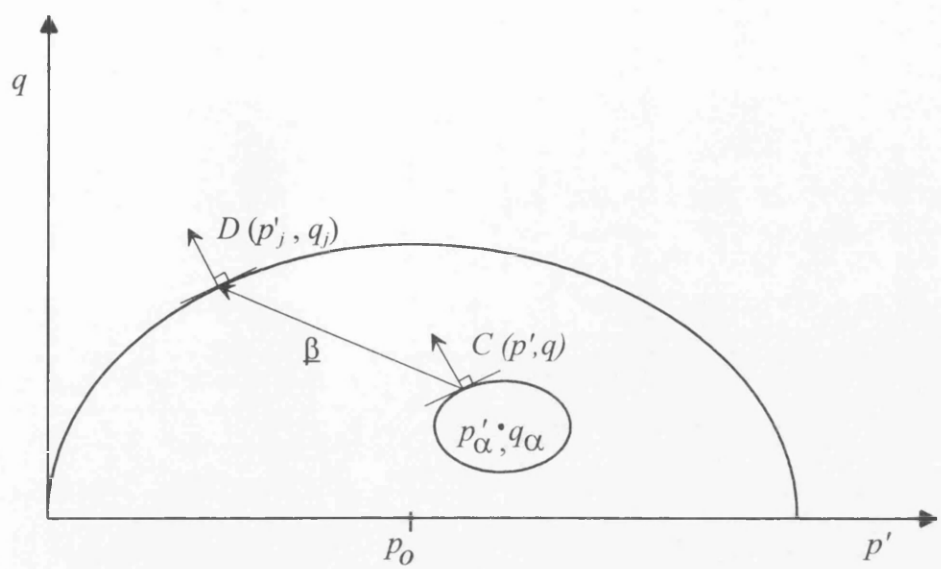


Figure 2.15 Assumed motion of the bubble yield surface within the Modified Cam clay (MCC) yield surface along the vector β .

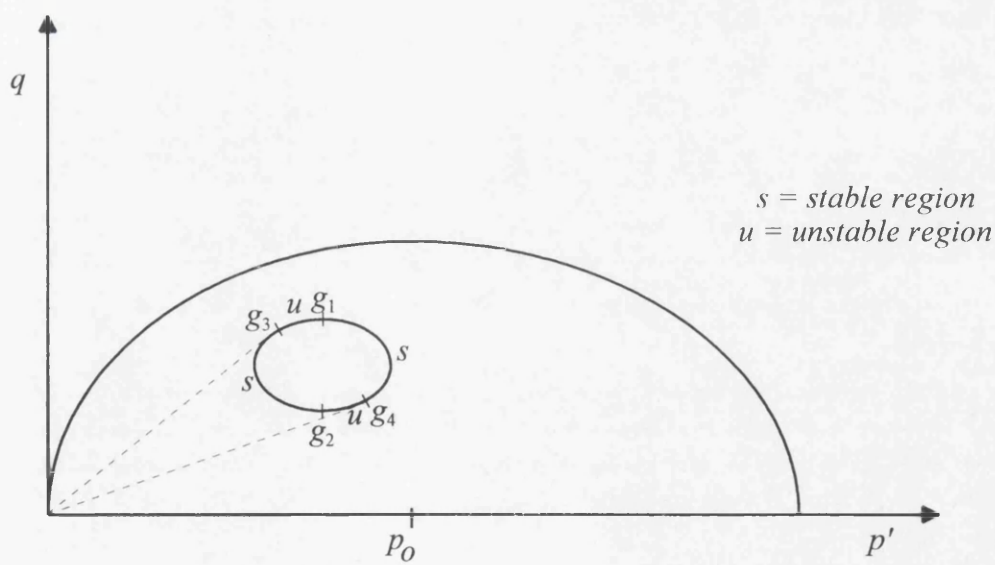


Figure 2.16 Diagram showing singularity points, stable and unstable regions on the bubble yield surface.

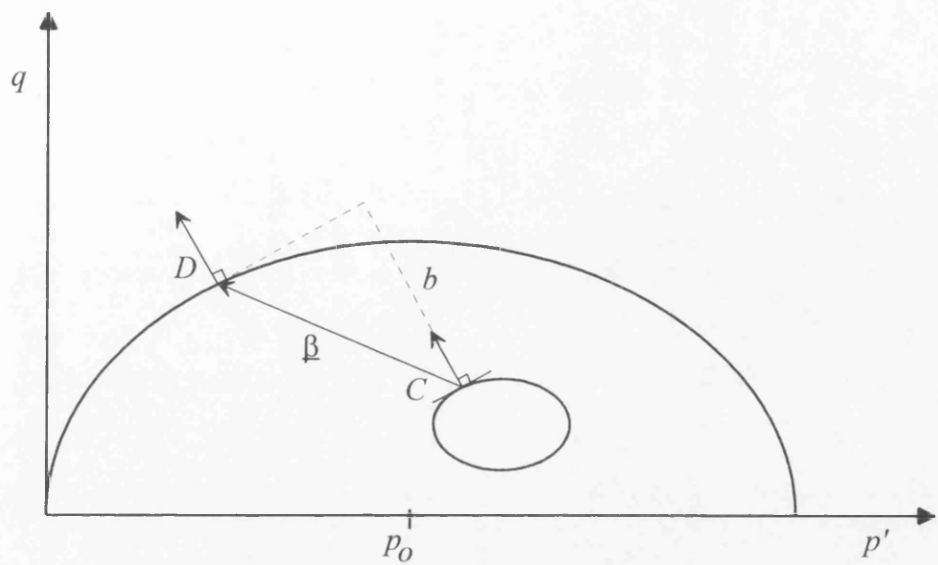
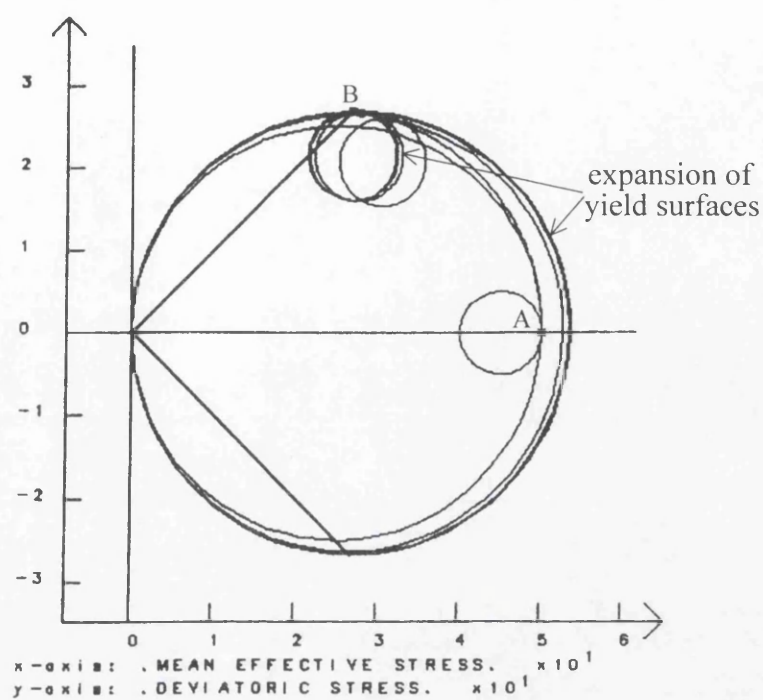
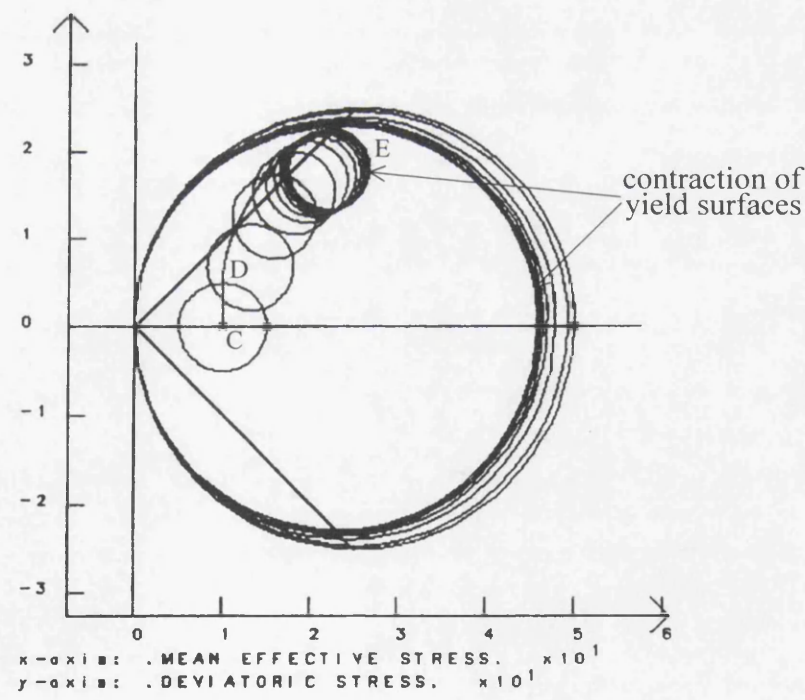


Figure 2.17 Definition of the vector β and the distance b .



(a)



(b)

Figure 2.18 Predicted relative motion of bubble and MCC yield surfaces for (a) normally consolidated clay and (b) overconsolidated clay, subjected to an undrained test.

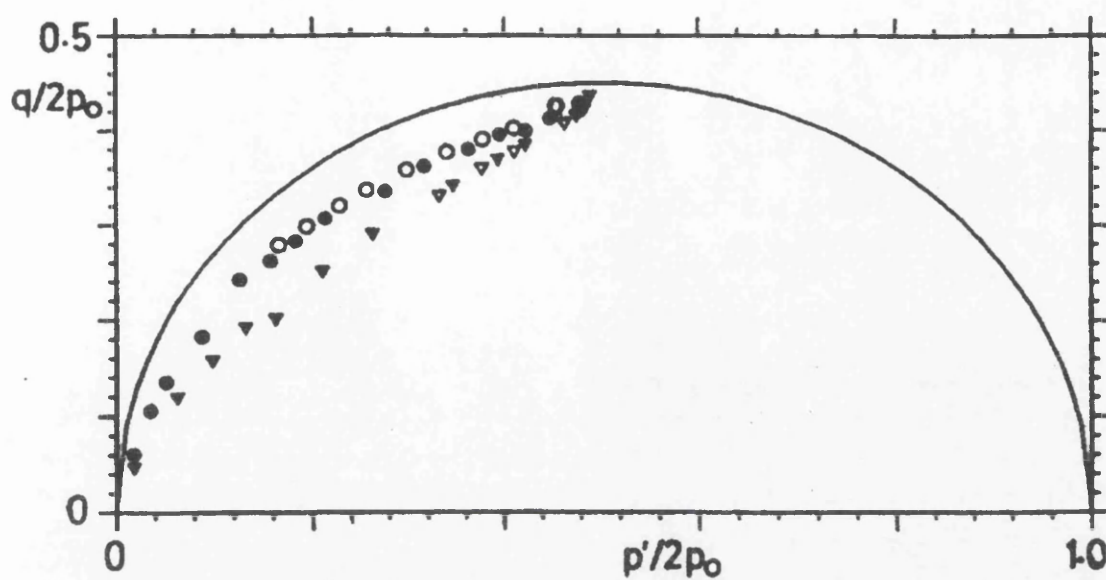


Figure 2.19 Failure points: \blacktriangledown isotropic undrained; \bullet isotropic drained; ∇ one-dimensional undrained; \circ one-dimensional drained (Al-Tabbaa and Wood, 1989).

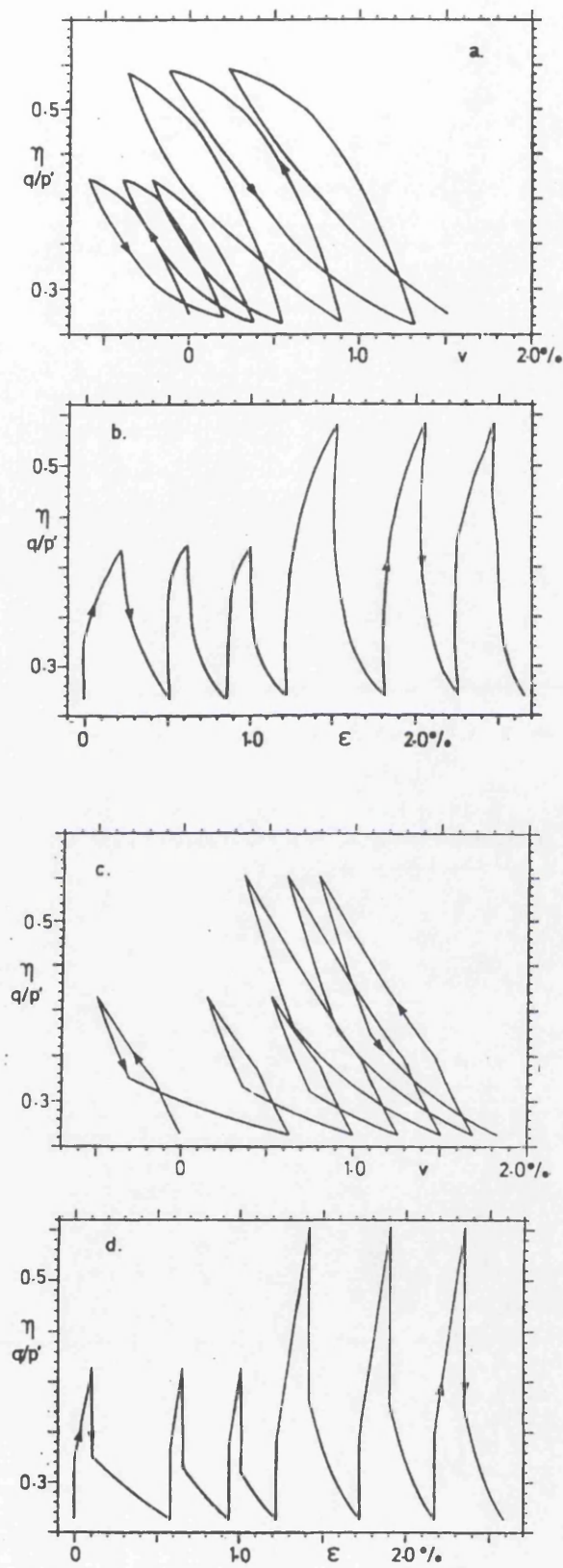


Figure 2.20 Constant q cycles: experimental observations of (a) volumetric strains and (b) shear strains; model predictions of (c) volumetric strains and (d) shear strains (Al-Tabbaa and Wood, 1989).

CHAPTER 3

Plane-Strain Finite Element Analyses

3.1 Summary

3.2 Introduction

3.3 Finite element packages

3.3.1 SWANDYNE

3.3.2 OASYS

3.4 Idealised model

3.4.1 Boundary conditions

3.4.2 Cyclic loading conditions

3.5 Maximum load and undrained shear strength

3.6 Mesh details

3.6.1 Mesh discretisation

3.7 Convergence study

3.7.1 SWANDYNE analysis

3.7.2 OASYS analysis

3.8 Parametric studies

3.8.1 The effect of soil strength parameter M

3.8.2 The effect of soil parameter R

3.8.3 The effect of soil parameter ψ

3.8.4 The effect of soil Poisson's ratio (ν)

3.8.5 The effect of soil parameters λ^* and κ^*

3.8.6 The effect of load level

3.8.7 The effect of overconsolidation ratio

3.9 SWANDYNE analysis and results

3.9.1 Fully bonded case

3.9.1.1 Comparisons of models' predictions

3.9.2 Half-debonded case

3.9.2.1 Comparisons of models' predictions

3.10 OASYS analysis and results

3.11 Boundary conditions review

3.12 Discussion of results

3.13 Concluding remarks

CHAPTER 3

Plane-Strain Finite Element Analyses

3.1 Summary

In this Chapter, pile foundations subjected to cyclic lateral loading are modelled using the finite element method under plane-strain conditions. The effect of the boundary conditions on the finite element predictions was examined and a convergence study was undertaken to determine the optimum number of load increments required to obtain results of good accuracy with minimum computational cost. Two different soil models, namely, the 'bubble' model and Mohr-Coulomb model, were employed in the finite element analyses in order to examine the interaction between pile and soil behaviour when subjected to cyclic loading.

3.2 Introduction

The primary objective of carrying out the two-dimensional finite element analyses described in this Chapter was to evaluate the implications of adopting advanced constitutive soil models for this complicated cyclic loading problem. This was intended to shed light on the detailed pile and soil behaviour, in particular at the pile-soil interface, and to provide insights for the development of the three-dimensional program APILEC, which employs a simpler soil model.

Although, it is now possible to perform fully three-dimensional finite element analyses for pile foundation problems (Brown and Shie, 1990, 1991; Bijlagte *et al.* 1991 among others), such analyses demand computer resources far beyond that which were available for this project.

For piles subjected to cyclic lateral loads, the horizontal displacements always dominate the deformation field; the vertical displacements are not very significant and can therefore be ignored. These assumptions allow modelling of pile foundations subjected to cyclic lateral loading as a two-dimensional plane-strain problem (horizontal section of the pile and soil in plan view) as shown in Figure 3.1. The pile-soil system can be subdivided

into a number of horizontal layers, as illustrated in Figure 3.2. For these layers, an elasto-plastic soil model can be employed for the analyses.

Two finite element packages, namely SWANDYNE and OASYS, were employed to predict pile behaviour under cyclic lateral loading.

3.3 Finite element packages

The finite element program SWANDYNE was chosen because it contains the cyclic soil model developed by Al-Tabbaa and Wood (1989) (known as the 'bubble' model described in Section 2.5); this model is not available in OASYS. Furthermore, cyclic (sinusoidal) loading conditions are also available. To compare with the predictions using the bubble model, the elastic-perfectly plastic Mohr-Coulomb model for soil was employed.

The OASYS finite element program was used to check the results obtained from the SWANDYNE analyses.

3.3.1 SWANDYNE

DIANA-SWANDYNE II is the acronym of Dynamic Interaction and Non-linear Analysis - SWANsea DYNamic version II, developed by Chan (1990). It is a two-dimensional program which incorporates plane-strain and axi-symmetric analyses. The program uses the Finite Element method with triangular and quadrilateral isoparametric elements in the spatial domain. The time integration is done using the Generalised Newmark method. Both the tangential stiffness method and the Quasi-Newton method are available for non-linear iterations. The program can deal with static, consolidating and dynamic conditions under drained and undrained conditions.

3.3.2 OASYS

The OASYS-SAFE (OASYS, 1991) finite element program was developed for the analysis of two-dimensional plane-stress, plane-strain, or axi-symmetric geotechnical problems. The elements available are 4-, 8- and 12-node isoparametric quadrilateral elements. Non-linear problems are dealt with by the 'initial stress' technique. The loading is applied incrementally. The sequences of cyclic loading can be divided into the loading and unloading stages.

3.4 Idealised model

The two-dimensional plane-strain model is shown in Figure 3.2. Taking advantage of the symmetry conditions, only half of the plane was modelled.

3.4.1 Boundary conditions

The boundary at *A* and *C* (see Figure 3.3) is assumed to be restrained by rollers, allowing displacements only in the *y-y* direction. The displacements beyond the 15 pile diameters in the *x-x* direction will not be significant, and can therefore be ignored. Due to the symmetry boundary condition, the boundary at *D* is assumed to be restrained by rollers, restricting displacements only in the *x-x* direction. The boundary at *B* is unrestrained, allowing the displacements of soil in the *x-x* and *y-y* directions during loading. The load is applied at the centre of the pile, at point *E*.

3.4.2 Cyclic loading conditions

One-way and two-way cyclic loading depicted in Figure 3.4 was used for SWANDYNE analysis. A period of ten seconds per cycle was adopted following Rao *et al.* (1992), Rao and Rao (1993) and Andersen *et al.* (1980). The design environmental condition for offshore works based on a 100 year wave has a period of around ten seconds (Tomlinson, 1994).

For OASYS analysis, the loading was applied in stages to simulate cyclic loading; see Figure 3.5.

3.5 Maximum load and undrained shear strength

The analyses are based on undrained loading conditions. The maximum lateral load was taken to be:

$$H_{max} = N_c C_u D \quad (3.1)$$

where N_c is the bearing capacity factor, depending on pile depth,

C_u is the undrained shear strength, and

D is the pile diameter.

For simplicity, N_c of ten is used (unless otherwise stated), indicating that the analysis is applicable for depths greater than $3D$ (Poulos and Davis, 1980; Tomlinson, 1994).

In the absence of undrained shear strength for normally consolidated clay, field data (Mersi, 1975; Larsson, 1980; Trak *et al.*, 1980; Wood, 1994) suggests a linear relationship between undrained shear strength and vertical effective stress, i.e.

$$C_u = 0.25 \sigma'_z \quad (3.2)$$

where σ'_z is the vertical effective stress.

The C_u value can be determined from the Modified Cam clay (MCC) model. The equation for the MCC yield surface is:

$$p'^2 - p'p_m + \frac{q^2}{M^2} = 0 \quad (3.3)$$

where p' is the mean effective stress,

p_m is the preconsolidation pressure,

q is the deviator stress, and

M is a function of the angle of shearing resistance.

The preconsolidation pressure can be expressed as:

$$p_m = N_p p' \quad (3.4)$$

where N_p is the overconsolidation ratio.

Coupling Equations (3.3) and (3.4), the deviator stress (for $N_p > 2$) becomes:

$$q = \frac{M}{N_p} p_m (N_p - 1)^{0.5} \quad (3.5)$$

Under isotropic condition, $p' = \sigma'_z$ and taking $C_u = q/2$, the undrained shear strength as a function of the overconsolidation ratio is:

$$C_u = 0.5 \sigma'_z M (N_p - 1)^{0.5} \quad (3.6)$$

This result is reasonable valid provided that the yield surface lies below the tension cut-off . The tension cut-off line ($q = 3p'$) is depicted in Figure 3.6. Combining this with Equations (3.4) and (3.5) gives:

$$N_p = 1 + \frac{9}{M^2} \quad (3.7)$$

The slope of the critical state line for a typical clay, ranges from 0.8 to 1.2 (corresponding to the angle of shearing resistance of 20° to 30° for clay), therefore the critical value of N_p will be around ten. For the purpose of this project, N_p up to eight are employed.

3.6 Mesh details

For the SWANDYNE analyses, eight-noded isoparametric quadrilateral elements were used to model the soil and the pile, while six-noded triangular isoparametric elements were used to model the inner core of the pile; see Figure 3.7a. The mesh consists of a total of 84 elements. The mesh adopted is shown in Figure 3.7a.

For the OASYS analyses, the same type of elements were used to model the pile and the soil, except that the inner core of the pile was deleted (Figure 3.7b) as OASYS does not provide a triangular element option. This meant that the pile was modelled as a hollow pile. This option should not affect the results as the pile elements were assumed to be very stiff.

3.6.1 Mesh discretisation

Based on a set of soil and pile parameter values, one-way cyclic loading was applied to the centre of the pile. A fully bonded pile-soil interface is assumed, i.e. the displacements of the pile and the soil are fully connected in all directions at the interface, and therefore displace equally.

The boundary was fixed at 30 pile diameters (D) and 15 pile diameters for the length and width of the mesh, respectively, after some experimentations; see Figures 3.7 and 3.8. Figure 3.8 shows the displacements (in the x - x direction) of the nodal points along the symmetric plane under the specified maximum load. It is observed that the largest displacement occurs at the pile-soil interface, and it decreases till the specified boundary is reached. Extending the length and breadth of the mesh (with additional elements) increases the computational cost without significant change to the results.

3.7 Convergence study

A convergence study using a simple mesh (Lee, 1995) assuming the fully bonded case was carried out. Typical load-displacement response of the pile (pile-soil interface) is depicted in Figure 3.9.

In this study, the number of load increments per cycle employed are 4, 10, 20, 40 and 100. Using these load increments, the maximum pile (pile-soil interface) displacements at the end of the five cycles were determined. Cyclic loads of 75 kN, 150 kN and 225 kN (arbitrarily chosen) with tolerances (i.e. convergence criteria) of 0.05 and 0.005, were used. The computational time required (based on an IBM-compatible 80486 DX2-66 computer) for these analyses were examined to assess the optimum number of load increments and tolerances for further analyses.

3.7.1 SWANDYNE analysis

A set of soil parameters was used for the bubble model. One hundred load increments per cycle was assumed to be the exact solutions for respective tolerances of 0.05 and 0.005. Using the maximum pile displacements for the fifth cycle, Figure 3.10 shows that reducing the number of load increments from 100 to 40, (20, 10, 4) for tolerance of 0.005, causes the displacements to be underestimated by 1%, (2%, 3%, 4%) for load of 75 kN, 2%, (4%, 7%, 11%) for load of 150 kN, and 5%, (8%, 12%, failure to converge) for load of 225 kN. For tolerance of 0.05, the underestimation is 3%, (7%, 11%, 21%) for load of 75 kN, 10%, (18%, 25%, 36%) for load of 150 kN, and 15%, (24%, 31%, 43%) for load of 225 kN. The above results (judging from the amount of underestimation) show that convergence to the exact solution is achieved with the use of a higher number of load increments and smaller

tolerances. For higher load levels, say 225 kN, the number of load increments used has greater effect on the displacement results, especially for tolerance of 0.05.

The times taken to execute the program for different load levels are depicted in Figure 3.11. It is shown that the computational time increases with the increase in both the load increments and the tolerances, except for the case of 4 and 10 load increments using tolerance of 0.005. The use of small load increments, say 4 and 10, cause the computational time to increase because of the increase in the number of iterations required to converge to the tolerance of 0.005, see Figure 3.11.

The displacement results, computational time, and the relative errors (defined as $\left(\frac{\text{exact value} - \text{predicted value}}{\text{exact value}} \right)$) for different load levels were tabulated in Tables 3.1 and 3.2 for tolerances of 0.05 and 0.005, respectively. The relative errors plotted against the number of load increments depicted in Figure 3.12, show that the relative errors reduced with the increase in the number of load increments. It is clearly shown that the relative errors for tolerance of 0.05 are considerably larger as compared with tolerance of 0.005 at the same number of load increments and load levels.

Assuming a maximum relative error of 10 % is acceptable in design, 20 and 40 load increments with tolerance of 0.005 were considered. From the computational (time) point of view, it is suggested that twenty load increments per cycle is probably the optimal choice.

3.7.2 OASYS analysis

For OASYS analyses, ten load increments with 5 and 10 iterations were used to compare their results with the SWANDYNE analyses (using Mohr-Coulomb model for soil and elastic model for pile). The comparison is deferred to Section 3.10.

3.8 Parametric studies

Parametric studies were carried out to examine the influence of the soil parameters on the pile and soil behaviour under cyclic loading conditions. The parametric studies were conducted at a depth of 5 m. Pile and soil are assumed to be fully bonded at their interface. The bubble model and elastic model were employed for the soil and pile, respectively. The details of the pile and soil data (unless stated otherwise) used in these parametric studies are:

Pile diameter (D)	= 1.0 m
Pile Young's modulus (E_p)	= 200 GPa

Pile Poisson's ratio (ν_p)	= 0.3
Soil Type	= Normally consolidated
Buoyant soil unit weight (γ)	= 10 kN/m ³
Undrained shear strength (C_u)	= 12.5 kPa (from Equation (3.2))
Bearing capacity factor (N_c)	= 10
Maximum cyclic load (H_{max})	= 125 kN (from Equation (3.1))

The details of the parameters (unless otherwise stated) for the bubble model are as follows:

M (slope of the critical state line)	= 1.0
R (ratio of the sizes of the bubble yield surface and the MCC yield surface)	= 0.2
ψ (exponent in the hardening function)	= 1.5
ν (Poisson's ratio)	= 0.2
λ^* (slope of the normal compression lines)	= 0.2

In addition, κ^* (initial slope of the unloading lines) is taken as $0.1 \lambda^*$.

One-way cyclic loading of five cycles was applied at the centre of the pile. Only the nodal maximum and residual displacements in the x - x direction along the symmetric plane at the fifth cycle will be reported. To avoid massive parametric studies to be conducted, only one parameter will vary at a time, while the others remain constant. This will help in evaluating the sensitivity of the particular parameter.

3.8.1 The effect of soil strength parameter M

The soil strength parameter (M) is taken as a function of the angle of shearing resistance, which is related to the shear strength of the soil. The higher the value of M , the greater the strength of the soil will be. For this study, M of 0.8, 1.0 and 1.2 were considered. Figure 3.13 clearly illustrates that the reducing M from 1.2 to 1.0, (0.8) increases the maximum pile (pile-soil interface) displacements by 1.7 times, (3.8 times) and residual pile displacements by 3.6 times, (6.0 times). The effect of M is greater for residual displacements than for maximum displacements. It is observed in Figure 3.13 that soil at two pile diameters away from the pile face is not greatly influenced by the loading as reflected by the steep drop in the soil displacements. Comparing the displacement results at a distance of 0.5 m (pile-soil interface) and 2.5 m from the centre of the pile, reduction in displacements averaging 3.3

times and 5 times were accounted for maximum and residual displacements, respectively, for all values of M . Figure 3.13 has indicated that the soil after seven pile diameters from the pile face is not sensitive to the parameter M as the difference in displacement results is minimal. Note that the assumption of fully bonded case has caused the nodal displacements along the symmetric plane to produce a 'mirror' image, with similar displacements experienced on both sides (left and right) of the pile.

3.8.2 The effect of soil parameter R

The ratio of the size of the bubble yield surface to the Modified Cam clay (MCC) yield surface, is defined by the parameter R . Increase in R will increase the magnitude of the elastic region of the soil. As such, one can expect a reduction in displacement as less soil yielding is taking place. For this study R of 0.2, 0.3 and 0.4 were considered. Figure 3.14 shows that increasing R from 0.2 to 0.3, (0.4) results in a reduction in maximum pile displacements by 21%, (45%) and residual pile displacement by 27%, (57%). The effect of R is greater for residual displacements than for maximum displacements. It is shown in Figure 3.14, that the soil at two pile diameters away from the pile face is not greatly influenced by the load as observed by the steep decline in displacement results. It is observed that the soil after five pile diameters away from the pile face is not affected by the change in R values.

3.8.3 The effect of soil parameter ψ

For the purpose of this parametric study, the exponent in the hardening function (ψ) of 1.0, 1.5 and 2.0 were used. The results depicted in Figure 3.15 show that increase in ψ results in the increase of both the maximum and residual displacements. This is due to the fact that increases in ψ will reduce the hardening function (h) in Equation (2.16), thus causing an increase in the plastic strain increments. The amount of increase in pile displacements when ψ increases from 1.0 to 1.5, (2.0) is 1.4 times, (2.0 times) for maximum displacements, and 1.8 times, (2.8 times) for residual displacements. The effect of ψ is greater for residual displacements than for maximum displacements. It is shown in Figure 3.15 that the effect of ψ after five pile diameters away from the pile is negligible.

3.8.4 The effect of soil Poisson's ratio (ν)

Poisson's ratio (ν) describes the ratio of the strain in the lateral direction to the strain in the vertical direction during the elastic response to the imposed change of stress. Therefore, increase in ν will increase the lateral displacement. In this study, ν of 0.2, 0.3 and 0.4 were employed. Figure 3.16 shows that increasing ν from 0.2 to 0.3, (0.4) causes an increase in maximum pile displacements by 25%, (92%) and residual pile displacements by 14%, (38%). The effect of ν is greater for maximum displacements than for residual displacements. Figure 3.16 also indicates that the maximum displacements of the soil are still influenced by ν after seven pile diameters away from the pile, unlike the parameters M , R and ψ , where the soil displacements are not affected.

3.8.5 The effect of soil parameters λ^* and κ^*

The slope of the normal compression line (λ^*) and the initial slope of the unloading line (κ^*) in the $\ln V$ - $\ln p'$ compression plane, indicate the specific volume of the soil. The higher the λ^* and κ^* values (at the same effective stress), indicate that the soil is more loosely packed, i.e. more compressible. For this study, λ^* of 0.1, 0.2, and 0.4, and corresponding κ^* of $0.1\lambda^*$ were considered. In Figure 3.17, it is shown that increasing λ^* from 0.1 to 0.2, (0.4) results in the increase in both the maximum and residual pile displacements by 2 times, (4 times). This indicates that increasing λ^* and corresponding κ^* by some factors (say 5 times), the maximum and residual pile displacements will increase by the same factors (i.e. 5 times). It is shown in Figure 3.17, that the maximum displacements of the soil are still influenced by λ^* and κ^* after seven pile diameters away from the pile.

3.8.6 The effect of load level

Loads of 100, 125 and 150 kN (0.8, 1.0 and 1.2 times of the maximum load H_{max}) were considered in this study. The displacement results depicted in Figure 3.18, show that an increase in the load levels, will cause an increase in both the pile and soil displacements. This is due to the fact that a greater number of soil elements yielding are taking place at higher load levels. Increasing the load of 125 kN by 1.2 times (i.e. 150 kN) has increased the maximum and residual pile displacements by 86% and 110%, respectively. Decreasing the load from 125 kN by 0.8 times (i.e. 100 kN), reduces the maximum and residual pile displacements by 50% and 59%, respectively. The effect of load level is greater for residual displacements than for maximum displacements. It is indicated in Figure 3.18, that the effect

of load level on the maximum displacements of the soil after seven pile diameters away from the pile are negligible.

3.8.7 The effect of overconsolidation ratio

Values of overconsolidation ratio (OCR) of 1, 4 and 8 were employed in this study. The preconsolidation pressure of the soil for OCR 4 and 8 are set to 200 and 400 kPa, respectively, while maintaining the initial effective stress of 50 kPa. The results depicted in Figure 3.19, show that an increase in OCR results in the reduction of both the pile and soil displacements. This is because the soils were consolidated to a past maximum effective stress of 200 and 400 kPa, and will naturally result in a denser packing than soil that is being consolidated to an effective stress of 50 kPa. Hence, its resistance to loading is higher, thereby giving a lower displacement. Increasing OCR from 1 to 4, (8) reduces the maximum pile displacements by 78%, (79%) and the residual pile displacements by 98%, (100%). The effect of OCR is greater for residual displacements than for maximum displacements. Increasing OCR from 4 to 8 has not much effect on displacements, because the soil at OCR of 4 might be close to its densest state to resist the load of 125 kN. Therefore further increase in OCR will only result in a further small decrease in displacements of less than 2%. It is observed that the effect of OCR on the maximum displacements of the soil after seven pile diameters away from the pile are negligible (Figure 3.19).

3.9 SWANDYNE analysis and results

From the parametric studies, it can be seen that the bubble model does give qualitatively reasonable predictions. The following analyses will be based on applying the maximum load (H_{max}) at the centre of the pile, and observing the maximum and residual displacements (in the x - x direction) of the pile and soil at their interface (along the symmetric plane). Information from the parametric studies has shown that it is not necessary to examine the soil elements further away from the pile, as the displacements are much less than the displacements at the pile-soil interface.

To simulate gap formation around the cyclic laterally loaded pile (see Figure 3.1), many researchers like Yegian and Wright (1973), Kooijman (1989a, 1989b), Desai and Appel (1976), Trochanis *et al.* (1991), Bhowmik and Long (1991) and Bijnagte *et al.* (1991) had modelled the pile-soil interface by an interface element. Unfortunately, the option for the

interface element is not available for the two finite element packages employed, hence recourse is made by assuming a 'half-debonded' case. The half-debonded case is to take account of the gap formation at the back of the advancing pile subjected to one-way cyclic loading. For this study, a fully bonded case and a half-debonded case are analysed, using the bubble model and the Mohr-Coulomb model. Typical pile and soil responses for these cases are illustrated in Figure 3.20.

The following analyses were carried out using the pile and soil data mentioned in Section 3.8, except that the undrained shear strength (C_u) and the bearing capacity factor (N_c) are now taken as 20 kPa and 9, respectively.

3.9.1 Fully bonded case

The fully bonded case is assumed where there is no relative displacement between the pile and the soil, i.e. pile and soil at their interface displacing at the same magnitude. No slippage or gap formation (pile-soil separation) is taken into account.

Bubble model predictions

The six soil parameter values required for the bubble model mentioned in Section 3.8 are taken as follows: $M = 1.0$, $R = 0.2$, $\psi = 1.5$, $\nu = 0.3$, $\lambda^* = 0.08$ and $\kappa^* = 0.008$. These values are chosen based on experimental tests conducted by Al-Tabbaa (1987). With C_u of 20 kPa, a maximum load (H_{max}) of 180 kN is determined from Equation (3.1). The results depicted in Figure 3.21, show that the maximum and residual pile (pile-soil interface) displacements were of the order of 150 mm and 120 mm, respectively, at the end of the fifth cycle. This is rather high (around 15% of the pile diameter), and hence, it is decided to reduced the H_{max} load by 50%. With H_{max} of 90 kN, a significant reduction in maximum and residual displacements is observed in Figure 3.22, giving maximum and residual pile displacements of 20 mm and 8 mm, respectively, at the end of the fifth cycle. This is a reduction of approximately 8 times and 15 times, respectively, when compared with H_{max} of 180 kN. This is due to the high plasticity involved within the soil under a load of 180 kN as compared with a load of 90 kN, where lots of soil elements would have yielded.

Mohr-Coulomb model predictions

For the Mohr-Coulomb model, the soil Young's modulus (E_s), undrained shear strength (C_u) and Poisson's ratio (ν) are taken to be 20 MPa, 20 kPa and 0.49 (undrained loading), respectively. Under H_{max} of 180 kN, the maximum and residual pile displacements at the end of the fifth cycle are 8.5 mm and 0.5 mm, respectively; see Figure 3.23. The Mohr-Coulomb model predicts an elastic pile response for loads up to 120 kN, after which, surrounding soil elements begin to yield. This is indicated by the change in gradient (point *A*) shown in Figure 3.23. Eventually, the pile stabilised to a shakedown response with a residual displacement of 0.5 mm.

3.9.1.1 Comparisons of models' predictions

Since different models are used in the analyses, one can expect differences in the predictions. For the bubble model, which is developed for cyclic loading, greater soil yielding can be anticipated (compare with the Mohr-Coulomb model) as the elastic region of the soil is only within the size of the bubble (Figure 2.14). Hence, a large amount of displacements and greater non-linearity can be observed; compare Figures 3.21 and 3.22 with Figure 3.23.

Using the Mohr-Coulomb model, the pile response is linearly elastic for loads below 120 kN, which subsequently shows signs of soil yielding. During unloading, the pile shows an almost linear elastic response and eventually shakedown. This is a large contrast, to the pronounced yielding of the soil and the progressive increase in pile displacements with cycling for the bubble model; compare Figures 3.21 and 3.23.

With further cycling, the bubble model shows that the areas between the reloading and unloading curves are reducing (Figure 3.21), indicating the amount of plastic work on the soil per cycle are progressively decreasing. Figure 3.21 also shows that the cyclic degradation (i.e. increase in maximum displacements with cycling) is reducing. Using the Mohr-Coulomb model (Figure 3.23), the pile has stabilised to an elastic response (shakedown) after the first cycle, indicating that no further plastic work is done on the soil.

Under H_{max} of 180 kN, it is observed that the bubble model gives much higher maximum and residual pile displacements as compared with the Mohr-Coulomb model. At the end of the fifth cycle, a difference of 18.2 times for maximum pile displacement and 200.5 times for the residual pile displacement is observed. Reducing H_{max} to 90 kN for the bubble model, the pile displacement differences between the Mohr-Coulomb model is

reduced, with an overestimation of maximum and residual pile displacements of 2.4 times and 14 times, respectively.

3.9.2 Half-debonded case

The left side of the soil was debonded from the pile (i.e. pile and soil nodes are not linked; see Figure 3.20c). This interface will be described as debonded interface. The right side of the pile remains bonded to the soil (i.e. pile and soil nodes are linked), and is described as bonded interface. The debonding and bonding of soil on the left and right sides of the pile, respectively, is to observe the gap formation on the left side of the pile (see Figure 3.20c), when the pile is subjected to one-way cyclic loading. The responses of the pile and soil displacements at the debonded interface are observed, where their behaviour may be simulated in the boundary element analysis.

Bubble model predictions

The same values for the pile and soil parameters mentioned in Section 3.9.1 were adopted. With maximum load (H_{max}) of 180 kN, Figure 3.24 shows that the maximum and residual pile displacements at the debonded interface are of the order of 600 mm. This will result in immediate failure of the pile, as the maximum pile displacement has exceeded 60 % of the pile diameter. Broms (1964) and Rao and Rao (1993) have suggested that the load corresponding to displacement of 20 % of the pile diameter (or width) is taken as the ultimate lateral capacity of the pile.

Due to the excessive displacement, H_{max} is reduced by 50% (i.e. 90 kN). This causes a significant reduction in the maximum and residual pile displacements of more than 7.5 times (see Figure 3.25), giving a gap of approximately 70 mm at the end of the fifth cycle.

It is observed in Figure 3.24, that during unloading from 180 kN to 160 kN, the pile displacement increases rather than decreases. For H_{max} of 90 kN, such strange phenomenon only takes place in the first cycle of unloading from 90 kN to 80 kN (point A in Figure 3.25). The mechanism of such occurrence is unclear.

The soil at the debonded interface responds in an almost elastic manner, though its displacement is moving 'backwards'. This is also a strange response as one would have expected the soil to move forward (in the positive x - x direction) due to the movement of the pile and the corresponding soil elements pulling effects. Nevertheless, the soil displacements

at the debonded interface are not significant as compared with the pile displacements. It can thus be assumed that the soil at the debonded interface responds elastically, unless the gap has been closed when the pile returns (say in a two-way cyclic loading).

Mohr-Coulomb model

The values for the soil and pile parameters are taken from Section 3.9.1. The pile and soil displacements at the debonded interface are depicted in Figure 3.26; a gap of around 15 mm is shown at the debonded interface at the end of the fifth cycle. It is evident in this plot, that the soil at the debonded interface is moving backwards, which is similar to the bubble model predictions; the cause of this phenomenon is unclear. It is also observed that the soil at the debonded interface has stabilised to an alternating plasticity response after the first cycle of loading. It can therefore be assumed that the soil at the debonded interface responds elastically. The pile at the debonded interface has shown signs of stabilisation to an alternating plasticity response with further cycling, as the rate of increase in maximum displacements with cycling is very small (less than 0.5%).

3.9.2.1 Comparisons of models' predictions

From the above results, the Mohr-Coulomb model seems to give more realistic pile and soil displacement results. The bubble model predicts very large (greater than $0.6D$) pile displacements at a load of 180 kN, which, in the actual field situation, the pile foundations will have collapsed. Under a load of 180 kN, the bubble model predicted much higher pile displacements as compared with the Mohr-Coulomb model. The differences are 26.4 times and 42.1 times for maximum and residual pile displacements, respectively, at the end of the fifth cycle. However, we cannot expect both models to give the same results, but the comparisons will indicate to us the suitable choice of soil models. That is, whether to employ a simple elastic-perfectly plastic Mohr-Coulomb, or an isotropic hardening model like MCC model, or a mixed hardening bubble model, for specific types of soils and environmental conditions.

Both the bubble model and Mohr-Coulomb model predicted that the soil at the debonded interface is moving backwards. This is a strange phenomenon. However, the magnitude of the soil displacements is insignificant in comparison with the pile

displacements; see Figures 3.24 to 3.26. From the analyses, it can thus be assumed that the soil at the debonded interface responds elastically.

3.10 OASYS analysis and results

The elastic-perfectly plastic Mohr-Coulomb model employed in SWANDYNE analysis is used for OASYS analysis. The values for the pile and soil parameters used in the analysis are identical to those used for SWANDYNE analysis (Section 3.9.1). To check on SWANDYNE results, 10 load increments with 5 and 10 iterations were used for OASYS analyses, and only the half-debonded case is reviewed. Different numbers of iterations were used, in order to see their effects and for comparisons with SWANDYNE results.

The pile and soil displacement results at the debonded interfaces are depicted in Figure 3.27a for 10 iterations and in Figure 3.27b for 5 iterations. Higher displacements are accounted for the 10 iterations than the 5 iterations' analyses, with a difference of about 10% at the end of the fifth cycle. Comparisons of the displacement predictions between OASYS (5 and 10 iterations) and SWANDYNE analyses are shown in Figures 3.28a and 3.28b. As observed in these plots, 10 load increments with 10 iterations (Figure 3.28a) gives a good match with SWANDYNE predictions, with differences of less than 0.2% at the end of the fifth cycle. From these comparisons, we can deduce that the results obtained from SWANDYNE analyses are correct, since both the finite element packages yield approximately the same load-displacement predictions. The slight difference in results may be due to the number of load increments and iterations used, the type of non linear iterations technique employed, etc.

3.11 Boundary conditions review

The soil at the debonded interface for the half-debonded case, appears to move (marginally) in the 'wrong' direction, for both the bubble model and Mohr-Coulomb model (Figures 3.24 to 3.28). It is suspected that this might be due to boundary conditions (denoted here as the initial case; see Figure 3.3). As such, the following boundary conditions were investigated using the SWANDYNE program.

Case (i) : All boundaries restrained by rollers.

Case (ii) : All boundaries are unrestrained, except rollers on the plane of symmetry, and fixity at the bottom right corner.

Case (iii) : Similar to case (ii) except fixed at the bottom left corner instead of the bottom right corner.

The Mohr-Coulomb model was used in this investigation.

Case (i)

With all the four boundaries of the mesh restrained by rollers, a reduction in both the pile and soil displacements at the debonded interface can be observed in Figure 3.29, when compared with the initial case. In terms of maximum and residual displacements of the pile, reductions of 39% and 41%, respectively, are observed at the end of the fifth cycle. For the soil displacements, the reductions are 55% and 74%, respectively. This is due to the constrained movement of the soil in the y - y direction at the boundary B in Figure 3.3, hence reducing soil displacements in the x - x direction. It can be seen in Figure 3.29, that the soil at the debonded interface is still moving backwards, though less noticeably than in the initial case.

Case (ii) and Case (iii)

For these cases, large pile and soil displacements occur at the debonded interface; see Figures 3.30 and 3.31. Obviously, these boundary conditions do not accord with reality and are not considered further.

3.12 Discussion of results

In regard to computational efficiency, the mesh discretisation study has shown that the mesh boundary can be confined to a length and breadth of thirty pile diameters and fifteen pile diameters, respectively. The convergence study has shown that twenty load increments (per ten seconds cycle) with tolerance of 0.005 can be employed to obtain predictions of good accuracy. For the OASYS analysis, ten load increments with ten iterations have shown to give similar displacement results to that obtained using SWANDYNE analysis (using elastic-perfectly plastic Mohr-Coulomb model).

Parametric studies

The parametric studies conducted based on the fully bonded case using the bubble model, have revealed that the pile (pile-soil interface) displacements are always the highest. The soil at two pile diameters away from the face of the pile is not greatly influenced by the cyclic loading on the pile. This is evident in Figures 3.13 to 3.19 where the displacements fall steeply from the pile-soil interface to a distance of 2.5 m from the centre of the pile. It is also shown in Figures 3.13 to 3.19 that the influence of most parameters are negligible at a distance of seven pile diameters from the face of the pile. In the fully bonded case, the nodal displacements along the symmetric plane are the same at the front and back of the pile.

Models' comparisons

Comparison of the bubble model and Mohr-Coulomb model predictions at the same load level for the fully bonded case, show that the former tends to predict much larger displacements than the latter. The differences for the maximum and residual pile displacements are 18.2 times and 200.5 times, respectively, at the fifth cycle.

For the half-debonded case, the bubble model also predicts much higher displacement than the Mohr-Coulomb model, with differences of 26.4 times and 42.1 times for maximum and residual pile displacements, respectively, at the fifth cycle. The predictions using bubble model for soil seem to be unrealistic.

The displacement predictions using the elastic-perfectly plastic Mohr-Coulomb model for soil and linearly elastic model for pile, yield reasonable results for gap formation, pile and soil displacements. The SWANDYNE and OASYS programs give similar results (if appropriate increments, iterations, loading conditions, etc., were used).

Comparisons between the fully bonded case and the half-debonded case using the bubble model (see Figures 3.21 and 3.24), reveal large differences (greater than four times) in the pile displacements. This is basically due to the fact that pile and soil nodes are not linked (allowing gap formation) for the left half of the pile-soil interface, which effectively reduces the soil resistance.

The evaluations of the half-debonded case for the bubble model and Mohr-Coulomb model show that the soil at the debonded interface will respond in an elastic manner (Figures 3.24 to 3.28). The pile displacements at the debonded interface increase with the number of load cycles. However, the cyclic degradation reduces and the pile may eventually stabilise to

an alternating plasticity state with further cycling, depending on the type of soil models and magnitude of cyclic loads.

3.13 Concluding remarks

The response of a pile subjected to cyclic lateral loads is influenced by various factors. The stress-strain behaviour of the soil, geometry and stiffness of the pile, boundary and drainage conditions at the site, and magnitude and nature of loading, are among the most important factors that control the behaviour of the pile-soil system.

The plane-strain finite element analyses, have given some insights into the pile and soil behaviour. For example, they show that the soil (at the debonded interface) will respond elastically when separated from the pile. With the information gathered, a simplified three-dimensional analysis, based on the indirect boundary element method (intended to reduce the computational time and data preparation effort), will be introduced in Chapter 5. Before advancing directly into the boundary element analysis, the model for soil strength degradation used in that analysis will be described in the next Chapter.

Table 3.1 Relative errors based on *tolerance* = 0.05

Load (kN)	No. of load increments	Displacement (mm)	Relative error (%)	Computational time (minutes)
75	100	55.2	0	16.7
	40	53.3	3.4	11.8
	20	51.5	6.7	8.8
	10	49.3	10.7	7
	4	43.8	20.7	6.1
150	100	22	0	17.8
	40	19.7	10.5	11.9
	20	18.1	17.7	10.4
	10	16.5	25	8.9
	4	14	36.4	8.5
225	100	52.2	0	19.9
	40	44.5	14.8	13
	20	39.7	23.9	12.1
	10	36.2	30.7	11.1
	4	30	42.5	11

Table 3.2 Relative errors based on *tolerance* = 0.005

Load (kN)	No. of load increments	Displacement (mm)	Relative error (%)	Computational time (minutes)
75	100	55.5	0	23.5
	40	54.9	1.1	14
	20	54.2	2.3	10.6
	10	53.7	3.2	9.6
	4	53.3	4	9.6
150	100	23	0	27
	40	22.4	2.6	20
	20	22	4.4	18.3
	10	21.4	7	19.4
	4	20.4	11.3	20.6
225	100	58	0	35.9
	40	55.3	4.7	30.9
	20	53.3	8.1	29.5
	10	51	12.1	31.2
	4	Failure to converge to tolerance specified		

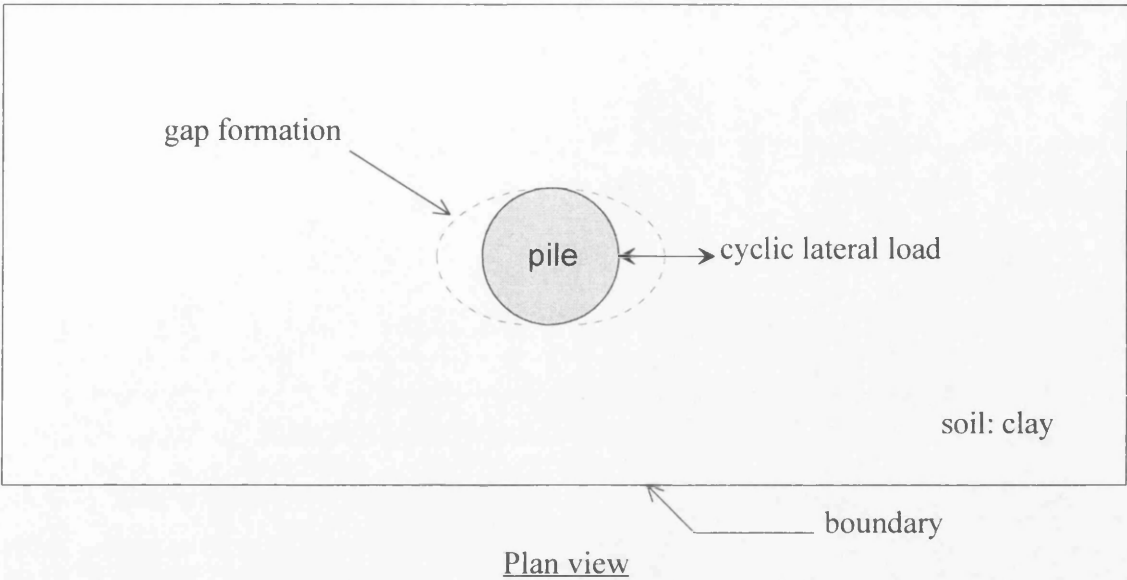


Figure 3.1 Idealised model under plane-strain conditions.

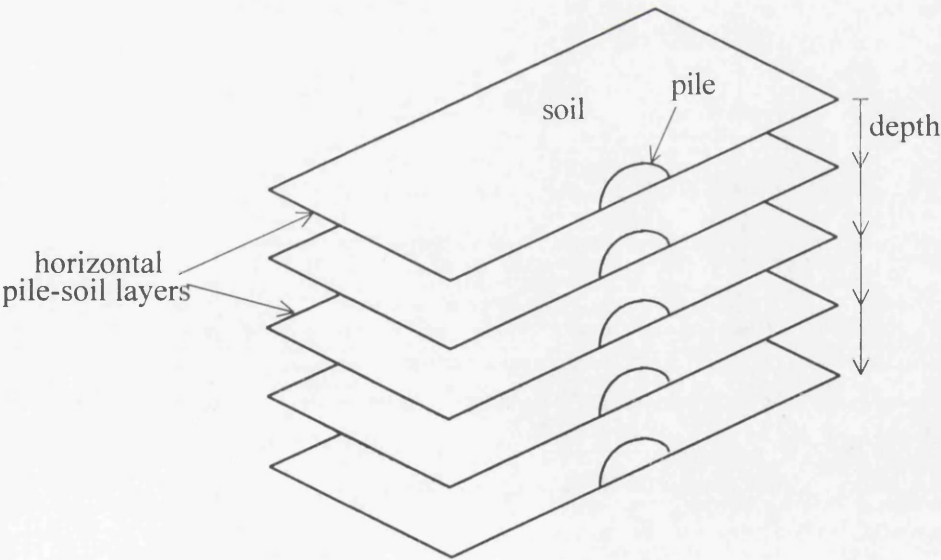


Figure 3.2 Two-dimensional half-layer systems.

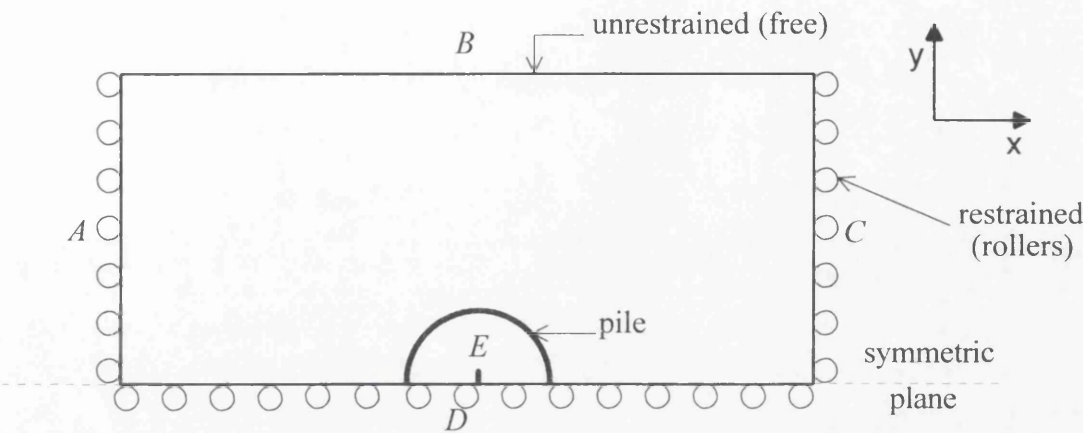
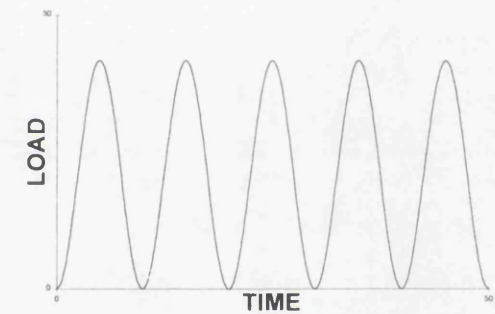
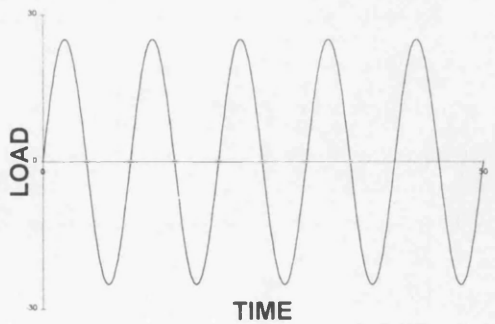


Figure 3.3 Mesh boundary conditions.



(a)



(b)

Figure 3.4 (a) One-way and (b) two-way cyclic loading.

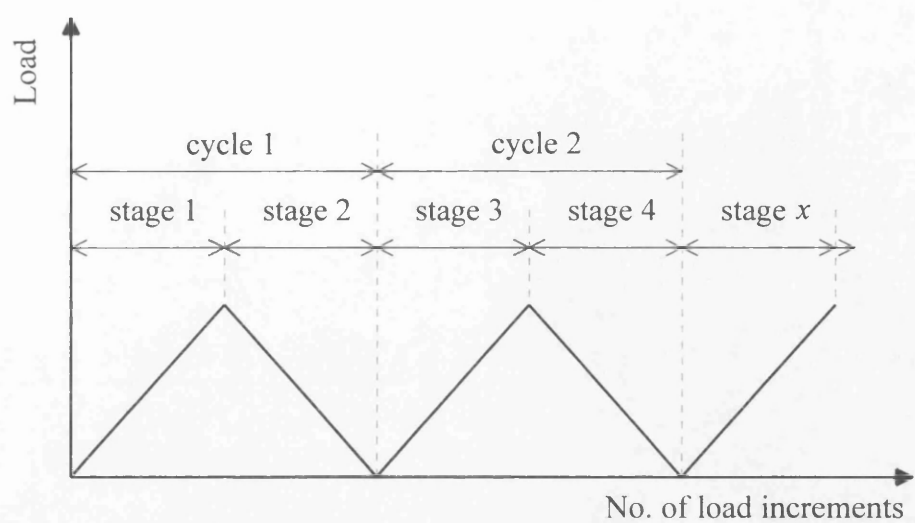


Figure 3.5 Stages of loading to simulate cyclic loading for OASYS analysis.

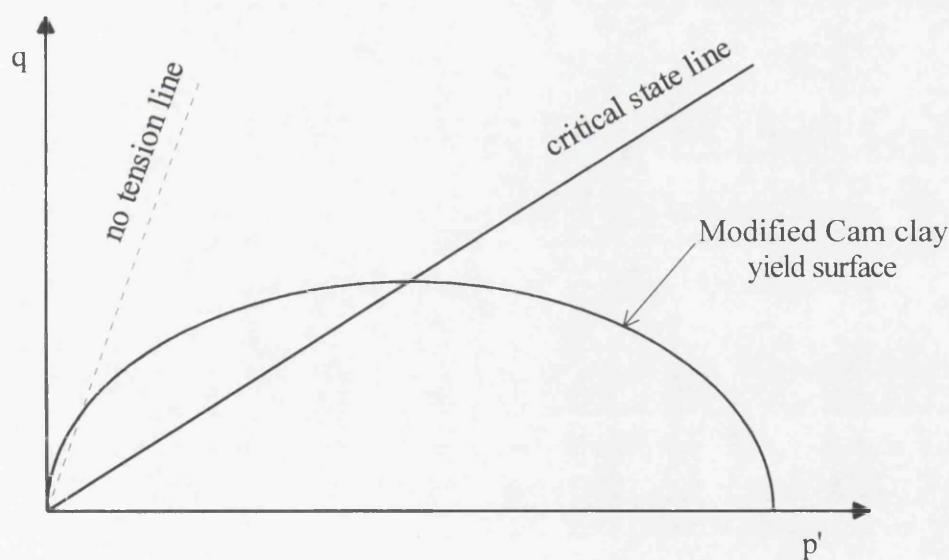


Figure 3.6 Modified Cam clay yield surface with tension cut-off line.

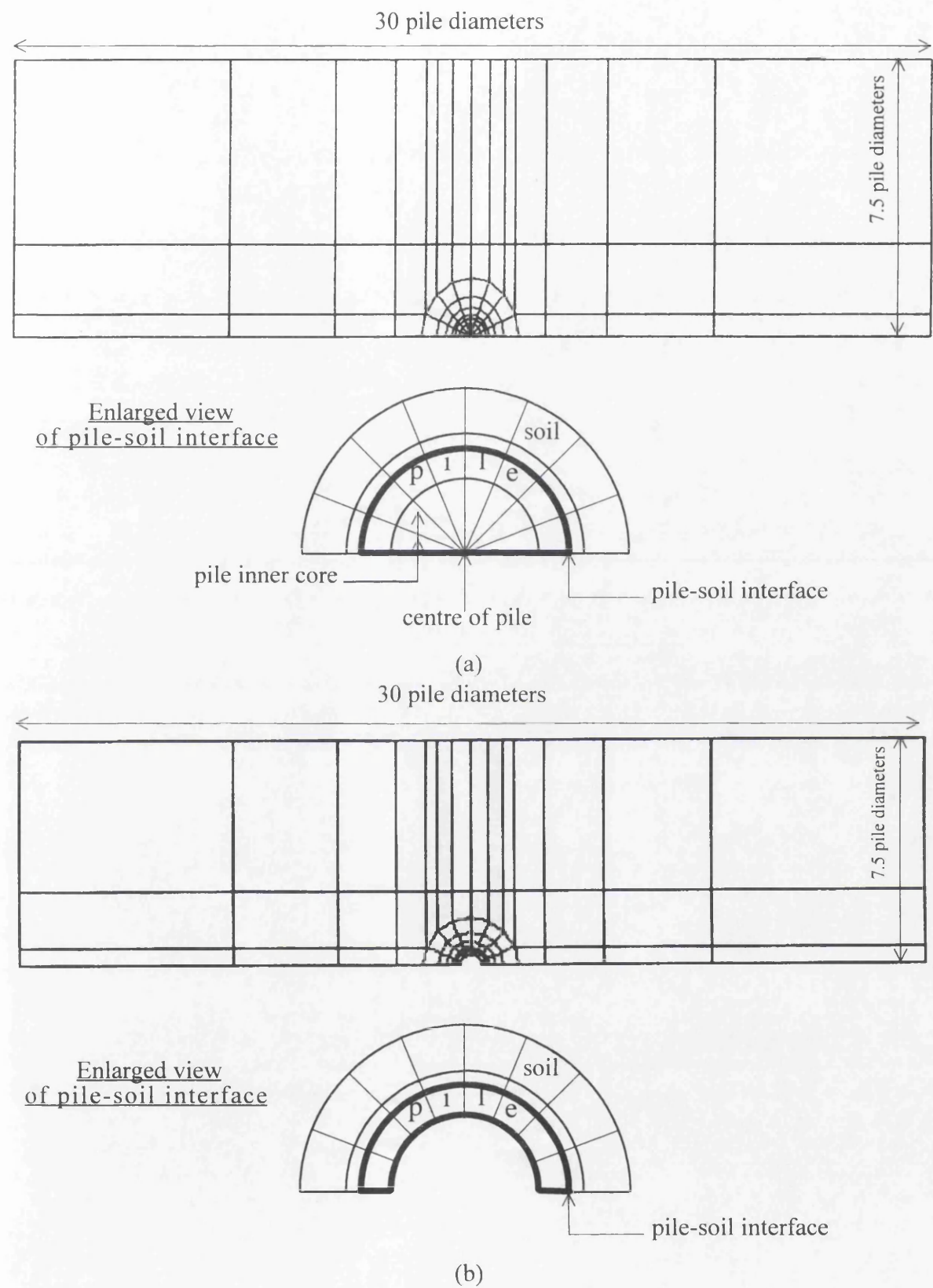


Figure 3.7 Mesh used for (a) SWANDYNE analysis and (b) OASYS analysis (not to scale).

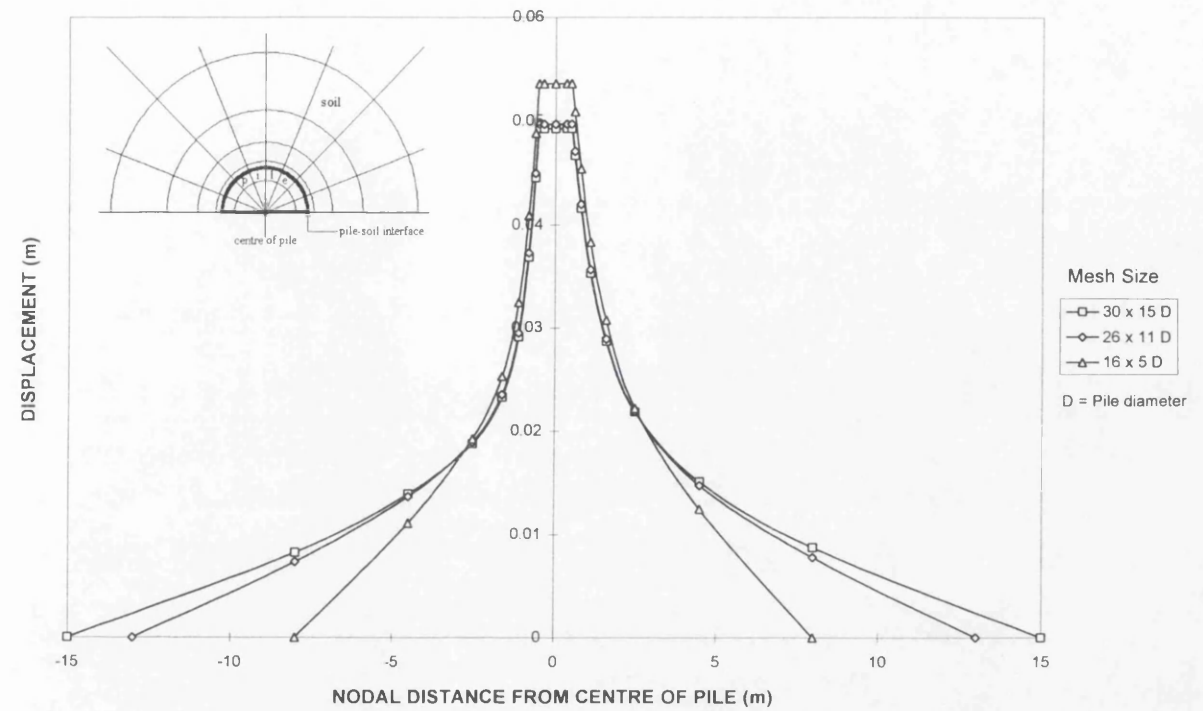


Figure 3.8 Comparisons of mesh sizes.

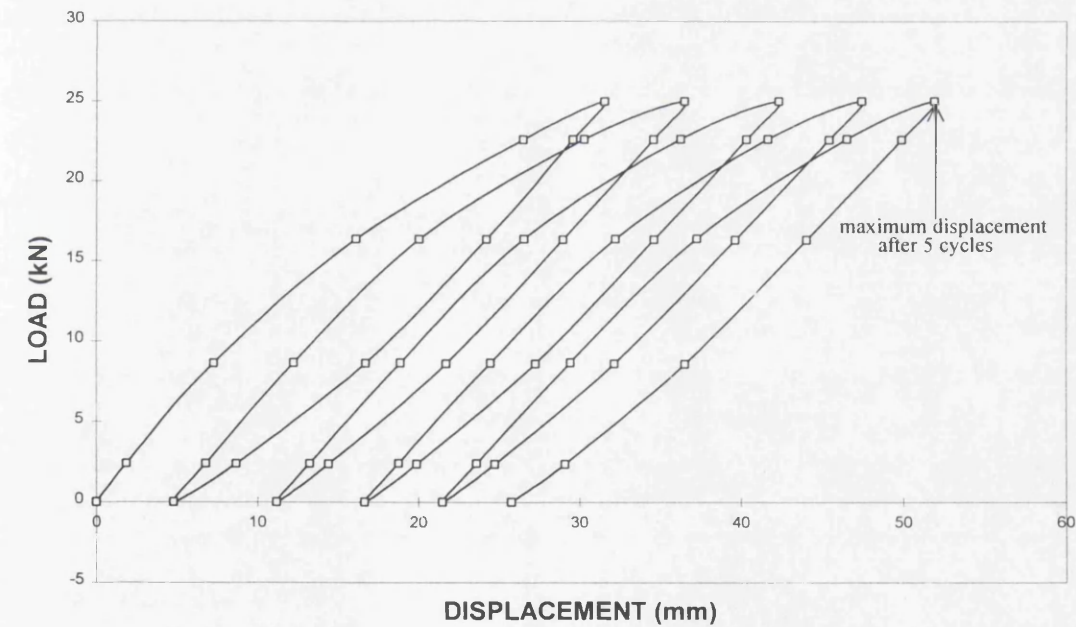


Figure 3.9 Typical pile load-displacement response for fully bonded case based on SWANDYNE analysis.

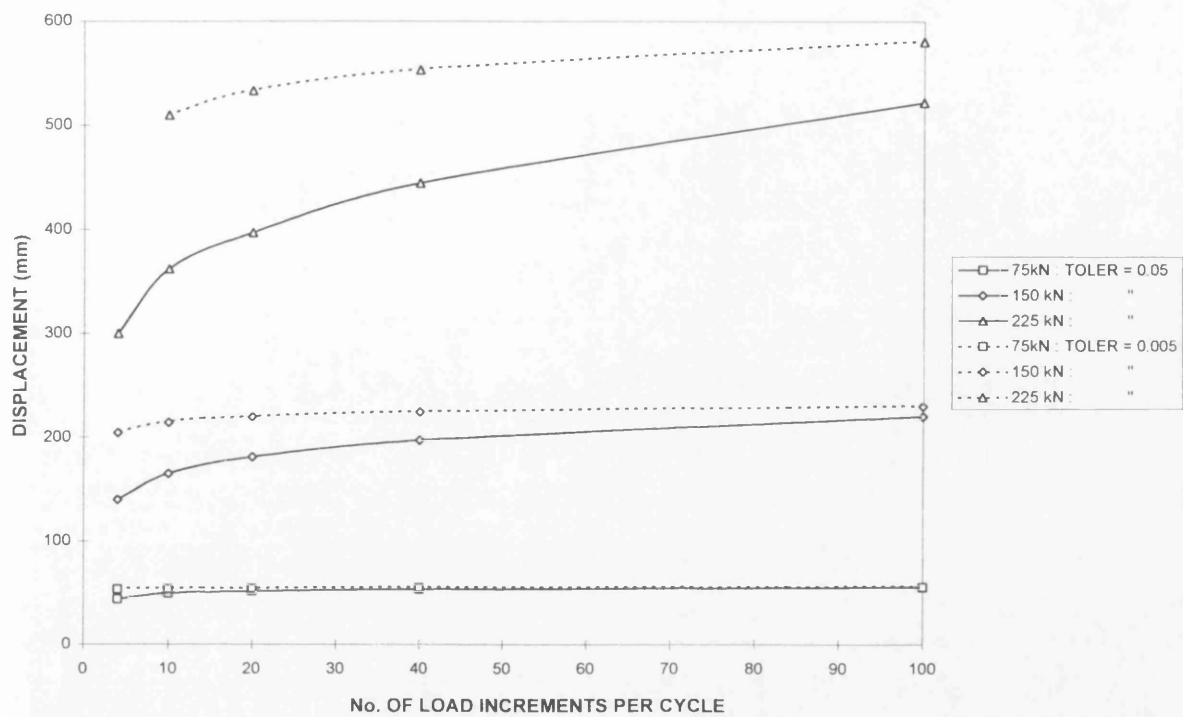


Figure 3.10 Convergence study based on maximum displacements at the fifth cycle.

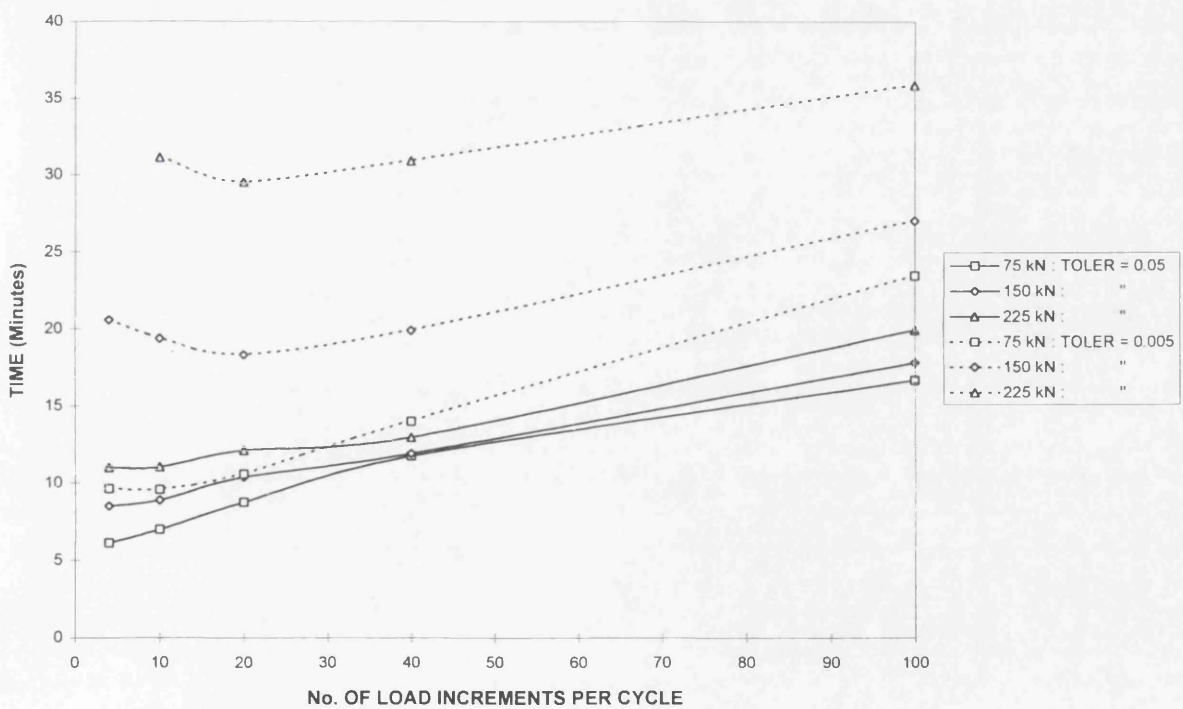


Figure 3.11 Effect of number of load increments per cycle on computational time.

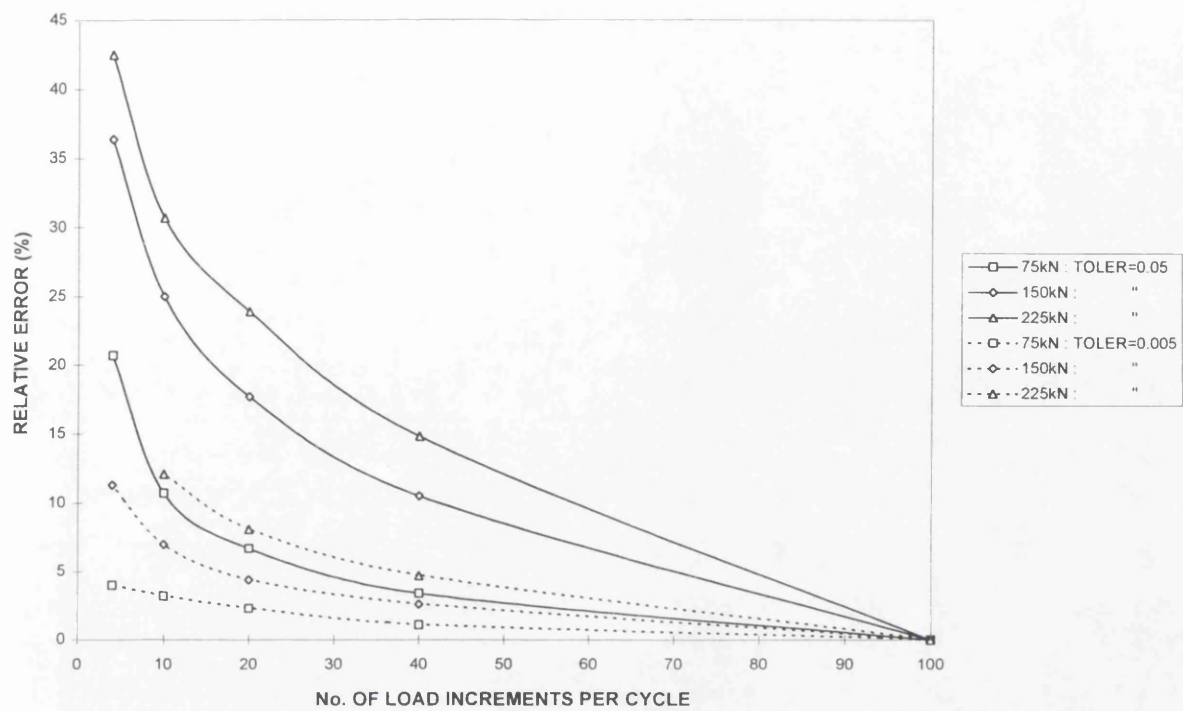


Figure 3.12 Relative error based on number of load increments.

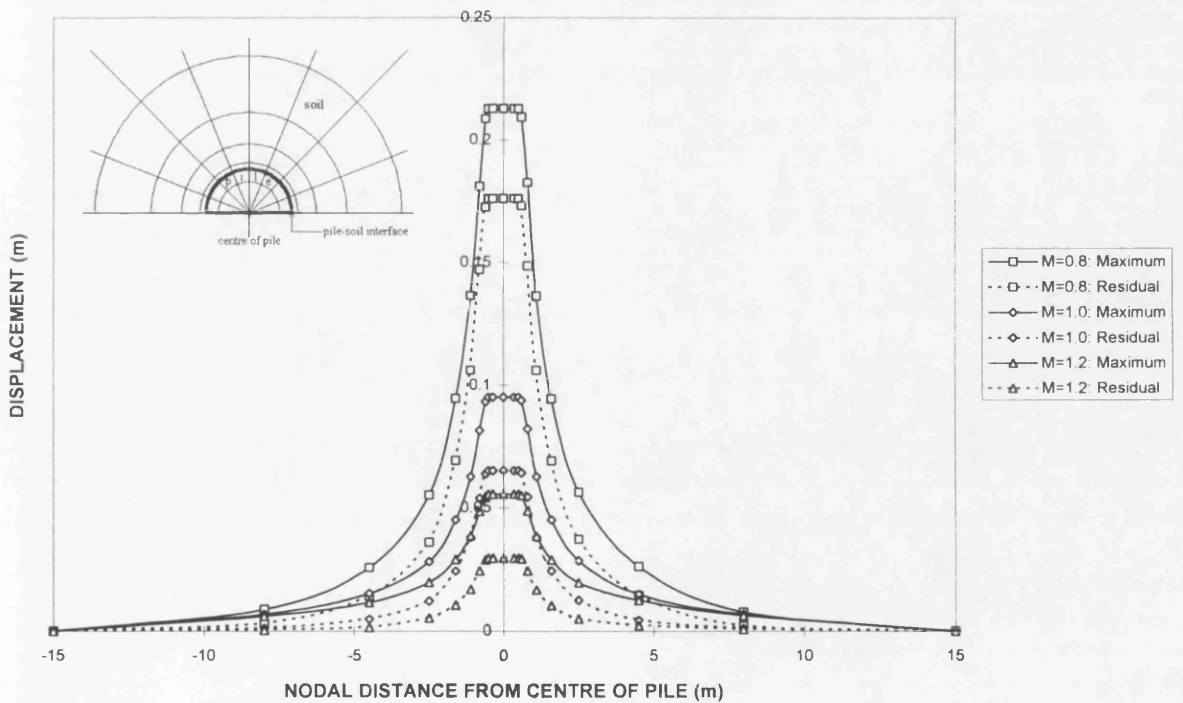


Figure 3.13 The effect of soil strength parameter M on maximum and residual displacements.

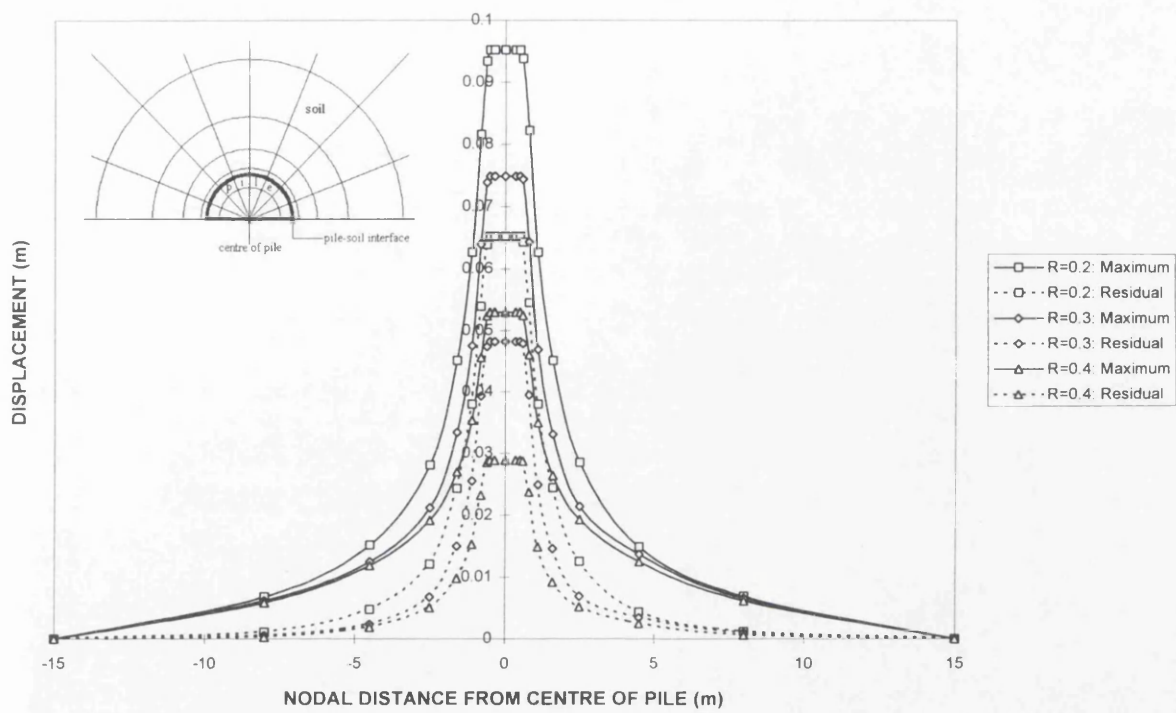


Figure 3.14 The effect of soil parameter R on maximum and residual displacements.

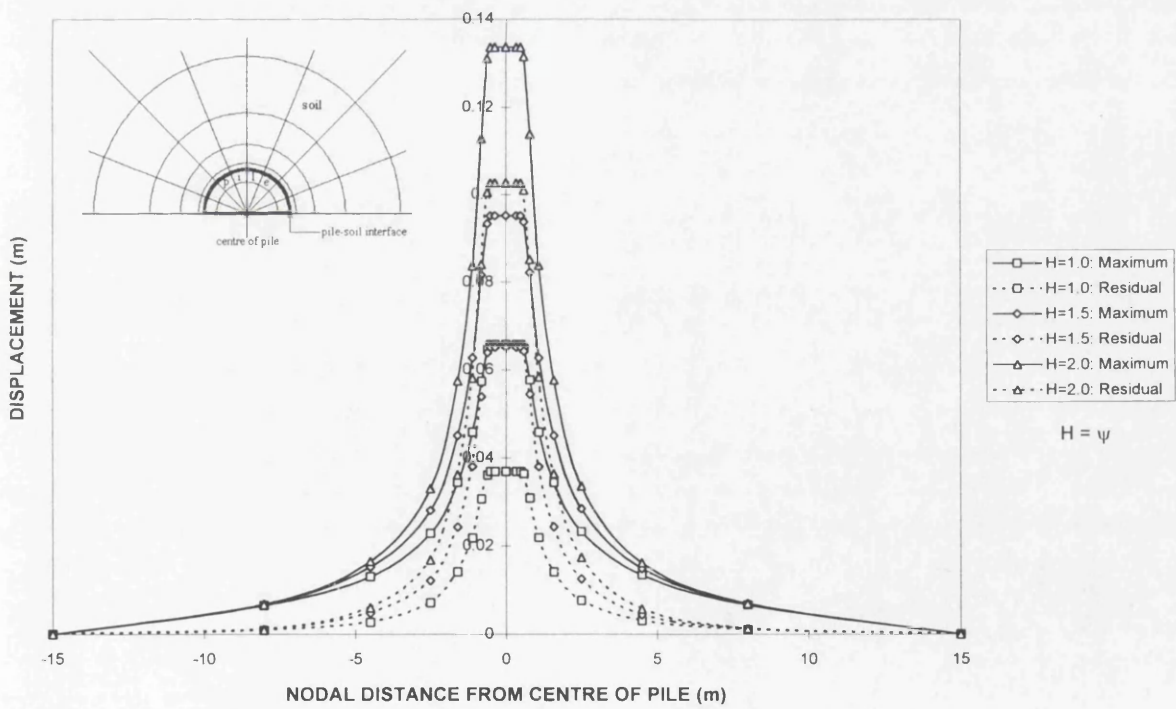


Figure 3.15 The effect of soil parameter ψ on maximum and residual displacements.

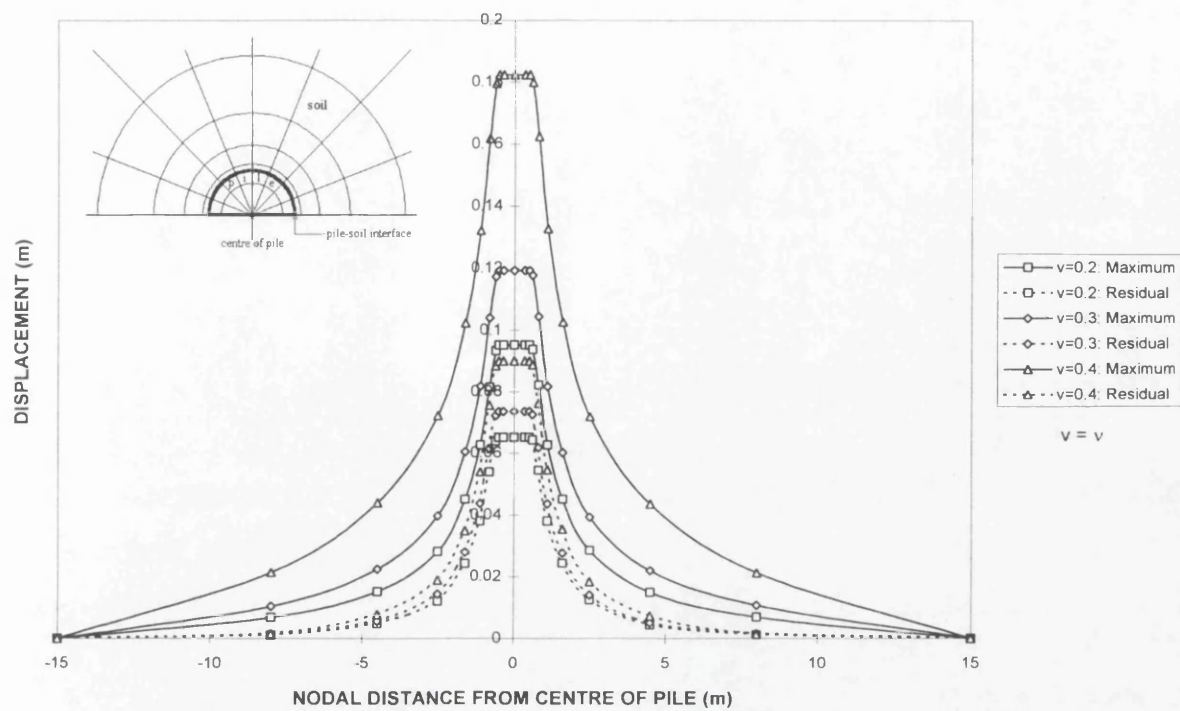


Figure 3.16 The effect of soil Poisson's ratio (ν) on maximum and residual displacements.

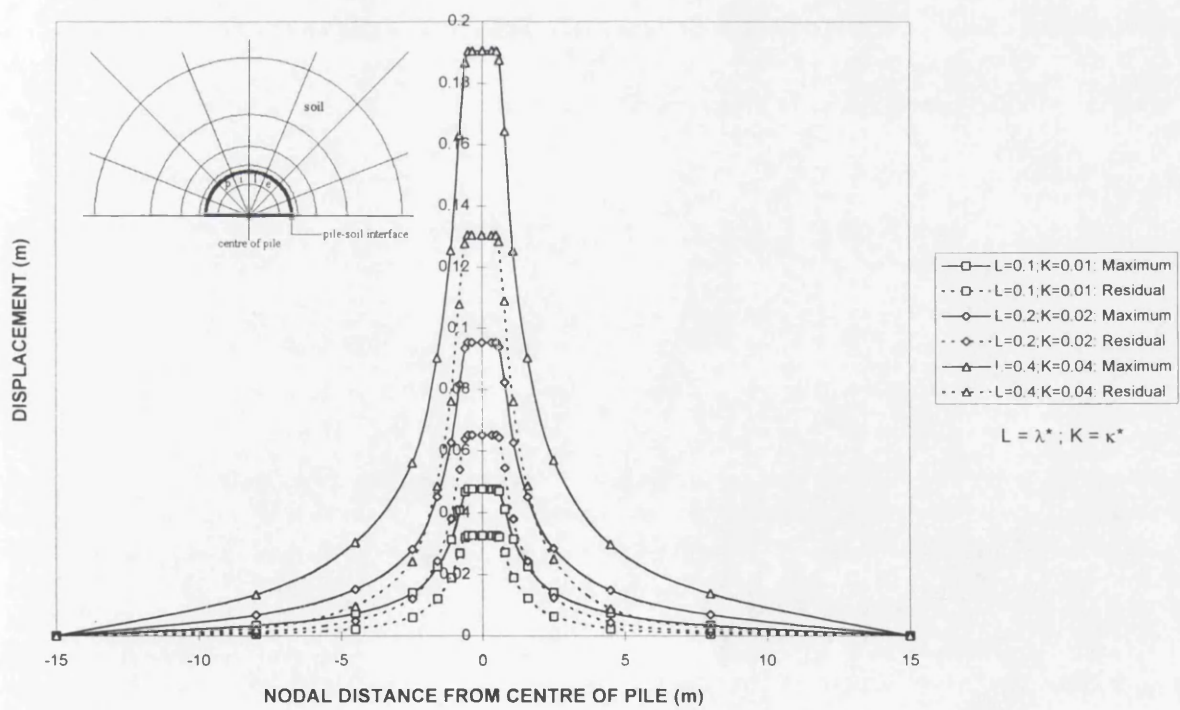


Figure 3.17 The effect of soil parameters λ^* and κ^* on maximum and residual displacements.

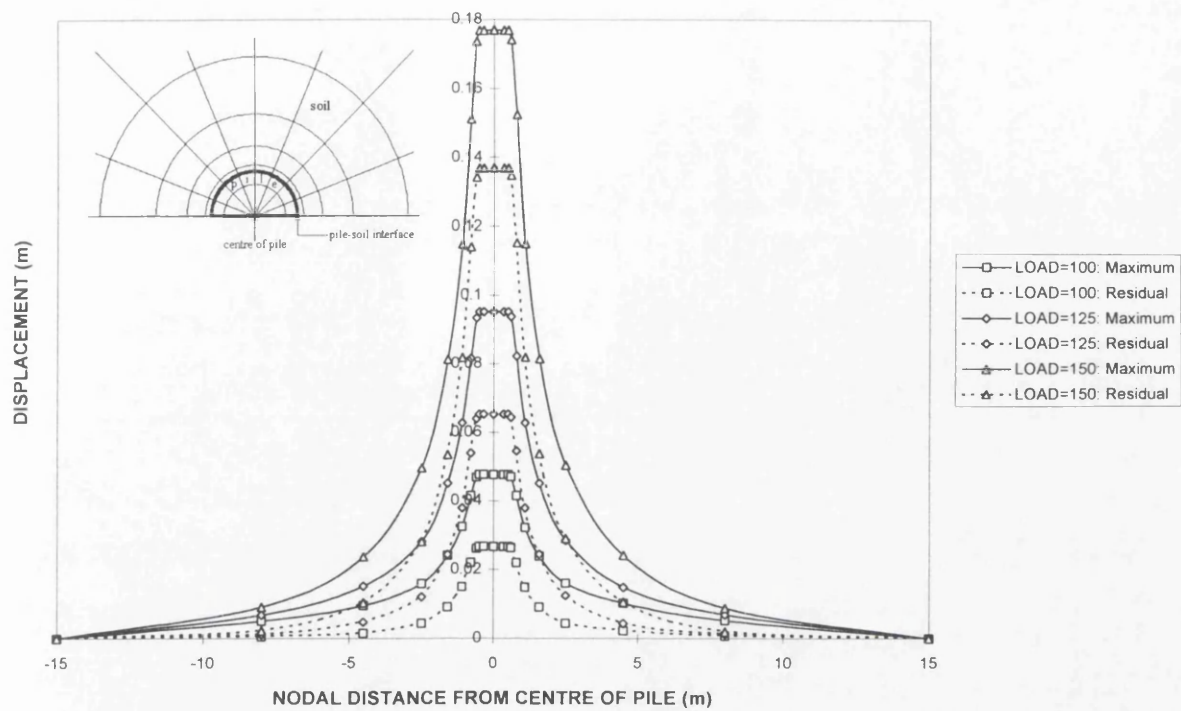


Figure 3.18 The effect of load level on maximum and residual displacements.

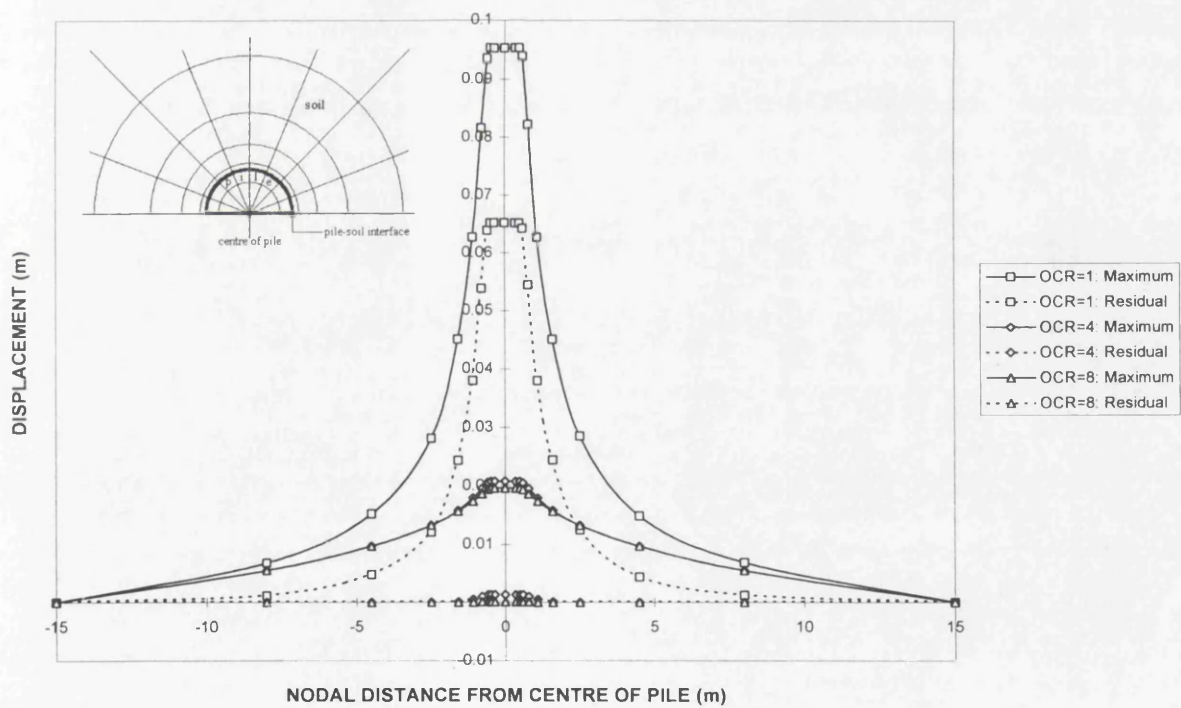


Figure 3.19 The effect of overconsolidation ratio (OCR) on maximum and residual displacements.

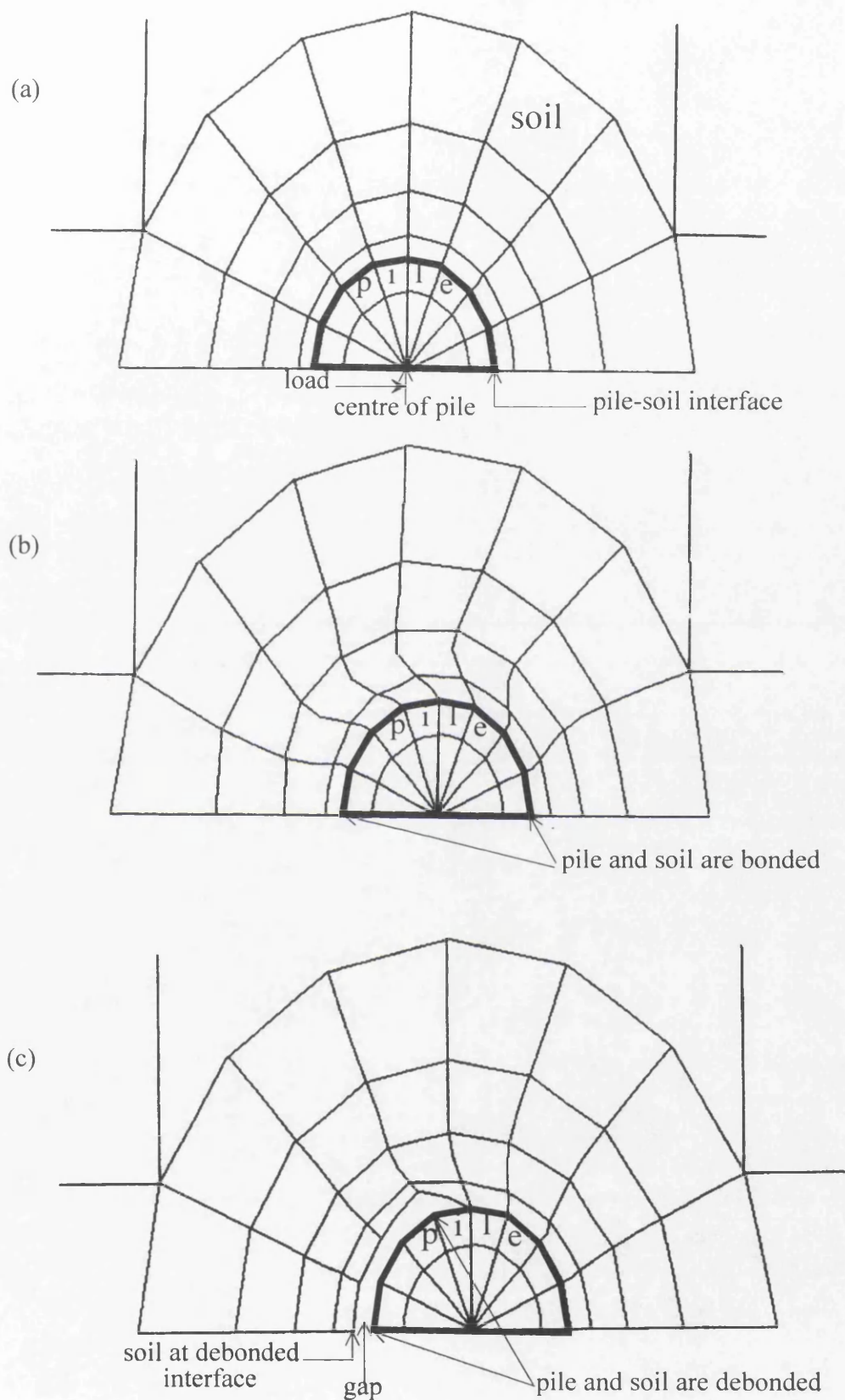


Figure 3.20 (a) Pile and soil elements at initial position. (b) Pile and soil element displacements for the fully bonded case. (c) Gap formation at the debonded interface for the half-debonded case.

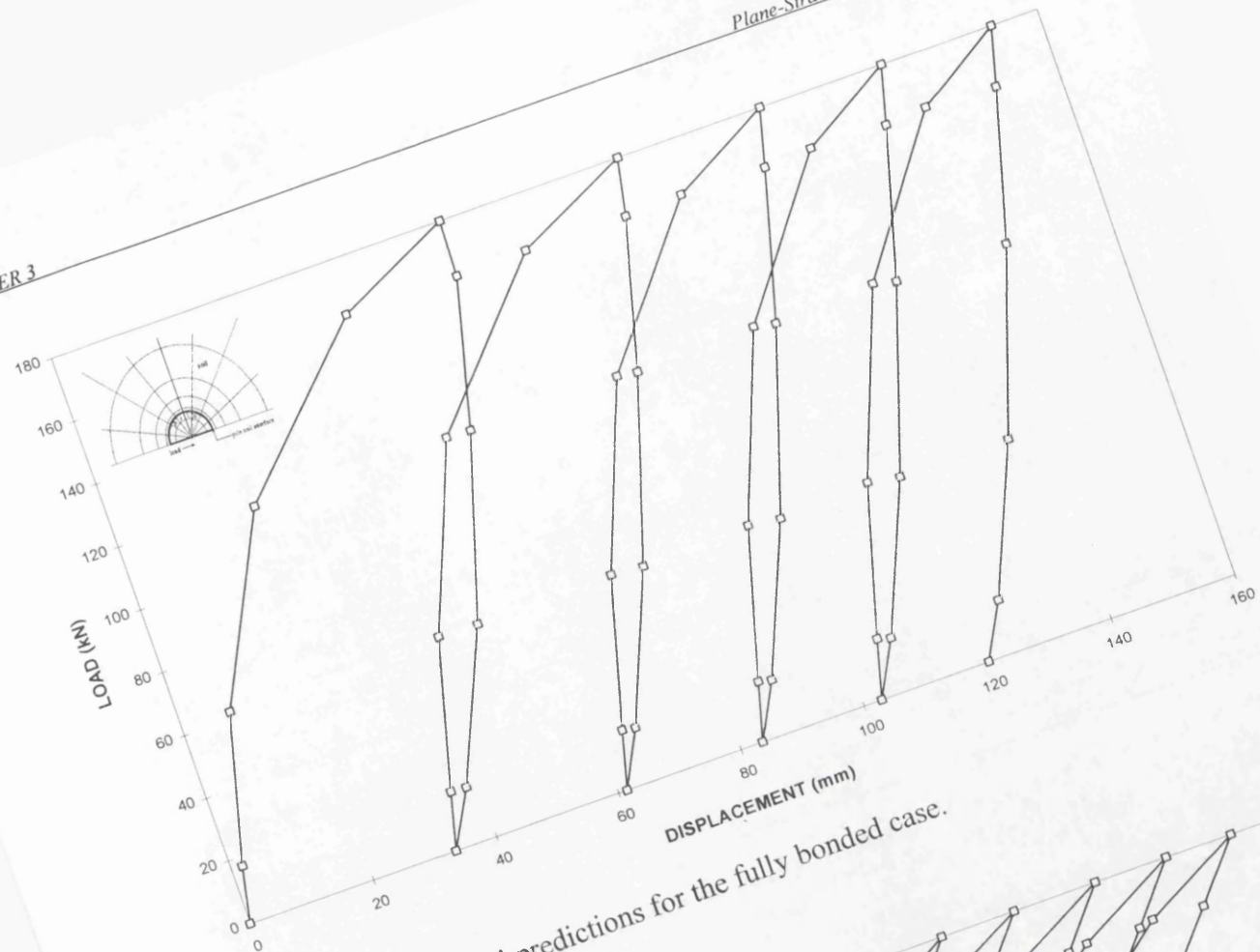


Figure 3.21 Bubble model predictions for the fully bonded case.

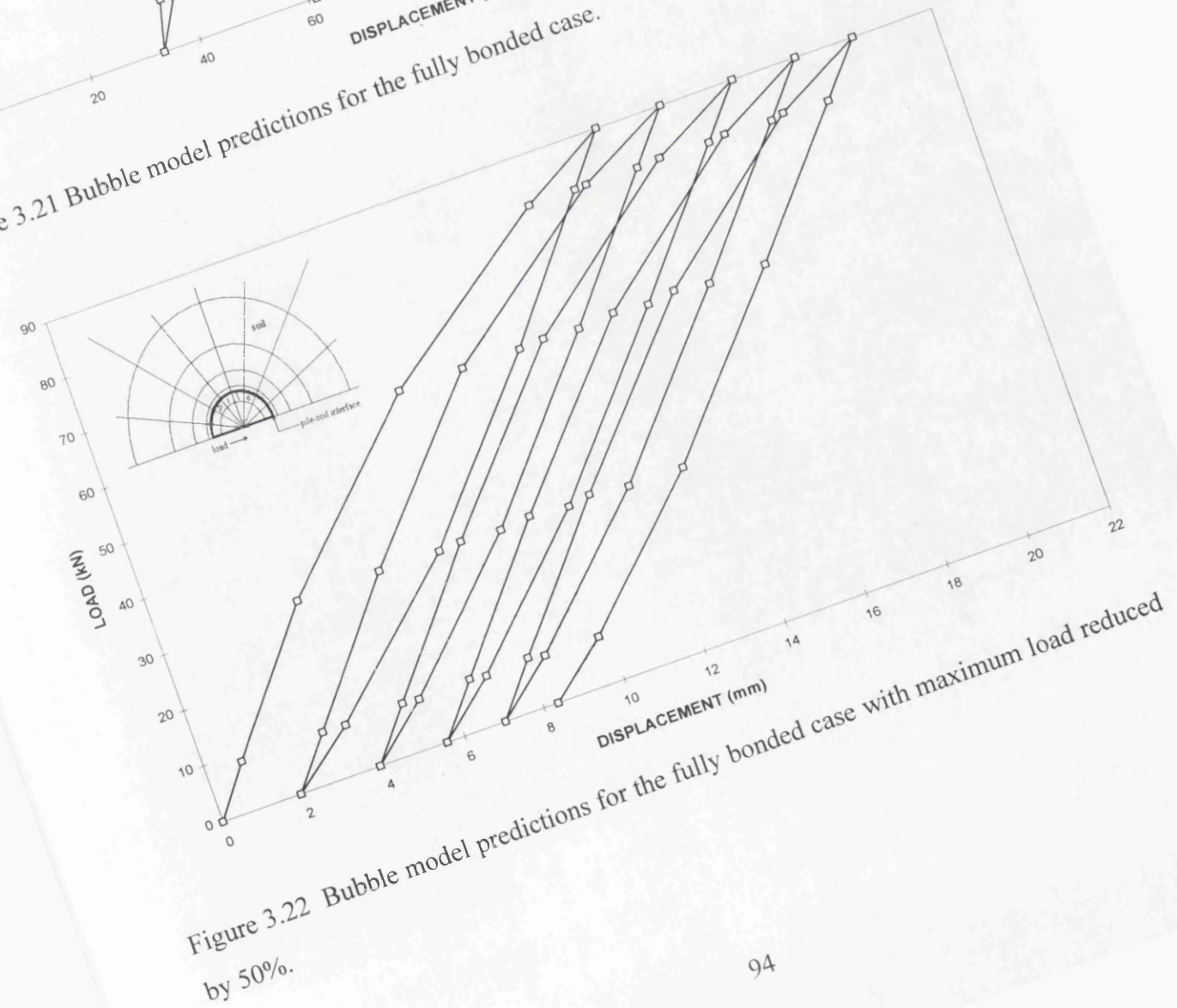


Figure 3.22 Bubble model predictions for the fully bonded case with maximum load reduced by 50%.

CHAPTER 3

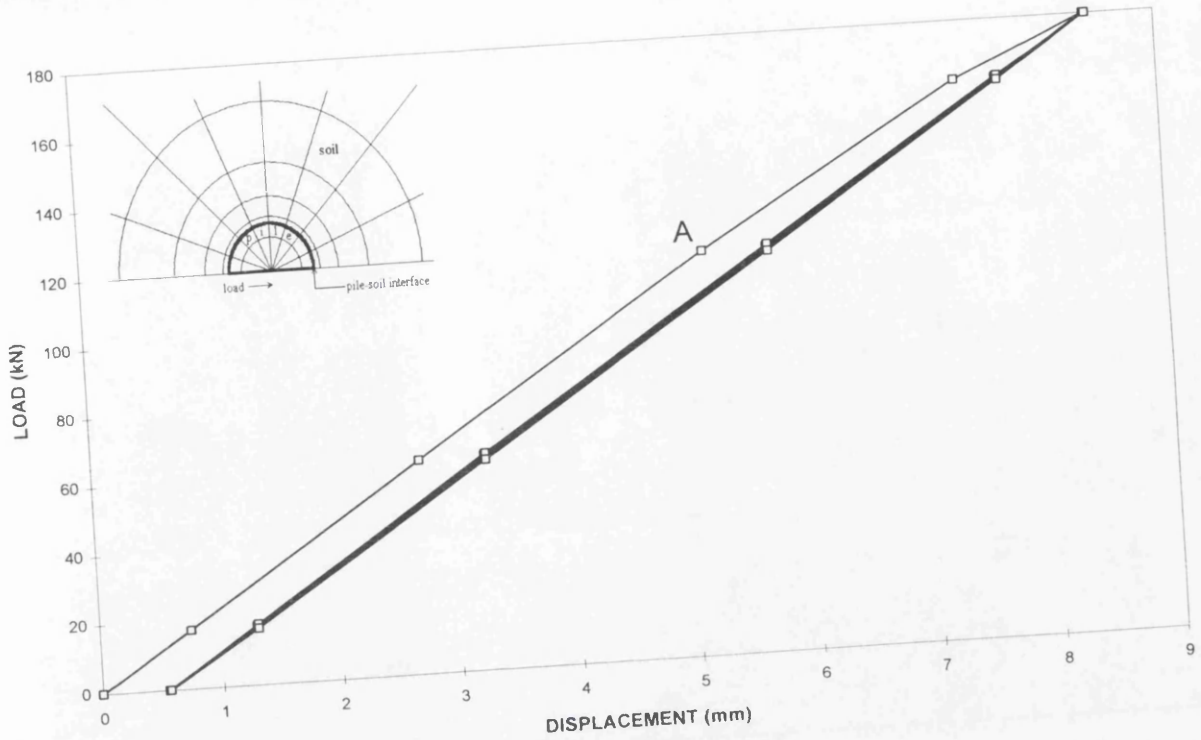


Figure 3.23 Mohr-Coulomb model predictions for the fully bonded case.

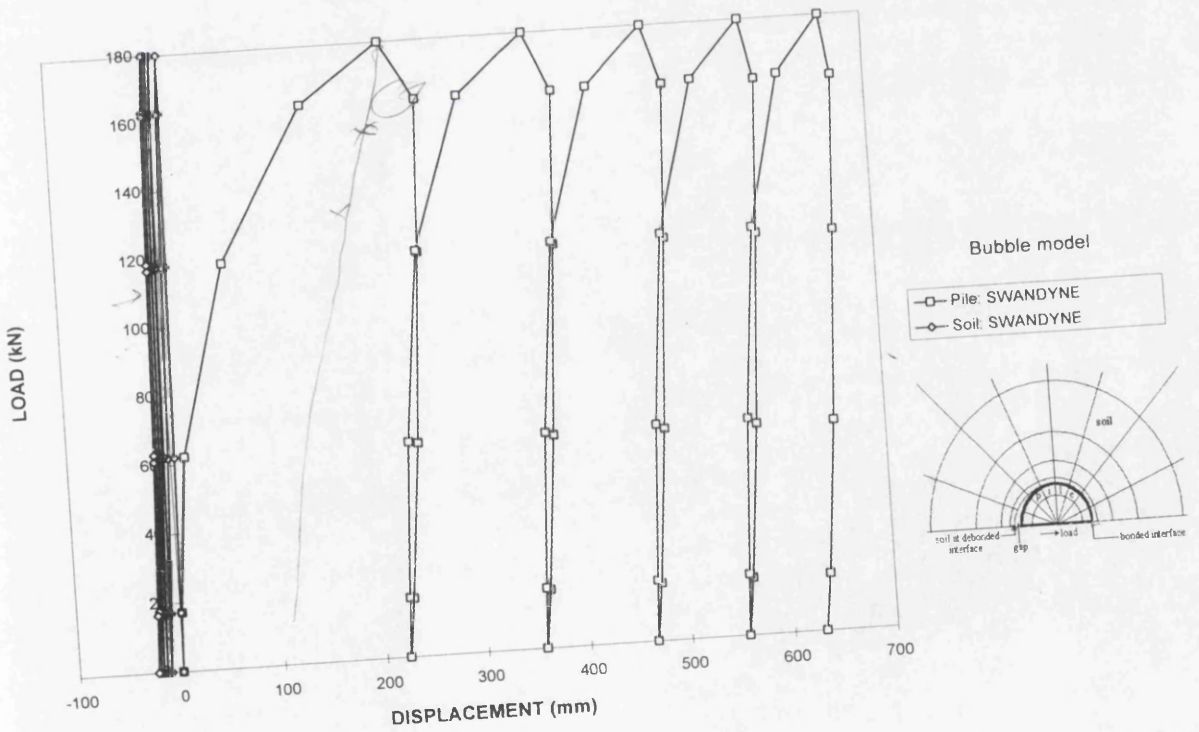


Figure 3.24 Bubble model predictions for the half-debonded case.

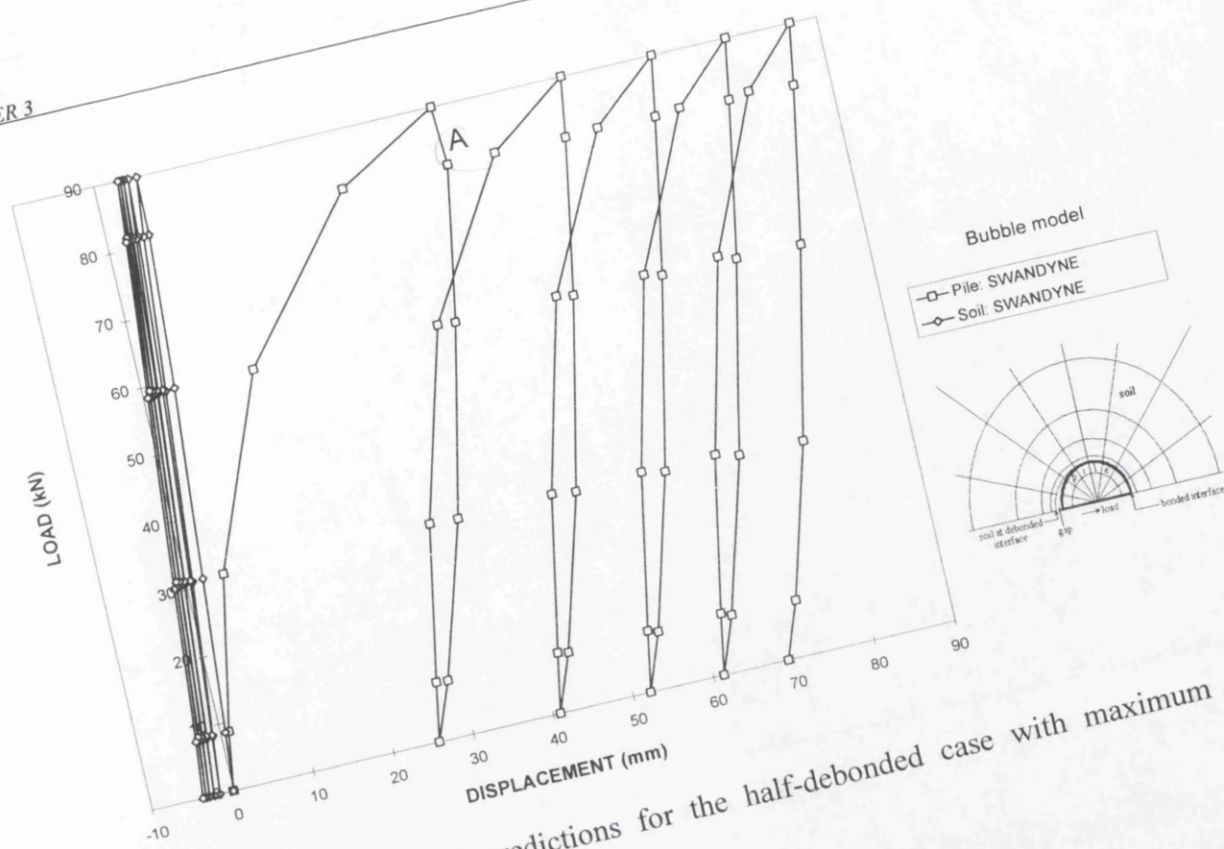


Figure 3.25 Bubble model predictions for the half-debonded case with maximum load reduced by 50%.

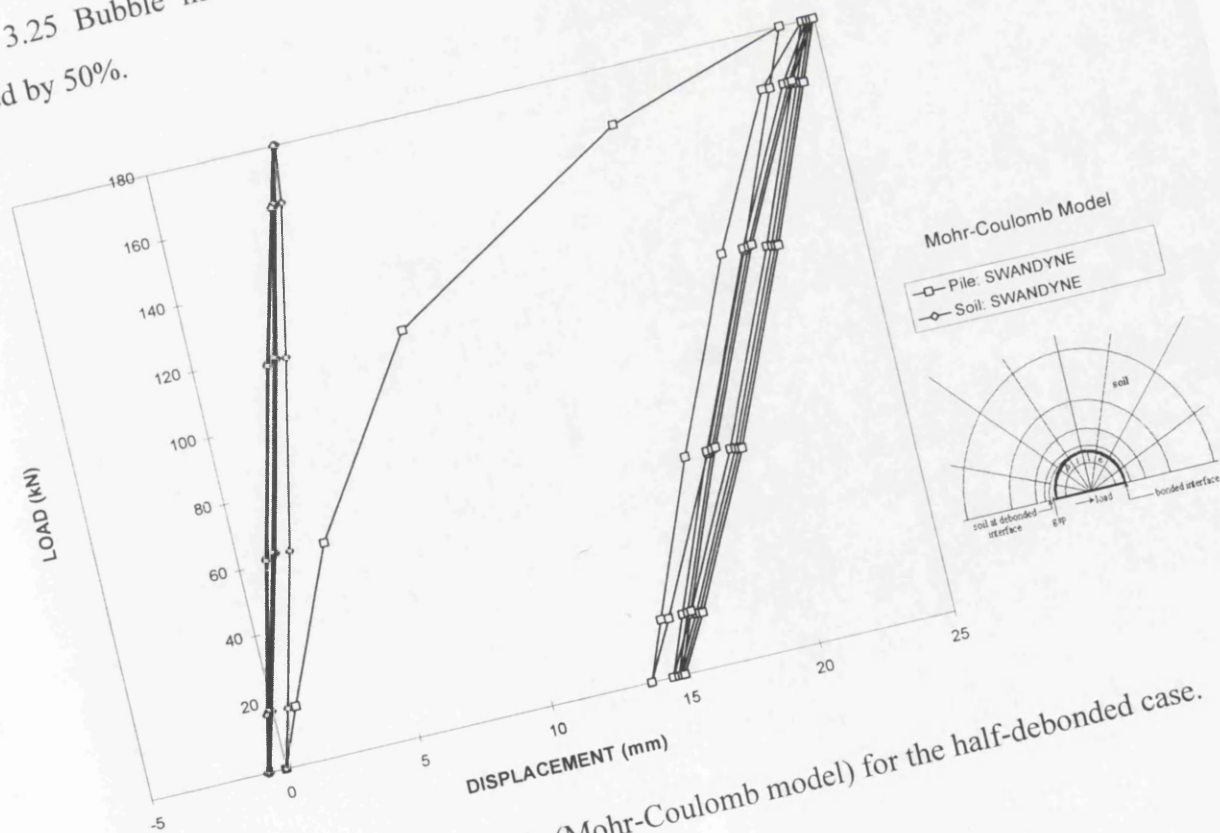
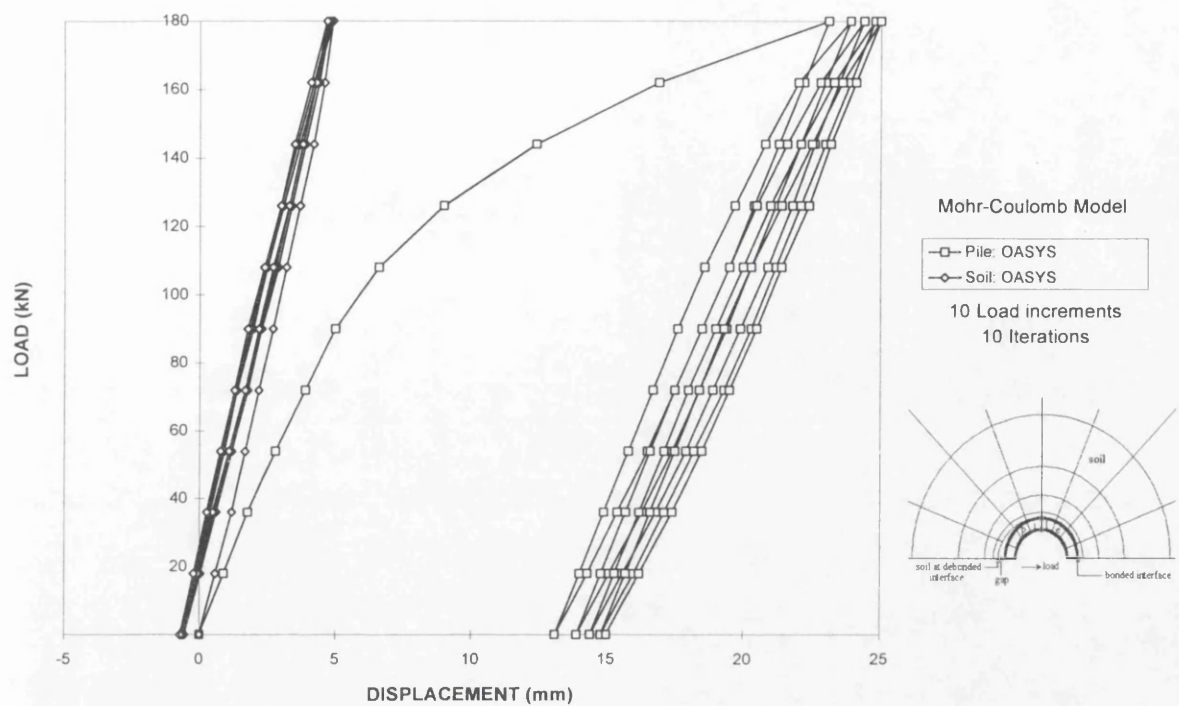
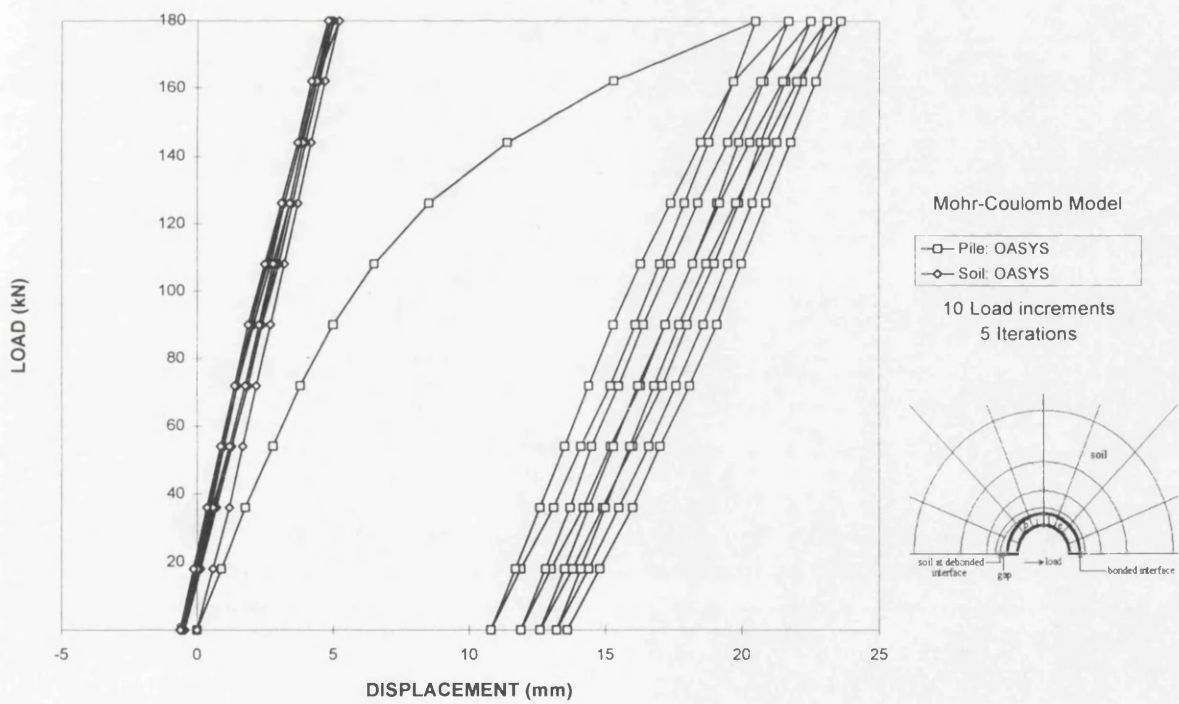


Figure 3.26 SWANDYNE analysis (Mohr-Coulomb model) for the half-debonded case.

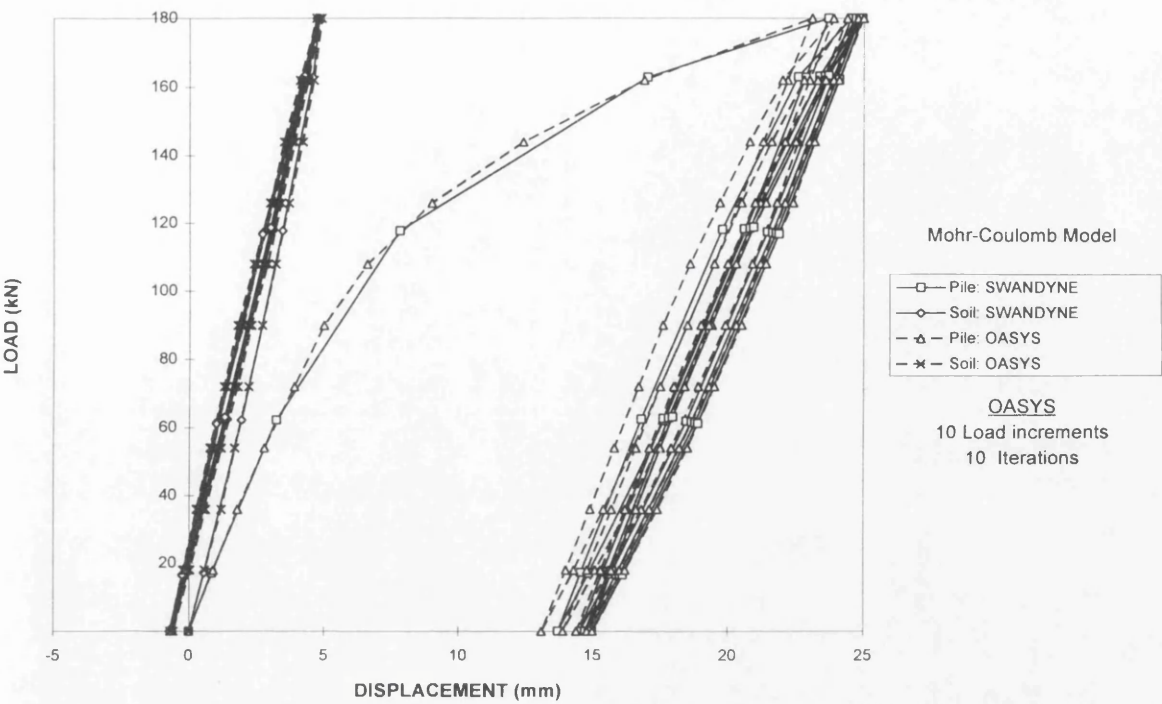


(a)

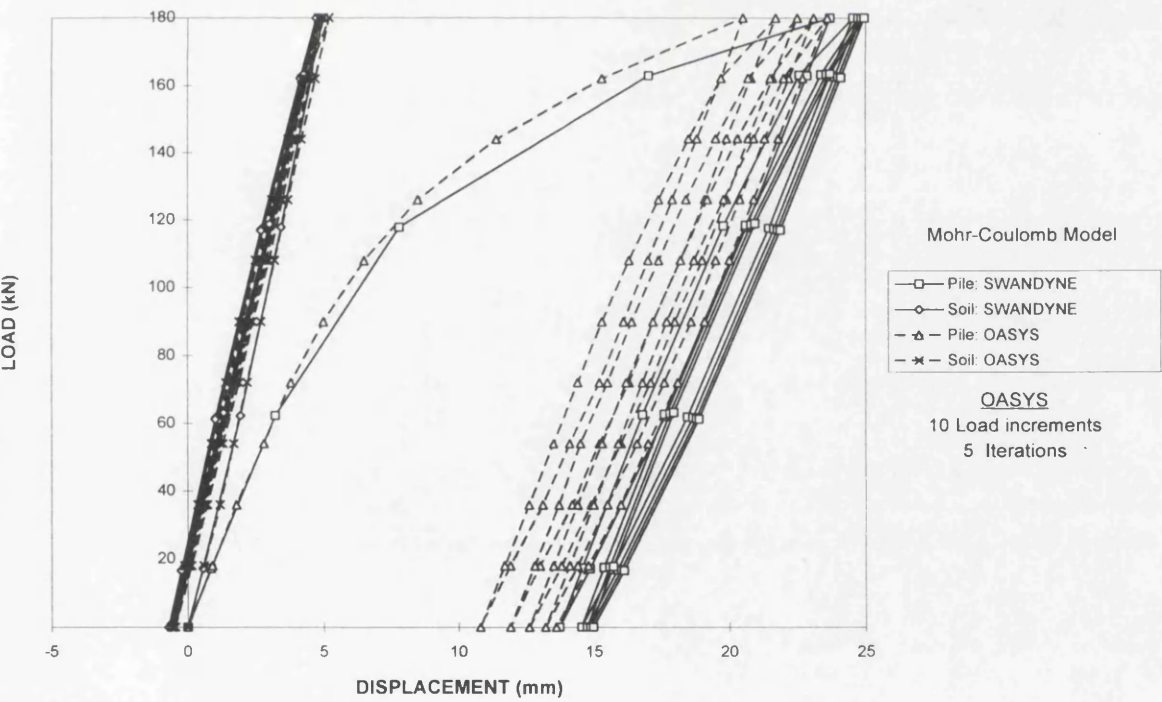


(b)

Figure 3.27 OASYS analysis (Mohr-Coulomb model) for the half-debonded case with (a) 10 load increments and 10 iterations and (b) 10 load increments and 5 iterations.



(a)



(b)

Figure 3.28 SWANDYNE and OASYS results (a) using 10 load increments and 10 iterations and (b) using 10 load increments and 5 iterations.

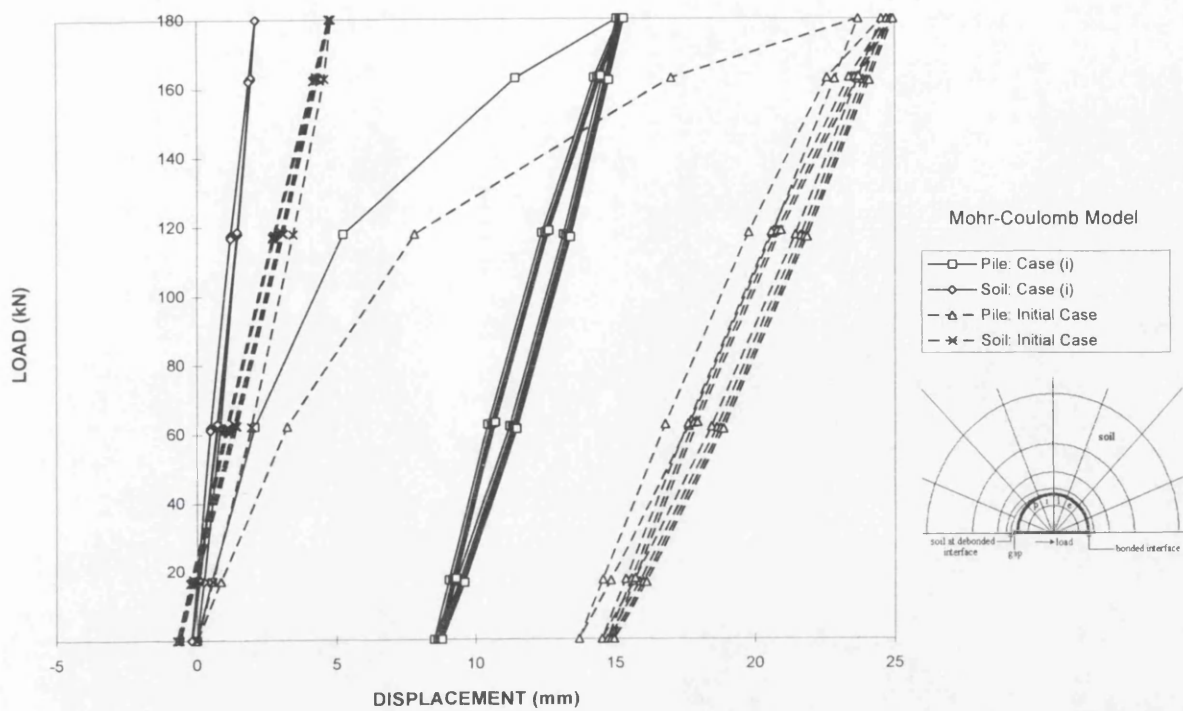


Figure 3.29 SWANDYNE analyses for *case (i)* and initial case using Mohr-Coulomb model.

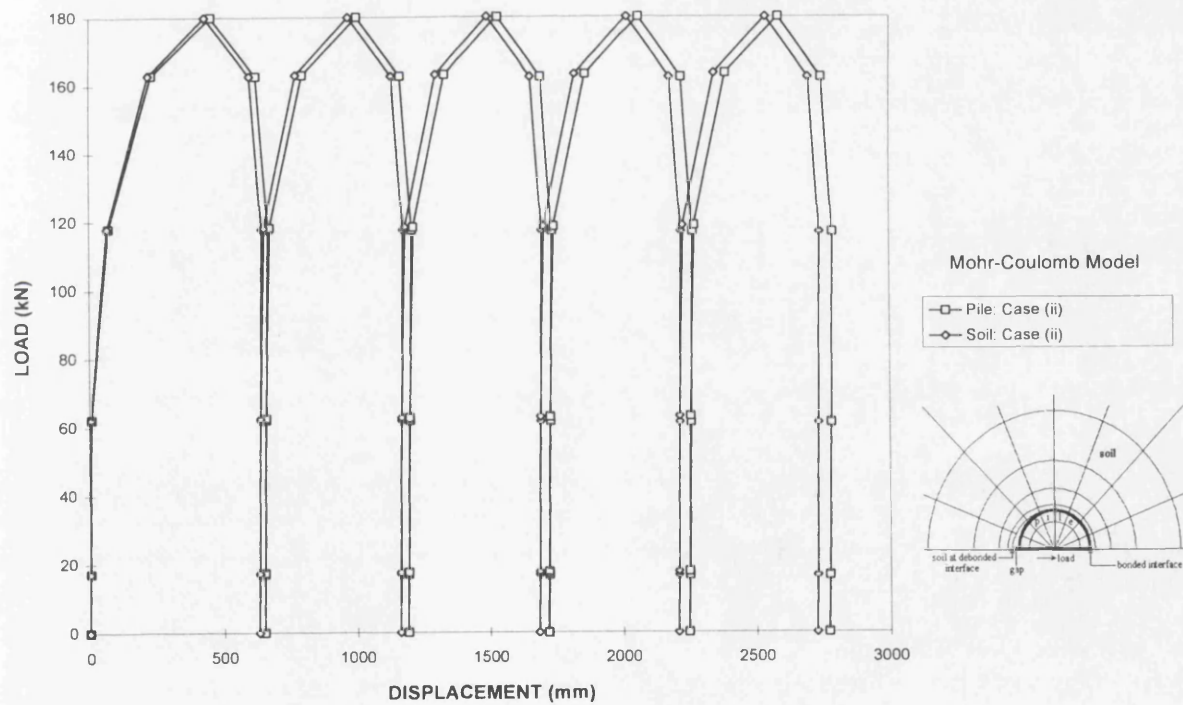


Figure 3.30 SWANDYNE analysis for *case (ii)* using Mohr-Coulomb model.

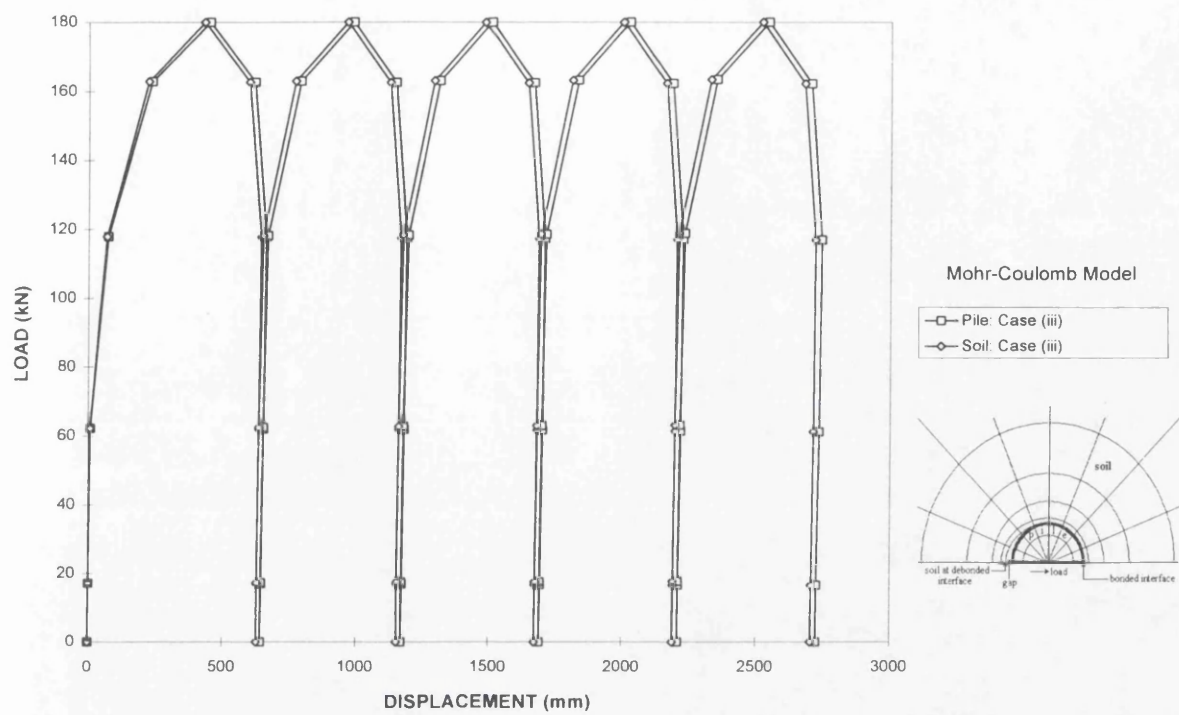


Figure 3.31 SWANDYNE analysis for *case (iii)* using Mohr-Coulomb model.

CHAPTER 4

Soil Strength Degradation

4.1 Summary

4.2 Introduction

4.3 Degradation of shear strength

4.3.1 Causes of shear strength degradation

4.3.2 Plastic displacement

4.4 Correlations of shear strength degradation with soil index properties

4.4.1 Correlations of residual angle of shearing resistance (ϕ'_r) with soil index properties

4.4.2 Correlations of residual/peak shear strength ratio (R_s) with soil index properties

4.4.2.1 Modifications of R_s for low normal effective stress

4.5 Rate of degradation of shear strength

4.5.1 Shear degradation rate factor (C_s) determination

4.6 Correlation of rate of shear strength degradation with soil index properties

4.7 Degradation of bearing strength

4.7.1 Experimental observations

4.8 Rate of degradation of bearing strength

4.8.1 Bearing degradation rate factor (C_b) determination

4.9 Application to cyclic analysis

4.10 Discussion

4.11 Concluding remarks

CHAPTER 4

Soil Strength Degradation

4.1 Summary

The phenomenon of soil strength degradation from peak to residual strength is described in this chapter. This provides important information to guide the development of the cyclic analysis of soil strength degradation at the pile-soil interface. Various correlations are established using the soil index properties to determine the residual angle of shearing resistance, and thereby the residual strength. Using experimental test results obtained by several researchers, simple correlations relating the degree (and rate) of strength degradation with soil index properties are presented. Some simple equations which describe the post-peak strength degradation of soil are proposed for use later in the cyclic analysis.

4.2 Introduction

Soil strength degradation plays an important role in the evaluation of cyclic pile response, as it can cause significant increases in pile displacements and moments, which may eventually cause failure of pile foundations. With increasing cycles, soil strengths may degrade from their peak values to a specific limit, known as the residual strength.

The degradation in strength is associated with an increase in the water content (drained condition), accumulation of excess pore water pressure (undrained condition), particle breakage, reorientation of the particles and loss of interparticle friction. To incorporate these effects into the analysis of cyclic loading of piles would be tedious and probably impossible. Hence, recourse is taken to a simpler approach: the fall in peak strength of soils to their residual values is assumed to be a function of the plastic displacement (soil displacement after peak strength is reached). This function is evaluated from the experimental results reported by various researchers.

The (pre-peak) cyclic degradation of soil strength and soil stiffness as described in Section 2.3 will not be dealt with. This is primarily due to the lack of data to quantify the amount of degradation and its correlation with cyclic shear strain (Lee and Focht, 1976; Idriss *et al.*, 1978a among others). The cyclic shear strains are difficult to relate to the deformation

of an element of soil in the field, especially for cyclic lateral loading on piles, where the amount of strain experienced by the soil along the entire pile depth varies and can hardly be determined.

When a pile is loaded laterally, the soil at the sides of the pile will be subjected, predominantly, to shearing, while the front face of an advancing pile will be subjected to compression (bearing). This behaviour can be seen in Figure 4.1 from the finite element analysis for the half-debonded case described in Section 3.9.2. The finite element results indicate a pattern of outward radial movement of the soil at the front and side of the pile, and inward movement behind the pile

From the orientation of the displacement vectors surrounding the pile, various failure mechanisms in the soil around the pile can be envisaged. In particular, the shear strength and bearing strength degradation can be isolated. It is observed that soils under shearing and bearing will exhibit the same trend of post-peak drop in strength, but that they may be of different magnitudes.

4.3 Degradation of shear strength

The shear strength behaviour of normally consolidated (N-C) and overconsolidated clays (O-C), with regard to peak and residual shear strengths and residual angle of shearing resistance (ϕ'_r), is depicted in Figure 4.2. This figure shows results typical of those obtained by carrying out slow drained tests in a shear box apparatus, in which the clay is subjected to displacements amounting to several centimetres.

As the clay is strained, so it builds up increasing resistance. However, under a given normal effective stress, there is a definite limit to the resistance the clay can offer (the peak strength). In ordinary practice, the test is stopped shortly after the peak strength has been clearly defined, and the peak strength is simply referred to as the 'shear strength' of the clay (under the given normal effective stress). If, however, the test is continued, the displacement will increase and the resistance of the clay decreases. This process, which may be called 'strain softening' or strength degradation, is not without limit, for ultimately, a certain 'residual strength' is reached which the clay maintains even when subjected to large displacements.

The peak and residual shear strengths, when plotted against normal effective stress, would show a relationship approximately in accordance with the Mohr-Coulomb law (Figure 4.2). The peak shear strengths can therefore be expressed as:

$$\tau_f = c' + \sigma'_n \tan \phi' \quad (4.1)$$

and the residual shear strength as:

$$\tau_r = c'_r + \sigma'_n \tan \phi'_r \quad (4.2)$$

where c' is the cohesion intercept,

ϕ' is the angle of shearing resistance,

σ'_n is the normal effective stress,

c'_r is the residual cohesion intercept, and

ϕ'_r is the residual angle of shearing resistance.

Test results reported by Skempton (1964), Bishop *et al.* (1965,1971), Skempton and Petley (1967), Lacasse *et al.* (1985), Head (1988), Burland (1990), among others, show almost invariably that c'_r is very small, and probably not significantly different from zero. Hence, the residual shear strength may be written simply as:

$$\tau_r = \sigma'_n \tan \phi'_r \quad (4.3)$$

This indicates that in moving from the peak to the residual shear strength, the cohesion intercept (c') disappears completely. During the same process, the angle of shearing resistance also decreases; in some clays, by only 1° or 2° , but in others by as much as 10° .

4.3.1 Causes of shear strength degradation

Skempton (1985) states that the post-peak drop in drained shear strength of an intact overconsolidated clay may be considered as being due, firstly, to an increase in water content (dilatancy) and, secondly, to the reorientation of the clay particles parallel to the direction of shearing. At the end of the first stage, the 'fully softened' or 'critical state' strength is reached.

Under larger displacements, when reorientation is completed, the shear strength falls to and remains constant at the residual value; see Figure 4.3a. In normally consolidated clays, which consolidate when sheared, the post-peak drop in shear strength is due entirely to particle reorientation, as depicted in Figure 4.3a.

The effects of particle reorientation are felt, to an appreciable extent, only in clays containing platy clay minerals and having a clay fraction (percentage by weight of particles smaller than 2 μm) exceeding about 20 - 25%. Silts and sandy clays, with lower clay fractions, exhibit nearly the classical 'critical state' type of behaviour in which, even at large displacements, the strength is scarcely less than the normally consolidated peak values, and the post-peak drop in shear strength of overconsolidated material of this kind is due almost entirely to water content increase, as shown in Figure 4.3b. Maksimovic (1996) suggests that particle breakage, interparticle friction and bond may also play an important role in shear strength degradation for normally and overconsolidated clays, depending on the magnitude of the normal effective stress.

For soil subjected to undrained loading conditions, the post-peak drop in undrained shear strength of the clay is mainly due to the accumulation of excess pore water pressure, particle reorientation and reduction of interparticle bonds.

Irrespective of the physical explanation of the drop in shear strength after passing the peak, the existence of this decrease in strength (especially in overconsolidated clays) must be accepted as a fact which has been fully established. Thus, if for any reason a clay is forced to pass the peak at some particular point within its mass, the strength at that point will decrease. This action will 'throw' additional stress on to the clay at some other point causing the peak to be passed at that point also. In this way, a progressive failure can be initiated and, in the limit, the soil shear strength at the side of the pile along its entire length will fall to the residual value, leading to a large reduction in pile lateral capacity.

4.3.2 Plastic displacement

It is noted that the plastic shear displacement (i.e. soil displacement after peak shear strength is reached) required to attain the residual shear strength varies for different test methods. For triaxial tests, this is relatively small (Bishop *et al.*, 1965; Burland, 1990), approximately 1 to 4 mm (corresponding to 1% to 5% axial strain), whereas for shear box

tests, the plastic displacement ranges from 5 mm to as high as 50 mm or even more (Skempton, 1964, 1985; Skempton and Hutchinson, 1969).

For triaxial tests, the failure plane is often not clearly defined on the $45^\circ + \phi^0/2$ plane, and the plastic displacement is a function of specimen height.

In the case of shear box tests, the failure plane is well-defined, by sliding on the horizontal plane. The plastic displacement is not restricted as the shear box can always be brought back to its starting position (multiple-reversal) during the test; see Figure 4.4. Thus the plastic displacement to reach residual strength may be much greater than for triaxial tests. Evidence of substantial discontinuity on the failure plane can be observed in these tests as opposed to triaxial tests.

For ring shear tests, the plastic displacement often exceeds 100 mm and in some cases an excess of 500 mm is necessary, before the shear strength of an intact clay falls to the residual value (Skempton, 1985; Bishop *et al.*, 1971; Lupini *et al.*, 1981). It is believed that the displacements required to establish residual conditions have been slightly overestimated, and the residual strength measured underestimated by these testing procedures.

The shear strength results obtained from the (multiple-reversal) shear box tests are probably most appropriate for the present study, as compared with triaxial and ring shear tests (which are more suitable for slope stability analyses, where shearing displacement is monotonic). However, shear strength results from ring shear tests and triaxial tests are also employed where necessary.

4.4 Correlations of shear strength degradation with soil index properties

Regarding the degradation from peak to residual shear strength, Figure 4.5 shows that this is not consistent for the overconsolidated clays presented by Skempton (1964). The cause of this happening may be related to the soil index properties listed in Table 4.1.

The Selset boulder clay has been consolidated under a moderate thickness of ice, but it is very sandy with a clay fraction of only 17%. Consequently, the cohesion intercept (for the peak shear strength) is not large and there is only a drop of 2° between the peak (ϕ') and the residual (ϕ'_r) angles of shearing resistance. The peak strength is 1.4 times the residual shear strength at a normal effective stress of 1000 lb/ft². The Jari clay has been consolidated under at least 2,000 ft of sediments. It is very strong in its undisturbed state as compared with the Selset, London and Walton's Wood clays, yet the residual shear strength indicates a zero

residual cohesion intercept and ϕ'_r of 18° . The peak shear strength is about 3.6 times greater than the residual shear strength at a normal effective stress of 1000 lb/ft^2 . The London clay, of Eocene age, has been consolidated under 500 ft to 1000 ft thickness of sediments, subsequently eroded. The peak shear strength is about 2.4 times the residual shear strength at a normal effective stress of 1000 lb/ft^2 with $\phi'_r = 16^\circ$. For Walton's Wood clay from Staffordshire, the peak shear strength is three times the residual shear strength at a normal effective stress of 1000 lb/ft^2 , and ϕ' is 1.6 times greater than ϕ'_r .

From the above evaluation, it may be implied that the degradation from peak to residual shear strength and ϕ'_r can be correlated with the index properties of the clays. This question is discussed in the next Section.

4.4.1 Correlations of residual angle of shearing resistance (ϕ'_r) with soil index properties

The peak and residual strengths of the overconsolidated clays described above are shown in Figure 4.5, and their index properties tabulated in Table 4.1. There appears to be a correlation between angle of shearing resistance (ϕ'_r) and these indices. For example, the Selset clay has low clay fraction and relatively high ϕ'_r . The clay fractions shown in Table 4.1 taken together with the results depicted in Figure 4.6, indicate that ϕ'_r decreases with increasing clay content.

Skempton (1985) states that the clay minerals can have little effect on residual strength when the clay fraction is less than 20%, as the strength is then controlled largely by the sand and silt particles. With clay fractions exceeding 40%, the residual strength depends almost entirely on the sliding friction of the clay particles, as well as their shape. A pictorial view of the influence of the clay fraction on post-failure given by Lupini *et al.* (1981) is shown in Figure 4.7. For higher clay contents, well-developed shear surfaces form due to the preferred reorientation of the clay particles.

A correlation of ϕ'_r with plasticity index (I_p) was given in Figure 4.8, after Fleischer (1972), for various stiff clays, based on ring shear tests with varying strain rates. Voight (1973) also found a relationship between ϕ'_r and I_p , using the results of others (Figure 4.8). Vaughan *et al.* (1978) summarised tests in the ring shear apparatus at Imperial College, mainly on natural clays of medium activity. They suggested the discontinuous relationship between ϕ'_r and I_p which is shown in Figure 4.8. They indicated that the controlling factor was likely to be the proportion of platy clay minerals present, and that this would correlate with I_p .

for clays of similar activity. Bucher (1975) used two strain-controlled ring shear devices of different design and multiple-reversal shear box tests to study the influence of stress history, stress level and temperature on residual friction angle. He presented a relationship between I_p and ϕ'_r similar to that of Vaughan *et al.* (1978), shown in Figure 4.8. He found that the ϕ'_r of two different clays ($I_p = 27\%$, $\phi'_r = 12.5^\circ$, and, $I_p = 30\%$, $\phi'_r = 25.6^\circ$) was unaffected by temperature changes between 10°C and 60°C .

Relationships between clay fraction and plasticity index with ϕ'_r for natural soils were given by Lupini *et al.* (1981), depicted in Figures 4.9 and 4.10, respectively. There seems to be a discontinuous change in shearing resistance at a clay fraction of 35% or I_p of 30%. However, a number of test results clearly fall outside any reasonable correlation band. The reason may be the shape of clay particles (proportions of platy and rotund particles), improper determination of the soil index properties, etc., as explained by Lupini *et al.* (1981).

Other correlations for ϕ'_r , for example, using liquid limit, have been presented by Mersi and Cepeda-Diaz (1986); see Figure 4.11. From the above, simple correlations with index properties may be adequate for the prediction of residual strength (using ϕ'_r) for engineering purposes, despite the scatter in the data.

4.4.2 Correlations of residual/peak shear strength ratio (R_s) with soil index properties

The degradation of shear strength obtained from shear box tests reported by Skempton (1964) and Bishop *et al.* (1971) is used as the basis for the following correlations. The soil strength parameters and index properties are tabulated in Table 4.2. Assuming normal effective stress (σ'_n) range of 5 to 300 kPa, applying Equations (4.1) to (4.3) and using the soil data from Table 4.2, the residual/peak shear strength ratios (R_s) of the clays are determined and is defined as:

$$R_s = \frac{\tau_r}{\tau_f} \quad (4.4)$$

where τ_r is the residual shear strength, and

τ_f is the peak shear strength.

The residual/peak shear strength ratios (R_s) are plotted against liquid limit in Figure 4.12a and against clay fraction in Figure 4.12b. It is observed that the range of R_s values for σ'_n of 5 to

300 kPa is small for plots *R/P 3A* and *R/P 4A* (see Table 4.2 for descriptions). This is due to the presence of residual cohesion intercept (c'_r) in these clays, giving a high value for the residual shear strength. However, setting c'_r to zero and using the average value of ϕ'_r from Petley (1966, 1969) results, have increased the range of R_s values. These are shown in Figures 4.13a and 4.13b; with plots *R/P 5A*, (*R/P 6A*) replacing *R/P 3A*, (*R/P 4A*).

The general trend from shear box tests shown in Figure 4.13, is that for a given increase in liquid limit and clay fraction, the amount of shear strength degradation is higher. It is shown in Figure 4.13, that for clays exceeding the 50% liquid limit or 40% clay fraction, R_s can be taken as 0.1, (0.5, 0.55) for $\sigma'_{vn} = 5$ kPa, (100 kPa, 300 kPa). For clays having liquid limit less than 30% or clay fraction less than 20%, R_s will be 0.3, (0.8, 0.85) for $\sigma'_{vn} = 5$ kPa, (100 kPa, 300 kPa). Comparing Figure 4.13a with 4.13b, it can be seen that the liquid limit is related to the clay fraction. It is noted that the increase in σ'_{vn} from 200 to 300 kPa causes only slight increase in R_s . The correlation of R_s with plastic limit is not good and has therefore not been presented.

The above correlations of R_s with liquid limit and clay fraction are based on drained tests, and are assumed to apply for undrained tests, so that it can be employed for the cyclic analysis under undrained loading conditions. This assumption is made due to the limited data for the post-peak drop of undrained shear strength of soil. From the triaxial test results of intact Corinth Marl and intact Todi clay reported by Burland *et al.* (1996), R_s values for drained tests are found to be similar to the values for undrained tests (tested under approximately the same effective consolidation pressures). The results obtained from Ward *et al.* (1965) on London clay (liquid limit = 70% and clay fraction = 57%) tested using quick undrained compression tests, gives $R_s = 0.6$. This agrees with the correlations of R_s based on liquid limit and clay fraction depicted in Figures 4.13a and 4.13b, respectively. It is therefore justifiable to assume that R_s for drained tests are equal to those for undrained tests.

4.4.2.1 Modifications of R_s for low normal effective stress

It is observed in Figure 4.13, that the shear strength degradation at low normal effective stress range (e.g. $R_s = 0.1$ for $\sigma'_{vn} = 5$ kPa) is very high, in comparisons with shear strength degradation for $\sigma'_{vn} > 50$ kPa. This is due to the linear extrapolation of the peak shear strength failure envelope at $\sigma'_{vn} > 100$ kPa towards the zero normal effective stress (see Figure 4.14), giving the cohesion intercept (c') and hence the peak shear strength of soil obtained via

Equation (4.1). This will give unsafe and high values of shear strength which the clay does not possess at low normal effective stresses ($\sigma'_n = 5$ to 50 kPa), thus leading to low R_s which is unduly conservative.

Maksimovic (1989a) shows that the shear strength failure envelope for compacted London clay is very much non-linear as observed in Figure 4.14, especially for $\sigma'_n = 5$ to 50 kPa. Experimental evidence of non-linear shear strength failure envelope can also be seen in Bishop *et al.* (1965, 1971) and Atkinson and Farrar (1985). Their results show that only when $\sigma'_n = 100$ to 400 kPa, can we define the shear strength failure envelope by a straight line.

Bilinear approach

Several expressions for the non-linear failure envelopes, mostly in the form of power or logarithmic relationships have been reported in the literature. The main shortcomings of these proposals are their validity in limited stress ranges. The hyperbolic expression proposed by Maksimovic (1989a, 1989b, 1996) offers good possibilities for simple description of the non-linear shear strength failure envelope within the widest possible range of stresses. However, the procedure is tedious and its application requires good experimental data.

For simplicity, the bilinear approach seems to be an appropriate and simple way to determine the soil shear strength at low to high normal effective stress range. Taking $c' = 0$ for clay subjecting to $\sigma'_n \leq 50$ kPa, while beyond the 50 kPa stress level, the c' value determined from the experimental tests can be used; see Figure 4.15. The selection of $\sigma'_n = 50$ kPa as the distinct mark for the transition of highly curved to a straight line failure envelope is based on the observation and results presented by Bishop *et al.* (1965) and Maksimovic (1996). This suggests that for $\sigma'_n \leq 50$ kPa, the peak shear strength will be determined as:

$$\tau_f = \tau_{50} \frac{\sigma'_n}{50} \quad (4.5)$$

where τ_{50} is the shear strength at $\sigma'_n = 50$ kPa based on Equation (4.1).

The above equation applies to the peak shear strength under low normal effective stress for normally consolidated and overconsolidated clays.

For the residual shear strength, though its failure envelope is curved with residual cohesion intercept approximately equal to zero (Maksimovic, 1996; Kenney, 1967 and

Bishop *et al.*, 1971), it is reasonably accurate to adopt the straight line residual strength failure envelope expressed in Equation (4.3).

Using the bilinear approach, the peak shear strengths for σ'_n from 0 to 300 kPa were determined using Equations (4.1) and (4.5). Adopting Equation (4.3) for residual shear strength determination, the results presented in Figures 4.13a and 4.13b were modified for R_s at low normal effective stress range ($\sigma'_n = 0$ to 50 kPa); see Figures 4.16a and 4.16b.

Based on the simple modification described above, R_s is now constant for $\sigma'_n = 0$ to 50 kPa. Figure 4.16 shows that for clays exceeding 50% liquid limit or 40% clay fraction, R_s can be taken as 0.3, (0.5, 0.55) for $\sigma'_n = 0$ to 50 kPa, (100 kPa, 300 kPa). For clay with liquid limit less than 30% or clay fraction lower than 20%, R_s can be taken as 0.7, (0.8, 0.85) for $\sigma'_n = 0$ to 50 kPa, (100 kPa, 300 kPa).

4.5 Rate of degradation of shear strength

From the shear box test results reported by Skempton (1964), it is shown in Figure 4.17 that the amount of shear strength degradation after passing its peak is dependent on the plastic shear displacement of the soil. It also illustrates that for different clays, the plastic shear displacements to reach residual shear strength will vary.

Considering only the peak to residual shear strength behaviour, the results in Figure 4.17 are replotted into Figure 4.18. From the trend of the shear strength degradation curves, it suggests that the exponential function can be used to describe the post-peak strength degradation. The current shear strength (post-peak) can be expressed as:

$$\tau = \tau_r + (\tau_f - \tau_r) \exp^{-C_s ds} \quad (4.6)$$

where C_s is the shear degradation rate factor in mm^{-1} , and d_s is the plastic shear displacement.

The first term on the RHS of Equation (4.6) describes the magnitude of residual shear strength. The second term describes the rate of degradation from peak to residual shear strength by using the shear degradation rate factor C_s , according to the magnitude of plastic shear displacement. To categorise the rate of shear strength degradation as slow, medium and fast, C_s values of 0.1, 0.5 and 1.0, respectively, are used and illustrated in Figure 4.19.

The use of Equation (4.6) to match the shear test results in Figure 4.18 is illustrated in Figure 4.20. The matches are reasonably good. $C_s = 0.2$ to 0.7 gives the best match to the post-peak strength degradation of Walton's Wood, Jackfield and London clays. The index properties of these clays listed in Table 4.3, suggest that C_s can be related to their indices.

4.5.1 Shear degradation rate factor (C_s) determination

In order to have a convenient quantitative expression by which the shear strength has fallen from peak to residual, for all types of clays with different magnitudes of peak and residual shear strengths, the residual shear ratio (R_{sr}) is used. It is defined as:

$$R_{sr} = \frac{\tau - \tau_r}{\tau_f - \tau_r} \quad (4.7)$$

Using the above expression, the residual shear ratio (R_{sr}) is plotted against the plastic shear displacement (d_s) to determine the rate of shear strength degradation. The post-peak shear strength degradation results obtained from various test methods described below, were used to determine C_s , and later, to establish correlations with the soil index properties.

Shear Box tests

The shear strength degradation results reported by Skempton (1964, 1985), using the shear box apparatus were considered. The descriptions of these clays are listed in Table 4.3. The residual shear ratios (R_{sr}) of these clays are plotted against the plastic shear displacement (d_s) in Figure 4.21. It shows that the clays from Jackfield, Barbara and Walton's Wood have a rapid rate of degradation as compared with the London clay, judging by the rapid decline of the initial curve at plastic shear displacements of 0 to 5 mm.

Using Equations (4.6) and (4.7) to best match the post-peak shear strength degradation curves shown in Figure 4.22, indicates that C_s is between 0.2 to 0.7. Note that it is important to have good curve matching in the initial portion of the degradation curve as the reduction of strength is more significant.

Ring Shear tests

The clays tested using the ring shear tests are listed in Table 4.4. The post-peak shear strength degradation curves of these clays are depicted in Figure 4.23. Using Equations (4.6)

and (4.7), Figure 4.23 shows that the best match C_s lies between 0.07 to 0.3 for Blue London clay and Kalabagh clay, with an exceptionally low C_s of 0.03 for the Brown London clay from Walthamstow.

Triaxial tests

The details of the clays tested using the triaxial tests are listed in Table 4.5. Figure 4.24 shows the post-peak shear strength degradation of the Norwegian marine clays, Todi and London clays. Applying Equations (4.6) and (4.7), the plot shows that Emmerstad clay, (Ellingsrud clay, Onsøy clay, London clay, Todi clay) can be matched using $C_s = 1.5$ to 2, (0.8 to 1.0, 0.4 to 0.5, 0.9 to 1.0, 2.0). The C_s values determined for the above mentioned test methods are summarised in Table 4.6.

4.6 Correlation of rate of shear strength degradation with soil index properties

The rate of shear strength degradation is described by the shear degradation rate factor (C_s). To establish correlations of C_s with soil index properties, the C_s values determined from the above tests were plotted against liquid limit, clay fraction and plasticity index as depicted in Figures 4.25a, 4.25b and 4.25c, respectively. From these figures, it appears that the triaxial tests (marked with *T* in the plots) give a very fast rate of shear strength degradation. Table 4.6 shows that London clay tested by shear box tests and ring shear tests give similar C_s values of around 0.2, while the tests conducted by triaxial apparatus gives C_s of 0.9 (differences of 4.5 times). The reasons may be due to the method of tests conducted, orientation of failure plane, etc. (Section 4.3.2). This may also suggest that the triaxial tests are not suitable for the accurate determination of the rate of shear strength degradation.

Discarding C_s determined from triaxial test results, Figure 4.26 indicates that C_s tends to be higher with lower liquid limit, clay fraction and plasticity index, but the results are scattered at higher liquid limit, clay fraction and plasticity index. The low $C_s = 0.03$ for Brown London clay from Walthamstow may be due to shearing along the fissure plane (numerous fissures and joints were found in the Brown London clay).

The wide range of normal effective stress (91 kPa to 525 kPa) applied to the specimens for simple shear box and ring shear tests may be one of the factors which caused

the scattered results. As seen in Table 4.6, lowering the normal effective stress from 283 to 207 kPa for the ring shear tests on Blue London clay, gives a decrease in C_s from 0.3 to 0.15. Different C_s values are also seen in the triaxial tests for the Norwegian clays listed in Table 4.6 tested using different consolidation pressures. Coupled with the normal effective stress effect, fissure conditions, particle breakage, etc. (in addition to the apparatus constraints and human errors), may have substantial influences on the rate of shear strength degradation

If field results on degradation rate are not available, one might use C_s of 0.5 for liquid limit, (clay fraction, plasticity index) of less than 50%, (40%, 30%). C_s of 0.2 can be used for liquid limit, (clay fraction, plasticity index) greater than 60%, (50%, 40%). Figure 4.26 can be used as a reference guide for the range of soil index properties.

4.7 Degradation of bearing strength

The soil at the front face of an advancing pile is subjected to compression (bearing). The degradation in its bearing strength can be expected to display a similar trend to that of shear strength degradation, i.e. the peak bearing strength reduces towards a residual value when the soil is subjected to large displacements. This is illustrated in Figure 4.27 using plate loading tests reported by Ward *et al.* (1965).

The failure mechanism involved in bearing, may be viewed as a footing embedded in cohesive soil resulting in a wedge failure as described by Whitaker (1970), and as illustrated in Figure 4.28. The soil will flow or shear along the interfaces of zones *A* and *B*, and along the boundary of zones *B* and *C*. Fleming *et al.* (1985) described the failure mechanism for circular piles; soil flows along two intersecting circular zones causing shear failure as depicted in Figure 4.29. Alternatively, bearing failure may be postulated as the failure mechanism at the base of a deep foundation as described by Meyerhof (1951). A bulb system of shear zones is developed as illustrated in Figure 4.30, and the soil will be sheared along the boundary of *BCEG* and *ACDF*.

Whatever the failure mechanism that one may adopt, a rigid zone in front of the pile is involved, pushing the soil forward and radially away from the pile as depicted in Figure 4.31. The soil will be sheared along *AC*, *BC*, *CD* and *DE*. However, the failure mechanism in bearing is not very well defined as compared with simple sliding along the side of the pile at points *A* and *B*. The causes of bearing strength degradation can be taken as similar to that

described for shear strength degradation in Section 4.3.1, involving accumulation of pore water pressure, particle reorientation, particle breakage, etc., but over a wider soil area.

4.7.1 Experimental observations

Bearing strength degradation has been examined using plate loading tests (Ward *et al.*, 1965). The tests were carried out on London clay at Ashford Common shaft at different soil depths, with liquid limits ranging between 60% to 71%, plastic limits between 24% to 29% and clay fractions between 44% to 60%.

The results from peak to residual bearing strength obtained from the plate loading tests are shown in Figure 4.27. To describe the magnitude of bearing strength degradation, the residual/peak bearing strength ratio (R_b) is used, and is defined as:

$$R_b = \frac{t_r}{t_f} \quad (4.8)$$

where t_r is the residual bearing strength, and

t_f is the peak bearing strength.

From the results depicted in Figure 4.27, the tests *ET/1* (Level *E* at depth of 34.8 m) and *CT/2* (Level *C* at depth of 20.1 m) give $R_b = 0.48$ and 0.41, respectively (based on extrapolation to assumed residual bearing strength). The minor difference in results between peak and residual bearing strength especially for *ET/2* and *FT/2* (Level *F* at depth of 42.1 m), is due to the position of the fissures in relation to the plate. Ward *et al.* (1965) explained that, if the fissures were located in positions which allowed the failure to occur almost entirely along the fissure, then the peak would be small as for Tests *ET/2* and *FT/2* in Figure 4.27. This is because the fissure acts as stress concentrator or discontinuous plane of weakness, whereby the strength of the soil will be greatly diminished. It is unlikely that the strength on a fissure or joint can be appreciably higher than the residual value. The largest peaks were obtained when the fissures were so located that part of the failure was forced to pass through some of the unfissured clays as in Tests *CT/2* and *ET/1*. The plastic bearing displacements (i.e. soil displacement after peak bearing strength is reached) attained by *ET/1* and *CT/2* based on extrapolation, are approximately 15 mm before reaching to the residual bearing strength.

Similar bearing strength degradation behaviour for plate loading tests, was obtained for the quick undrained compression tests on cylindrical specimens of 76 mm long by 38 mm diameter prepared from blocks in the laboratory (Ward *et al.*, 1965); see Figure 4.32. Very pronounced peaks were obtained for intact specimens containing no fissures, giving $R_b = 0.6$ and a plastic displacement of 5 mm (greater than 6% axial strain) by extrapolation to assumed residual strength. When failure occurred partly along existing fissures, smaller peaks were found and where the failure occurred entirely along a fissure, little or no peak was noted.

Further investigation on bearing strength degradation was obtained from the plate loading tests reported by Andersen and Stenhamar (1983). The in-situ plate loading tests were carried out on a medium stiff overconsolidated clay at Haga in Norway. The plasticity index is 15% and clay fraction is 45%.

The load-displacement curves from the plate loading tests are presented in Figures 4.33 and 4.34 for Test 1 and Test 3, respectively. The vertical load or bearing strength (area of square steel plate is 1 m^2) for Test 1, loaded to failure in 24 minutes is 340 kPa. For the more rapid Test 3 with vertical loading to failure in 45 seconds (60 times faster than the rate of testing for Test 1), the bearing strength is 10% higher, i.e. 375 kPa. It is evident that the loading rate is not an important factor in the present study.

The residual bearing strength for Test 1 was not fully registered as observed in Figure 4.33. After the vertical load reaches its peak, the soil degrades slowly as seen from the gentle decline of the load till it reaches about 260 kN, after which, there is a vertical drop in load. This may be due to the quick release of pressure in the hydraulic jack. Obviously, the load at residual will be less than 260 kN, giving R_b of less than 0.76 and a plastic bearing displacement of more than 40 mm. The stepping of the curve prior to reaching to its peak is due mainly to the sequence of unloading and reloading, which does not show significant change to the load-displacement response for loads up to 300 kN; compare Test 1 with Test 3 in Figure 4.34. The degradation from peak to residual for Test 3 was not recorded, but a vertical drop of load can be clearly seen in Figure 4.34, suggesting a sudden release of hydraulic pressure.

It is difficult with the scant information available to make firm recommendations. However, based on the limited amount of data available, one can assume $R_b = 0.4$ to 0.7. The soil depth did not seem to have a significant influence on R_b , as noted from the results from

Ashford Common and Haga sites. Details of R_b and soil index properties are listed in Table 4.7.

4.8 Rate of degradation of bearing strength

The bearing strength degradation from peak to residual depicted in Figures 4.27 and 4.33, shows that it is influenced by the plastic bearing displacement of the soil. Since the trend of bearing strength degradation is similar to the shear strength degradation, it suggests the use of exponential function to describe the post-peak bearing strength degradation.

The current bearing strength (post-peak) as a result of bearing strength degradation is expressed as:

$$t = t_r + (t_f - t_r) \exp^{(-C_b db/D)} \quad (4.9)$$

where C_b is the bearing degradation rate factor,

d_b is the plastic bearing displacement, and

D is the plate diameter or width.

The first term on the RHS of Equation (4.9) describes the magnitude of residual bearing strength. The second term describes the rate of bearing strength degradation from peak to residual bearing strength by the use of the bearing degradation rate factor (C_b), according to the magnitude of the plastic bearing displacement. The diameter (or width) of the plate is used to normalise the plastic bearing displacement since there appears to be a scale effect. Ward *et al.* (1965) and Golder and Leonard (1954) have reported that the bearing strengths of the clays are strongly influenced by the size of the plate used in the plate loading tests.

Rate of bearing strength degradation (C_b) of 10, 50 and 100 are identified as slow, medium and fast rates, respectively, and are illustrated in Figure 4.35.

4.8.1 Bearing degradation rate factor (C_b) determination

The results from Ward *et al.* (1965) were employed for this study. Relevant results are taken from plate loading tests on intact clays, i.e. ET/1 and CT/2 in Figure 4.27. To have a convenient quantitative expression for the amount by which the peak bearing strength has

reduced to its residual, for all types of clays, the residual bearing ratio (R_{br}) is used, and is expressed as:

$$R_{br} = \frac{t - t_r}{t_f - t_r} \quad (4.10)$$

Considering only the peak to residual bearing strength, the results of R_{br} were plotted against the plastic bearing displacement (d_b). Different C_b values were used to determine the rates of bearing strength degradation which match closely the experimental results.

For the result of $ET/1$, the best match C_b values were between 30 to 50, and for $CT/2$ were between 10 to 20 as depicted in Figure 4.36. The value for C_b is dependent upon the type of soil encountered in the site. With the lack of information on the rate of bearing strength degradation, C_b can simply be taken as ranging between 30 to 50. Details of C_b and soil index properties are listed in Table 4.7.

4.9 Application to cyclic analysis

For simplicity, the cyclic analysis is based on an elastic-perfectly plastic model for soils, which are assumed to behave linearly elastically at small strains, but yield when certain limit stresses (peak strength) are reached. After the soil yields, its limit stress will degrade according to the magnitude of plastic displacement, as described in Section 4.5.

Shear strength degradation

The soil elements at the side face of the pile are subjected to shearing. They will yield when the yield stresses (t_{sys}) for shearing (taken as the limit shear stresses (t_{ss}), i.e. $t_{sys} = t_{ss}$), are attained. After which, the limit shear stress will degrade to the residual limit shear stress at large plastic shear displacements. The residual limit shear stress for each shearing soil element can be determined as:

$$t_{ssr} = R_s t_{ss} \quad (4.11)$$

where R_s is the residual/peak shear strength ratio, and

t_{ss} is the limit shear stress.

In the absence of experimental data for the residual/peak shear strength ratio (R_s), Figure 4.6 and Figures 4.8 to 4.11 can be used to determine the residual angle of shearing resistance ϕ' , based on the soil index properties. Thereafter, using Equation (4.3) to determine the residual shear strength, and with the knowledge of the peak shear strength (Equation (4.5) may be required for low σ'_n), to determine R_s using Equation (4.4). For a simple estimation of R_s for different types of clays, Figure 4.16 can be used as a guide, provided that the index properties of the clay are known.

The shear strength degradation only applies to the shearing soil elements that have yielded in shear, i.e. the shear stress reaches t_{sys} . The plastic shear displacements (d_s) are determined (from the pile displacements) when the shearing soil elements are plastic. While the shearing soil elements continue to yield with increasing loads, d_s will increase. When the shearing soil elements have recovered from plastic to elastic (e.g. initial stage of unloading and reloading), the limit shear stresses will degrade according to an exponential function (analogous to Equation (4.6)) to a new value. This value is known as the reduced limit shear stress (t_{ssd}), and is determined based on the plastic shear displacement (accumulated from the loading/reloading and unloading cycles):

$$t_{ssd} = t_{ssr} + (t_{ss} - t_{ssr}) \exp(-C_s ds) \quad (4.12)$$

where C_s is the shear degradation rate factor in mm^{-1} .

The value of C_s can be determined from Figure 4.26 with knowledge of the soil index properties. After determining the reduced limit shear stress, it is now set to be the yield stress for shearing, i.e. $t_{sys} = t_{ssd}$ for that loading/reloading or unloading cycle.

The plastic shear displacement for the plastic shearing soil elements will progressively increase for each cycle, and the reduced limit shear stress will progressively decrease until the residual limit shear stress is reached. This is illustrated in Figure 4.37.

Bearing strength degradation

The soil elements at the front face of the advancing pile are subjected to bearing. They will yield when the yield stresses (t_{sys}) for bearing (taken as the limit bearing stresses (t_{sc}), i.e. $t_{sys} = t_{sc}$), are reached. After which, the limit bearing stress will degrade to the residual limit

stress, at large plastic bearing displacements. The residual limit bearing stress for each bearing soil element is determined as:

$$t_{scr} = R_b t_{sc} \quad (4.13)$$

where R_b is the residual/peak bearing strength ratio, and
 t_{sc} is the limit bearing stress.

Recommendations for the values of R_b are found in Section 4.7.1 and Table 4.7.

The bearing strength degradation only applies to the bearing soil elements that have yielded in bearing, i.e. the bearing stress reaches t_{sys} . The plastic bearing displacements (d_b) are determined (from pile displacements) when the bearing soil elements are plastic. While the bearing soil elements continue to yield with increasing loads, d_b will increase. When the bearing soil elements have recovered from plastic to elastic (e.g. in the initial stage of unloading and reloading), the limit bearing stresses will degrade according to the exponential function (analogous to Equation (4.9)) to a new value. This value is known as the reduced limit bearing stress (t_{scd}), and is determined based on the plastic bearing displacement (accumulated from the loading/reloading and unloading cycles):

$$t_{scd} = t_{scr} + (t_{sc} - t_{scr}) \exp^{-C_b db/D} \quad (4.14)$$

where C_b is the bearing degradation rate factor, and
 D is the pile diameter or width.

Recommendations for the value of C_b can be found in Section 4.8.1 and Table 4.7. The reduced limit bearing stress is now set to be the yield stress for bearing, i.e. $t_{sys} = t_{scd}$ for that loading/reloading or unloading cycle.

The plastic bearing displacement for the plastic bearing soil elements will progressively increase for each cycle, and the reduced limit bearing stress will progressively decrease until the residual limit bearing stress is reached. This is shown in Figure 4.38.

4.10 Discussion

In practice, the maximum shear strength of the soil or the strength parameters c' and ϕ' are easily available, but not the residual strength. As such, correlations of residual angle of shearing resistance (ϕ'_r) with soil index properties have been presented, to enable the determination of residual strength of the soils. After which, R_s (residual/peak shear strength ratio) can be calculated, and used in the cyclic analysis to determine the residual limit shear stress of the soil.

From the shear test results, it appears that R_s is dependent on the magnitude of the normal effective stress applied. Peak shear strengths of the clays are over-predicted using the Mohr-Coulomb's straight line equation. As such, the bilinear approach is adopted to give reasonable estimates of the R_s values over a wide range of normal effective stresses. For practical purposes, correlations of R_s with soil index properties are presented in Figure 4.16.

From the experimental results, it appears that the rate of shear strength degradation, described by the shear degradation rate factor (C_s), can be related to the soil index properties. As such correlations of C_s with soil index properties were presented in Figures 4.25 and 4.26.

For post-peak bearing strength degradation, the parameters R_b (residual/peak bearing strength ratio) and C_b (bearing degradation rate factor) are used to describe the magnitude of residual bearing strength and the rate of degradation, respectively. These parameters may also be correlated with the soil index properties. However, due to the limited test results on bearing strength degradation, such correlations have not been presented. The recommended values for R_b and C_b are discussed in Sections 4.7.1 and 4.8.1, respectively. With the knowledge of the soil index properties, Table 4.7 can be used as a guide.

The use of the exponential functions to describe the post-peak shear strength and bearing strength degradation via Equations (4.6) and (4.9), respectively, appear to be satisfactory. These equations (in a modified form: Equations (4.12) and (4.14)) are employed in the cyclic analysis, to determine the reduced limit stress for each cycle of loading, depending on the plastic displacement of the soil.

4.11 Concluding remarks

The subject of soil strength degradation is presented based on the experimental results provided by various researchers. From their results, it appears that the degree and rate of strength degradation can be related to the index properties of the soil.

To describe the post-peak shear strength and bearing strength degradation of the soils, the strength degradation parameters, namely R_s , C_s , R_b and C_b are required for the soil model. These parameters can be obtained from experimental tests with few of the complications and difficulties of the other soil models described in Chapter 2. Alternatively, these parameters can be correlated with the soil index properties as discussed in this Chapter.

For the post-peak strength degradation of soil to their residual limits, Equations (4.6) and (4.9) have been proposed. These equations provide a description of the shear strength and bearing strength degradation, as observed in experimental tests. The application of these equations to the soil model for cyclic analysis is straight forward: we determine the reduced limit stress for each cycle of loading as a function of the plastic displacement of the soil.

With the soil strength degradation model now defined, the boundary element analysis of cyclic laterally loaded piles can now be developed.

Table 4.1 Index properties of clays, after Skempton (1964).

Clay type	Liquid Limit (%)	Plastic Limit (%)	Plasticity Index (%)	Clay Fraction (%)
Selset clay	26	13	13	17
Jari clay	70	27	43	47
London clay	82	29	53	55
Walton's Wood clay	53	28	25	69

Table 4.2 Soil index properties and strength parameters determined from shear box tests.

Plot Name	Soil type & site	Test method and index properties	Peak		Residual		Reference
			c' (kPa)	ϕ' (°)	c'_r (kPa)	ϕ'_r (°)	
R/P 1	Jackfield clay from Shropshire	Drained shear box test $LL=41, PL=22, CF=36, PI=22$	10.5	25	0	19	Skempton, 1964
R/P 2	Boulder clay from Selset, north Yorkshire	Drained shear box test $LL=26, PL=13, CF=17, PI=13$	8.6	32	0	30	
R/P 3	London clay from Ashford Common	Drained multiple-reversal shear box test $LL=82, PL=29, CF=55, PI=53$	15.3	20	0	16	
R/P 4	Jari clay from Himalayas	Drained shear box test $LL=70, PL=27, CF=47, PI=43$	37.3	22	0	18	
R/P 5	Walton's Wood clay from Staffordshire	Casagrande shear box $LL=53, PL=28, CF=69, PI=25$	15.3	21	0	13	
R/P 1A	Blue London clay from Leigh on Sea	Drained multiple-reversal shear box test $LL=67, PL=26, CF=51, PI=41$	17.2	23.5	0	14.5	Bishop, 1971 after Petley, 1966
R/P 2A	Blue London clay from Wraybury	Drained multiple-reversal shear box test $LL=70, PL=29, CF=58, PI=41$	29.7	20	0	13.5	Bishop, 1971 after Agarwal, 1967
R/P 3A	Brown London clay from Hendon	Drained multiple-reversal shear box test $LL=82, PL=33, CF=60, PI=49$	17.9	23	3.5	14.6	Bishop, 1971 after Petley, 1966
R/P 4A	Weald clay from Arlington	Drained multiple-reversal shear box test $LL=73, PL=30, CF=45, PI=43$	13.1	18.2	6.2	10.5	Bishop, 1971 after Petley, 1969
R/P 5A	Brown London clay from Hendon	Drained multiple-reversal shear box test $LL=82, PL=33, CF=60, PI=49$	17.9	23	0	16.7	Bishop, 1971 after Petley, 1966
R/P 6A	Weald clay from Arlington	Drained multiple-reversal shear box test $LL=73, PL=30, CF=45, PI=43$	13.1	18.2	0	12.6	Bishop, 1971 after Petley, 1969

Note: All clays are undisturbed and tested under drained conditions.

LL = Liquid Limit, PL = Plastic Limit, CF = Clay Fraction and PI = Plasticity Index in %.

Table 4.3 Index properties of clays, from shear box tests.

Plot Name	Soil type & site	Test method	Liquid Limit (%)	Clay fraction (%)	Plasticity index (%)	Reference
Walton's Wood	Walton's Wood clay from Staffordshire	Casagrande shear box test	53	69	25	Skempton, 1964
Jackfield clay	Jackfield clay from Shropshire	Drained shear box test	41	36	22	
London clay	London clay from Ashford Common	Drained multiple-reversal shear box test	82	55	53	
Barbara: Intact	S.Barbara clay from Florence	Drained multiple-reversal shear box test	76	37	33	Skempton, 1985 after Calebresi & Manfredini, 1973

Table 4.4 Index properties of clays, from ring shear tests.

Plot Name	Soil type & site	Test method	Liquid Limit (%)	Clay fraction (%)	Plasticity index (%)	Reference
Brown London clay	Brown London clay from Walthamstow	Ring shear test	66	53	42	Bishop, 1971
Blue London clay; RS-2	Blue London clay from Wraysbury		72	57	43	
Blue London clay; RS-5	Blue London clay from Wraysbury		72	57	43	
Kalabagh	Kalabagh clay		62	47	36	Skempton, 1985

Table 4.5 Index properties of clays, from triaxial tests.

Plot Name	Soil type & site	Test method	Liquid Limit (%)	Clay fraction (%)	Plasticity index (%)	Reference
Onsoy	Onsøy clay from Norway	Consolidated undrained	56 - 74	60	30 - 44	Lacasse <i>et al.</i> , 1985
Ellingsrud	Ellingsrud clay from Norway		25 - 29	37	5 - 8	
Emmerstad	Emmerstad clay from Norway		24 - 32	40	3 - 12	
Todi clay	Todi clay	Unconsolidated undrained	50	35	28	Burland, 1990
London clay	London clay	Consolidated undrained	71	53	42	Webb, 1969

Table 4.6 Shear degradation rate factors (C_s).

Clay type	Test method	Normal effective stress (kPa)	C_s (mm ⁻¹)	Figure Reference
Walton's Wood clay	Shear box test	153	0.4	Figure 4.22
Jackfield clay		110	0.6	
London clay		91	0.2	
S.Barbara clay		300	0.5 - 0.6	
Brown London clay	Ring shear test	214	0.03	Figure 4.23
Blue London clay; RS-2		207	0.15	
Blue London clay; RS-5		283	0.3	
Kalabagh clay		525	0.07	
Onsøy clay	Triaxial test	-	0.4 - 0.5	Figure 4.24
Ellingsrud clay		-	0.8 - 1.0	
Emmerstad clay		-	1.5 - 2.0	
Todi clay		-	2	
London clay		-	0.9	

Table 4.7 Residual/peak bearing strength ratios (R_s) and bearing degradation rate factors (C_b).

Soil type & site	Test method and description	Soil depth (m)	LL (%)	PL (%)	CF (%)	PI (%)	R_b	C_b	Reference
London clay from Ashford Common	Plate loading test: $CT/2$	20.1	71	29	53	42	0.41	10 - 20	Ward <i>et al.</i> , 1965
	Plate loading test: $ET/1$	34.8	70	27	57	43	0.48	30 - 50	
	Quick undrained compression test	34.8	70	27	57	43	0.6	-	
Haga clay from Norway	Plate loading test	2.3 - 2.5	40	25	45	15	< 0.76	-	Andersen & Stenhamar, 1983

LL = Liquid Limit, PL = Plastic Limit, CF = Clay Fraction and PI = Plasticity Index in %.

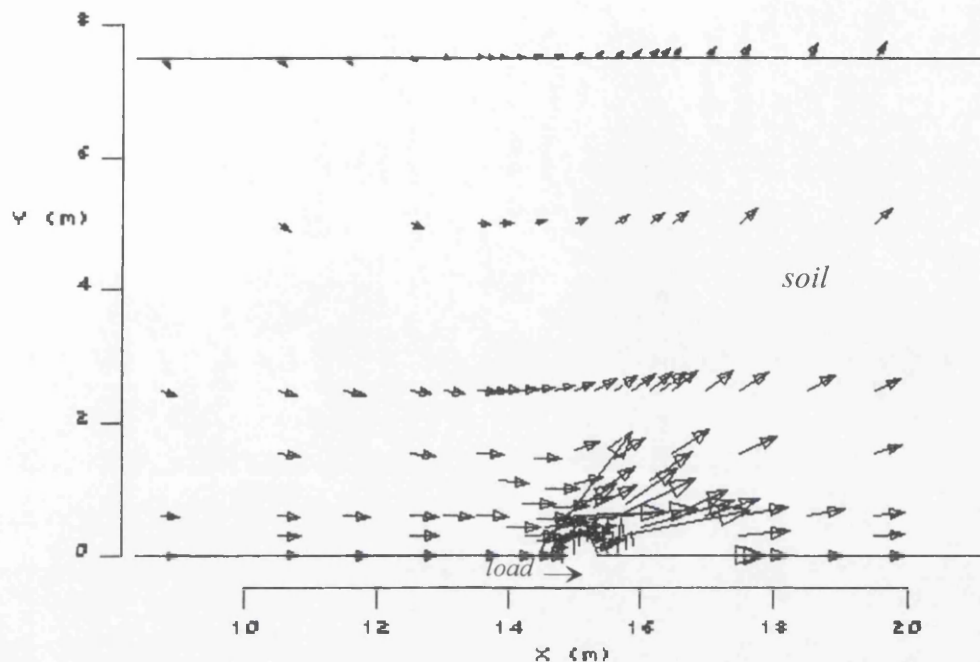


Figure 4.1 Soil displacement vectors from a finite element analysis for a pile subjected to lateral load.

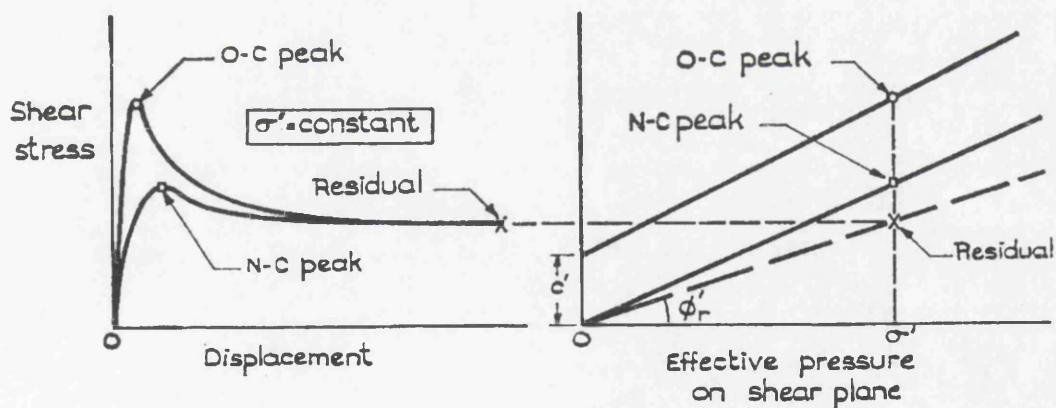


Figure 4.2 Peak and residual strengths of normally consolidated and overconsolidated clays (Skempton, 1964).

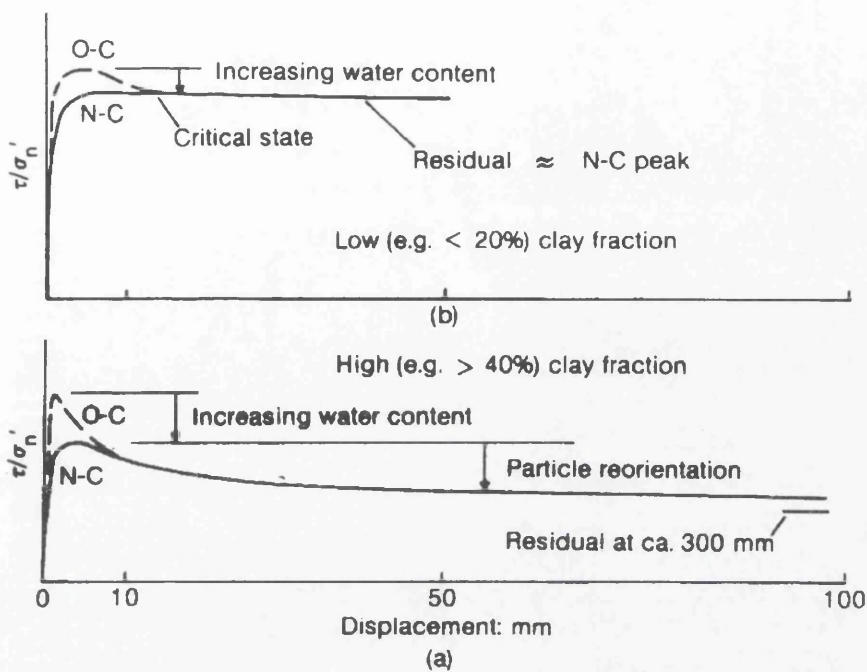


Figure 4.3 Stress-displacement curves at constant normal effective stress (σ'_n) (Skempton, 1985).

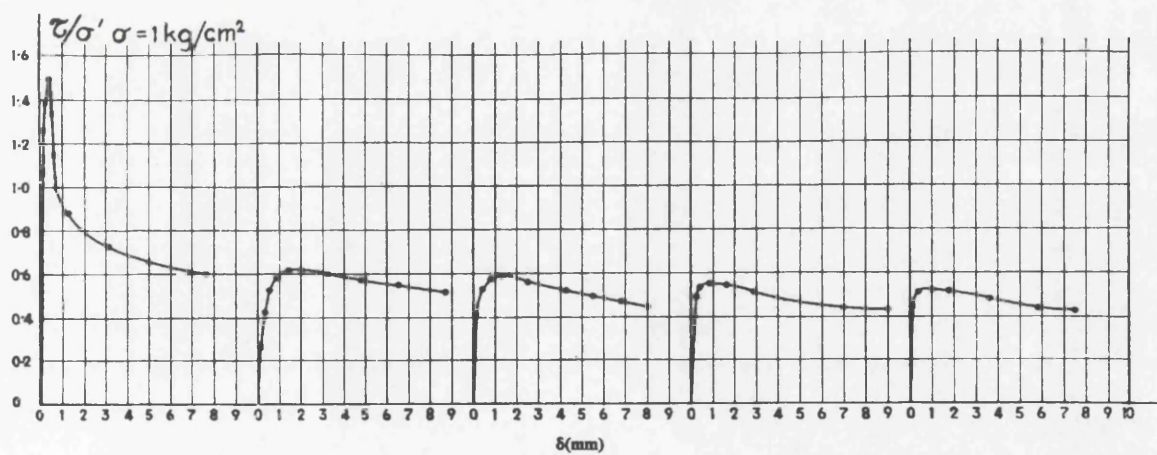


Figure 4.4 Stress-displacement curves for intact clay using multiple-reversal shear box test (Calabresi and Manfredini, 1973).

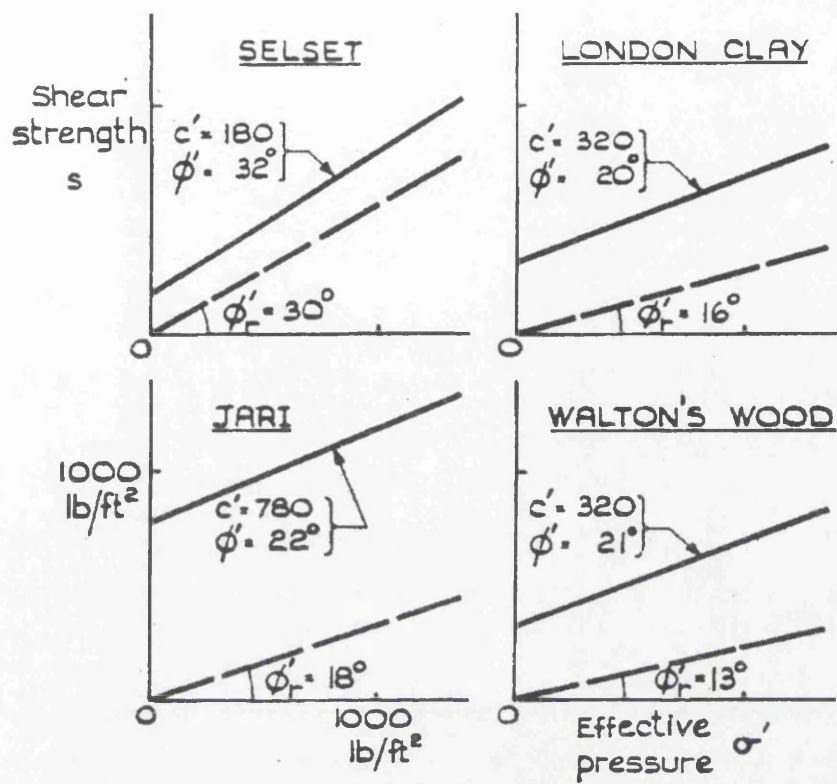


Figure 4.5 Peak and residual strengths of overconsolidated clays (Skempton, 1964).

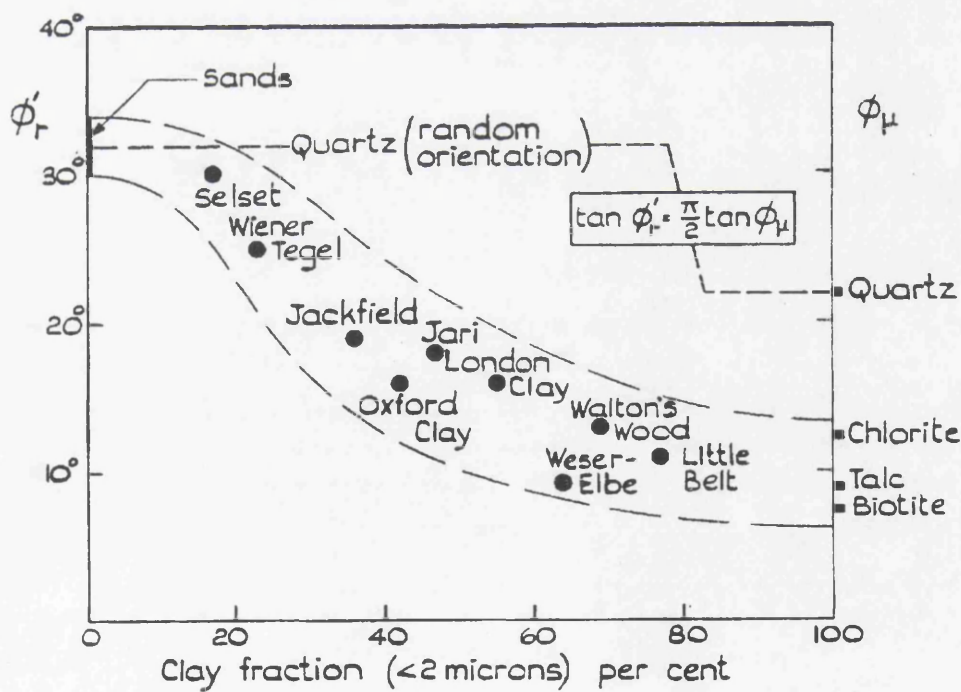


Figure 4.6 Decrease in residual angle of shearing resistance (ϕ'_r) with increasing clay fraction (Skempton, 1964).

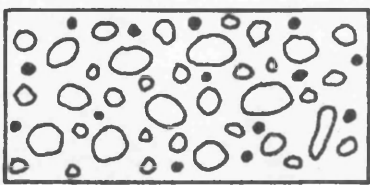
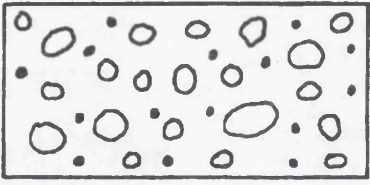
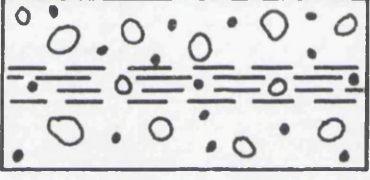
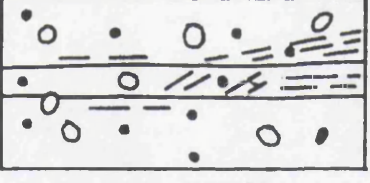

Test no.	Clay fraction: %	Thin section	Description
2	20		No separation on shear zone. Thin section showed no preferred orientation of the clay matrix (Figs 19, 20)
3	27		No separation on shear zone. Thin section showed no preferred orientation of the clay matrix
4	34		No separation on shear zone. Thin section showed shear zone about 1.5 mm thick containing discontinuous shear surfaces parallel to the direction of shear
5	40		Specimen separated on heavily striated (slickensided) shear surface. Thin section showed two continuous shear surfaces, undulating in the direction of shear, about 2.5 mm apart. Clay particles between them orientated 0–45° to direction of shear (Fig. 23)
6	48		Specimen separated on shear surface, more polished than test 5, with less well developed striations and no undulations in direction of shear. This surface bounded one side of zone of strongly orientated clay 0.5–2.0 mm thick; other side bounded by less well developed shear surface. Clay on either side of this zone showed partial orientation (Figs 21, 22)

Figure 4.7 Summary of post-failure structure from Happisburgh-London clay mixtures. (Lupini *et al.*, 1981).

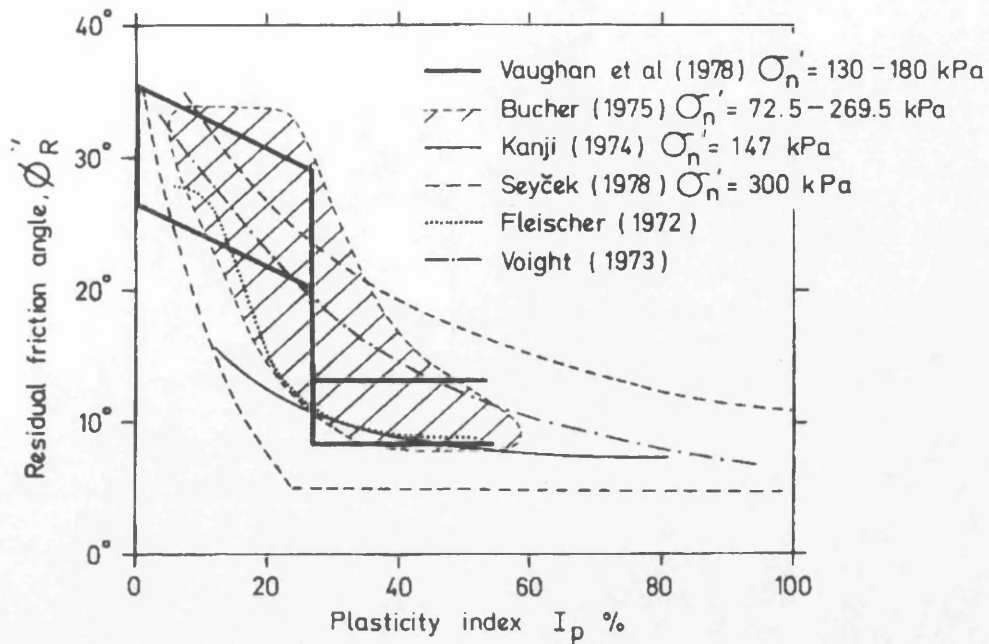


Figure 4.8 Correlation of residual friction angle (ϕ'_R) with plasticity index (Lupini *et al.*, 1981).

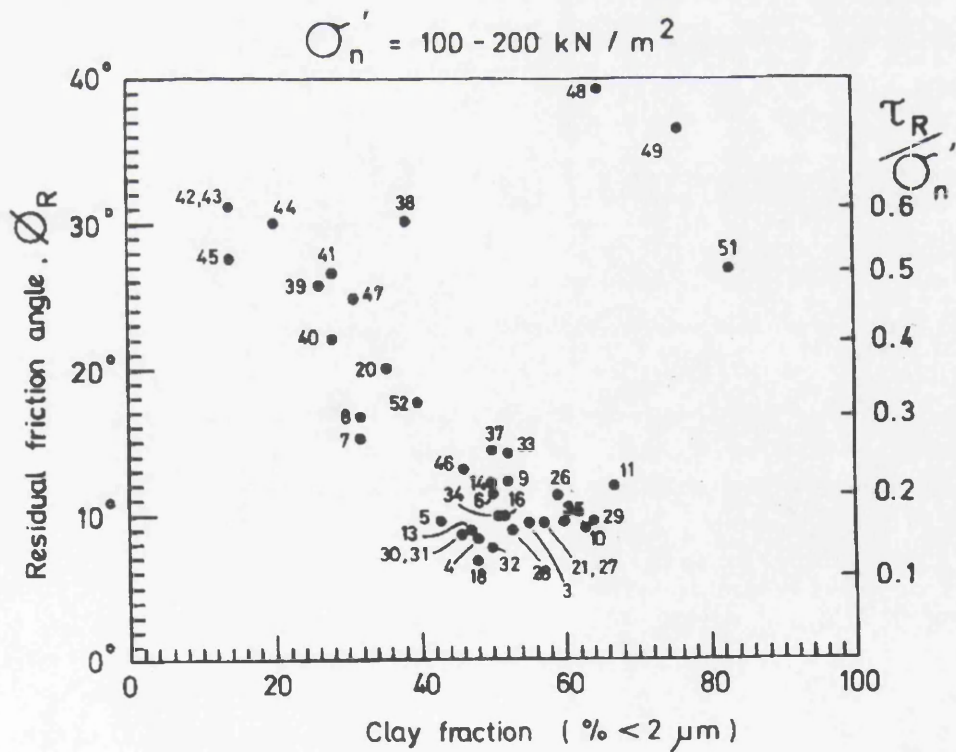


Figure 4.9 Correlation of residual friction angle (ϕ'_R) with clay fraction for natural soils (Lupini *et al.*, 1981).

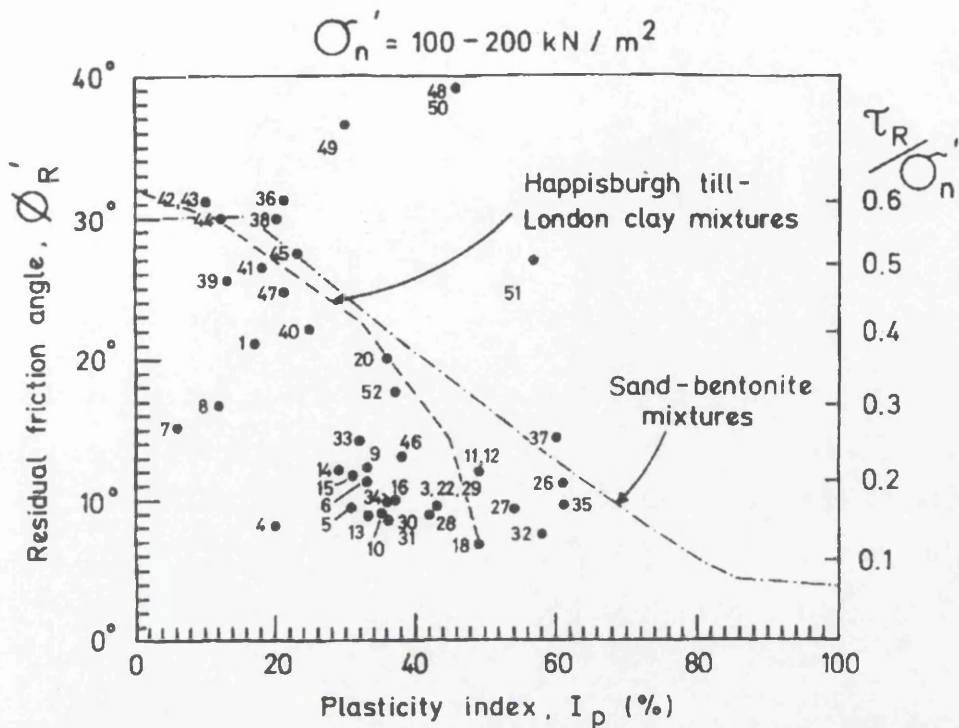


Figure 4.10 Correlation of residual friction angle (ϕ'_R) with plasticity index for natural soils (Lupini *et al.*, 1981).

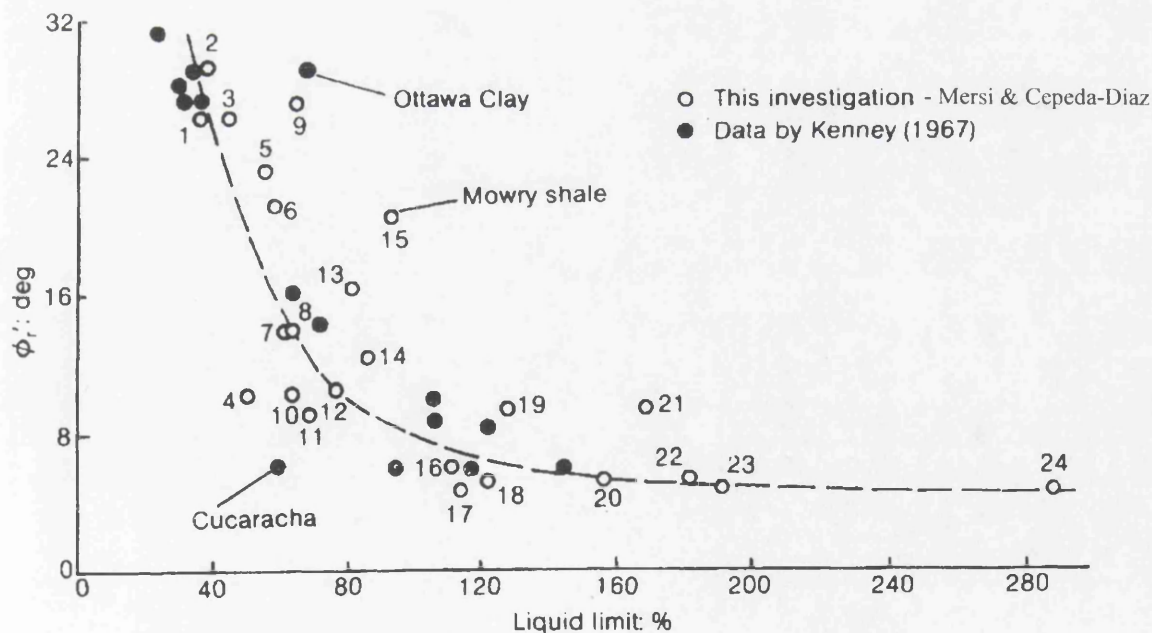
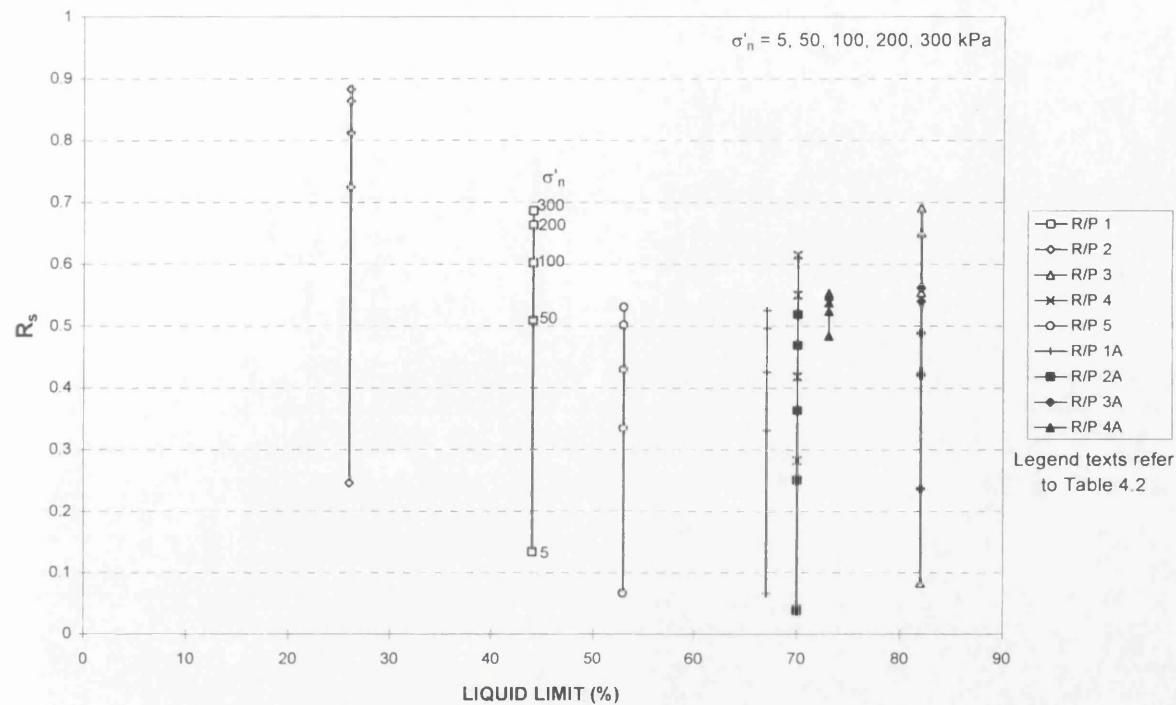
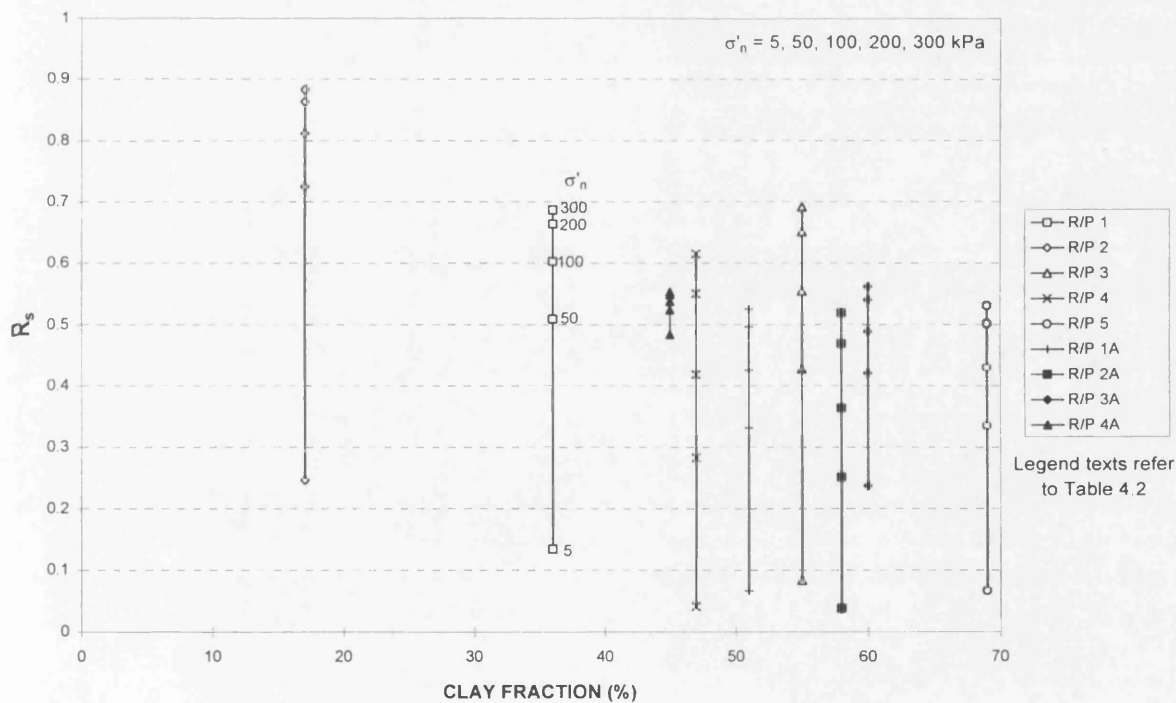


Figure 4.11 Correlation of residual friction angle (ϕ'_R) with liquid limit (Mersi and Cepeda-Diaz, 1986).

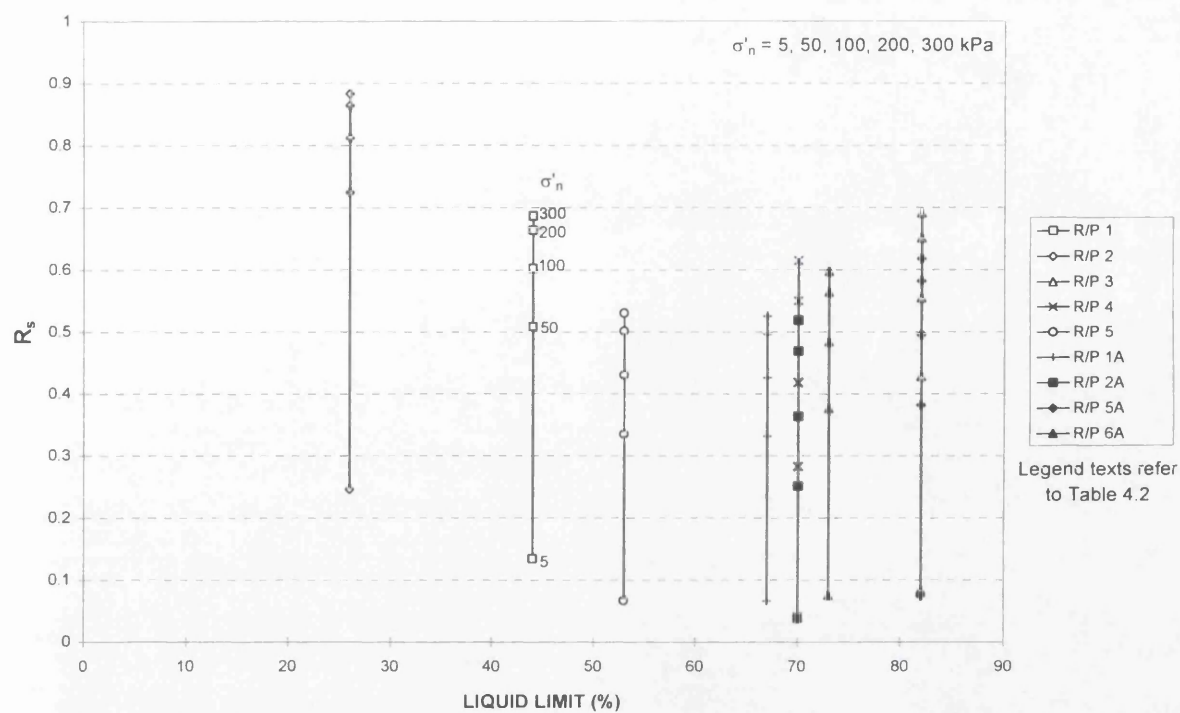


(a)

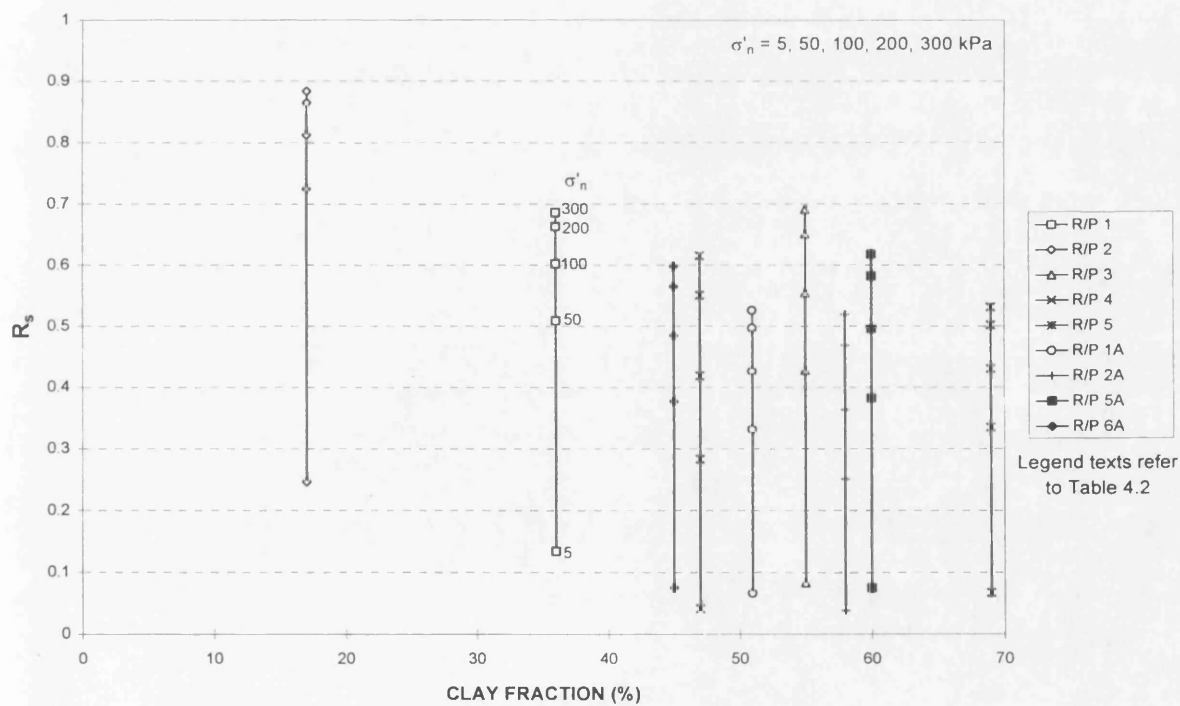


(b)

Figure 4.12 Correlation of residual/peak shear strength ratio (R_s) with (a) liquid limit and (b) clay fraction.



(a)



(b)

Figure 4.13 Correlation of residual/peak shear strength ratio (R_s) with (a) liquid limit and (b) clay fraction (with residual cohesion intercept c' , set to zero).

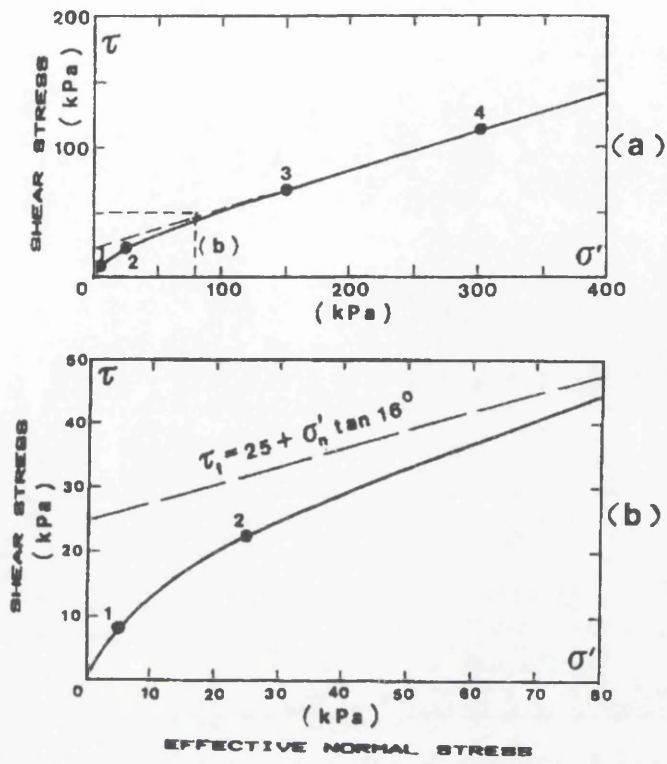


Figure 4.14 Failure envelope for compacted London clay; (a) investigated stress range with detail and (b) in the low stress range (Maksimovic, 1989a).

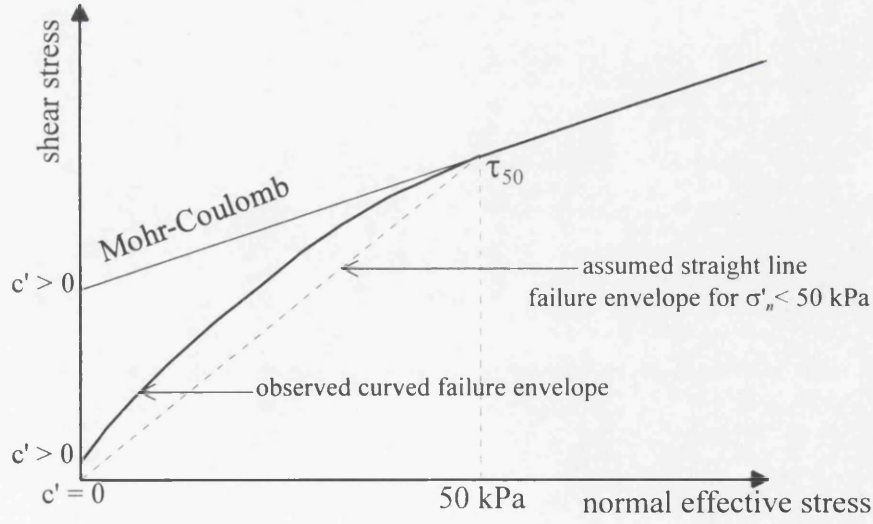
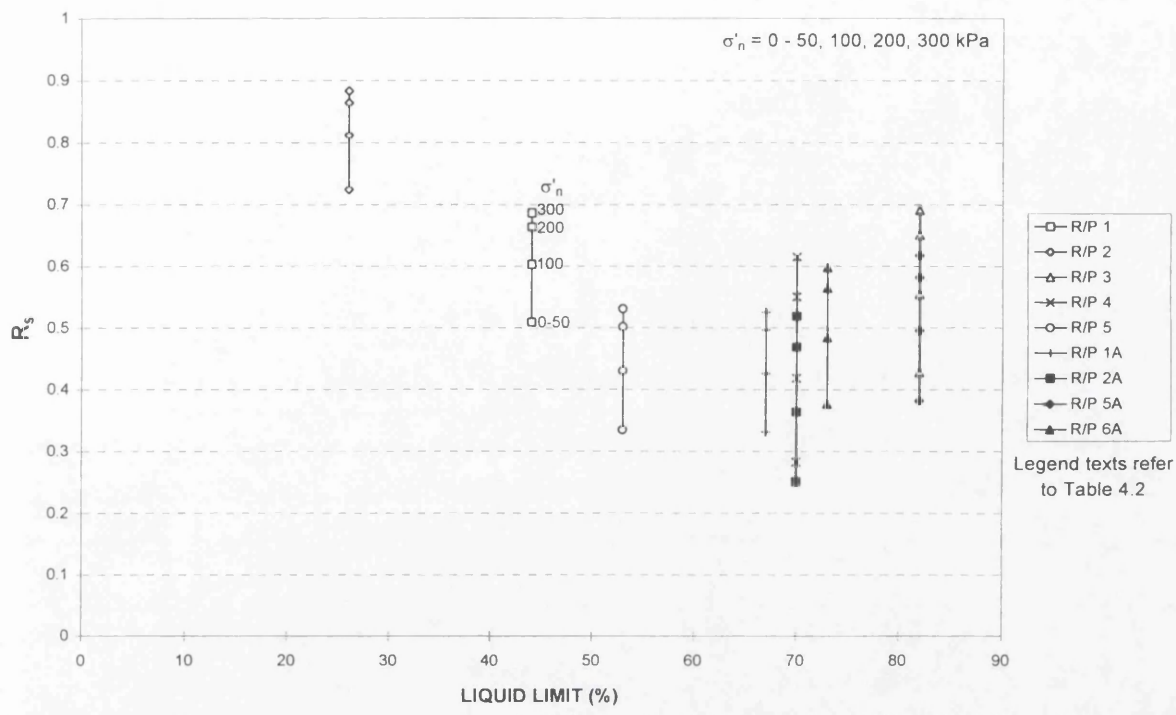
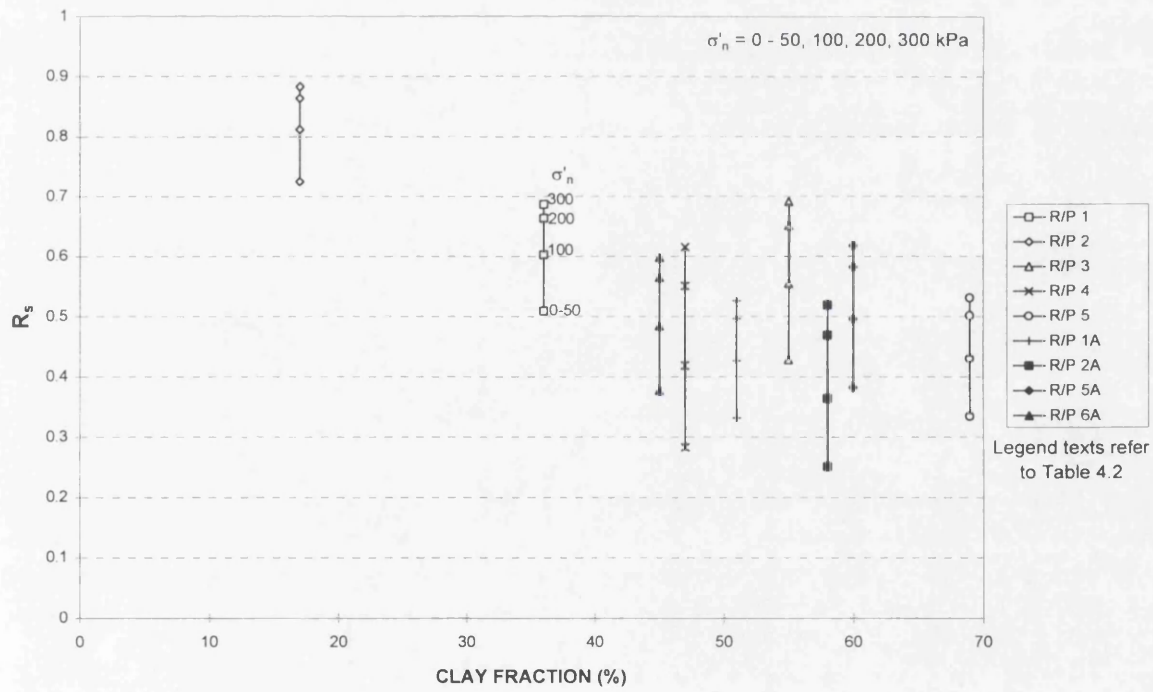


Figure 4.15 Shear strength failure envelope using bilinear approach.



(a)



(b)

Figure 4.16 Correlation of residual/peak shear strength ratio (R_s) with (a) liquid limit and (b) clay fraction (with residual cohesion intercept c'_r set to zero and modification for low stress range).

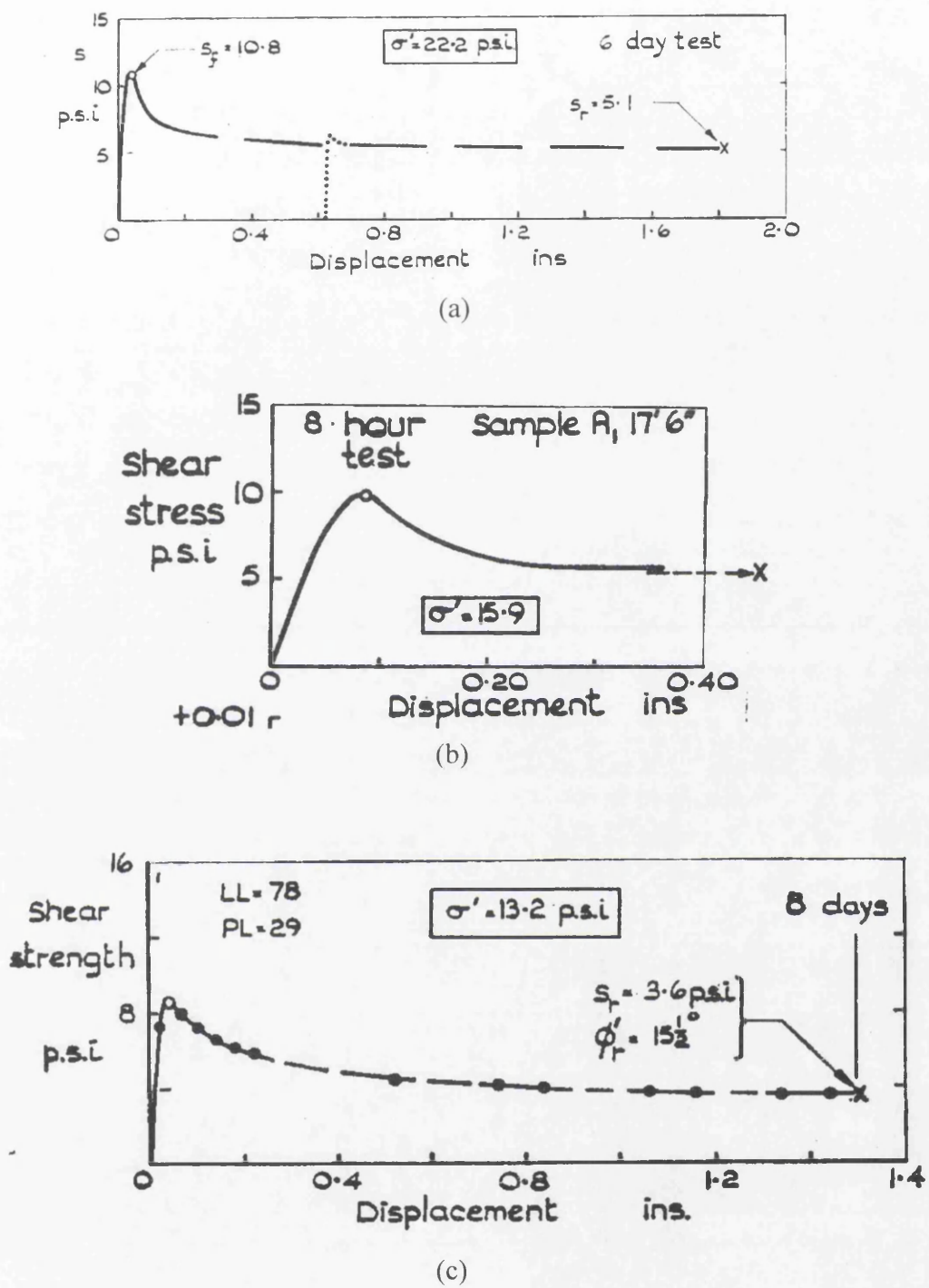


Figure 4.17 Shear test results on (a) Walton's Wood clay, (b) Jackfield clay and (c) London clay (Skempton, 1964).

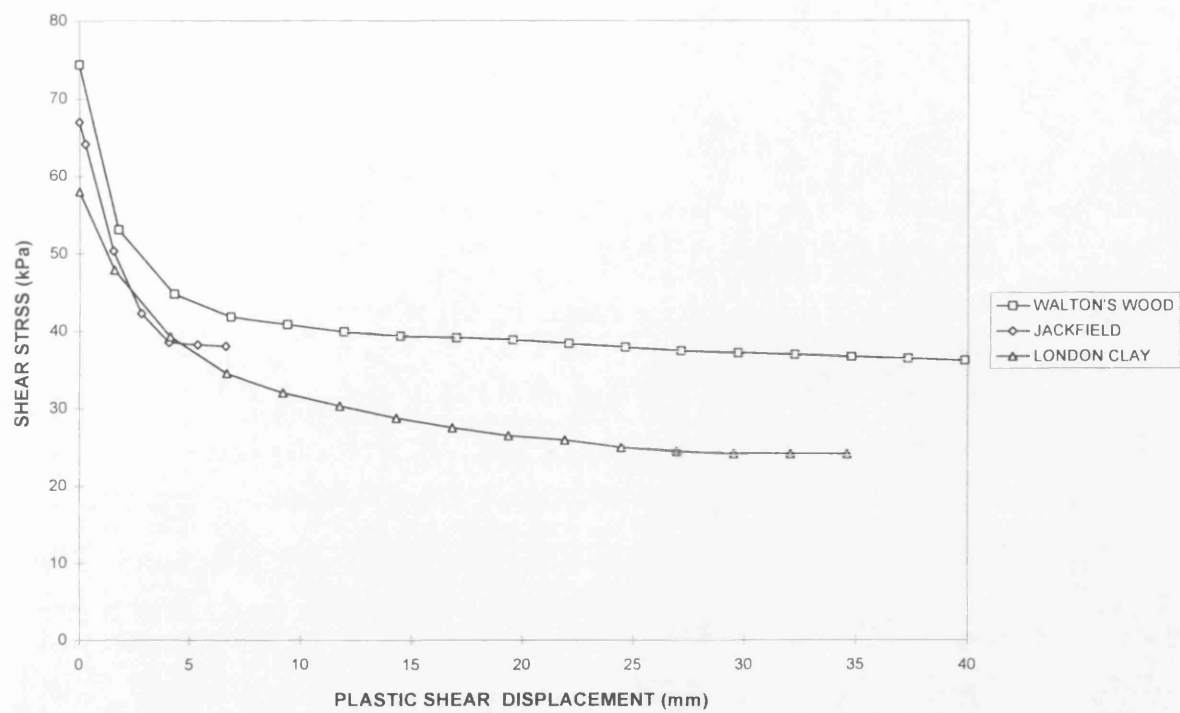


Figure 4.18 Post-peak shear strength degradation after Skempton (1964).

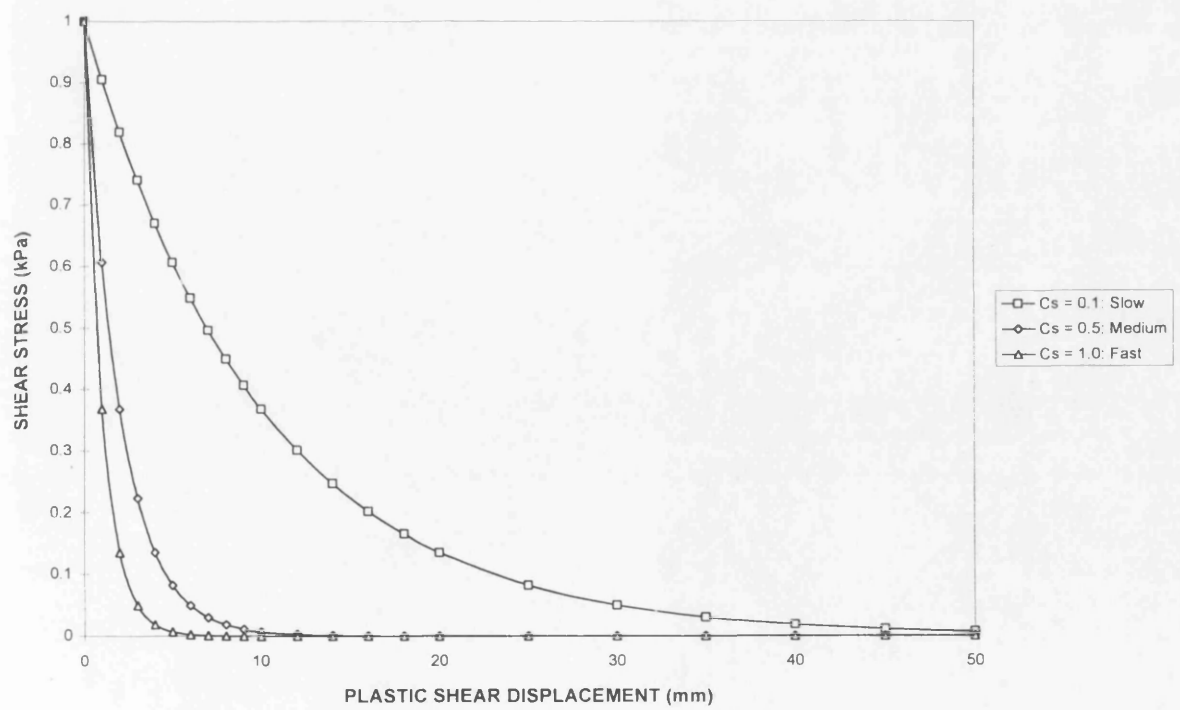


Figure 4.19 Identification of shear strength degradation rate factor (C_s).

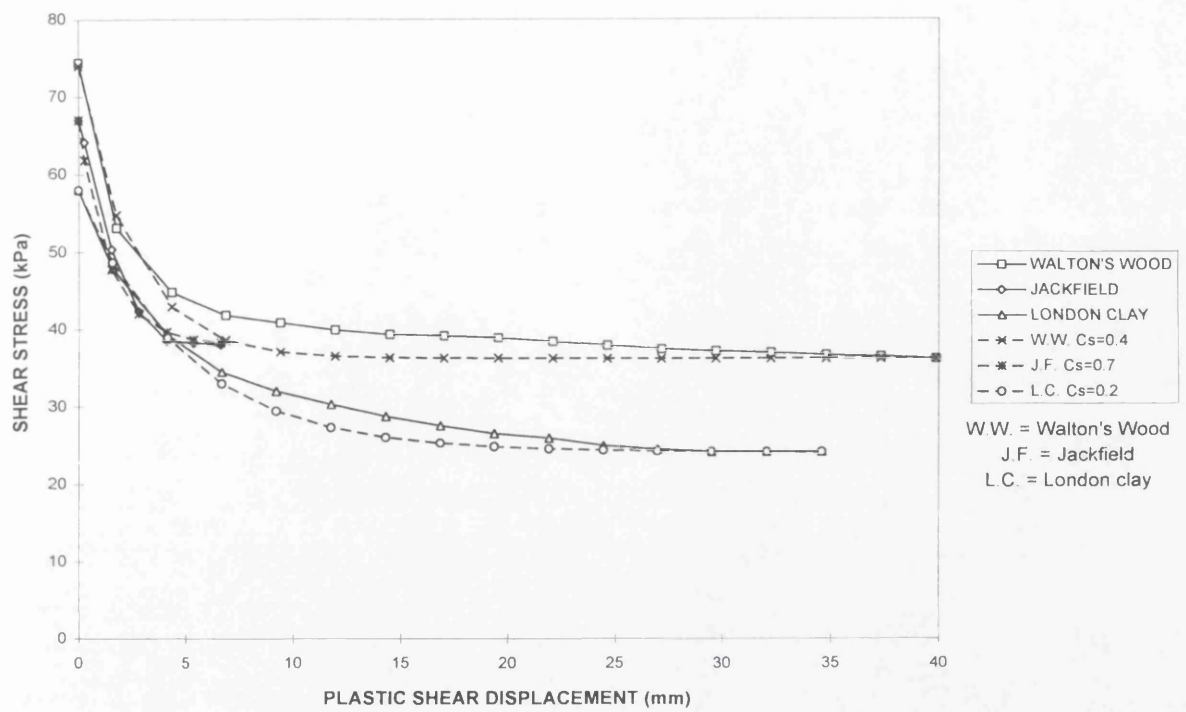


Figure 4.20 Determination of shear degradation rate factor (C_s) from post-peak shear strength degradation results.

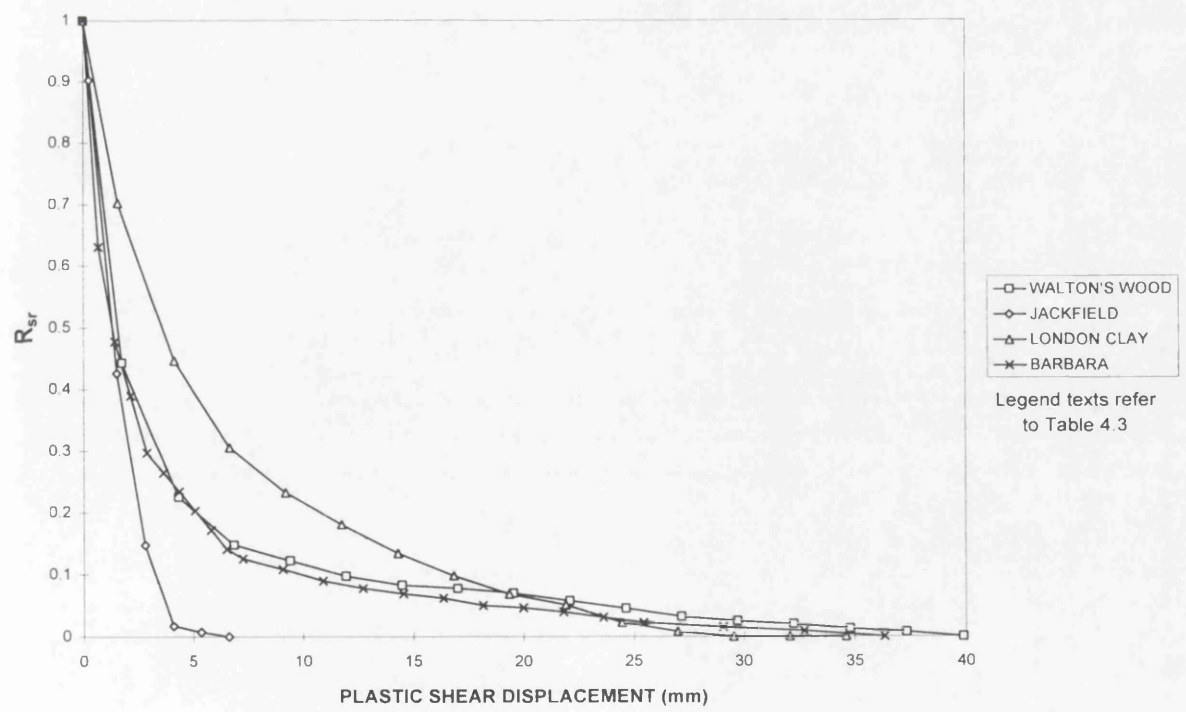


Figure 4.21 Rate of shear strength degradation from shear box tests.

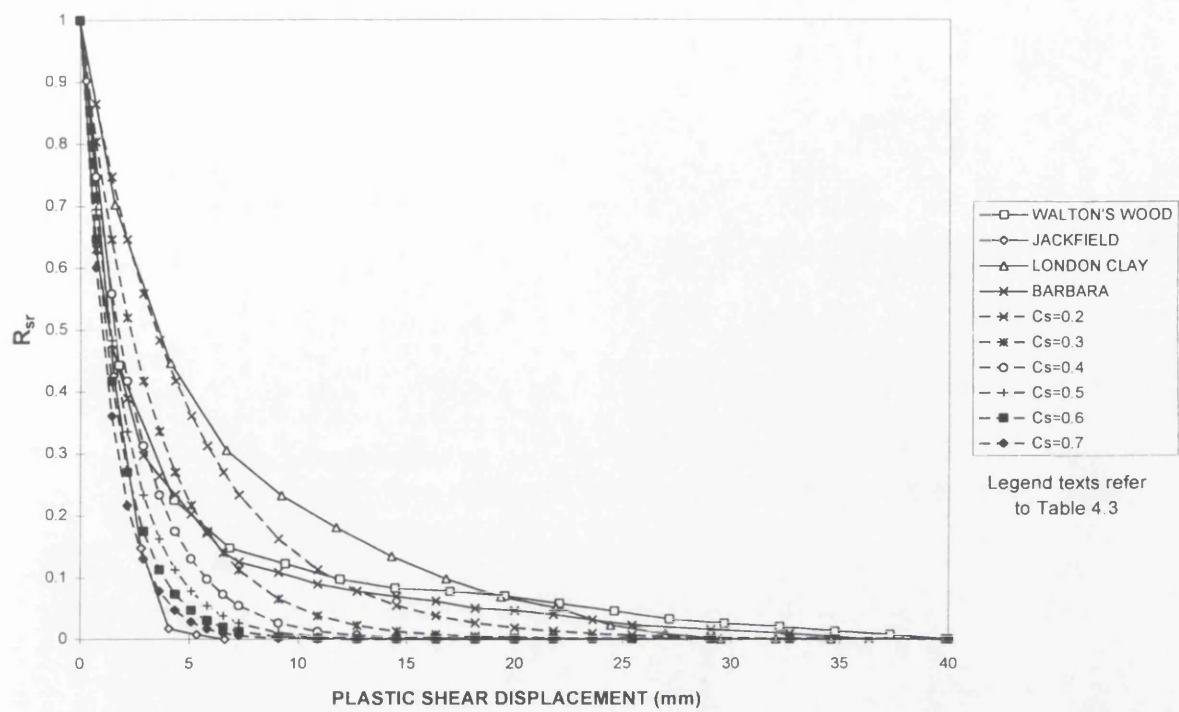


Figure 4.22 Determination of shear degradation rate factor (C_s) from post-peak shear strength degradation results using shear box tests.

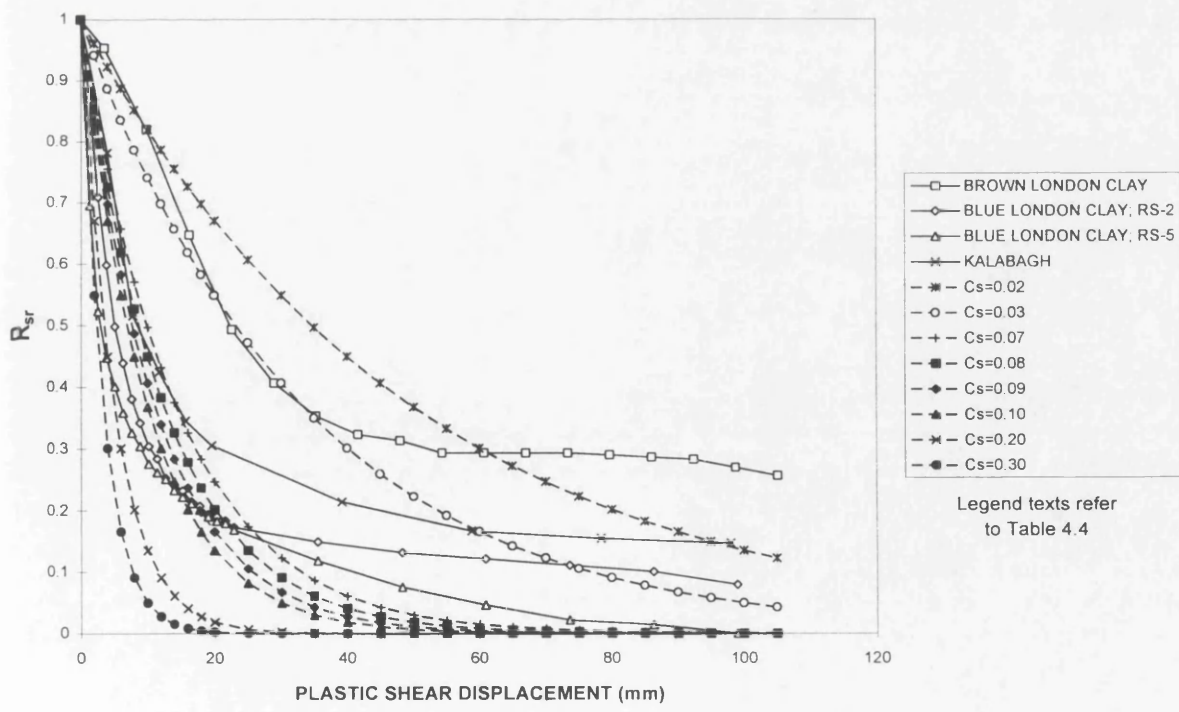


Figure 4.23 Determination of shear degradation rate factor (C_s) from post-peak shear strength degradation results using ring shear tests.

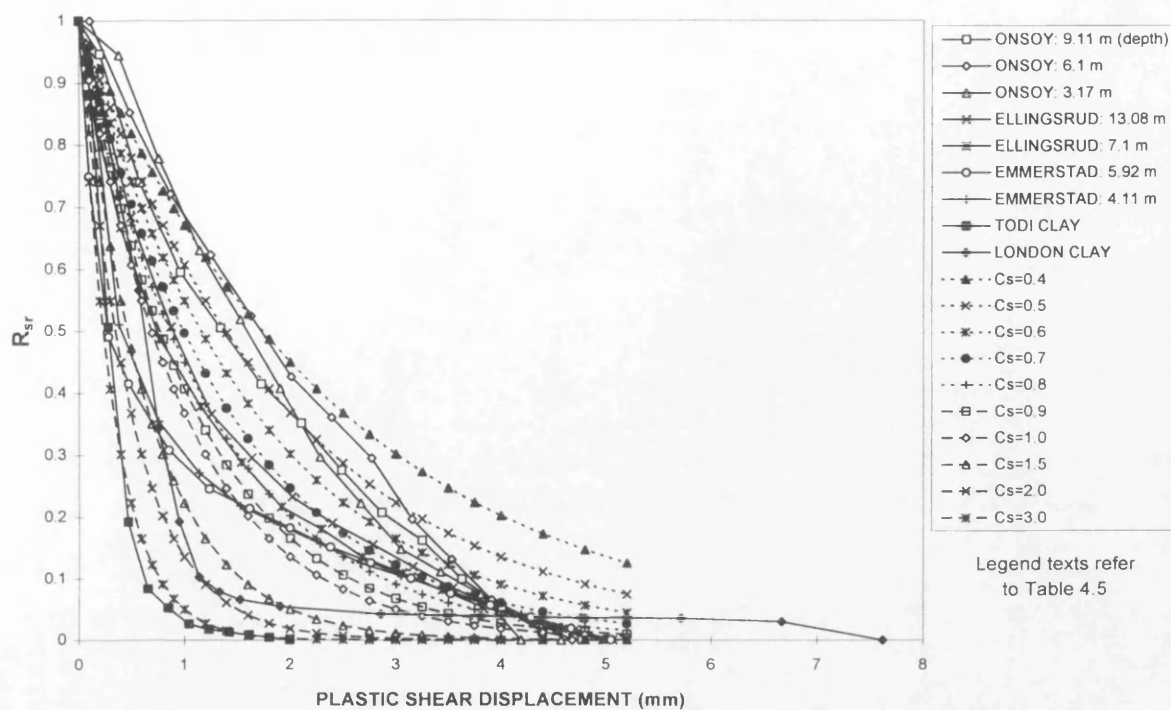
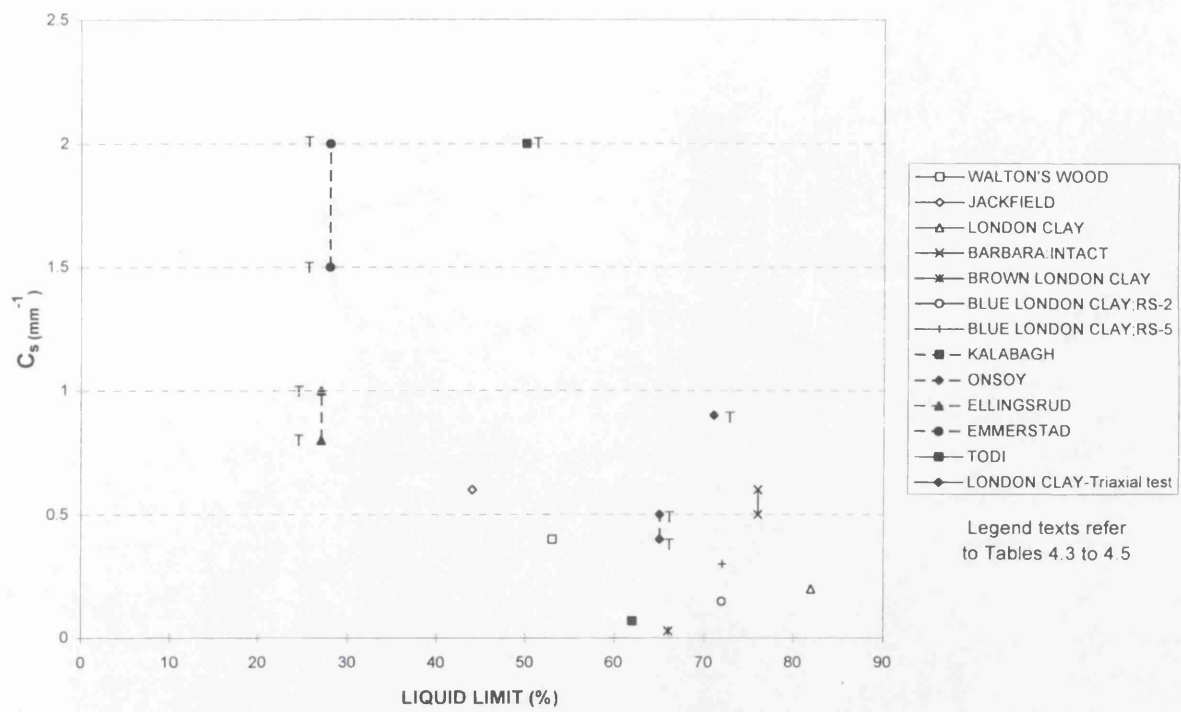
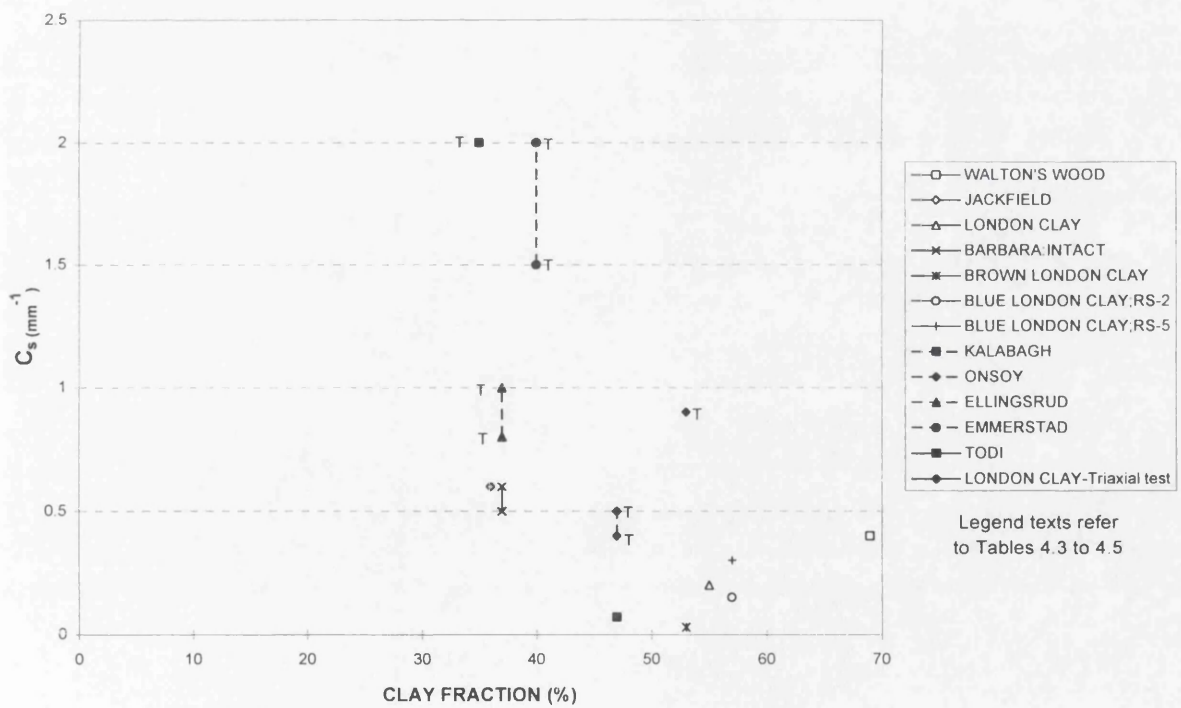


Figure 4.24 Determination of shear degradation rate factor (C_s) from post-peak shear strength degradation results using triaxial tests.



(a)



(b)

Figure 4.25 Correlation of shear degradation rate factor (C_s) with (a) liquid limit, (b) clay fraction and (c) plasticity index (see overleaf).

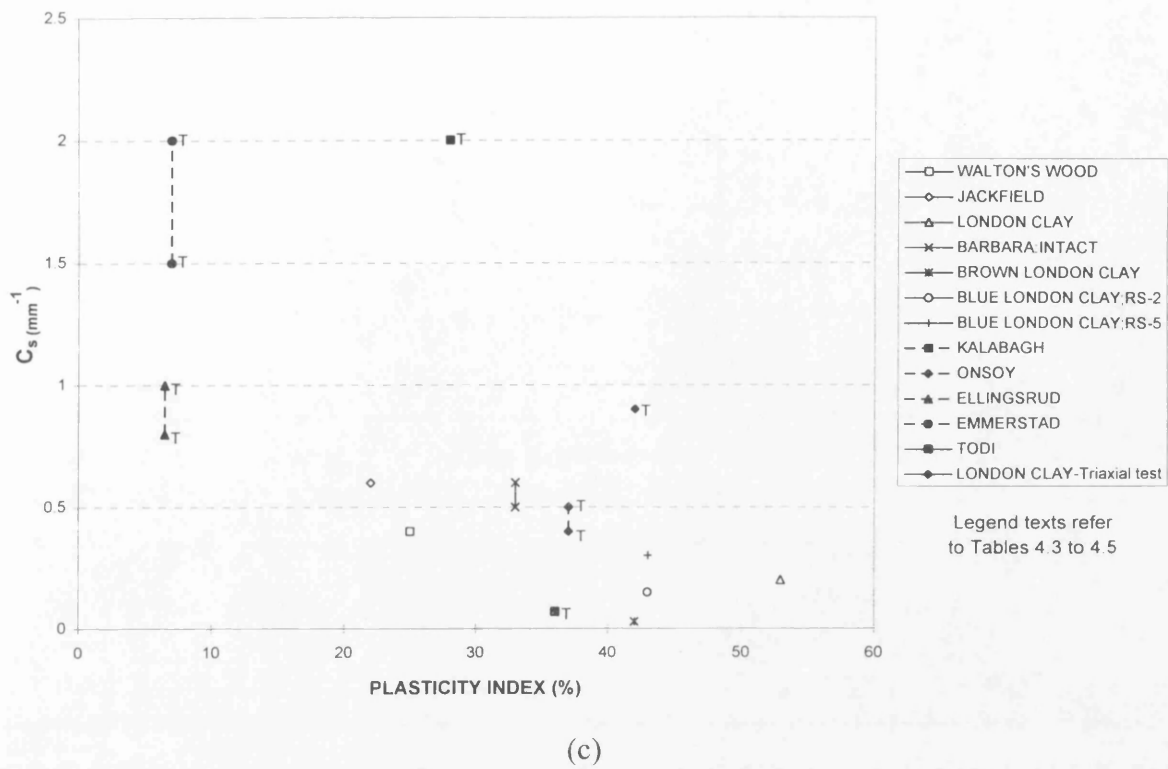


Figure 4.25 (c) Correlation of shear degradation rate factor (C_s) with plasticity index.

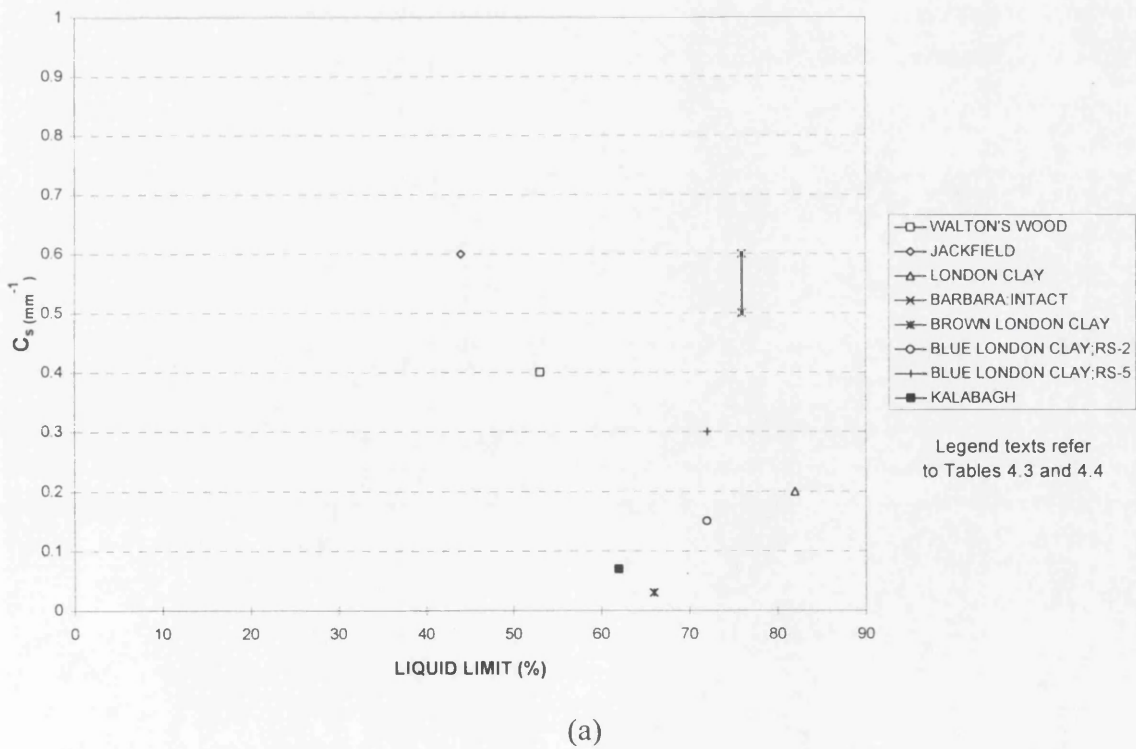
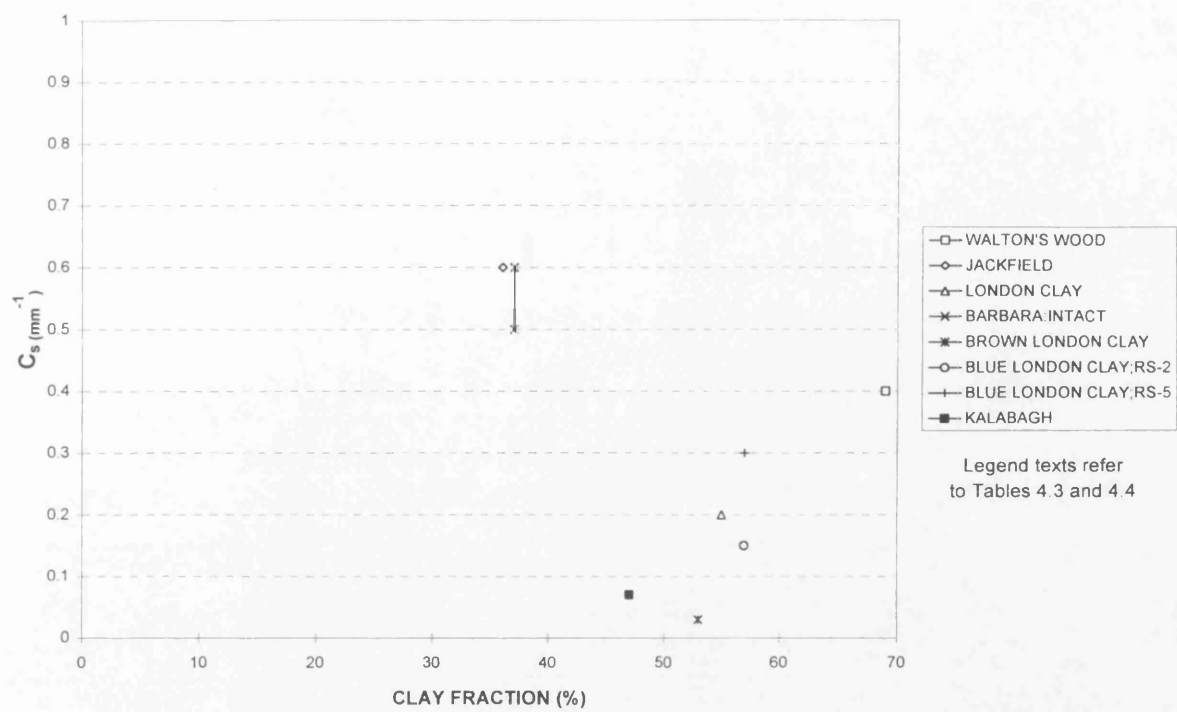
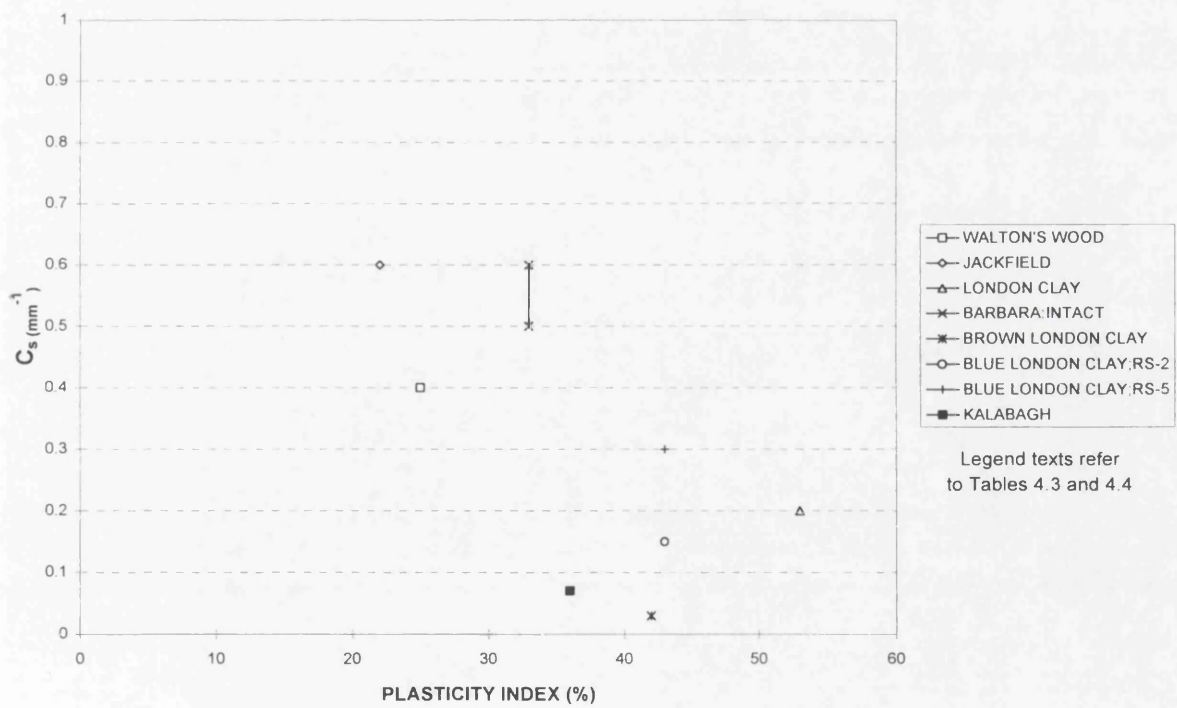


Figure 4.26 Correlation of shear degradation rate factor (C_s) with (a) liquid limit, (b) clay fraction (see overleaf), and (c) plasticity index (see overleaf), discarding triaxial test results.



(b)



(c)

Figure 4.26 Correlation of shear degradation rate factor (C_s) with (b) clay fraction and (c) plasticity index, discarding triaxial test results.

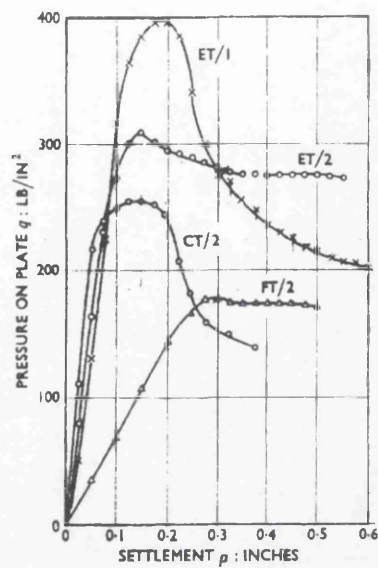


Figure 4.27 Typical load-settlement curves from plate loading tests (Ward *et al.*, 1965).

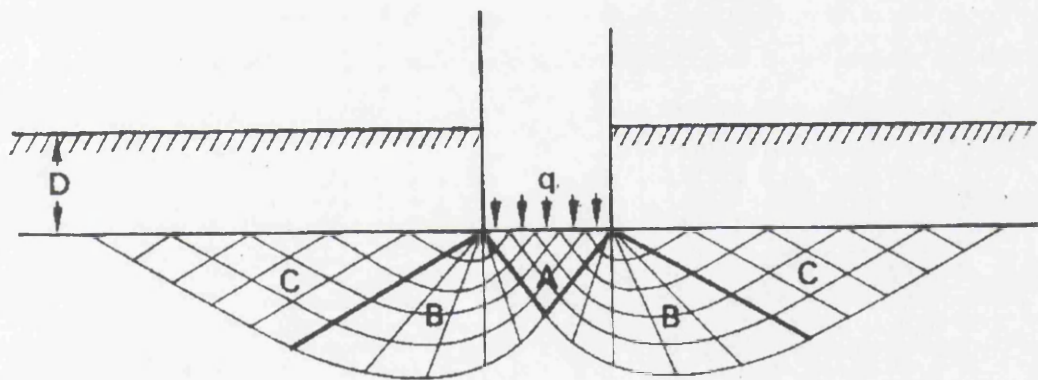


Figure 4.28 Shear zones beneath a shallow foundation according to Terzaghi. *A*, zone of elastic equilibrium; *B*, zones of radial shear; *C*, zones of passive shear; *D*, depth of foundation (Whitaker, 1970).

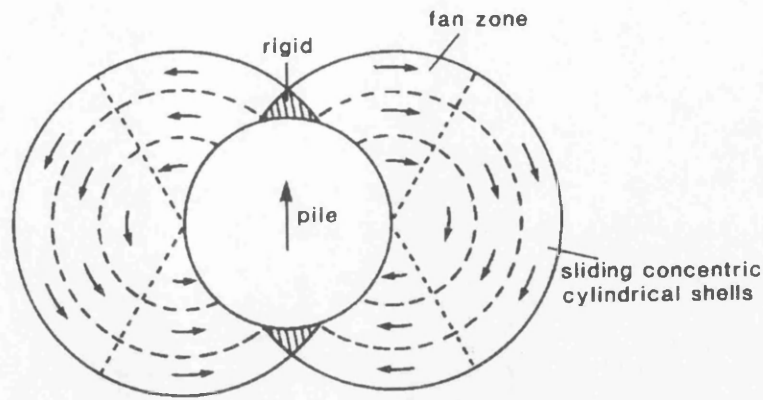


Figure 4.29 Failure mechanism for soil around laterally loaded pile. (Fleming *et al.*, 1985).

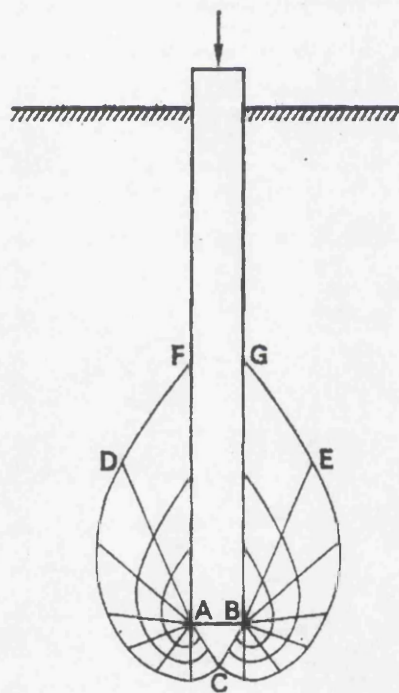


Figure 4.30 Shear zones around the base of a pile (Whitaker, 1970).

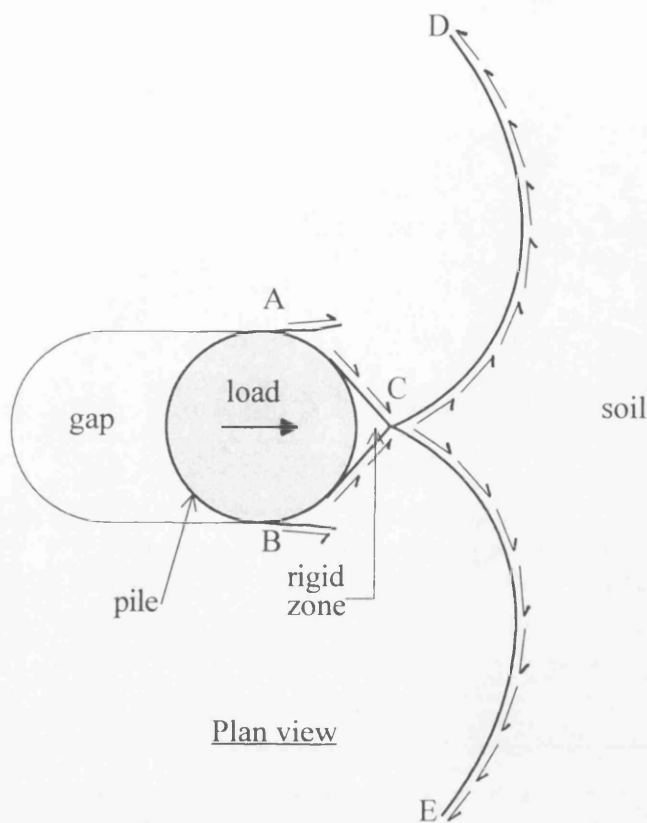


Figure 4.31 Failure mechanism of soil when a pile is loaded laterally.

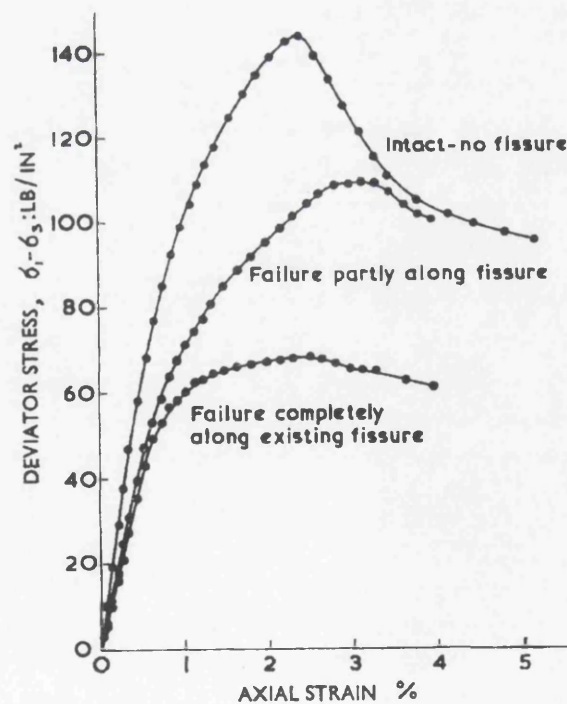


Figure 4.32 Undrained triaxial compression tests on block specimens (Ward *et al.*, 1965).

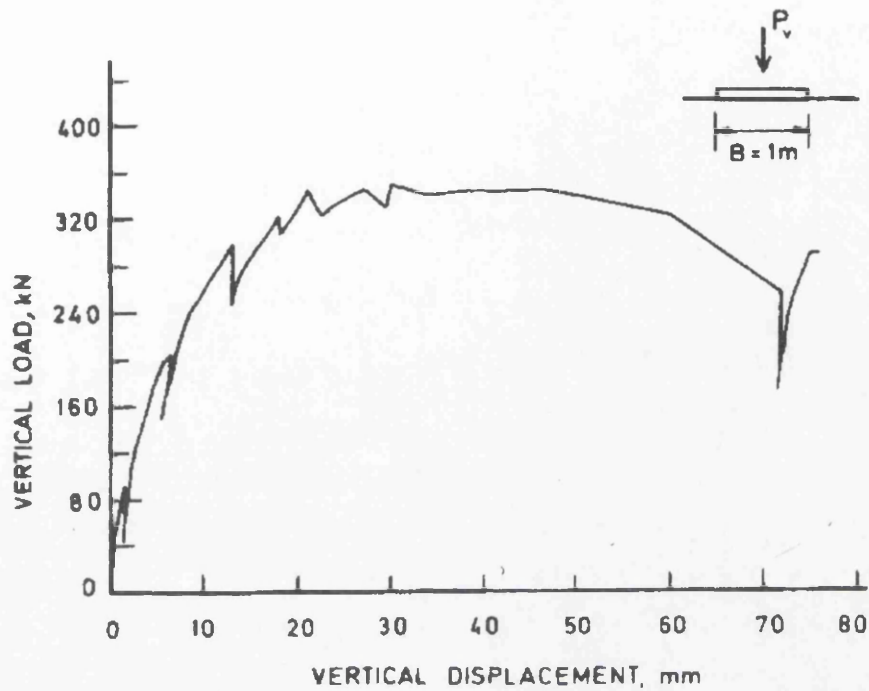


Figure 4.33 Measured load-displacement curve from plate loading tests for Test 1 (Andersen and Stenhamar, 1983).

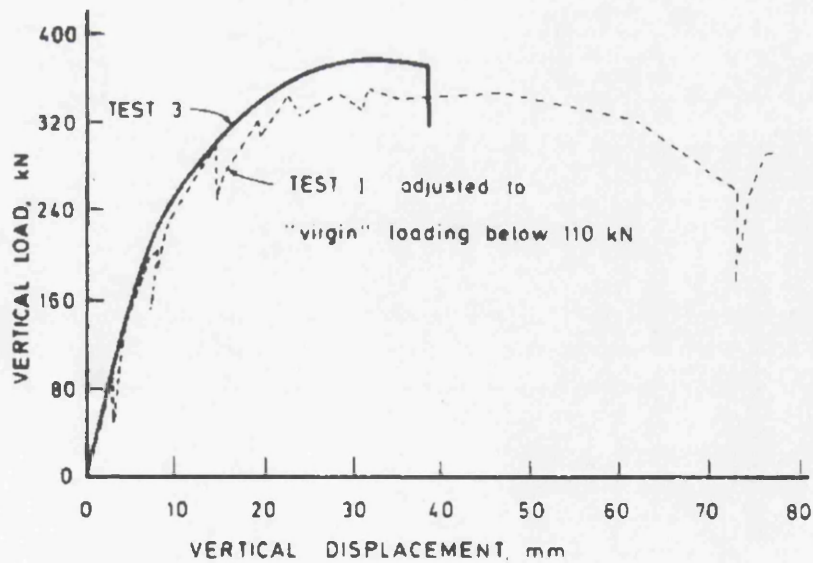


Figure 4.34 Measured load-displacement curve from plate loading tests for Tests 1 and 3 (Andersen and Stenhamar, 1983).

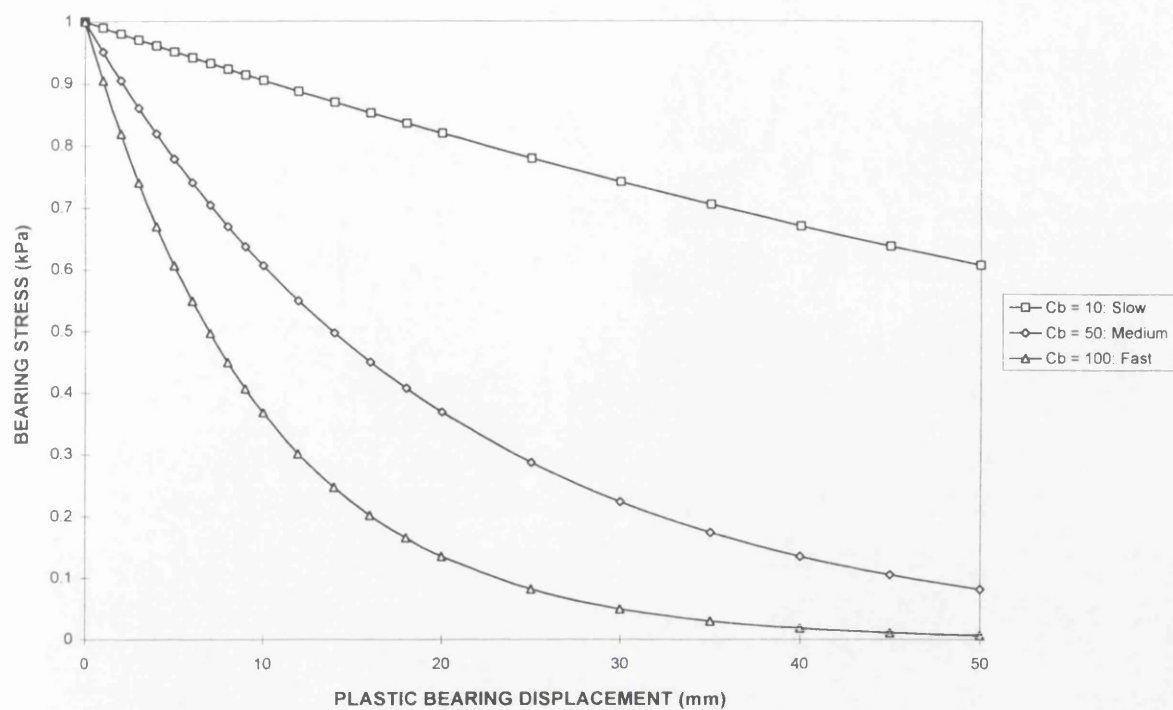


Figure 4.35 Identification of bearing strength degradation rate factor (C_b).

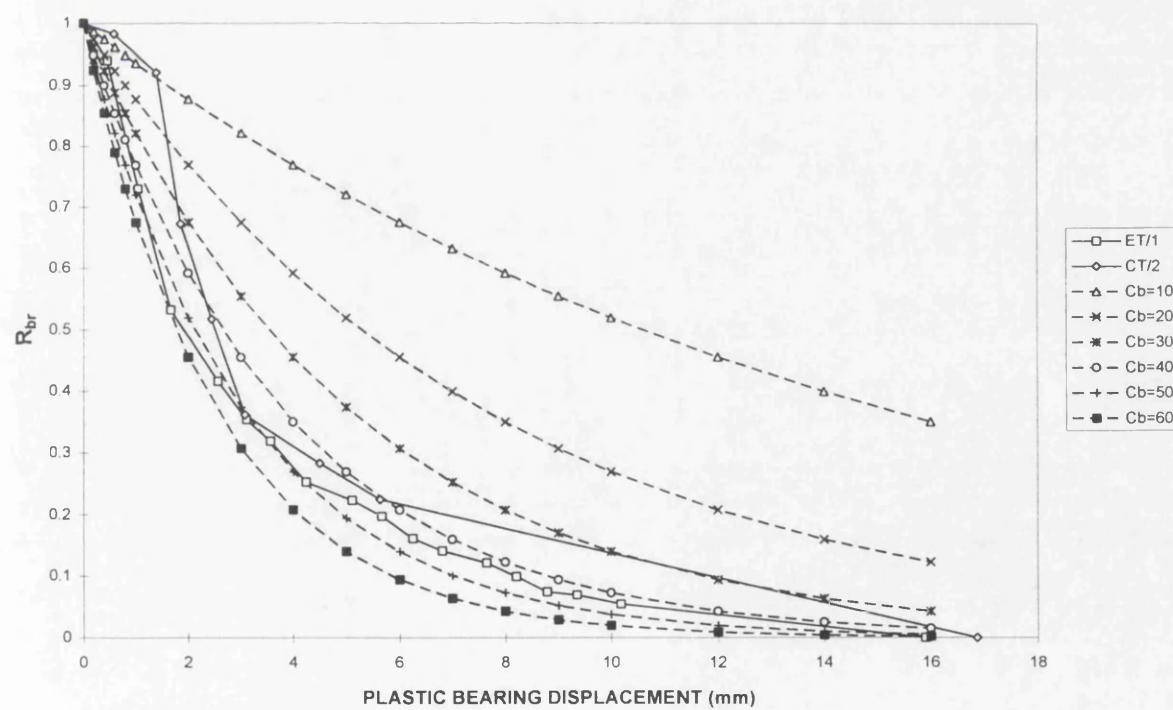
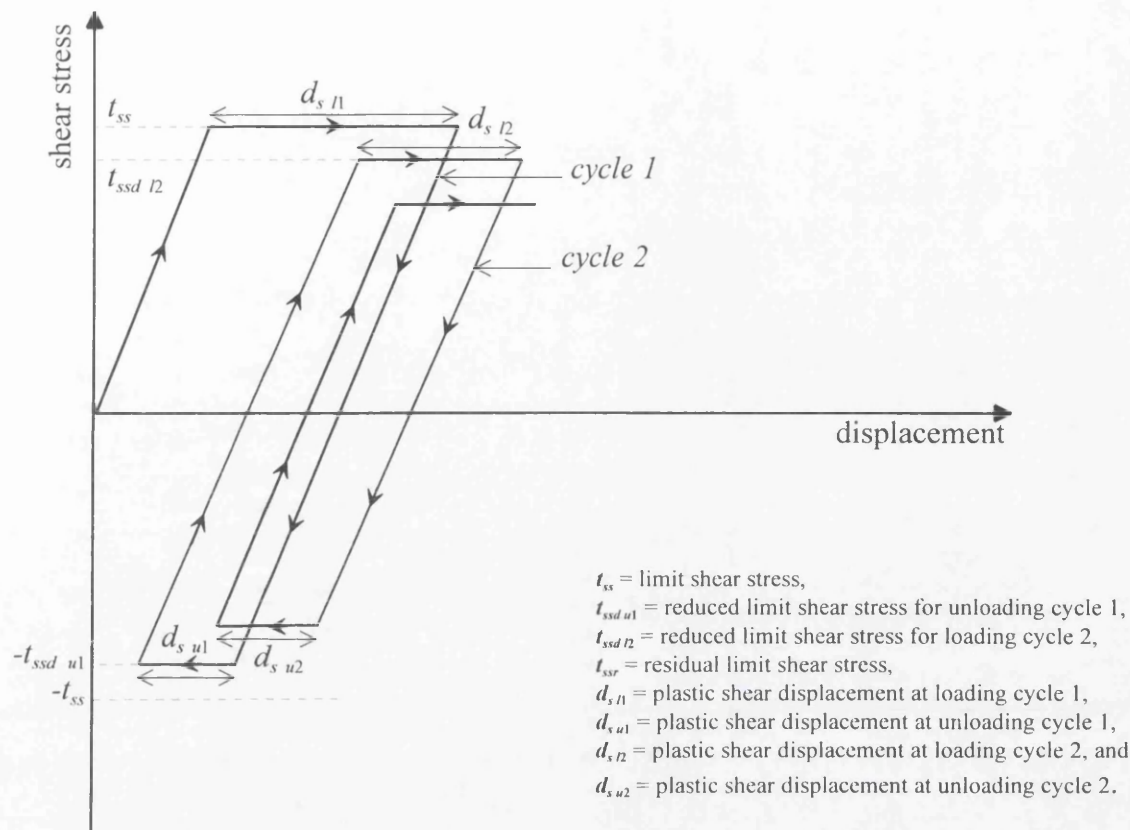
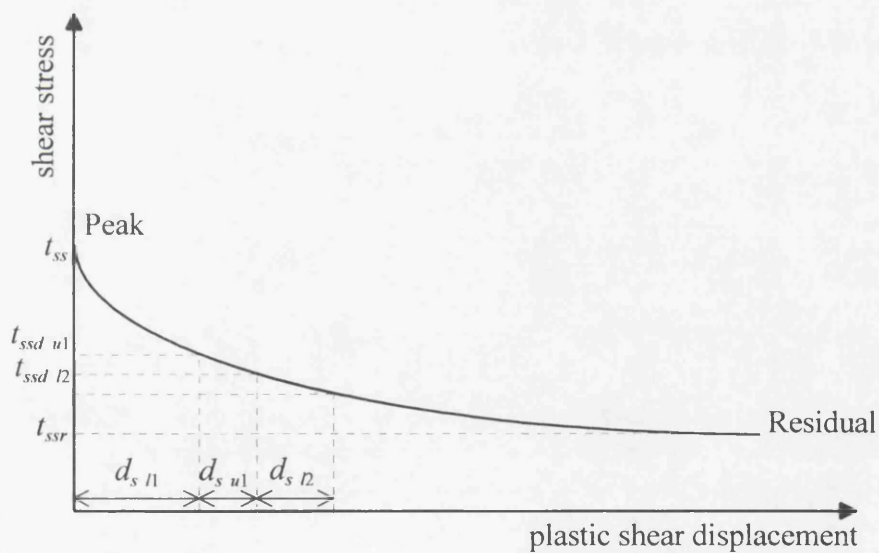


Figure 4.36 Determination of bearing degradation rate factor (C_b) from post-peak bearing strength degradation results using plate loading tests.

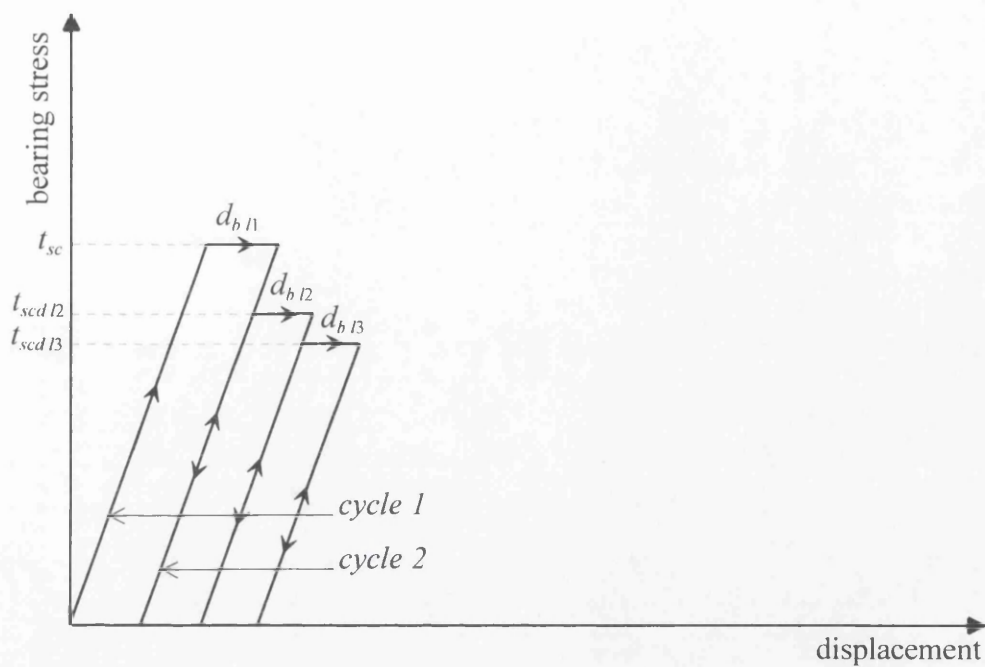


(a)

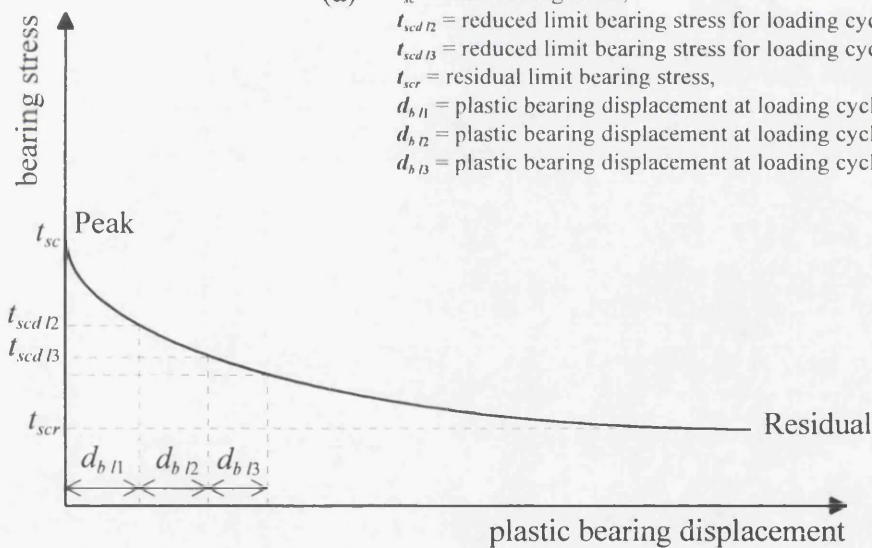


(b)

Figure 4.37 (a) Determination of plastic shear displacement (d_v) and reduced limit shear stress (t_{ssd}), and (b) shear strength degradation based on plastic shear displacement.



- (a) t_{sc} = limit bearing stress,
 t_{scd12} = reduced limit bearing stress for loading cycle 2,
 t_{scd13} = reduced limit bearing stress for loading cycle 3,
 t_{scr} = residual limit bearing stress,
 d_{b11} = plastic bearing displacement at loading cycle 1,
 d_{b12} = plastic bearing displacement at loading cycle 2, and
 d_{b13} = plastic bearing displacement at loading cycle 3.



(b)

Figure 4.38 (a) Determination of plastic bearing displacement (d_b) and reduced limit bearing stress (t_{scd}), and (b) bearing strength degradation based on plastic bearing displacement.

CHAPTER 5

Boundary Element Analysis

5.1 Summary

5.2 Introduction

5.3 Soil model

5.3.1 Clay types

5.3.2 Limit stresses

5.3.3 Gap formation

5.3.4 Backsliding

5.3.5 Soil strength degradation

5.4 Boundary element formulation

5.4.1 Pile flexure

5.4.2 Soil deformation

5.4.3 Pile-soil system interaction

5.4.4 Pile-head stiffness matrix and compliance matrix

5.4.5 Pile tractions and displacements

5.4.6 Elastic unloading

5.4.7 Gap formation

5.4.8 Pile-head reactions

5.4.9 Shear strength degradation

5.4.10 Bearing strength degradation

5.4.11 Modified soil segment stiffness matrix

5.4.12 Unloading and reloading

5.5 Discussion

5.6 Concluding remarks

Appendix 5.1 Bernoulli-Euler Beam Theory

Appendix 5.2 Mindlin's Solution

CHAPTER 5

Boundary Element Analysis

5.1 Summary

The formulation used in the cyclic analysis of laterally loaded pile foundations embedded in cohesive soils, based on the indirect boundary element method, is described here. The analysis is capable of determining the pile-head load-displacement and rotation response. In addition, the pile tractions, displacements, shear forces and bending moments along the length of the pile can also be evaluated. Phenomena observed in cyclic pile-load tests, such as gapping, backsliding and soil strength degradation effects are accounted for in the analysis, by the use of a simple soil model.

5.2 Introduction

A continuum approach based on incremental analysis, via the indirect boundary element method, is presented based on a method employed by Davies and Budhu (1986) and Budhu and Davies (1988) for static analyses of laterally loaded piles. This approach is capable of analysing the three-dimensional pile-soil behaviour of cyclic laterally loaded piles without undue computational cost. A significant simplification of the method is that although the yield (failure) conditions at the pile-soil interface are satisfied, the yield conditions within the soil continuum are not explicitly satisfied. While such an analysis fails to account fully for the complex mechanics of the continuum, the studies referred to above suggest that it is capable of producing excellent results, and it captures all of the essential features of the problem.

The non-linear elasto-plastic analysis is based on an elastic-perfectly plastic model for soils, which are assumed to behave linearly elastically at small strain levels, but fail, when they reach certain yield stresses, namely, bearing failure in the compression zone, tension failure in the tensile zone and shear failure in the slip zone. After the soil yields, its strength may degrade depending on the magnitude of the plastic displacement (i.e. strain-softening).

Cyclic loading of piles embedded in cohesive soil, generally results in gaps forming at the tension face of the pile (Matlock, 1970; Bijmagne *et al.*, 1991; Dunnavant and O'Neill,

1989; Long *et al.*, 1993), resulting in degradation of the pile responses. Due to the cyclic loading, soils will also degrade, resulting in increasing pile displacements, moments etc. For cohesive soils, backsliding may reduce gap sizes (Grashius *et al.*, 1990; Bijlagte *et al.*, 1991). These phenomena (described by a simple soil model) are included in the computer program, APILEC, based on the existing program, APILES (Davies and Budhu, 1994). The main extensions to the program are the following:

- 1.) Unload and reload cycles accounting for one-way and two-way cyclic loadings, with the option of load-controlled (or displacement-controlled) conditions.
- 2.) Gap formation, i.e. separation between the pile and the soil, when the soil is subjected to tensile stresses.
- 3.) Backsliding of soil into the gap.
- 4.) Soil strength degradation.

5.3 Soil model

The equivalent linear and cyclic non-linear soil models for cyclic loading (described in Sections 2.4.1 and 2.4.2) cannot be applied, because the cyclic shear strain induced in soils during cyclic loading cannot be readily determined. Furthermore, the parameters required for these models are not easily determined experimentally. On the other hand, the advanced constitutive models (described in Sections 2.4.3 and 2.5), for example, the bubble model, are too complex.

For simplicity, it is assumed that the soil behaves like an elastic-perfectly plastic material. While such a simple model cannot fully describe the behaviour of the soils, it is sufficiently adequate for most practical problems. It can reproduce the non-linear load-displacement response of laterally loaded piles from the interaction of elastic and plastic (yielded) soil elements.

The soil parameters required in the static analysis are the undrained shear strength (C_u) of the soil and its Young's modulus (E_s). Poisson's ratio (ν) is assumed to be equal to 0.5 under undrained loading conditions. For cyclic analysis, residual/peak shear strength ratio (R_s), the shear degradation rate factor (C_s), the residual/peak bearing strength ratio (R_b), and the bearing degradation rate factor (C_b) are required to account for soil strength degradation. A further backsliding factor (β) is needed if the backsliding phenomenon is taken into consideration.

5.3.1 Clay types

Two clay profiles are considered in the analysis, corresponding to soft (lightly overconsolidated) clays and stiff (heavily overconsolidated) clays.

Soft clays

The undrained shear strength (C_u) is to be linearly proportional to the depth (z) below ground level:

$$C_u = cz \quad (5.1)$$

where c is the rate of increase in undrained shear strength with depth.

For very soft clays, if the groundwater level and ground level coincides, then the (minimum) magnitude of the parameter c is approximately 3 kPa/m (Budhu and Davies, 1988). If field measurements of shear strength are available, selection of the parameter c should be governed by the strength profile over the effective length of the pile, typically the upper ten diameters.

For soft clays, Equation (3.2) can be used, i.e.

$$C_u = 0.25 \sigma'_z \quad (5.2) \quad (3.2 \text{ bis})$$

where σ'_z is the vertical effective stress.

Alternatively, the undrained shear strength (Skempton, 1954, 1957) can be deduced from the relationship:

$$C_u = (0.11 + 0.37 I_p) \sigma'_z \quad (5.3)$$

where I_p is the plasticity index.

The Young's modulus (E_s) of the soil is similarly assumed to be proportional to depth:

$$E_s = mz \quad (5.4)$$

where m is the rate of increase in Young's modulus with depth.

Stiff clays

The undrained shear strength (C_u) and the Young's modulus (E_s) for stiff clays are assumed to be constant throughout the pile depth.

5.3.2 Limit stresses

In the analysis, elastic behaviour is assumed until the tractions on the pile-soil interface reach certain yield stresses (determined from the limit stresses). In the compression soil zone (see Figure 5.1a), the limiting bearing stress is given by the equation:

$$t_{sc} = N_c C_u \quad (5.5)$$

where N_c is the bearing capacity factor.

The bearing capacity factor is assumed to increase linearly from two at the surface to a constant value of nine at a depth of three pile diameters and below. These values are suggested by Skempton (1959), Poulos and Davis (1980) and Tomlinson (1994).

In the slip (shear) soil zone (see Figure 5.1b), i.e. along the side of the pile, the limiting shear stress is taken as:

$$t_{ss} = \alpha C_u \quad (5.6)$$

where α is an empirical adhesion factor.

The adhesion factor (α) depends mainly on the undrained shear strength of the soil, and the method of pile installation. For driven piles, α ranges from 0.2 for very stiff clays to 1.0 for soft clays (Tomlinson, 1994). For bored piles, data on α are limited, and an average value of 0.5 is recommended.

Since soils cannot sustain tension, the total change in normal stress in the tension soil zone (see Figure 5.1a) cannot be greater than the in-situ lateral effective stress. Thus, the limiting tensile stress is:

$$t_{st} = K_i \gamma z \quad (5.7)$$

where K_i is the lateral earth pressure coefficient,
 γ is the effective unit weight of the soil, and
 z is the depth.

The lateral earth pressure coefficient (K_i) should reflect the method of installation. For driven piles, a value of unity or higher is appropriate, whereas for bored piles, K_i may be less than unity.

From the limit stresses determined using Equations (5.5) to (5.7), the yield stresses for the soil elements are established. The yield stress for bearing is:

$$t_{syc} = t_{sc} \quad (5.8)$$

yield stress for shear is:

$$t_{sys} = t_{ss} \quad (5.9)$$

and yield stress for tension is:

$$t_{syl} = t_{sl} \quad (5.10)$$

5.3.3 Gap formation

A principal effect of cyclic loading is the development of a permanent gap between the pile and the soil when the soil yields in tension (Figure 5.1a). Gaps play a vital role in the cyclic analysis, as they can determine whether a soil element remains plastic or elastic during the unloading and reloading processes. When gaps occur at the pile-soil interface, the resistance provided by the soil element at that particular section is reduced to zero until

pile-soil contact is established again. Careful monitoring of gap formation throughout the whole pile length is required and care must be taken to ensure that the gaps do not 'overclose' when the pile returns.

From the plane-strain finite element analysis presented in Chapter 3, it is observed that the soil elements at the debonded pile-soil interface (gaps present), responded elastically (in terms of load-displacement responses); see Figures 3.24 to 3.29. This suggests that for cyclic analysis, the soil element that has yielded in tension (gap occurs at the pile-soil interface), will undergo an elastic load-displacement response according to the initial pile-soil system stiffness. For simplicity, it can be assumed that when the soil element fails in tension, it will remain stationary, unless the pile-soil contact is established again (e.g. gap closed during unloading).

5.3.4 Backsliding

During loading, tensile stresses may occur at the pile-soil contact zone. The adhesive properties of cohesive soil will result in backsliding of the soil into the gap, resulting in the reduction in gap size, as depicted in Figure 5.1a. This phenomenon has been observed by Matlock (1970) in his laboratory model pile tests and implemented by Bijnagte *et al.* (1991) in their discrete element numerical model (described in Section 1.3.5).

Backsliding is incorporated here by increasing the limit tensile stress of the soil. This reduces the number of soil elements yielding in tension, and thereby reduces the gap sizes. The limit adhesive stress of the soil is calculated from the equation:

$$t_{stb} = \beta C_u + t_{st} \quad (5.11)$$

where β is a backsliding factor; $0 < \beta < 1$.

If backsliding is included in the analysis, the yield stress for tension (t_{syl}) in Equation (5.10) will be replaced:

$$t_{syl} = t_{stb} \quad (5.12)$$

In many reported cyclic pile-load tests, backsliding has not been mentioned. This is probably because its influence on the overall pile behaviour is not significant, or it may be that the amount of soil sliding back into the gap cannot be measured in the field. However, it is felt that the implementation of the backsliding effect is essential for the complete analysis of pile-soil interface behaviour.

5.3.5 Soil strength degradation

Cyclic loading on soil will result in strength degradation as described in Chapter 4. The soil strength degradation is based on the post-peak strength degradation to residual strength, which are evident in shear tests and bearing tests depicted in Figures 5.2a and 5.2b, respectively. The magnitude of strength degradation can be taken as a function of the plastic soil displacement (i.e. displacement after peak strength is reached), as illustrated in Figure 5.1c. The soil strength degradation applies only to plastic soil elements where their stresses have reached the yield stresses. Such situation occurs mostly for the soil elements at the upper region of the pile. For soil elements subjected to stresses below their yield stresses, their strength will not degrade. This applies to soil elements that are at the lower portion of the pile, where the stresses subjected upon them are minimal.

Shear strength degradation

From Section 4.9, it was shown that the residual limit shear stress of the soil in the slip (shear) zone can be determined as:

$$t_{ssr} = R_s t_{ss} \quad (5.13) \quad (4.11 \text{ bis})$$

where R_s is the residual/peak shear strength ratio.

Due to shear strength degradation, the limit shear stress will reduce. The reduced limit shear stress is given by the equation:

$$t_{ssd} = t_{ssr} + (t_{ss} - t_{ssr}) \exp(-C_s ds) \quad (5.14) \quad (4.12 \text{ bis})$$

where C_s is the shear degradation rate factor in mm^{-1} , and

d_s is the plastic shear displacement.

The correlations of R_s and C_s with soil index properties are found in Figures 4.16 and 4.26, respectively.

If shear strength degradation is allowed for the particular soil element, the yield stress for shear will be:

$$t_{sys} = t_{ssd} \quad (5.15)$$

Bearing strength degradation

From Section 4.9, it was shown that the residual limit bearing stress of the soil in the compression zone can be determined as:

$$t_{scr} = R_b t_{sc} \quad (5.16) \quad (4.13 \text{ bis})$$

where R_b is the residual/peak bearing strength ratio.

As a result of bearing strength degradation, the limit bearing stress will reduce. The reduced limit bearing stress is determined by the equation:

$$t_{scd} = t_{scr} + (t_{sc} - t_{scr}) \exp^{(-C_b db/D)} \quad (5.17) \quad (4.14 \text{ bis})$$

where C_b is the bearing degradation rate factor,

d_b is the plastic bearing displacement, and

D is the pile diameter or width.

Discussion on the values for R_b and C_b is found in Sections 4.7.1 and 4.8.1, respectively.

If bearing strength degradation is allowed for the particular soil element, the yield stress for bearing will be:

$$t_{syc} = t_{scd} \quad (5.18)$$

5.4 Boundary element formulation

The non-linear response of piles to lateral loading is obtained by coupling the equations describing the non-linear load-displacement behaviour of the soil with the equations describing the flexural behaviour of the pile, treated as a solid cylindrical elastic beam. An approximate solution to this elasto-plastic problem is obtained by means of an incremental analysis via the indirect boundary element method, where only the pile-soil interface is discretised (Davies and Budhu, 1986; Budhu and Davies, 1988).

5.4.1 Pile flexure

The pile of length (L) is divided into a number (n) of cylindrical segments, see Figure 5.3a. Following the subdivision of the pile length into segments, the mean lateral displacements and tractions over each segment (nodal values) in the pile domain can be related to each other via the elementary (Bernoulli-Euler) beam theory, giving:

$$\{u_p\} = [G_p]\{t_p\} + \{B_p^u\} + \{B_p^\theta\} \quad (5.19)$$

where $\{u_p\}$ are the pile segment displacements,

$[G_p]$ is the matrix of coefficients obtained by integration of the Bernoulli-Euler kernel; for further details see Appendix 5.1,

$\{t_p\}$ are the pile segment tractions,

$\{B_p^u\}$ are the pile segment displacements, due to unit lateral translation of the pile (see Figure 5.4a), giving $[1, 1, 1 \dots]^T$, and, T denotes transpose, and

$\{B_p^\theta\}$ are the pile segment displacements, due to unit rotation of the pile about its head (see Figure 5.4b), giving $[-0.5h, -1.5h, -2.5h \dots]^T$, and, h is the height of pile segment.

The pile segment displacements due to unit boundary conditions are taken as:

$$\{B_p\} = \{B_p^u\} + \{B_p^\theta\} \quad (5.20)$$

Applying Equation (5.20), Equation (5.19) is simplified as:

$$\{u_p\} = [G_p]\{t_p\} + \{B_p\} \quad (5.21)$$

5.4.2 Soil deformation

Assuming linearly elastic behaviour in the soil domain, the soil deformations and tractions at the pile-soil interface nodes can be obtained by integration of Mindlin's (Mindlin, 1936) kernel, yielding:

$$\{u_{se}\} = [G_{se}]\{t_{se}\} \quad (5.22)$$

where $\{u_{se}\}$ are the soil displacements at the pile-soil interface,

$\{t_{se}\}$ are the soil tractions at the pile-soil interface, and

$[G_{se}]$ is the matrix of coefficients obtained from Mindlin's solution; for further details see Appendix 5.2.

Evaluations of the $[G_{se}]$ matrix are carried out by integration of the Mindlin's solution for the horizontal displacement caused by a point load within the interior of a semi-infinite mass. Although the solution is only applicable for an elastic isotropic homogenous mass with uniform Young's modulus (E_s), inhomogenous material with varying E_s can also be considered. To allow approximately for soil non-homogeneity, the representative modulus E_s for i -th element, when considering the influence of j -th element, may be taken as the larger E_s value at i -th and j -th elements (Davies and Budhu, 1994).

From the four faces of the pile segment (Figure 5.3b), a full soil matrix $[G_{se}]$ of $4n \times 4n$ is formed. The full soil matrix is then inverted to give the $[F]$ matrix, i.e.

$$[F] = [G_{se}]^{-1} \quad (5.23)$$

Employing elastic theory and utilising the principle of superposition, the four soil element (surrounding a pile segment) stiffnesses can be condensed into one soil segment (see Figure 5.5a), resulting in an $n \times n$ matrix. This is compatible with the pile coefficients matrix $[G_p]$ of $n \times n$. The condensation yields the 'soil segment' stiffness matrix $[K_s]$; see Figure 5.5b. Each coefficient of the $[K_s]$ matrix is taken as:

$$K_{s\ ij} = \sum_{I=4i-3}^{4i} \sum_{J=4j-3}^{4j} F_{IJ} \quad (5.24)$$

where $K_{s\,ij}$ is the coefficient at the i -th row and the j -th column of $[K_s]$ matrix,
 F_{IJ} is the coefficient at the I -th row and the J -th column of $[F]$ matrix, and
 i and $j = 1, 2, 3$ to n .

It is worthy of note that the soil segment stiffness matrix generated using the Mindlin's solution (Mindlin, 1936) is fully populated (in the initial loading stage) in contrast with the p - y method which supposes a diagonal stiffness matrix. The soil segment stiffness matrix $[K_s]$ is inverted to give the compliance matrix $[G_s]$, i.e.

$$[G_s] = [K_s]^{-1} \quad (5.25)$$

Knowing the $[G_s]$ matrix, the soil segment displacements are determined as:

$$\{u_s\} = [G_s] \{t_s\} \quad (5.26)$$

where $\{u_s\}$ are the soil segment displacements, and
 $\{t_s\}$ are the soil segment tractions.

5.4.3 Pile-soil system interaction

Invoking compatibility of the deformations of the pile and the soil:

$$\{u_p\} = \{u_s\} \quad (5.27)$$

and equilibrium of the tractions at the pile-soil interface:

$$\{t_p\} = -\{t_s\} \quad (5.28)$$

Coupling of Equations (5.21) and (5.26) by applying Equations (5.27) and (5.28) gives the pile segment tractions as:

$$\{t_p\} = -[G_p + G_s]^{-1} \{B_p\} \quad (5.29)$$

Incremental analysis

For load-displacement response to be non-linear, Equation (5.29) is solved incrementally by applying unit boundary conditions on the pile head (Figure 5.4). For convenience and to avoid confusion, the symbol Δ is used to identify the tractions (or displacements) obtained, and Equation (5.29) is rewritten as:

$$\{\Delta t_p\} = -[G_p + G_s]^{-1} \{B_p\} \quad (5.30)$$

where $\{\Delta t_p\}$ are the pile segment tractions.

During each increment, the matrix $[G_p]$ is unaltered since the pile is assumed to remain elastic, but the soil compliance matrix $[G_s]$ is altered because of soil yielding, elastic unloading or gap closure.

Soil yielding

In the event, when a soil segment yields (i.e. the four soil elements that constitute the soil segment reach their yield stresses), the stiffness coefficients of the $[K_s]$ matrix corresponding to that segment (rows and columns) will be zero. The determination of $[G_s]$ matrix is not possible as the inverse of $[K_s]$ matrix with zero terms in either the row or column cannot be evaluated. This means that Equation (5.30) cannot be applied to determined the pile segment traction.

In the above situation, based on equilibrium condition, the traction for the pile segments corresponding to the plastic soil segments will be:

$$\{\Delta t_p^n\} = -\{\Delta t_s^n\} = 0 \quad (5.31)$$

where $\{\Delta t_p^n\}$ are the pile segment tractions corresponding to the plastic soil segments, and $\{\Delta t_s^n\}$ are the plastic soil segment tractions.

The compatibility criterion is no longer justified, i.e.

$$\{\Delta u_p^n\} \neq \{\Delta u_s^n\} \quad (5.32)$$

where $\{\Delta u_p^n\}$ are the pile segment displacements corresponding to the plastic soil segments,

and

$\{\Delta u_s^n\}$ are the plastic soil segment displacements.

The interaction between elastic and plastic soil segments during the incremental analysis, can be solved by using matrix partitioning. Equation (5.21) can be partitioned as:

$$\begin{Bmatrix} \Delta u_p^e \\ \Delta u_p^n \end{Bmatrix} = \begin{bmatrix} G_p^{ee} & G_p^{en} \\ G_p^{ne} & G_p^{nn} \end{bmatrix} \begin{Bmatrix} \Delta t_p^e \\ \Delta t_p^n \end{Bmatrix} + \begin{Bmatrix} B_p^e \\ B_p^n \end{Bmatrix} \quad (5.33)$$

where $\{\Delta u_p^e\}$ are the pile segment displacements corresponding to the elastic soil segments,

$\{\Delta t_p^e\}$ are the pile segment tractions corresponding to the elastic soil segments,

$[G_p^{ee}]$ and $[G_p^{ne}]$ are the pile coefficients corresponding to the elastic soil segments,

$[G_p^{en}]$ and $[G_p^{nn}]$ are the pile coefficients corresponding to the plastic soil segments,

and

$\{B_p^e\}$ and $\{B_p^n\}$ are the pile segment displacements due to unit boundary conditions corresponding to elastic and plastic soil segments, respectively.

The soil segment displacements from Equation (5.26) is partitioned as:

$$\begin{Bmatrix} \Delta u_s^e \\ \Delta u_s^n \end{Bmatrix} = \begin{bmatrix} G_s^{ee} & G_s^{en} \\ G_s^{ne} & G_s^{nn} \end{bmatrix} \begin{Bmatrix} \Delta t_s^e \\ \Delta t_s^n \end{Bmatrix} \quad (5.34)$$

where $\{\Delta u_s^e\}$ are the elastic soil segment displacements,

$\{\Delta t_s^e\}$ are the elastic soil segment tractions,

$[G_s^{ee}]$ and $[G_s^{ne}]$ are the soil coefficients corresponding to the elastic soil segments,

and

$[G_s^{en}]$ and $[G_s^{nn}]$ are the soil coefficients corresponding to the plastic soil segments.

If the soil segments are elastic, compatibility and equilibrium implies:

$$\{\Delta u_p^e\} = \{\Delta u_s^e\} \quad (5.35)$$

$$\{\Delta t_p^e\} = -\{\Delta t_s^e\} \quad (5.36)$$

Inverting Equation (5.34), we obtain:

$$\begin{Bmatrix} \Delta t_s^e \\ \Delta t_s^n \end{Bmatrix} = \begin{bmatrix} K_s^{ee} & K_s^{en} \\ K_s^{ne} & K_s^{nn} \end{bmatrix} \begin{Bmatrix} \Delta u_s^e \\ \Delta u_s^n \end{Bmatrix} \quad (5.37)$$

where $[K_s^{ee}]$ and $[K_s^{ne}]$ are the soil stiffness coefficients corresponding to the elastic soil segments, and

$[K_s^{en}]$ and $[K_s^{nn}]$ are the soil stiffness coefficients corresponding to the plastic soil segments.

Invoking Equation (5.31) and noting that the plastic soil segment displacements are arbitrary, implies that:

$$[K_s^{ne}] = [K_s^{nn}] = 0 \quad (5.38)$$

and applying symmetry:

$$[K_s^{en}] = 0 \quad (5.39)$$

Making the assumption that the stiffness submatrix $[K_s^{ee}]$ of elastic soil segments are only altered based on the number of elastic soil segments (described in Section 5.4.11), from Equations (5.37) to (5.39), we obtain:

$$\{\Delta t_s^e\} = [K_s^{ee}]\{\Delta u_s^e\} \quad (5.40)$$

Inverting the above equation gives:

$$\{\Delta u_s^e\} = [G_{s*}^{ee}]\{\Delta t_s^e\} \quad (5.41)$$

where $[G_{s*}^{ee}] = [K_s^{ee}]^{-1}$

Hence, for elastic and plastic soil segment displacements, Equation (5.34) is written as:

$$\begin{Bmatrix} \Delta u_s^e \\ \Delta u_s^n \end{Bmatrix} = \begin{bmatrix} G_{s*}^{ee} & G_{s*}^{en} \\ G_{s*}^{ne} & G_{s*}^{nn} \end{bmatrix} \begin{Bmatrix} \Delta t_s^e \\ \Delta t_s^n \end{Bmatrix} \quad (5.42)$$

The plastic soil segment displacements $\{\Delta u_s^n\}$ are undetermined as there are no unique solutions. It is important to note that $[G_{s*}^{ee}]$ is not equal to $[G_s^{ee}]$ in Equation (5.34). The $[G_{s*}^{ne}]$ and $[G_{s*}^{nn}]$ are undetermined terms, as the inverse of zero terms from Equation (5.38) will be infinity. This suggests that the soil segment displacements after yielding cannot be determined. However, this is not a major concern, as the pile segment displacements corresponding to the yielded soil segments can still be evaluated as shown in Equation (5.33); $[G_p]$ is assumed to be unaltered, as the pile segments remain elastic at all times. For convenience, rewrite Equation (5.33) using Equation (5.31) yields:

$$\{\Delta u_p^e\} = [G_p^{ee}]\{\Delta t_p^e\} + \{B_p^e\} \quad (5.43)$$

$$\{\Delta u_p^n\} = [G_p^{ne}]\{\Delta t_p^e\} + \{B_p^n\} \quad (5.44)$$

Enforcing compatibility and equilibrium at the elastic pile-soil interfaces via Equations (5.35) and (5.36), Equations (5.41) and (5.43) can be combined to give:

$$\{\Delta t_p^e\} = -[G_{s*}^{ee} + G_p^{ee}]^{-1}\{B_p^e\} \quad (5.45)$$

The pile-soil system stiffness matrix is defined as:

$$[K] = [G_{s*}^{ee} + G_p^{ee}]^{-1} \quad (5.46)$$

Once the tractions for the elastic and plastic segments are known, further analyses can then be carried out.

5.4.4 Pile-head stiffness matrix and compliance matrix

In practice, the unit translation and rotation problems are solved independently by applying Equations (5.45) and (5.46). The pile segment tractions due to unit lateral translation of the pile are:

$$\{\Delta t_p^{eu}\} = -[K]\{B_p^{eu}\} \quad (5.47)$$

where $\{\Delta t_p^{eu}\}$ are the pile segment tractions due to unit lateral translation of the pile, corresponding to the elastic soil segments, and
 $\{B_p^{eu}\}$ are the pile segment displacements due to unit lateral translation of the pile, corresponding to the elastic soil segments.

The pile segment traction increments due to unit rotation of the pile about its head are:

$$\{\Delta t_p^{e\theta}\} = -[K]\{B_p^{e\theta}\} \quad (5.48)$$

where $\{\Delta t_p^{e\theta}\}$ are the pile segment traction increments due to unit rotation of the pile about its head, corresponding to the elastic soil segments, and
 $\{B_p^{e\theta}\}$ are the pile segment displacements due to unit rotation of the pile about its head, corresponding to the elastic soil segments.

The lateral load at the pile-head due to unit lateral translation of the pile is determined as:

$$H_u = \sum_{i=1}^n \Delta t_{pi}^{eu} A_p \quad (5.49)$$

and due to unit rotation of the pile about its head is determined as:

$$H_\theta = \sum_{i=1}^n \Delta t_{pi}^{e\theta} A_p \quad (5.50)$$

where Δt_{pi}^{eu} is the pile segment traction for the i -th segment, due to unit lateral translation of the pile, corresponding to the elastic soil segment,
 A_p is the pile segment cross sectional area, and
 $\Delta t_{pi}^{e\theta}$ is the pile segment traction for the i -th segment, due to unit rotation at the pile about its head, corresponding to the elastic soil segment.

The moment at the pile-head due to unit lateral translation of the pile is:

$$M_u = - \sum_{i=1}^n \Delta t_{pi}^{eu} A_p z_i \quad (5.51)$$

and due to unit rotation of the pile about its head is:

$$M_\theta = - \sum_{i=1}^n \Delta t_{pi}^{e\theta} A_p z_i \quad (5.52)$$

where z_i is the depth at the i -th segment.

The system pile-head stiffness matrix $[SM]$ can be assembled into:

$$\begin{Bmatrix} H \\ M \end{Bmatrix} = \begin{bmatrix} H_u & H_\theta \\ M_u & M_\theta \end{bmatrix} \begin{Bmatrix} u \\ \theta \end{Bmatrix} \quad (5.53)$$

where H is the pile-head lateral load,

M is the pile-head moment,

H_u, H_θ, M_u and M_θ are coefficients of the pile-head stiffness matrix $[SM]$ determined from Equations (5.49) to (5.52),

u is the lateral translation of the pile-head, and

θ is the rotation of the pile-head.

The inverse of the stiffness matrix $[SM]$ yields the pile-head compliance matrix $[CM]$ as:

$$\begin{Bmatrix} u \\ \theta \end{Bmatrix} = \begin{bmatrix} F_{uH} & F_{uM} \\ F_{\theta H} & F_{\theta M} \end{bmatrix} \begin{Bmatrix} H \\ M \end{Bmatrix} \quad (5.54)$$

where $F_{uH}, F_{uM}, F_{\theta H}$ and $F_{\theta M}$ are coefficients of the pile-head compliance matrix $[CM]$.

5.4.5 Pile tractions and displacements

The matrix $[CM]$ is employed to determine the pile segment tractions and displacements through the following equations for various pile-head conditions, except the fixed-head case where the pile-head rotation is zero. The pile segment tractions for a fixed-head case are:

$$\{\Delta t_p^e\} = \{\Delta t_p^{eu}\} \quad (5.55)$$

The pile segment displacements corresponding to the elastic soil segment are:

$$\{\Delta u_p^e\} = [G_p^{ee}]\{\Delta t_p^e\} + \{B_p^{eu}\} \quad (5.56)$$

and corresponding to the plastic soil segment are:

$$\{\Delta u_p^n\} = [G_p^{ne}]\{\Delta t_p^e\} + \{B_p^{nu}\} \quad (5.57)$$

where $\{B_p^{nu}\}$ are the pile segment displacements due to unit lateral translation of the pile, corresponding to the plastic soil segments.

For a general free-head with eccentricity case, the pile segment tractions are expressed as:

$$\{\Delta t_p^e\} = F_{uH}\{\Delta t_p^{eu}\} + F_{\theta H}\{\Delta t_p^{e\theta}\} + \left(F_{uM}\{\Delta t_p^{eu}\} + F_{\theta M}\{\Delta t_p^{e\theta}\}\right) e \quad (5.58)$$

The pile segment displacements corresponding to the elastic soil segment are:

$$\begin{aligned} \{\Delta u_p^e\} = & [G_p^{ee}]\{\Delta t_p^e\} + F_{uH}\{B_p^{eu}\} + F_{\theta H}\{B_p^{e\theta}\} \\ & + \left(F_{uM}\{B_p^{eu}\} + F_{\theta M}\{B_p^{e\theta}\}\right) e \end{aligned} \quad (5.59)$$

and corresponding to the plastic soil segment are:

$$\begin{aligned} \{\Delta u_p^n\} = & [G_p^{ne}]\{\Delta t_p^e\} + F_{uH}\{B_p^{nu}\} + F_{\theta H}\{B_p^{n\theta}\} \\ & + \left(F_{uM}\{B_p^{nu}\} + F_{\theta M}\{B_p^{n\theta}\}\right) e \end{aligned} \quad (5.60)$$

where e is the eccentricity of loading, and

$\{B_p^{n\theta}\}$ are the pile segment displacements due to unit rotation of the pile about its head, corresponding to the plastic soil segments.

The pile segment tractions, which are equal in magnitude but opposite in direction to the soil segment tractions, are distributed accordingly to the elastic soil element(s) surrounding the pile segments, i.e.

$$\{\Delta t_{st}^e\} = - \frac{\{\Delta t_p^e\}}{n_e} \quad (5.61)$$

where $\{\Delta t_{st}^e\}$ are the elastic soil element tractions, and
 n_e is the number of elastic soil elements within the segment.

These soil element tractions are compared with the yield stresses established for each soil element (described in Section 5.3). A yield factor is applied to all elastic soil elements (see Figure 5.6), expressed as:

$$\{p_f\} = \frac{\{\Delta t_{st}^e\}}{\{t_{sy}\} - \{t_{str}\}} \quad (5.62)$$

where $\{p_f\}$ are the yield factors for the elastic soil elements,
 $\{t_{str}\}$ are the current soil element tractions (end of previous increment), and
 $\{t_{sy}\}$ are the yield stresses for the soil elements.

The yield factors $\{p_f\}$ determined for all the elastic soil elements were compared against one another, and the largest yield factor (f_y) was chosen. This implies that the current soil element traction (end of previous increment) for the particular soil element is closest to its yield stress in the current increment. Subsequently, the soil element upon which the largest yield factor is chosen, is regarded as plastic, as the current soil element traction in the current increment will reach the yield stress (when f_y is employed to determine the soil element traction increment). At any one increment, only one soil element is allowed to yield unless other elements (e.g. side soil elements of a soil segment) are having the same yield factor. No increase in tractions are permitted for the plastic elements.

The soil elements traction increments are determined as:

$$\{\delta t_{st}\} = \frac{\{\Delta t_{st}^e\}}{f_y} \quad (5.63)$$

and the current soil element tractions are determined as:

$$\{t_{st}\} = \{t_{str}\} + \{\delta t_{st}\} \quad (5.64)$$

The pile segment (corresponding to both elastic and plastic soil segments) displacement increments are determined as:

$$\{\delta u_p\} = \frac{\{\Delta u_p\}}{f_y} \quad (5.65)$$

and the current pile segment displacements are determined as:

$$\{u_p\} = \{u_{pr}\} + \{\delta u_p\} \quad (5.66)$$

where $\{\Delta u_p\}$ is equal to $\{\Delta u_p^e\}$ or $\{\Delta u_p^n\}$, and $\{u_{pr}\}$ are the current pile displacements (end of previous increment).

The current pile segment traction is obtained by summation of the tractions of the four soil elements surrounding it, i.e.

$$t_{pi} = - \sum_{j=1}^4 t_{stij} \quad (5.67)$$

where t_{pi} is the current pile segment traction for the i -th segment,

t_{stij} is the current soil element traction for the j -th element of the i -th segment, and

$i = 1, 2, 3$ to n .

Knowing the traction of each pile segment, the shear force and bending moment for the pile segments along the pile length can be readily determined.

5.4.6 Elastic unloading

Some soil elements tend to regain elasticity after yielding due to changes in their traction increment directions during incremental loading. Consequently, it is necessary to include provisions for elastic unloading to occur. These plastic elements are identified and brought back to elastic when:

$$\{\Delta t_p^e\} \{t_{str}\} < 0 \quad (5.68)$$

For the case when the soil segments have yielded, the pile segment traction for that segment will be zero (i.e. $\Delta t_p^e = 0$), and the above Equation (5.68) for soil elements elastic unloading cannot be applied. Elastic unloading of a plastic soil segment is allowed for when:

$$t_{pr\ i} \left[\Delta t_{p\ i+1}^e + \Delta t_{p\ i-1}^e \right] < 0 \quad (5.69)$$

where $t_{pr\ i}$ is the current pile segment traction (end of previous increment) for the i -th segment,

$\Delta t_{p\ i+1}^e$ is the pile segment traction for the $i+1$ segment; if $i = n$, then $\Delta t_{p\ i+1}^e = 0$, and

$\Delta t_{p\ i-1}^e$ is the pile segment traction for the $i-1$ segment; if $i = 1$, then $\Delta t_{p\ i-1}^e = 0$.

The elastic unloading will result in an increase in the stiffness of the system as the elements are set back to elastic, resulting in a stiffer pile response. Note that elastic unloading is not provided for plastic soil elements where gaps are present at the pile-soil interfaces.

5.4.7 Gap formation

Gap distances are determined at the pile-soil interfaces when the soil elements yield in tension. At the right pile face (see Figure 5.7a), the current right gap distances are:

$$\{d_{gr}\} = \{u_{gr}\} - \{u_p\} \quad (5.70)$$

and for the left pile face, the current left gap distances are:

$$\{d_{gl}\} = \{u_p\} - \{u_{gl}\} \quad (5.71)$$

where $\{u_{gr}\}$ and $\{u_{gl}\}$ are the pile displacements when soil elements yield in tension at the right and left faces of the pile, respectively.

Since overclosing of the gap is not allowed, this implies:

$$\{d_{gr}\} \geq 0 \quad \text{and} \quad \{d_{gl}\} \geq 0 \quad (5.72)$$

To ensure that Equation (5.72) is satisfied, the gap closing factors are determined when d_{gr} and d_{gl} are less than zero (see Figure 5.7b). The gap closing factors for the right pile face are:

$$\{C_{gr}\} = \frac{\{\Delta u_p\}}{\frac{\{\Delta u_p\}}{f_y} + \{d_{gr}\}} \quad (5.73)$$

and for the left pile face are:

$$\{C_{gl}\} = \frac{\{\Delta u_p\}}{\frac{\{\Delta u_p\}}{f_y} - \{d_{gl}\}} \quad (5.74)$$

As many of the soil elements may experience gap closing in a particular increment, the gap closing factors determined from Equations (5.73) and (5.74) are compared against one another. The largest gap closing factor (f_g) is then chosen. This will ensure that only one gap is closed in the current increment. Due to gap closure, the pile-soil contact is established and the plastic soil element is brought back to elastic. The soil resistance for that element is provided and the stiffness of the pile-soil system is increased.

The element once determined as plastic, where f_y is chosen in the current increment, is now set back to elastic as f_g is always greater than f_y . The largest yield factor (f_y) is now taken to be:

$$f_y = f_g \quad (5.75)$$

In what follows, Equations (5.63) to (5.67) are recalculated by applying Equation (5.75). The shear force and bending moments for the pile segments are subsequently determined.

5.4.8 Pile-head reactions

The incremental pile-head lateral load for a fixed-head pile is determined as:

$$\delta H = \frac{H_u}{f_y} \quad (5.76)$$

the incremental pile-head moment is:

$$\delta M = \frac{M_u}{f_y} \quad (5.77)$$

and the incremental pile-head lateral displacement is:

$$\delta u = \frac{1}{f_y} \quad (5.78)$$

where H_u and M_u are stiffness coefficients in the $[SM]$ matrix from Equation (5.53).

For a general free-head case with eccentricity, the incremental pile-head lateral load is:

$$\delta H = \frac{1}{f_y} \quad (5.79)$$

the incremental pile-head moment is:

$$\delta M = -\frac{e}{f_y} \quad (5.80)$$

the incremental lateral pile-head displacement is:

$$\delta u = \left[\frac{F_{uH}}{f_y} + \frac{F_{uM} e}{f_y} \right] \quad (5.81)$$

and incremental lateral pile-head rotation is:

$$\delta \theta = \left[\frac{F_{\theta H}}{f_y} + \frac{F_{\theta M} e}{f_y} \right] \quad (5.82)$$

where F_{uH} , F_{uM} , $F_{\theta H}$ and $F_{\theta M}$ are coefficients in the $[CM]$ matrix from Equation (5.54).

The current pile-head lateral load is:

$$H = H_r + \delta H \quad (5.83)$$

the current pile-head moment is:

$$M = M_r + \delta M \quad (5.84)$$

the current pile-head lateral displacement is:

$$u = u_r + \delta u \quad (5.85)$$

and the current pile-head rotation is:

$$\theta = \theta_r + \delta \theta \quad (5.86)$$

where H_r , M_r , u_r and θ_r are current pile-head lateral load, moment, lateral displacement and rotation (end of previous increment), respectively.

5.4.9 Shear strength degradation

For shear strength degradation, the incremental plastic shear displacements (δd_s) are determined when the side soil elements yield under two or more consecutive increments or change to elastic (due to elastic unloading only) after being plastic. The incremental plastic shear displacements are calculated from the current pile segment displacements:

$$\{\delta d_s\} = |\{u_p\} - \{u_{pr}\}| \quad (5.87)$$

where $| \cdot |$ denotes absolute value,

$\{u_p\}$ are the current pile segment displacements, and

$\{u_{pr}\}$ are the current pile segment displacements (end of previous increment).

The current plastic shear displacements are determined as:

$$\{d_s\} = \{d_{sr}\} + \{\delta d_s\} \quad (5.88)$$

where $\{d_{sr}\}$ are the current plastic shear displacements (end of previous increment).

Using the appropriate residual/peak shear strength ratio (R_s) and shear degradation rate factor (C_s), as discussed in Section 5.3.5, the limit shear stress for each soil element will degrade to a new value using Equation (5.14), according to current plastic shear displacement. This new value, known as the reduced limit shear stress (t_{ssd}), is only determined when the element has recovered from plastic to elastic. The yield stress for shear, for a particular element is now:

$$t_{sys} = t_{ssd} \quad (5.89)$$

5.4.10 Bearing strength degradation

For bearing strength degradation, the incremental plastic bearing displacements (δd_b) are determined when the bearing soil elements yield under two or more consecutive increments or changes from the plastic to elastic (due to elastic unloading only). The incremental plastic bearing displacements are determined from the current pile segment displacements, i.e.

$$\{\delta d_b\} = |\{u_p\} - \{u_{pr}\}| \quad (5.90)$$

The current plastic bearing displacements are determined as:

$$\{d_b\} = \{d_{br}\} + \{\delta d_b\} \quad (5.91)$$

where $\{d_{br}\}$ are the current bearing plastic displacements (end of previous increments).

Using the appropriate residual/peak bearing strength ratio (R_b) and bearing degradation rate factor (C_b), as discussed in Sections 5.3.5. The limit bearing stress of each soil element will degrade to a new value using Equation (5.17), according to the current plastic bearing displacements. The new limit, known as the reduced limit bearing stress (t_{scd}), is only calculated when the element has recovered from plastic to elastic. The yield stress for bearing, for a particular element is now taken to be:

$$t_{\text{sync}} = t_{\text{scd}} \quad (5.92)$$

5.4.11 Modified soil segment stiffness matrix

At the end of each increment, the 'original' soil segment stiffness matrix $[K_s^o]$ (coefficients determined from Equation (5.24) at the beginning of the analysis) is modified for soil yielding, elastic unloading or gap closure. The $[K_s^o]$ matrix is modified according to the number of yielded soil elements in each soil segment, by using an influence factor (f). For soil element(s) yielded in the k -th segment, the stiffness coefficients for the k -th row is modified as:

$$K_{s\ ki} = f(n_p) K_{s\ ki}^o \quad (5.93)$$

and the stiffness coefficient for the k -th column is modified as:

$$K_{s\ jk} = f(n_p) K_{s\ jk}^o \quad (5.94)$$

where $K_{s\ ki}$ is the stiffness coefficient at the k -th row and the i -th column of $[K_s]$ matrix,
 n_p is the number of yielded soil elements within the segment; $f(1) = 0.75, f(2) = 0.5,$
 $f(3) = 0.25, f(4) = 0,$
 $K_{s\ ki}^o$ is the stiffness coefficient at the k -th row and the i -th column of $[K_s^o]$ matrix,
 $i = 1, 2, 3$ to n ,
 $K_{s\ jk}$ is the stiffness coefficient at the j -th row and the k -th column of $[K_s]$ matrix,
 $K_{s\ jk}^o$ is the stiffness coefficient at the j -th row and the k -th column of $[K_s^o]$ matrix, and
 $j = 1, 2, 3$ to n .

The above process is repeated for each yielded soil segment. The lower value of stiffness coefficients determined from Equations (5.93) and (5.94) is taken to form the $[K_s]$ matrix.

The stiffness coefficients are then partitioned to correspond to the elastic and plastic soil segments as shown in Equation (5.37). The matrix $[K_s^{ee}]$ is then inverted to give the $[G_{s^{*}}^{ee}]$ matrix to be used in Equation (5.45) for the next increment. No direct interaction is allowed to occur between elastic and plastic soil segments, as the stiffness coefficients (rows and columns) of the plastic soil segments are taken as zero ($f(4) = 0$). The use of the influence

factor (f) enforces load transfer to other elastic soil segments and results in monotonic decrease in the system stiffness as yielding progresses.

5.4.12 Unloading and reloading

At the beginning of unloading, all soil elements are set back to elastic due to changes in the load direction, except for soil elements that have yielded in tension. The pile segment tractions $\{\Delta t_p\}$ and displacements $\{\Delta u_p\}$ obtained from unit boundary conditions are now set in opposite directions in contrast to the loading/reloading stage. This will lead to reduction in the soil element tractions, pile segment displacements and tractions, pile-head lateral loads, etc., in each increment, until the specified minimum load (or displacement for displacement-controlled conditions) is reached.

At the beginning of reloading, all soil elements are set back to elastic due to changes in the load direction, except for soil elements that have yielded in tension. The pile segment tractions $\{\Delta t_p\}$ and displacements $\{\Delta u_p\}$ obtained from unit boundary conditions are now set in opposite directions in contrast to the unloading stage. This will lead to increases in the soil element tractions, pile segment displacements and tractions, pile-head lateral loads, etc., in each increment, until the specified maximum load (or displacement for displacement-controlled conditions) is reached.

The unloading and reloading processes continue until the specified number of cycles is reached.

5.5 Discussion

A simple and realistic soil model based on experimental observations is established. The model assumes an elastic-perfectly plastic soil behaviour, with modifications that allow soil strength degradation, taken as a function of the plastic displacement. To account for gap formation, the gap sizes are determined when the soil elements yield in tension. To account for backsliding, the backsliding factor (β) and the undrained shear strength of the soil is used.

The general formulation for the cyclic analysis via the indirect boundary method is presented. The analysis has taken into consideration the four faces of the pile via the Mindlin's solution (Mindlin, 1936), that allows interaction with the neighbouring soil elements. The analysis has employed matrix partitioning, so that there will not be any direct interaction between elastic and plastic soil segments during incremental loading. The

modifications of the soil segment stiffness matrix using the influence factors, enforce load transfer to other elastic elements, resulting in the reduction in the pile-soil system stiffness as soil yielding progresses. The unloading and reloading cycles are carried out by simply reversing the pile traction and displacement increments.

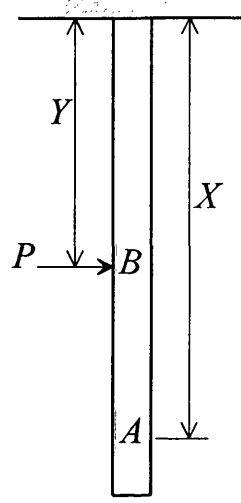
The yield factor approach adopted, ensures that only one soil element yields at any one increment. Among other things, this reduces the computational time required for analysis as compared with equal loading increments to the specified load. This leads to the application of a gap closing factor to ensure that, at any one increment, only one gap is allowed to close, at the same time, ensuring that the pile does not overclose other gaps.

5.6 Concluding remarks

The principal aspects of cyclic soil behaviour are accounted for in this model of cyclic pile-load behaviour. The analysis is capable of determining the pile-head load, moment, displacement and rotation, and shear forces and bending moments along the pile length for piles subjected to cyclic lateral loading. The method takes into consideration soil continuity, pile-head fixity and relative stiffness of the pile and soil as opposed to the established p - y analysis. The implementation will be described in the next Chapter.

Appendix 5.1

Bernoulli-Euler Beam Theory



Using the Bernoulli-Euler beam theory, the displacement at A due to a point load (P) at B is:

$$u(A) = G(A,B) P(B) \quad (\text{A5.1-1})$$

$$\text{where } G(A, B) = \frac{[3YX^2 - X^3]}{6E_p I_p} \quad \text{for } X \leq Y \quad (\text{A5.1-2})$$

$$G(A, B) = \frac{[3XY^2 - Y^3]}{6E_p I_p} \quad \text{for } X \geq Y \quad (\text{A5.1-3})$$

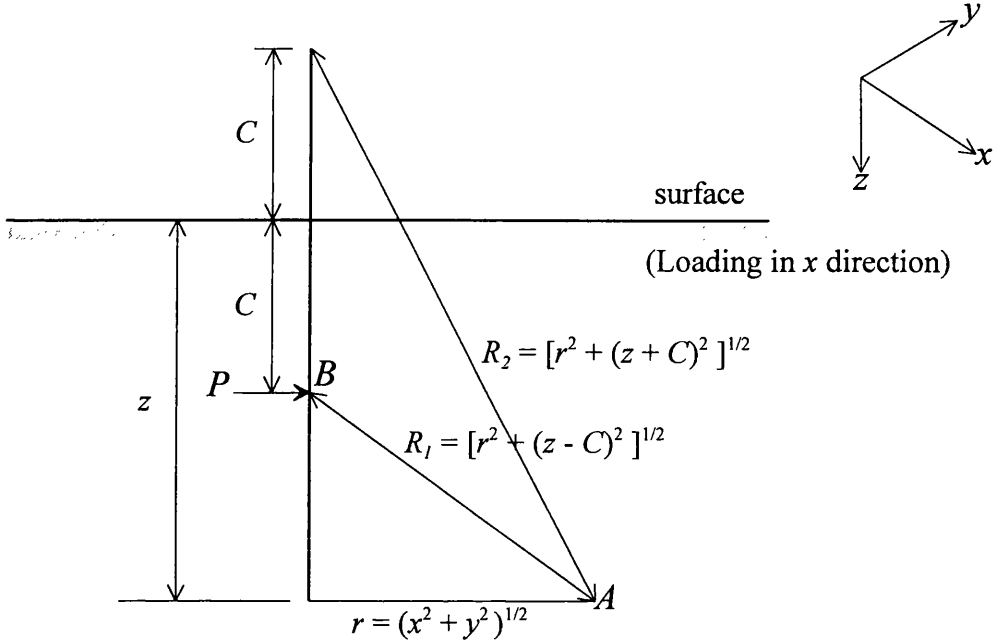
For distributed traction (t), between Y_1 and Y_2 over a beam of width D , we obtain:

$$u(A) = D \int_{Y_1}^{Y_2} t(B) G(A, B) dY \quad (\text{A5.1-4})$$

The above integration is performed analytically.

Appendix 5.2

Mindlin's Solution (Mindlin, 1936)



The horizontal displacement at A caused by a horizontal point load (P) at B within the interior of a semi-infinite elastic-isotropic homogenous mass is expressed as:

$$u(A) = G(A,B) P(B) \quad (\text{A5.2-1})$$

where:

$$G(A,B) = \frac{1}{16\pi G'(1-\nu)} \left[\frac{(3-4\nu)}{R_1} + \frac{1}{R_2} + \frac{x^2}{R_1^3} + \frac{(3-4\nu)x^2}{R_2^3} + \frac{2Cz}{R_2^3} \left(1 - \frac{3x^2}{R_2^2} \right) + \frac{4(1-\nu)(1-2\nu)}{R_2+z+C} \left(1 - \frac{x^2}{R_2(R_2+z+C)} \right) \right] \quad (\text{A5.2-2})$$

where G' is the shear modulus, and

ν is the Poisson's ratio.

For distributed (constant) traction (t) over a surface (S), we obtain:

$$u(A) = t(B) \int_S G(A, B) dS(B) \quad (\text{A5.2-3})$$

The above integration is performed numerically.

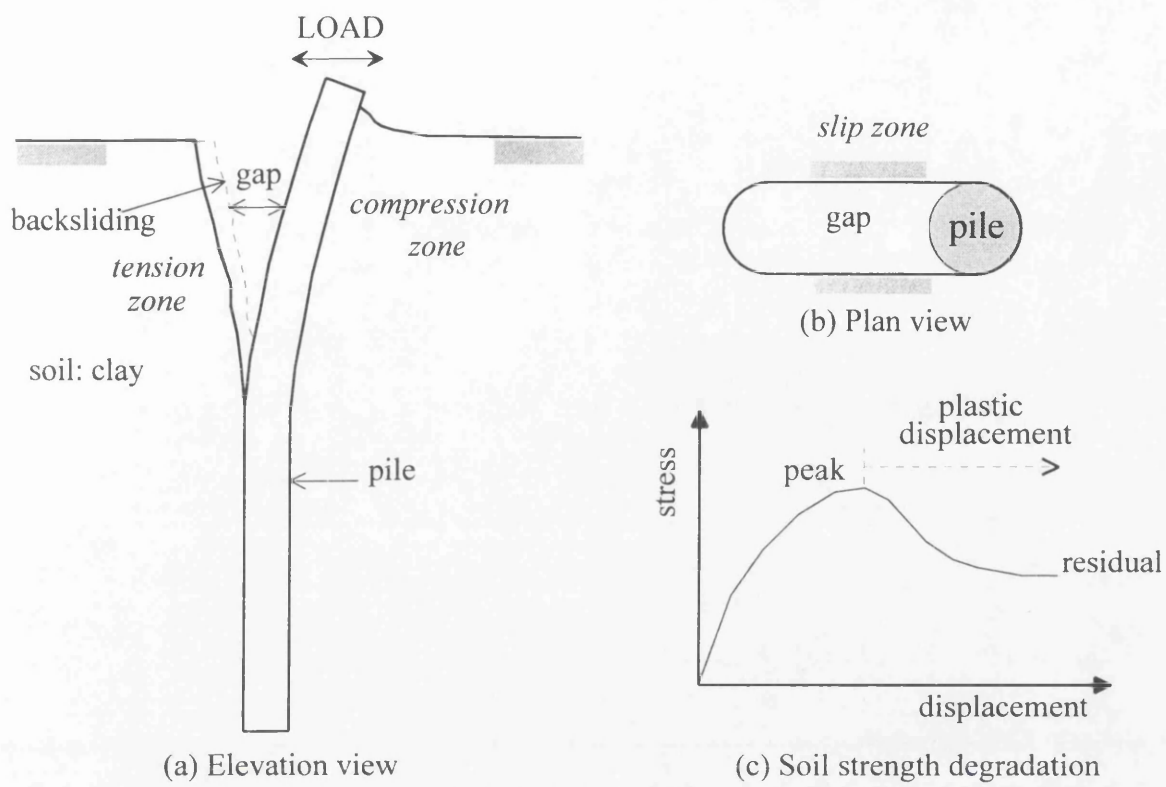


Figure 5.1 Phenomena observed and soil zones developed during cyclic pile-load tests.

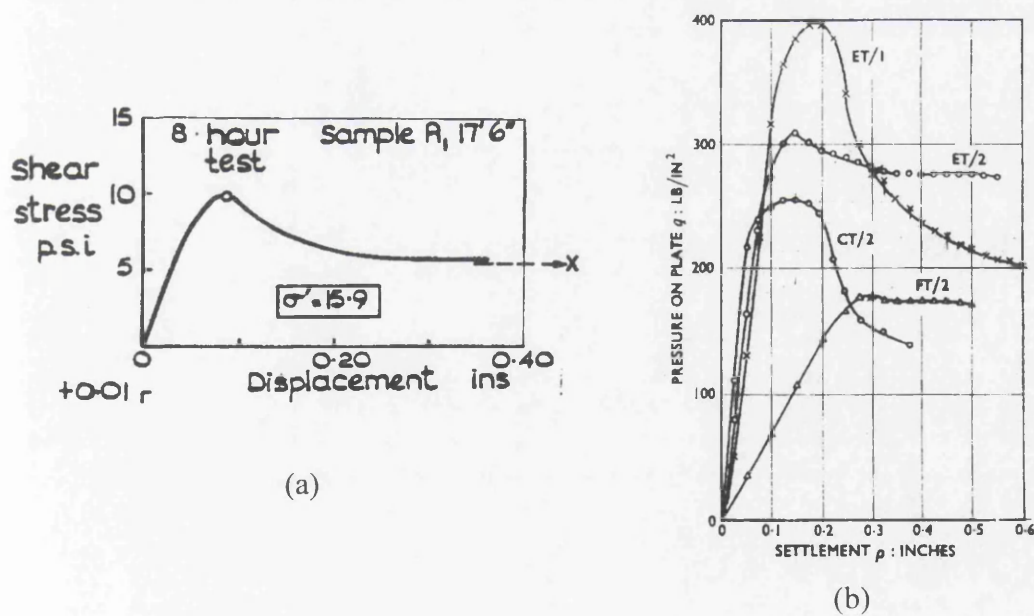


Figure 5.2 (a) Shear test results on Jackfield clay (Skempton, 1964) and (b) typical load-settlement curves for plate loading tests (Ward *et al.*, 1965).

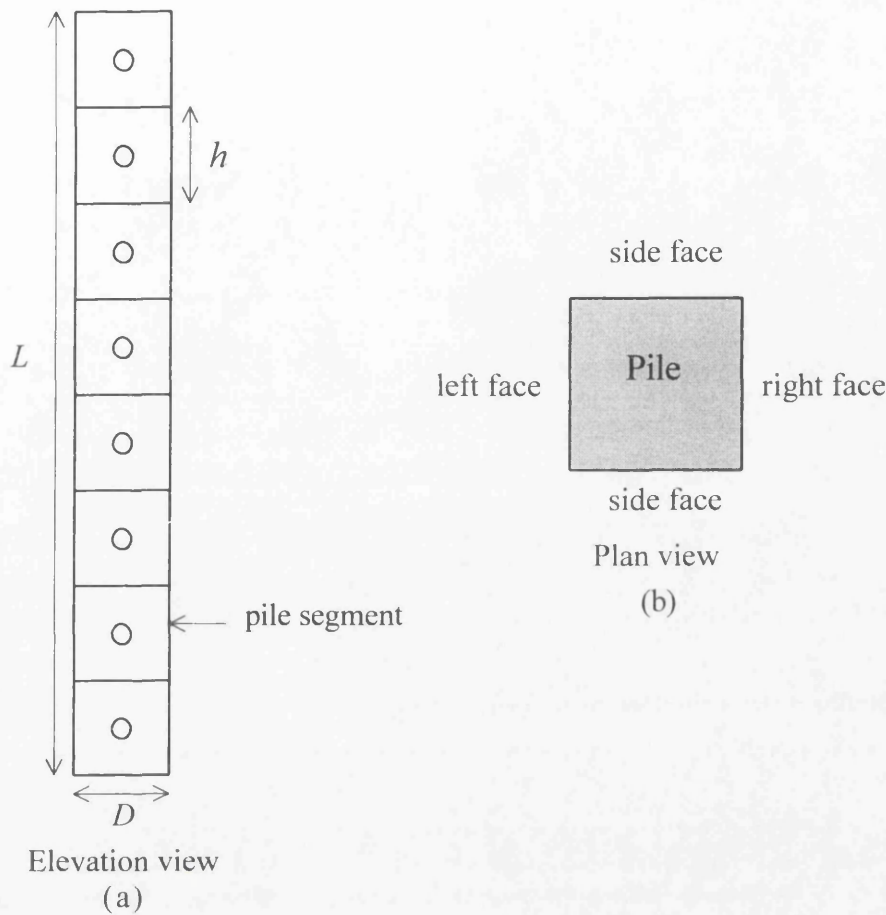


Figure 5.3 (a) Pile discretisation and (b) four faces of a pile segment.

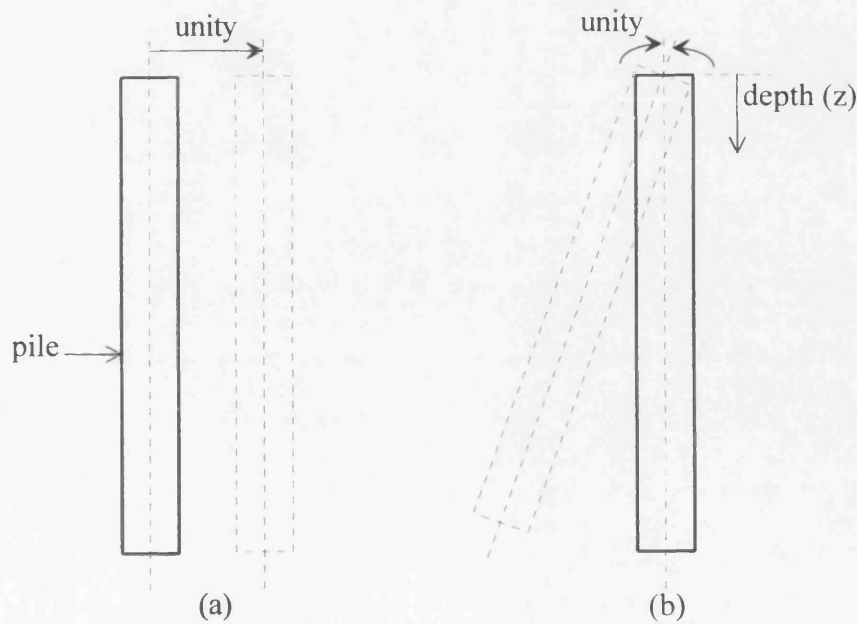
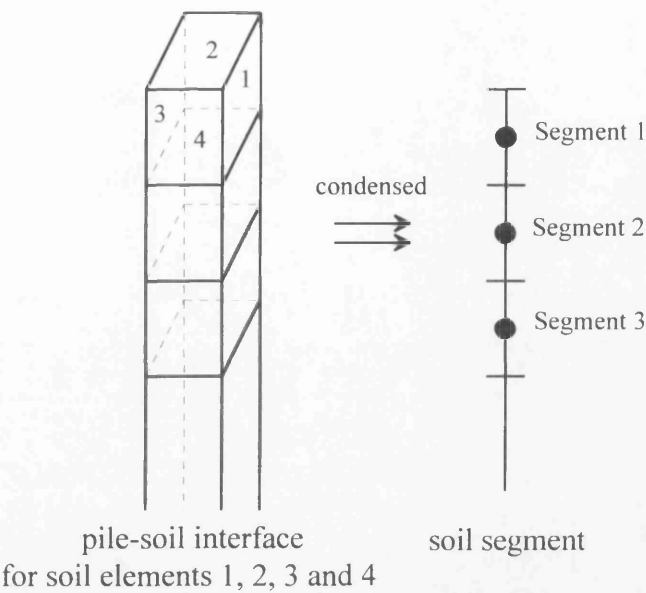


Figure 5.4 Unit boundary conditions; (a) unit lateral translation of the pile and (b) unit rotation of the pile about its head.



(a)

$$[F] = \left[\begin{array}{c|c|c} \begin{array}{cccc} F_{1,1} & F_{1,2} & F_{1,3} & F_{1,4} \\ F_{2,1} & F_{2,2} & F_{2,3} & F_{2,4} \\ F_{3,1} & & & \\ F_{4,1} & & & \end{array} & \begin{array}{cc} = K_{s1,1} & \\ & = K_{s1,2} \end{array} & \begin{array}{cccc} F_{1,5} & F_{1,6} & . & . \\ F_{2,5} & F_{2,6} & . & . \\ . & . & . & . \\ . & . & . & . \end{array} \\ \begin{array}{c} F_{5,1} \\ F_{6,1} \\ . \\ . \\ . \end{array} & \begin{array}{c} = K_{s2,1} \\ \\ \\ \\ \end{array} & \begin{array}{cccc} . & F_{1,n} \\ . & F_{2,n} \\ . & . \\ . & . \\ . & . \end{array} \\ F_{n,1} & . & . & . & . & . & . & . & F_{n,n} \end{array} \right]$$

(b)

Figure 5.5 (a) Four soil elements on the faces of a pile segment treated as one soil segment and (b) full soil stiffness matrix $[F]$ condensed into a soil segment stiffness matrix $[K_s]$.

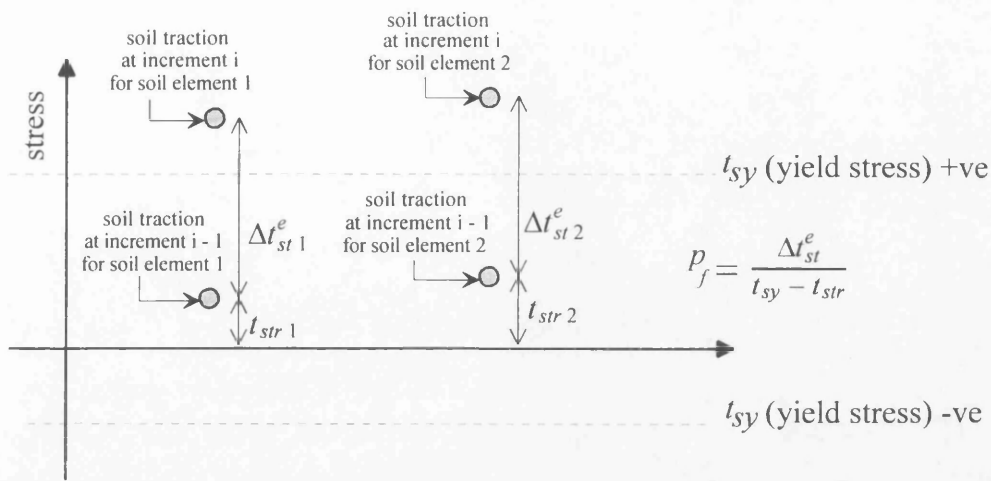


Figure 5.6 Determination of yield factors (p_f) for soil elements.

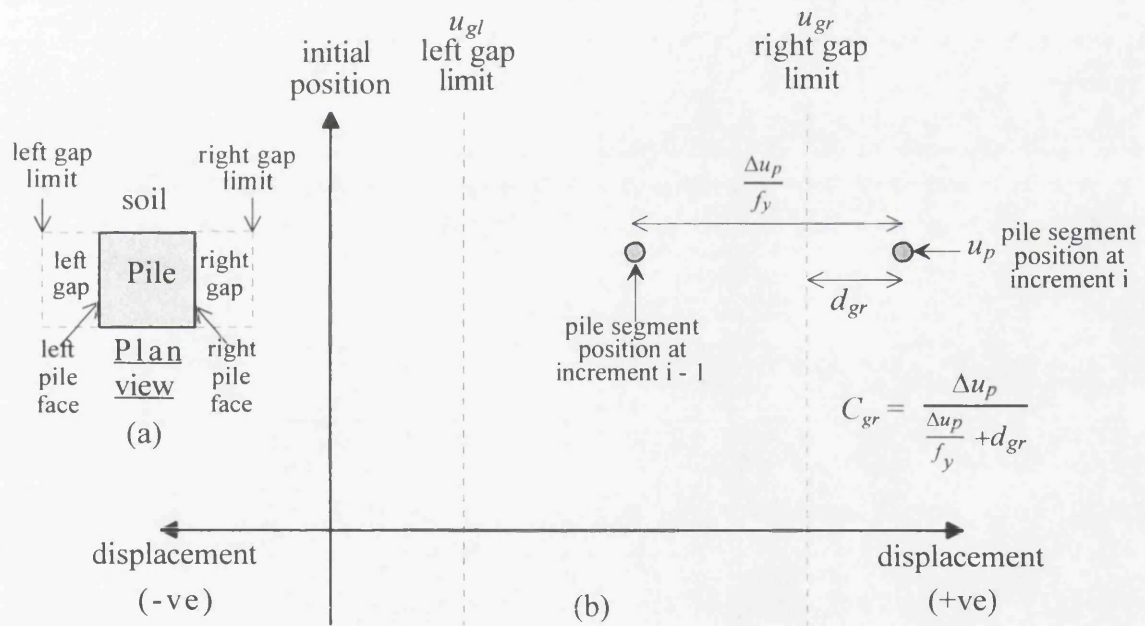


Figure 5.7 (a) Gap terminology and (b) determination of gap closing factor for soil element.

CHAPTER 6

Numerical Implementation of Cyclic Loading Algorithm

6.1 Summary

6.2 Introduction

6.3 Computational procedure for cyclic analysis

6.3.1 Pile-soil system interaction

6.3.2 Pile-head stiffness matrix and compliance matrix

6.3.3 Pile traction and displacement due to unit boundary conditions

6.3.4 Elastic unloading

6.3.5 Yield factor

6.3.6 Pile traction and displacement

6.3.7 Gap formation

6.3.8 Pile-head reactions

6.3.9 Shear strength degradation

6.3.10 Bearing strength degradation

6.3.11 Modified soil segment stiffness matrix

6.3.12 At specified loads and displacements

6.3.13 Unloading and reloading

6.4 Description of the program

6.5 Typical illustrative results

6.5.1 Load-controlled conditions

6.5.2 Displacement-controlled conditions

6.5.3 Gap formation

6.5.4 Backsliding

6.5.5 Shear strength degradation

6.5.6 Bearing strength degradation

6.6 Investigation of cyclic degradation

6.6.1 Beam-On-Spring model

6.6.1.1 Beam-On-Spring model results

6.6.2 Beam-On-Interactive-Spring model

6.6.2.1 Beam-On-Interactive-Spring model results

6.7 Discussion of results

6.8 Concluding remarks

CHAPTER 6

Numerical Implementation of Cyclic Loading Algorithm

6.1 Summary

This Chapter describes the implementation of cyclic loading algorithm, the APILEC program. The program allows for load-controlled and displacement-controlled conditions as well as one-way and two-way cycling. Other features of the program are also described, including gap formation, backsliding and strength degradation. An investigation of the causes of cyclic degradation observed in this analysis is undertaken by means of the simple Beam-On-Spring and Beam-On-Interactive-Spring models.

6.2 Introduction

The implementation of the formulations presented in Chapter 5 is described in this Chapter. To account for different loading conditions, the computer program (APILEC) is designed to be capable of analysing one-way and two-way cyclic loadings. Two methods of cycling are also considered here, namely the load-controlled and displacement-controlled methods. For the load-controlled method, the unloading or reloading stage begins once the specified maximum load or minimum load is attained. For the displacement-controlled method, unloading or reloading begins once the specified maximum or minimum displacement is reached. Phenomena observed during cyclic pile-load tests, for example, gap formation, backsliding and strength degradation, are included in the analysis. The effects of these phenomena on pile response will be examined.

6.3 Computational procedure for cyclic analysis

Sign conventions

The sign conventions adopted for loads, pile and soil tractions, shear forces, bending moments and displacements are shown in Figure 6.1.

Procedure

For a pile subjected to cyclic lateral loads or moments, the computational procedure is described in terms of the following Steps.

Step (1)

Discretise the pile into n equal segments (say height D) as depicted in Figure 6.2a.

Step (2)

Set up the fully populated soil matrix of coefficients $[G_{se}]$ via integration of the Mindlin's solution (Mindlin, 1936). The elements on the four faces of the pile (see Figure 6.2b) are taken into consideration. This will yield a $4n \times 4n$ $[G_{se}]$ matrix.

Step (3)

Set up the fully populated pile matrix of coefficients $[G_p]$ via integration of the Bernouli-Euler (beam theory) kernel, with the beam assumed as a circular section. This will yield a $n \times n$ $[G_p]$ matrix.

Step (4)

Determine the undrained shear strength (C_u) and soil Young's modulus (E_s) values at the mid-points of each soil element (nodal points), and thereby calculate the limiting stresses:

limit bearing stress

$$t_{sc} = N_c C_u \quad (6.1) \quad (5.5 \text{ bis})$$

limit shear stress

$$t_{ss} = \alpha C_u \quad (6.2) \quad (5.6 \text{ bis})$$

limit tensile stress

$$t_{st} = K_t \gamma z \quad (6.3) \quad (5.7 \text{ bis})$$

limit adhesive stress (for backsliding)

$$t_{stb} = \beta C_u + t_{st} \quad (6.4) \quad (5.11 \text{ bis})$$

residual limit shear stress (for shear strength degradation)

$$t_{ssr} = R_s t_{ss} \quad (6.5) \quad (5.13 \text{ bis})$$

residual limit bearing stress (for bearing strength degradation)

$$t_{scr} = R_b t_{sc} \quad (6.6) \quad (5.16 \text{ bis})$$

where N_c is the bearing capacity factor,
 α is an empirical adhesion factor,
 K_r is the lateral earth pressure coefficient,
 γ is the effective unit weight of the soil,
 z is the depth,
 β is the backsliding factor; $0 < \beta < 1$,
 R_b is the residual/peak bearing strength ratio, and
 R_s is the residual/peak shear strength ratio.

From the limiting stresses, the yield stresses for the soil elements are defined:

yield stress for bearing

$$t_{syc} = t_{sc} \quad (6.7) \quad (5.8 \text{ bis})$$

yield stress for shear

$$t_{sys} = t_{ss} \quad (6.8) \quad (5.9 \text{ bis})$$

yield stress for tension

$$t_{syl} = t_{st} \quad (6.9) \quad (5.10 \text{ bis})$$

If backsliding is considered, the yield stress for tension is:

$$t_{syl} = t_{stb} \quad (6.10) \quad (5.12 \text{ bis})$$

6.3.1 Pile-soil system interaction

Step (5)

The full soil matrix $[G_{se}]$ is inverted, i.e.

$$[F] = [G_{se}]^{-1} \quad (6.11) \quad (5.23 \text{ bis})$$

The matrix $[F]$ is then condensed to form the $n \times n$ $[K_s]$ matrix, known as the 'soil segment' stiffness matrix; see Figure 6.3. Each coefficient of the $[K_s]$ matrix is computed as:

$$K_{s\,ij} = \sum_{I=4i-3}^{4i} \sum_{J=4j-3}^{4j} F_{IJ} \quad (6.12) \quad (5.24 \text{ bis})$$

where $K_{s\,ij}$ is the coefficient at the i -th row and the j -th column of $[K_s]$ matrix,
 F_{IJ} is the coefficient at the I -th row and the J -th column of $[F]$ matrix, and
 i and $j = 1, 2, 3$ to n .

The $[K_s]$ matrix is then inverted to give the soil segment compliance matrix $[G_s]$, i.e.

$$[G_s] = [K_s]^{-1} \quad (6.13) \quad (5.25 \text{ bis})$$

Step (6)

Based on the compatibility and equilibrium conditions at the pile-soil interfaces, the pile segment tractions are determined in each increment by applying unit boundary conditions on the pile-head, i.e.

$$\{\Delta t_p\} = -[G_p + G_s]^{-1} \{B_p\} \quad (6.14) \quad (5.30 \text{ bis})$$

where symbol Δ denotes tractions (or displacements) obtained by applying unit boundary conditions in each increment,

$\{\Delta t_p\}$ are the pile segment tractions, and

$\{B_p\}$ pile segment displacements due to unit boundary conditions, taken as:

$$\{B_p\} = \{B_p^u\} + \{B_p^0\} \quad (6.15) \quad (5.20 \text{ bis})$$

where $\{B_p^u\}$ are the pile segment displacements, due to unit lateral translation of the pile, giving $[1, 1, 1 \dots]^T$, and, T denotes transpose, and

$\{B_p^0\}$ are the pile segment displacements, due to unit rotation of the pile about its head, giving $[-0.5h, -1.5h, -2.5h \dots]^T$, and, h is the height of pile segment.

Step (7)

For plastic soil segments (i.e. all the four soil elements surrounding the pile segment which have reached their yield stresses), the corresponding stiffness coefficients (rows and columns) of the $[K_s]$ matrix are taken as zero. This results in no interaction being allowed for the elastic

and plastic soil segments. The tractions of the plastic soil segments and the corresponding pile segments are therefore:

$$\{\Delta t_p^n\} = -\{\Delta t_s^n\} = 0 \quad (6.16) \quad (5.31 \text{ bis})$$

where $\{\Delta t_p^n\}$ are the pile segment tractions corresponding to the plastic soil segments, and $\{\Delta t_s^n\}$ are the plastic soil segment tractions.

Enforcing compatibility and equilibrium conditions at the pile-soil interface for the elastic soil segments and equilibrium conditions for the plastic soil segments (Equation (6.16)), the pile segment tractions correspond to the elastic soil segments (by matrix partitioning) are determined as:

$$\{\Delta t_p^e\} = -[G_{s*}^{ee} + G_p^{ee}]^{-1} \{B_p^e\} \quad (6.17) \quad (5.45 \text{ bis})$$

where $\{\Delta t_p^e\}$ are the pile segment tractions corresponding to the elastic soil segments, $[G_{s*}^{ee}]$ are soil coefficients obtained from the inversion of the modified (due to soil yielding) soil segment stiffness matrix $[K_s]$ corresponding to the elastic soil segments, $[G_p^{ee}]$ are pile coefficients obtained from the $[G_p]$ matrix corresponding to the elastic soil segments, and $\{B_p^e\}$ are the pile segment displacements due to unit boundary conditions corresponding to elastic soil segments.

6.3.2 Pile-head stiffness matrix and compliance matrix

Step (8)

Apply unit lateral translation and unit rotation at the pile-head, and determine the pile segment tractions:

due to unit lateral translation

$$\{\Delta t_p^{eu}\} = -[K]\{B_p^{eu}\} \quad (6.18) \quad (5.47 \text{ bis})$$

due to unit rotation

$$\{\Delta t_p^{e\theta}\} = -[K]\{B_p^{e\theta}\} \quad (6.19) \quad (5.48 \text{ bis})$$

where $[K] = [G_{s*}^{ee} + G_p^{ec}]$,

$\{\Delta t_p^{eu}\}$ are the pile segment tractions due to unit lateral translation of the pile, corresponding to the elastic soil segments,

$\{B_p^{eu}\}$ are the pile segment displacements due to unit lateral translation of the pile, corresponding to the elastic soil segments,

$\{\Delta t_p^{e\theta}\}$ are the pile segment traction increments due to unit rotation of the pile about its head, corresponding to the elastic soil segments, and

$\{B_p^{e\theta}\}$ are the pile segment displacements due to unit rotation of the pile about its head, corresponding to the elastic soil segments.

Step (9)

Determine the lateral load at the pile-head due to unit lateral translation of the pile:

$$H_u = \sum_{i=1}^n \Delta t_{pi}^{eu} A_p \quad (6.20) \quad (5.49 \text{ bis})$$

and due to unit rotation of the pile about its head:

$$H_\theta = \sum_{i=1}^n \Delta t_{pi}^{e\theta} A_p \quad (6.21) \quad (5.50 \text{ bis})$$

where Δt_{pi}^{eu} is the pile segment traction for the i -th segment, due to unit lateral translation of the pile, corresponding to the elastic soil segment,

A_p is the pile segment cross sectional area, and

$\Delta t_{pi}^{e\theta}$ is the pile segment traction for the i -th segment, due to unit rotation at the pile about its head, corresponding to the elastic soil segment.

Determine the moment at the pile-head due to unit lateral translation of the pile:

$$M_u = - \sum_{i=1}^n \Delta t_{pi}^{eu} A_p z_i \quad (6.22) \quad (5.51 \text{ bis})$$

and due to unit rotation of the pile about its head:

$$M_\theta = - \sum_{i=1}^n \Delta t_{pi}^{e\theta} A_p z_i \quad (6.23) \quad (5.52 \text{ bis})$$

where z_i is the depth at the i -th segment.

The above process yields the 2×2 pile-head stiffness matrix $[SM]$:

$$\begin{Bmatrix} H \\ M \end{Bmatrix} = \begin{bmatrix} H_u & H_\theta \\ M_u & M_\theta \end{bmatrix} \begin{Bmatrix} u \\ \theta \end{Bmatrix} \quad (6.24) \quad (5.53 \text{ bis})$$

and by inversion, the compliance matrix $[CM]$ is obtained:

$$\begin{Bmatrix} u \\ \theta \end{Bmatrix} = \begin{bmatrix} F_{uH} & F_{uM} \\ F_{\theta H} & F_{\theta M} \end{bmatrix} \begin{Bmatrix} H \\ M \end{Bmatrix} \quad (6.25) \quad (5.54 \text{ bis})$$

where H is the pile-head lateral load,

M is the pile-head moment,

H_u , H_θ , M_u and M_θ are coefficients of the pile-head stiffness matrix $[SM]$ determined from Equations (6.20) to (6.23),

u is the lateral translation applied at the pile-head; $u = 1$,

θ is the rotation applied at the pile-head, $\theta = 1$, and

F_{uH} , F_{uM} , $F_{\theta H}$ and $F_{\theta M}$ are coefficients of the pile-head compliance matrix $[CM]$.

6.3.3 Pile traction and displacement due to unit boundary conditions

Step (10)

Compute the pile segment tractions and displacements depending on the pile-head fixity. For a fixed-head case, the pile segment tractions corresponding to the elastic soil segments are:

$$\{\Delta t_p^e\} = \{\Delta t_p^{eu}\} \quad (6.26) \quad (5.55 \text{ bis})$$

The pile segment displacements corresponding to the elastic soil segments are:

$$\{\Delta u_p^e\} = [G_p^{ee}] \{\Delta t_p^e\} + \{B_p^{eu}\} \quad (6.27) \quad (5.56 \text{ bis})$$

and corresponding to the plastic soil segment are:

$$\{\Delta u_p^n\} = [G_p^{ne}] \{\Delta t_p^e\} + \{B_p^{nu}\} \quad (6.28) \quad (5.57 \text{ bis})$$

where $\{B_p^{nu}\}$ are the pile segment displacements due to unit lateral translation of the pile, corresponding to the plastic soil segments.

For a general free-head with eccentricity case, the pile segment tractions corresponding to the elastic soil segments are:

$$\{\Delta t_p^e\} = F_{uH}\{\Delta t_p^{eu}\} + F_{\theta H}\{\Delta t_p^{e\theta}\} + \left(F_{uM}\{\Delta t_p^{eu}\} + F_{\theta M}\{\Delta t_p^{e\theta}\}\right) e \quad (6.29) \quad (5.58 \text{ bis})$$

The pile segment displacements corresponding to the elastic soil segments are:

$$\begin{aligned} \{\Delta u_p^e\} = & \left[G_p^{ee} \right] \{\Delta t_p^e\} + F_{uH}\{B_p^{eu}\} + F_{\theta H}\{B_p^{e\theta}\} \\ & + \left(F_{uM}\{B_p^{eu}\} + F_{\theta M}\{B_p^{e\theta}\} \right) e \end{aligned} \quad (6.30) \quad (5.59 \text{ bis})$$

and corresponding to the plastic soil segments are:

$$\begin{aligned} \{\Delta u_p^n\} = & \left[G_p^{ne} \right] \{\Delta t_p^e\} + F_{uH}\{B_p^{nu}\} + F_{\theta H}\{B_p^{n\theta}\} \\ & + \left(F_{uM}\{B_p^{nu}\} + F_{\theta M}\{B_p^{n\theta}\} \right) e \end{aligned} \quad (6.31) \quad (5.60 \text{ bis})$$

where e is the distance of the load point to the ground surface or mudline, and $\{B_p^{n\theta}\}$ are the pile segment displacements due to unit rotation of the pile about its head, corresponding to the plastic soil segments.

Step (11)

Determine the soil element tractions by distributing the pile segment tractions according to the elastic soil elements within the soil segment:

$$\{\Delta t_{st}^e\} = - \frac{\{\Delta t_p^e\}}{n_e} \quad (6.32) \quad (5.61 \text{ bis})$$

where $\{\Delta t_{st}^e\}$ are the elastic soil element tractions, and n_e is the number of elastic soil elements within the segment.

6.3.4 Elastic unloading

Step (12)

Provide for elastic unloading of the plastic soil elements when:

$$\{\Delta t_p^e\} \{t_{str}\} < 0 \quad (6.33) \quad (5.68 \text{ bis})$$

where $\{t_{str}\}$ are the current soil element tractions (end of previous increment).

If the whole soil segment yielded, elastic unloading of a plastic soil segment is provided when:

$$t_{pr i} [\Delta t_{p i+1}^e + \Delta t_{p i-1}^e] < 0 \quad (6.34) \quad (5.69 \text{ bis})$$

where $t_{pr i}$ is the current pile segment traction (end of previous increment) for the i -th segment,

$\Delta t_{p i+1}^e$ is the pile segment traction for the $i+1$ segment; if $i = n$, then $\Delta t_{p i+1}^e = 0$, and

$\Delta t_{p i-1}^e$ is the pile segment traction for the $i-1$ segment; if $i = 1$, then $\Delta t_{p i-1}^e = 0$.

Elastic unloading does not apply to plastic soil elements where gaps are present at the pile-soil interfaces. If elastic unloading is allowed for, the soil elements will be set to elastic and Step (23) will be executed to modify the soil segment stiffness matrix $[K_s]$. If no elastic unloading occurs, this step is ignored.

6.3.5 Yield factorStep (13)

Determine the yield factors for the elastic soil elements:

$$\{p_f\} = \frac{\{\Delta t_{st}^e\}}{\{t_{sy}\} - \{t_{str}\}} \quad (6.35) \quad (5.62 \text{ bis})$$

where $\{p_f\}$ are the yield factors for the elastic soil elements, and

$\{t_{sy}\}$ are the yield stresses for the soil elements.

From all the yield factors (p_f) determined, the largest yield factor (f_y) is chosen and the element from which f_y is selected is regarded as plastic. This is because when f_y is employed

to determine the soil element traction increment (described in the next Section) in the current increment, the current soil element traction will reach the yield stress.

6.3.6 Pile traction and displacement

Step (14)

Determine the soil element traction increments:

$$\{\delta t_{st}\} = \frac{\{\Delta t_{st}^e\}}{f_y} \quad (6.36) \quad (5.63 \text{ bis})$$

and subsequently the current soil element tractions:

$$\{t_{st}\} = \{t_{str}\} + \{\delta t_{st}\} \quad (6.37) \quad (5.64 \text{ bis})$$

Determine the pile segment displacement increments:

$$\{\delta u_p\} = \frac{\{\Delta u_p\}}{f_y} \quad (6.38) \quad (5.65 \text{ bis})$$

and subsequently, the current pile segment displacements:

$$\{u_p\} = \{u_{pr}\} + \{\delta u_p\} \quad (6.39) \quad (5.66 \text{ bis})$$

where $\{\Delta u_p\}$ are pile segment displacements corresponding to both elastic and plastic soil segments, and

$\{u_{pr}\}$ are the current pile displacements (end of previous increment).

Step (15)

Compute the current pile segment traction:

$$t_{pi} = - \sum_{j=1}^4 t_{stij} \quad (6.40) \quad (5.67 \text{ bis})$$

where t_{pi} is the current pile segment traction for the i -th segment,

$t_{s\ ij}$ is the current soil element traction for the j -th element of the i -th segment, and
 $i = 1, 2, 3$ to n .

From the current pile segment tractions, the shear forces and bending moments at nodal points and at the top of the pile segments, respectively, for the entire pile length are calculated:

current shear forces

$$H_{s\ n-i} = \sum_{j=n-i}^n t_{pj} A_p \quad (6.41)$$

current bending moments

$$M_{p\ n-i} = - \sum_{j=n-i}^n t_{pj} A_p h [j - (n-i) + 0.5] \quad (6.42)$$

where $H_{s\ n-i}$ is the shear force for the $n-i$ pile segment,
 $M_{p\ n-i}$ is the bending moment for the $n-i$ pile segment,
 t_{pj} is the current pile segment traction for the j -th segment,
 h is the height of the pile segment, and
 $i = 0, 1, 2$ to $n-1$.

6.3.7 Gap formation

Gap size

Step (16)

Compute the right and left gap distances (see Figure 6.4) at the pile-soil interfaces for those soil elements that have yielded in tension. For the right pile face, the current right gap distances are:

$$\{d_{gr}\} = \{u_{gr}\} - \{u_p\} \quad (6.43) \quad (5.70 \text{ bis})$$

and for the left pile face, the current left gap distances are:

$$\{d_{gl}\} = \{u_p\} - \{u_{gl}\} \quad (6.44) \quad (5.71 \text{ bis})$$

where $\{u_{gr}\}$ and $\{u_{gl}\}$ are the pile displacements when soil elements yield in tension at the right and left faces of the pile, respectively.

Gap closure

Step (17)

After determining the gap distance, some gaps may have overclosed by the pile (see Figure 6.5), i.e. when d_{gr} or d_{gl} is less than zero. If no overclosing of gaps is experienced, this step is ignored. The gap closing factors for the right pile face are:

$$\{C_{gr}\} = \frac{\{\Delta u_p\}}{\frac{\{\Delta u_p\}}{f_y} + \{d_{gr}\}} \quad (6.45) \quad (5.73 \text{ bis})$$

and for the left pile face are:

$$\{C_{gl}\} = \frac{\{\Delta u_p\}}{\frac{\{\Delta u_p\}}{f_y} - \{d_{gl}\}} \quad (6.46) \quad (5.74 \text{ bis})$$

From all the gap closing factors determined, the largest factor (f_g) is used so that it ensures that the pile closes only one gap in the current increment and the rest of the gaps are not overclosed.

The element once determined as plastic (where f_y is chosen in the current increment) is now set back to elastic as f_g is always greater than f_y . Due to gap closure, the plastic soil element, is brought back to elastic. Steps (14) to (16) are re-evaluated with $f_y = f_g$ in the current increment. The progressive stages of soil elements yielding and gap closure are illustrated in Figure 6.6.

6.3.8 Pile-head reactions

Step (18)

Depending on pile-head fixity, the incremental pile-head lateral load (δH) for a fixed-head pile is determined as:

$$\delta H = \frac{H_u}{f_y} \quad (6.47) \quad (5.76 \text{ bis})$$

the incremental pile-head moment as:

$$\delta M = \frac{M_u}{f_y} \quad (6.48) \quad (5.77 \text{ bis})$$

and the incremental pile-head lateral displacement as:

$$\delta u = \frac{1}{f_y} \quad (6.9) \quad (5.78 \text{ bis})$$

where H_u and M_u are stiffness coefficients in the $[SM]$ matrix from Equation (6.24).

For a general free-head case with eccentricity, the incremental pile-head lateral load is:

$$\delta H = \frac{1}{f_y} \quad (6.50) \quad (5.79 \text{ bis})$$

the incremental pile-head moment is:

$$\delta M = -\frac{e}{f_y} \quad (6.51) \quad (5.80 \text{ bis})$$

the incremental pile-head lateral displacement is:

$$\delta u = \left[\frac{F_{uH}}{f_y} + \frac{F_{uM} e}{f_y} \right] \quad (6.52) \quad (5.81 \text{ bis})$$

the incremental pile-head rotation is:

$$\delta \theta = \left[\frac{F_{\theta H}}{f_y} + \frac{F_{\theta M} e}{f_y} \right] \quad (6.53) \quad (5.82 \text{ bis})$$

where F_{uH} , F_{uM} , $F_{\theta H}$ and $F_{\theta M}$ are coefficients in the $[CM]$ matrix from Equation (6.25).

The current pile-head lateral load is subsequently calculated:

$$H = H_r + \delta H \quad (6.54) \quad (5.83 \text{ bis})$$

the current pile-head moment:

$$M = M_r + \delta M \quad (6.55) \quad (5.84 \text{ bis})$$

the current pile-head lateral displacement:

$$u = u_r + \delta u \quad (6.56) \quad (5.85 \text{ bis})$$

and the current pile-head rotation:

$$\theta = \theta_r + \delta \theta \quad (6.57) \quad (5.86 \text{ bis})$$

where H_r , M_r , u_r and θ_r are current pile-head lateral load, moment, lateral displacement and rotation (end of previous increment), respectively.

As a check, the current pile-head lateral load and moment, must be equal to the current shear force and bending moment for the top pile segment, determined from Equations (6.41) and (6.42).

6.3.9 Shear strength degradation

Plastic shear displacement

Step (19)

Compute the incremental plastic shear displacements (δd_p) from the current pile segment displacements (see Figure 6.7a) when:

- side soil elements under two consecutive increments are plastic,
- side soil elements have changed from plastic to elastic (due to elastic unloading and not for the beginning of unloading or reloading).

Satisfied with the above requirements, the incremental plastic shear displacements are determined as:

$$\{\delta d_s\} = |\{u_p\} - \{u_{pr}\}| \quad (6.58) \quad (5.87 \text{ bis})$$

where $| \cdot |$ denotes absolute value,

$\{u_p\}$ are the current pile segment displacements, and

$\{u_{pr}\}$ are the current pile segment displacements (end of previous increment).

Subsequently, the current plastic shear displacements are determined:

$$\{d_s\} = \{d_{sr}\} + \{\delta d_s\} \quad (6.59) \quad (5.88 \text{ bis})$$

where $\{d_{sr}\}$ are the current plastic shear displacements (end of previous increment).

The flow chart for the determination of d_s is illustrated in Figure 6.8.

Reduced limit shear stress

Step (20)

Determine the reduced limit shear stress (t_{ssd}) for each soil element that has recovered from plastic to elastic (Figure 6.7a):

$$t_{ssd} = t_{ssr} + (t_{ss} - t_{ssr}) \exp(-C_s ds) \quad (6.60) \quad (5.14 \text{ bis})$$

where C_s is the shear degradation rate factor in mm^{-1} .

The yield stress for shear can now be taken as:

$$t_{sys} = t_{ssd} \quad (6.61) \quad (5.15 \text{ bis})$$

However, due to the constraint that the current shear stress (t_{s2}) may be higher than t_{ssd} (see Figure 6.7b), t_{sys} is determined as such:

- ♦ if $t_{ssd} > t_{s2}$ then $t_{sys} = t_{ssd}$,
- ♦ if $t_{ssd} < t_{s2}$ then $t_{sys} = 1.01t_{s2}$ provided that $t_{sys} < t_{ys*}$, else $t_{sys} = t_{ys*}$.

where t_{ys*} is the yield stress for shear (end of previous increment).

The flow chart for the determination of t_{sys} is illustrated in Figure 6.9. A constant value of 1.01 is applied to the current shear stress, in order to bring the yield stress close to the current shear stress (Figure 6.7b). This is because the particular side element might yield due to changes in the direction of traction increment, before reaching to its reduced limit shear stress (t_{ssd}). The yield stress for shear applies to shearing in both positive and negative directions.

6.3.10 Bearing strength degradation

Plastic bearing displacement

Step (21)

Compute the incremental plastic bearing displacements (δd_b) from the current pile segment displacements (see Figure 6.10a) when:

- ♦ bearing soil elements under two consecutive increments are plastic
- ♦ bearing soil elements have changed from plastic to elastic (due to elastic unloading and not the beginning of unloading or reloading)

Satisfied with the above requirements, the incremental plastic bearing displacements are determined as:

$$\{\delta d_b\} = |\{u_p\} - \{u_{pr}\}| \quad (6.62) \quad (5.90 \text{ bis})$$

The current plastic bearing displacement are subsequently determined:

$$\{d_b\} = \{d_{br}\} + \{\delta d_b\} \quad (6.63) \quad (5.91 \text{ bis})$$

where $\{d_{br}\}$ are the current plastic bearing displacements (end of previous increments).

The flow chart for the determination of d_b is shown in Figure 6.11.

Reduced limit bearing stress

Step (22)

The reduced limit bearing stress (t_{scd}) is calculated for each soil element that has recovered from plastic to elastic (see Figure 6.10a):

$$t_{scd} = t_{scr} + (t_{sc} - t_{scr}) \exp^{(-C_b db/D)} \quad (6.64) \quad (5.17 \text{ bis})$$

where C_b is the bearing degradation rate factor, and

D is the pile diameter or width.

The yield stress for bearing can be taken as:

$$t_{syc} = t_{scd} \quad (6.65) \quad (5.18 \text{ bis})$$

Since the current bearing stress (t_{sl}) might be greater than t_{scd} (see Figure 6.10b), the yield stress for bearing (t_{syc}) is determined as such:

- if $t_{scd} > t_{sl}$ then $t_{syc} = t_{scd}$,
- if $t_{scd} < t_{sl}$ then $t_{syc} = 1.01t_{sl}$ provided that $t_{syc} < t_{yc*}$, else $t_{syc} = t_{yc*}$.

where t_{yc*} is the yield stress for bearing (end of previous increment).

The constant $1.01t_{sl}$ is used to bring the yield stress for bearing close to the current bearing stress, in case the particular soil element might yield due to changes in the direction of traction increment, before reaching to its reduced limit bearing stress (t_{scd}). The flow chart for the determination of t_{scd} is illustrated in Figure 6.12.

As the magnitude of plastic bearing displacements of the soil elements are different for the right face and left face of the corresponding pile segments, the reduced limit bearing stress determined will be different (Figure 6.10c). Care has to be taken on the sign conventions adopted.

6.3.11 Modified soil segment stiffness matrix

Step (23)

Modify the soil segment stiffness matrix for soil yielding or elastic unloading or gap closure. An influence factor (f) is used to modify the 'original' soil segment stiffness matrix $[K_s^o]$ (coefficients obtained from Equation (6.12) at the beginning of the analysis) depending on the number of yielded soil elements. For soil element(s) yielded in the k -th segment, the stiffness coefficients for the k -th row is modified as:

$$K_{s\ ki} = f(n_p) K_{s\ ki}^o \quad (6.66) \quad (5.93 \text{ bis})$$

and the stiffness coefficient for the k -th column is modified as:

$$K_{s\ jk} = f(n_p) K_{s\ jk}^o \quad (6.67) \quad (5.94 \text{ bis})$$

where $K_{s\ ki}$ is the stiffness coefficient at the k -th row and the i -th column of $[K_s]$ matrix,

n_p is the number of yielded soil elements within the segment; $f(1) = 0.75, f(2) = 0.5,$

$f(3) = 0.25, f(4) = 0,$

$K_{s\ ki}^o$ is the stiffness coefficient at the k -th row and the i -th column of $[K_s^o]$ matrix,

$i = 1, 2, 3 \text{ to } n,$

$K_{s\ jk}$ is the stiffness coefficient at the j -th row and the k -th column of $[K_s]$ matrix,

$K_{s\ jk}^o$ is the stiffness coefficient at the j -th row and the k -th column of $[K_s^o]$ matrix, and

$j = 1, 2, 3 \text{ to } n.$

The above process is repeated for each yielded soil segment. The lower value of the stiffness coefficients determined from Equations (6.66) and (6.67) is taken to form the $[K_s]$ matrix. The use of the influence factor, $f(1), f(2), f(3)$ and $f(4)$ implies that the stiffness of the soil segment is reduced by 25, 50, 75 and 100%, respectively. No direct interaction is allowed for plastic and elastic soil segments as the stiffness coefficients (rows and columns) for the plastic soil segments are taken as zero. The stiffness coefficients are then partitioned accordingly to correspond with the elastic and plastic soil segments. The stiffness coefficients corresponding to the elastic soil segments are inverted and substituted into Equation (6.17) for the next increment.

6.3.12 At specified loads and displacements

Step (24)

The procedure for Steps (7) to (23) is repeated for each increment, until the current pile-head lateral load has exceeded the specified load (maximum or minimum) after Step (18). At this stage, an interpolation factor (I_F) is required to bring the former load exactly to the latter load.

The interpolation factor is determined as:

$$I_F = \frac{H_F - H_r}{H - H_r} \quad (6.68)$$

where H_F is the specified pile-head lateral load.

For displacement-controlled conditions, the interpolation factor is determined when the current pile-head lateral displacement has exceeded the specified displacement (maximum or minimum), and is calculated as:

$$I_F = \frac{u_F - u_r}{u - u_r} \quad (6.69)$$

where u_F is the specified pile-head lateral displacement.

The current soil element tractions at the specified load or displacement is then computed as:

$$\{t_{st*}\} = [\{t_{st}\} - \{t_{str}\}] I_F + \{t_{str}\} \quad (6.70)$$

and the current pile segment displacements at the specified load or displacement as:

$$\{u_{p*}\} = [\{u_p\} - \{u_{pr}\}] I_F + \{u_{pr}\} \quad (6.71)$$

The current pile-head lateral load at the specified load or displacement is subsequently determined as:

$$H_* = (H - H_r) I_F + H_r \quad (6.72)$$

the current pile-head moment at the specified load or displacement as:

$$M_* = (M - M_r) I_F + M_r \quad (6.73)$$

the current pile-head lateral displacement at the specified load or displacement as:

$$u_* = (u - u_r) I_F + u_r \quad (6.74)$$

and the current pile-head rotation at the specified load or displacement as:

$$\theta_* = (\theta - \theta_r) I_F + \theta_r \quad (6.75)$$

After solving Equations (6.70) to (6.75), the following were carried out for the current values:

current soil element tractions

$$\{t_{st}\} = \{t_{st*}\} \quad (6.76)$$

current pile segment displacements

$$\{u_p\} = \{u_{p*}\} \quad (6.77)$$

current pile-head lateral load

$$H = H_* \quad (6.78)$$

current pile-head moment

$$M = M_* \quad (6.79)$$

current pile-head lateral displacement

$$u = u_* \quad (6.80)$$

current pile-head rotation

$$\theta = \theta_* \quad (6.81)$$

Steps (15) and (16) are re-evaluated and Steps (19) to (23) are then carried out. It follows that when the specified load (maximum or minimum) was attained, the particular soil element (where f_y was determined) was set back to elastic. This is because the element could not have yielded, as the predicted load in that increment is always greater (or lesser in the case of specified minimum load) than the specified maximum load. If gap closure is encountered, the

soil element (where f_g was determined) was set back to plastic, because the pile could not have closed the gap in that increment at the specified load. Step (25) is subsequently executed.

For displacement-controlled conditions, when the specified displacement (maximum or minimum) was attained, the particular soil element where f_y was determined was set back to elastic. This is because the element could not have yielded, as the predicted displacement in that increment is always greater (or lesser in the case of specified minimum displacement) than the specified maximum displacement. Also, if gap closure is encountered, the soil element (where f_g was determined) was set back to plastic, because the pile could not have closed the gap in that increment at the specified displacement. Step (25) is subsequently executed.

6.3.13 Unloading and reloading

Step (25)

At the beginning of unloading, all soil elements are set back to elastic due to changes in loading direction, except for soil elements that have yielded in tension as illustrated in Figure 6.13. The pile segment tractions (Δt_p) and displacements (Δu_p) due to unit boundary conditions are now set to reverse direction in contrast to the loading/reloading stage. This will lead to reduction in the pile segment tractions and displacements, soil element tractions, pile-head loads, etc., in each increment. Steps (7) to (24) were then carried out till the specified minimum load (load-controlled) or displacement (displacement-controlled) was reached.

At the beginning of reloading, all soil elements are set back to elastic except soil elements that have yielded in tension. The pile segment tractions (Δt_p) and displacements (Δu_p) due to unit boundary conditions are now reversed in direction in contrast to the unloading stage. This will lead to the increase in the pile segment tractions and displacements, soil element tractions, pile-head loads, etc., in each increment. Steps (7) to (24) were then carried out till the specified maximum load (load-controlled) or displacement (displacement-controlled) was attained.

The above was repeated for unloading and reloading stages, until the required number of cycles was reached.

6.4 Description of the program

The computer program is written in FORTRAN 77 language, containing approximately 3000 lines. Rather than giving explicit details of the program, only the main subroutines involved (see Figure 6.14) and the tasks performed will be described here.

Subroutine **DRIVE**

- Calls for Subroutines **DATGEN**, **GMAT**, **SVEC** and **START** at the start of the analysis.
- Calls for Subroutines **PLAST** and **SOLV** for incremental analyses.
- Contains the cyclic counter to generate to the specific number of cycles, and defines whether the analysis is carried out based on the reloading or unloading process.

Subroutine **DATGEN**

- Reads all the input data and assigns files for the output of results (e.g. pile displacements, bending moments, etc.). The required input data are described in Table 6.1.
- Discretise the pile into n segments; Step (1) in Section 6.3.

Subroutine **GMAT**

- Sets up the soil matrix of coefficients $[G_{se}]$ by integration of the Mindlin's solution (Mindlin, 1936) for the four faces of the pile; Step (2) in Section 6.3.

Subroutine **DMAT**

- Sets up the pile matrix of coefficient $[G_p]$ by integration of the Bernoulli-Euler (beam theory) kernel; Step (3) in Section 6.3.

Subroutine **SVEC**

- Determines the limit stresses for the soil elements, e.g. the limit bearing, shear, tensile stresses, etc. Assigns these limit stresses as yield stresses for bearing, shear, tension, etc.; Step (4) in Section 6.3.

Subroutine **START**

- Sets the specific variables to zero.

Subroutine **SOLV**

- ♦ Sets up the pile-soil system stiffness matrix; Steps (5) to (7) in Section 6.3.1.
- ♦ Solves for pile segment traction for unit lateral translation of the pile and unit rotation of the pile about its head; Step (8) in Section 6.3.2.
- ♦ Determines the pile-head stiffness matrix $[SM]$ and the compliance matrix $[CM]$; Step (9) in Section 6.3.2.
- ♦ Computes the pile segment tractions and displacements for unit boundary conditions for free-head and fixed-head cases; Step (10) in Section 6.3.3.
- ♦ Computes soil element tractions for unit boundary conditions; Step (11) in Section 6.3.3.
- ♦ Checks for elastic unloading of plastic soil elements and soil segments; Step (12) in Section 6.3.4.
- ♦ Determines the yield factors for all elastic soil elements; Step (13) in Section 6.3.5.
- ♦ Checks for soil element closest to yield and determines the largest yield factor (f_y); Step (13) in Section 6.3.5.
- ♦ Computes soil element traction increments and current tractions, and pile segment displacement increments and current displacements; Step (14) in Section 6.3.6.
- ♦ Computes pile tractions, shear forces and bending moments for the pile segments; Step (15) in Section 6.3.6.
- ♦ Calls for Subroutines **QCGAP** and **QDISP**.
- ♦ Computes incremental and current pile-head lateral load, displacement, moment and rotation; Step (18) in Section 6.3.8.
- ♦ Calls for Subroutines **QDEGRAD**, **QRFACT**, **QDEGRADB** and **QRFACTB**.
- ♦ Determine the interpolation factor when the predicted load or displacement exceeded the specified load or displacement; Step (24) in Section 6.3.12.
- ♦ Return back to Subroutine **DRIVE** for the next increment.

Subroutine **QCGAP**

- ♦ Computes gap sizes at the pile-soil interfaces for soil elements that have yielded in tension; Step (16) in Section 6.3.7.

Subroutine **QDISP**

- Searches for gaps experiencing gap closures and determines the gap closing factors; Step (17) in Section 6.3.7.
- Check for gaps nearest to gap closure and determines the largest gap closing factor (f_g); Step (17) in Section 6.3.7.

Subroutine **QDEGRAD**

- Computes the incremental and current plastic shear displacement for soil elements that have yielded in shear; Step (19) in Section 6.3.9.

Subroutine **QRFACT**

- Determines the reduced limit shear stresses and thereby the yield stresses for shear, when the side soil elements have recovered from plastic to elastic; Step (20) in Section 6.3.9

Subroutine **QDEGRADB**

- Computes the incremental and current plastic bearing displacement for soil elements that have yielded in bearing; Step (21) in Section 6.3.10.

Subroutine **QRFACTB**

- Determines the reduced limit bearing stresses and thereby the yield stresses for bearing, when the bearing soil elements have recovered from plastic to elastic; Step (22) in Section 6.3.10.

Subroutine **PLAST**

- Modifies the soil segment stiffness matrix for soil yielding or elastic unloading or gap closure; Step (23) in Section 6.3.11.

6.5 Typical illustrative results

Some cases were analysed using the program to demonstrate its features. The analyses were carried out using a free-head pile embedded in a stiff clay, subjected to one-way and two-way cyclic loadings. The details of the parameters involved are as follows (unless otherwise stated):

Pile length (L)	= 10 m
Pile Diameter (D)	= 1.0 m
Pile Young's modulus (E_p)	= 50 GPa
Eccentricity of loading (e)	= 0 m
Type of controlled conditions	= Load-controlled
Soil unit weight (γ)	= 10 kN/m ³
Lateral earth pressure coefficient (K_l)	= 1.0
Adhesion factor (α)	= 0.5
Undrained shear strength (C_u)	= 100 kPa
Soil Young's modulus (E_s)	= 100 MPa
Backsliding factor (β)	= 0
Residual/peak shear strength ratio (R_s)	= 0.5
Shear degradation rate factor (C_s)	= 0.5 mm ⁻¹
Residual/peak bearing strength ratio (R_b)	= 0.5
Bearing degradation rate factor (C_b)	= 50

6.5.1 Load-controlled conditions

The results of one-way and two-way cyclic loadings with load-controlled conditions are depicted in Figures 6.15a and 6.15b, respectively. The plots clearly indicate the increase in pile-head displacement with the increase in the number of cycles. At the end of unloading for the one-way cyclic analysis, a permanent or residual displacement can be seen, which is indicative of the plastic yielding of soil. Gap closure can be observed from the sudden increase in gradient of the load-displacement curves (point *A* in Figure 6.15a). It is observed that the second cycle has a considerable effect on the pile-head load-displacement response. This is because gaps are created at the first cycle, and the stiffness of the pile-soil system is subsequently reduced.

For two-way cyclic loading depicted in Figure 6.15b, the maximum and minimum pile-head displacements at maximum and minimum loads, respectively, are almost of the same magnitude (differences less than 2%) but in opposite directions. Gap closure, for two-way cyclic loading, normally occurs near to the initial position of the pile. This is marked by the sudden increase in gradient of the load-displacement curves (point *A* in Figure 6.15b).

It is observed that the maximum pile-head displacement for one-way cyclic loading is larger than (by approximately 15% at the fifth cycle) the two-way cyclic loading. The reason is that there are more yielded soil elements (especially for elements yielded in tension) at the beginning of the reloading stage for the former than the latter, hence a greater reduction in the pile-soil system stiffness, leading to higher pile displacements.

The bending moment distribution along the pile for cycles 1 to 5 is depicted in Figures 6.16a and 6.16b for one-way and two-way cyclic loadings, respectively. In Figure 6.16a, an increase in maximum bending moment with cycling is observed. Also, the depth at which the maximum moment occurs has moved from 3 to 4 m, as greater amount of soil yielding have taken place near the top of the pile. For two-way cyclic loading (Figure 6.16b), similar trend of positive bending moment distribution for one-way cyclic loading is observed. The negative bending moment distribution at the end of unloading is almost identical (less than 1% difference) to the positive bending moment distribution at the end of the reloading for that cycle, displaying a mirror image.

The results of the pile displacement, left and right soil profiles together with the size of the gaps at the end of the first cycle of one-way cyclic loading are depicted in Figure 6.17. It is observed that left and right gaps are present near the top of the pile at the end of the cycle.

6.5.2 Displacement-controlled conditions

The load-controlled conditions usually apply during cyclic pile-load tests. However, in some circumstances, displacement-controlled testing is employed (e.g. test is easier to control as mentioned by Long *et al.*, 1993).

The pile-head load-displacement plots for the one-way and two-way cyclic loadings using displacement-controlled conditions are depicted in Figures 6.18a and 6.18b, respectively. The results indicate that with the increase in the number of cycles, the load applied to reach to the specified maximum pile-head displacement (say at 15 mm) decreases due to the increase in the amount of soil yielding. The reduction in load from the first cycle to the fifth cycle is 20% for the one-way cyclic loading (Figure 6.18a) and 17% for the two-way cyclic loading (Figure 6.18b).

6.5.3 Gap formation

The effect of inclusion and exclusion of gap formation in the analysis on pile responses is examined. The exclusion of gap formation, implies that the soil elements that had yielded in tension in the unloading (or reloading) stage are all set to elastic at the beginning of reloading (or unloading) stage. This assumes that the soil is adhering to the pile at all times, though the soil might have yielded in tension. No soil strength degradation is included, and one-way and two-way cyclic loadings under load-controlled conditions are used for the analysis.

The results of pile-head load-displacement responses depicted in Figure 6.19, show that cyclic degradation (i.e. increase in pile-head displacements with cycling) is evident for analysis with gap formation. For the case without gap formation, the pile response stabilises to an alternating plasticity state after the second cycle. This shows that with gap formation included in the analysis, it will cause a significant increase in the pile-head displacements, and may also indicate that gap formation is the cause of cyclic degradation. However, if the load is increased to 1500 kN, cyclic degradation is evident in both cases with and without gap formation included; see Figure 6.20. This shows that the process of unloading and reloading in itself, is capable of producing the cyclic degradation, and that the gap formation inclusion simply aggravates the rate of cyclic degradation.

It is shown in Figure 6.20, that the residual displacement with gap formation included in the analysis, is much less than (around 60% at the end of the fifth cycle) the case without gap formation. This is due to the fact that with gap formation included, all soil elements that have yielded in tension have remained plastic in the beginning of the unloading or reloading cycles, unlike the case without gap formation. This results in a lower pile-soil system stiffness, hence, less stiff pile responses with higher maximum and lower residual displacements.

For the two-way cyclic loading depicted in Figure 6.21, the exclusion of gap formation in the analysis, has caused the pile to stabilise to an alternating plasticity response in the second cycle. Significant differences (end of five cycles) in the magnitude of maximum and minimum pile-head displacements, are observed between the case with and without gap formation (Figure 6.21). It is observed in the case without gap formation, that the positive displacement is greater than the negative displacement by approximately 70% at the end of the fifth cycle. For the case with gap formation, the minimum pile-head displacements are

similar to the maximum pile-head displacements (differences less than 1%) at the end of the fifth cycle.

6.5.4 Backsliding

The effect on pile responses with backsliding included in the analysis, is examined in this section. The backsliding factor (β) is assumed a value of 0.5 and no strength degradation is included. Comparing the case with and without backsliding, it is observed in Figure 6.22, that the maximum and residual pile-head displacements are reduced by 15% and 32%, respectively, at the end of the fifth cycle. This is because the inclusion of backsliding will increase the yield stress for tension of the soil according to Equations (6.4) and (6.10), hence lesser soil yielding in tension can be anticipated. This results in the reduction of gap size, simulating cohesive soil sliding back into the gap during loading.

6.5.5 Shear strength degradation

In this study, the residual/peak shear strength ratio (R_s) and rate of shear degradation factor (C_s) are both set to 0.5, signifying a 50% degradation of the shear strength and a medium rate of shear strength degradation. Bearing strength degradation is not included in the analysis. The pile-head load-displacement response depicted in Figure 6.23, shows that the inclusion of shear strength degradation has caused an increase in the maximum pile-head displacement, but a reduction in the residual displacement as compared with the case of no shear strength degradation. This is due to the greater amount of soil yielding taking place during the unloading and reloading cycles, as the yield stress for shear is reduced because of shear strength degradation. Figure 6.23 also indicates that the magnitude of residual displacement is mainly controlled by the side (shear) soil elements. This means that, if the adhesion factor (α) for the soil is set to a small value of 0.1, the yield stress for shear for the side soil elements will be very low, and, we can therefore expect a very small residual displacement as depicted in Figure 6.24. It is shown that reducing the yield stress for shear will reduce the rate of cyclic degradation.

6.5.6 Bearing strength degradation

The analysis was carried out with residual/peak bearing strength ratio (R_b) and rate of bearing degradation factor (C_b) taken as 0.5 and 50, respectively. This implies 50% of bearing

strength degradation, degrading at a medium rate. Shear strength degradation is not included in the analysis. Figure 6.25 shows that the analysis with bearing strength degradation included has shown larger maximum and residual pile-head displacements than the analysis without bearing strength degradation. In contrast to the shear strength degradation (Figures 6.23 and 6.24), larger residual displacements are observed for the analysis with bearing strength degradation than without (see Figure 6.25). This is because of the lower amount of soil yielding in bearing taking place in the unloading stage than with the reloading stage. A larger reduction in the yield stress for bearing is accounted for in the latter stage than in the former stage.

6.6 Investigation of cyclic degradation

The pile-head load-displacement responses depicted in Figures 6.20 and 6.23 to 6.25 have indicated that the reason for cyclic degradation is not simply caused by the inclusion of gap formation or soil strength degradation in the analysis, but simply the inclusion of unloading and reloading cycles. To examine the cause of cyclic degradation within the APILEC analysis, a Beam-On-Spring (BOS) model and a Beam-On-Interactive-Spring (BOIS) model were employed.

6.6.1 Beam-On-Spring model

The Beam-On-Spring (BOS) model is similar to the Winkler or subgrade reaction approach, in which the pile is supported by an array of uncoupled springs and sliders (giving a rigid perfectly-plastic response). The use of springs and sliders is to model the elastic-perfectly plastic soil behaviour which is similar to APILEC soil model. The pile is modelled as an elastic beam via beam theory. The use of uncoupled springs to model the soil behaviour will create a diagonal soil matrix rather than the fully populated soil matrix in APILEC analysis.

The model assumed that the pile segments are surrounded by four springs with sliders (known as 'spring segments') as shown in Figure 6.26. The springs consist of the side springs to take account of the shear loadings. For an advancing pile towards the right direction, the right and left springs will take account of the compressive and tensile loadings, respectively, and vice versa. A stiffness value is assigned to each spring, and likewise a limit load. Beyond the limit load, i.e. the spring yields and slides, simulating the elastic-perfectly plastic soil

behaviour; see Figure 6.27. Assuming that the soil takes no tension, the limit load for tension for the spring is taken to be zero. Gaps will occur when the springs at the back face of an advancing pile are subjected to tensile loads greater than zero.

The method of analysis for APILEC was adopted for BOS model, so as to avoid the complication of rewriting a new set of programs, compared with changes made only to specific Subroutine, namely the soil matrix generation Subroutine **GMAT** (see Section 6.4). Gap formation, gap closure and strength degradation are accounted for in the analysis.

The 'spring segment' stiffness is generated by simply summing the four spring stiffnesses connecting the pile segment, i.e.

$$K_{sp\ i} = \sum_{j=1}^4 K_{se\ ij} \quad (6.82)$$

where $K_{sp\ i}$ is the spring segment stiffness for the i -th segment,
 $K_{se\ ij}$ is the individual spring stiffness for the j -th spring of i -th segment, and
 $i = 1, 2, 3$ to n .

The diagonal terms of the soil segment stiffness matrix $[K_s]$ is then computed as:

$$K_{s\ ii} = K_{sp\ i} \quad (6.83)$$

where $K_{s\ ii}$ is the stiffness coefficients at the i -th row and i -th column of the $[K_s]$ matrix, and
 $i = 1, 2, 3$ to n .

The stiffness coefficients for the non-diagonal terms in the $[K_s]$ matrix are zeros. The $[K_s]$ matrix is then inverted to give the soil segment compliance matrix $[G_s]$ to be used in Equation (6.14). The pile is discretised into n segments, and the pile matrix $[G_p]$ is set up via the beam theory. With the limit loads specified for all the springs (taken as the yield stresses for the soil elements), Steps (7) to (25) described in Section 6.3, are then applied until the specified number of cycles is reached.

6.6.1.1 Beam-On-Spring model results

For the analysis, the limit compression, tensile and shear loads for the springs are taken to be 10, 0 and 0.5 kN, respectively. These limit loads of the springs are taken to be the yield stress of the soil elements for compression, tension and shear. The ratio of the limit compression loads in the springs to their limit shear loads was taken to be around ten; this reflects the ratio of bearing to shear limit stress used in APILEC analysis. All the spring stiffnesses are assumed to be 100 kN/m, simulating stiff clay with constant Young's modulus. The pile data are similar to those described in Section 6.5. Ten cycles of one-way cyclic loading were applied. Gap formation and soil strength degradation were also included in the analysis.

The analysis carried out with and without gap formation, saw no cyclic degradation in Figure 6.28, even when the load is very high (i.e. close to pile collapse). Comparing the case with and without gap formation, reveals higher residual pile-head displacements for the latter as depicted in Figure 6.28; reasons as explained in Section 6.5.3.

With the inclusion of bearing strength degradation and gap formation in the analysis, cyclic degradation is observed in Figure 6.29, and eventually stabilised to an alternating plasticity response at about ten cycles. With gap formation and shear strength degradation included in the analysis, cyclic degradation can also be seen in Figure 6.30, and the pile-head stabilised to an alternating plasticity response at the fifth cycle. The cyclic degradation is produced, as a result of degradation of the yield stress in each stage of unloading and reloading. The stabilisation to an alternating plasticity response can be anticipated when the residual strength for the soil elements is reached. This eventually reduces to gap formation alone where no cyclic degradation is produced (see Figure 6.28).

6.6.2 Beam-On-Interactive-Spring model

Since the BOS model, does not provide the answer for the cause of cyclic degradation due simply to the unloading and reloading cycles observed in APILEC analysis, the Beam-On-Interactive-Spring (BOIS) model with interactive springs was used to model the soil behaviour. The model is similar to the BOS model (see Figure 6.26), except that interaction with neighbouring spring segments are allowed. This is to simulate the soil segments interaction approach adopted by APILEC analysis.

For a simple interactive four spring segments, the soils segment compliance matrix $[G_s]$ is:

$$[G_s] = \begin{bmatrix} \frac{1}{K_{sp1}} & Ir_{12} & Ir_{13} & Ir_{14} \\ Ir_{21} & \frac{1}{K_{sp2}} & Ir_{23} & Ir_{24} \\ Ir_{31} & Ir_{32} & \frac{1}{K_{sp3}} & Ir_{34} \\ Ir_{41} & Ir_{42} & Ir_{43} & \frac{1}{K_{sp4}} \end{bmatrix} \quad (6.84)$$

The interactive term (Ir_{ij}) for the i -th segment due to loading at the j -th segment is taken as:

$$Ir_{ij} = \frac{1}{K_{spi}} \frac{I_c}{r_{ij}} \quad (6.85)$$

where I_c is a interactive constant,

r_{ij} is the distance between the i -th segment and the j -th segment (see Figure 6.31), and i and $j = 1, 2, 3$ to n .

Using the above method of obtaining the $[G_s]$ matrix, a fully populated soil matrix will be created, which is similar to the APILEC continuum approach. With the limit loads specified for the springs (taken as the yield stresses for the soil elements) and $[G_s]$ obtained from Equation (6.84), Steps (7) to (25) described in Section 6.3, are then applied until the specified number of cycles were attained.

6.6.2.1 Beam-On-Interactive-Spring model results

For the analysis, all the spring stiffnesses are assumed to be 100 MN/m. The limit compression, tension and shear loads are taken to be 900, 0 and 50 kN, respectively. These values are selected after observation from the BOS model, where the maximum pile-head displacements were found to be too excessive (greater than 150 mm). The above limit loads are taken to be the yield stress for compression, tension and shear for the soil elements. One-way cyclic loading was applied in five cycles, with gap formation included in the analysis. The interactive constant (I_c) for the interactive terms in Equation (6.85) is assumed to be 0.1 (unless otherwise stated).

With the inclusion of the interactive terms (Ir) in the soil matrix, cyclic degradation was clearly observed in Figure 6.32. In comparison with the BOS model, a less stiff response

is observed in Figure 6.33, which implies that the use of interactive terms in the soil matrix will cause a decrease in the stiffness of the pile-soil system. With the exclusion of gap formation in the analysis for the BOIS model, no cyclic degradation is observed in Figure 6.33. However, increasing the applied load to a higher value (close to pile collapse), cyclic degradation is clearly evident in Figure 6.34, which is similar to the APILEC analysis at high load level (see Figure 6.20).

It is observed in Figure 6.32, that the rate of cyclic degradation is quite small. This is due to the value of I_c that was employed in the $[G_s]$ matrix in Equation (6.84). Changing the I_c value from 0.1 to 0.4, will increase the interactive terms (I_r in Equation (6.85)) in the $[G_s]$ matrix, leading to a lower pile-soil system stiffness. Hence, higher pile-head displacements and higher rate of cyclic degradation can be anticipated as shown in Figure 6.35.

For the soil strength degradation, bearing strength degradation will be dealt with first. Using a residual/peak bearing strength ratio (R_b) of 0.5 and a bearing degradation rate factor (C_b) of 100 for the analysis, cyclic degradation can clearly be seen in Figure 6.36. No sign of stabilisation to an alternating plasticity response was observed, which is similar to APILEC results depicted in Figure 6.25; note that the BOS model has shown that the pile will stabilise to an alternating plasticity response with further cycling as shown in Figure 6.29. Comparing the case with and without bearing strength degradation included in the analysis (Figure 6.36), shows that the former predicts higher maximum and residual displacements than the latter by 44% and 81%, respectively, at the end of the fifth cycle.

For shear strength degradation, residual/peak shear strength ratio (R_s) of 0.5 and a shear degradation rate factor (C_s) of 0.1 were used. Cyclic degradation is clearly observed in Figure 6.37 with no evidence of stabilisation to an alternating plasticity response at the end of the fifth cycle. Comparing the case with and without shear strength degradation included in the analysis, shows that the former gives higher maximum displacement but a lower residual displacement than the latter (Figure 6.37). Such behaviour is similar to the APILEC analysis shown in Figure 6.23.

From the results of BOS and BOIS analyses, it seems to suggest that the cause of cyclic degradation is due to the interactive terms involved, i.e. when interaction between neighbouring spring segments is taken into consideration. The degree of interaction can be simply adjusted by the value of I_c in Equation (6.85). With higher I_c values (i.e. greater interaction), higher rate of cyclic degradation is shown in Figure 6.38, whereby setting I_c to

zero, i.e. essentially the BOS model, will lead to no cyclic degradation as depicted in Figure 6.38.

6.7 Discussion of results

The results revealed from the analyses with gap formation, backsliding and soil strength degradation included, show similar trends of pile responses to those observed in the cyclic pile-load tests, depicted in Figures 1.1 to 1.3. They indicate an increase in pile-head displacement and maximum bending moment with cycling for the load-controlled conditions, and a reduction in the pile-head load with cycling to the specified displacement for the displacement-controlled conditions.

Gap formation

The inclusion of gap formation and likewise the gap closure in the analysis is vital, because its exclusion can give a too stiff pile response during unloading and subsequent reloading cycles, as observed in Figures 6.19 to 6.21. It is also a more realistic approach, as gaps will form when the soil yields in tension, compared with the assumption that the soil adheres to the pile at all times, as assumed by many researchers like Matlock (1970), Reese *et al.* (1975), Poulos (1982) and Hamilton and Dunnavant (1993), among others.

Backsliding

Analyses with backsliding included (Figure 6.22) show that the pile-head displacements (both maximum and residual) and gap sizes will decrease. It can therefore simulate cohesive soils sliding back into the gap to reduce the gap sizes during loading, resulting in the reduction of pile-head displacements.

Soil strength degradation

The soil strength degradation was only employed when the soil elements had reached their yield stresses. Analyses with only shear strength degradation included (Figure 6.23) show an increase in the maximum pile-head displacement and decrease in the residual displacement with cycling as compared with the case where no shear strength degradation is included. This is because of the greater amount of soil yielding taking place in the unloading and reloading stages, as the yield stress for shear is reduced with cycling. Figure 6.24 shows

that the magnitude of residual displacement is mainly controlled by the side face soil elements. If the yield stresses of these elements are low, low residual displacements result.

With only bearing strength degradation included in the analysis (depicted in Figure 6.25), larger maximum and residual pile-head displacements with cycling occur, as compared with the case where no bearing degradation is included. This is due to the much larger amount of soil yielding taking place in the reloading stage than the unloading stage. As shear strength and bearing strength degradation always occur together, this results in an increase of maximum and residual pile-head displacements with cycling as compared with the case where no soil strength degradation is assumed.

Spring models

The investigation on the cause of cyclic degradation (as observed in APILEC analysis) using BOS and BOIS models, suggests that it is because soil continuity is accounted for in the analysis, where interaction with neighbouring soil elements is considered. The inclusion of gap formation and soil strength degradation will increase the rate of cyclic degradation, due to the greater amount of soil yielding.

6.8 Concluding remarks

The analysis was successfully implemented using the procedure described here. From the analyses of some simple cases described in Section 6.5, the predicted pile responses appear to be similar to those observed during cyclic pile-load tests. The use of BOS and BOIS models suggests that the cyclic degradation observed in APILEC analysis, arises from the soil element interactions. With the assurance that the algorithm produces plausible results, a number of parametric studies can now be conducted.

Table 6.1 Input data for the program APILEC.

Description	SI Units	Variable
Pile length (L)	m	al
Diameter (D)	m	diam
Pile Young's modulus (E_p)	kPa	ep
Pile working stress	kPa	sigw
Pile-head conditions <ul style="list-style-type: none">▪ 0 = Fixed▪ 3 = Free	- - -	iload " "
Eccentricity of loading (e)	m	xcent
Type of analysis <ul style="list-style-type: none">▪ 0 = Static▪ 1 = One-way cycling▪ 2 = Two-way cycling	- - - -	iqcyclf " " "
Gap formation analysis <ul style="list-style-type: none">▪ 0 = No▪ 1 = Yes	- - -	igap " "
Number of cycles	-	nqcycl
Backsliding analysis <ul style="list-style-type: none">▪ 0 = No▪ 1 = Yes► Backsliding factor (β)	- - - -	iqback " " qbeta

continued ...

Description	SI Units	Variable
Displacement-controlled conditions	-	iqdisco
▪ 0 = No	-	"
▪ 1 = Yes	-	"
▶ Displacement-controlled value	mm	qdisco
Shear strength degradation analysis	-	iqdegr
▪ 0 = No	-	"
▪ 1 = Yes	-	"
▶ Residual/peak shear strength ratio (R_s)	-	qresi
▶ Shear degradation rate factor (C_s)	mm ⁻¹	qcs
Bearing strength degradation analysis	-	iqdegrb
▪ 0 = No	-	"
▪ 1 = Yes	-	"
▶ Residual/peak bearing strength ratio (R_b)	-	qresib
▶ Bearing degradation rate factor (C_b)	-	qcb
Soil type	-	iopt
▪ 1 = Stiff clay	-	iopt
▶ Effective unit weight (γ)	kN/m ³	gama
▶ Lateral earth pressure coefficient (K_r)	-	ako
▶ Adhesion factor (α)	-	alfa
▶ Young's modulus (E_s)	kPa	esa
▶ Undrained shear strength (C_u)	kPa	cua
▪ 2 = Soft clay	-	iopt
▶ Effective unit weight (γ)	kN/m ³	gama
▶ Lateral earth pressure coefficient (K_r)	-	ako
▶ Adhesion factor (α)	-	alfa
▶ Young's modulus at ground level (m_o)	kPa	esa
▶ Rate of increase in Young's modulus (m)	kPa/m	esm
▶ Undrained shear strength at ground level (c_o)	kPa	cua
▶ Rate of increase in undrained shear strength (c)	kPa/m	cum

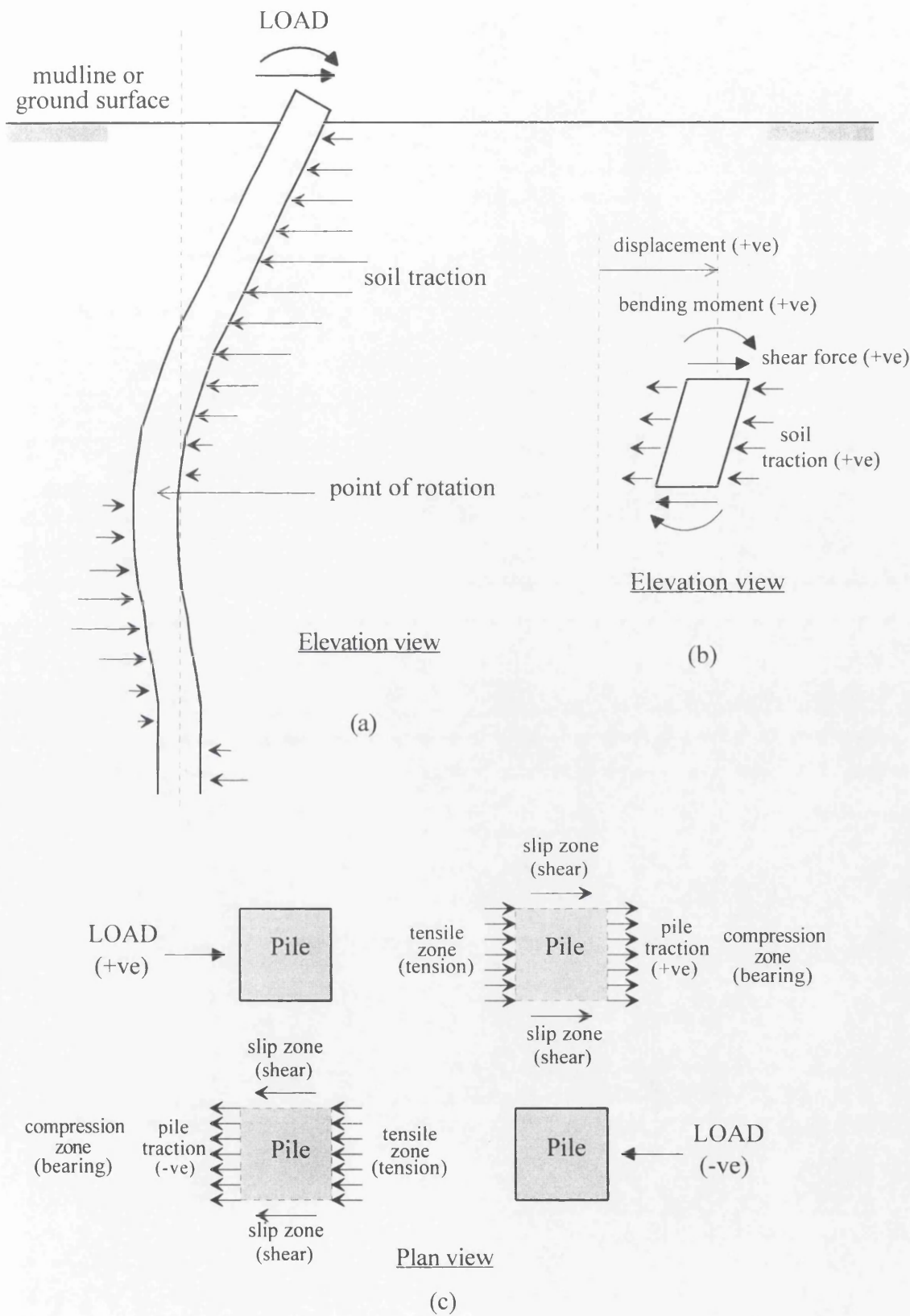


Figure 6.1 (a) Response of a laterally loaded pile, (b) sign conventions for a pile segment and (c) zones encountered when load direction changes.

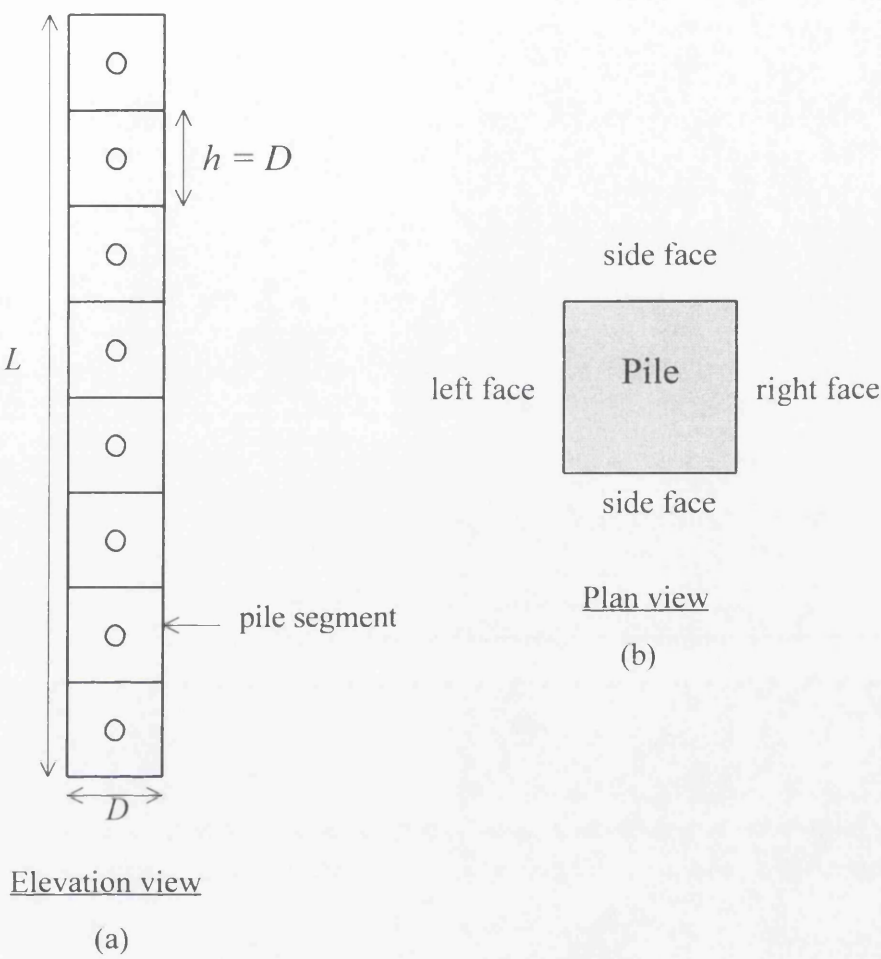
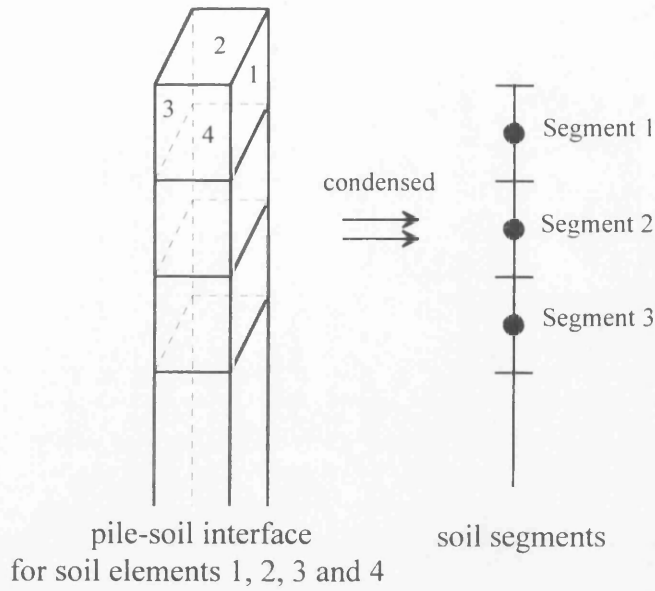


Figure 6.2 (a) Pile discretisation and (b) four faces of a pile segment.



(a)

$$[F] = \begin{bmatrix} \boxed{\begin{matrix} F1,1 & F1,2 & F1,3 & F1,4 \\ F2,1 & F2,2 & F2,3 & F2,4 \\ F3,1 & & & \\ F4,1 & & & \end{matrix}} = K_s1,1 & \boxed{\begin{matrix} F1,5 & F1,6 & . & . \\ F2,5 & F2,6 & . & . \\ & & & \end{matrix}} = K_s1,2 \\ \boxed{\begin{matrix} F5,1 \\ F6,1 \\ . \\ . \end{matrix}} = K_s2,1 & \\ . & \\ Fn,1 & . & . & . & . & . & . & . & Fn,n \end{bmatrix}$$

(b)

Figure 6.3 (a) Four soil elements on the faces of a pile segment treated as one soil segment and (b) full soil matrix $[F]$ condensed into a soil segment stiffness matrix $[K_s]$.

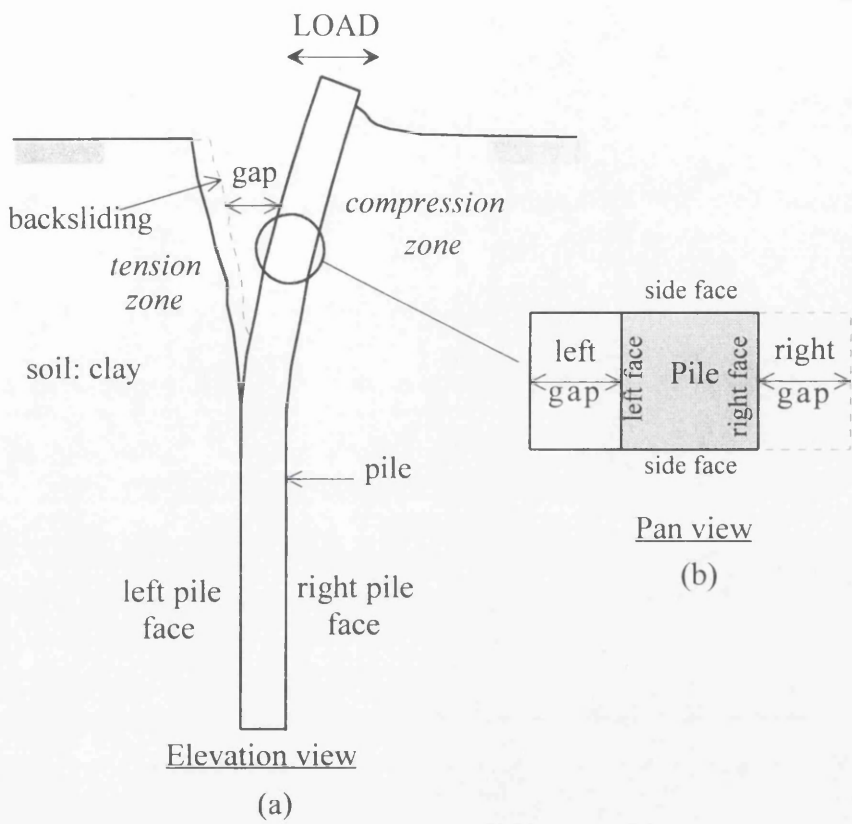


Figure 6.4 (a) Phenomena observed and soil zones developed during cyclic pile load test and (b) pile faces and gaps terminology.

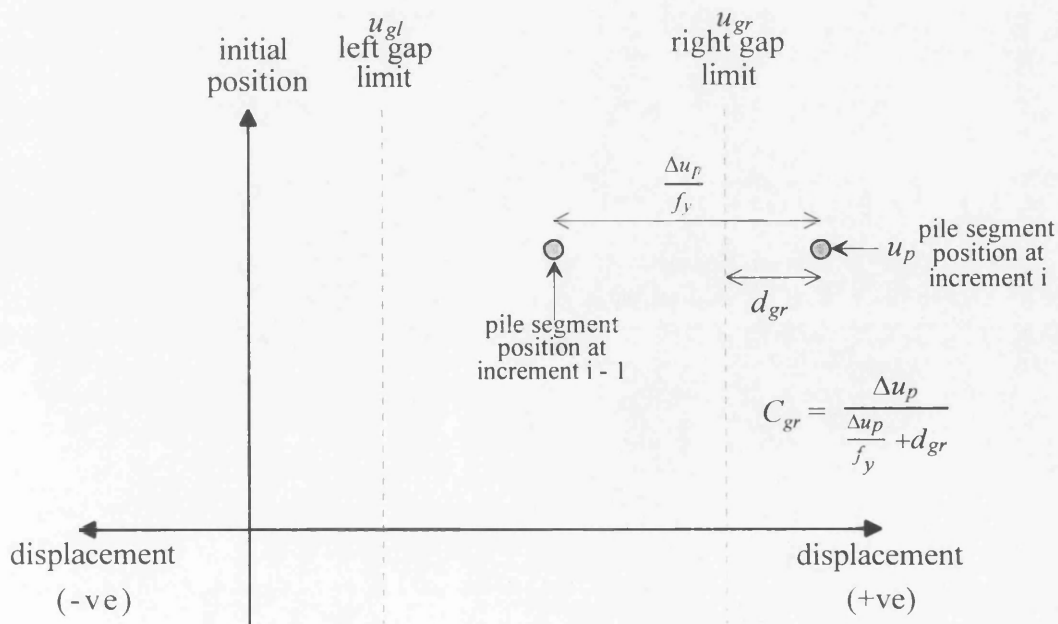


Figure 6.5 Determination of gap closing factor for soil element.

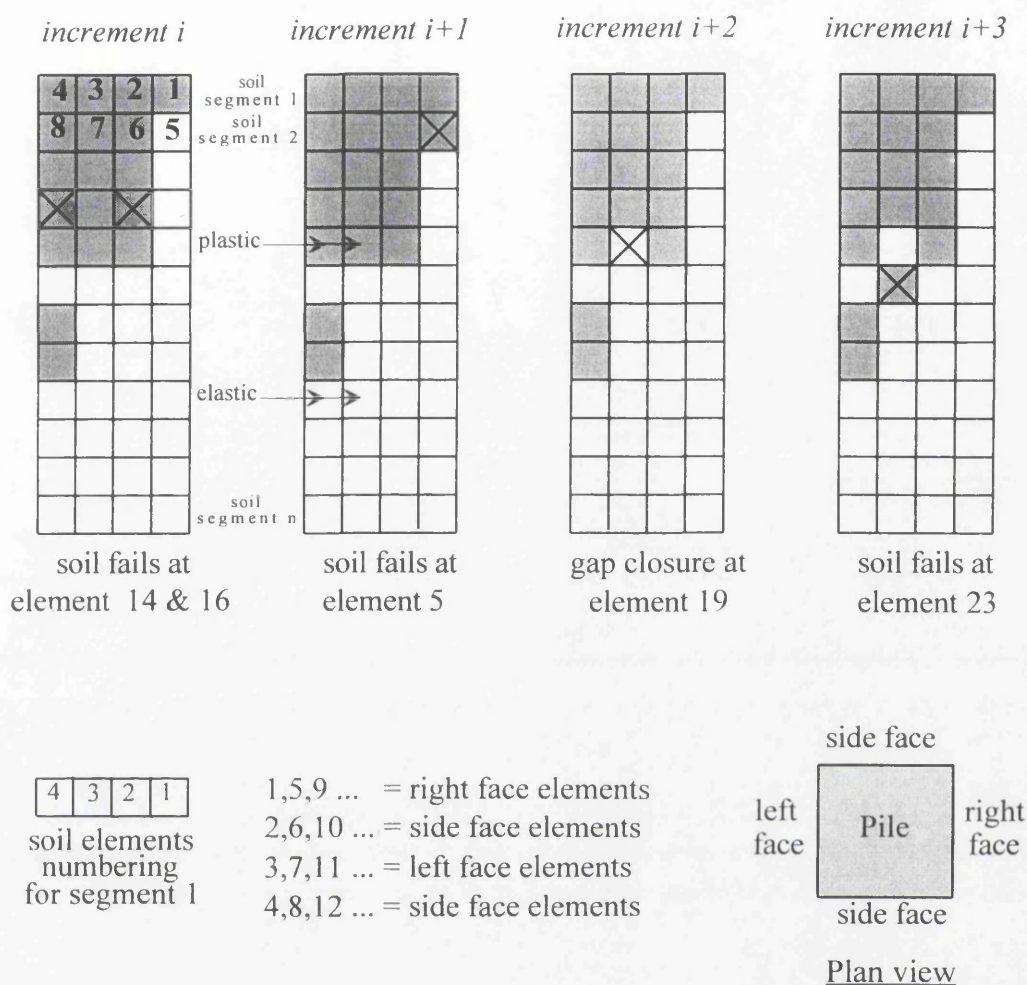


Figure 6.6 Soil elements elastic and plastic identification at different increments and elements numbering system.

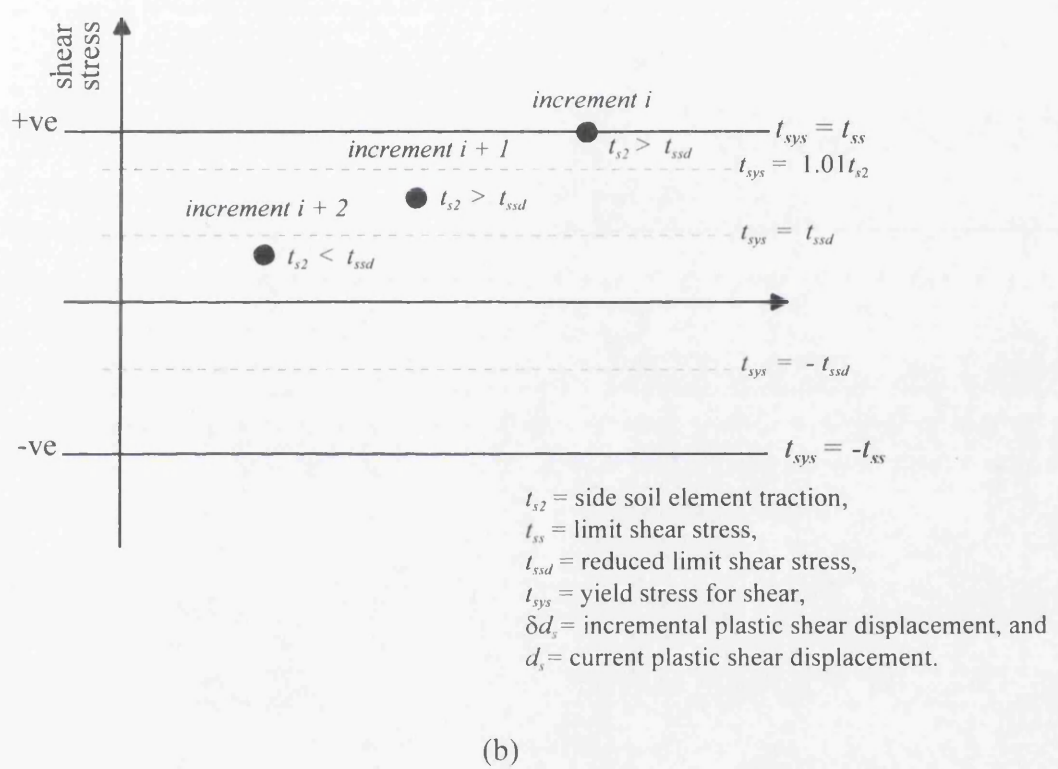
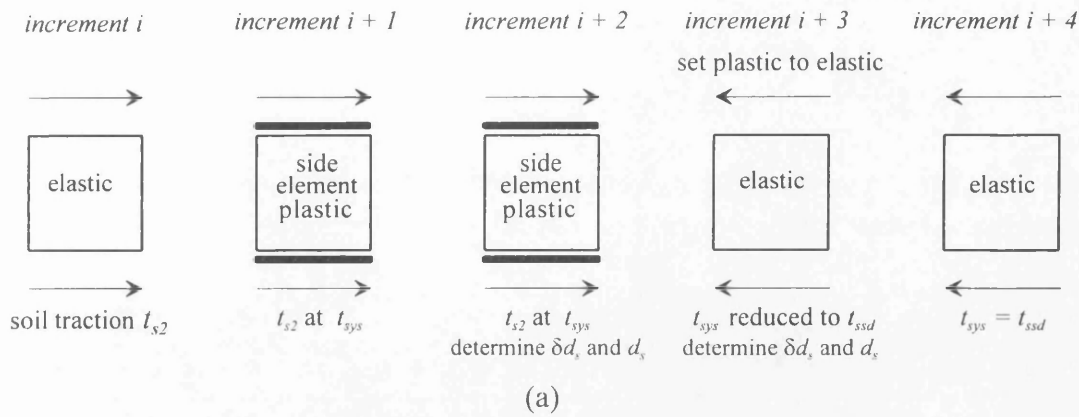


Figure 6.7 (a) Progressive yielding of side face soil elements and (b) determination of yield stress for shear.

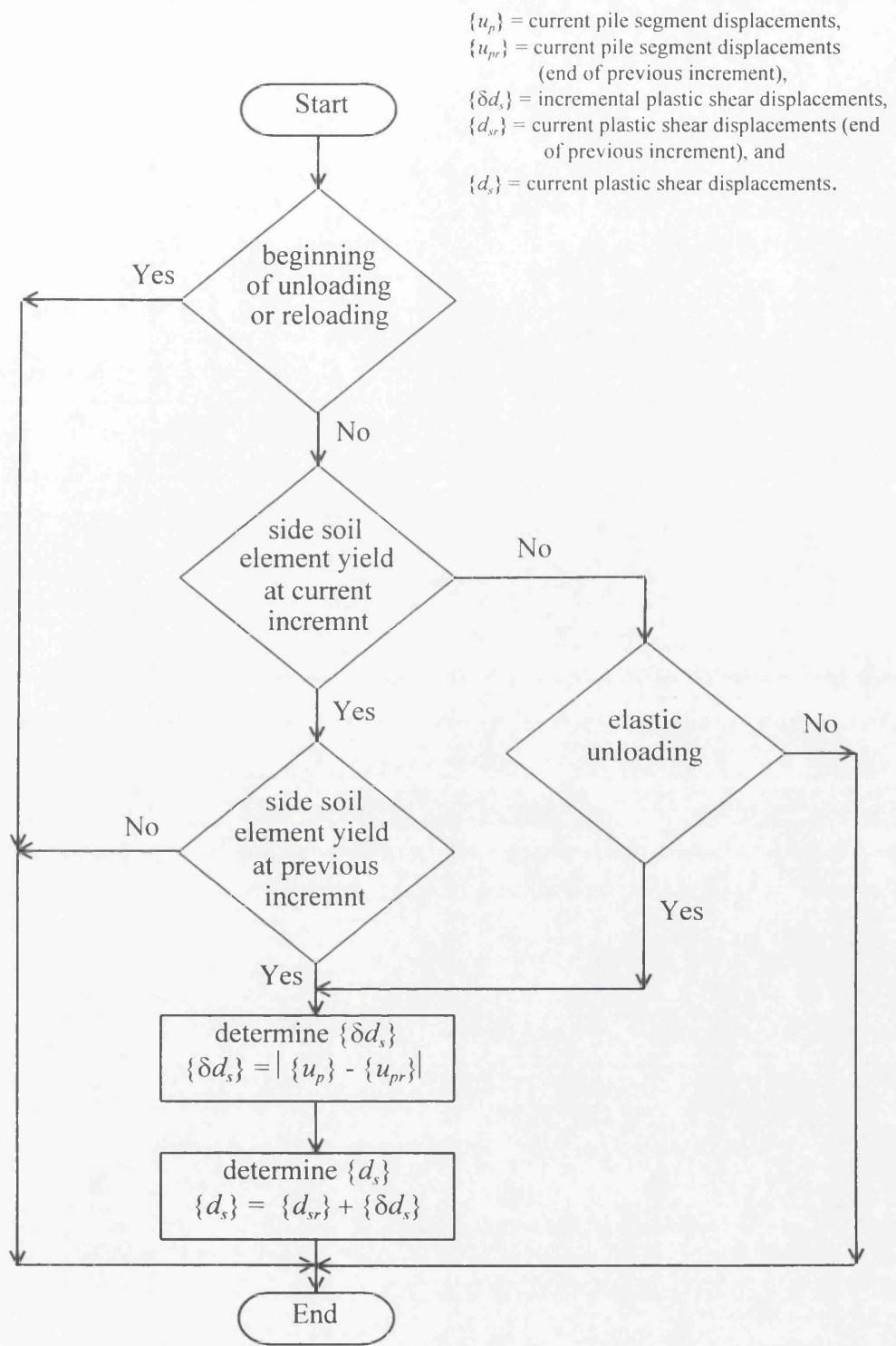


Figure 6.8 Flow chart for the determination of incremental and current plastic shear displacements.

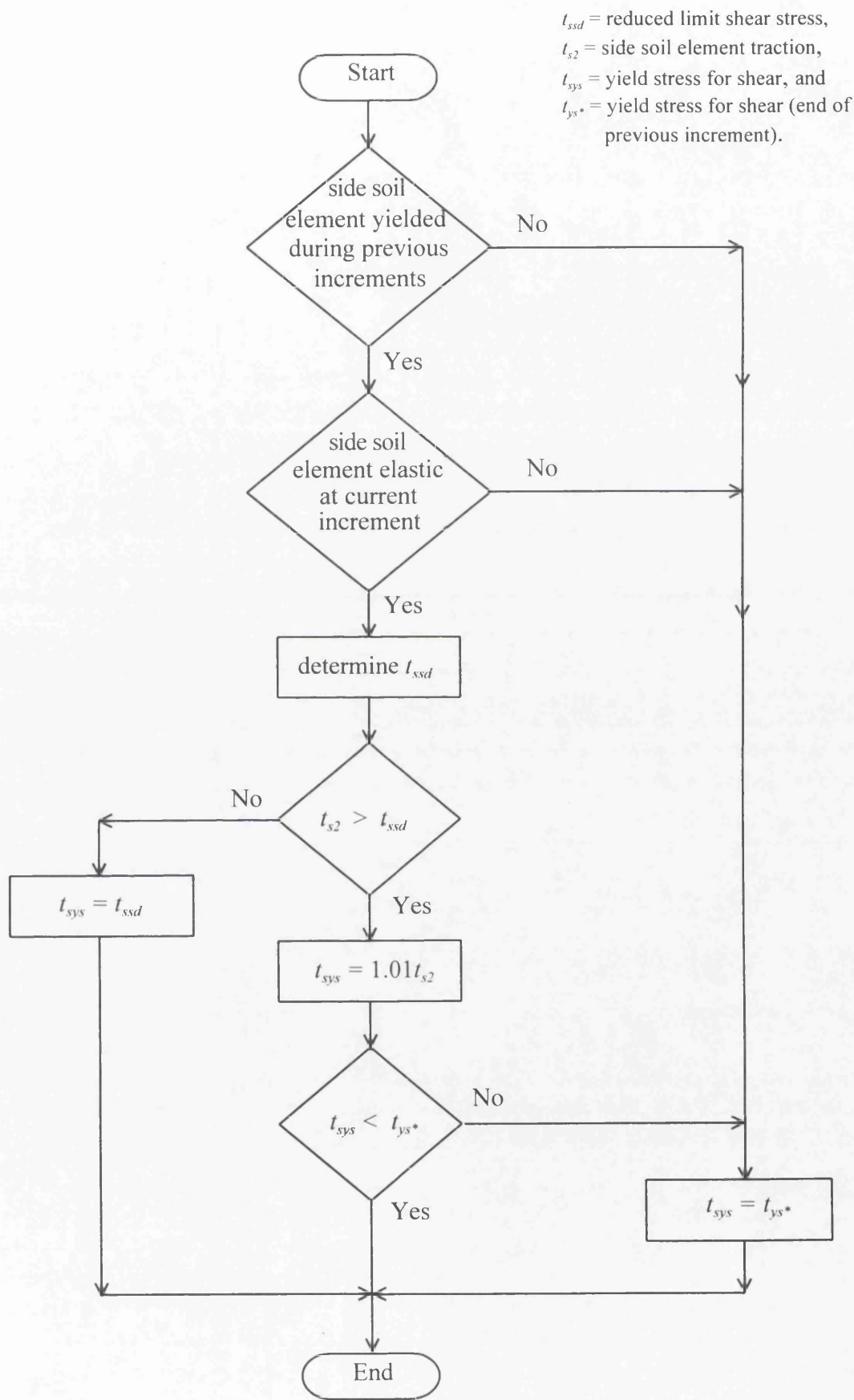


Figure 6.9 Flow chart for the determination of yield stress for shear.

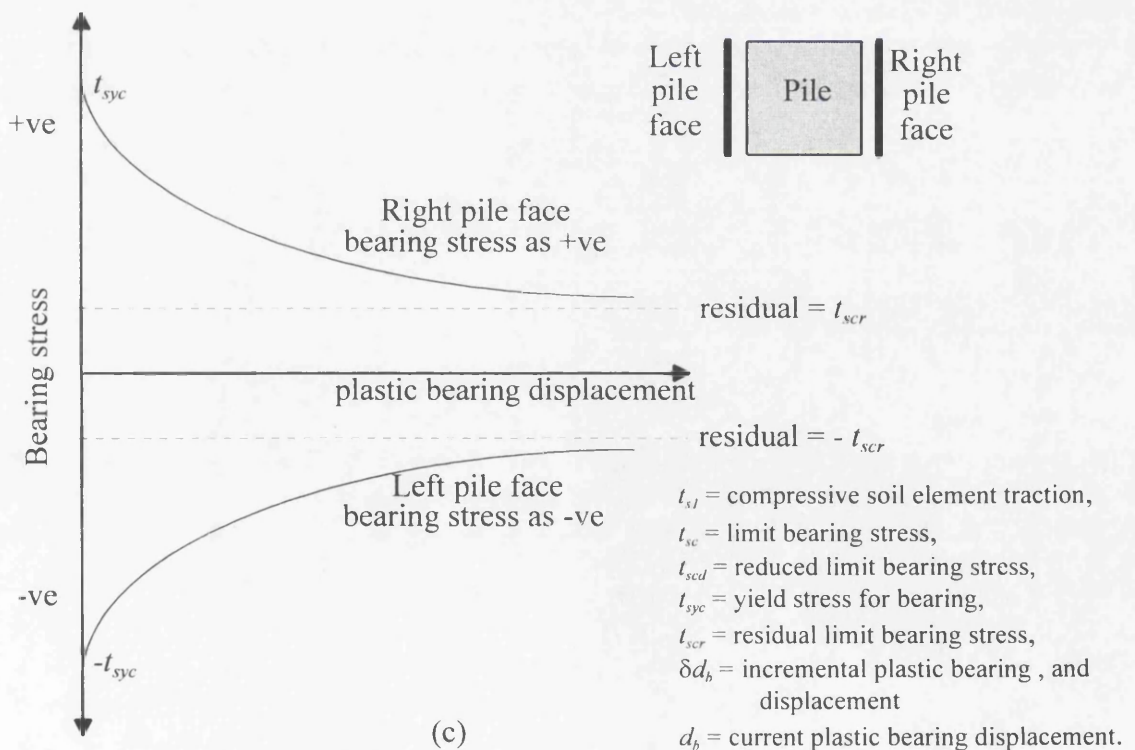
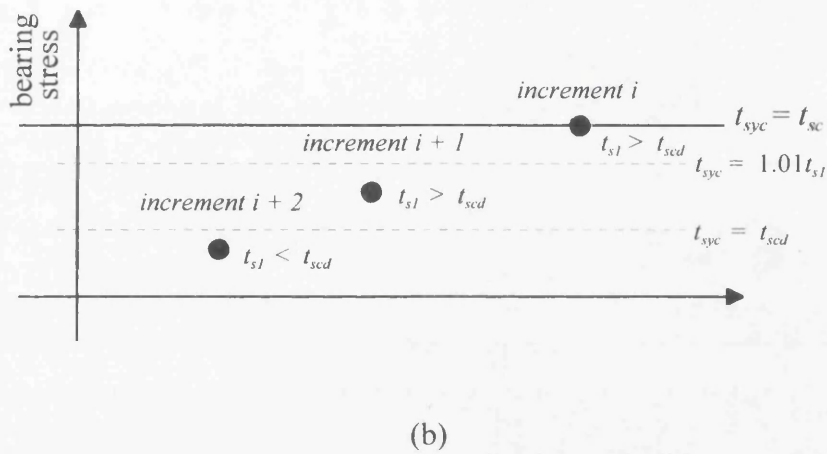
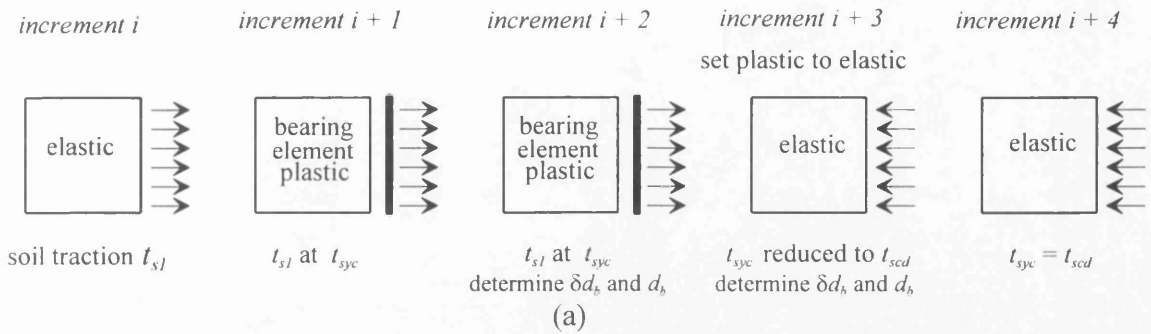


Figure 6.10 (a) Progressive yielding of bearing soil element, (b) determination of yield stress for bearing and (c) bearing strength degradation as a function of the residual limit bearing stress and the plastic bearing displacement.

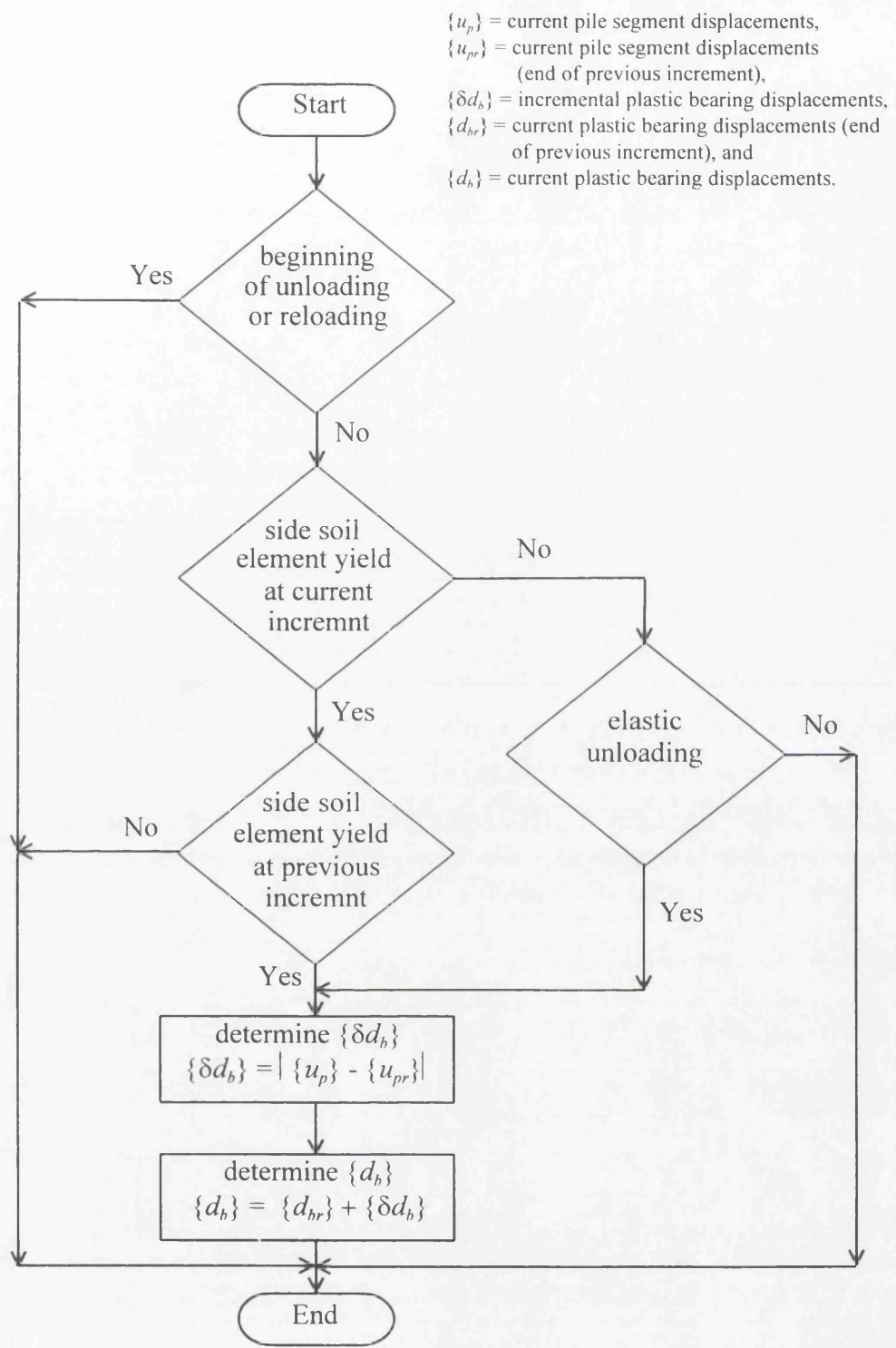


Figure 6.11 Flow chart for the determination of incremental and current plastic bearing displacements.

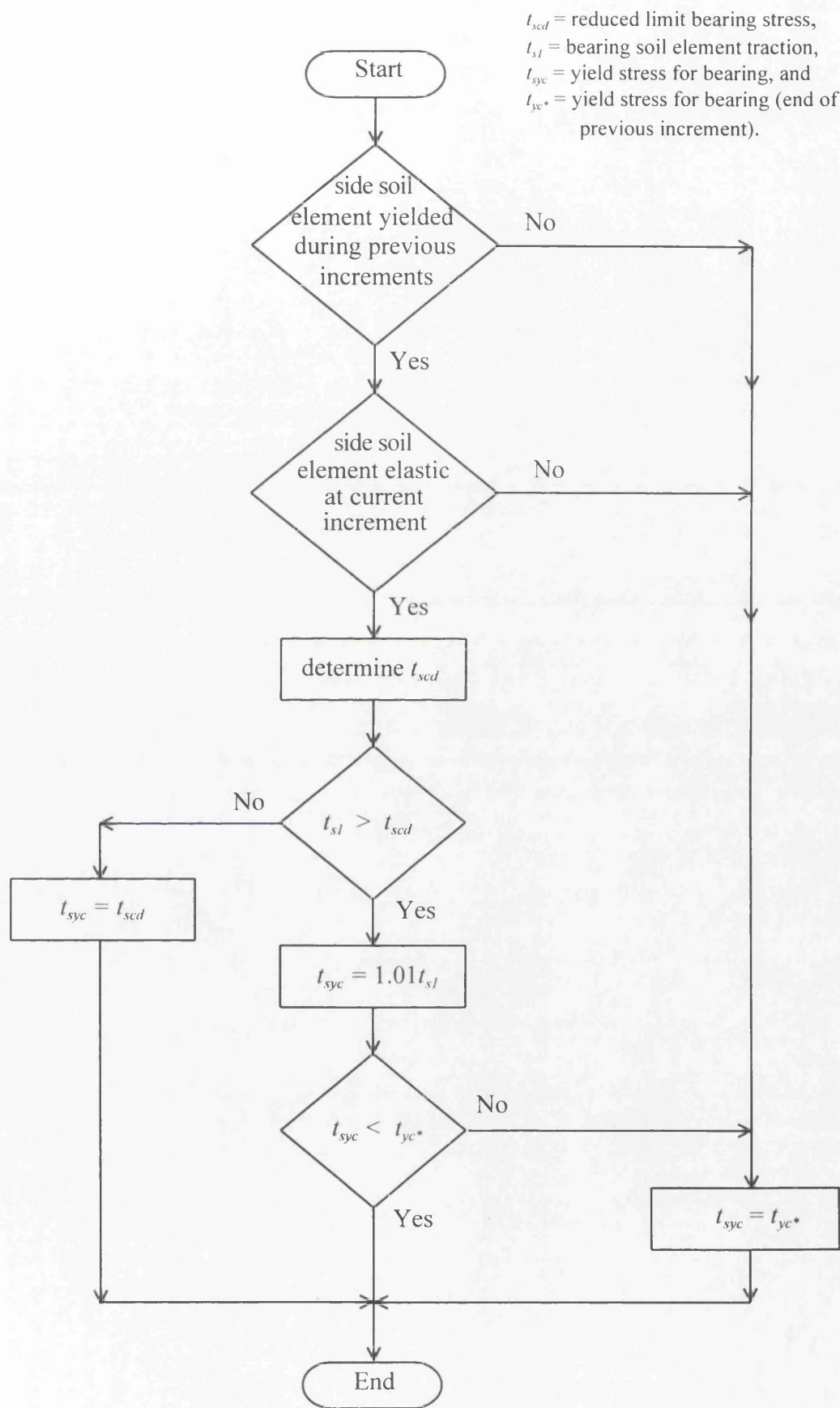


Figure 6.12 Flow chart for the determination of yield stress for bearing.

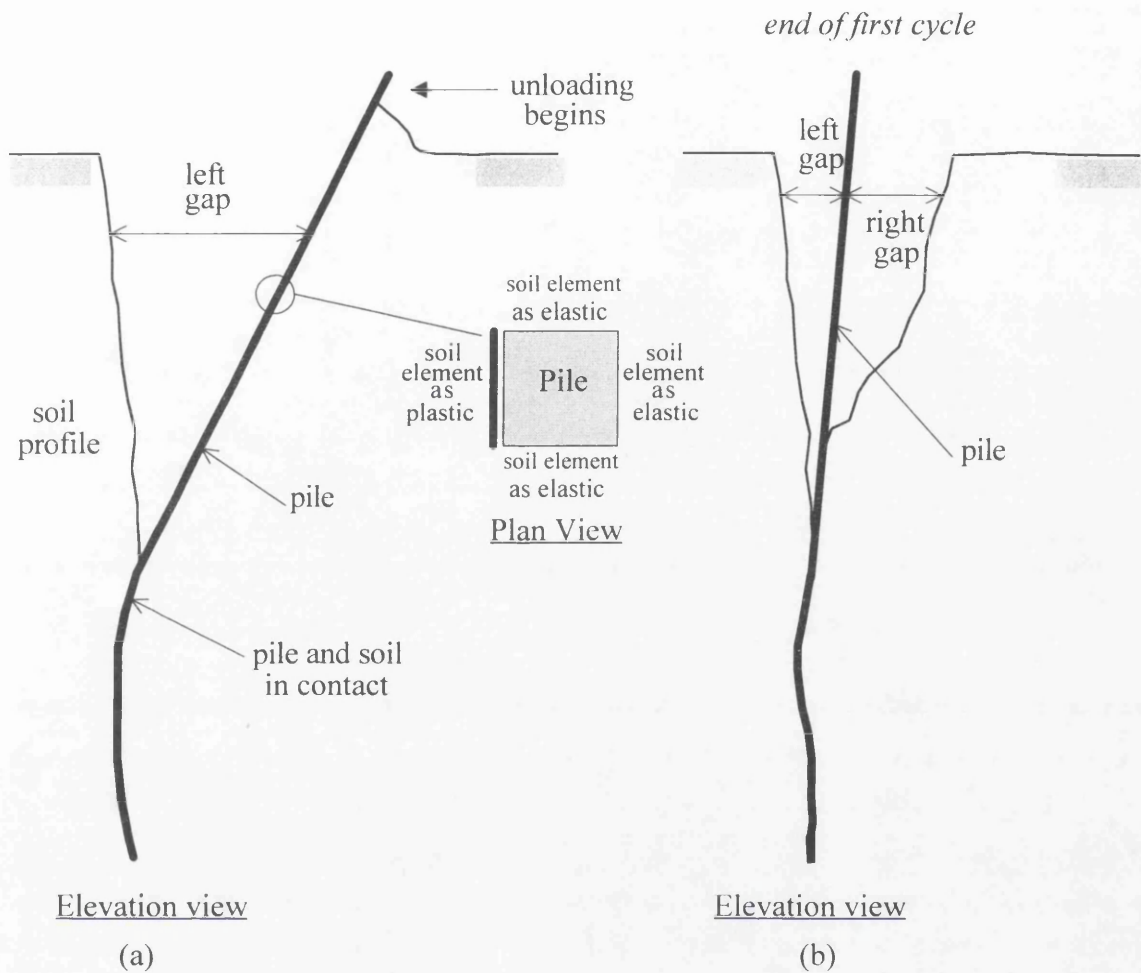


Figure 6.13 Gap formation; (a) at the beginning of unloading and (b) end of first cycle of one-way cyclic loading.

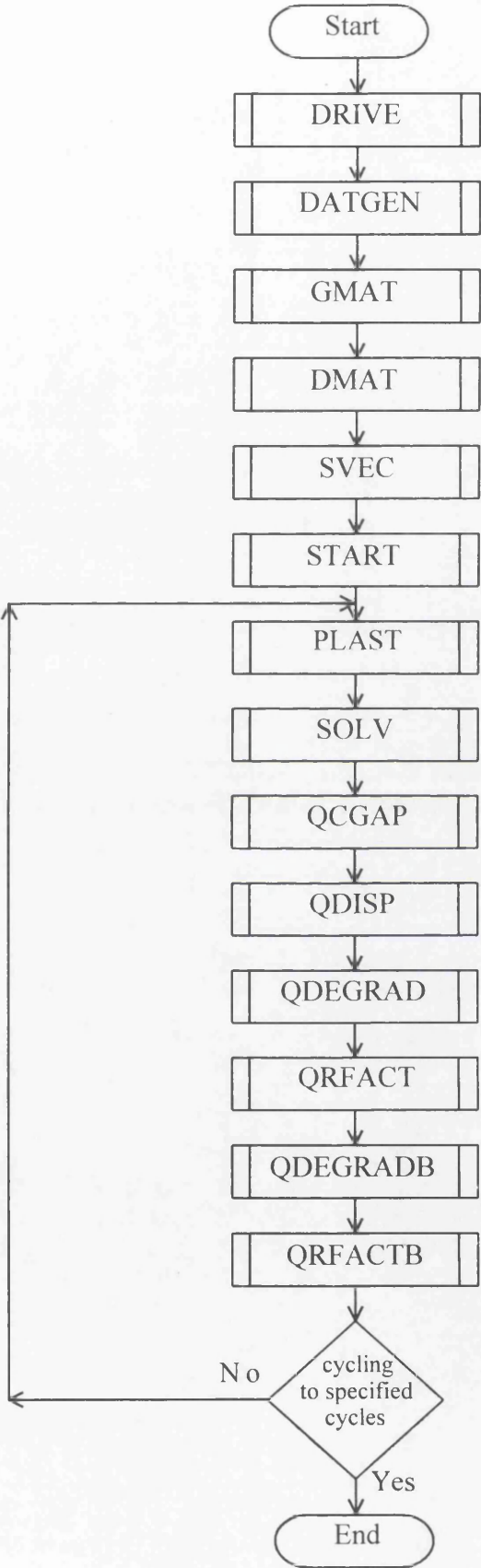
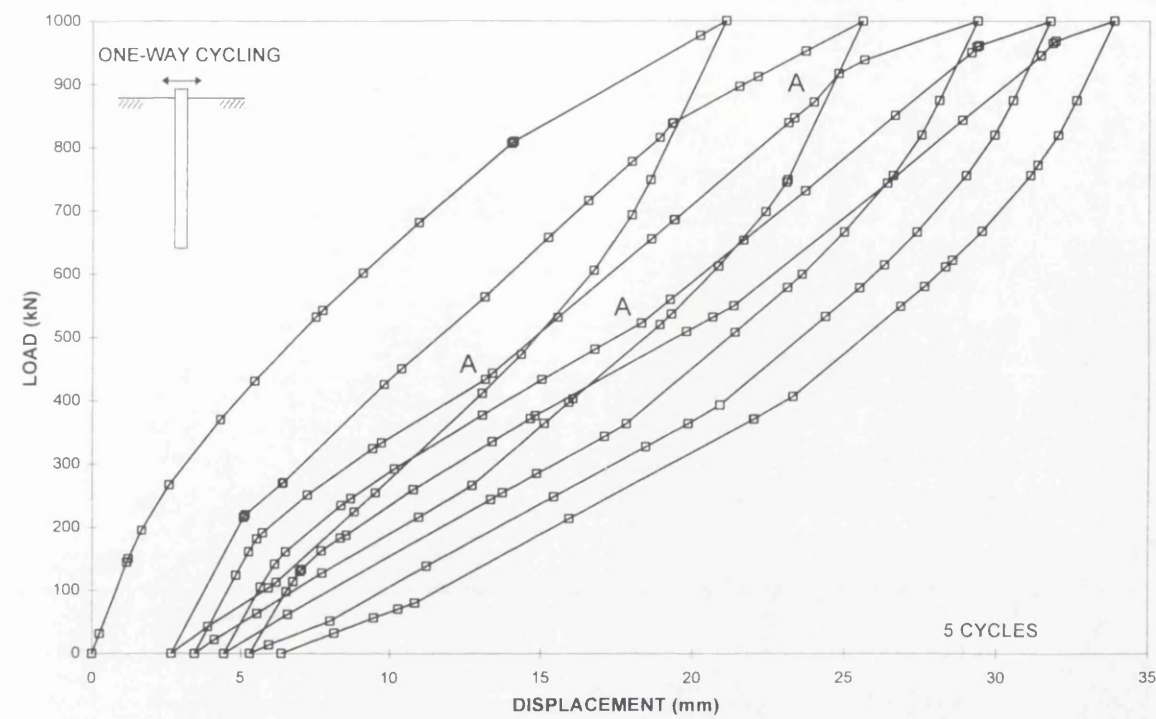
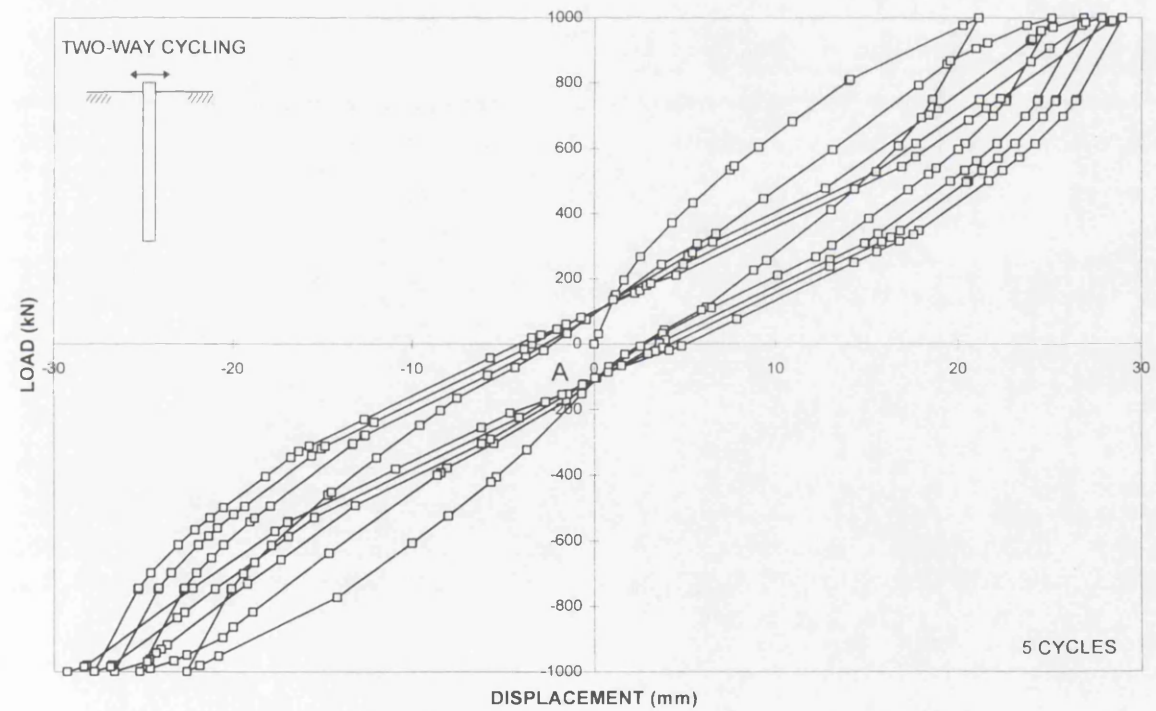


Figure 6.14 Structure of APILEC program with its subroutine.

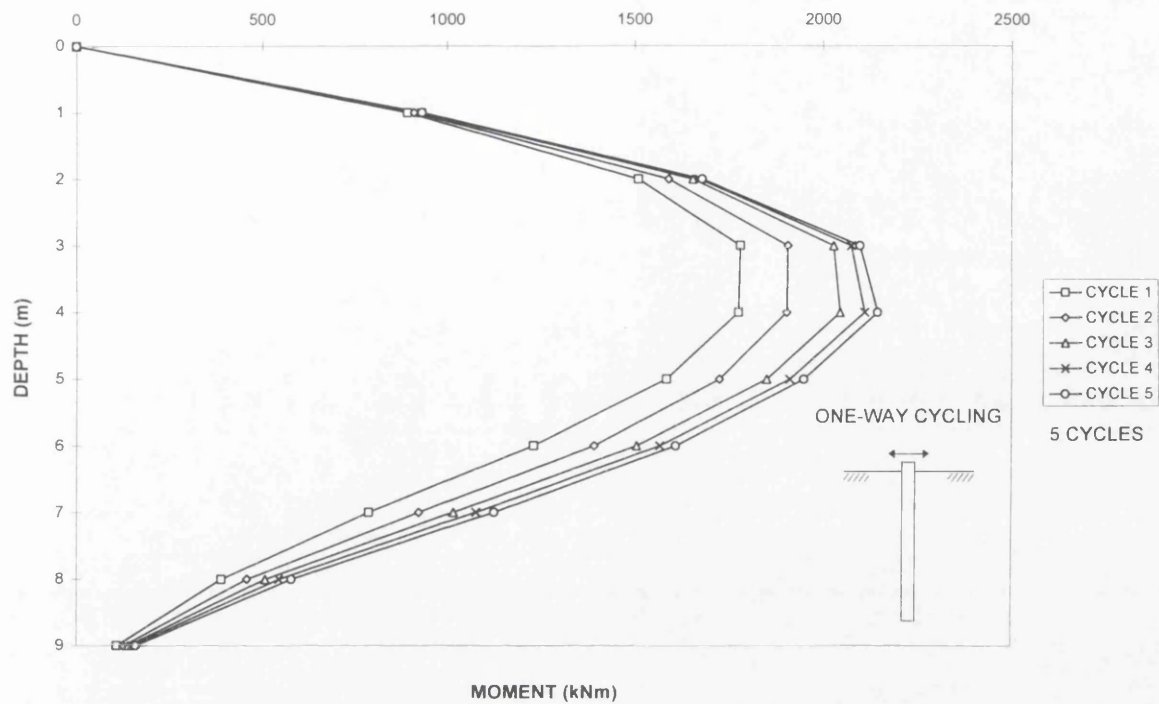


(a)

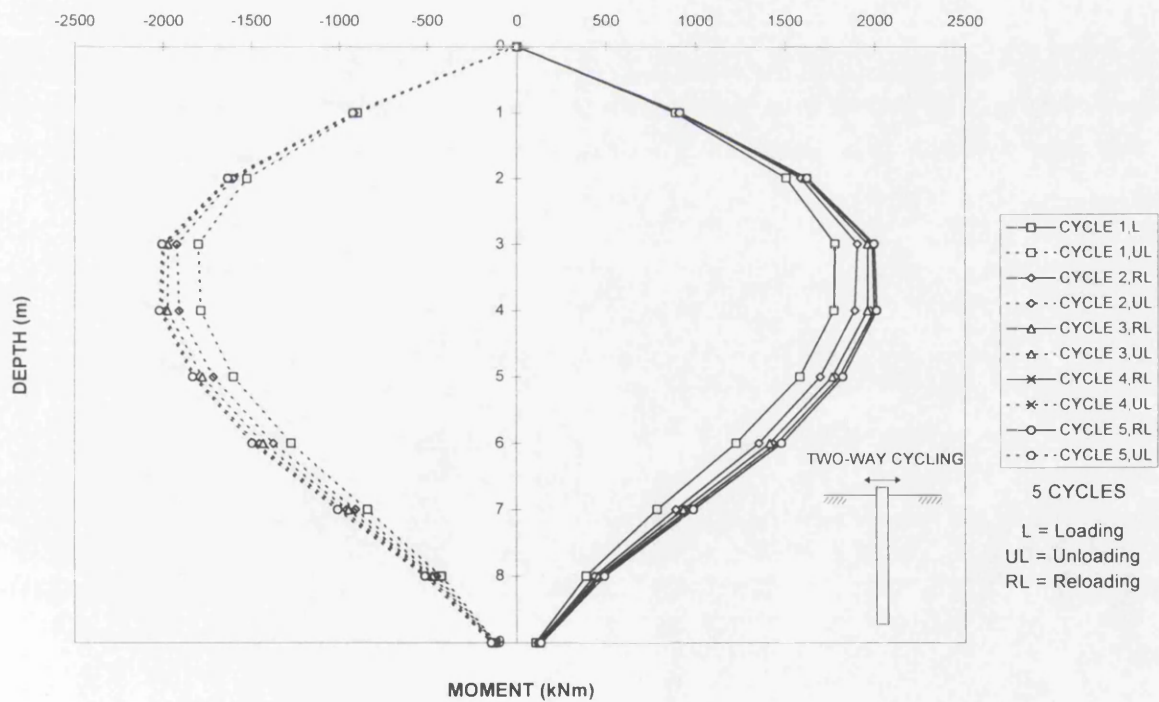


(b)

Figure 6.15 Pile-head load-displacement responses for (a) one-way and (b) two-way cyclic loading under load-controlled conditions.



(a)



(b)

Figure 6.16 Pile bending moment distributions for (a) one-way and (b) two-way cyclic loading under load-controlled conditions.

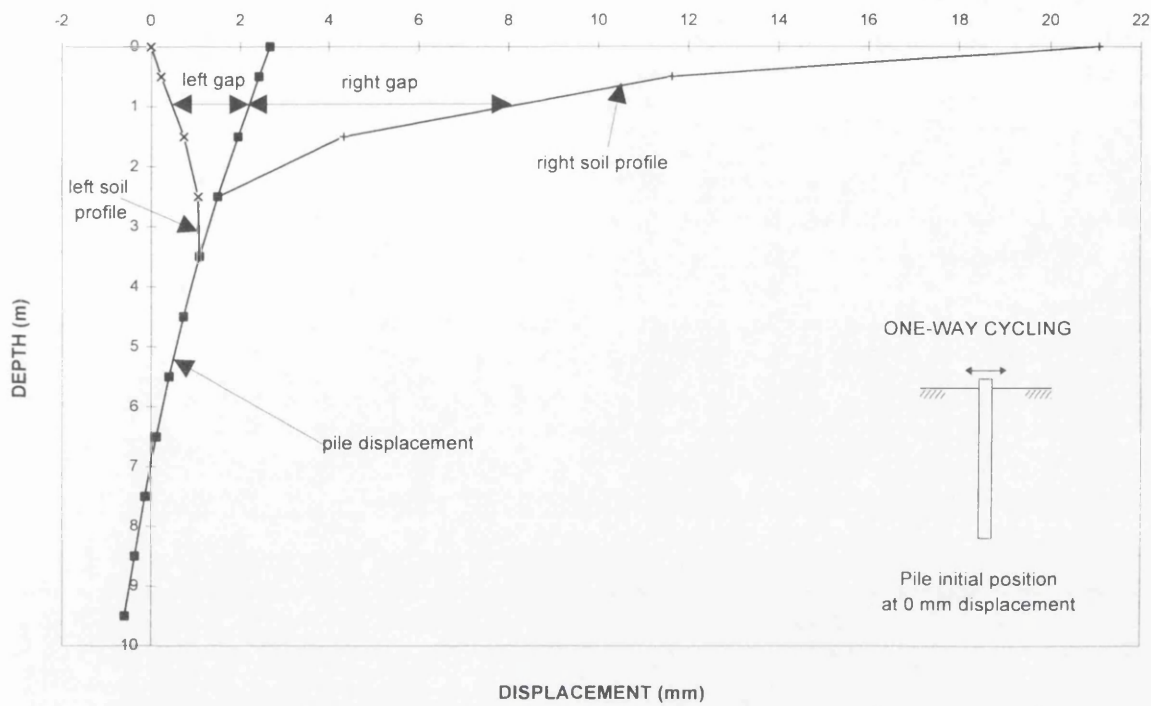


Figure 6.17 Pile displacement, soil profiles and gap distances at the end of first cycle of one-way cyclic loading.

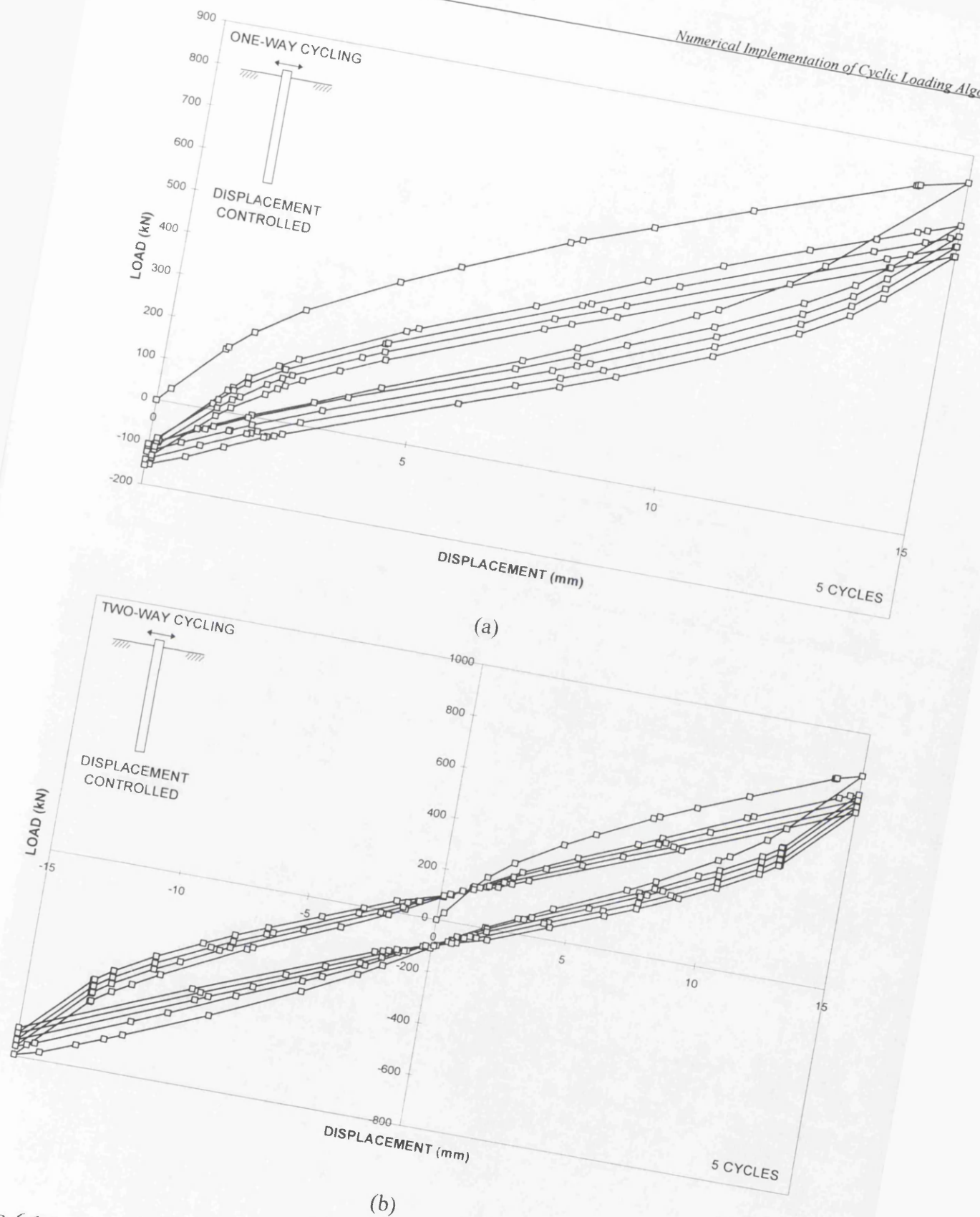


Figure 6.18 Pile-head load-displacement responses for (a) one-way and (b) two-way cyclic loading under displacement-controlled conditions.

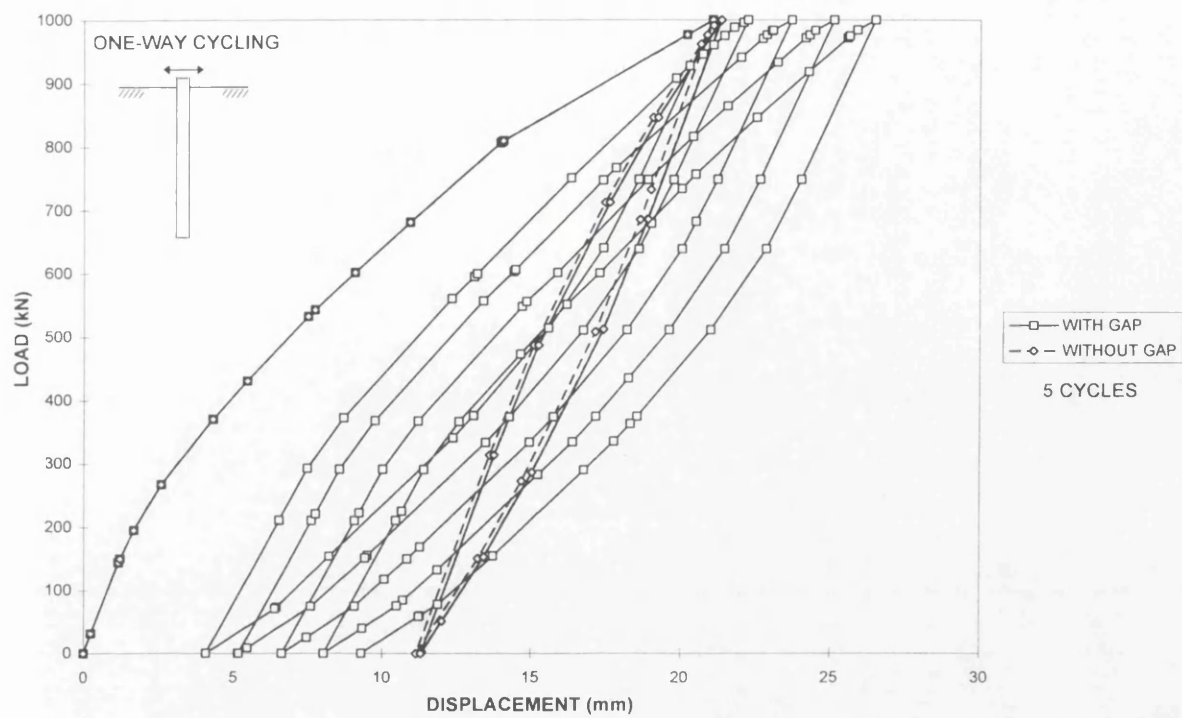


Figure 6.19 Pile-head load-displacement responses for one-way cyclic loading with and without gap formation.

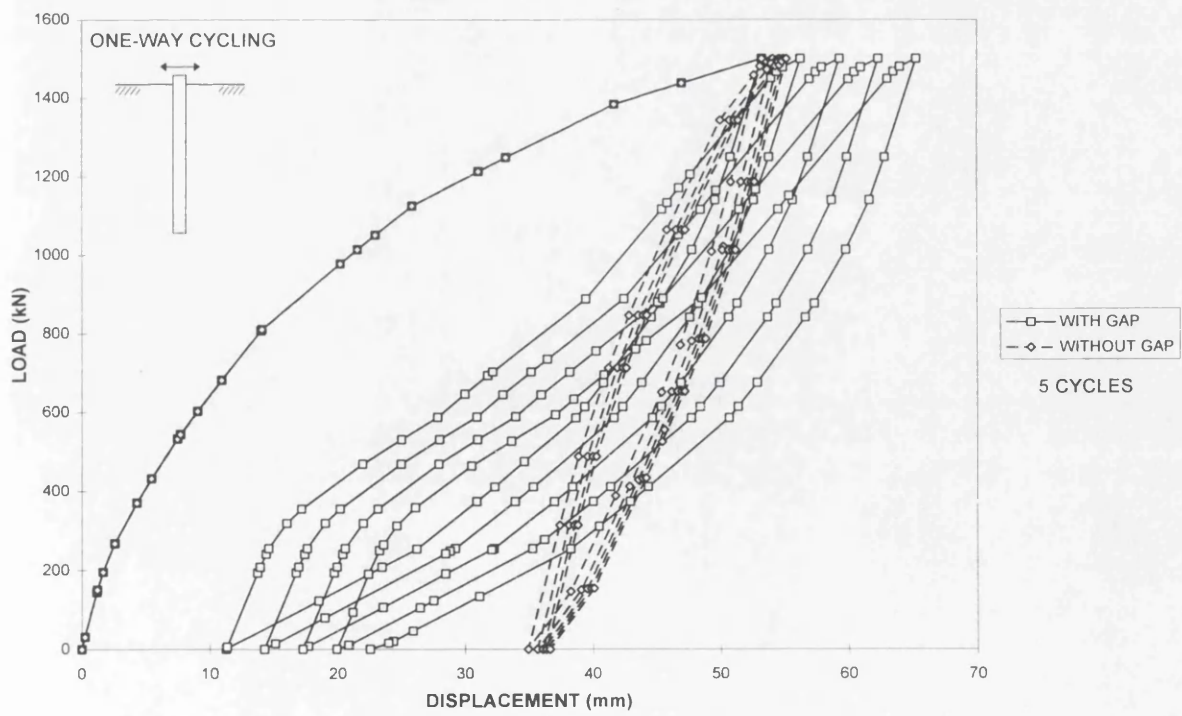


Figure 6.20 Pile-head load-displacement responses for one-way cyclic loading at high load level with and without gap formation.

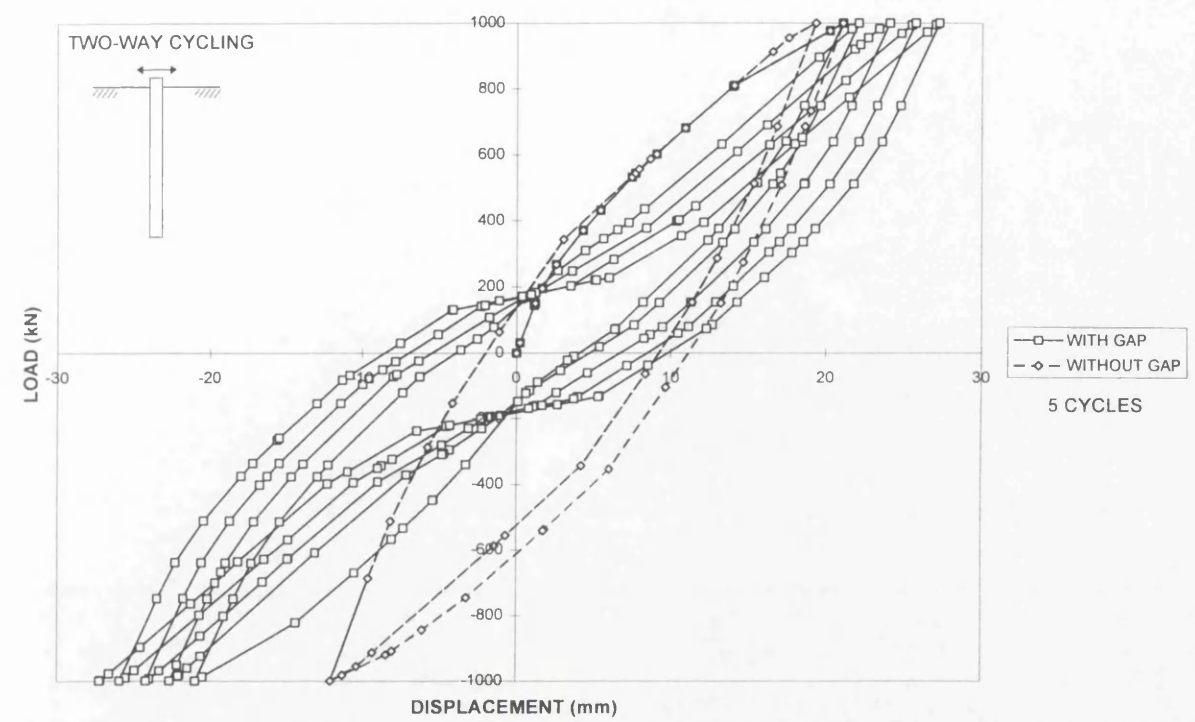


Figure 6.21 Pile-head load-displacement responses for two-way cyclic loading with and without gap formation.

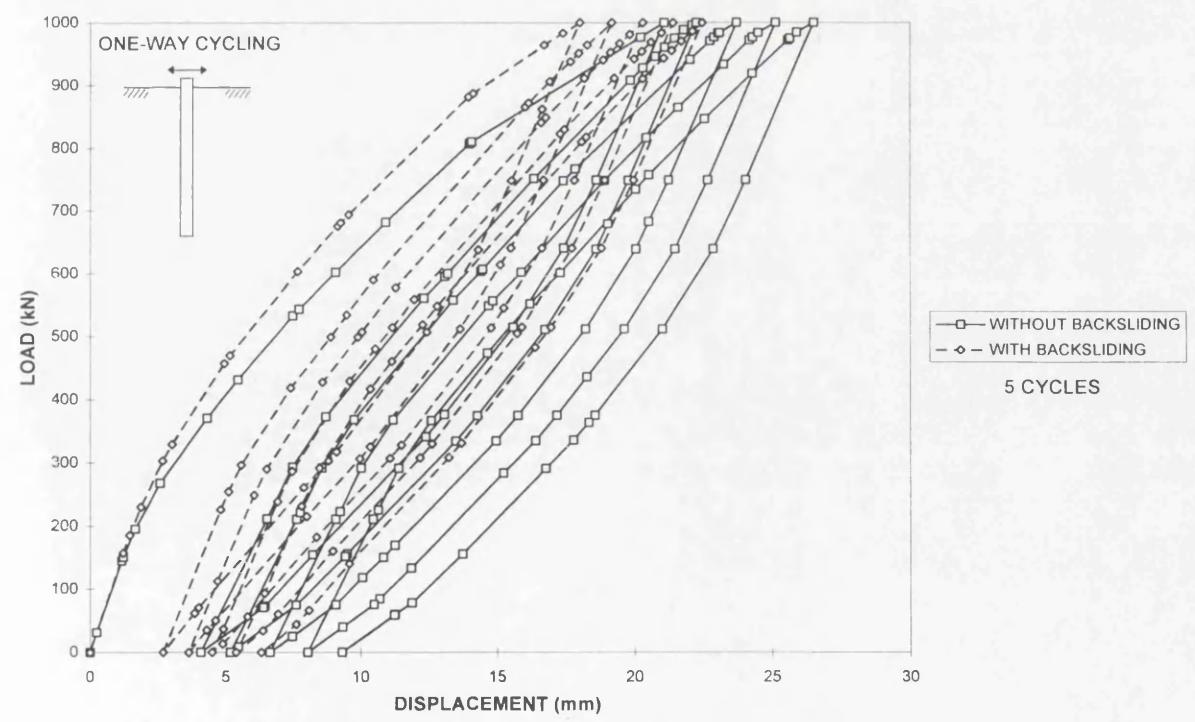


Figure 6.22 Pile-head load-displacement responses for one-way cyclic loading with and without backsliding.

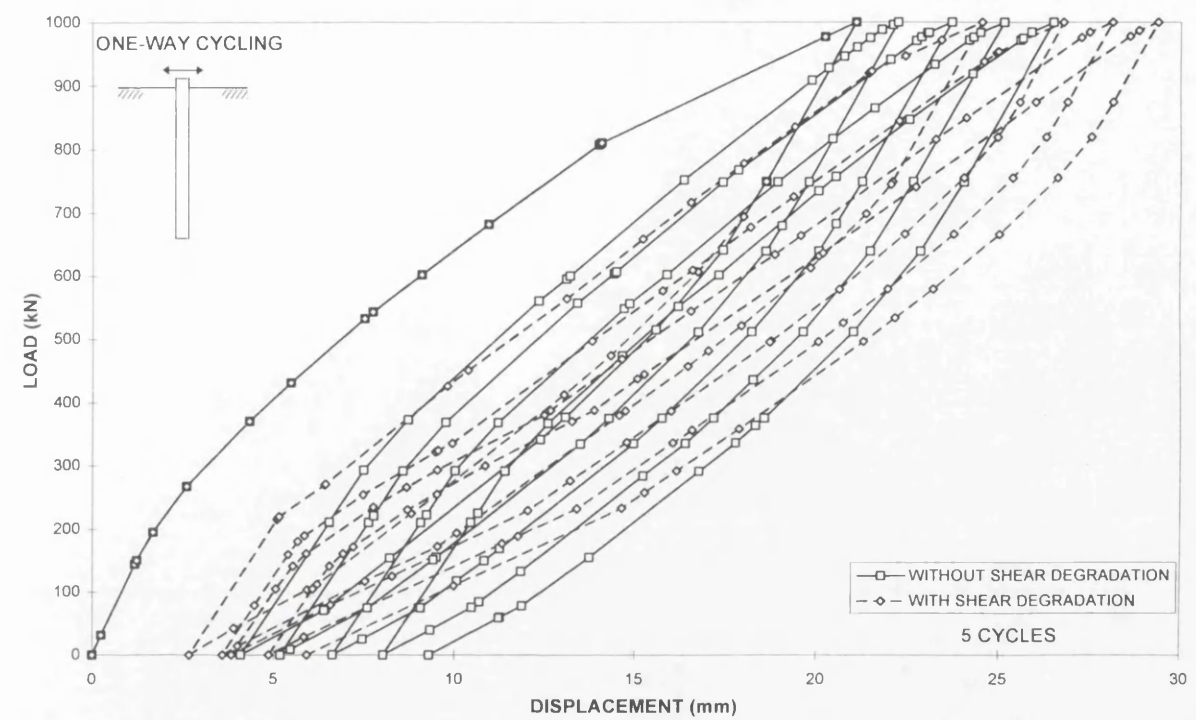


Figure 6.23 Pile-head load-displacement responses for one-way cyclic loading with and without shear strength degradation.

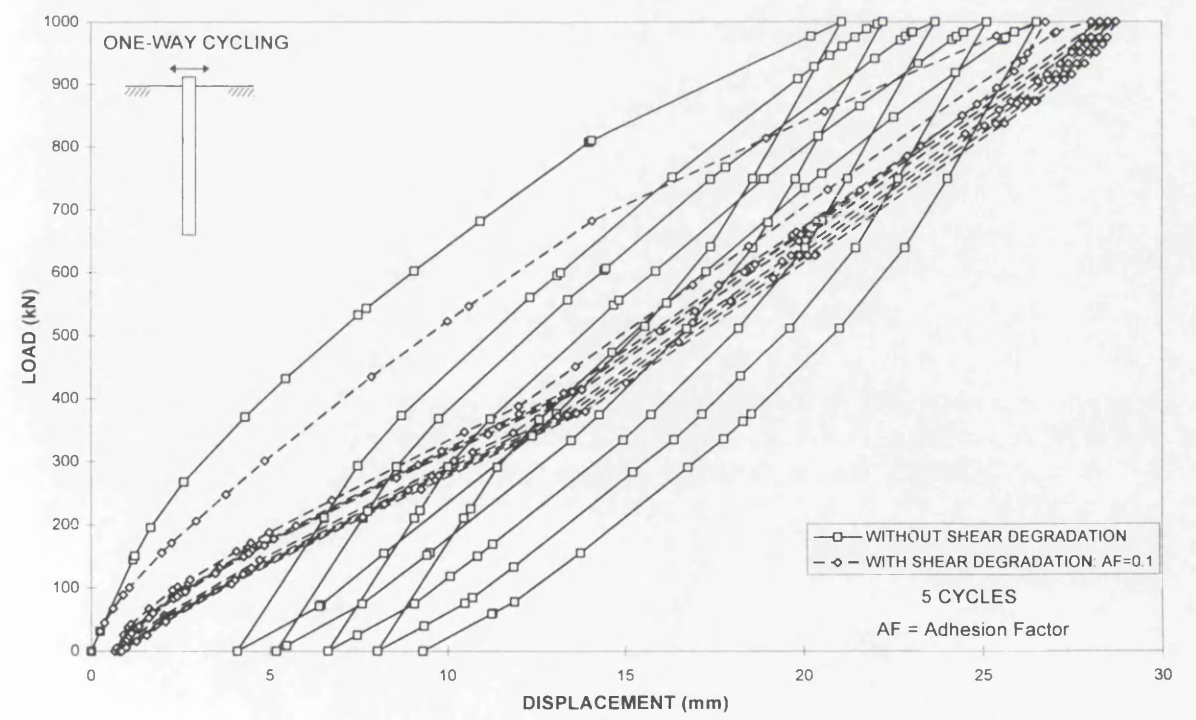


Figure 6.24 Pile-head load-displacement responses for one-way cyclic loading with and without shear strength degradation at low limit shear stress.

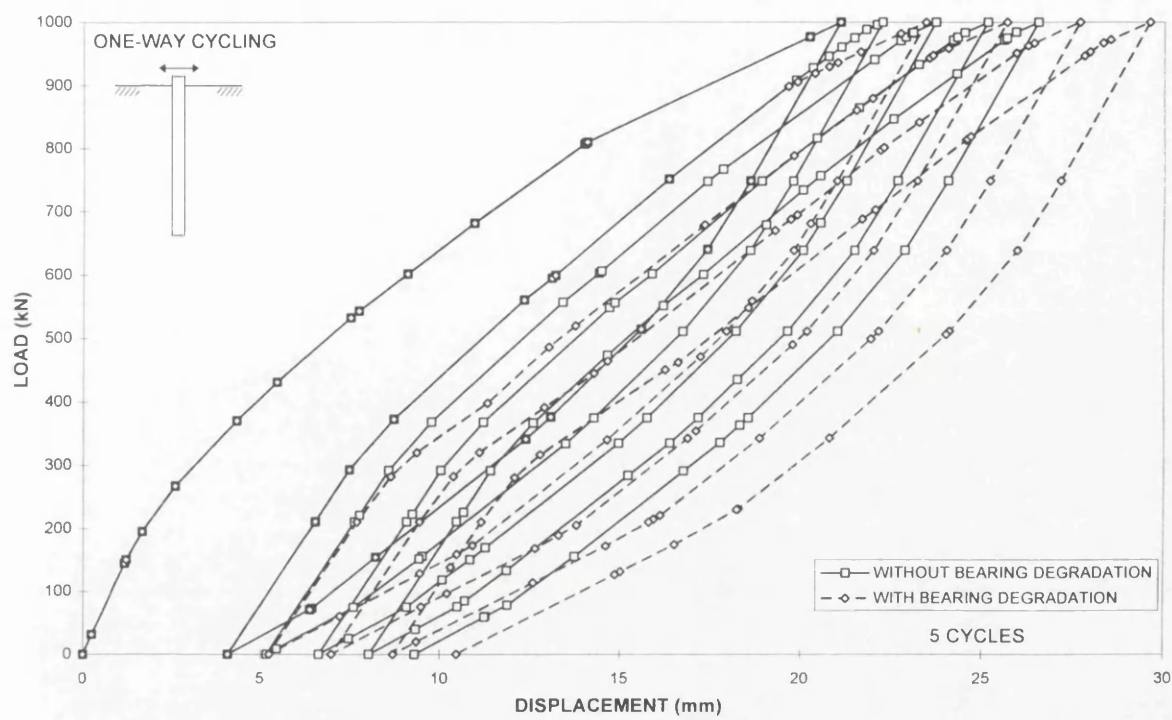


Figure 6.25 Pile-head load-displacement responses for one-way cyclic loading with and without bearing strength degradation.

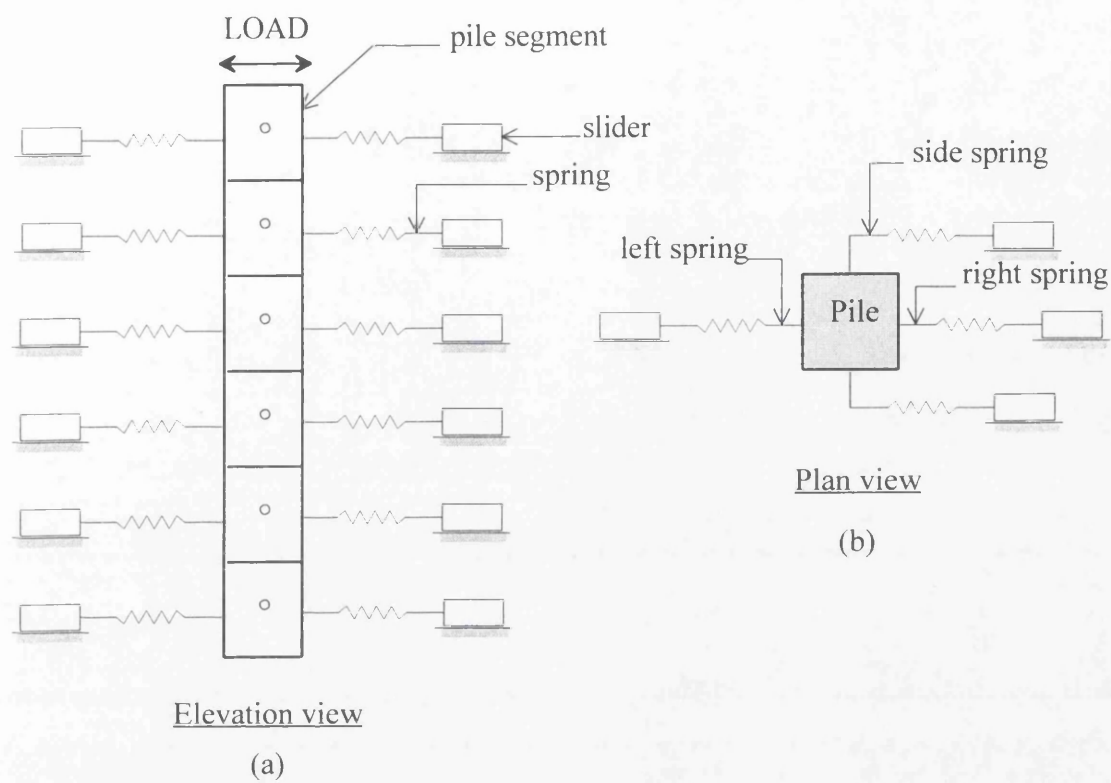


Figure 6.26 Beam-On-Spring (BOS) model.

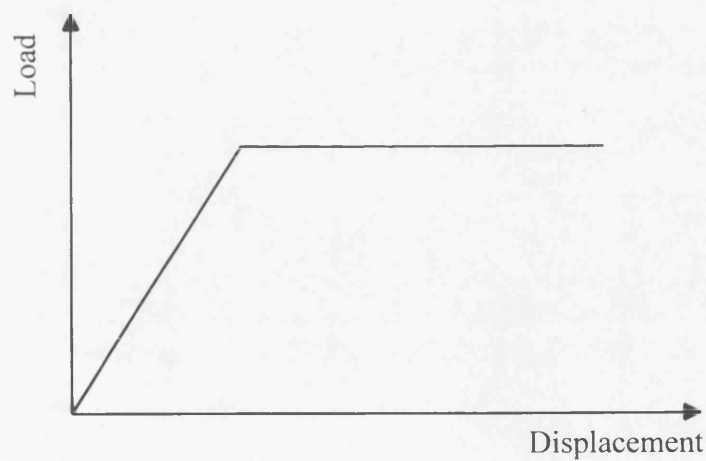


Figure 6.27 Elastic-perfectly plastic soil behaviour.

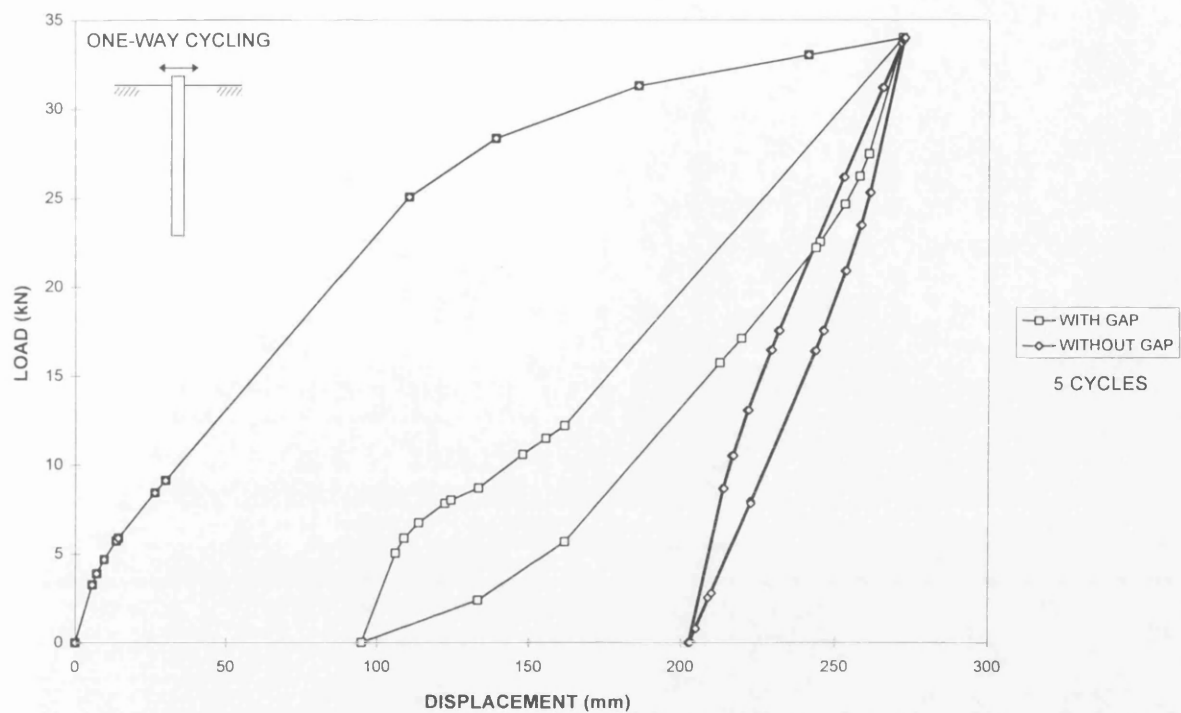


Figure 6.28 Pile-head load-displacement responses for one-way cyclic loading with and without gap formation using BOS model.

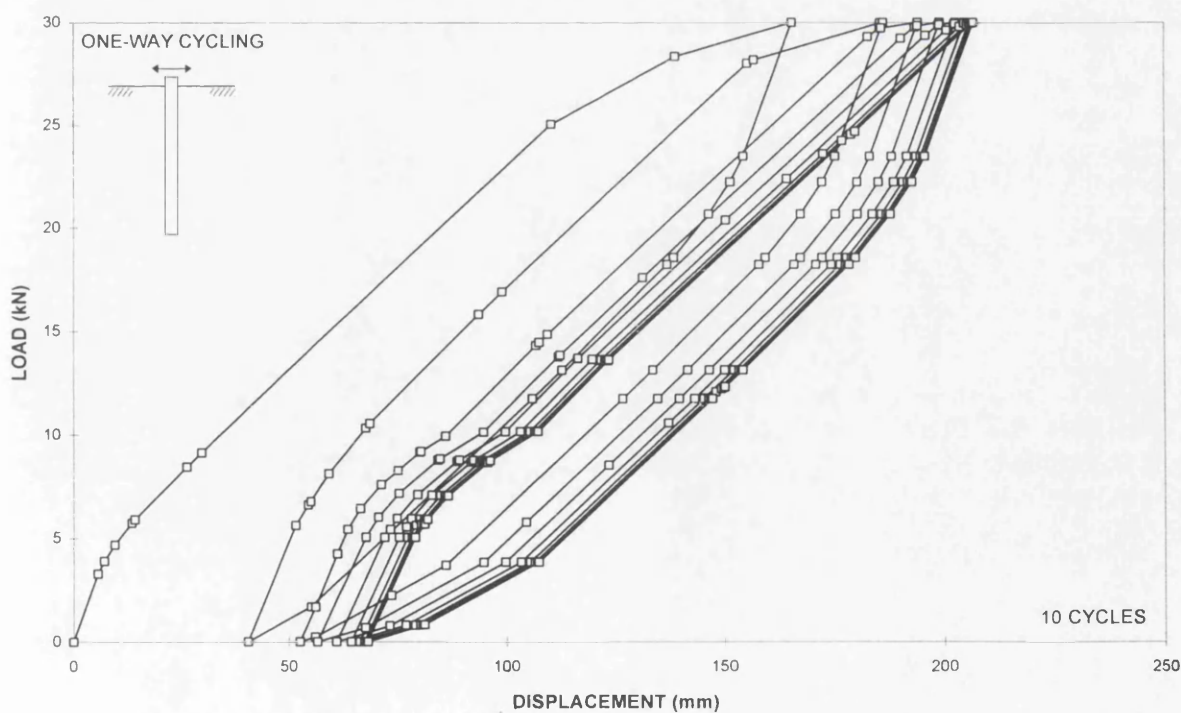


Figure 6.29 Pile-head load-displacement responses for one-way cyclic loading with gap formation and bearing strength degradation using BOS model.

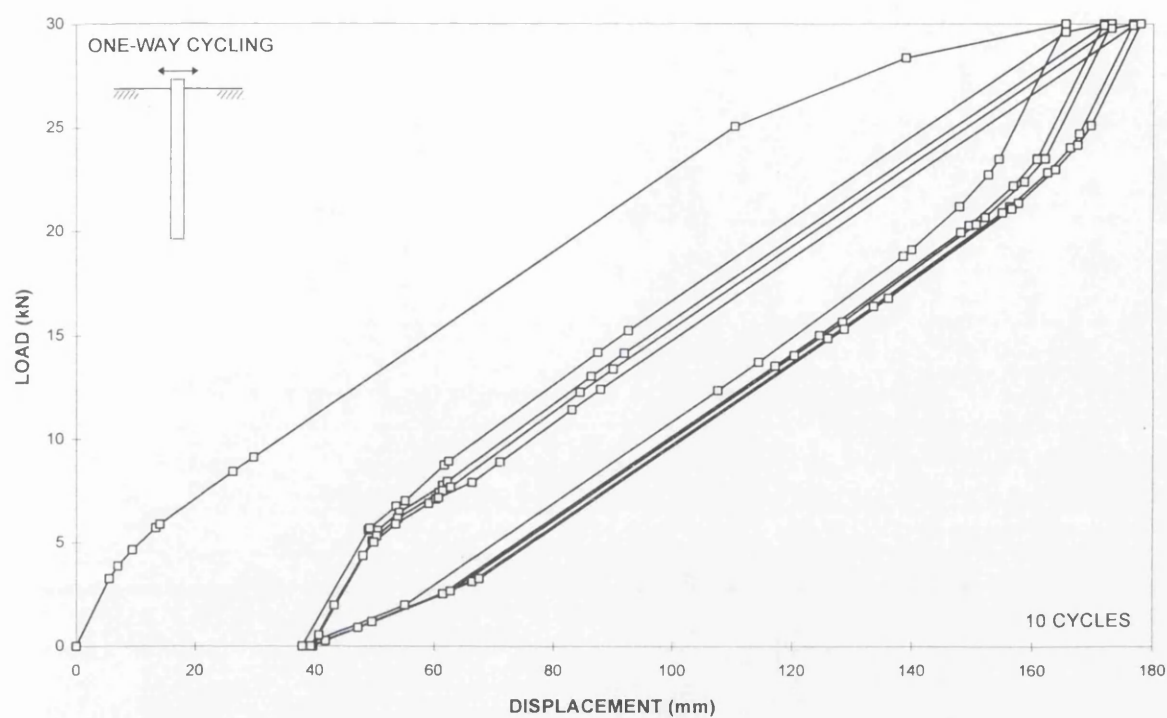


Figure 6.30 Pile-head load-displacement responses for one-way cyclic loading with gap formation and shear strength degradation using BOS model.

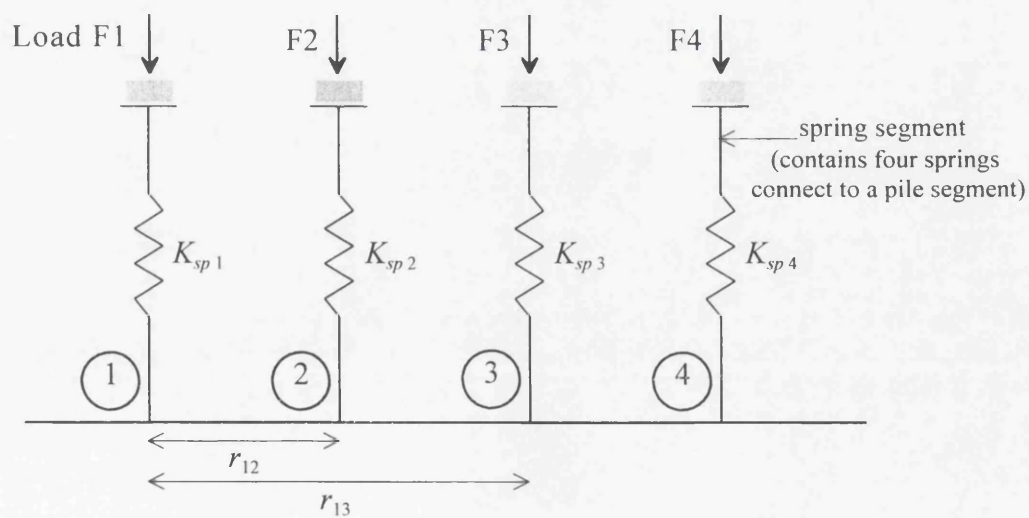


Figure 6.31 Distance between neighbouring spring segments for Beam-On-Interactive-Spring (BOIS) model.

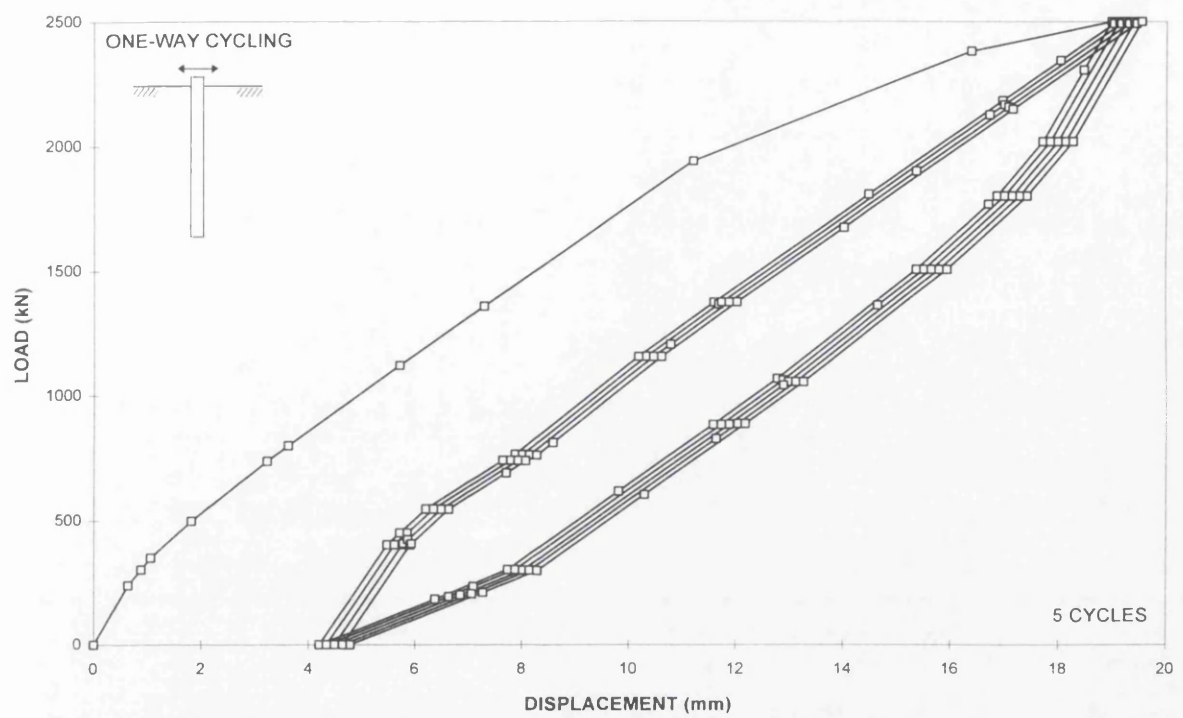


Figure 6.32 Pile-head load-displacement responses for one-way cyclic loading with gap formation using BOIS model.

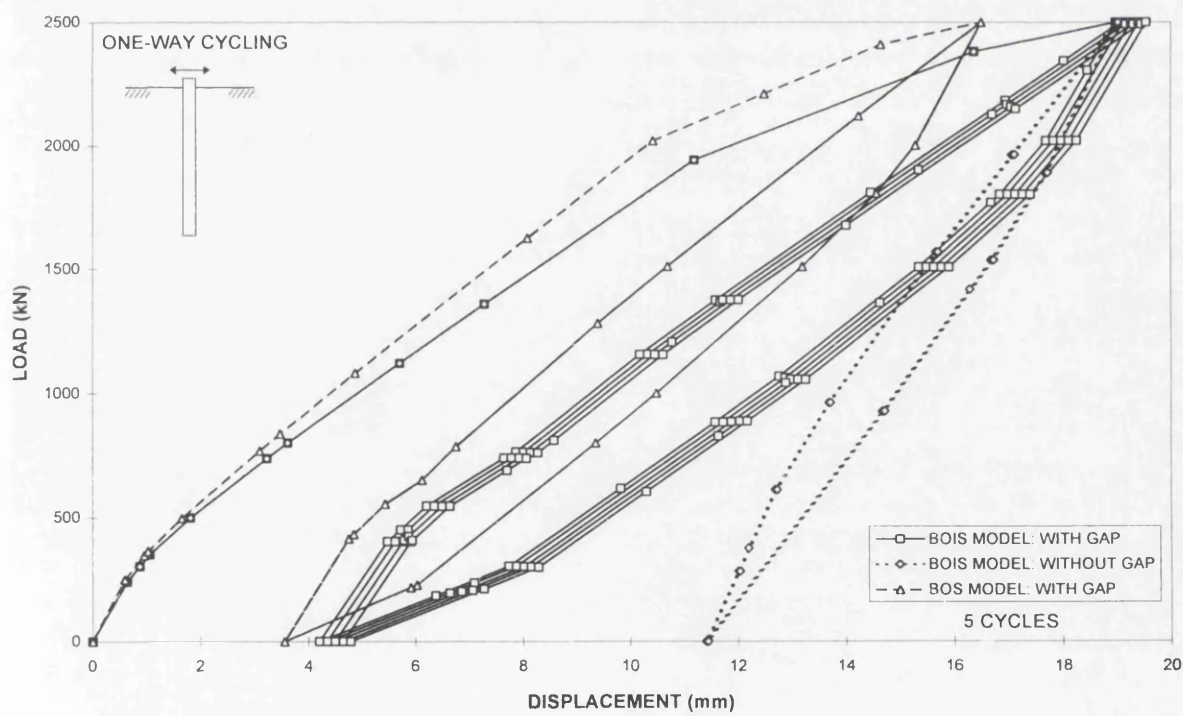


Figure 6.33 Pile-head load-displacement responses for one-way cyclic loading with and without gap formation using BOS and BOIS models.

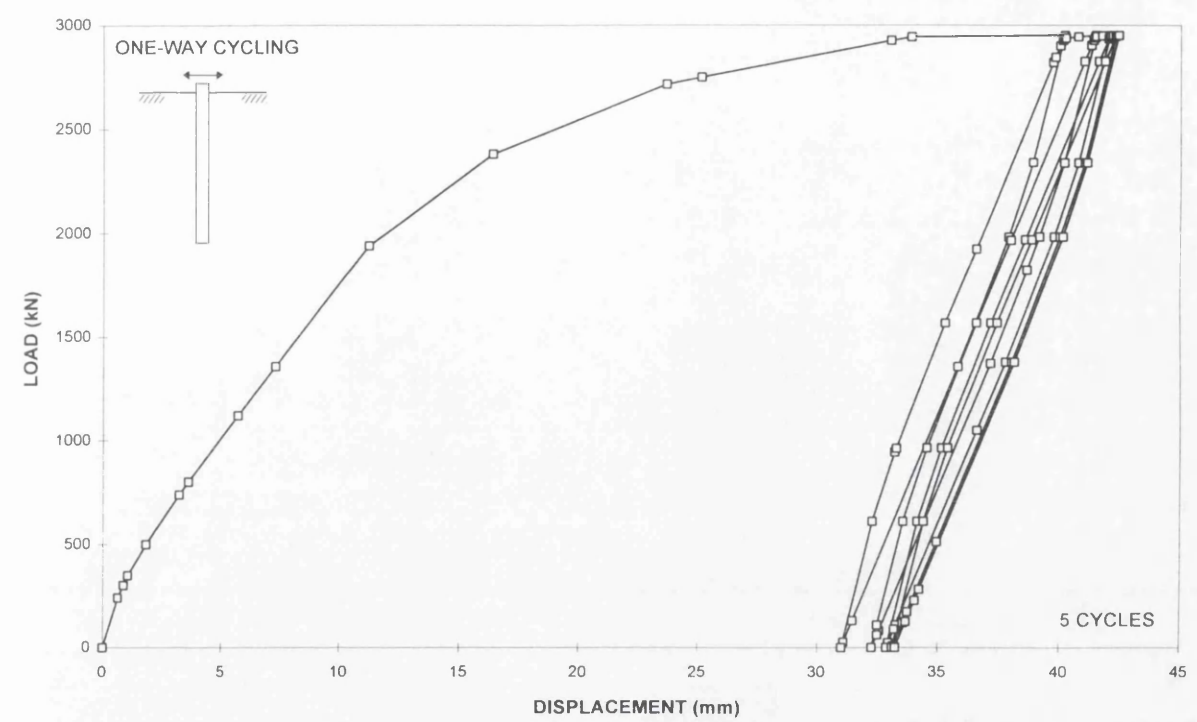


Figure 6.34 Pile-head load-displacement responses for one-way cyclic loading without gap formation at high load level using BOIS model.

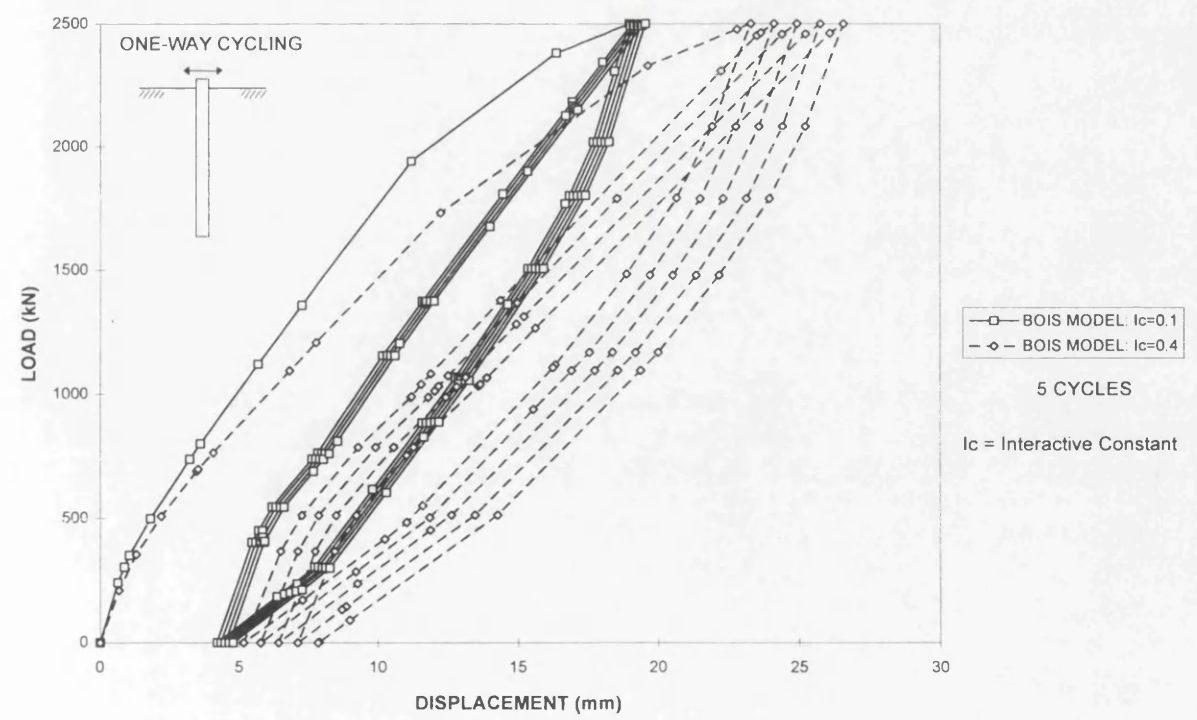


Figure 6.35 Comparison on the magnitude and rate of cyclic degradation with different interactive constant (I_c) for BOIS model.

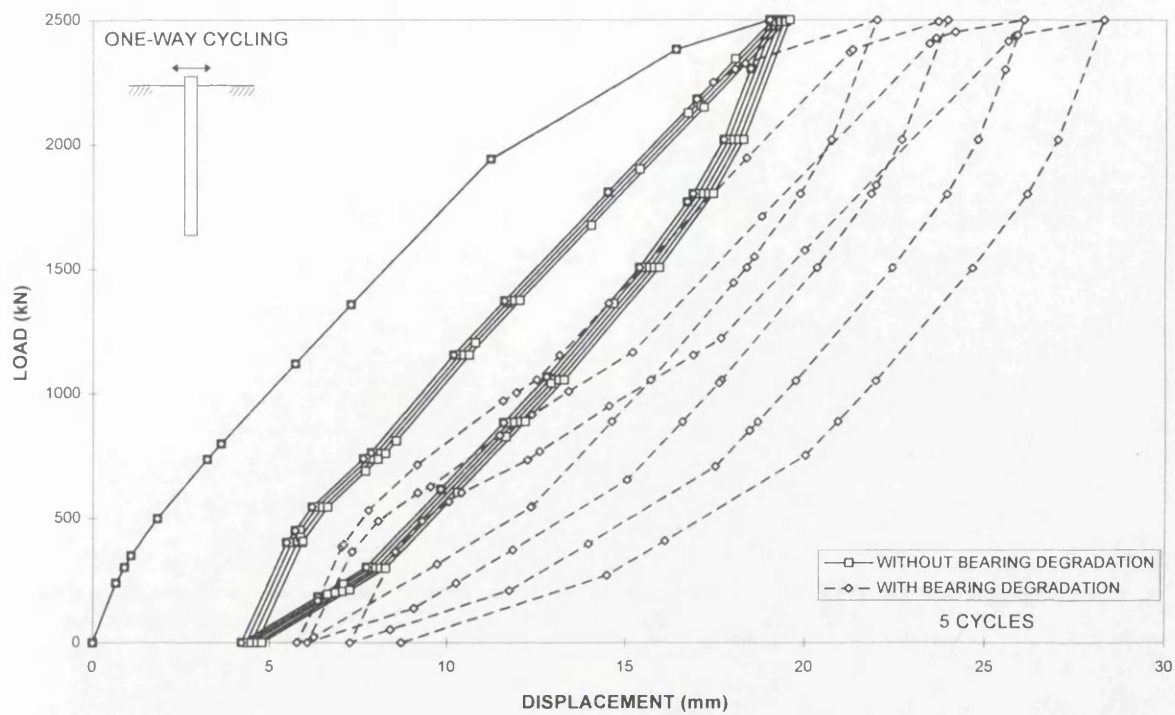


Figure 6.36 Pile-head load-displacement responses for one-way cyclic loading with gap formation and bearing strength degradation using BOIS model.

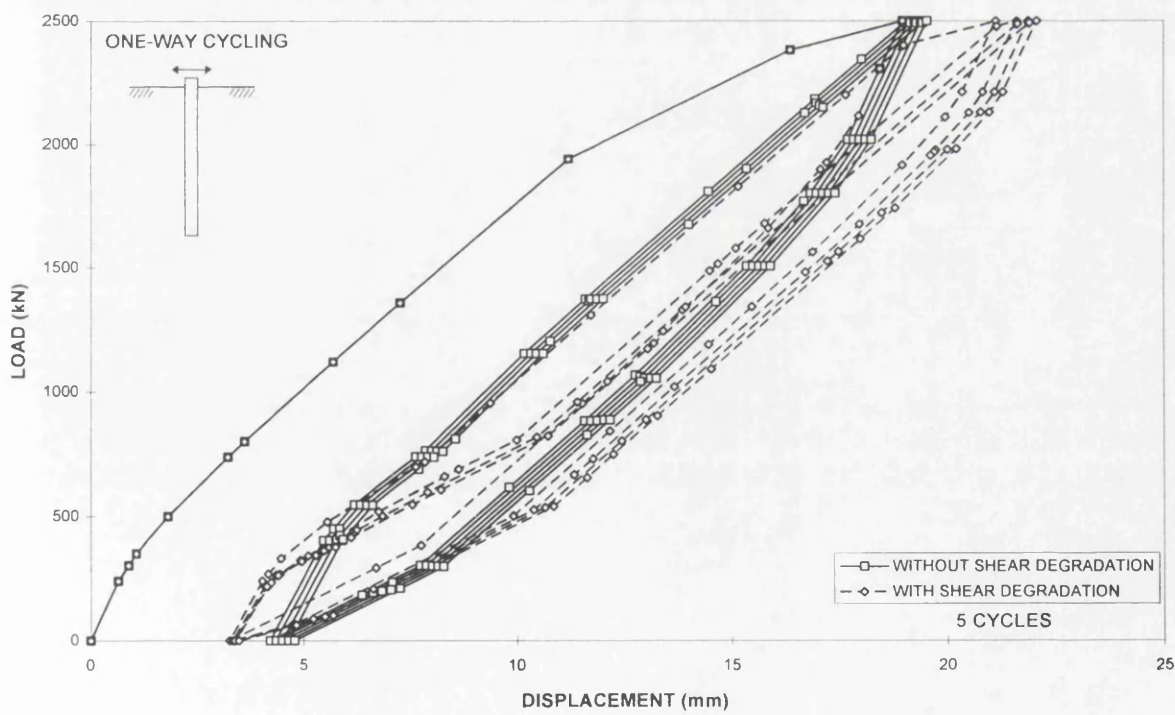


Figure 6.37 Pile-head load-displacement responses for one-way cyclic loading with gap formation and shear strength degradation using BOIS model.

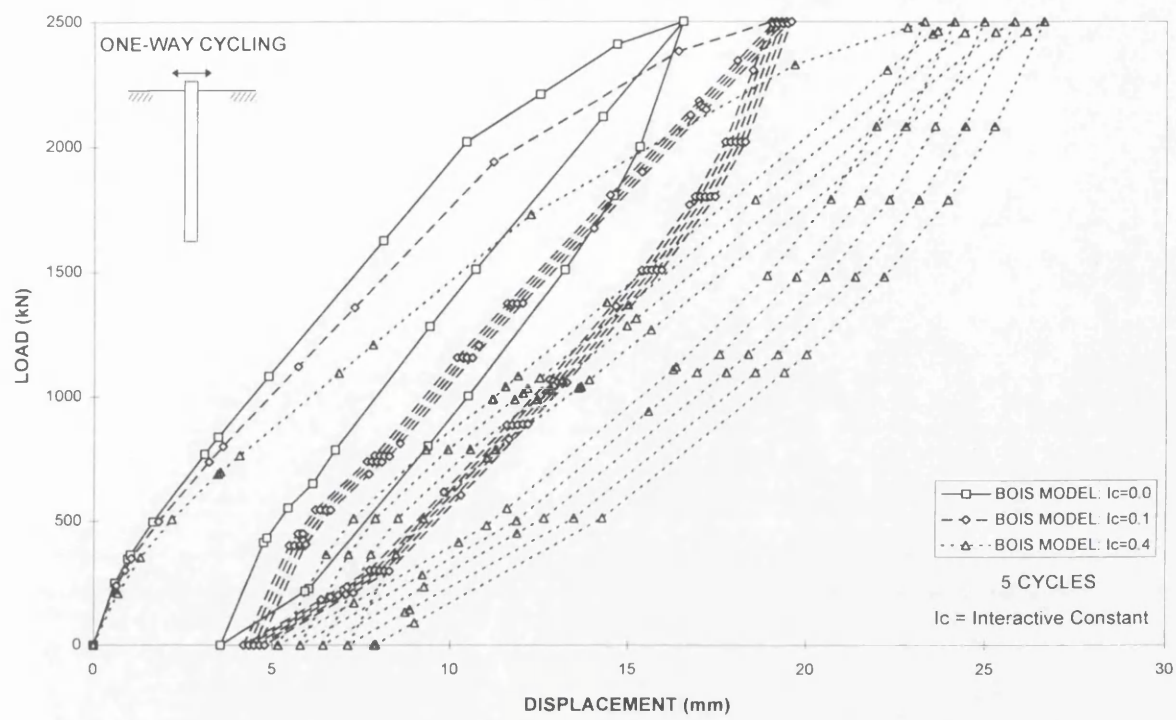


Figure 6.38 Comparison on the magnitude and rate of cyclic degradation with interactive constant $I_c = 0$ using BOIS model.

CHAPTER 7

Parametric Studies

7.1 Summary

7.2 Introduction

7.3 Pile discretisation

7.4 Standard parameters

7.5 Stiff clay

7.5.1 The effect of load levels

7.5.2 The effect of pile Young's modulus (E_p)

7.5.3 The effect of backsliding factor (β)

7.5.4 The effect of residual/peak bearing strength ratio (R_b)

7.5.5 The effect of bearing degradation rate factor (C_b)

7.5.6 The effect of residual/peak shear strength ratio (R_s)

7.5.7 The effect of shear strength degradation rate factor (C_s)

7.5.8 The effect of adhesion factor (α)

7.5.9 The effect of eccentric loading (e)

7.6 Soft clay

7.6.1 The effect of load levels

7.6.2 The effect of pile Young's modulus (E_p)

7.6.3 The effect of backsliding factor (β)

7.6.4 The effect of residual/peak bearing strength ratio (R_b)

7.6.5 The effect of bearing degradation rate factor (C_b)

7.6.6 The effect of residual/peak shear strength ratio (R_s)

7.6.7 The effect of shear strength degradation rate factor (C_s)

7.6.8 The effect of adhesion factor (α)

7.6.9 The effect of eccentric loading (e)

7.7 Discussion of results

7.8 Concluding remarks

CHAPTER 7

Parametric Studies

7.1 Summary

This Chapter begins with a study into the optimum pile discretisation for cyclic loading analyses. The main part of the Chapter contains the results of an extensive parametric study of the principal soil and pile variables and their effects on pile performance under cyclic loading conditions.

7.2 Introduction

There are many parameters that will influence the behaviour of piles subjected to cyclic lateral loading. Generally, these parameters can be classified into two categories. The first category contains the pile parameters, namely: pile Young's modulus, diameter, length, etc. The second category contains the soil parameters, namely: undrained shear strength, soil Young's modulus, adhesion factor, backsliding factor, etc. As the variations of these parameters are large, only major parameters will be explored here.

The parametric studies are based on free-head and fixed-head piles subjected to one-way cyclic loading under load-controlled conditions. The following parameters are examined:

- ♦ Pile Young's modulus,
- ♦ Backsliding factor,
- ♦ Residual/peak bearing strength ratio,
- ♦ Bearing degradation rate factor,
- ♦ Residual/peak shear strength ratio,
- ♦ Shear degradation rate factor,
- ♦ Adhesion factor, and
- ♦ Eccentricity of loading.

In addition, pile discretisation is studied to determine the optimum height to width ratio of each pile segment, such that computational efficiency with adequate accuracy is achieved.

The two main factors that govern the design of laterally loaded pile foundations are the (maximum) pile-head displacements and the maximum bending moments. The parametric studies which follow focus mainly on these two criteria.

7.3 Pile discretisation

An important practical aspect of this study was the requirement to limit the computational time, while retaining reasonable accuracy. In this section, the results of numerical experiments aimed at determining an optimal pile discretisation strategy were reported.

A pile (of length (L) = 20 m and diameter (D) = 1 m), was discretised into n segments of 10, 20, 30 and 40, yielding height to width ratios (h/D) for each pile segment of 2, 1, 0.67 and 0.5, respectively. The time taken to execute the APILEC program (using the Salford Fortran FTN77 compiler) and based on an IBM-compatible 80486 DX2-66 computer was determined.

The pile-head load-displacement results for different n segments are depicted in Figure 7.1. It is indicated that with higher n , the displacement (both maximum and residual) is lower. At the end of the ten cycles, it is shown in Figure 7.2, that the plastic zone (defined as zone with yielded soil elements) has extended to a pile depth of 10 m, (8 m, 7.37 m, 7.5 m) for n of 10, (20, 30, 40). The results indicate that with the increase in n , the depths of plastic zone and the percentage of soil yielding are lower (Figure 7.2), hence lower pile-head displacements can be anticipated as shown in Figure 7.1. An initial stiffer pile-head load-displacement response is due to the fact that the pile is discretised into more segments as evident in Table 7.1.

Figures 7.3a and 7.3b show the reduction in pile-head displacement and increase in maximum bending moment responses with increases in n , for up to ten cycles. The plot in Figure 7.4 shows the increase in the time taken for the analysis with increases in n segments.

Taking the results of $n = 40$ as the exact solution, Figure 7.3a shows that using n of 10, (20, 30) has overestimated the pile-head displacements by 14%, (9%, 4%) for the first cycle. Increasing the number of cycles to ten, the overestimation is reduced, with overestimation of 3%, (3%, 1%) for n of 10, (20, 30). Figure 7.3b shows that using n of 10, (20, 30) has overestimated the maximum bending moments by 1.8%, (1.1%, 0.3%) in the first cycle. With further cycling to the tenth cycle, the underestimation is 5.8%, (0.5%, 0.9%).

The relative errors, defined as $\left(\frac{\text{exact value} - \text{predicted value}}{\text{exact value}} \right)$, for pile-head displacements and maximum bending moments are shown in Table 7.2 and 7.3, respectively. Taking an error of approximately 5% or less as the allowable tolerance, suggests that 20 or 30 segments are necessary. From the computational (time) point of view (see Figure 7.4), twenty segments is probably an optimal choice, i.e. assuming an unit aspect ratio ($h/D = 1$).

From this study, it appears that the use of unit aspect ratio segments (as for static analyses) can be adopted for cyclic loading analyses, in order to obtain results of good accuracy without excessive computational costs.

7.4 Standard parameters

For piles subjected to lateral loading, the principal design criteria are the (maximum) pile-head lateral displacements and the maximum bending moments at the working load levels. The results of this study are presented in dimensionless forms. The advantage of presenting the results in this way is that the wide range of practical parameters can be presented in very few plots.

Since many parameters would be required to undertake a comprehensive study, only the major parameters that influence pile behaviour are explored here. In what follows, several non-dimensional groups are identified. The principal values (unless otherwise stated) of the parameters used in the subsequent parametric studies are as shown below.

Pile length	$L = 20 \text{ m}$
Pile diameter	$D = 1 \text{ m}$
Pile length-diameter ratio	$L/D = 20$
Eccentricity-diameter ratio	$e/D = 0$
Lateral earth pressure coefficient	$K_t = 1$
Buoyant soil unit weight	$\gamma = 10 \text{ kN/m}^3$
Backsliding factor	$\beta = 0$
Residual/peak shear strength ratio	$R_s = 0.5$
Shear strength degradation rate factor	$C_s = 0.5 \text{ mm}^{-1}$
Residual/peak bearing strength ratio	$R_b = 0.5$
Bearing strength degradation rate factor	$C_b = 50$

Stiff clay

Undrained shear strength	$C_u = 50 \text{ kPa}$
Soil Young's modulus	$E_s = 25 \text{ MPa}$
Load-strength ratio	$H/C_u D^2 = 10 \text{ (free-head)}$
(describes the load level)	$H/C_u D^2 = 20 \text{ (fixed-head)}$
Pile Young's modulus	$E_p = 25 \text{ GPa}$
Pile-soil stiffness ratio	$E_p/E_s = K' = 1000$
Soil stiffness-strength ratio	$E_s/C_u = 500$
Adhesion factor	$\alpha = 0.5$

Soft clay

Rate of increase in undrained shear strength	$c = 2 \text{ kPa/m}$
Rate of increase in soil Young's modulus	$m = 25 \text{ MPa/m}$
Load-strength ratio	$H/cD^3 = 150 \text{ (free head)}$
(describes the load level)	$H/cD^3 = 300 \text{ (fixed head)}$
Pile Young's modulus	$E_p = 10 \text{ GPa}$
Pile-soil stiffness ratio	$E_p/mD = K' = 5000$
Soil stiffness-strength ratio	$m/c = 1000$
Adhesion factor	$\alpha = 1$

Only ten cycles of loading are considered in these parametric studies. Further load cycles (usually of 50 to 100 cycles or more) can result, in some circumstances, in numerical instability which lead to apparently anomalous results.

7.5 Stiff clay

The 'stiff clay' model is intended to simulate the heavily consolidated clay conditions commonly encountered in many site situations. The undrained shear strength (C_u) and the Young's modulus (E_s) of the clays are assumed to be constant with depth.

In the following studies, the results are expressed in terms of normalised pile displacement $\left(\frac{\delta_{\max} E_s D}{H}\right)$ and normalised maximum bending moment $\left(\frac{M_{\max}}{HD}\right)$ against the parameters considered; where δ_{\max} , M_{\max} , H , and D , are the (maximum) pile-head displacement, maximum bending moment, lateral load and pile diameter, respectively.

7.5.1 The effect of load levels

Pile failure usually precedes soil failure. Yielding of a cylindrical cross section is initiated, in the absence of axial loading, when the bending moment at the section is:

$$M_y = \frac{\pi \sigma_y D^3}{32} \quad (7.1)$$

where σ_y is the yield stress of the material.

Collapse occurs only when the full section yields which requires a further increase in bending moment. For a cylindrical free-head pile subjected to lateral loading only, Davies and Budhu (1986) show that yielding of the pile section (in bending) begins when the normalised load level $\left(\frac{H}{C_u D^2}\right)$ is:

$$\frac{H_y}{C_u D^2} = \left(2 \frac{\sigma_y}{C_u}\right)^{0.5} \quad (7.2)$$

where H_y is the yield load.

For fixed-head piles, which can sustain much higher lateral loads than the free-head piles, the yield load can be taken as:

$$\frac{H_y}{C_u D^2} = \left(4 \frac{\sigma_y}{C_u}\right)^{0.5} \quad (7.3)$$

Taking a typical $\frac{\sigma_y}{C_u}$ value of 200, based on Equations (7.2) and (7.3), the yield load is $20C_u D^2$ for free-head piles and approximately $30C_u D^2$ for fixed-head piles.

Free-head piles

Loads of 5, 10, 15 and $20(C_u D^2)$ were employed to explore the effects of load levels on pile response. Figure 7.5a shows that increasing the loads causes an increase in the pile-head displacements, and Figure 7.5b shows an increase in the maximum bending moments. It is observed that the rate of cyclic degradation and the rate of increase in maximum bending moment with cycling, increased with increasing load levels. The above

results are because of the greater amounts of soil yielding taking place with increasing load levels.

The above Figures show that the second cycle has a considerable effect on the pile-head displacements and maximum bending moments. This is due to the fact that gaps are created by the first cycle, and hence the stiffness of the pile-soil system, in subsequent cycles, is lower. Comparing loads of $5C_u D^2$ with $10C_u D^2$, ($15C_u D^2$, $20C_u D^2$), Figure 7.5a shows that the pile-head displacements have increased by 1.5 times, (2.5 times, 3.2 times) for the tenth cycle. For maximum bending moments depicted in Figure 7.5b, the increase is 13%, (41%, 72%) for the tenth cycle. The effect of load levels is greater for pile-head displacements than for maximum bending moments.

Fixed-head piles

Loads of 5, 10, 20 and $30(C_u D^2)$ were used to examine the effect of increasing load levels. The pile-head displacement and maximum bending moment results depicted in Figures 7.6a and 7.6b, respectively, show that at the low load level of $5C_u D^2$, the pile responds elastically. At higher load levels of $10C_u D^2$ to $30C_u D^2$, cyclic degradation and increase in maximum bending moments with cycling occur, and the rate of increase is higher with increasing load levels (reasons as explained for the free-head piles). Increasing the load from $5C_u D^2$ to $10C_u D^2$, ($20C_u D^2$, $30C_u D^2$), increases the pile-head displacements by 1.6 times, (2.2 times, 2.9 times) and the maximum bending moments by 33%, (45%, 69%) for the tenth cycle. The effect of load levels is greater for pile-head displacements than for maximum bending moments.

Comparing the influence of pile-head conditions for pile-head displacements (Figures 7.5a and 7.6a) at cycles 1 and 10 under a load of $20C_u D^2$, indicates that the fixed head pile has undergone lesser pile-head displacements than free-head piles by 2.6 times for the first cycle and 3.8 times for the tenth cycle. This is due to the fact that the pile-head is restrained against rotation for fixed-head piles. For bending moment comparison, the fixed-head piles show lower maximum positive bending moments (not shown in figure) than free-head piles by 3.1 times for the first cycle and 3.6 times for the tenth cycle. The maximum negative bending moments shown in Figure 7.6b are the restrained moments at the pile-head. Comparing the maximum bending moments which the pile is experiencing (regardless whether it is positive or negative), it is observed that the fixed-head piles experience higher

maximum bending moments than the free-head piles with cycling; compare Figures 7.5b and 7.6b.

The results of the free-head and fixed-head piles, have indicated that provision of restraint at the pile-head, will effectively decrease the pile-head displacements as well as the maximum positive bending moments of the piles. However, precautions have to be taken to ensure that the maximum negative bending moment at the pile-head of fixed-head piles does not exceed the yield moment

7.5.2 The effect of pile Young's modulus (E_p)

For this parametric study, the pile-soil stiffness ratio ($K' = E_p/E_s$) of 250, 1000, 2000 and 4000 were considered. The soil Young's modulus (E_s) is assumed to remain constant, while the pile Young's modulus (E_p) varies. Piles with lower E_p are more flexible than those with higher E_p .

Free-head piles

Figure 7.7a shows the decrease in pile-head displacements as E_p increases. It is observed that a slower rate of cyclic degradation, is associated with the higher E_p . Such results are because of the increase in the stiffness of the pile-soil system as E_p increases, resulting in the lower amount of soil yielding. Increasing K' from 250 to 500, (1000, 2000, 4000) reduces the pile-head displacements by 24%, (58%, 66%, 73%) for the tenth cycle. Further increase in E_p from $2000E_s$ to $4000E_s$ does not show significant reduction in the pile-head displacements. This is due to the fact that the stiffness of the pile-soil system is already very high at $E_p = 2000E_s$, and therefore further increase in E_p only reduces the pile-head displacements slightly. This is why hollow steel piles (with appropriate E_p) are more commonly used than solid steel piles, where the latter E_p is obviously higher and more economical.

Though the lower E_p results in the increase in the pile-head displacements, it causes lower maximum bending moments as depicted in Figure 7.7b. This is because E_p is directly proportional to bending moment and inversely proportional to displacement. Increasing K' from 250 to 500, (1000, 2000, 4000) results in the increase in the maximum bending moments by 15%, (15%, 39%, 68%) for the tenth cycle. It is observed that the rate of increase in maximum bending moment with cycling, is higher for $E_p = 250E_s$ than for $E_p = 1000E_s$.

This is in consequence of the large pile-head displacements for low E_p , as a result of large amount of soil yielding. The large increase in the maximum bending moment from cycles 5 to 10 for $K' = 500$ (point A in Figure 7.7b), is due to the change in pile depth position (from 3 to 4 m) at which the maximum bending moment occurs.

Fixed-head piles

Similar trends of pile responses in terms of pile-head displacements and maximum bending moments for free-head piles (Figure 7.7) are observed for fixed-head piles (Figure 7.8). The only difference, is that the phenomenon of large increase in the maximum bending moment from cycles 5 to 10 for $K' = 500$ is not seen. It is indicated that the effect of E_p is greater for pile-head displacements than for maximum bending moments for both free-head and fixed-head piles.

7.5.3 The effect of backsliding factor (β)

The backsliding factor (β) is used to increase the yield stress for tension for the soil according to Equations (6.4) and (6.10). Soils with high β is indicative of high adhesive strength. In this parametric study, β of 0.0, 0.1, 0.2 and 0.5 were considered.

Free-head piles

Increase in β reduces the pile-head displacements and maximum bending moments as depicted in Figures 7.9a and 7.9b, respectively. This is because of the lesser soil elements yielding in tension, which reduce the gap sizes, as the yield stress for tension for the elements is increased. Increasing β from 0.0 to 0.1, (0.2, 0.5) decreases the pile-head displacements by 3%, (5%, 17%) and the maximum bending moments by 1%, (1%, 7%) at the fifth cycle. It is observed that the rate of cyclic degradation and the rate of increase in maximum bending moment with cycling, are similar for all values of β for up to five cycles. With further cycling, say at the tenth cycle, it is noted that the pile-head displacements and maximum bending moments for $\beta = 0.1$ and 0.2 are greater than $\beta = 0.0$. The reason for such occurrence is unclear. It is indicated that the effect of β on both the pile-head displacements and the maximum bending moments is negligible for $\beta = 0.1$ and 0.2. This suggests that the parameter β can be ignored as β rarely exceeds 0.2.

Fixed-head piles

Similar trends of pile responses in terms of pile-head displacements and maximum bending moments for free-head piles (Figure 7.9) are observed for fixed-head piles (Figure 7.10). The differences are that the rate of cyclic degradation and the rate of increase in maximum bending moment with cycling, are similar for all values of β for up to ten cycles. The phenomenon of pile-head displacements and maximum bending moments for $\beta = 0.1$ and 0.2 greater than $\beta = 0.0$ is not produced.

7.5.4 The effect of residual/peak bearing strength ratio (R_b)

For this study, residual/peak bearing strength ratio (R_b) of 0.1, 0.2, 0.5 and 1.0 were considered. This simulates the degradation of bearing strength of the soil at the front face of an advancing pile by 90%, 80%, 50% and 0%, respectively. Soils with high R_b , i.e. approaching unity suffer very little bearing strength degradation after peak. Conversely, a low R_b is indicative of low residual bearing strength.

Free-head piles

The results for pile-head displacements and maximum bending moments under a load of $10C_u D^2$ (full line) are shown in Figures 7.11a and 7.11b, respectively. They show the effect of R_b is negligible. As such, the load is increased to $20C_u D^2$ (dotted line). With this higher load, the reduction in R_b gives higher pile-head displacements and maximum bending moments. This is because of the greater amount of soil yielding taking place as a result of the larger degradation in the bearing strength of the soil. This is also reflected in the higher rate of cyclic degradation, and the higher rate of increase in maximum bending moment with cycling, for lower R_b . Reducing R_b from 1.0 to 0.5, (0.2, 0.1) causes an increase in the pile-head displacements by 1.2 times, (1.8 times, 2.8 times), and the maximum bending moments by 1.2 times, (1.8 times, 2.2 times) for the tenth cycle. The effect of R_b is greater for pile-head displacements than for maximum bending moments. Note that the effect of R_b usually applies after the first loading cycle, when the elements have recovered from plastic to elastic.

Fixed-head piles

Under a load of $20C_u D^2$ (full line), Figures 7.12a and 7.12b show that R_b has virtually no effect on the pile-head displacements and maximum bending moments. As such, the load is increased to $30C_u D^2$ (dotted line). With this increase in load, Figures 7.12a and 7.12b show similar pile responses as for the free-head piles (see Figure 7.11). The difference is that the rate of cyclic degradation and the rate of increase in maximum bending moment with cycling, is lower for fixed-head than for free-head piles, due to lesser soil yielding.

From the analyses of free-head and fixed-head piles under loads of $20C_u D^2$ and $30C_u D^2$, respectively, it is indicated that the effect of R_b is more significant at higher load levels. At load levels less than $10C_u D^2$ and $20C_u D^2$ for free-head and fixed-head piles, respectively, the parameter R_b can be safely ignored.

7.5.5 The effect of bearing degradation rate factor (C_b)

The bearing degradation rate factor (C_b) quantifies the rate of bearing strength degradation of soil after peak. For this study, C_b of 10, 20, 50 and 100 are considered. This is to simulate slow ($C_b = 10$ and 20), medium ($C_b = 50$) and fast ($C_b = 100$) rates of bearing strength degradation.

Free-head piles

The effect of C_b on pile-head displacements and maximum bending moments are depicted in Figures 7.13a and 7.13b, respectively. They show that for a low load level of $10C_u D^2$ (full line), the effect of C_b is negligible. At a higher load level of $20C_u D^2$ (dotted line), the pile-head displacements and maximum bending moments increase with C_b . This is because of the greater amount of soil elements yielding in bearing, as the bearing strength is degraded more rapidly for higher C_b .

It is observed that the rate of cyclic degradation and the rate of increase in maximum bending moment with cycling, increases with increasing C_b (up to $C_b = 50$). There is very little difference between the results for C_b greater than 50. This is because for low C_b (10 and 20), the bearing strength of the soil elements lie between the peak strength and residual strength. For high C_b (greater than 50), the bearing strength of the soil elements is at the residual strength.

It is indicated that when C_b increases from 10 to 20, (50, 100) the pile-head displacements are increased by 1%, (15%, 16%), and the maximum bending moments

increased by 3%, (17%, 22%) for the tenth cycle. The results suggest that C_b has greater effect on the maximum bending moments than the pile-head displacements.

Fixed-head piles

Under a load of $20C_u D^2$ (full line), C_b has negligible effect on pile-head displacements and maximum bending moments as seen in Figures 7.14a and 7.14b. Increasing the load up to $30C_u D^2$ (dotted line) did not cause significant changes to the pile-head displacements and maximum bending moments. It is observed that the rate of cyclic degradation and the rate of increase in maximum bending moment with cycling, are not significantly influenced by C_b . This is because the residual bearing strength of the soil elements has been reached at $C_b = 50$ and 100, and closely reached at $C_b = 10$ and 20, due to large residual bearing displacements. A slight increase in pile-head displacements (less than 3%) and maximum bending moments (less than 5%) of up to ten cycles were experienced, when C_b increased from 10 to 100. The results suggest that C_b has greater effect on the maximum bending moments than the pile-head displacements.

From the above evaluation, it is observed that C_b has greater effect on free-head than fixed-head piles, when the piles are subjected to load levels close to their yield loads (described in Section 7.5.1). Note that the effect of C_b usually applies after the first loading cycle, when the elements have recovered from plastic to elastic.

7.5.6 The effect of residual/peak shear strength ratio (R_s)

For this parametric study, residual/peak shear strength ratio (R_s) of 0.1, 0.2, 0.5 and 1.0 were considered. This simulates the degradation of shear strength of the soil at the side face of the pile by 90%, 80%, 50% and 0%, respectively. Soils with high R_s , i.e. approaching unity suffer very little shear strength degradation after peak. Conversely, a low R_s is indicative of low residual shear strength.

Free-head piles

Figures 7.15a and 7.15b show that reducing R_s causes the pile-head displacements and maximum bending moments to increase, due to greater amount of soil yielding as a result of greater degradation in the shear strength. It is observed that the pile responds elastically for $R_s = 1.0$, while cyclic degradation occurs for $R_s < 1.0$. This is because shear strength degradation

is allowed for $R_s < 1.0$, and therefore the shear strength is reduced for each reloading and unloading cycle. Decreasing R_s from 1.0 to 0.5, (0.2, 0.1) increases the pile-head displacements by 31%, (67%, 59%) for the tenth cycle. It is observed in the tenth cycle, that the pile-head displacement for $R_s = 0.2$ (point *A* in Figure 7.15a) is greater than for $R_s = 0.1$. This is because the rate of cyclic degradation is higher for $R_s = 0.2$ than for $R_s = 0.1$ after the fifth cycle when the residual strength of the soil for $R_s = 0.1$ is reached; see Figure 7.15c.

The maximum bending moment results depicted in Figure 7.15b show that reducing R_s from 1.0 to 0.5, (0.2, 0.1) increases the moment by 11%, (20%, 19%) for the tenth cycle. The higher maximum bending moments predicted for $R_s = 0.2$ than for $R_s = 0.1$, is a consequence of the pile-head displacement responses (Figure 7.15a).

The above results show that the effect of R_s is greater for pile-head displacements than for maximum bending moments. The effect of R_s is seen after the first loading cycle, when the elements have recovered from plastic to elastic.

Fixed-head piles

Figures 7.16a and 7.16b show that reducing R_s causes the pile-head displacements and maximum bending moments to increase (reasons as explained for free-head piles). It is observed that the rate of cyclic degradation and the rate of increase in maximum bending moment with cycling, is higher for lower R_s . This is due to the fact that higher shear strength degradation is allowed for the soil elements. However, with further cycling of up to five cycles, the rate of cyclic degradation for $R_s = 0.2$ and 0.5, is higher than $R_s = 0.1$ when the residual strength of the elements is about to be reached. Comparing the pile-head displacements for $R_s = 1.0$ with 0.5, (0.2, 0.1) show an increase of 27%, (29%, 29%) for the tenth cycle. For maximum bending moments, the increase is 8%, (11%, 11%) for the tenth cycle. The effect is greater for pile-head displacements than for maximum bending moments.

The phenomenon of $R_s = 0.2$ having greater pile-head displacements and maximum bending moments than $R_s = 0.1$ at the tenth cycle (as for the case of free-head piles; see Figures 7.15a and 7.15b) was not observed in Figures 7.16a and 7.16b. However, with further cycling, say for twenty cycles, such phenomenon may occur.

7.5.7 The effect of shear strength degradation rate factor (C_s)

The shear strength degradation rate factor (C_s) is to quantify the rate of shear strength degradation of soil after passing its peak. In this parametric study, C_s of 0.1, 0.2, 0.5 and 1.0 were considered. This simulates slow ($C_s = 0.1$ and 0.2), medium ($C_s = 0.5$) and fast ($C_s = 1.0$) rates of shear strength degradation.

Free-head piles

Figures 7.17a and 7.17b show that increasing C_s results in the increase in the pile-head displacements and maximum bending moments. This is because of a greater amount of soil yielding taking place as the rate of shear strength degradation is increased, especially for cycles 2 and 5. At the tenth cycle, the effect of C_s is negligible, as the residual strength of the soil elements is reached, regardless of the rate specified, due to large plastic shear displacement. Note that the effect of C_s usually applies after the first loading cycle, when the elements have recovered from plastic to elastic.

Fixed-head piles

Similar trends of pile responses in terms of pile-head displacements and maximum bending moments for free-head piles (Figure 7.17) are observed for fixed-head piles (Figure 7.18).

From the above evaluation, it may suggest that the parameter C_s can be safely ignored for the analysis of free-head and fixed-head piles under loads of $10C_u D^2$ and $20C_u D^2$, respectively.

7.5.8 The effect of adhesion factor (α)

The adhesion factor (α) is used to determine the limit shear stress of the soil elements at the side faces of the pile according to Equations (6.2). For the purpose of this parametric study, four values were considered, namely: 0.1, 0.2, 0.5 and 1.0.

Free-head piles

A reduction in α increases the pile-head displacements and the maximum bending moments for cycles 1 to 5, as depicted in Figures 7.19a and 7.19b, respectively. This is because of the greater amount of soil yielding taking place as a result of lower limit shear stress. However, with the increase in cycling, $\alpha = 0.2$ (point A in Figure 7.19a) gives higher

pile-head displacements than $\alpha = 0.1$. This is due to the higher rate of cyclic degradation for $\alpha = 0.2$ than for $\alpha = 0.1$ (see Figure 7.19c). The maximum bending moment for $\alpha = 0.2$ is higher than for $\alpha = 0.1$, as a consequence of the pile-head displacement responses. Reducing α from 1.0 to 0.5, (0.2, 0.1) increases the pile-head displacements by 29%, (60%, 52%), and the maximum bending moments by 5%, (17%, 14%) for the tenth cycle. The effect of α is greater for pile-head displacements than for maximum bending moments.

Fixed-head piles

The increase in the pile-head displacements and maximum bending moments with the reduction in α is clearly shown in Figures 7.20a and 7.20b, for cycles 1 and 2 (reasons as explained for the free-head piles). With further cycling, $\alpha = 0.1$ and 0.2 has stabilised to an alternating plasticity response. It is observed in the tenth cycle, that the maximum pile-head displacements for $\alpha = 0.5$ is greater than for $\alpha = 0.2$. This is because of the higher rate of cyclic degradation for higher α . Reducing α from 1.0 to 0.5, (0.2, 0.1) increases the pile-head displacements by 24%, (21%, 26%) and the maximum bending moments by 6%, (10%, 10%) for the tenth cycle. The effect of α is greater for pile-head displacements than for maximum bending moments.

7.5.9 The effect of eccentric loading (e)

Eccentric loading (e) decreases the lateral capacity of the pile due to the increase in bending moments in the pile. The eccentricity of 0.0, 0.5, 1.0 and 2.0D (D is the pile diameter) will be examined in this study.

Free-head piles

An increase in e causes the pile-head displacements and maximum bending moments to increase, as depicted in Figures 7.21a and 7.21b, respectively. This is because of greater soil yielding as a result of the increase in the bending moments in the piles. This is also reflected in the rate of cyclic degradation and the rate of increase in maximum bending moment with cycling. The above Figures show that increasing e from zero to 0.5D, (1.0D, 2.0D) increases the pile-head displacements by 1.7 times, (2.2 times, 3.2 times) and the maximum bending moments by 1.4 times, (1.6 times, 2.1 times) for the tenth cycle. The

results show that the effect of eccentricity is greater for pile-head displacements than for maximum bending moments.

Fixed-head piles

It is assumed in APILEC analysis that eccentric loading does not have any effect on the fixed-head piles. As such, the effect of eccentricity is not examined.

7.6 Soft clay

The 'soft clay' model is intended to simulate the normally consolidated (or lightly-overconsolidated) clay conditions encountered in many site situations, where the undrained shear strength of the clay increases linearly with depth.

In the following studies, the normalised displacement $\left(\frac{\delta_{\max} m D^2}{H}\right)$ and normalised maximum bending moment $\left(\frac{M_{\max}}{H D}\right)$ are plotted against the parameters concerned; where δ_{\max} , M_{\max} , H , m and D are the (maximum) pile-head displacement, maximum bending moment, lateral load, rate of increase in soil Young's modulus and pile diameter, respectively.

7.6.1 The effect of load levels

In practice, most piles fail by yielding of the pile section (in bending) itself, well before the load capacity of the surrounding soil. Following Brom's (1964) limit-equilibrium approach, Budhu and Davies (1988) showed that the horizontal load at yield for free-head piles is:

$$\frac{H_y}{cD^3} = 0.5 \left(\frac{\sigma_y}{cD} \right)^{\frac{2}{3}} \quad (7.6)$$

For fixed-head piles, the yield load is:

$$\frac{H_y}{cD^3} = 0.8 \left(\frac{\sigma_y}{cD} \right)^{\frac{2}{3}} \quad (7.7)$$

Taking a typical value $\frac{\sigma_y}{cD}$ of 10000, based on Equations (7.6) and (7.7), the yield load is around $200cD^3$ for free-head piles and $400cD^3$ for fixed-head piles.

Free-head piles

Loads of 50, 100, 150 and 200(cD^3) were used to examine the effect of load levels on pile responses. Figures 7.22a and 7.22b show that the pile-head displacements and maximum bending moments increase with load levels and cycling, as a result of the increase in soil yielding. It is shown that the second cycle has a considerable effect on the pile-head displacements and maximum bending moments. This is due to the fact that gaps are created by the first cycle, and hence the stiffness of the pile-soil system in subsequent cycles is lower. At a low load of $50cD^3$, the pile stabilised to an alternating plasticity response. At load levels higher than $100cD^3$, cyclic degradation is observed and the rate is higher with an increase in load levels, due to the larger amount of soil yielding taking place. The rate of increase in the maximum bending moment with cycling, is as a consequence of the pile-head displacements. Increasing the load from $50cD^3$ to $100cD^3$, ($150cD^3$, $200cD^3$) gives an increase in the pile-head displacements by 1.3 times, (1.8 times, 2.9 times) and the maximum bending moments by 20%, (52%, 81%) for the tenth cycle. The effect of load levels is greater for pile-head displacements than for maximum bending moments.

Fixed-head piles

Similar trends of pile responses in terms of pile-head displacements and maximum bending moments for free-head piles (Figure 7.22) are observed for fixed-head piles (Figure 7.23).

The comparison of free-head with fixed-head pile results under a load of $200cD^3$, shows that the use of fixed-head piles instead of a free-head piles, reduces the pile-head displacements by 77% for the first cycle and 82% for the tenth cycle. For the maximum bending moments (ignoring positive or negative), the reduction is 17% and 27% for the first and tenth cycle, respectively. From the above evaluation, we can deduce that fixing the pile-head will definitely improve the lateral load capacity of the pile.

7.6.2 The effect of pile Young's modulus (E_p)

For this parametric study, the pile-soil stiffness ratio K' (E_p/mD) of 1000, 2000, 5000, 10000 and 20000 are considered. With mD (m is the rate of increase in Young's modulus and

D is the pile diameter) remains constant, E_p is varied accordingly. Piles with lower E_p are more flexible.

Free-head piles

Figure 7.24a shows that the pile-head displacements are increasing with reduction in E_p or K' , due to the increase in soil yielding as a result of reduction in the pile-soil system stiffness. It is observed that for $K' = 10000$ and 20000 , the piles stabilised to an alternating plasticity response as the stiffness of the pile-soil system is very high. Cyclic degradation occurs at K' less than 5000 , with higher rate of cyclic degradation associated with lower K' . Reducing K' from 20000 to 10000 , (5000 , 2000 , 1000) causes the pile-head displacements to increase by 1.5 times, (2.9 times, 7.8 times, 15.3 times) for the tenth cycle. It is observed in Figure 7.24a, that the further increase of K' from 10000 to 20000 does not affect the pile-head displacements significantly. This is because the stiffness of the pile-soil system is very high for $K' = 10000$, where the pile responded almost elastically; further increase in K' only gives a slight reduction in the pile-head displacements.

It is shown in Figure 7.24b, that the maximum bending moments increase with K' as E_p is directly proportional to the bending moment and inversely proportional to the displacement. Increasing K' from 1000 to 2000 , (5000 , 10000 , 20000) causes the maximum bending moments to increase by 0.0%, (0.2%, 3%, 9%) for the first cycle. With further cycling, however, due to the large pile-head displacements for low K' values (say K' of 1000 , 2000 and 5000), it produces large bending moments as a result of the large amount of soil yielding. This off-sets the directly proportional effect of E_p with bending moment (see Figure 7.24b for the first cycle), producing higher maximum bending moments for K' of 1000 , 2000 , and 5000 than for K' of 20000 with cycling. The above results indicate that the effect of E_p is greater for pile-head displacements than for maximum bending moments.

Fixed-head piles

Similar trends of pile responses in terms of pile-head displacements and maximum bending moments for free-head piles (Figure 7.24) are observed for fixed-head piles (Figure 7.25).

The above results, suggest that the further increase in E_p from $10000mD$ to $20000mD$, does not reduce significantly the pile-head displacements and maximum bending moments.

This applies to both free-head and fixed-head piles. To economise on pile material costs, hollow piles (with appropriate E_p) may be more preferable than solid steel piles.

7.6.3 The effect of backsliding factor (β)

Similar to the stiff clay model described in Section 7.5.3, the backsliding factor (β) of 0.0, 0.1, 0.2, and 0.5 were considered in this study.

Free-head piles

Figures 7.26a and 7.26b show that increasing β results in the reduction of the pile-head displacements and maximum bending moments, respectively. This is because of the lesser amount of soil yielding taking place, as the increase in β increases the yield stress for tension for the soil elements. This is reflected in the reduction in the rate of cyclic degradation and the rate of increase in maximum bending moment with cycling. Increasing β from 0.0 to 0.1, (0.2, 0.5) causes the pile-head displacements to reduce by 1%, (2%, 5%), and the maximum bending moments by 0.5%, (0.9%, 2.2%) for the tenth cycle. The results show that β has negligible effect on the pile-head displacements and maximum bending moments. It suggests that β may be safely ignored in the analysis for load levels less than $150cD^3$.

Fixed-head piles

Similar trends of pile responses in terms of pile-head displacements and maximum bending moments for free-head piles (Figure 7.26) are observed for fixed-head piles (Figure 7.27). The results suggest that β may be safely ignored in the analysis for load levels less than $300cD^3$.

7.6.4 The effect of residual/peak bearing strength ratio (R_b)

For this parametric study, the residual/peak bearing strength ratio (R_b) of 0.1, 0.2, 0.5 and 1.0 are considered. This simulates the degradation of bearing strength of the soil by 90%, 80%, 50% and 0%, respectively. Other details are described in Section 7.5.4 for the stiff clay model.

Free-head piles

Figures 7.28a and 7.28b show that reducing R_b increases the pile-head displacements and the maximum bending moments, respectively. This is due to the fact that more soil elements are taking place as a result of higher degradation of bearing strength. This is also reflected in the increase in the rate of cyclic degradation and the rate of increase in maximum bending moment with cycling. Reducing R_b from 1.0 to 0.5, (0.2, 0.1) causes the pile-head displacements to increase by 13%, (34%, 51%) and the maximum bending moments by 8%, (15%, 24%) for the tenth cycle. The effect of R_b is greater for pile-head displacements than for maximum bending moments. Note that the effect of R_b usually applies after the first loading cycle, when the elements have recovered from plastic to elastic.

Fixed-head piles

Similar trends of pile responses in terms of pile-head displacements and maximum bending moments for free-head piles (Figure 7.28) are observed for fixed-head piles (Figure 7.29). The only difference is that for $R_b = 1.0$, the pile has stabilised to an alternating plasticity response, where no degradation of bearing strength is being allowed.

7.6.5 The effect of bearing degradation rate factor (C_b)

Similar values of bearing degradation rate factor (C_b) for the stiff clay model (Section 7.5.5) were employed here. This is to simulate slow ($C_b = 10$ and 20), medium ($C_b = 50$) and fast ($C_b = 100$) rates of bearing strength degradation.

Free-head piles

Figures 7.30a and 7.30b, show that an increase in C_b causes an increase in the pile-head displacements and the maximum bending moments, respectively. This is because of the increase in soil elements yielding as the rate of bearing strength degradation is increased. This explains the increase in the rate of cyclic degradation and the rate of increase in maximum bending moment with cycling, with increasing C_b . Increasing C_b from 10 to 20, (50, 100) increases the pile-head displacements by 2%, (11%, 19%), and the maximum bending moment by 2%, (6%, 10%) for the tenth cycle. The effect of C_b is greater for pile-head displacements than for maximum bending moments. Note that the effect of C_b is usually observed after the first loading cycle, when the elements have recovered from plastic to elastic.

Fixed-head piles.

Similar trends of pile responses in terms of pile-head displacements and maximum bending moments for free-head piles (Figure 7.30) are observed for fixed-head piles (Figure 7.31). It is observed that for $C_b = 10$ and 20, the pile tends to stabilise to an alternating plasticity response with further cycling. This is because of the slow rate of bearing strength degradation, which causes little degradation of bearing strength. The rate of cyclic degradation and the rate of increase in maximum bending moment with cycling, are higher for $C_b > 50$

7.6.6 The effect of residual/peak shear strength ratio (R_s)

For this study, the residual/peak shear strength ratio (R_s) of 0.1, 0.2, 0.5 and 1.0 were employed. This simulates the degradation of shear strength of soil by 90%, 80%, 50% and 0%, respectively. Other details are described in Section 7.5.6 for the stiff clay model.

Free-head piles

Figures 7.32a and 7.32b show that the increase in pile-head displacements and maximum bending moments, respectively, is associated with the reduction in R_s . This is due to the fact that a greater amount of soil yielding occurs for lower R_s , as the degradation in the shear strength of the clay is higher. It is observed that the rate of cyclic degradation and the rate of increase in maximum bending moment with cycling, for $R_s = 0.1$ is initially higher than $R_s > 0.2$. However, with cycling greater than five cycles, the rate of cyclic degradation and the rate of increase in maximum bending moment decreases, when the residual strength of the soil elements is reached. Reducing R_s from 1.0 to 0.5, (0.2, 0.1) increases the pile-head displacements by 4%, (9%, 12%), and the maximum bending moments by 4%, (6%, 6%) for the tenth cycle. The effect of R_s is greater for pile-head displacements than for maximum bending moments. The effect of R_s usually applies after the first loading cycle, when the plastic elements are brought back to elastic.

Fixed-head piles

Similar trends of pile responses in terms of pile-head displacements and maximum bending moments for free-head piles (Figure 7.32) are observed for fixed-head piles (Figure

7.33), except that $R_s = 0.1$ and 0.2 have stabilised to an alternating plasticity response with further cycling. This is because the residual shear strength of the soil elements were reached.

7.6.7 The effect of shear strength degradation rate factor (C_s)

Similar values of shear strength degradation rate factor (C_s) for the stiff clay model (Section 7.5.7) were considered in this study. This is to simulate slow ($C_s = 0.1$ and 0.2), medium ($C_s = 0.5$) and fast ($C_s = 1.0$) rates of shear strength degradation.

Free-head piles

The increase in pile-head displacements and maximum bending moments with the increase in C_s are depicted in Figures 7.34a and 7.34b, respectively. It is observed that the effect of C_s for both pile-head displacements and maximum bending moments are negligible. This is because the residual strength of the soil elements have been reached regardless of the rate specified, as the plastic shear displacement for the elements is very high. For example, it is shown that the increase in C_s from 0.1 to 0.2 , (0.5 , 1.0) increases the pile-head displacements by only 0.2% , (0.2% , 0.4%), and the maximum bending moments by only 0.7% , (1.5% , 1.6%) for the tenth cycle.

Fixed-head piles

Similar trends of pile responses in terms of pile-head displacements and maximum bending moments for free-head piles (Figure 7.34) are observed for fixed-head piles (Figure 7.35).

The above results imply that C_s can be ignored for both free-head and fixed-head piles in the analysis, for loads below $150cD^3$ and $300cD^3$, respectively.

7.6.8 The effect of adhesion factor (α)

Similar adhesion factor (α) of 0.1 , 0.2 , 0.5 and 1.0 for the stiff clay model (Section 7.5.8) were considered in this study.

Free-head piles

Figures 7.36a and 7.36b show the increase in pile-head displacements and maximum bending moments when α decreases. This is because of the greater amount of soil elements

yielding taking place as the limit shear stress is lower. It is observed that the lower rate of cyclic degradation and lower rate of increase in maximum bending moment with cycling, is associated with a lower α . This is due to the greater amount of soil elements yielding in both the loading/reloading and unloading cycles. Decreasing α from 1.0 to 0.5, (0.2, 0.1) causes the pile-head displacements to increase by 5%, (10%, 14%), and the maximum bending moments by 1%, (2%, 2%) for the tenth cycle. The effect of α is greater for pile-head displacements than for maximum bending moments.

Fixed-head piles

Similar trends of pile responses in terms of pile-head displacements and maximum bending moments for free-head piles (Figure 7.36) are observed for fixed-head piles (Figure 7.37).

7.6.9 The effect of eccentric loading (e)

As for the stiff clay model (Section 7.5.9), the eccentricity (e) of 0.0, 0.5, 1.0 and 2.0D (D is the pile diameter) were considered in this parametric study.

Free-head piles

An increase in e causes the increase in the pile-head displacements and maximum bending moments as depicted in Figures 7.38a and 7.38b, respectively. This is due to the fact that a greater amount of soil elements yielding are taking place, as the bending moments in the piles are increased. This also causes the rate of cyclic degradation to increase. Increasing e from 0.0 to 0.5D, (1.0D, 2.0D) increases the pile-head displacements by 1.3 times, (1.7 times, 2.7 times), and the maximum bending moments by 14%, (27%, 55%) for the tenth cycle. The results suggest that the effect of e is greater for pile-head displacements than for maximum bending moments.

Fixed-head piles

It is assumed in APILEC analysis that eccentric loading will not have any effect on the fixed-head piles. As such, the effect of eccentricity on pile responses is not examined.

7.7 Discussion of results

Pile discretisation

The pile discretisation study showed that unit aspect ratio for the pile segments should be adopted during analysis, to obtain an optimum balance between computational cost and accuracy.

Parametric studies

The parametric studies indicate the parameters that have significant influence on the pile responses in terms of pile-head displacements and maximum bending moments. They also indicated the parameters which can be safely ignored.

Load levels

The study has shown that the load levels have significant effect on the pile-head displacements and the maximum bending moments. The effect is greater for pile-head displacements than on maximum bending moments. The rate of cyclic degradation and the rate of increase in maximum bending moment with cycling, are higher with increasing load levels. Comparing the responses of free-head and fixed-head piles under the same load level, indicates that the latter reduces the pile-head displacements and the maximum bending moments for both stiff clay and soft clay models. The results indicate that fixing the pile-head will improve the cyclic lateral load capacity of the pile.

Pile Young's modulus (E_p)

The study has shown that E_p has significant effect on the pile-head displacements and the maximum bending moments. Increase in E_p reduces the pile-head displacements but increases the maximum bending moments. The effect is greater for pile-head displacements than for maximum bending moments. It is observed for the stiff clay model, that further increase in E_p from $2000E_s$ to $4000E_s$ shows only slight reduction in the pile-head displacements and a slight increase in the maximum bending moments. For the soft clay model, a further increase in E_p from $10000mD$ to $20000mD$ shows negligible effect on pile-head displacements and maximum bending moments. This evaluation indicates that piles of reasonable E_p should be employed to reduce the pile foundation costs.

Backsliding factor (β)

The study on β shows that it did not have significant effect on the pile-head displacements and the maximum bending moments for both stiff clay and soft clay models. This suggests that this parameter can be ignored in the analysis.

Residual/peak bearing strength ratio (R_b)

For the stiff clay model, R_b has shown to have significant effect on the pile-head displacements and the maximum bending moments, only when the load level is at the yield load. The parameter R_b can be ignored if the load levels are below $10C_u D^2$ for free-head piles and $20C_u D^2$ for fixed-head piles. For the soft clay model, R_b has shown to have significant effect on the pile-head displacements and maximum bending moments at load levels of 75% of the yield load. The effect is greater for pile-head displacements than for maximum bending moments for both models.

Bearing degradation rate factor (C_b)

For the stiff clay model, C_b has shown to have significant effect on pile-head displacements and maximum bending moments for free-head piles subjected only to the yield load level. C_b can be ignored for fixed-head piles. The effect is greater for maximum bending moments than for pile-head displacements. For the soft clay model, C_b has shown to have significant effect on pile-head displacements and maximum bending moments at load levels of 75% of the yield load. The effect is greater for pile-head displacements than for maximum bending moments.

Residual/peak shear strength ratio (R_s)

The study shows that R_s has significant effect on pile-head displacements and maximum bending moments for both soft clay and stiff clay models. The effect is greater for pile-head displacements than for maximum bending moments.

Shear degradation rate factor (C_s)

The study shows that C_s does not have significant effect on pile-head displacements and maximum bending moments. For the stiff clay model, C_s can be ignored for free-head and fixed-head piles subjected to load levels less than $10C_u D^2$ and $20C_u D^2$, respectively. For

the soft clay model, C_s can be ignored for free-head and fixed-head piles subjected to load levels less than $150cD^3$ and $300cD^3$, respectively.

Adhesion factor (α) and eccentric loading (e)

The study shows that α and e have significant effect on the pile-head displacements and maximum bending moments for both soft clay and stiff clay models. The effect is greater for pile-head displacements than for maximum bending moments.

7.8 Concluding remarks

The results obtained in this parametric study have shed light on the performance of cyclic laterally loaded piles, and provides some useful data for design purposes. In the next Chapter, a number of published case histories are examined in order to assess the usefulness of this method of analysis in practice.

Table 7.1 Effect of pile discretisation on the initial stiffnesses of the pile-soil system.

No. of pile segments (<i>n</i>)	Initial stiffness (MN/m)
10	61.1
20	64.1
30	65.4
40	65.7

Table 7.2 Effect of pile discretisation on the relative errors in pile-head displacements.

No. of pile segments (<i>n</i>)	Relative errors (%)		
	Cycle 1	Cycle 5	Cycle 10
10	14	7.5	3.2
20	8.6	4.1	2.6
30	3.5	3.3	1
40	0	0	0

Table 7.3 Effect of pile discretisation on the relative errors in maximum bending moments.

No. of pile segments (<i>n</i>)	Relative errors (%)		
	Cycle 1	Cycle 5	Cycle 10
10	1.8	-6.8	-5.8
20	1.1	-2.8	-0.5
30	0.3	-0.7	-0.9
40	0	0	0

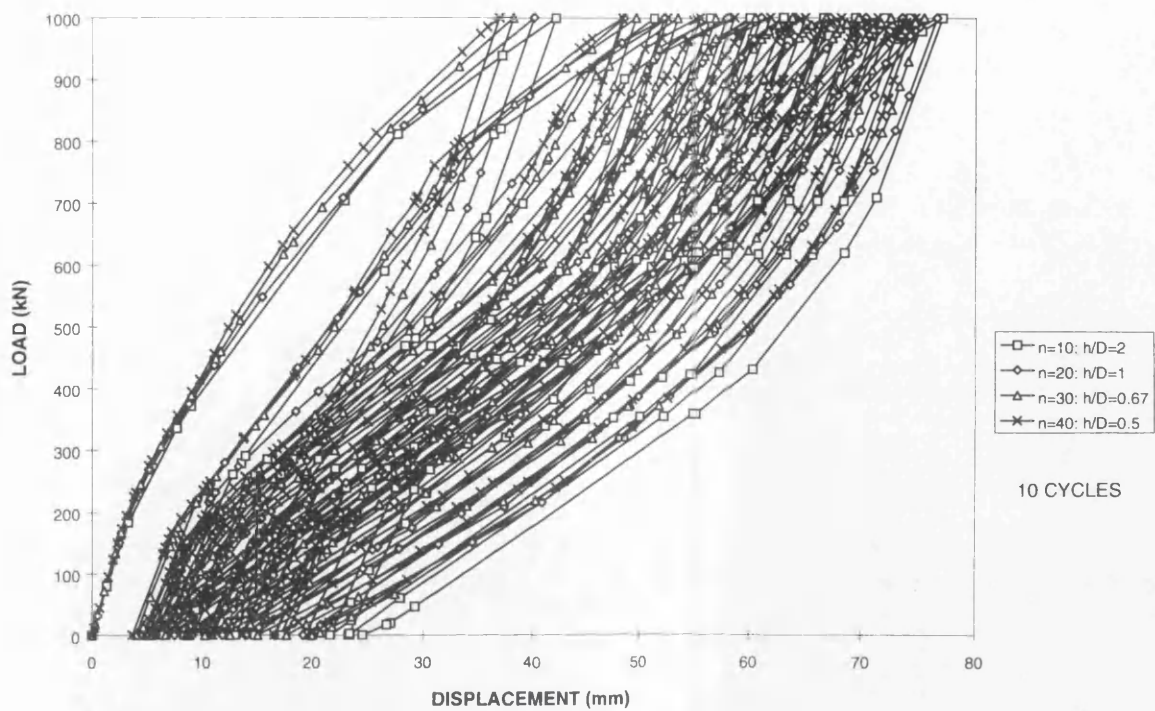


Figure 7.1 The effect of pile discretisation on pile-head load-displacement responses.

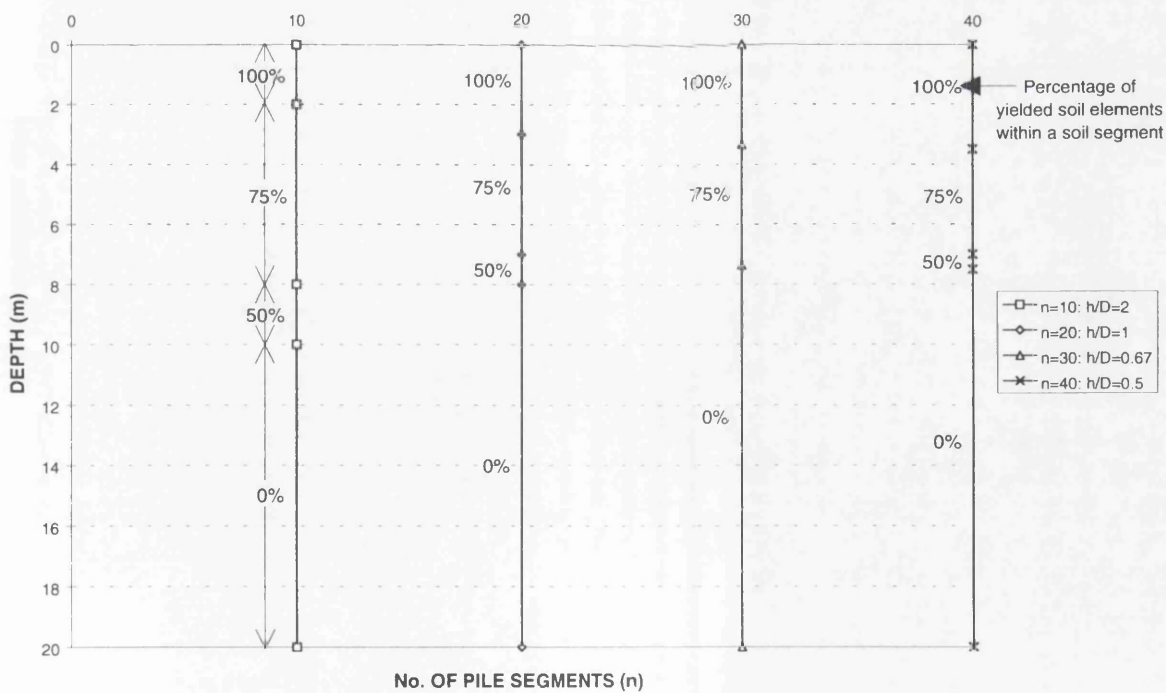
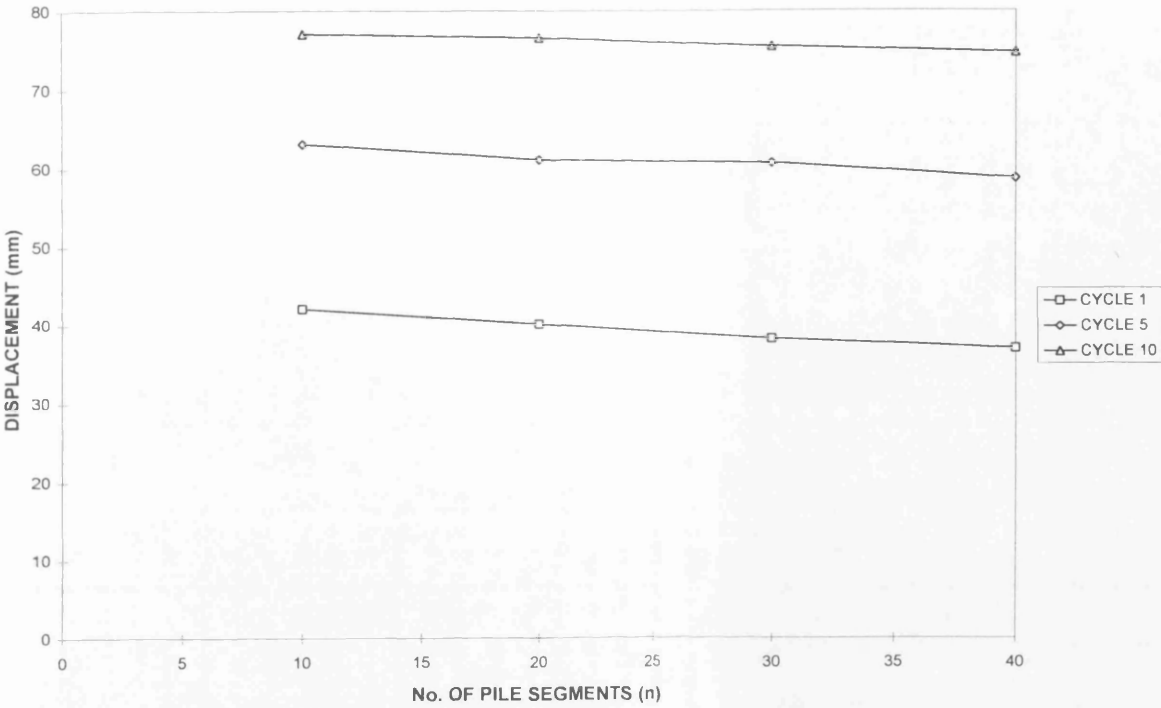
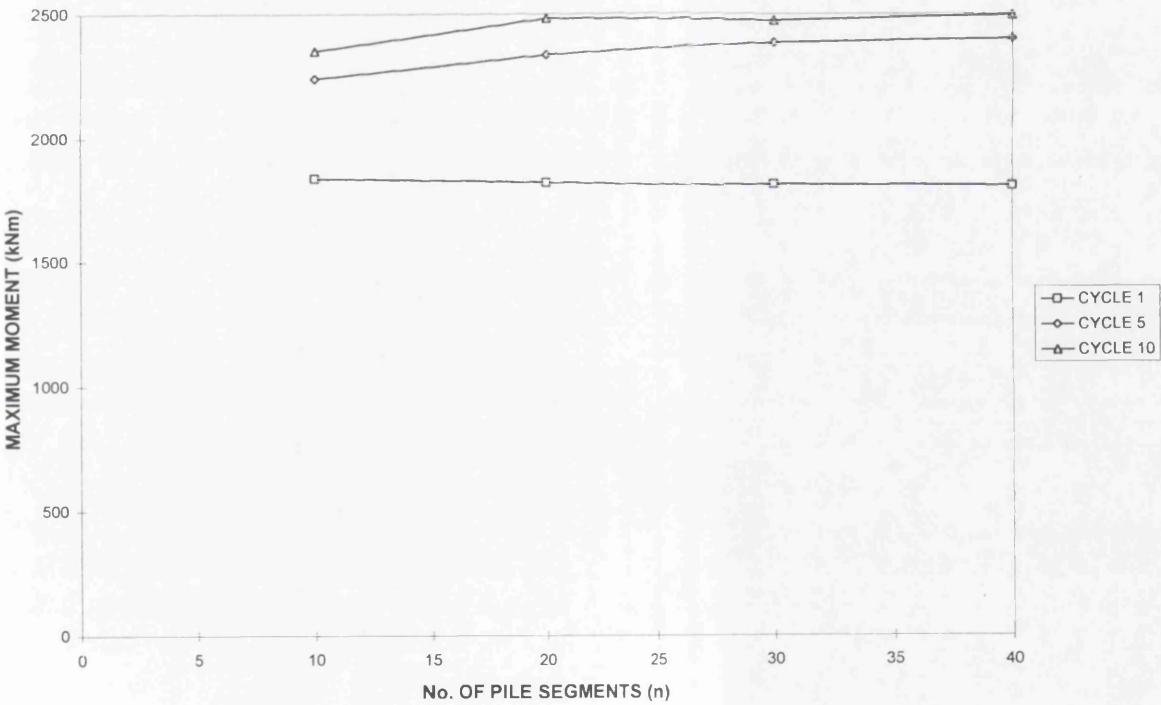


Figure 7.2 The effect of pile discretisation on soil segments yielding.



(a)



(b)

Figure 7.3 The effect of pile discretisation on (a) pile-head displacements and (b) maximum bending moments.

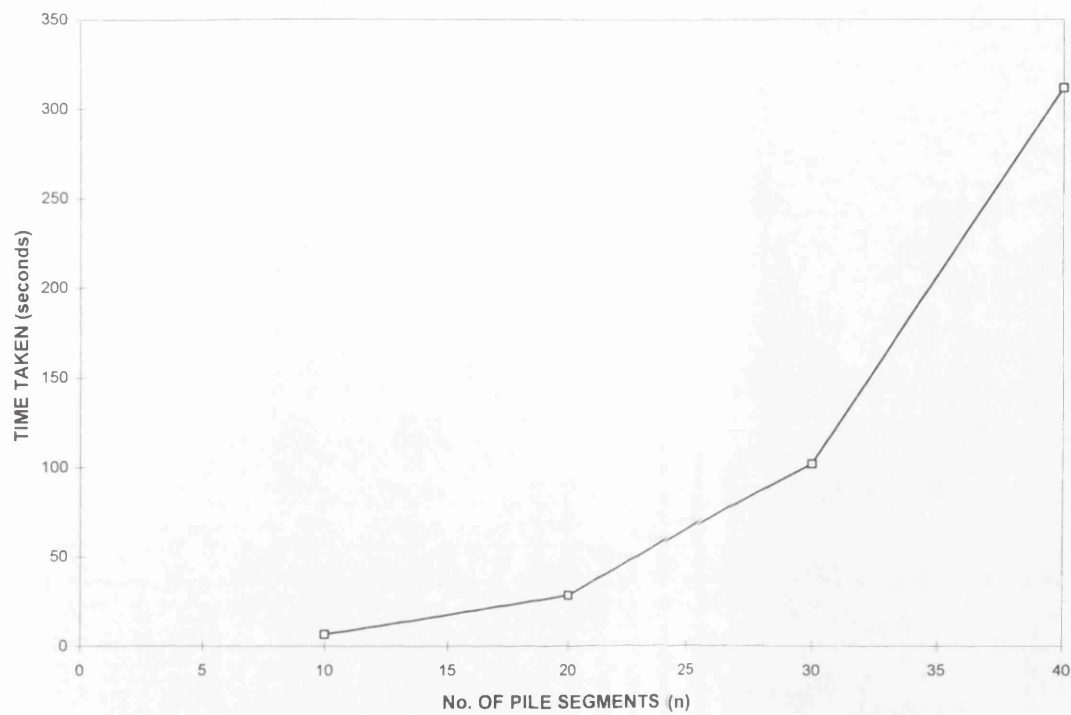
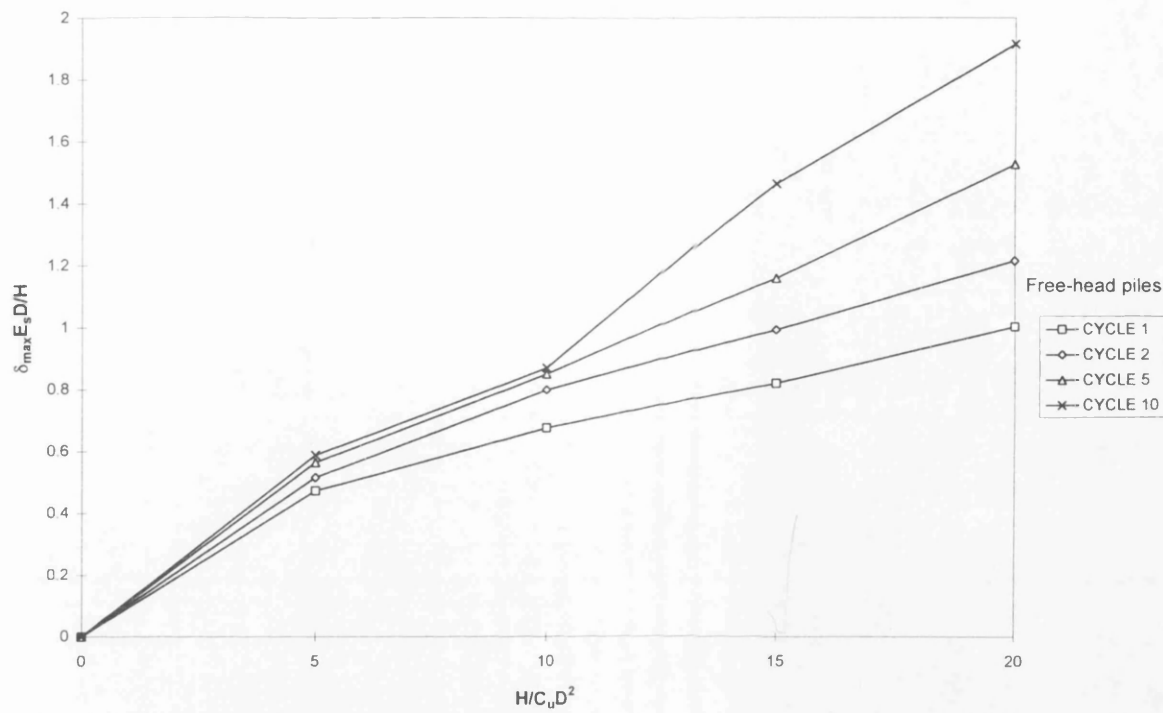
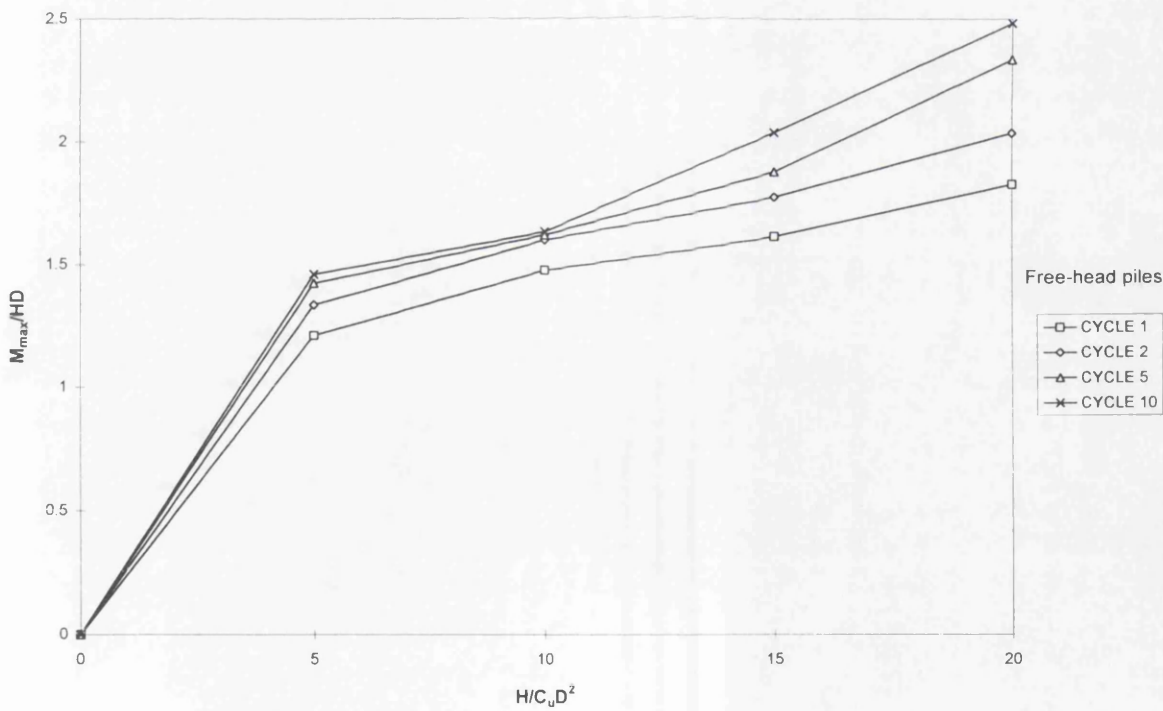


Figure 7.4 The effect of pile discretisation on time required for analysis.

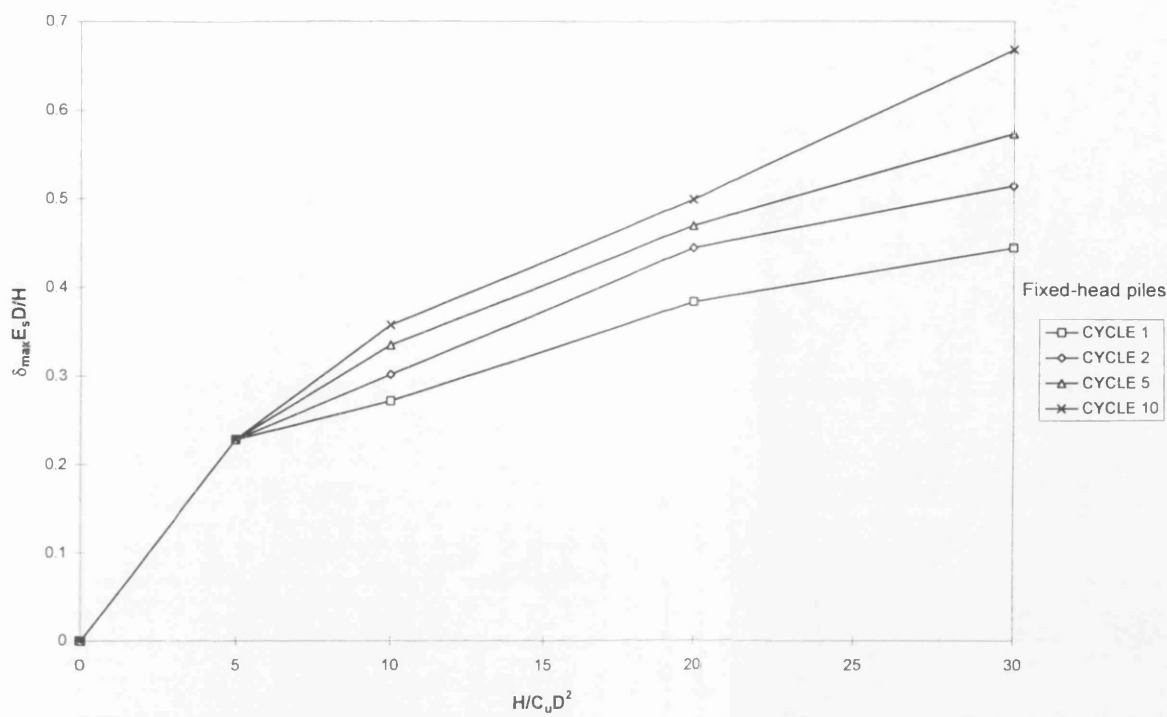


(a)

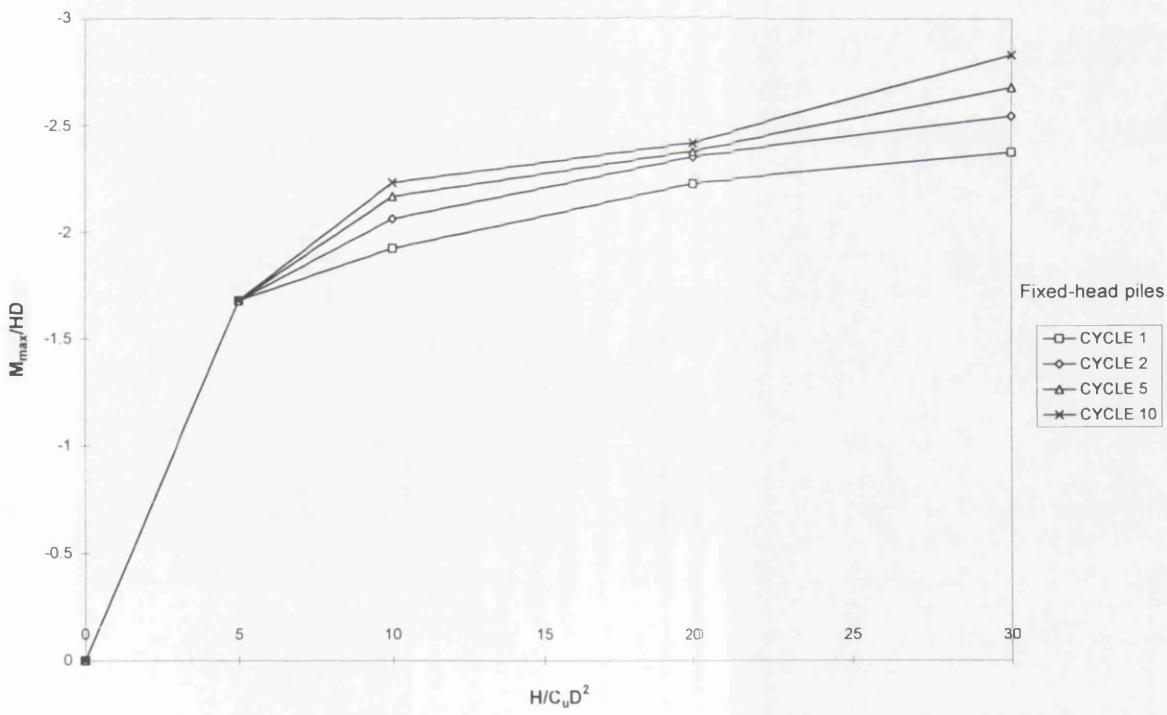


(b)

Figure 7.5 The effect of load levels on (a) pile-head displacements and (b) maximum bending moments, for free-head piles in stiff clay.

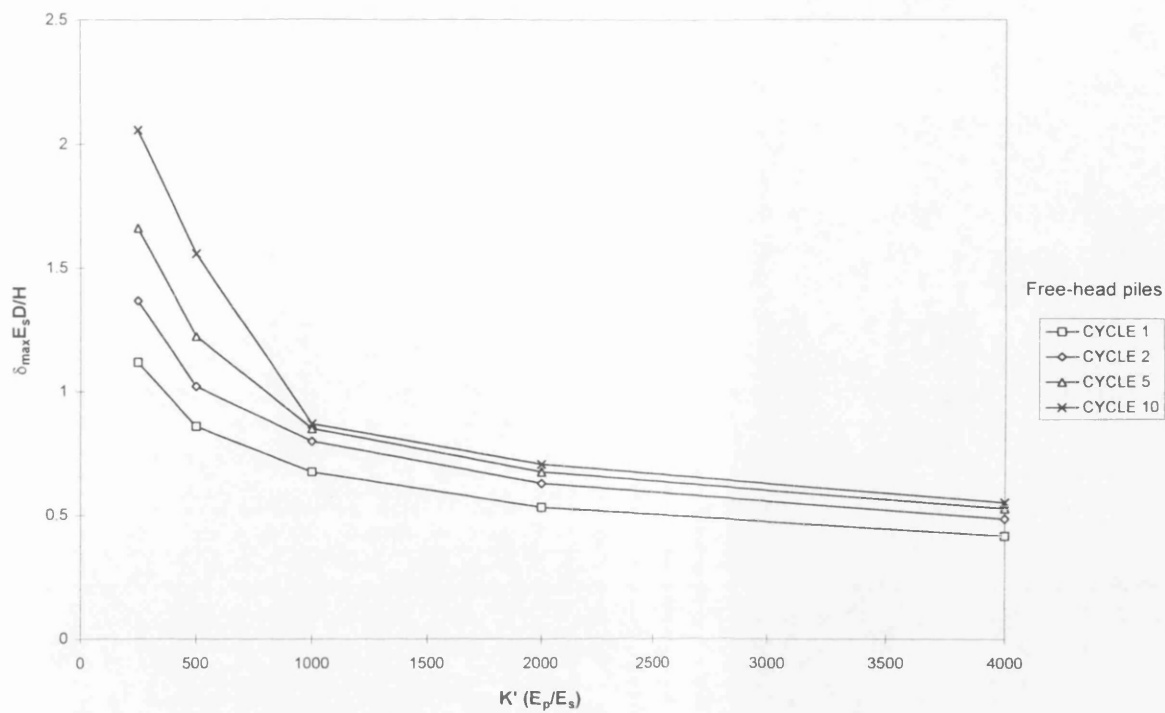


(a)

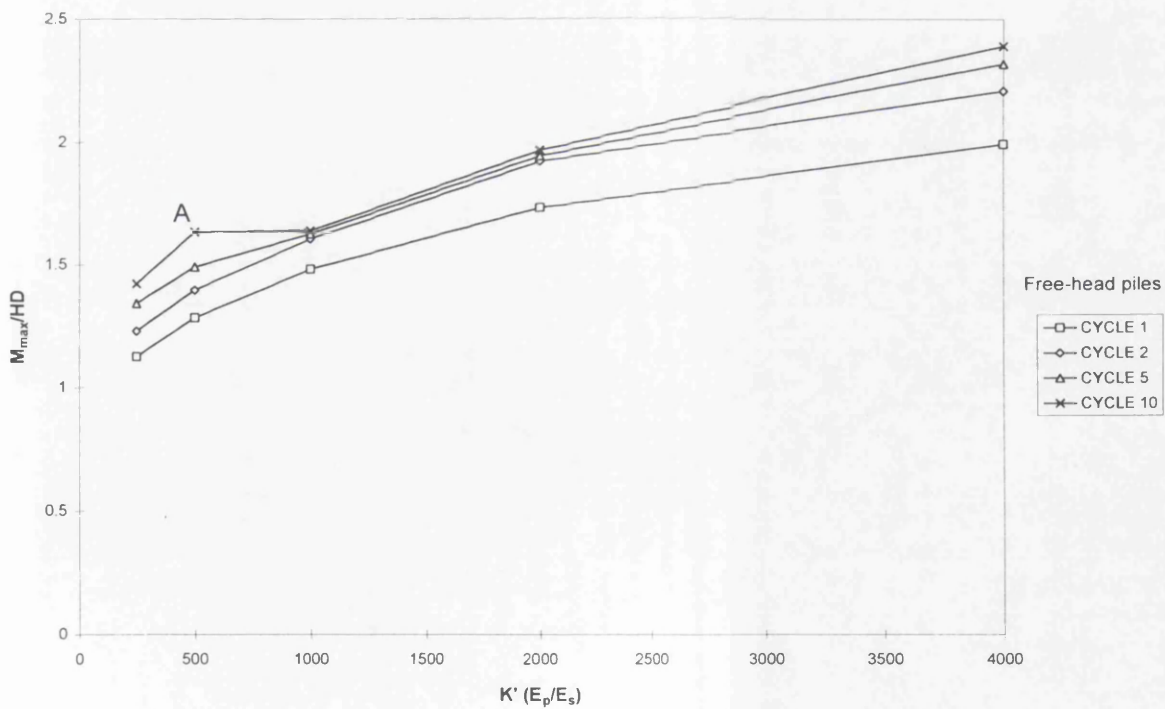


(b)

Figure 7.6 The effect of load levels on (a) pile-head displacements and (b) maximum bending moments, for fixed-head piles in stiff clay.

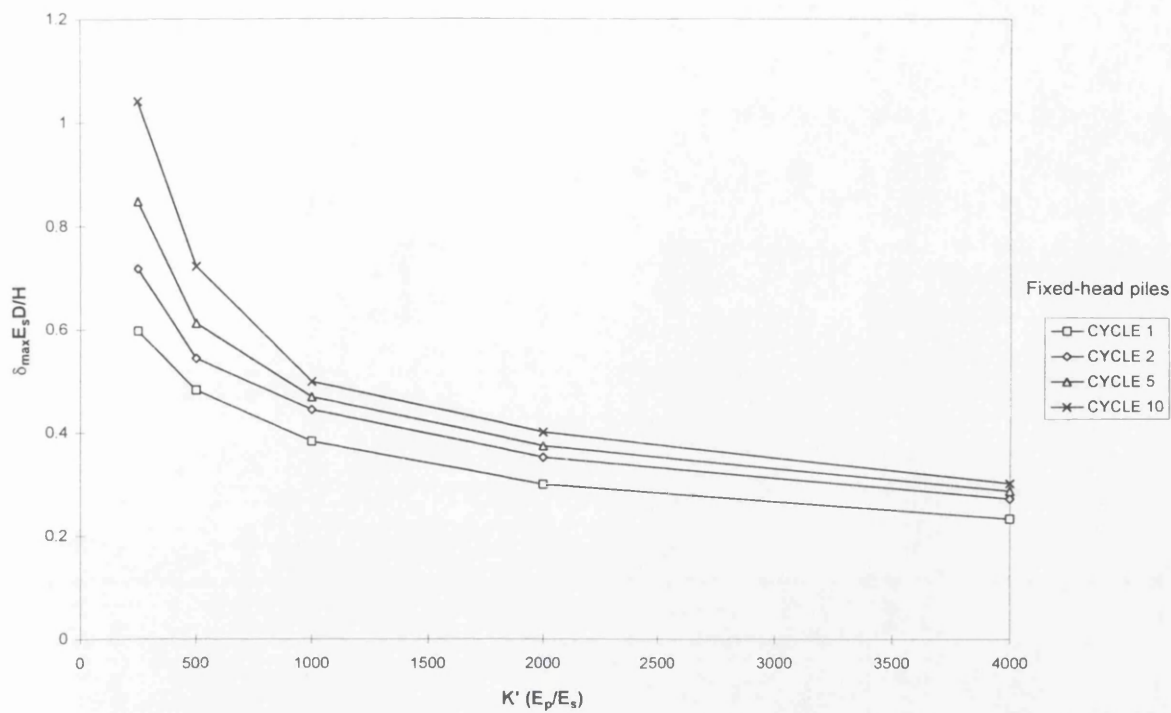


(a)

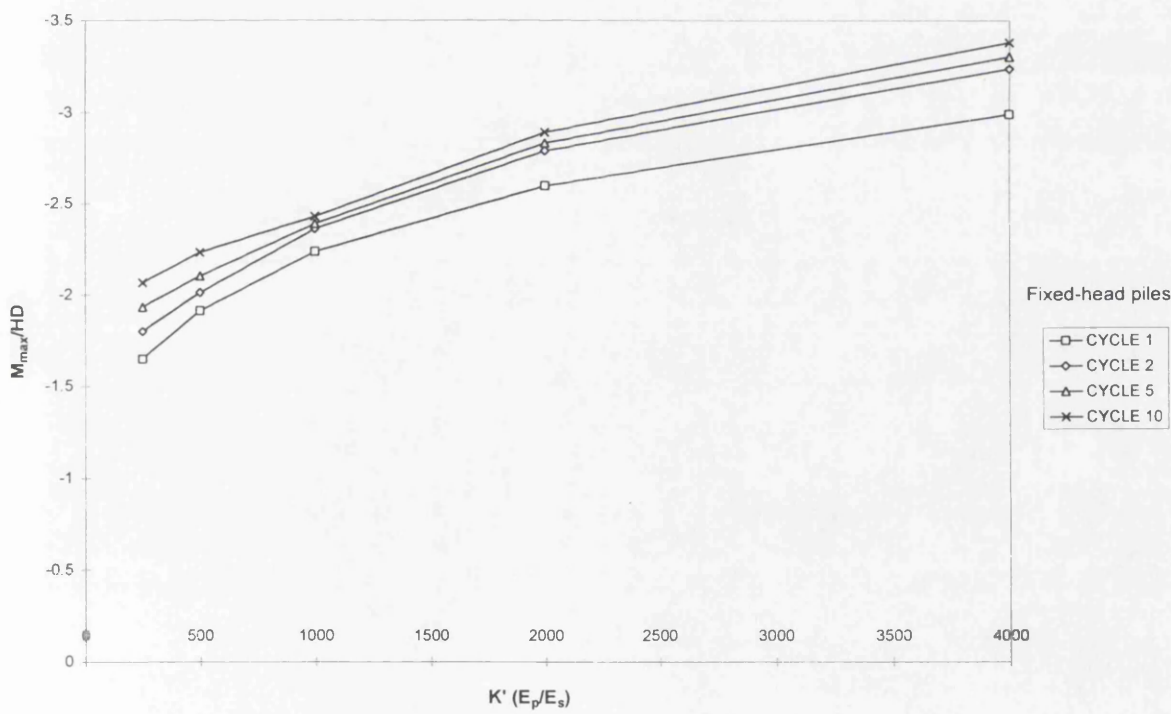


(b)

Figure 7.7 The effect of pile Young's modulus (E_p) on (a) pile-head displacements and (b) maximum bending moments, for free-head piles in stiff clay.

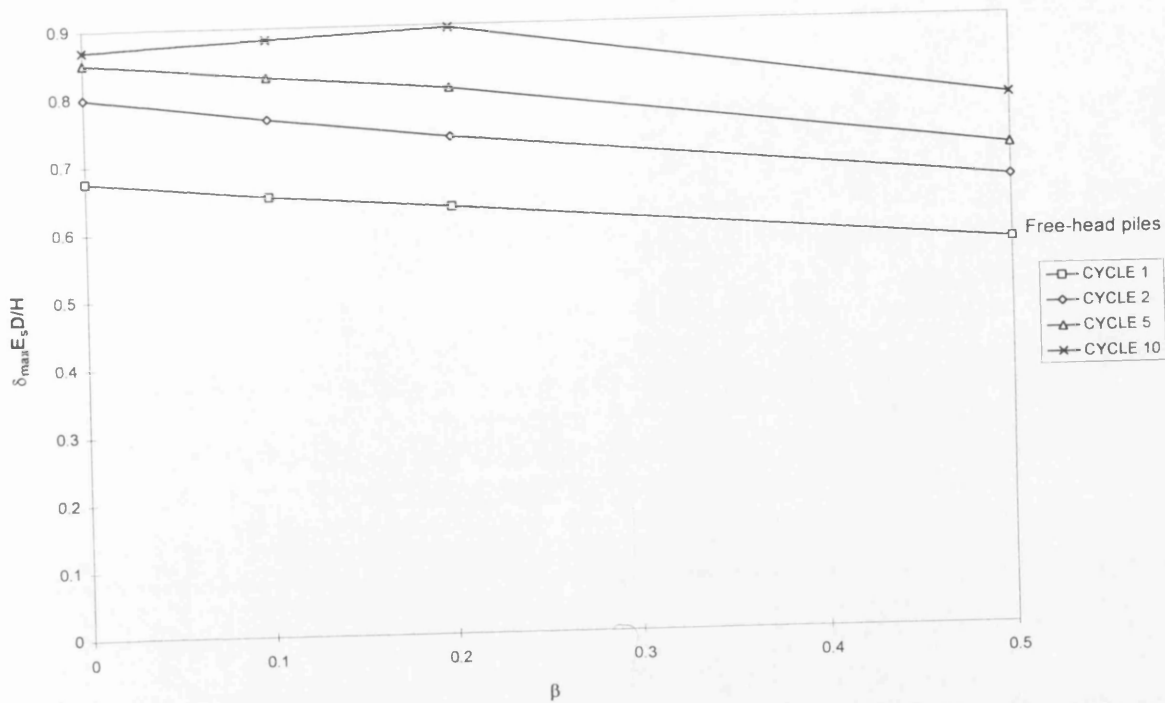


(a)

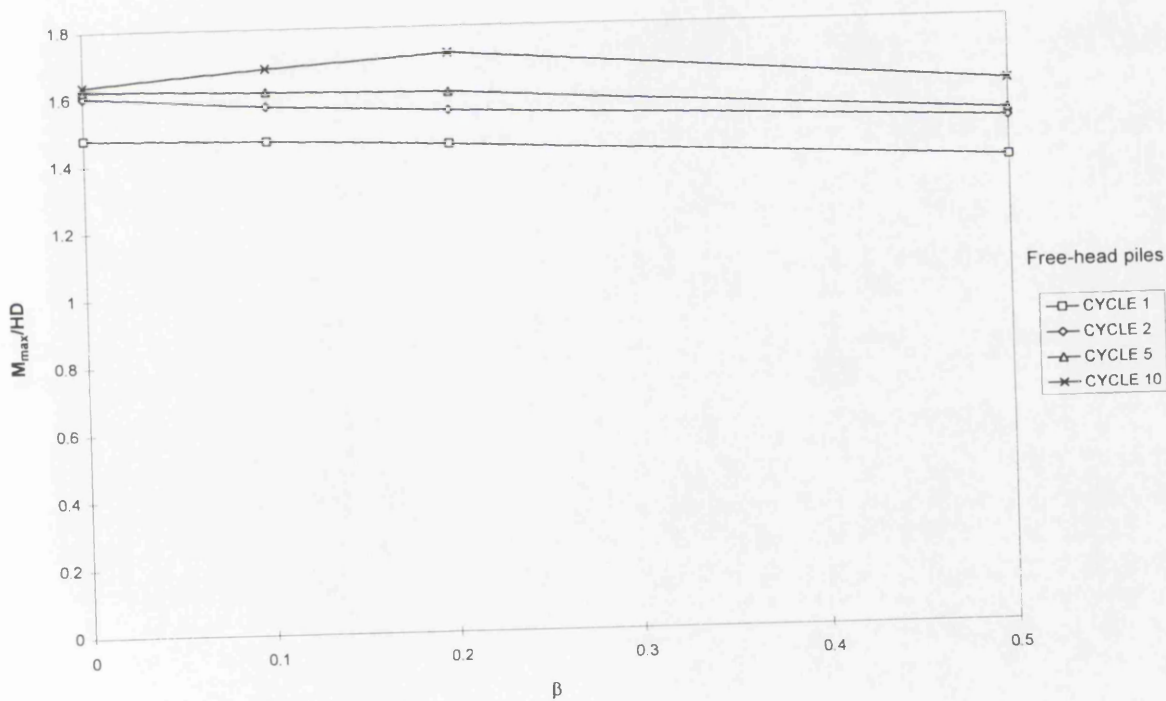


(b)

Figure 7.8 The effect of pile Young's modulus (E_p) on (a) pile-head displacements and (b) maximum bending moments, for fixed-head piles in stiff clay.

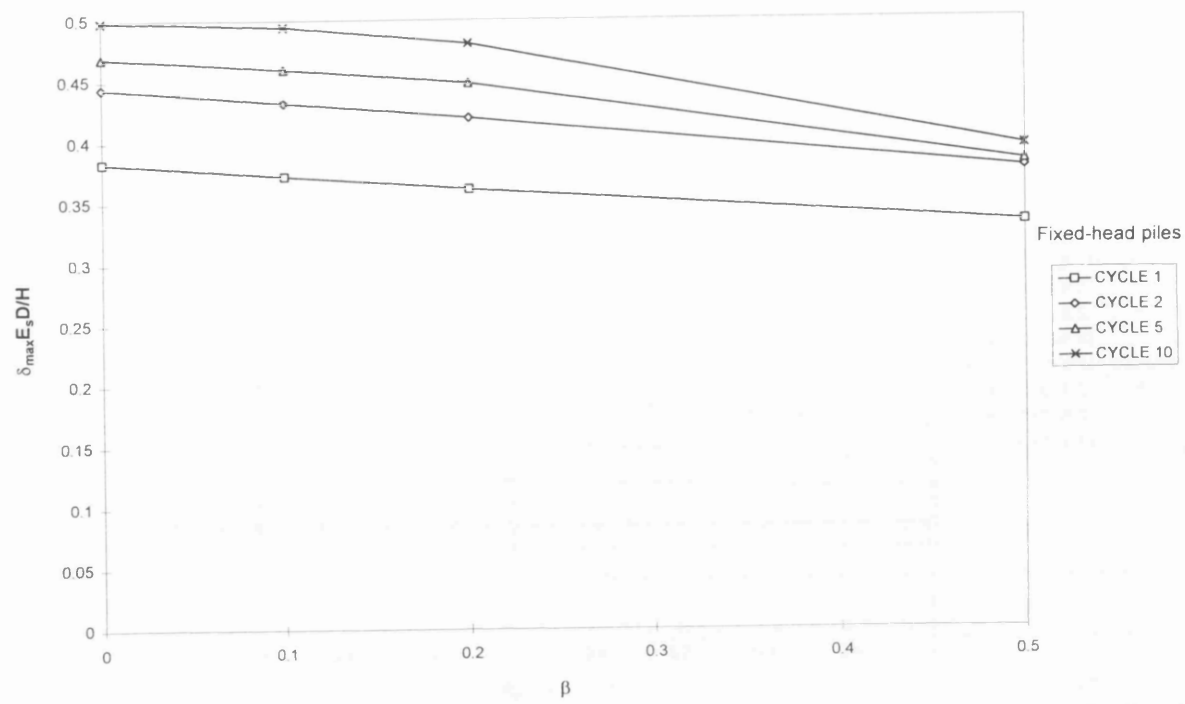


(a)

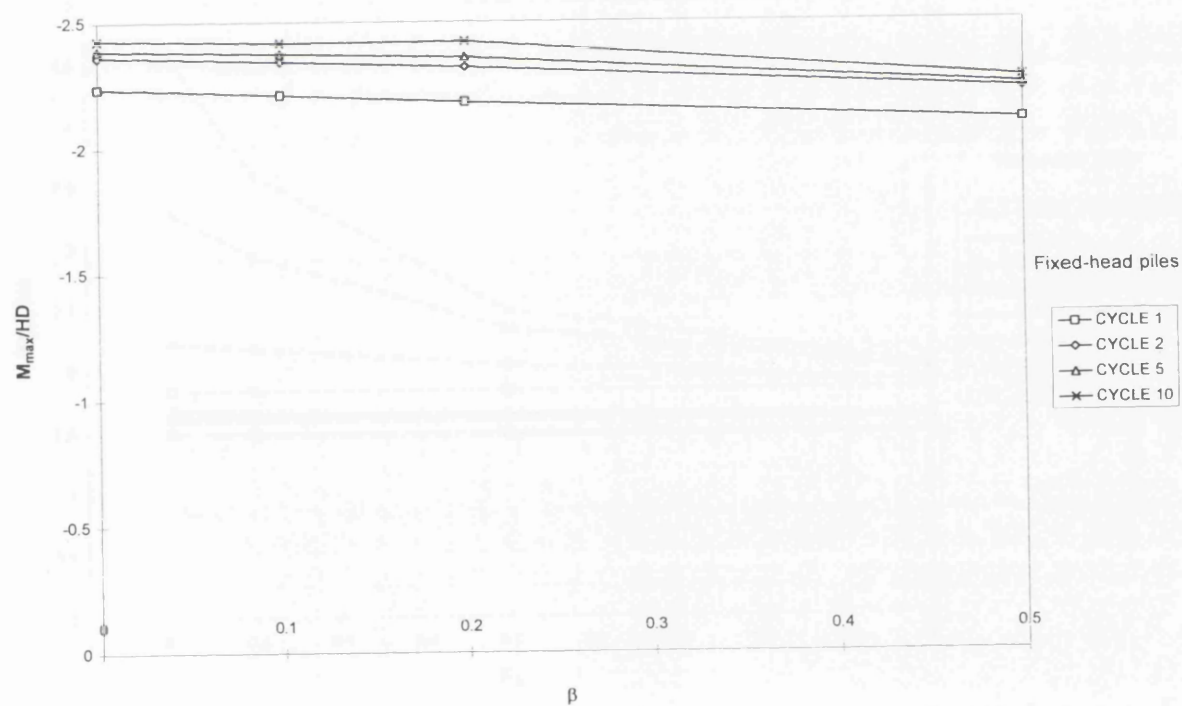


(b)

Figure 7.9 The effect of backsliding factor (β) on (a) pile-head displacements and (b) maximum bending moments, for free-head piles in stiff clay.

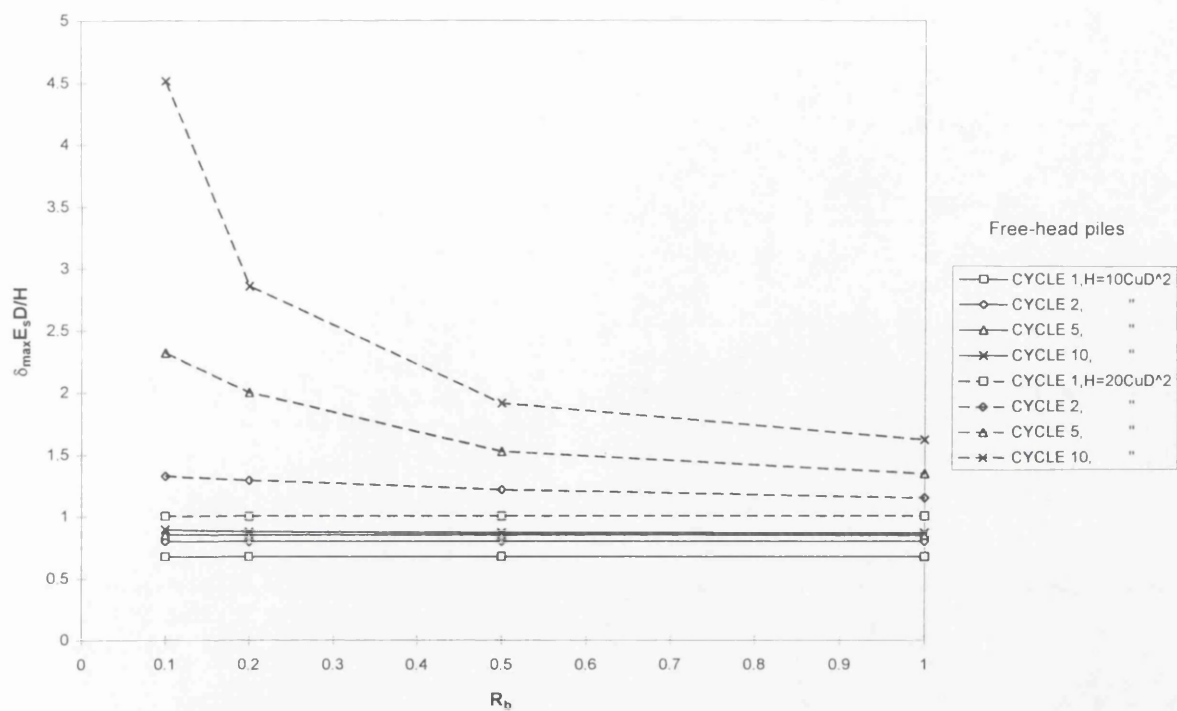


(a)

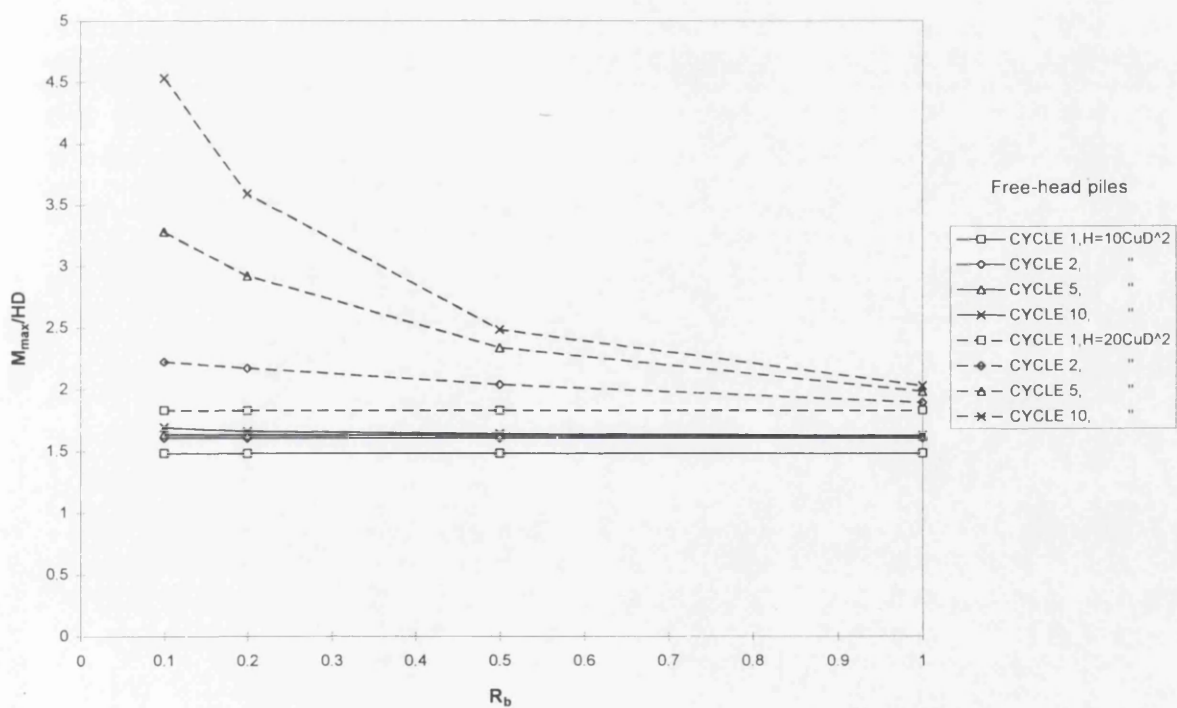


(b)

Figure 7.10 The effect of backsliding factor (β) on (a) pile-head displacements and (b) maximum bending moments, for fixed-head piles in stiff clay.

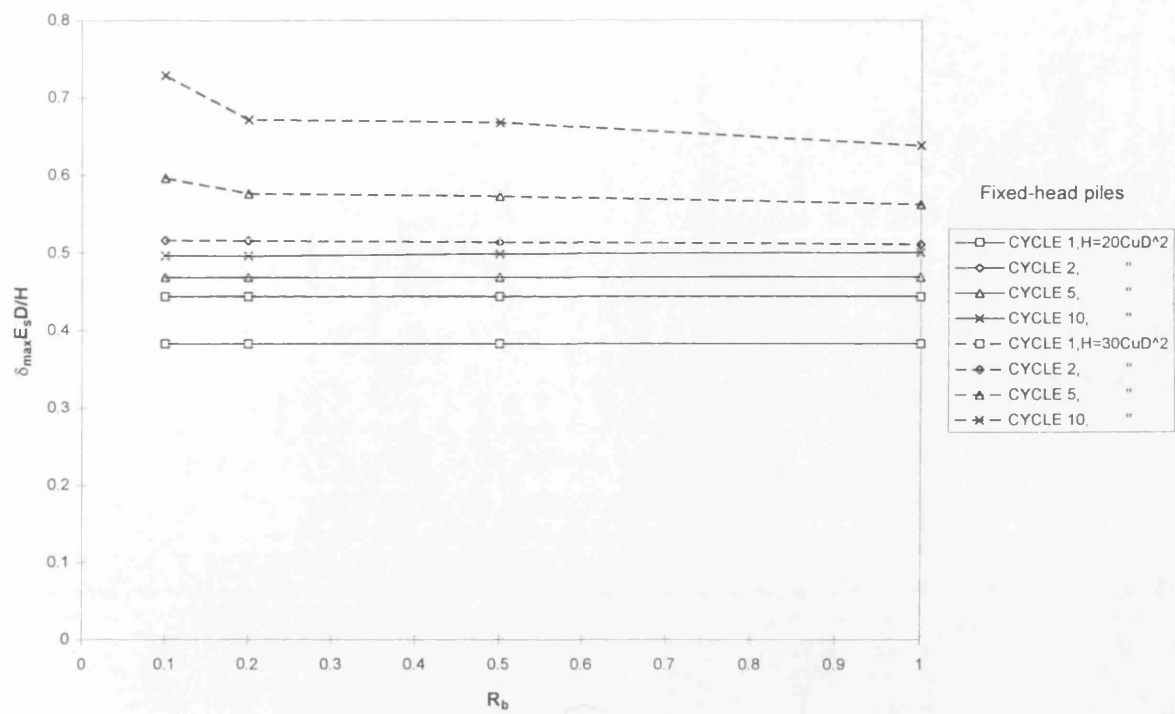


(a)

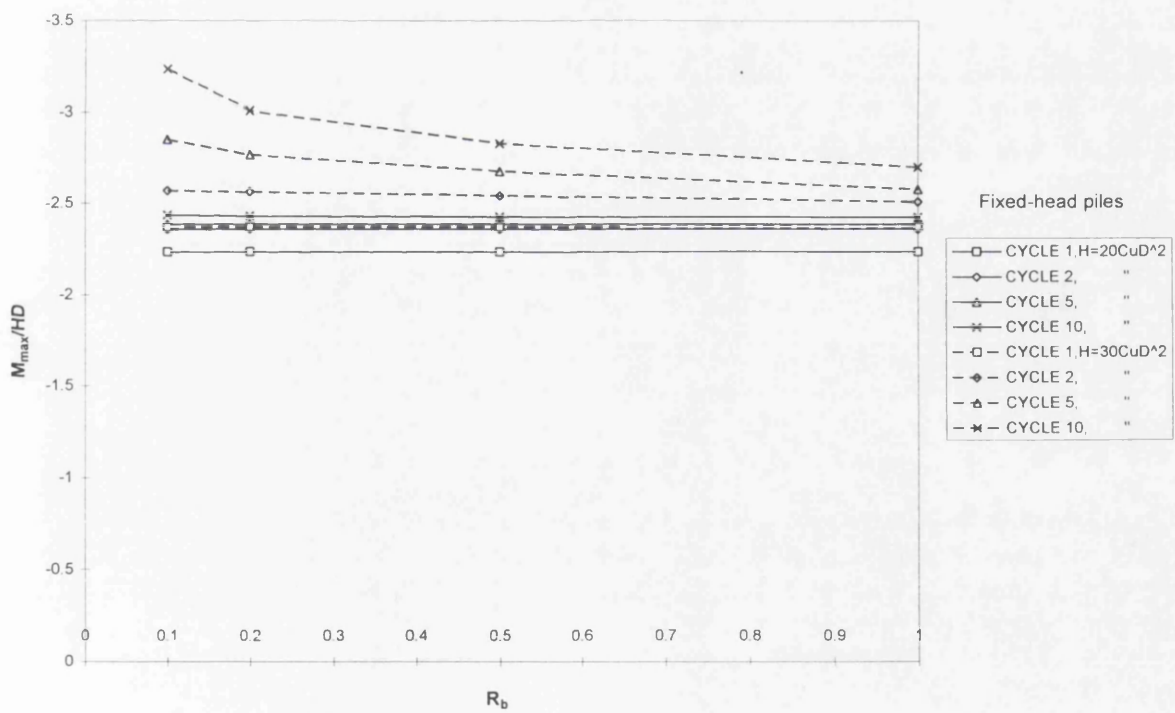


(b)

Figure 7.11 The effect of residual/peak bearing strength ratio (R_b) on (a) pile-head displacements and (b) maximum bending moments, for free-head piles in stiff clay.

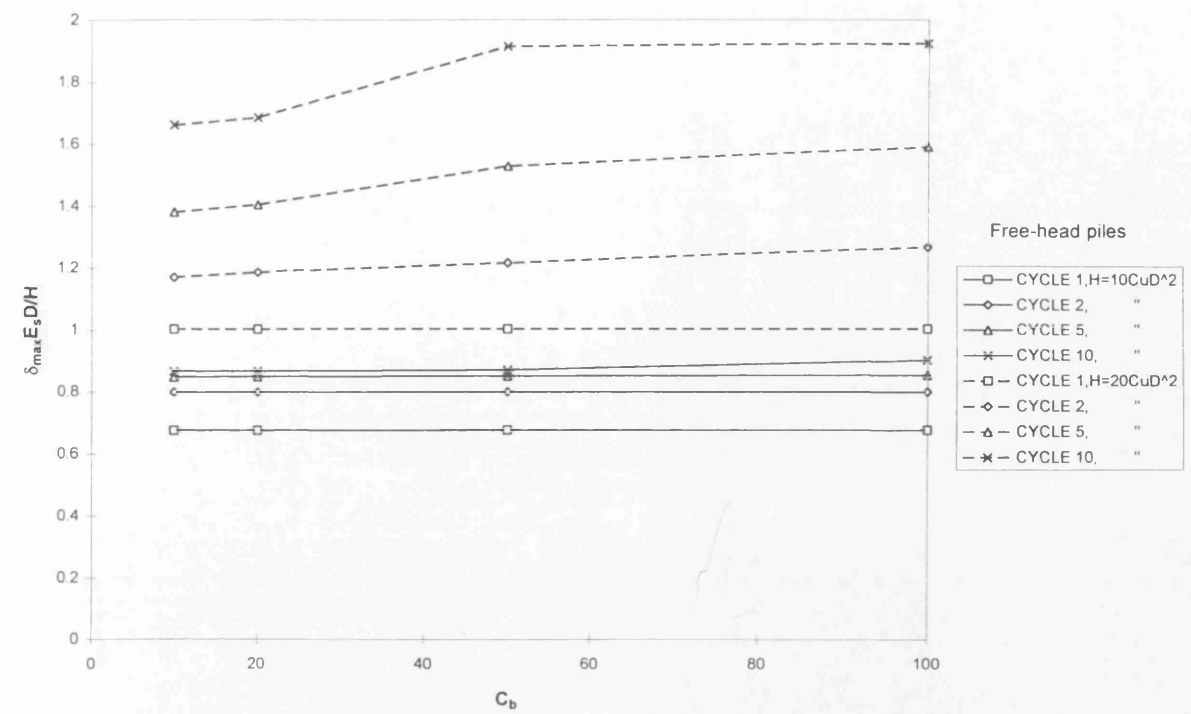


(a)

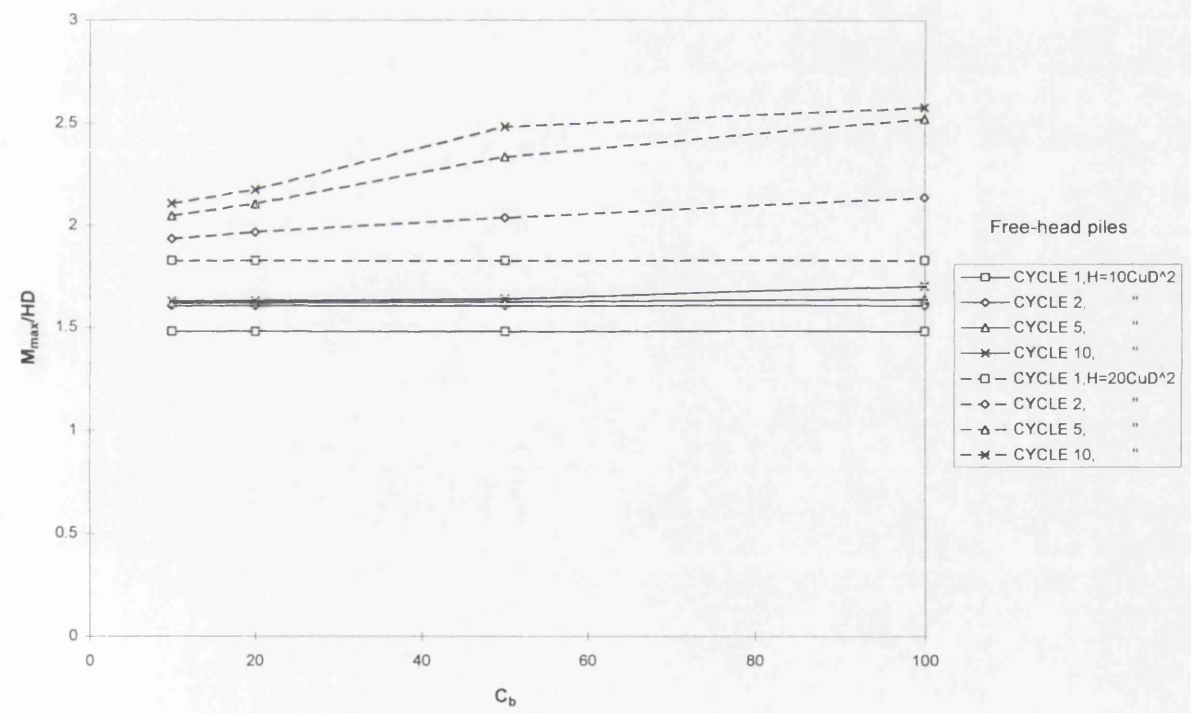


(b)

Figure 7.12 The effect of residual/peak bearing strength ratio (R_b) on (a) pile-head displacements and (b) maximum bending moments, for fixed-head piles in stiff clay.

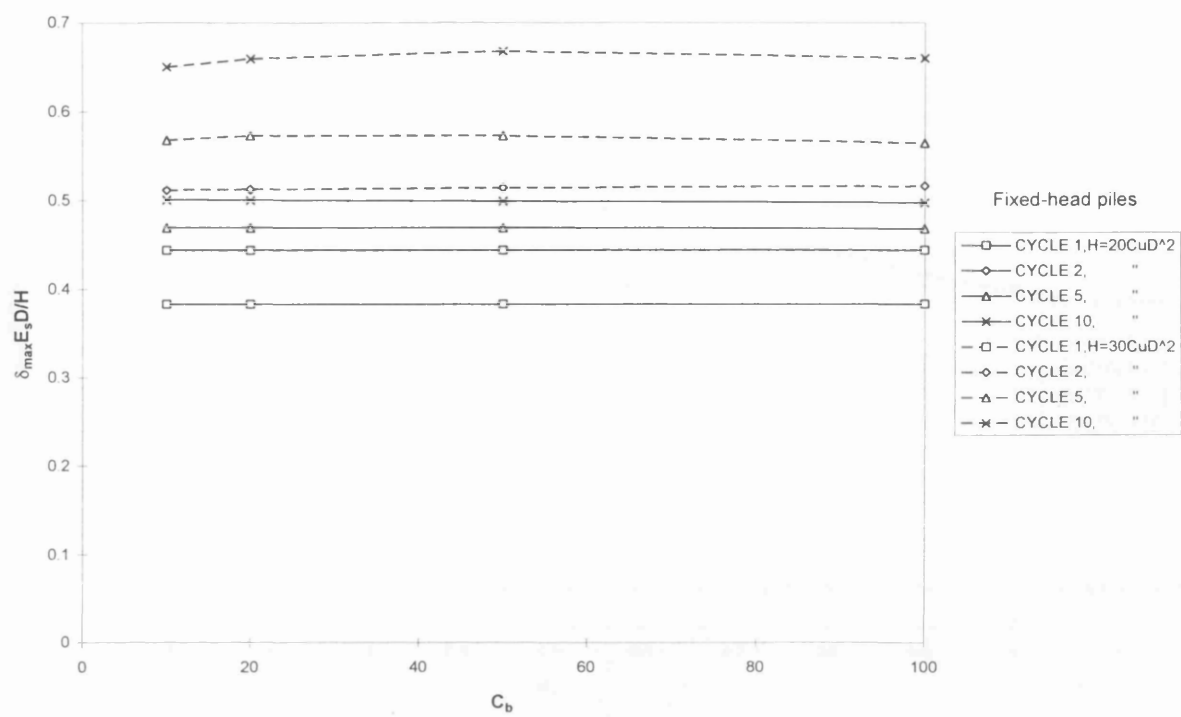


(a)

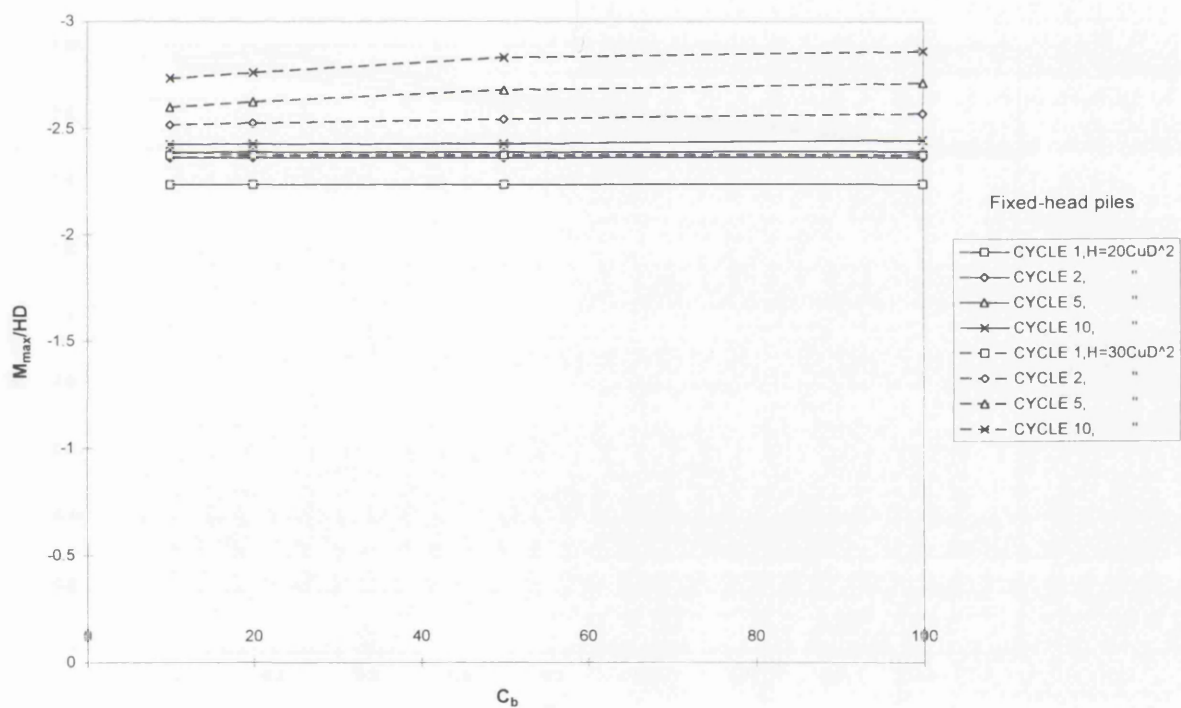


(b)

Figure 7.13 The effect of bearing degradation rate factor (C_b) on (a) pile-head displacements and (b) maximum bending moments, for free-head piles in stiff clay.

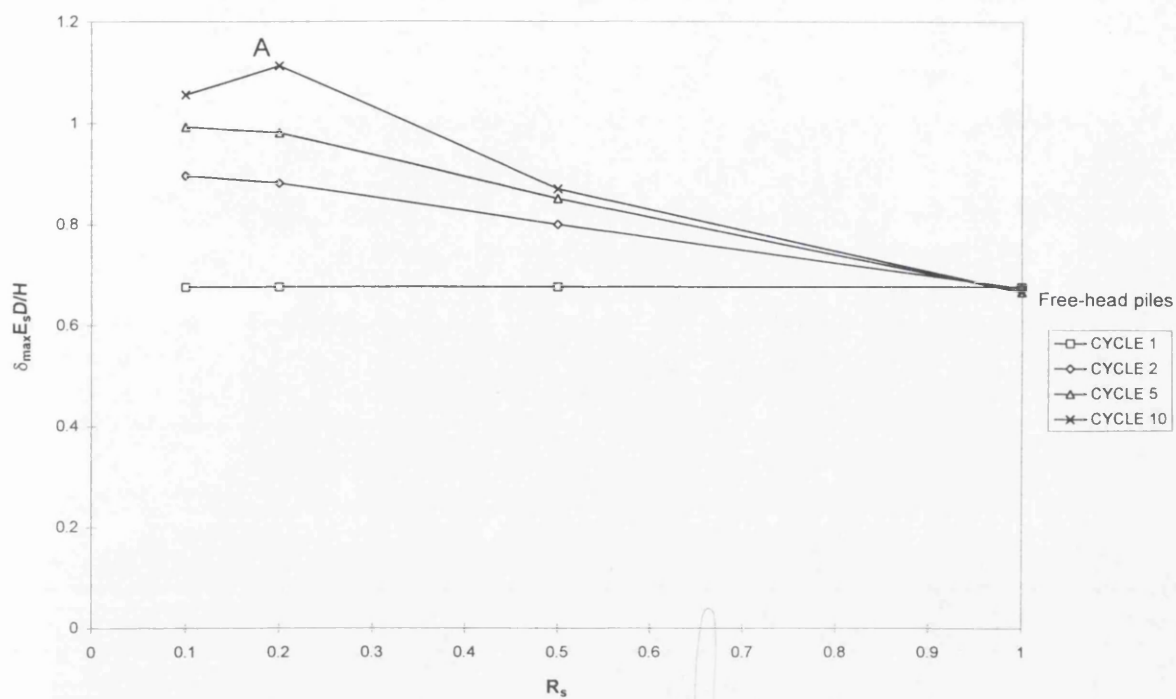


(a)

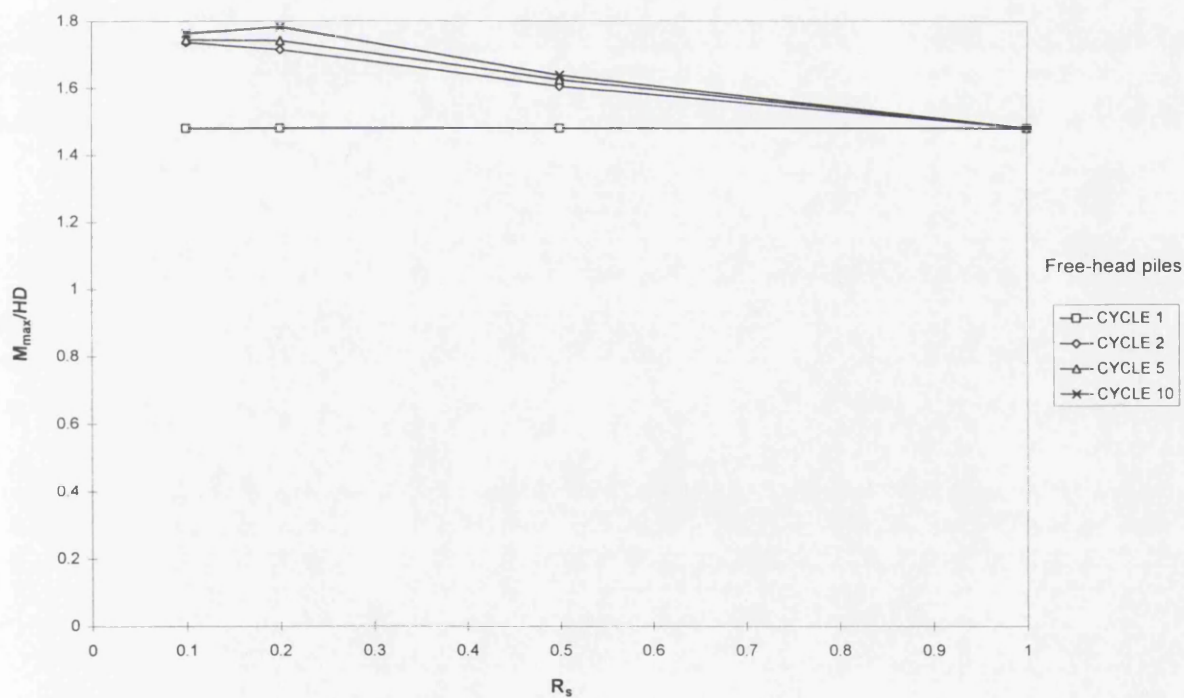


(b)

Figure 7.14 The effect of bearing degradation rate factor (C_b) on (a) pile-head displacements and (b) maximum bending moments, for fixed-head piles in stiff clay.

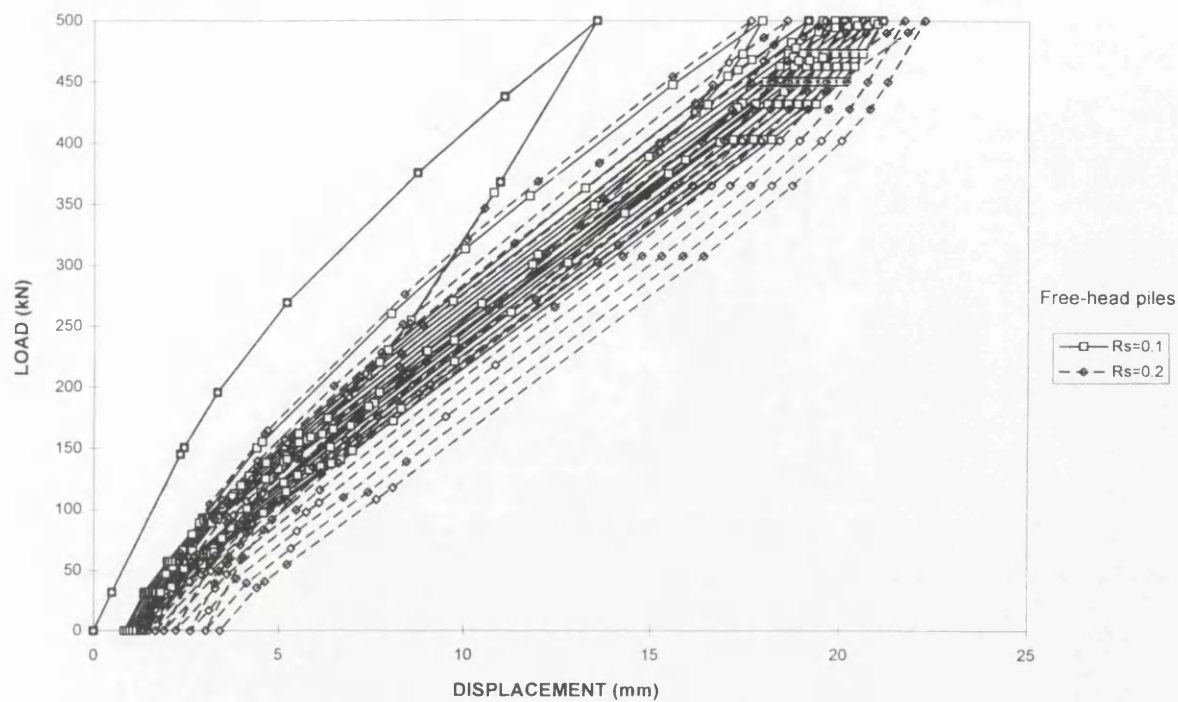


(a)



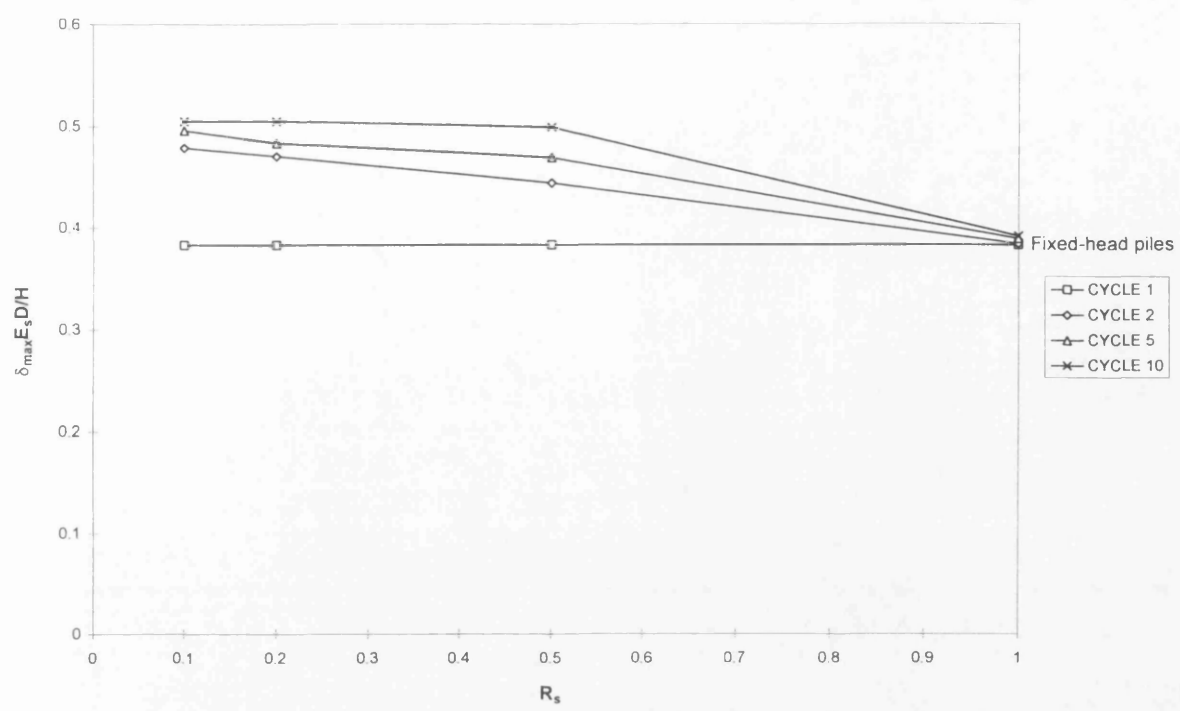
(b)

Figure 7.15 The effect of residual/peak shear strength ratio (R_s) on (a) pile-head displacements, (b) maximum bending moments and (c) pile-head load-displacement responses for R_s of 0.1 and 0.2 (see overleaf), for free-head piles in stiff clay.

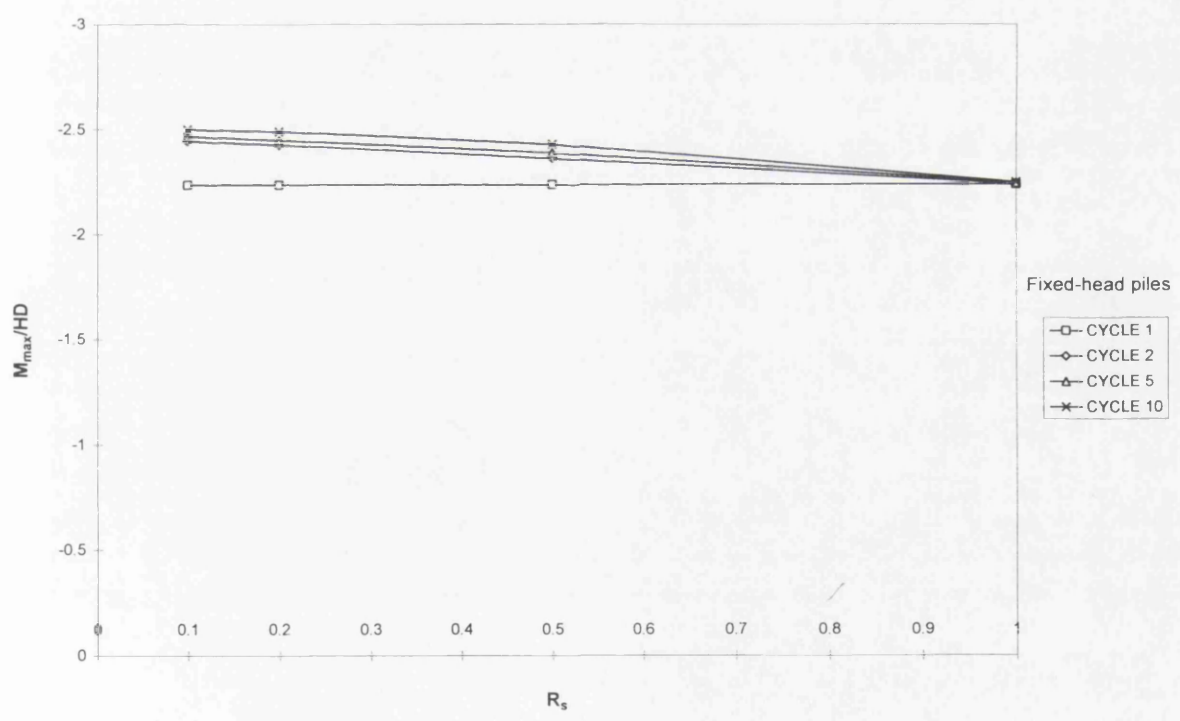


(c)

Figure 7.15 (c) The effect of residual/peak shear strength ratio (R_s) on pile-head load-displacement responses for R_s of 0.1 and 0.2, for free-head piles in stiff clay.

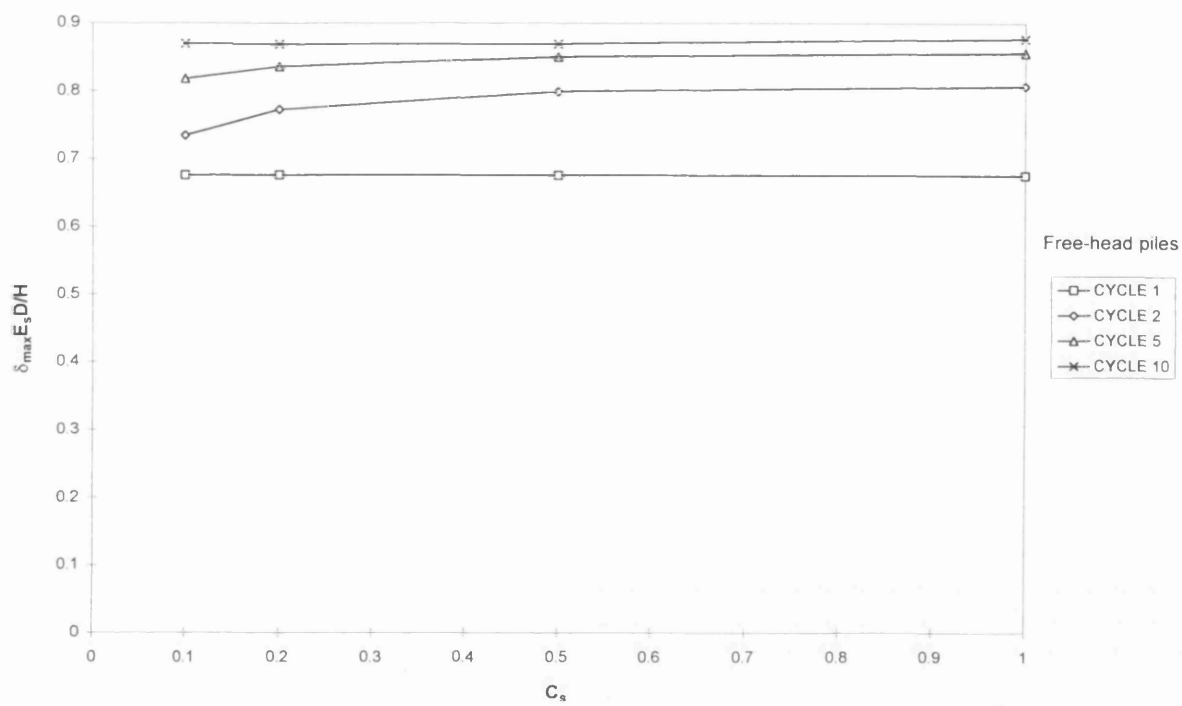


(a)

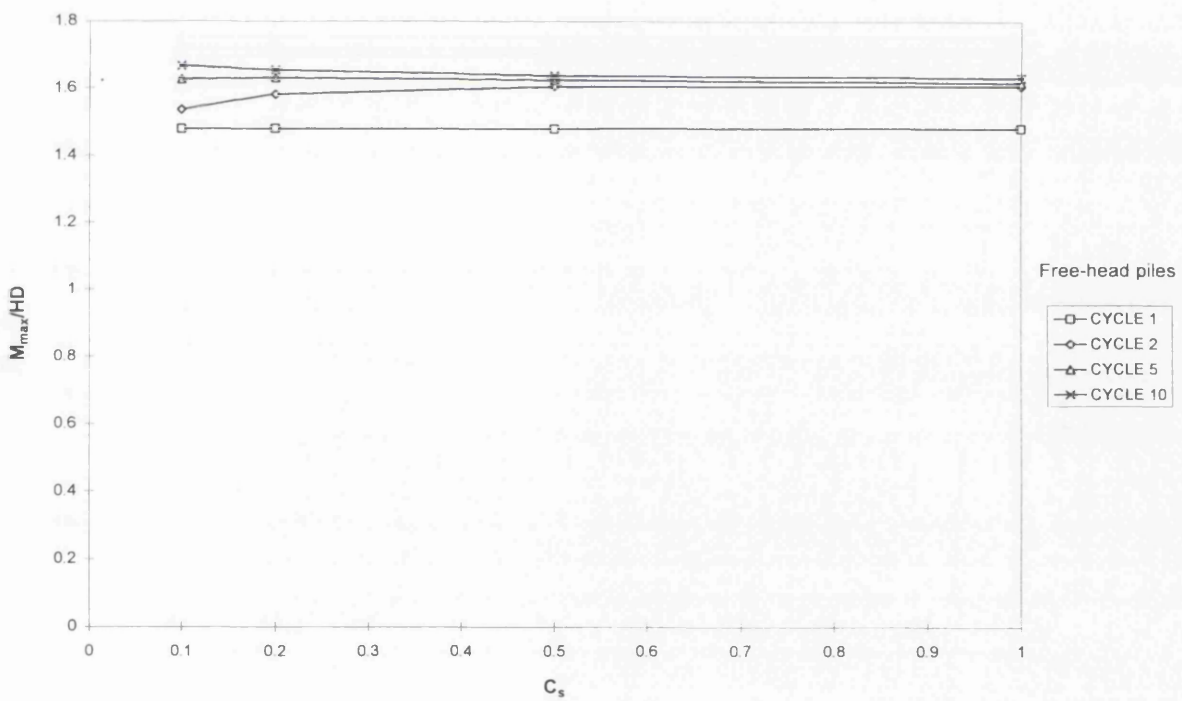


(b)

Figure 7.16 The effect of residual/peak shear strength ratio (R_s) on (a) pile-head displacements and (b) maximum bending moments, for fixed-head piles in stiff clay.

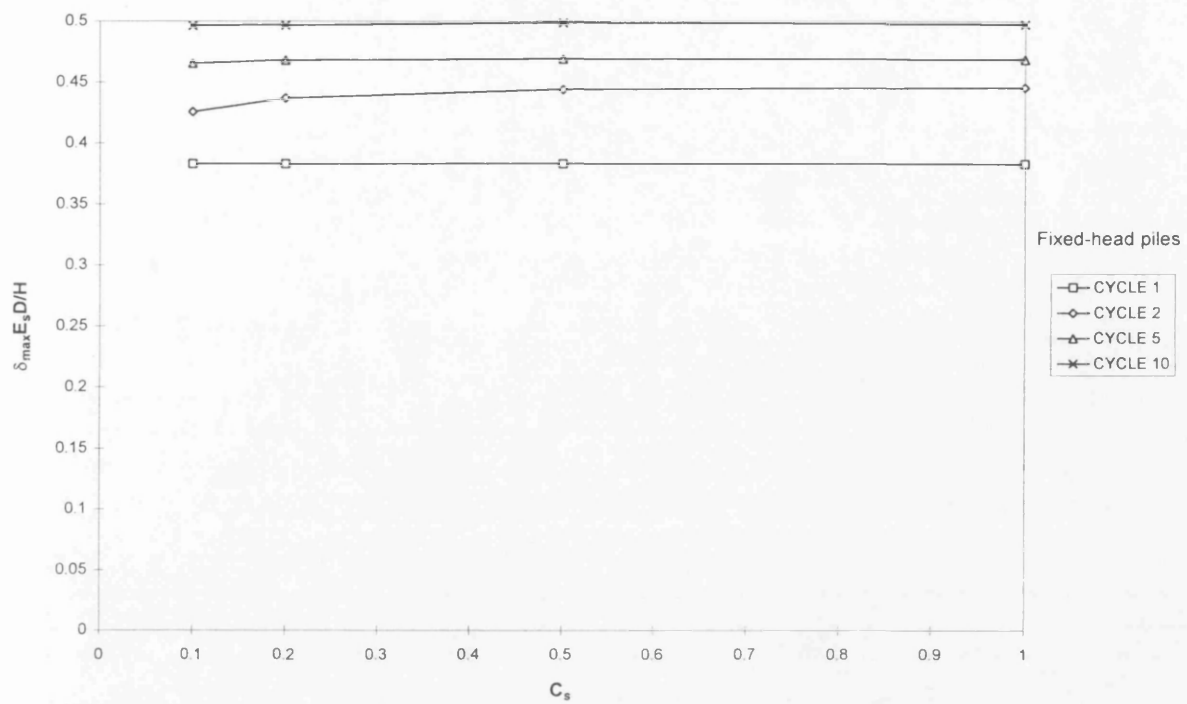


(a)

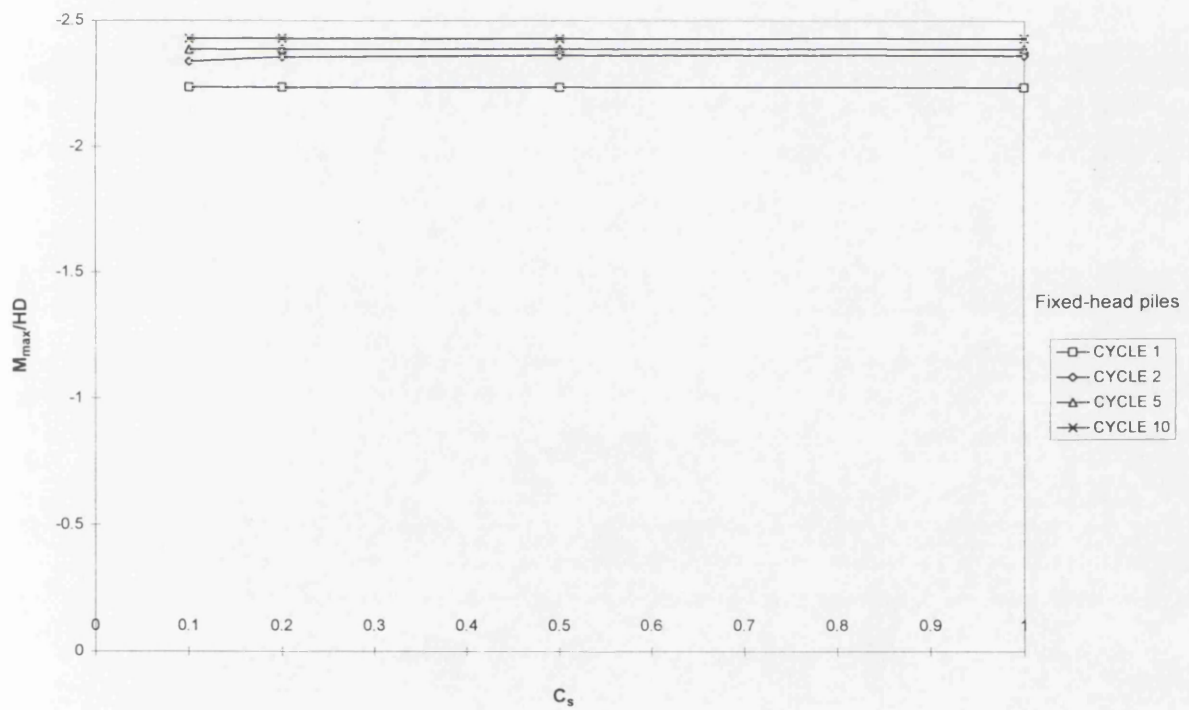


(b)

Figure 7.17 The effect of shear strength degradation rate factor (C_s) on (a) pile-head displacements and (b) maximum bending moments, for free-head piles in stiff clay.

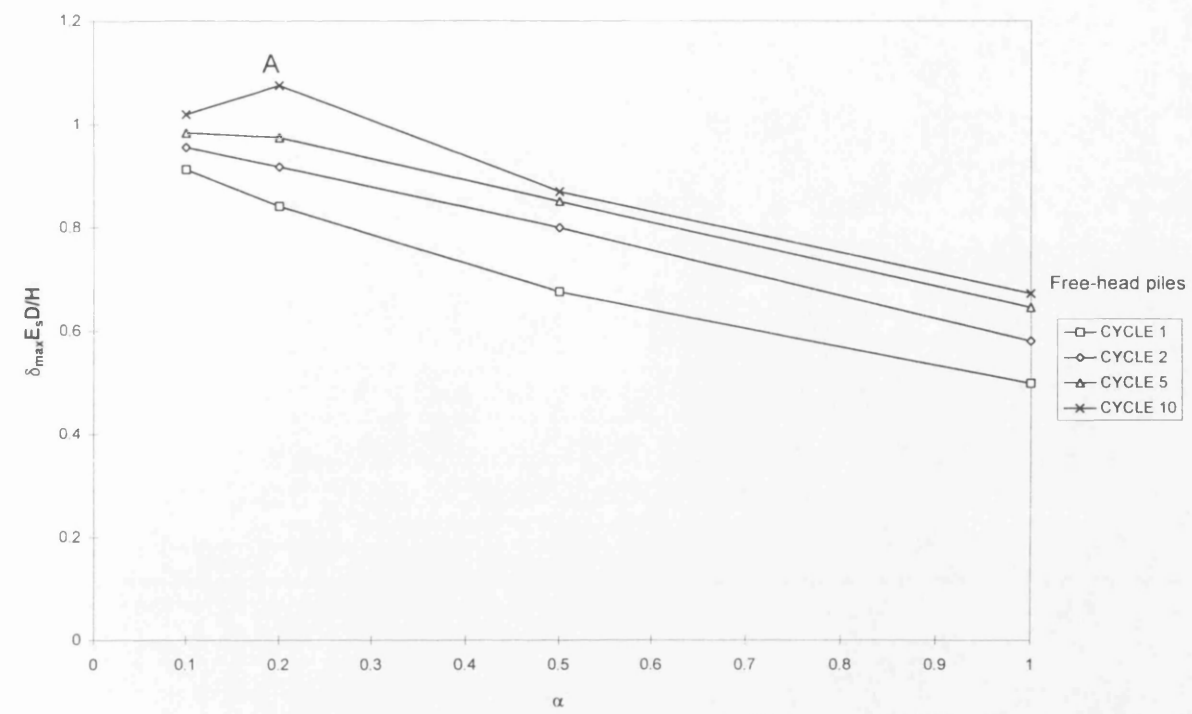


(a)

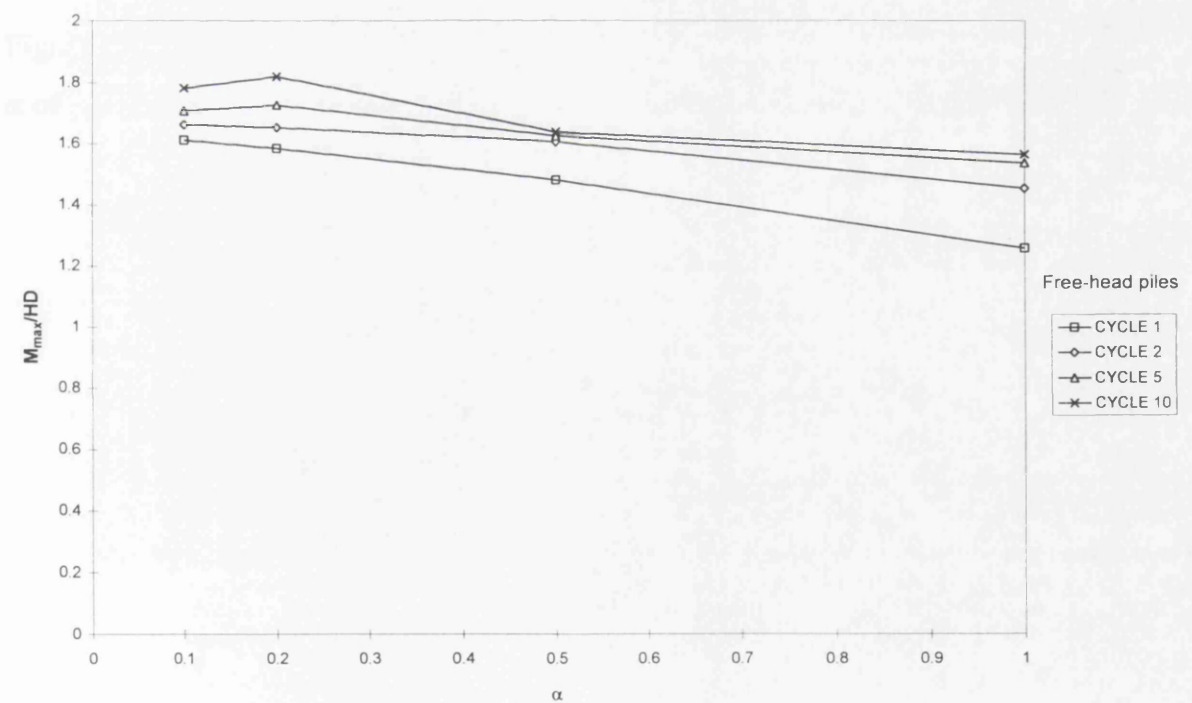


(b)

Figure 7.18 The effect of shear strength degradation rate factor (C_s) on (a) pile-head displacements and (b) maximum bending moments, for fixed-head piles in stiff clay.

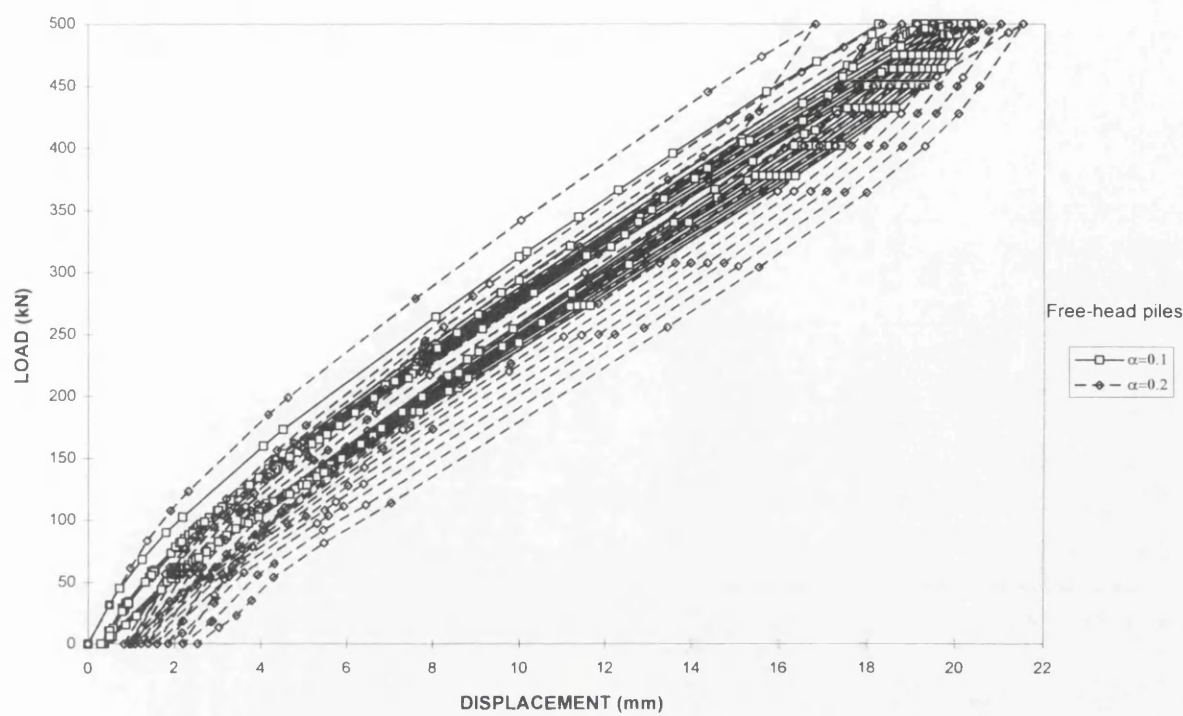


(a)



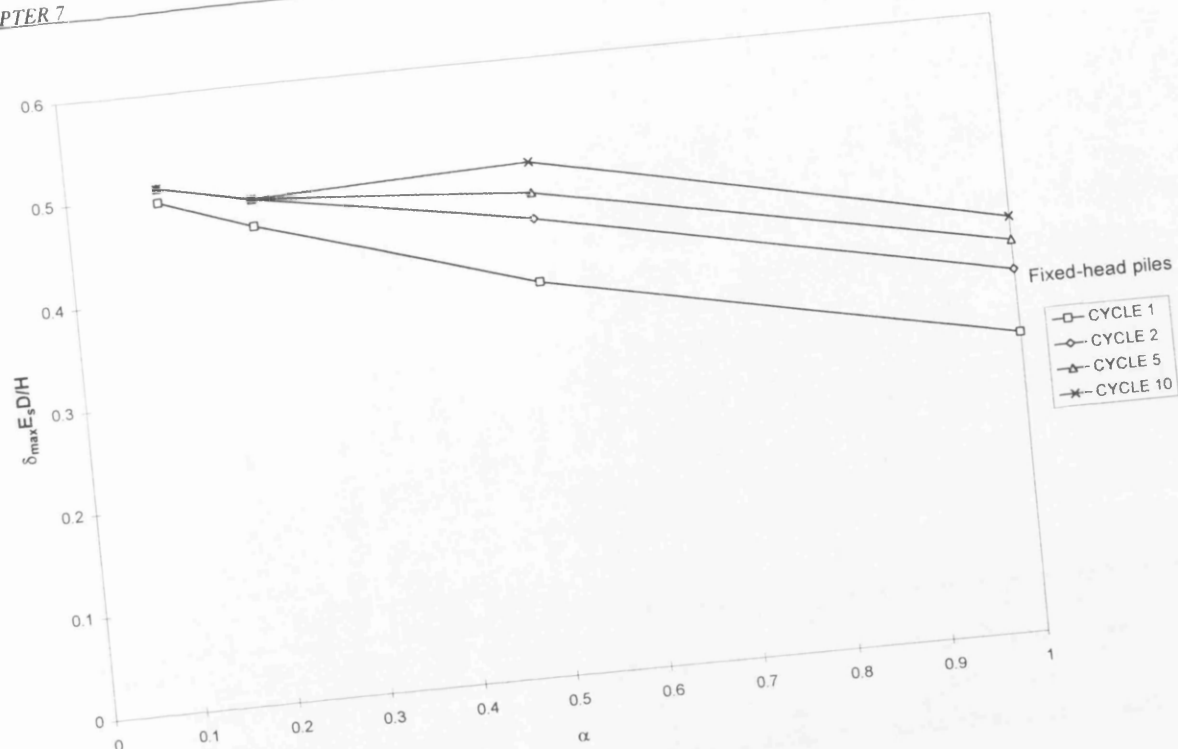
(b)

Figure 7.19 The effect of adhesion factor (α) on (a) pile-head displacements, (b) maximum bending moments and (c) pile-head load-displacement responses for α of 0.1 and 0.2 (see overleaf), for free-head piles in stiff clay.

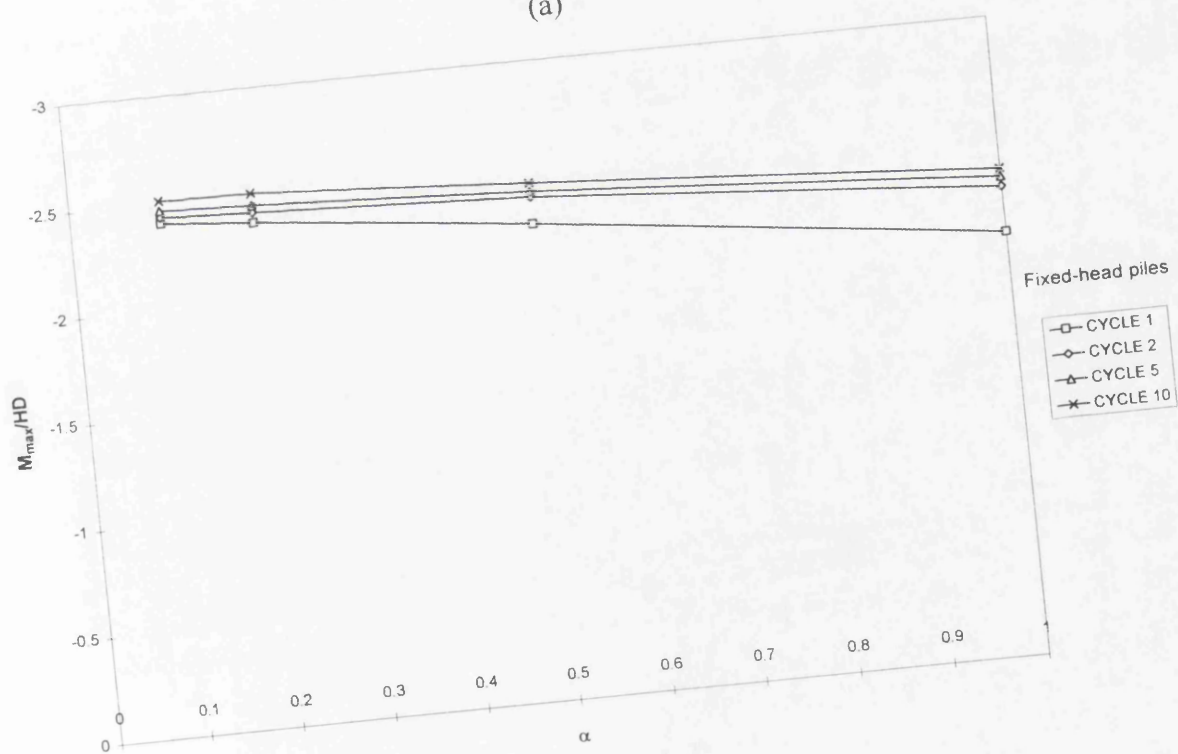


(c)

Figure 7.19 (c) The effect of adhesion factor (α) on pile-head load-displacement responses for α of 0.1 and 0.2, for free-head piles in stiff clay.



(a)



(b)

Figure 7.20 The effect of adhesion factor (α) on (a) pile-head displacements and (b) maximum bending moments, for fixed-head piles in stiff clay.

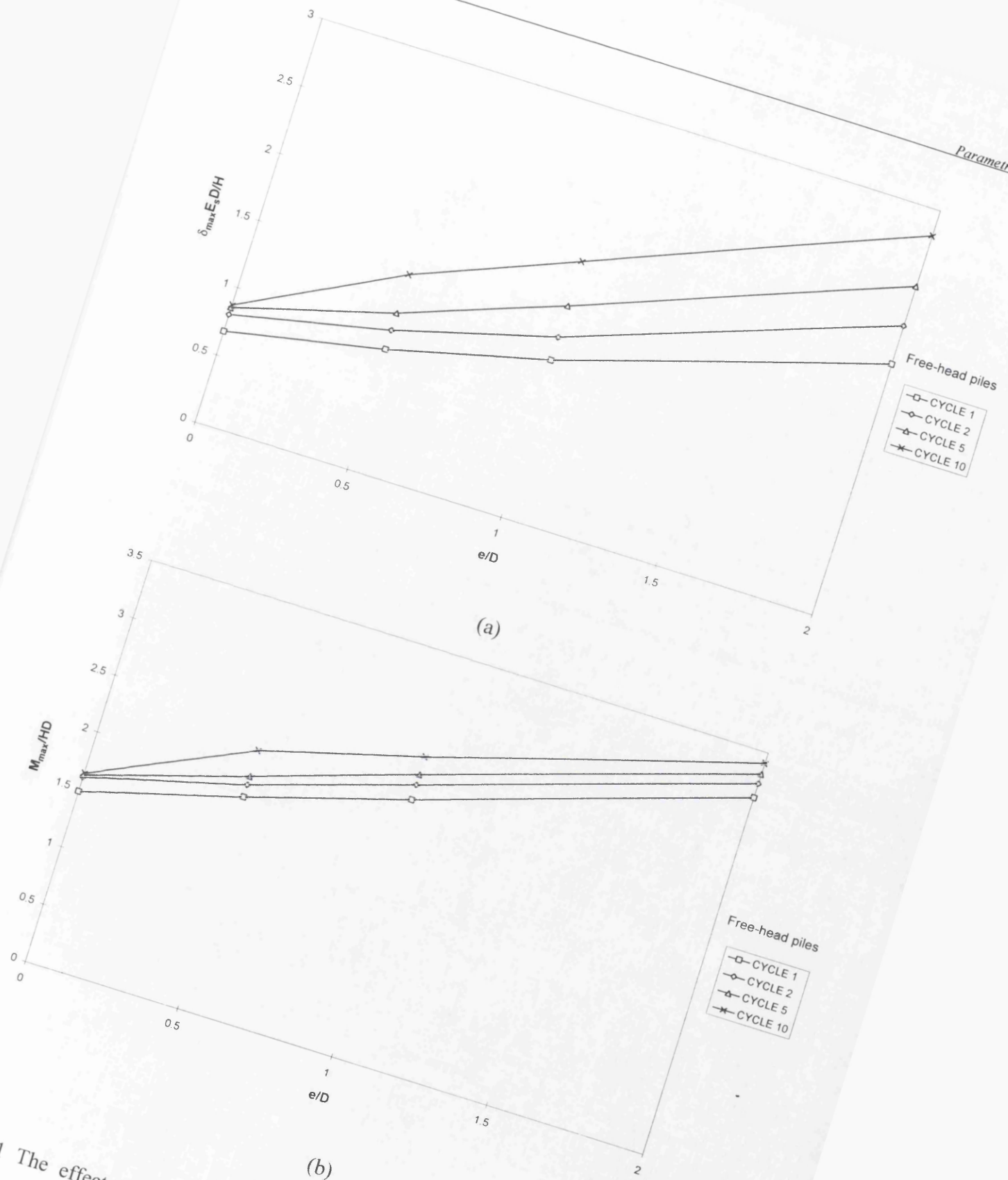
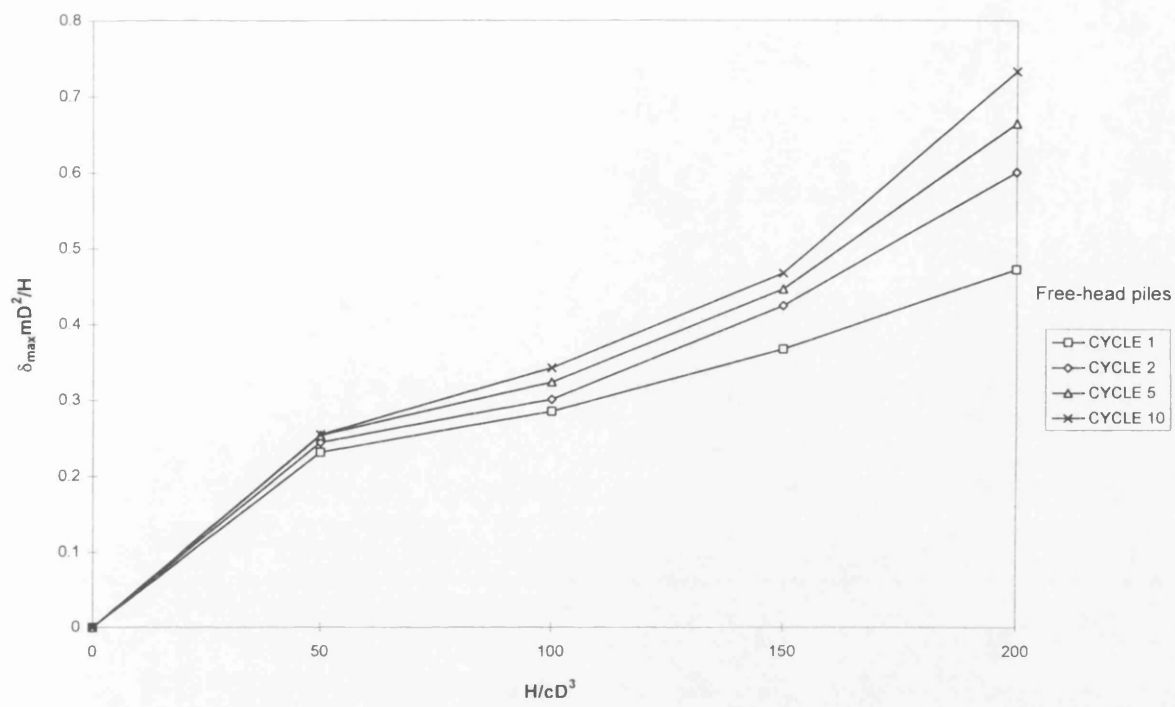
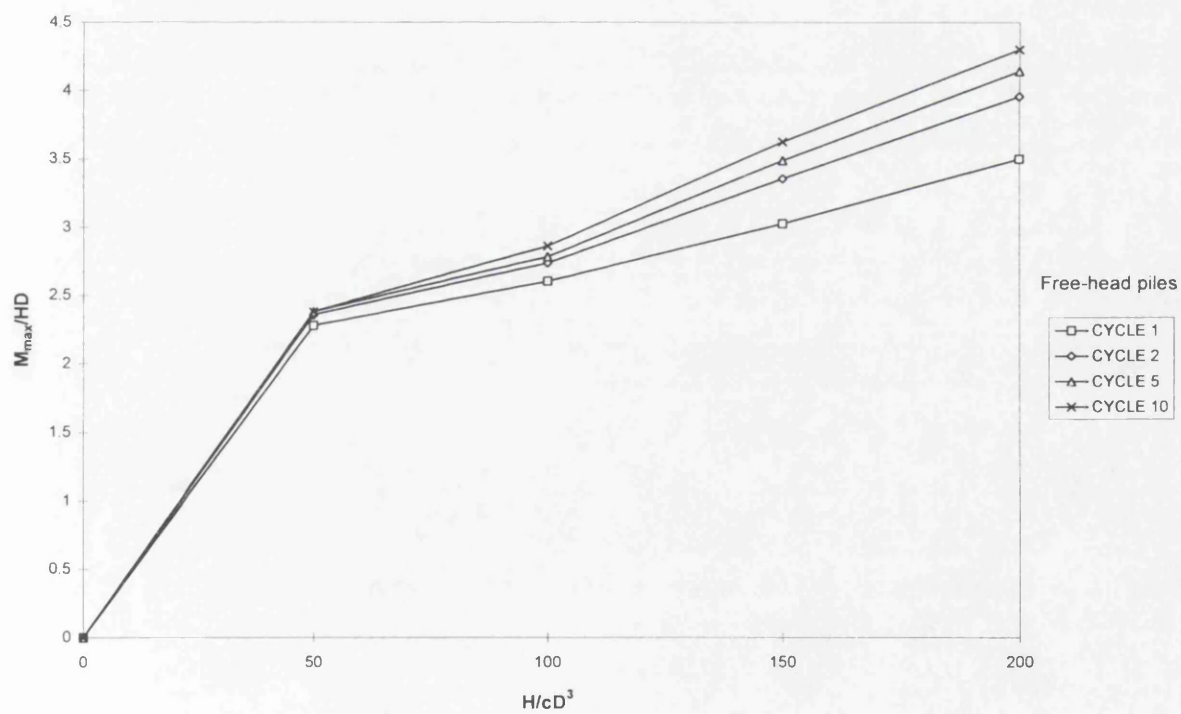


Figure 7.21 The effect of eccentric loading (e) on (a) pile-head displacements and (b) maximum bending moments, for free-head piles in stiff clay.

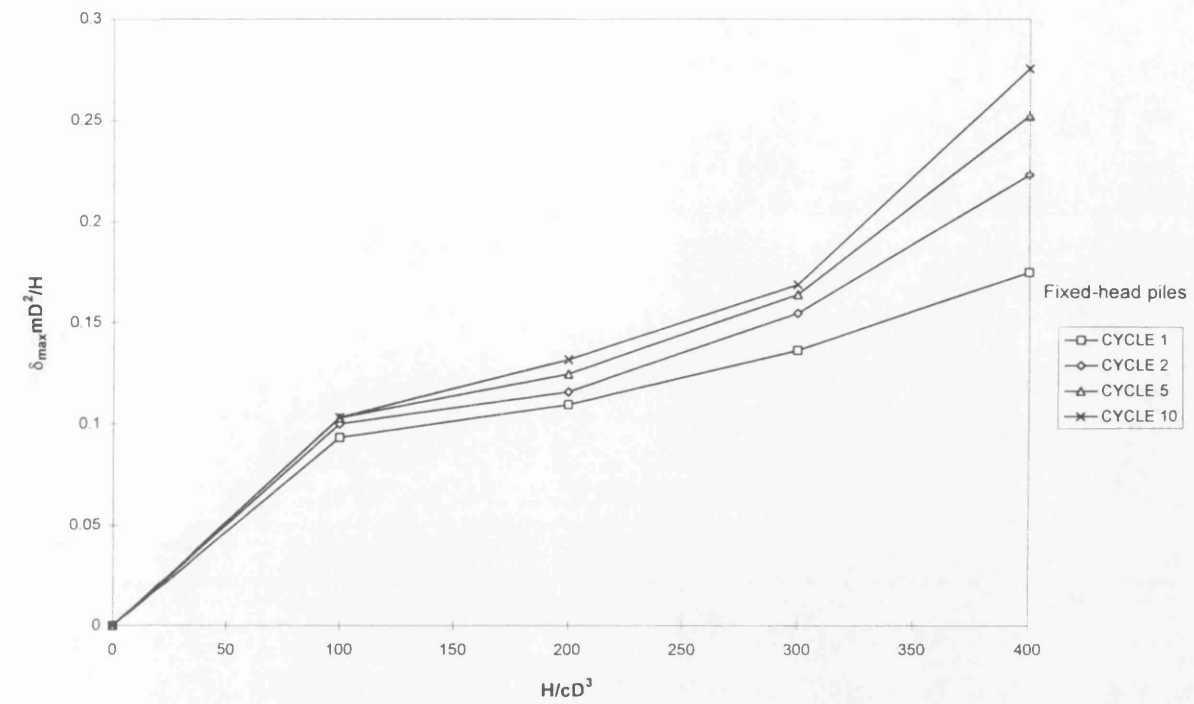


(a)

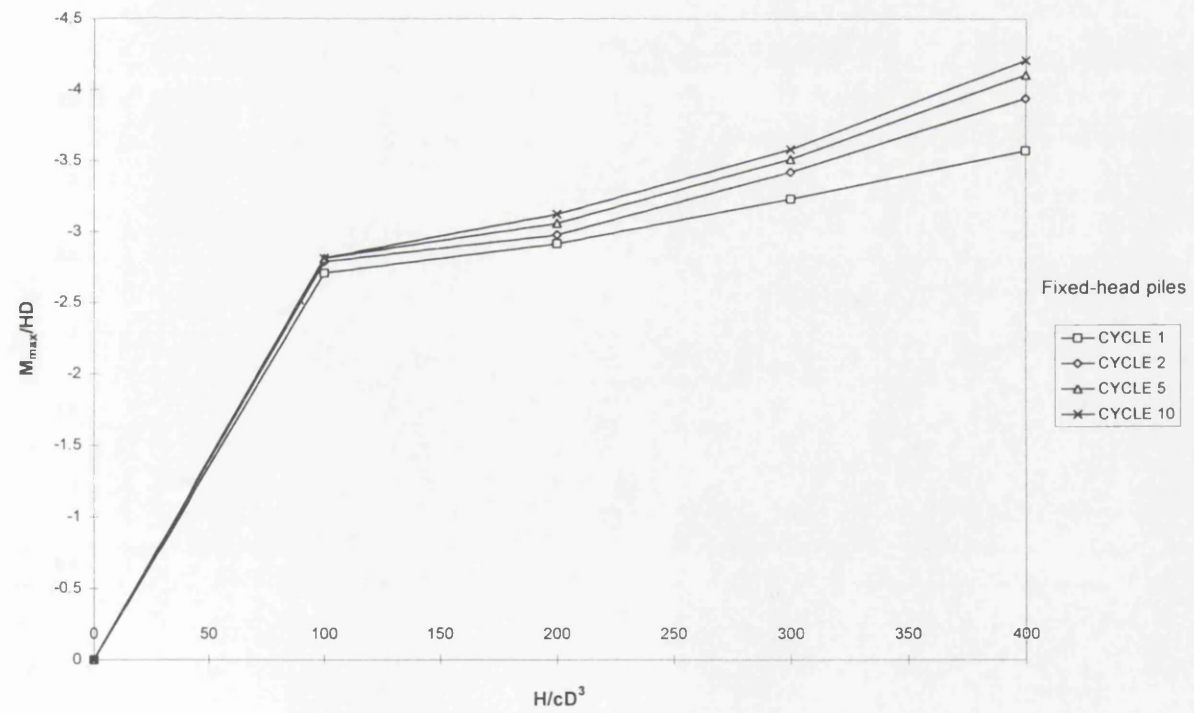


(b)

Figure 7.22 The effect of load levels on (a) pile-head displacements and (b) maximum bending moments, for free-head piles in soft clay.

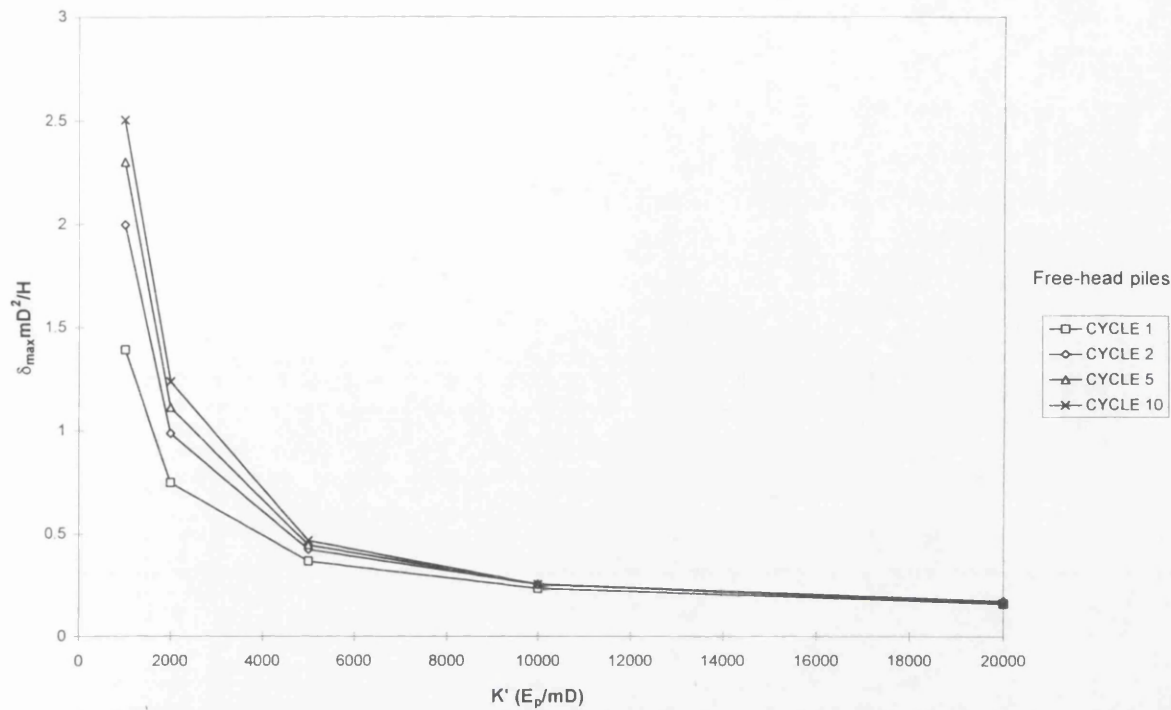


(a)

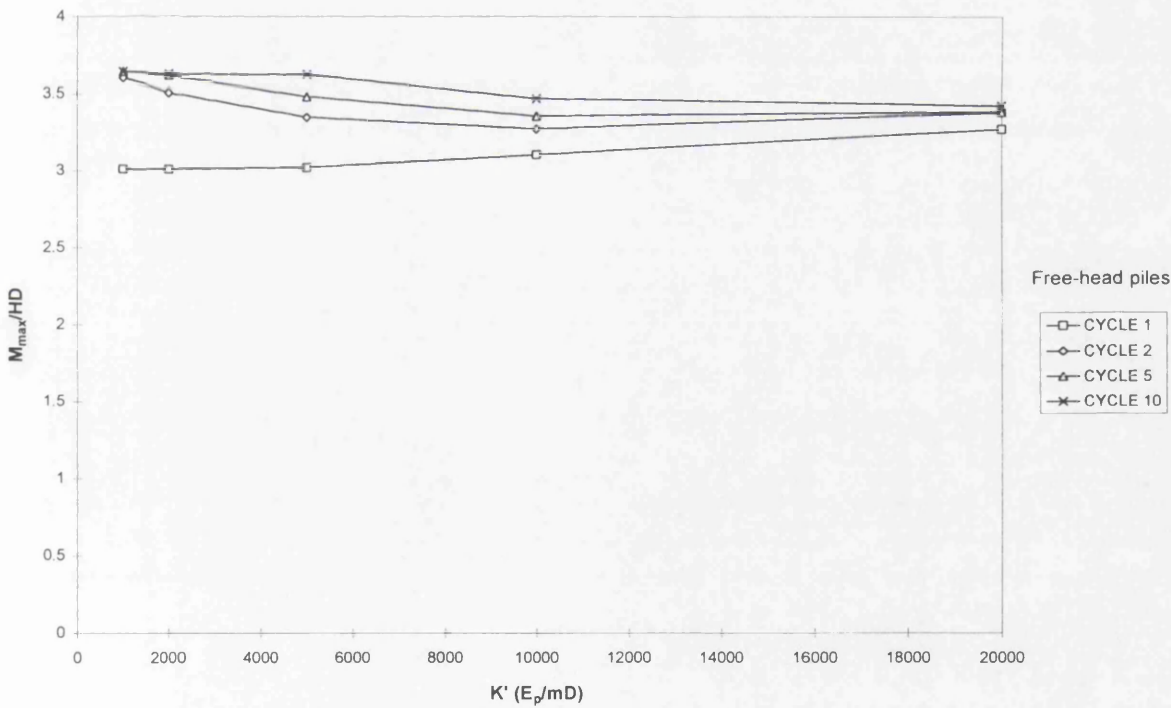


(b)

Figure 7.23 The effect of load levels on (a) pile-head displacements and (b) maximum bending moments, for fixed-head piles in soft clay.

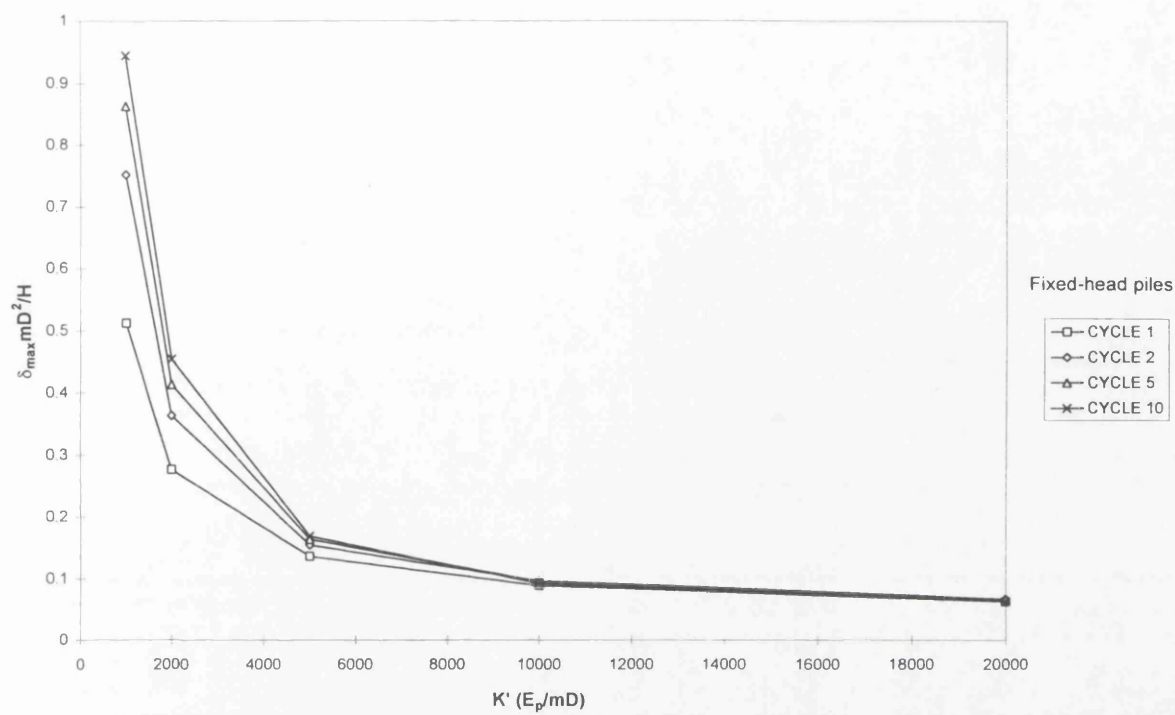


(a)

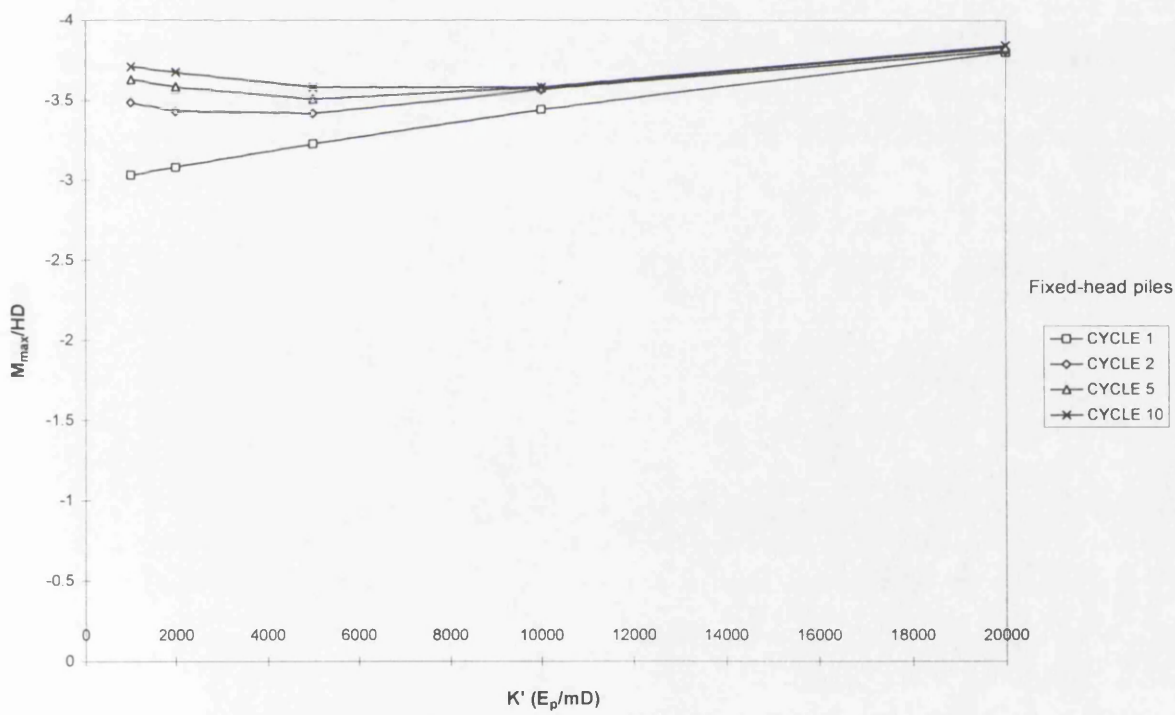


(b)

Figure 7.24 The effect of pile Young's modulus (E_p) on (a) pile-head displacements and (b) maximum bending moments, for free-head piles in soft clay.

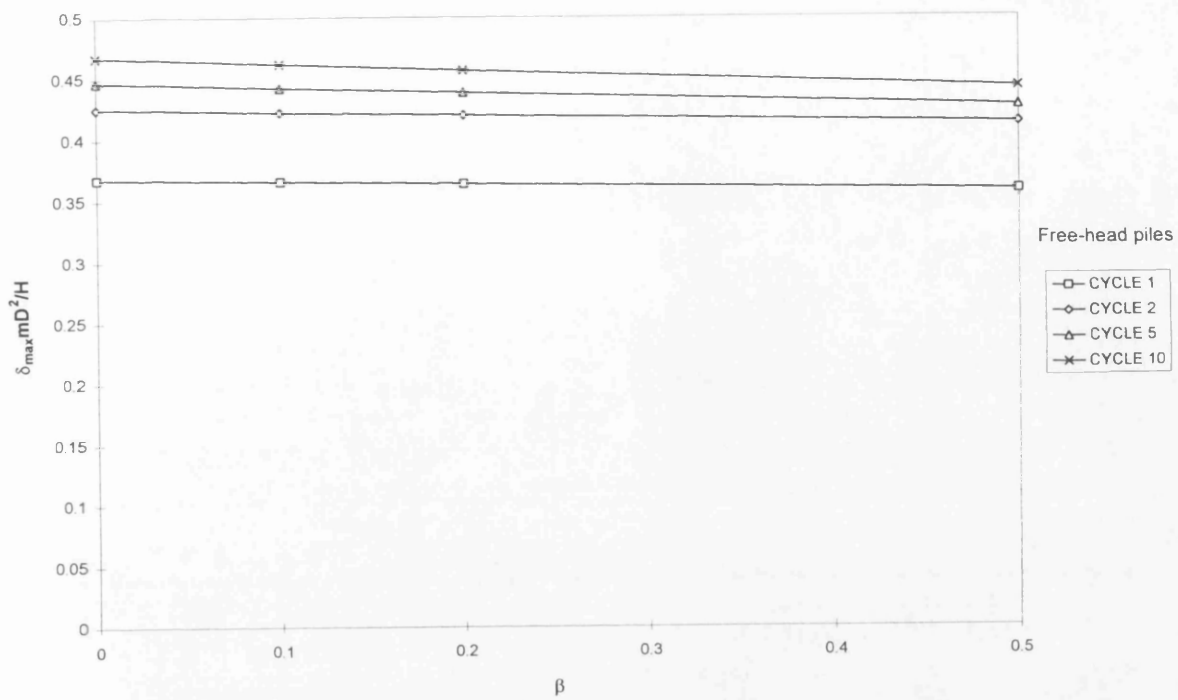


(a)

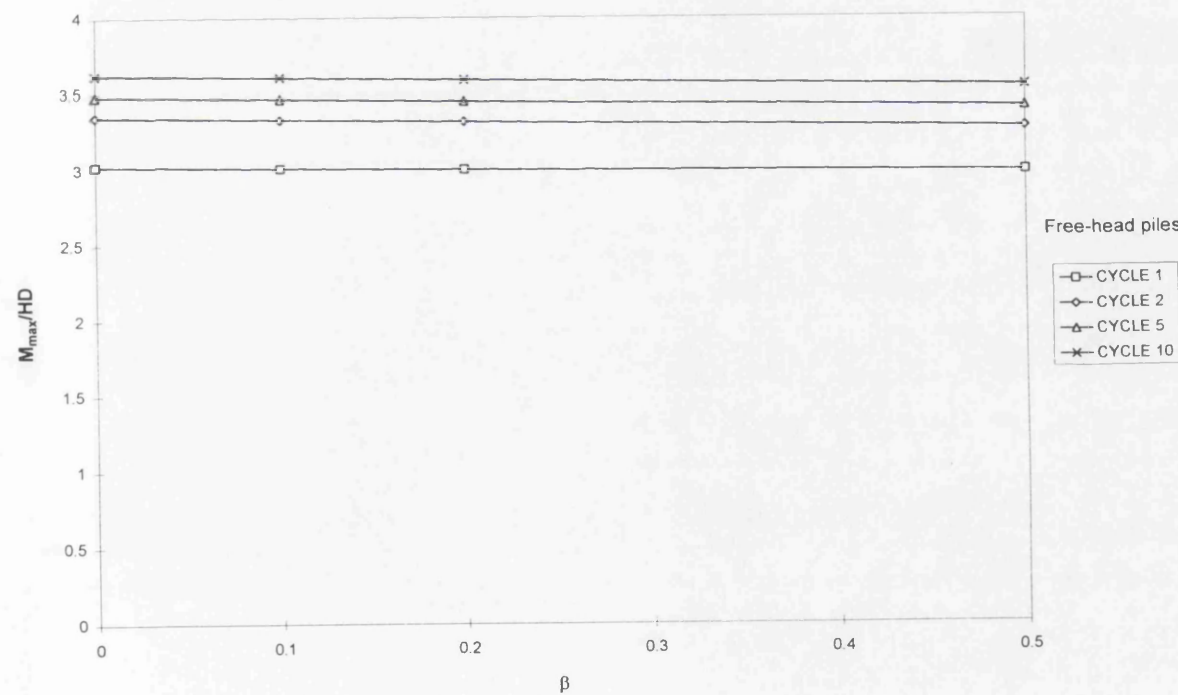


(b)

Figure 7.25 The effect of pile Young's modulus (E_p) on (a) pile-head displacements and (b) maximum bending moments, for fixed-head piles in soft clay.

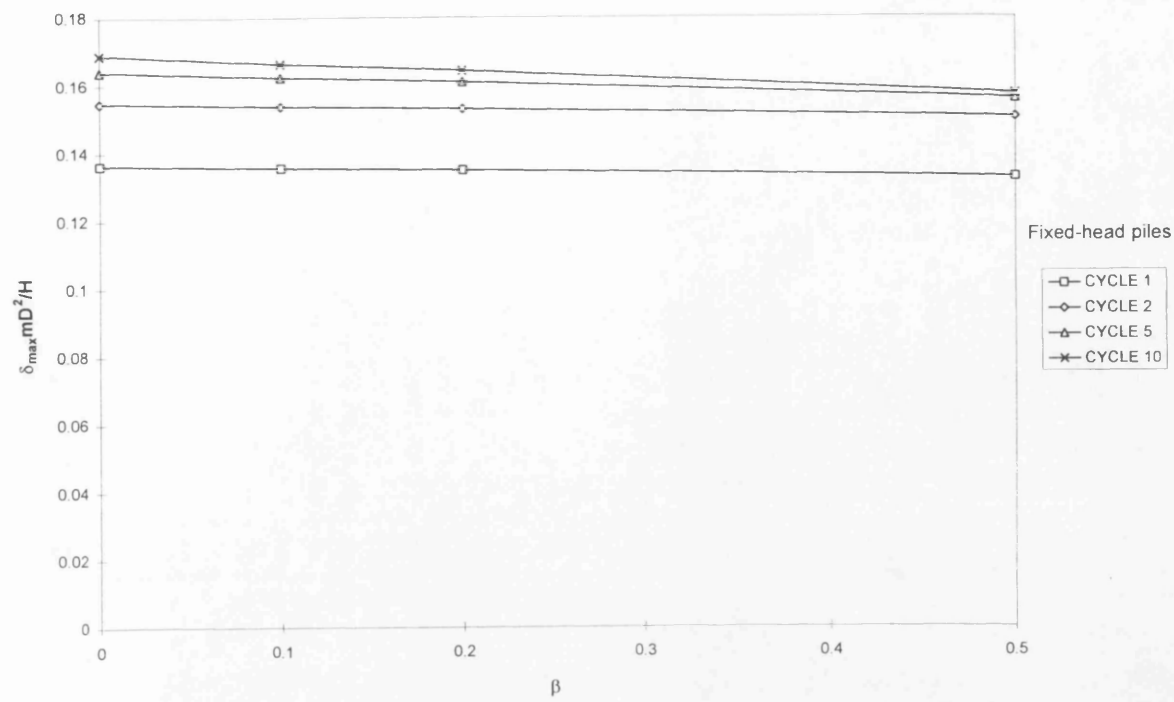


(a)

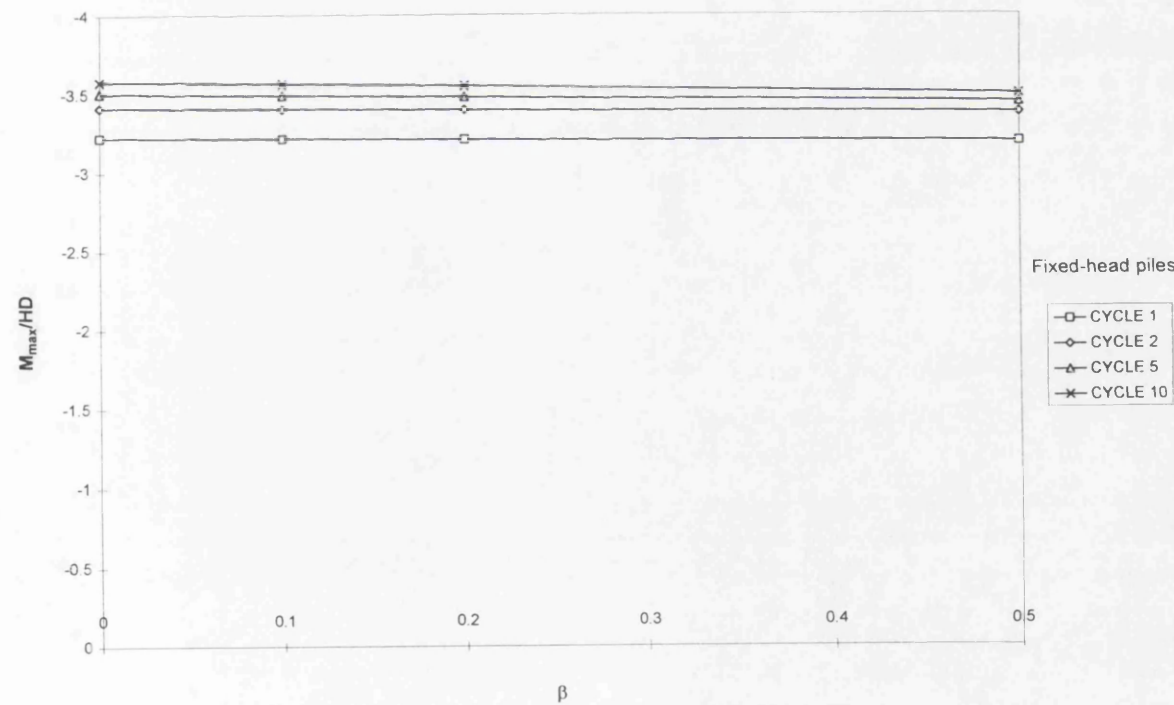


(b)

Figure 7.26 The effect of backsliding factor (β) on (a) pile-head displacements and (b) maximum bending moments, for free-head piles in soft clay.

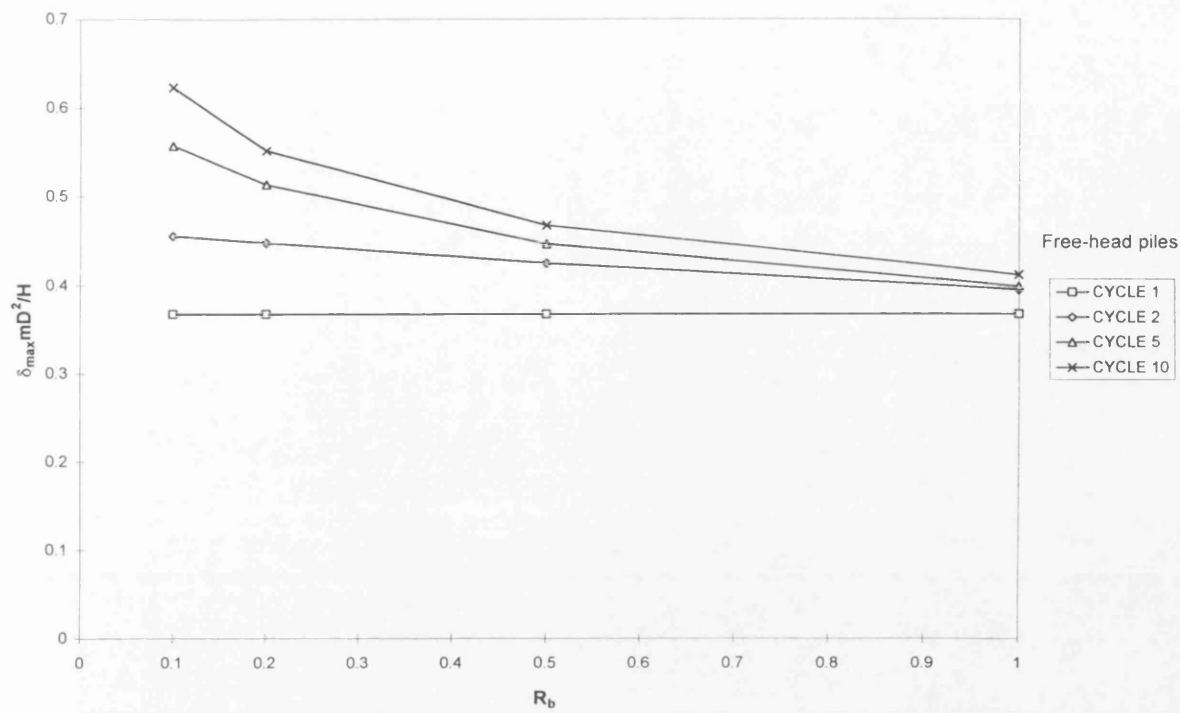


(a)

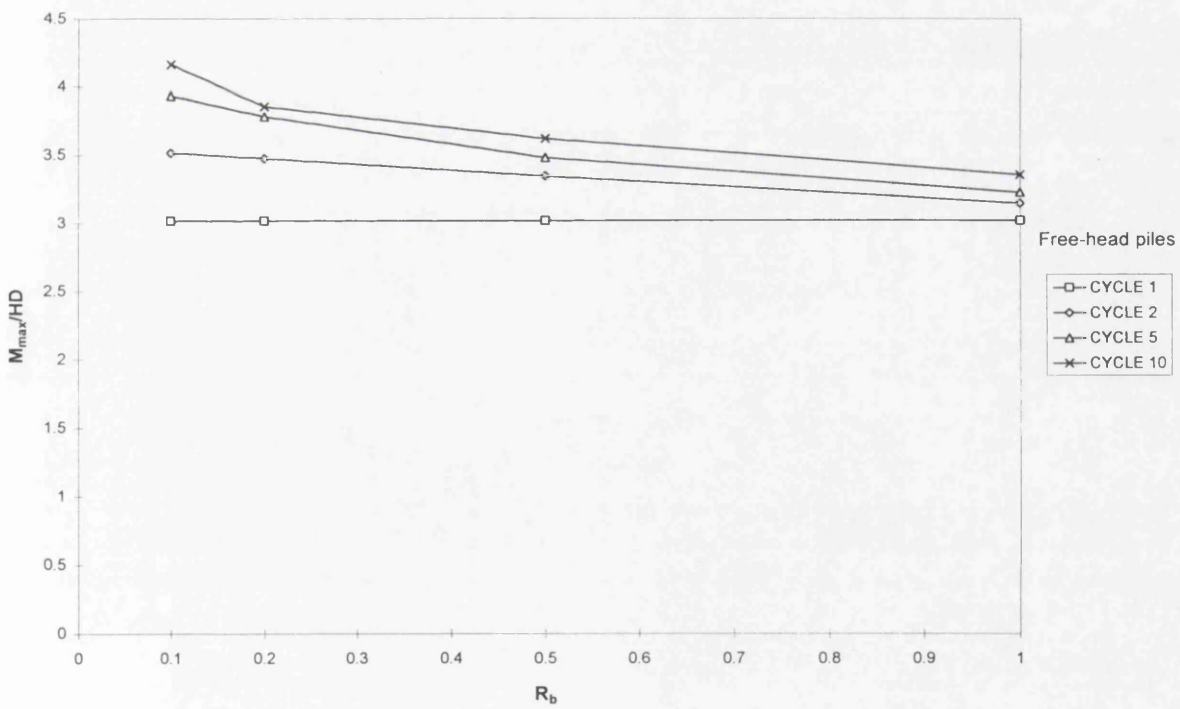


(b)

Figure 7.27 The effect of backsliding factor (β) on (a) pile-head displacements and (b) maximum bending moments, for fixed-head piles in soft clay.

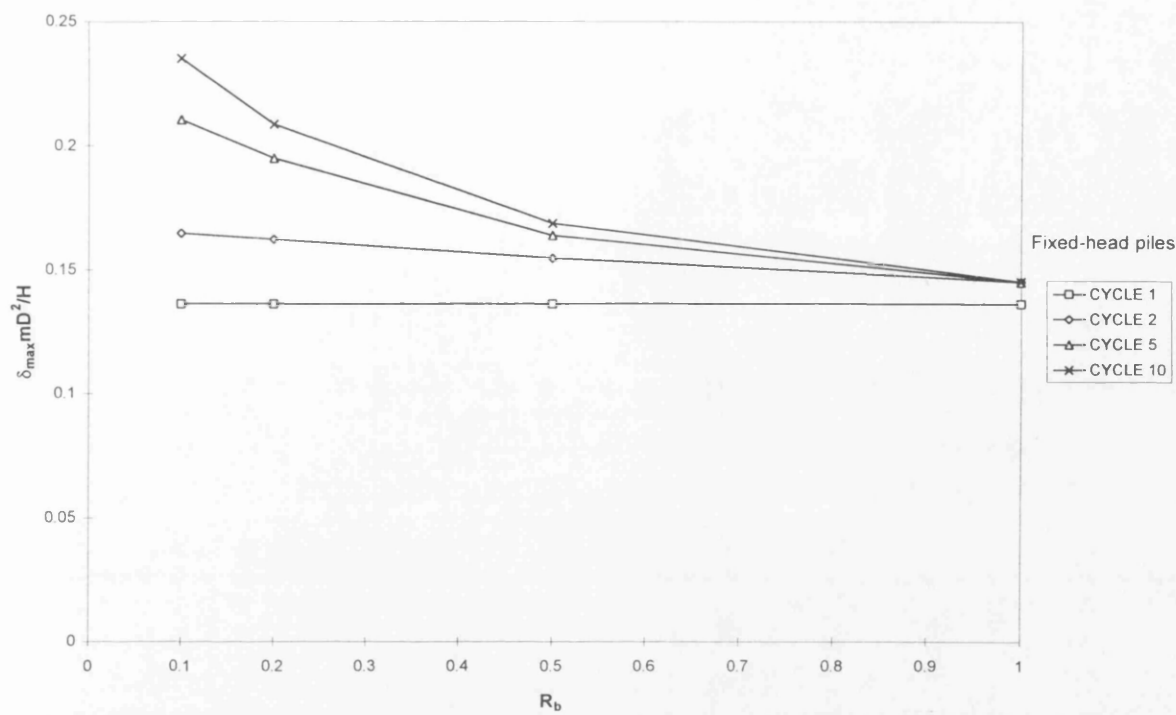


(a)

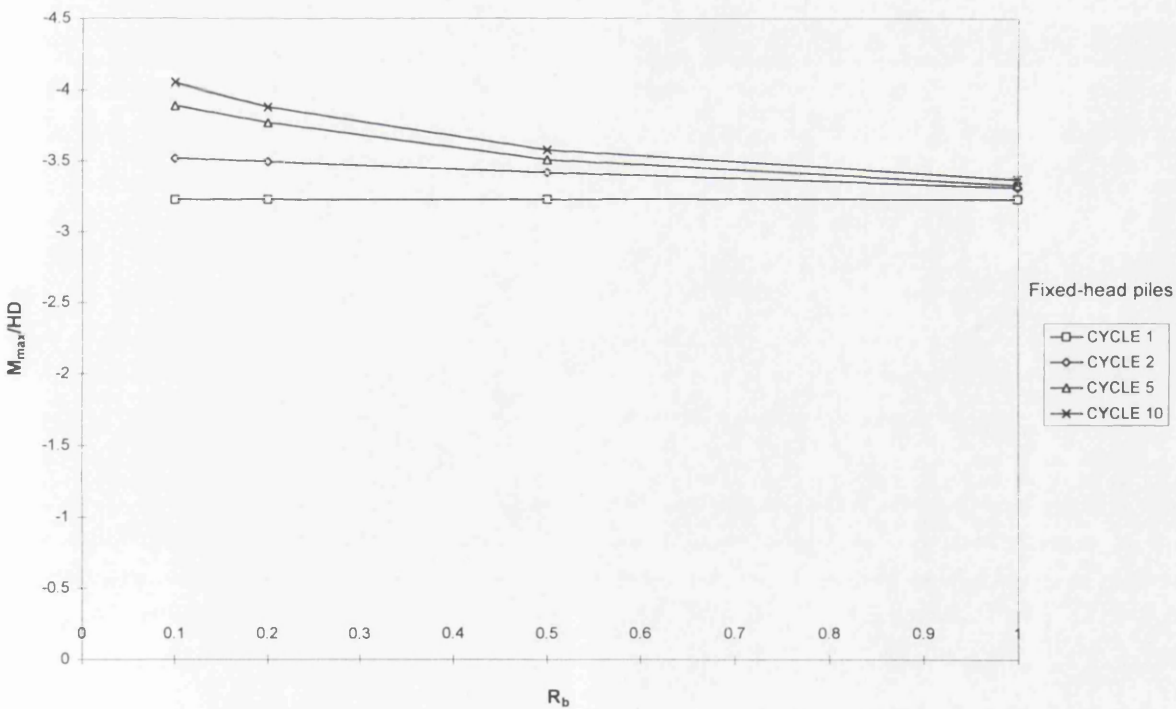


(b)

Figure 7.28 The effect of residual/peak bearing strength ratio (R_b) on (a) pile-head displacements and (b) maximum bending moments, for free-head piles in soft clay.

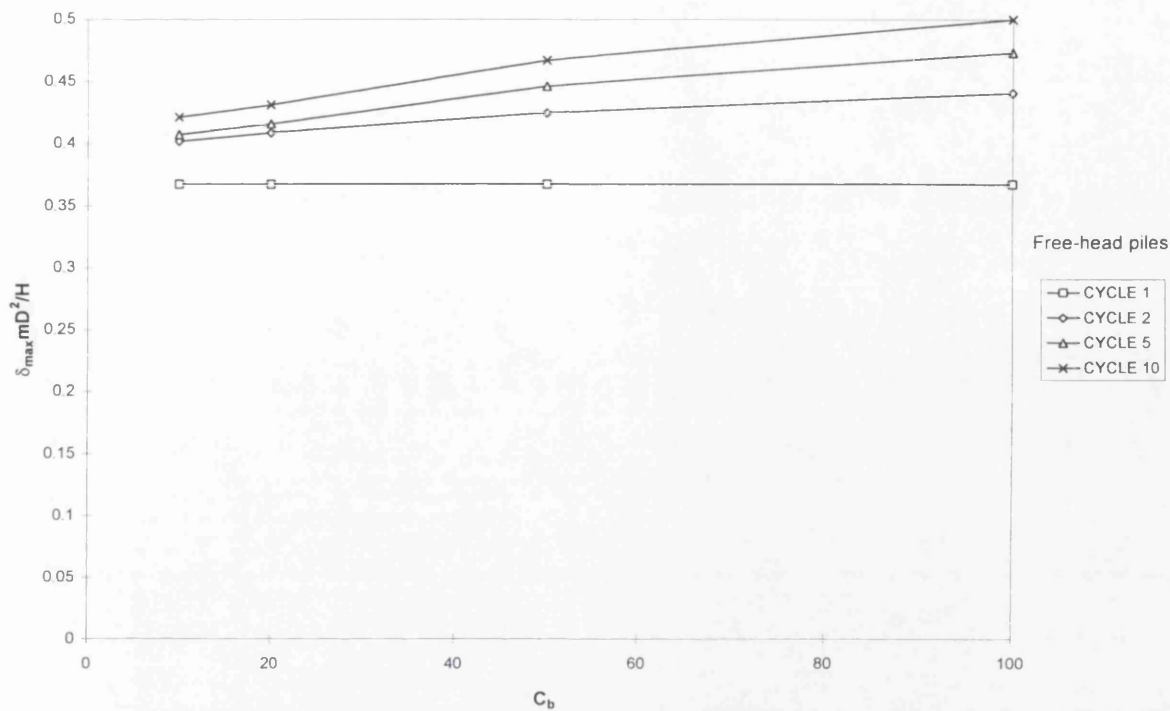


(a)

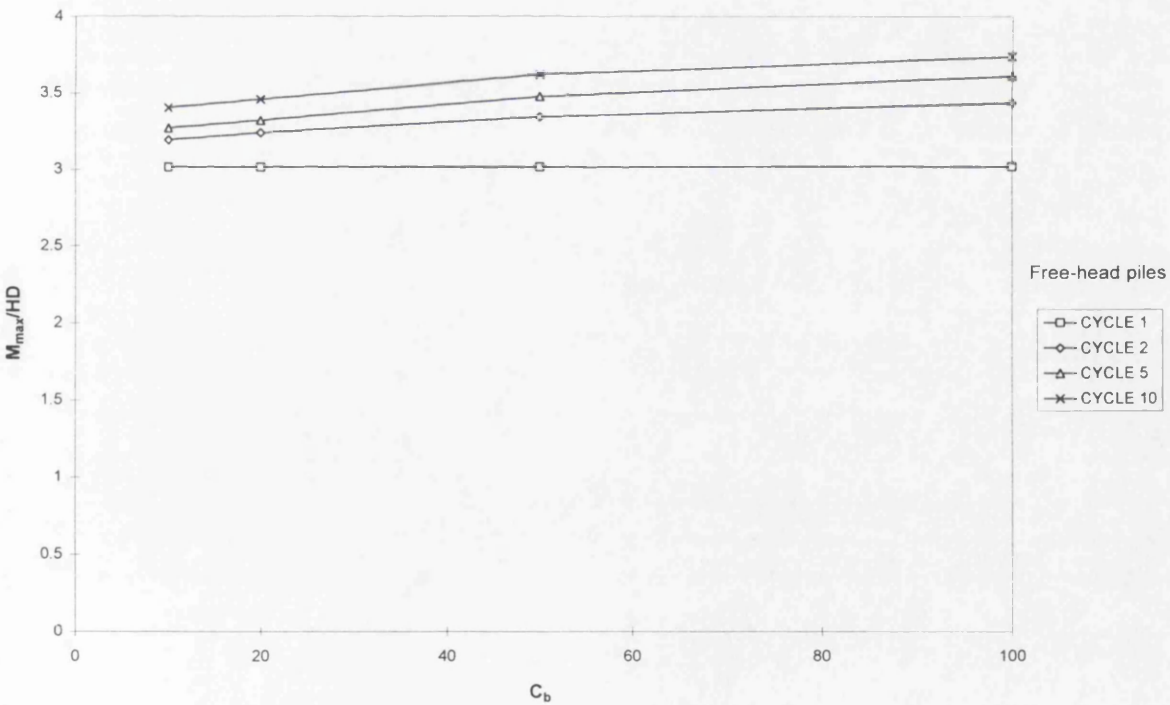


(b)

Figure 7.29 The effect of residual/peak bearing strength ratio (R_b) on (a) pile-head displacements and (b) maximum bending moments, for fixed-head piles in soft clay.

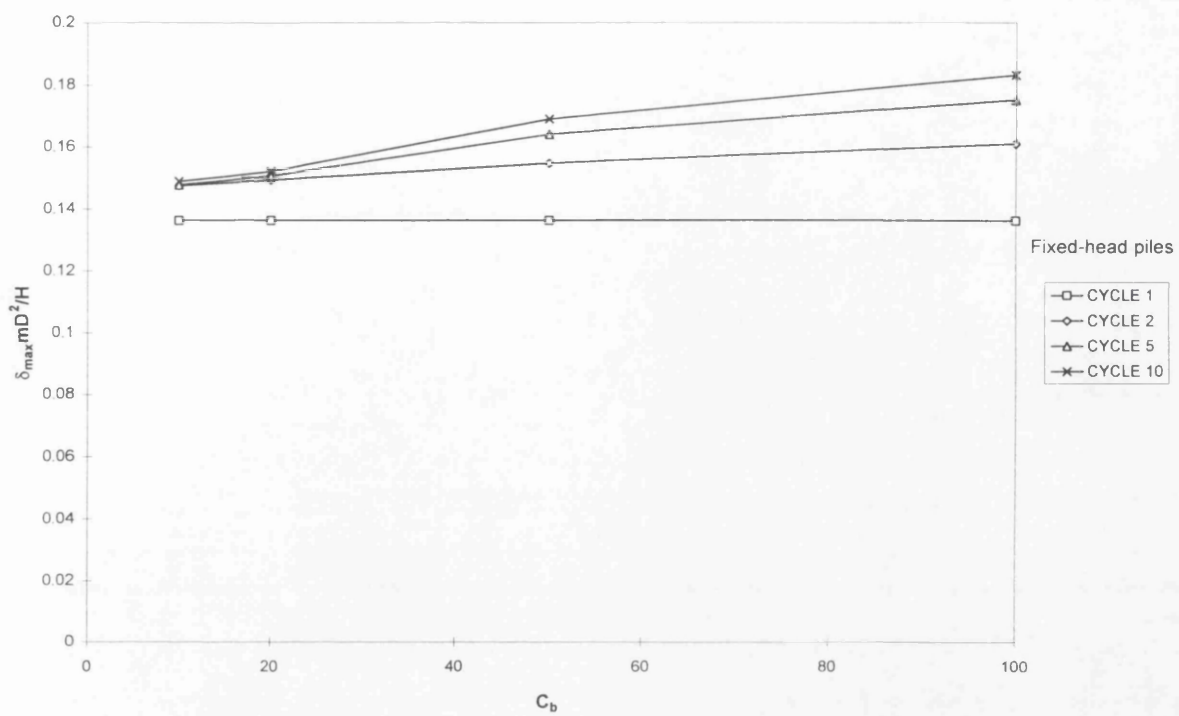


(a)

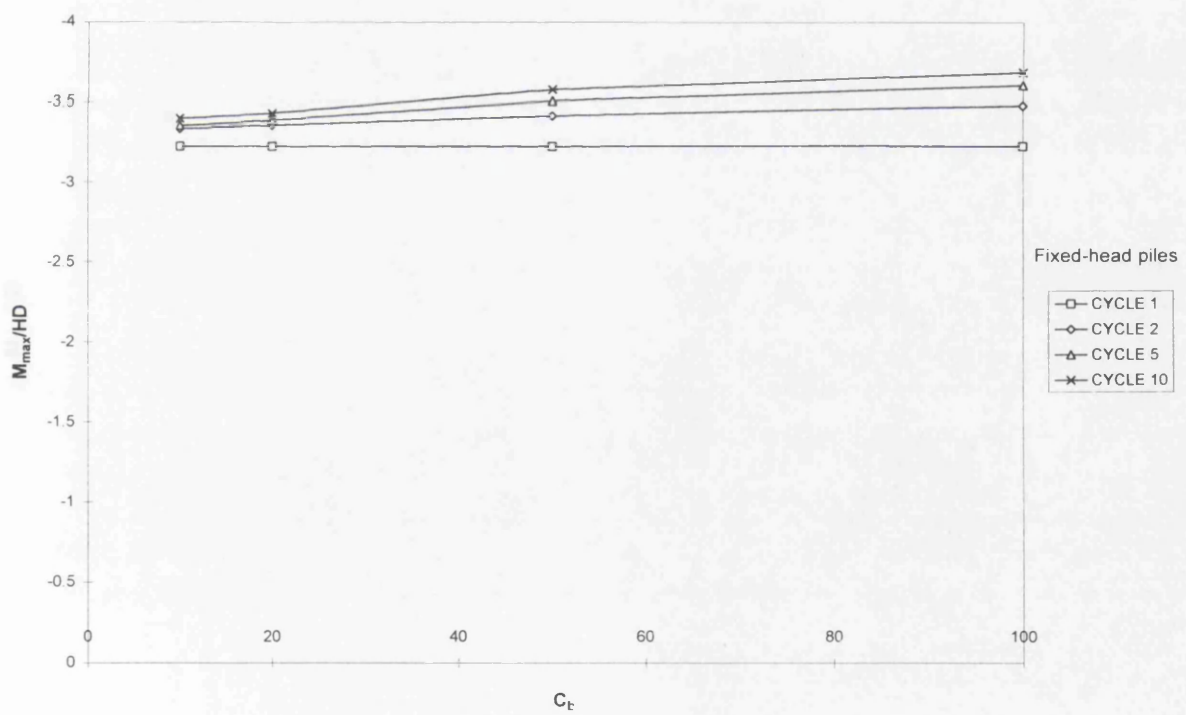


(b)

Figure 7.30 The effect of bearing degradation rate factor (C_b) on (a) pile-head displacements and (b) maximum bending moments, for free-head piles in soft clay.

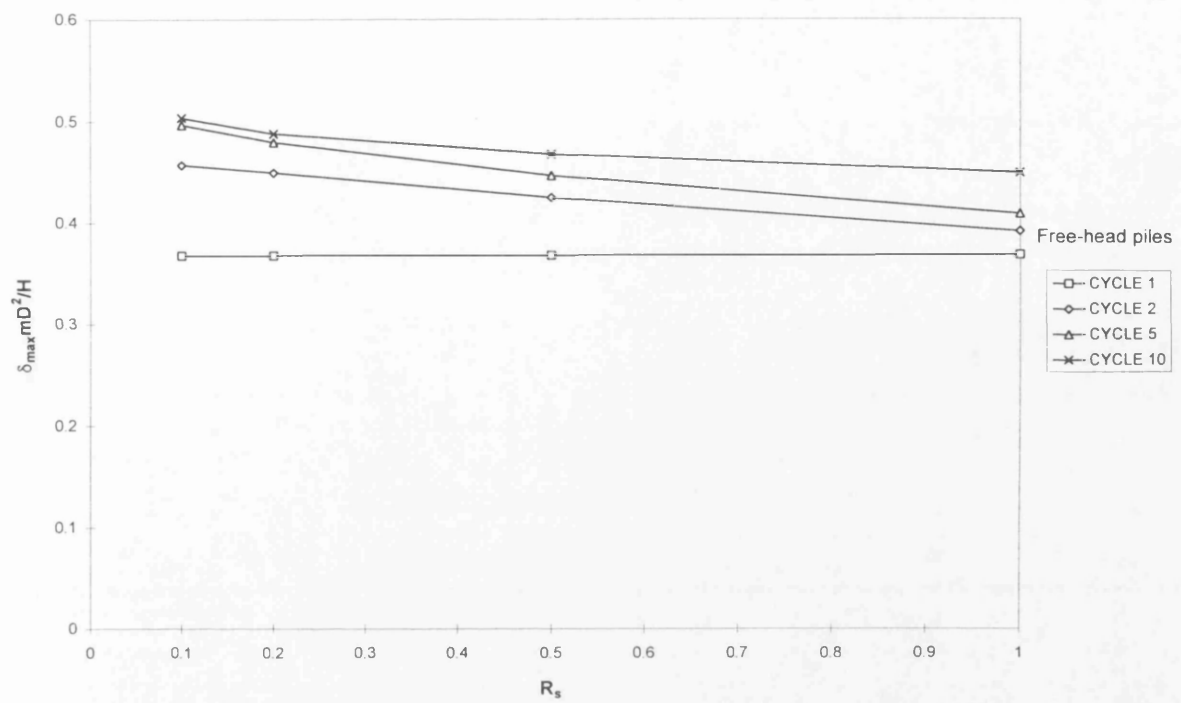


(a)

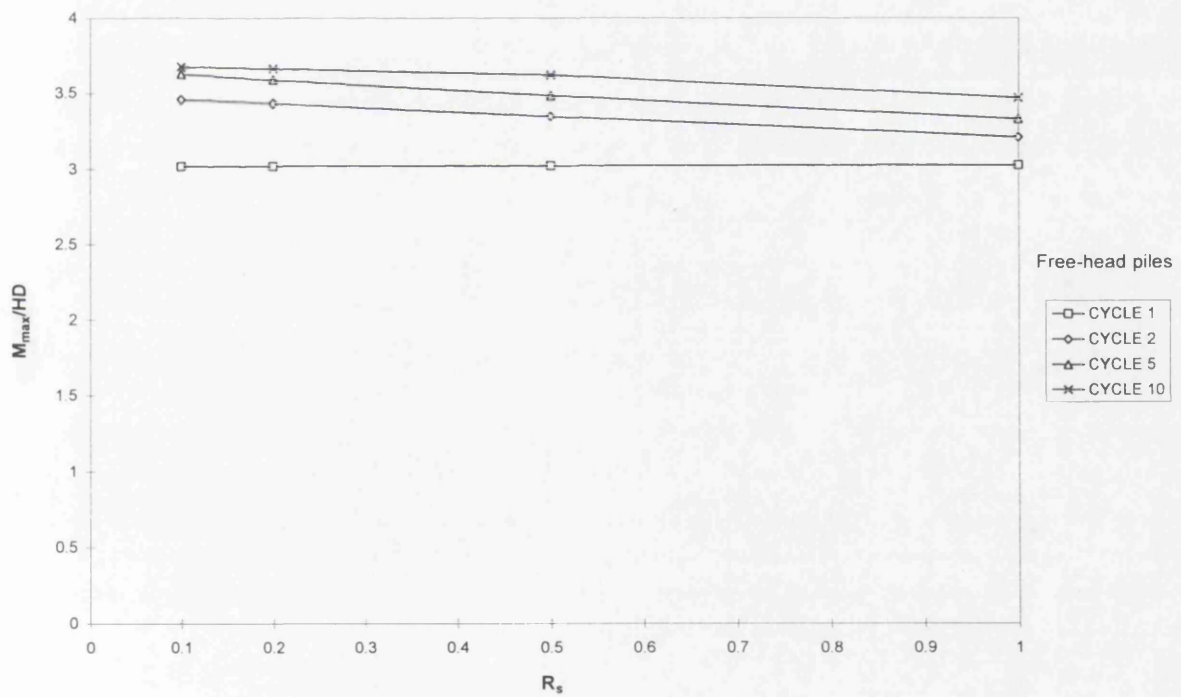


(b)

Figure 7.31 The effect of bearing degradation rate factor (C_b) on (a) pile-head displacements and (b) maximum bending moments, for fixed-head piles in soft clay.

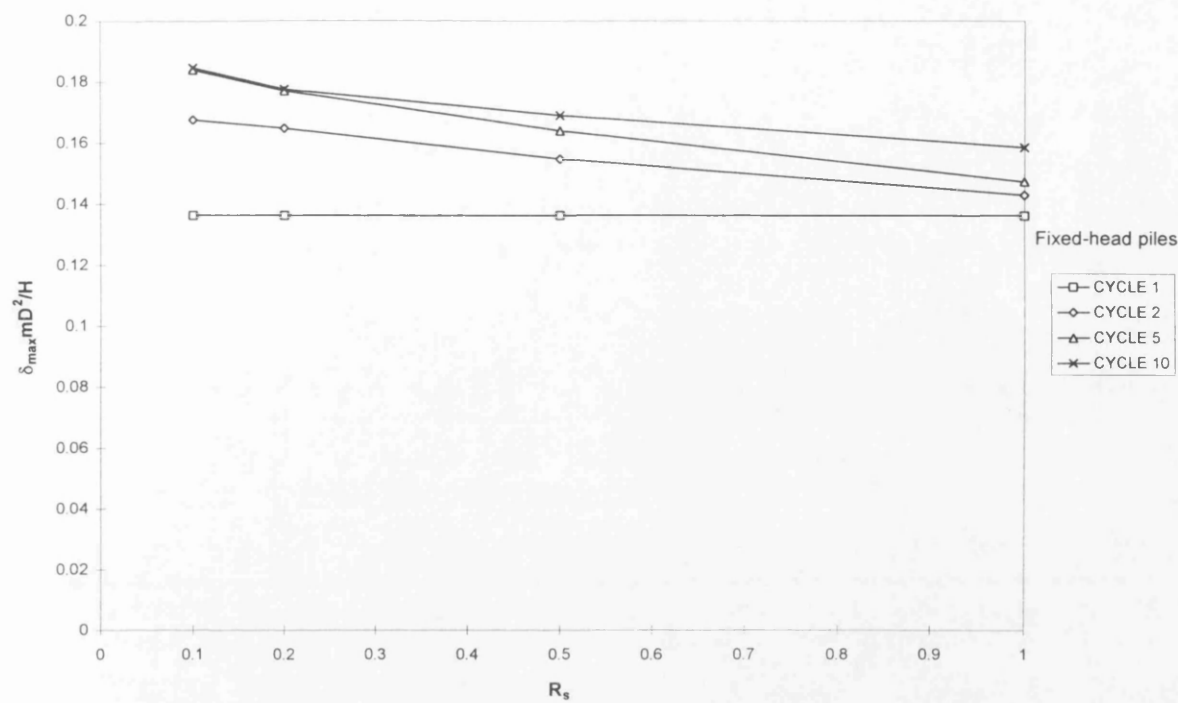


(a)

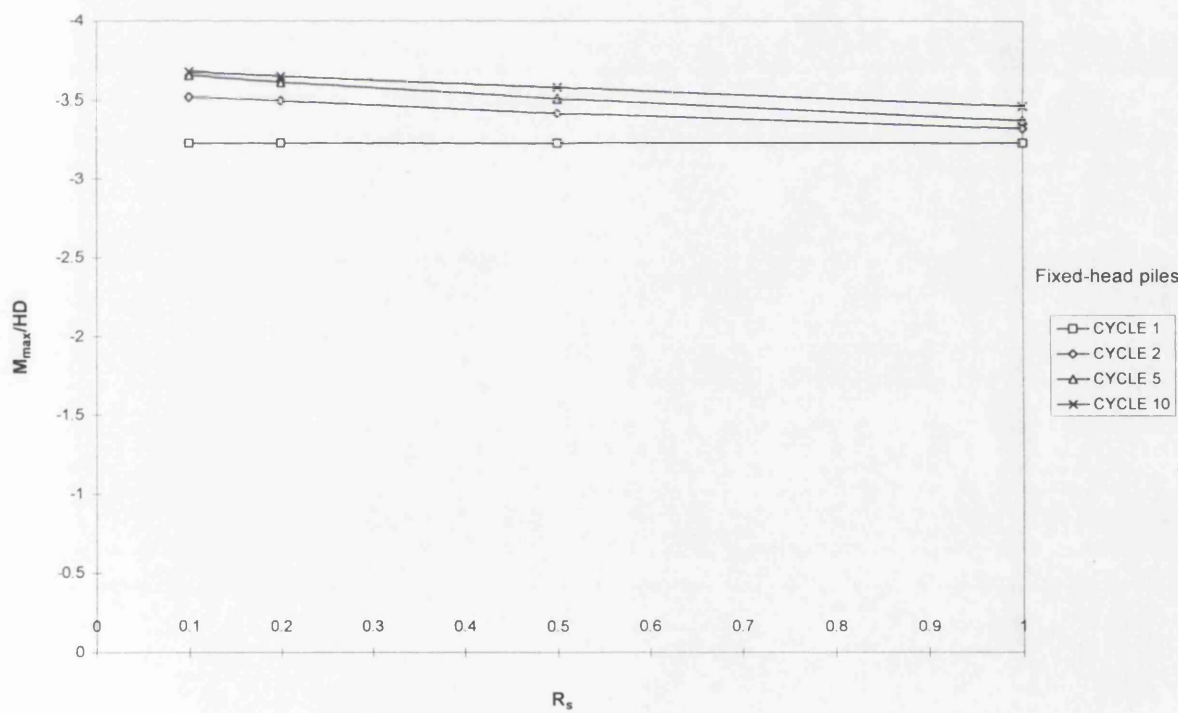


(b)

Figure 7.32 The effect of residual/peak shear strength ratio (R_s) on (a) pile-head displacements and (b) maximum bending moments, for free-head piles in soft clay.

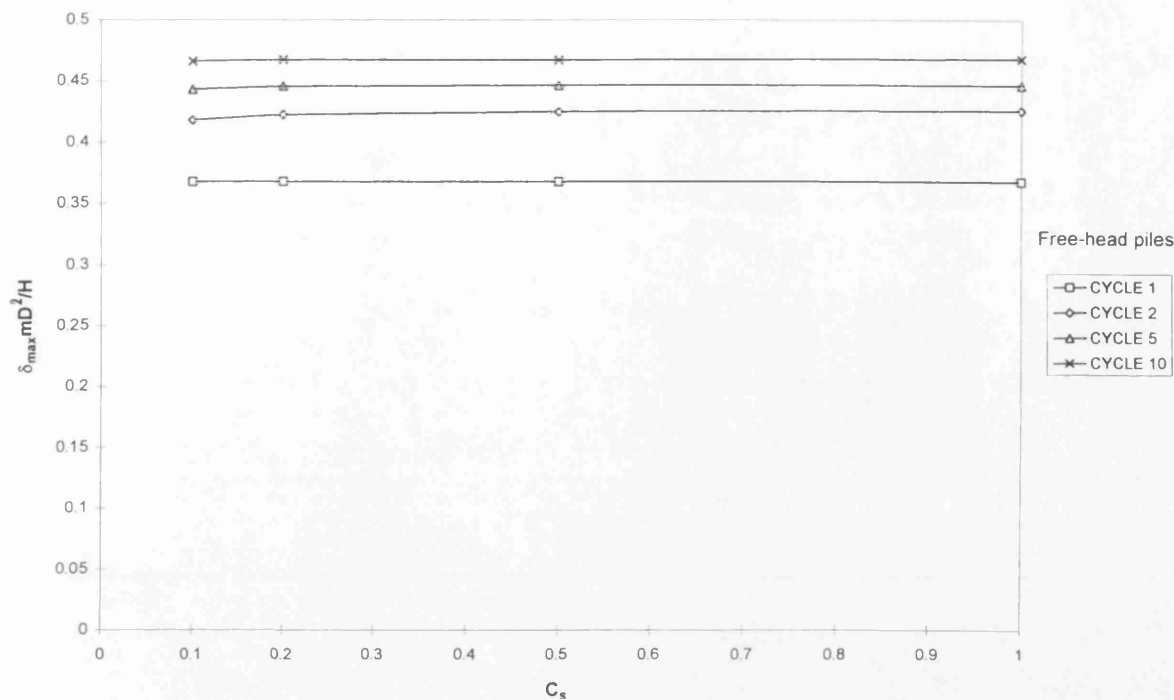


(a)

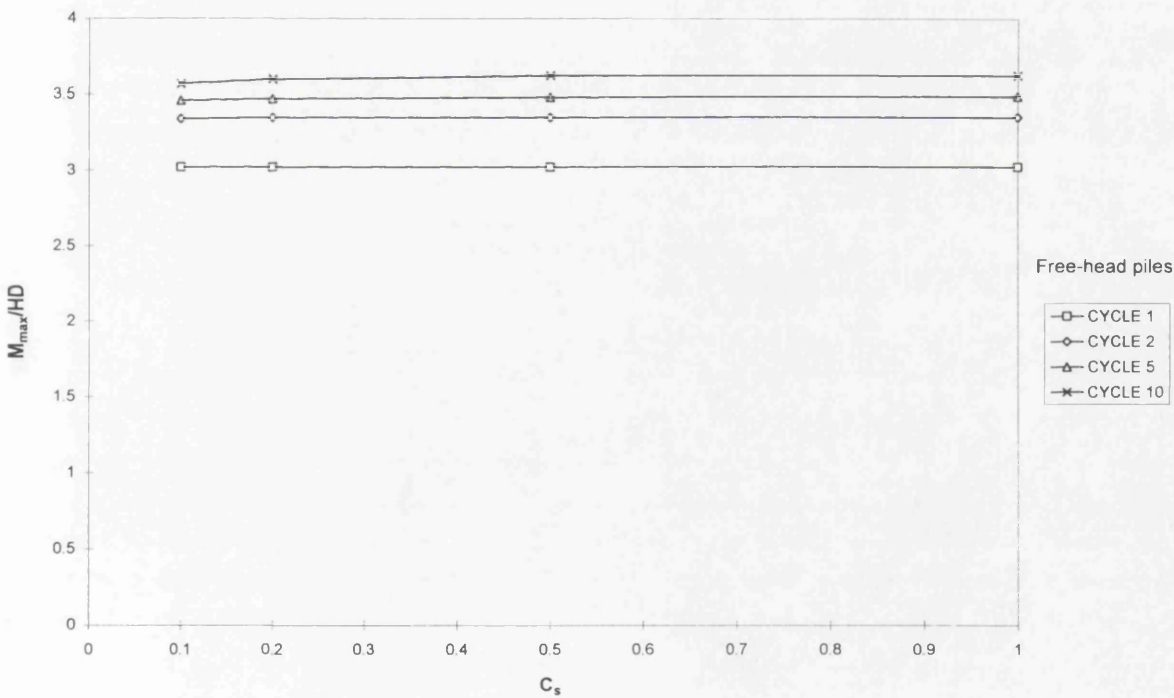


(b)

Figure 7.33 The effect of residual/peak shear strength ratio (R_s) on (a) pile-head displacements and (b) maximum bending moments, for fixed-head piles in soft clay.

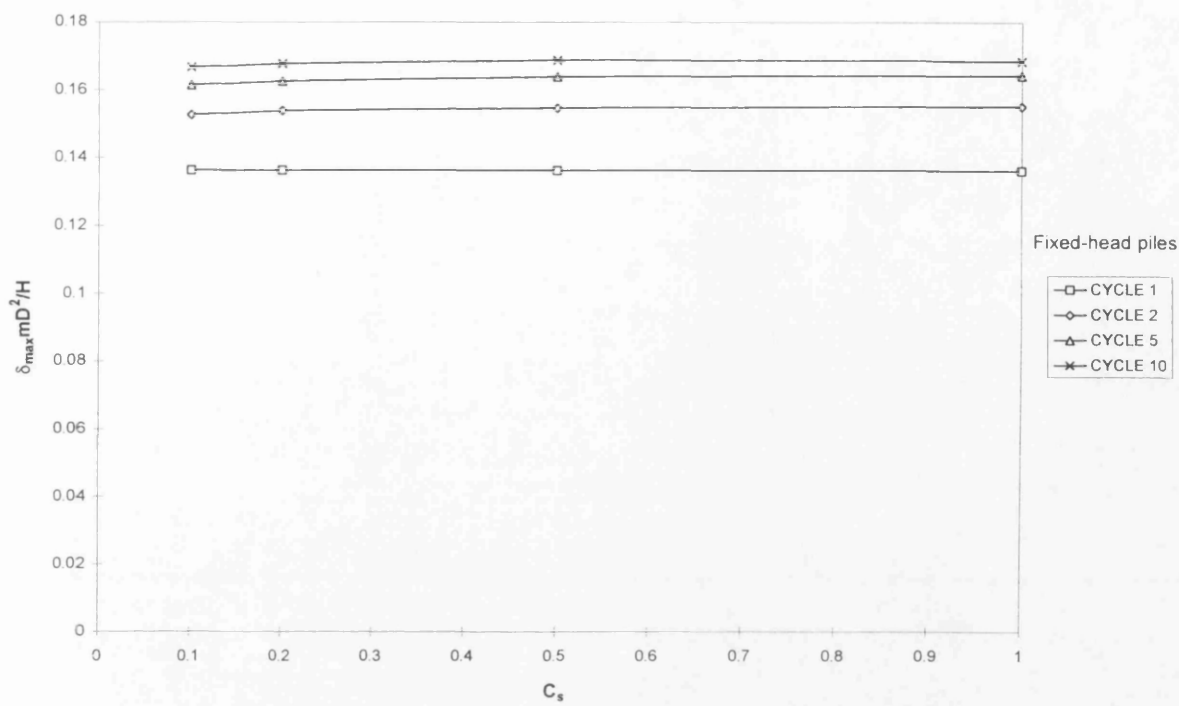


(a)

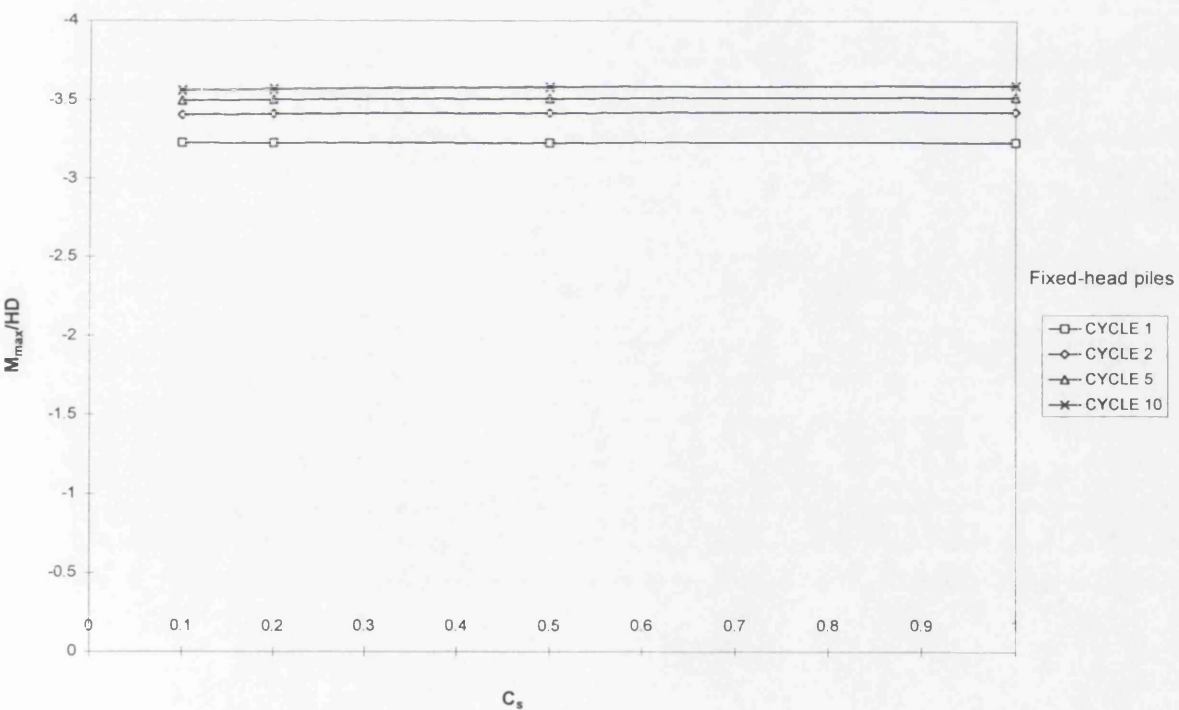


(b)

Figure 7.34 The effect of shear strength degradation rate factor (C_s) on (a) pile-head displacements and (b) maximum bending moments, for free-head piles in soft clay.

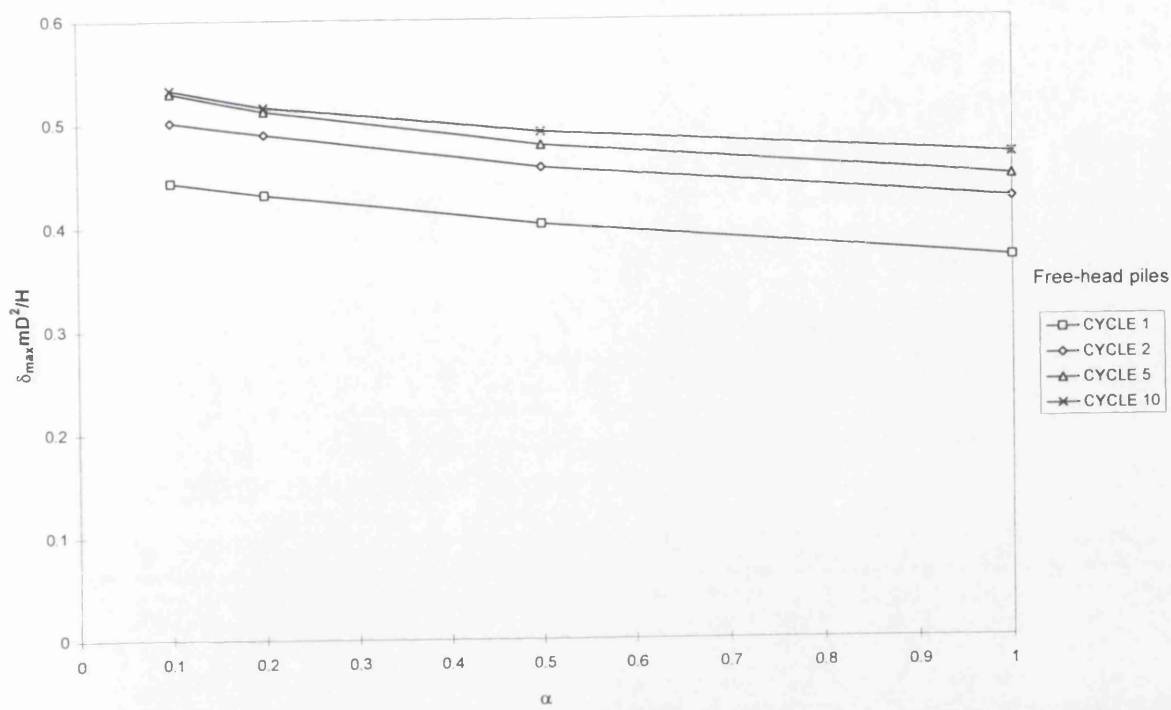


(a)

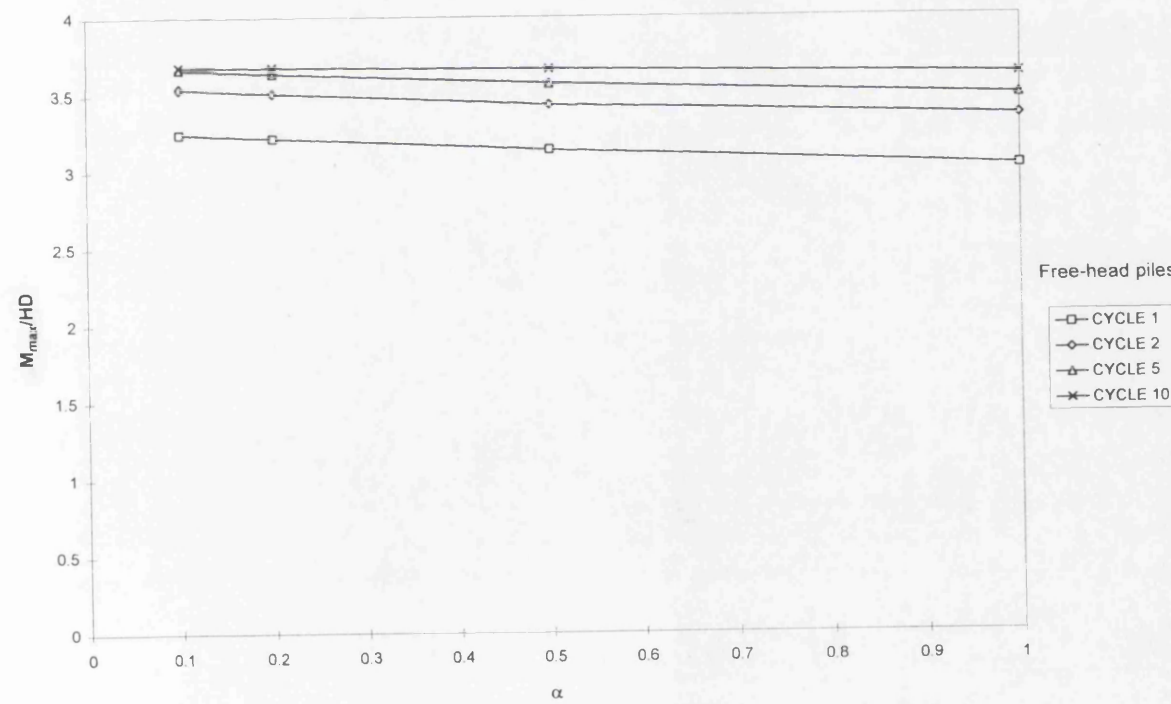


(b)

Figure 7.35 The effect of shear strength degradation rate factor (C_s) on (a) pile-head displacements and (b) maximum bending moments, for fixed-head piles in soft clay.

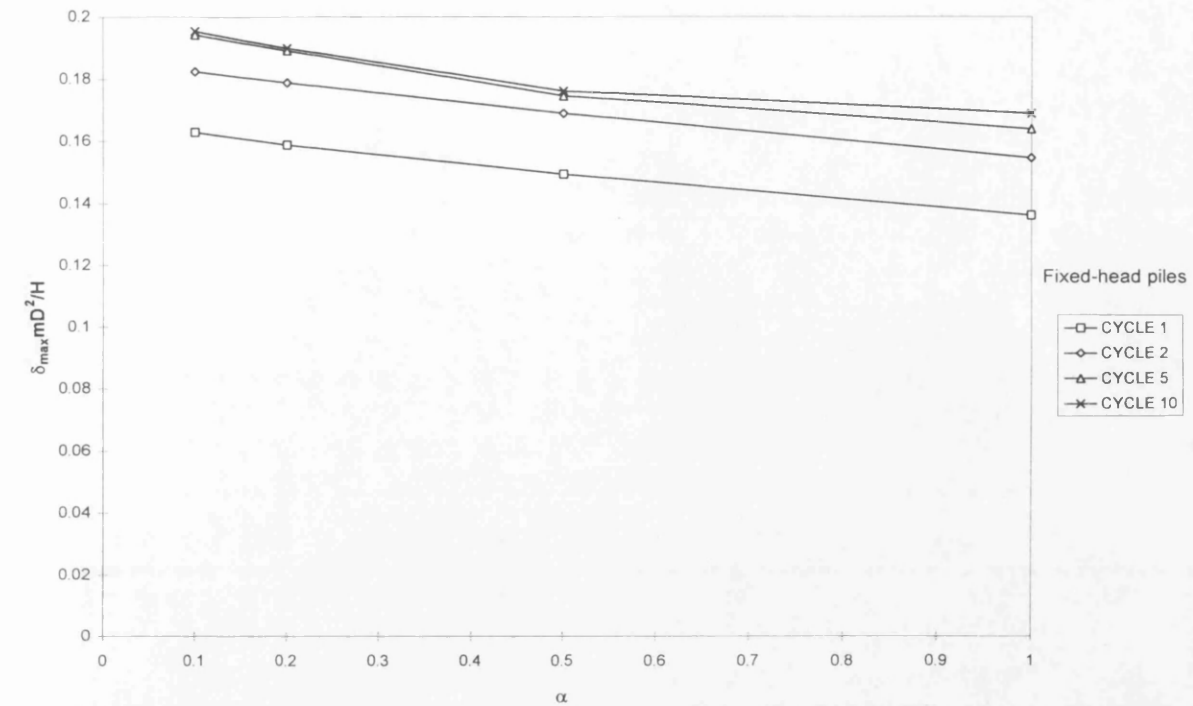


(a)

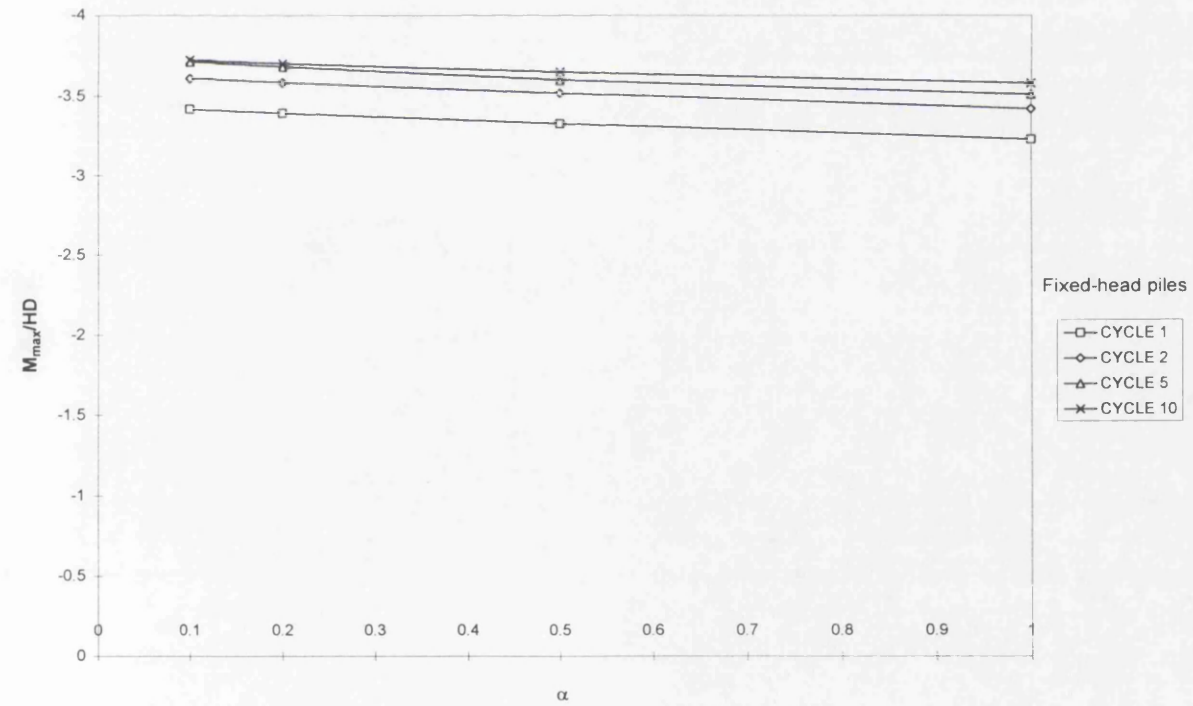


(b)

Figure 7.36 The effect of adhesion factor (α) on (a) pile-head displacements and (b) maximum bending moments, for free-head piles in soft clay.

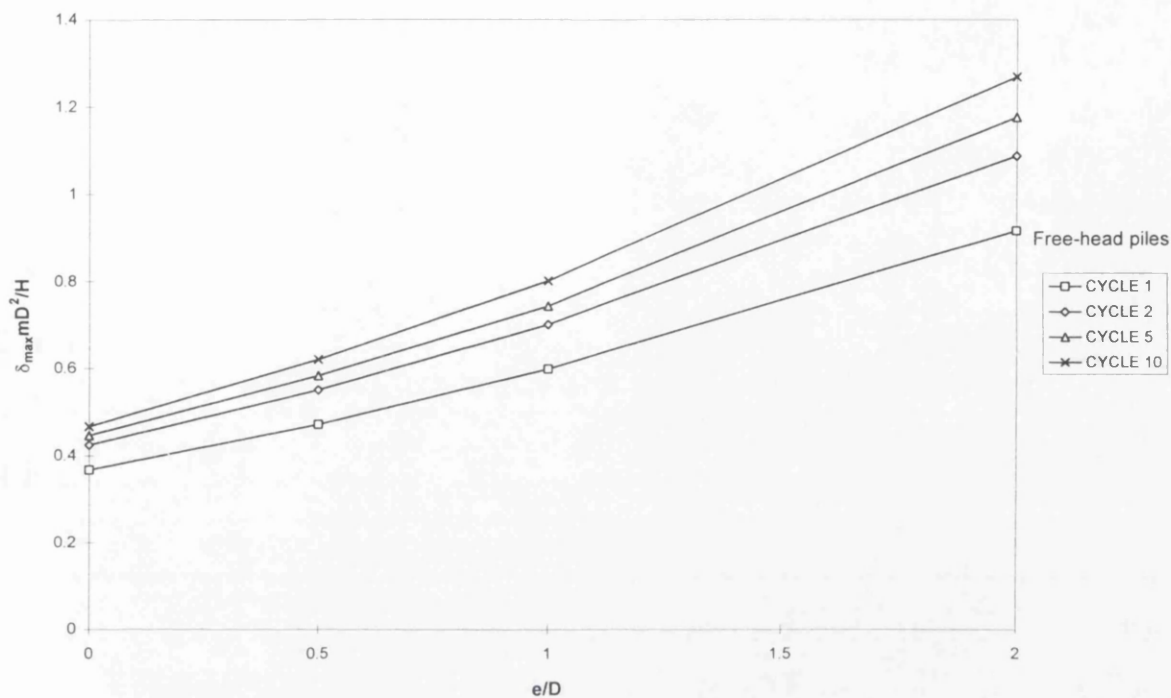


(a)

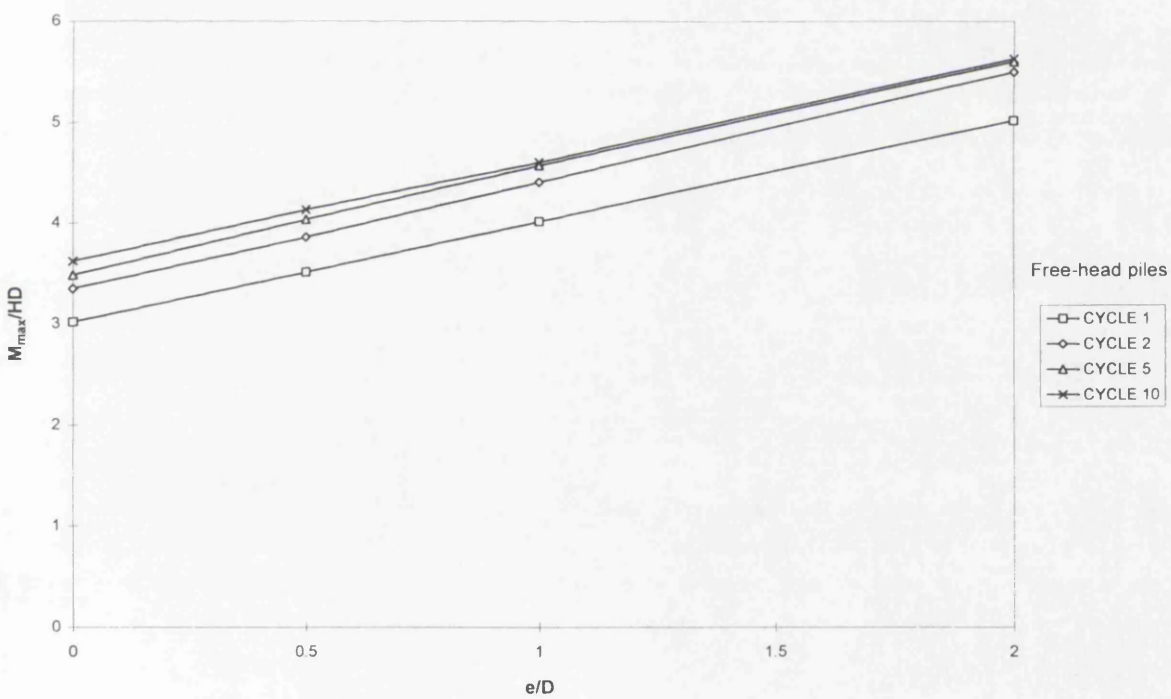


(b)

Figure 7.37 The effect of adhesion factor (α) on (a) pile-head displacements and (b) maximum bending moments, for fixed-head piles in soft clay.



(a)



(b)

Figure 7.38 The effect of eccentric loading (e) on (a) pile-head displacements and (b) maximum bending moments, for free-head piles in soft clay.

CHAPTER 8

Analyses of Published Field Test Data

8.1 Summary

8.2 Introduction

8.3 Selection of soil parameters

8.4 Field tests reported by Matlock

8.4.1 Field tests at Lake Austin

8.4.1.1 Soil conditions

8.4.1.2 Predictions by previous workers

8.4.1.3 Current analysis

8.4.1.4 Discussion

8.4.2 Field tests at Sabine

8.4.2.1 Soil conditions

8.4.2.2 Predictions by previous workers

8.4.2.3 Current analysis

8.4.2.4 Discussion

8.5 Field tests reported by Reese *et al.*

8.5.1 Soil conditions

8.5.2 Predictions by previous workers

8.5.3 Current analysis

8.5.4 Discussion

8.6 Field tests reported by Tassios and Levendis

8.6.1 Soil conditions

8.6.2 Field test observations

8.6.3 Current analysis

8.6.4 Discussion

8.7 Field tests reported by Hamilton and Dunnivant

8.7.1 Soil conditions

8.7.2 Predictions by previous workers

8.7.3 Current analysis

8.7.4 Discussion

8.8 Discussion of results

8.9 Concluding remarks

Appendix 8.1 Equivalent Pile Young's Modulus

CHAPTER 8

Analyses of Published Field Test Data

8.1 Summary

The cyclic loading analysis developed in Chapter 6 is employed to interpret the test data obtained from five published full-scale field tests. These studies concentrate on lateral pile-head displacements, maximum bending moments and bending moment distributions along the pile length. In addition, the predictions of the present numerical analysis are compared with those obtained by a number of other workers. Before attempting to interpret the pile responses, the selection of soil parameters to be used in the current analysis is discussed.

8.2 Introduction

The objective of this Chapter is to examine the accuracy and usefulness of the current analysis (APILEC), developed in Chapter 6. This is carried out by comparisons with cyclic pile-load test results from published case histories. The case histories examined in this study are:

- ♦ Field tests at Lake Austin reported by Matlock (1970).
- ♦ Field tests at Sabine reported by Matlock (1970).
- ♦ Field tests reported by Reese *et al.* (1975).
- ♦ Field tests reported by Tassios and Levendis (1974).
- ♦ Field tests at Tilbrook Grange reported by Hamilton and Dunnavant (1993).

For each case, the soil conditions of the site were studied carefully, in order to determine the appropriate soil parameters to be employed for the current analysis. The predictions of other researchers were then discussed, and subsequently compared with the current analysis.

For the analyses, the comparisons with static loading tests were carried out first, so as to determine if the selected soil parameters (e.g. soil Young's modulus) to be employed are appropriate, before proceeding to the complex cyclic loading tests. In what follows, the

selection of the appropriate soil parameters to be used in the current analysis will be discussed.

8.3 Selection of soil parameters

The soil parameters required for the static analysis are the undrained shear strength (C_u) of the soil and its Young's modulus (E_s). Poisson's ratio (ν) is assumed to be equal to 0.5 under cyclic (undrained) loading conditions. For cyclic analysis, the strength degradation parameters are required. They are: residual/peak shear strength ratio (R_s), the shear degradation rate factor (C_s), the residual/peak bearing strength ratio (R_b), and the bearing degradation rate factor (C_b) are required to account for soil strength degradation. A further backsliding factor (β) is needed to account for the backsliding phenomenon.

Soil stiffness-strength ratio (E_s/C_u)

The most satisfactory method of obtaining E_s appears to be to carry out full-scale pile-load tests and back-figure the average value of E_s from the measured displacement. However, in situations where pile-load test data are not available, empirical correlations between E_s and C_u , which may be determined more readily from laboratory or field tests are frequently used. However, the reliability of determining E_s from laboratory tests is often questionable, because they are significantly affected by the anisotropic nature of the soils, sampling disturbance, uncertainties of test equipments and testing procedures.

In the absence of data from good quality tests, it is preferable and convenient to assume a value for the soil stiffness-strength ratio (E_s/C_u). Simons (1976) reviewed published data and found E_s/C_u ratios ranging from 40 to 3000. The low values certainly incorporate within them the effects of soil disturbance and non-linearity. D'Appolonia *et al.* (1971) reported E_s/C_u ratios of 1000 to 1500 for inorganic clays of moderate sensitivity. Bjerrum (1972) reported E_s/C_u ratios from 500 to 1500 obtained from field shear vane tests whereas Poulos (1971) reported ratios ranging from 15 to 95 from back-calculated load-displacement measurements of full-scale pile-load tests. These ratios correspond to secant values of Young's modulus and in a later publication (Poulos and Davis, 1980) ratios of 250 to 400 were tentatively suggested for the tangent modulus/strength ratio. Ottaviani and Marchetti (1979) obtained E_s/C_u ratio of 1000 from the results of a single pile-load test. In another

pile-load test conducted by Cooke *et al.* (1979), E_s/C_u ratio of 1250 was obtained. From the results of two pile-load tests, Meyerhof *et al.* (1981) reported that the average E_s/C_u ratio is approximately 400. Results reported by Butterfield and Ghosh (1980) on the study of 20 laboratory model pile tests, give an average E_s/C_u ratio of 470. The results of Aschenbrener and Olson (1984) seem to indicate that E_s/C_u ratios lie between 400 and 1000. Davies and Budhu (1986) and Budhu and Davies (1988) advocated E_s/C_u ratios in the range of 500 to 1500 from their case history studies. Quek, Chow and Phoon (1992) analysed published results of pile-load tests and laboratory model pile tests and found that E_s/C_u ratio is averaging about 740. It is apparent from the above results, that the E_s/C_u ratio is quite uncertain, and the proposals of E_s/C_u ratios by Davies and Budhu (1986) and Budhu and Davies (1988) were adopted for the cyclic analysis. Note that for soft clay model, the m/c ratio is used instead of E_s/C_u (where m is the rate of increase in soil Young's modulus and c is the rate of increase in undrained shear strength).

Strength degradation parameters

The strength degradation parameters, namely: residual/peak shear strength ratio (R_s), the shear degradation rate factor (C_s), the residual/peak bearing strength ratio (R_b), and the bearing degradation rate factor (C_b) can be correlated with soil index properties as described in Chapter 4. However, if the soil index properties are not available, R_s , C_s , R_b and C_b can be taken as 0.5, 0.5 mm^{-1} , 0.5 and 50, respectively, assuming 50% degradation of the shear strength and bearing strength, and medium rate of shear strength and bearing strength degradation.

Backsliding factor (β)

The backsliding factor (β) to account for backsliding phenomenon is taken as zero, as there appears to be no field tests that can quantify the magnitude of backsliding. Nevertheless, the parametric study on the effect on β (described in Sections 7.5.3 and 7.6.3), had shown that its influence on pile-head displacements and maximum bending moments is negligible.

8.4 Field tests reported by Matlock

Matlock (1970) has described six series of load-controlled tests performed at two different locations using instrumented steel pipe piles. Two series of free-head tests (one static and one cyclic) were conducted at Lake Austin, Texas. The other four series of loadings (two static and two cyclic) tested under both free-head and fixed-head conditions were conducted at Sabine, Texas. The details of the pile are:

Embedded length of pile (L)	= 12.8 m
Outer diameter of the pile (D)	= 0.32 m
Inner diameter of the pile	= 0.30 m

Incremental lateral loads were applied by the loading strut; see Figure 8.1 for the test set up for fixed-head pile at Sabine. A trench was excavated and filled with water to simulate the offshore environment.

8.4.1 Field tests at Lake Austin

8.4.1.1 Soil conditions

The soils at Lake Austin consist of clays and silts deposited relatively recently behind the Lake Austin Dam, Texas. The clays are somewhat jointed and fissured due to desiccation, with an average vane shear strength of 38 kPa. Unconfined triaxial tests were also carried out (Kay *et al.*, 1986), giving shear strengths of about 24 kPa. The average submerged unit weight of the clay was estimated to be 8 kN/m³ (Grashuis *et al.*, 1990).

The current analysis has adopted a soft clay model (since the clay in which the pile is embedded, is described as soft clay by Matlock). The details of the parameters are:

Buoyant soil unit weight (γ)	= 8 kN/m ³
Lateral earth pressure coefficient (K_t)	= 1.0
Adhesion factor (α)	= 0.5
Rate of increase in undrained shear strength (c)	= 10 kPa/m
Rate of increase in soil Young's modulus (m)	= 5 MPa/m
Backsliding factor (β)	= 0
Residual/peak shear strength ratio (R_s)	= 0.5
Shear degradation rate factor (C_s)	= 0.5 mm ⁻¹
Residual/peak bearing strength ratio (R_b)	= 0.5
Bearing degradation rate factor (C_b)	= 50

The C_u at the mudline is taken as zero. The values for the strength degradation parameters suggested above, are because the index properties of the soil are not available. The m/c ratio is taken as 500, following the suggestion in Section 8.3. From the pile data and reference to Appendix 8.1, the equivalent pile Young's modulus is taken as 55 GPa.

8.4.1.2 Predictions by previous workers

The relationship between pile-head loads and displacements were not published, and comparisons with results can only be based on the pile-head load-maximum bending moment responses and the bending moment distributions along the pile length.

Matlock used the p - y method (described in Section 1.3.2), with some adjustments to the empirical values, to give the predictions for static and cyclic pile-head load-maximum bending moment responses depicted in Figures 8.2 and 8.3. Good agreement with field results were achieved by Matlock, with underestimation of maximum bending moments for both static (only at load levels below 60 kN) and cyclic loading tests.

Kay *et al.* (1986) used the finite element method together with the soil parameters determined from the in-situ pressuremeter testing to validate the load-displacement responses reported by Matlock. The shear strength values obtained from the pressuremeter tests were about 20 kPa, which were lower than the values previously obtained by Matlock. The E_s values adopted by Kay *et al.* are around $300C_u$. In comparison with the measured field results for static loading only, Kay *et al.* predictions gave much stiffer pile responses, typically 45% higher.

Grashuis *et al.* (1990) used the discrete element method (described in Section 1.3.5) to verify their proposed method of analysis, for static loading only. The C_u and E_s values adopted were 20 kPa and 40 MPa, respectively. The analysis gave reasonable agreement with the measured field results reported by Matlock.

Poulos (1982) employed the modified boundary element (described in Section 1.3.7) to analyse the pile test data under both static and cyclic loading obtained by Matlock. The shear strength value adopted is not mentioned. However, E_s is assumed to vary linearly with depth, with a rate of increase of 40 MPa per metre. The results of Poulos' analyses for static and cyclic loading tests are shown in Figures 8.2 and 8.3, respectively. An underestimation of the maximum bending moments at low load levels (below 70 kN) and an overestimation of

the maximum bending moments at high load levels (above 70 kN) for static tests can be clearly seen in Figure 8.2. For cyclic analysis, an underestimation and overestimation of maximum bending moments at low and high load levels, respectively, can again be seen in Figure 8.3.

8.4.1.3 Current analysis

The static and cyclic analyses were carried out based on the soil data described in Section 8.4.1.1. The predictions for the static analyses depicted in Figure 8.2, show that APILEC gives excellent predictions (differences less than 1%) of the maximum bending moments for loads up to 30 kN, but it overestimated the maximum bending moments at higher load levels. However, the differences are less than 20%.

For cyclic analyses, Figure 8.3 shows that the APILEC predictions for maximum bending moments provide an excellent estimate (differences less than 1%) of the actual field results for loads less than 70 kN. Slight underestimation of the maximum bending moments of less than 10% are accounted for a load of 75 kN. It should be noted that only ten cycles were considered. The bending moment distributions, depicted in Figure 8.4, show comparisons between the predictions and the measured values at a load level of 75 kN. At the tenth cycle, APILEC has underestimated the maximum bending moments by approximately 10%. However, with further cycling of up to fifty cycles, APILEC gives a more accurate prediction of the bending moment distribution, with overestimation of the maximum bending moments by only 3%. It is clearly shown in Figure 8.4, that the depth at which the maximum bending moment occurs, is correctly predicted by APILEC.

8.4.1.4 Discussion

The soil strength properties adopted by previous researchers (described in Section 8.4.1.2) are often inconsistent. The current analysis (APILEC) has adopted a soft clay model, giving good predictions of pile responses for both static and cyclic loading.

APILEC has successfully predicted the increase in maximum bending moments with increasing load levels for both static and cyclic loadings. The predictions clearly show that the position at which the maximum bending moment occurs moves down the pile length with increased cycling.

The predictions by APILEC for ten cycles are sufficient to give accurate estimates of the pile responses measured in the field. It is shown that with further cycling of up to fifty cycles, the predictions are better especially at higher load levels. However, this will greatly increase the computational cost.

Overall, APILEC certainly gives better predictions of the measured pile responses than other methods of analyses developed by Matlock and Poulos, for static and cyclic loadings (especially for cyclic loading); see Figures 8.2 and 8.3.

8.4.2 Field tests at Sabine

At Sabine, tests were carried out on free-head and fixed-head piles, in order to assess pile-head fixity effects. The pile data is similar to that described in Section 8.4.1.

8.4.2.1 Soil conditions

The soils at the Sabine site are mainly soft, slightly overconsolidated marine clays with vane shear strengths averaging about 14 kPa.

Since the pile is embedded in soft clay as described by Matlock, the shear strength is assumed to vary linearly with depth. The details of the parameters employed for the current analysis are:

Buoyant soil unit weight (γ)	= 10 kN/m ³
Lateral earth pressure coefficient (K_t)	= 1.0
Adhesion factor (α)	= 1.0
Rate of increase in undrained shear strength (c)	= 6 kPa/m
Rate of increase in soil Young's modulus (m)	= 3 MPa/m
Backsliding factor (β)	= 0
Residual/peak shear strength ratio (R_s)	= 0.5
Shear degradation rate factor (C_s)	= 0.5 mm ⁻¹
Residual/peak bearing strength ratio (R_b)	= 0.5
Bearing degradation rate factor (C_b)	= 50

The C_u at the mudline is taken as zero since the pile tests were performed in a pit flooded with water. The adhesion factor (α) is taken as unity, since the clay is probably very soft (shear strength is only 14 kPa). The values for the strength degradation parameters suggested above,

are because the index properties of the soil are not available. The (m/c) ratio is taken as 500, following the suggestion in Section 8.3.

8.4.2.2 Predictions by previous workers

Due to the limited field data, comparisons can only be based on the pile-head load-maximum bending moment responses and the bending moment distributions along the pile length.

Free-head pile

Matlock employed the p - y method to predict the response of free-head piles to static and cyclic loading tests. Good agreement with field test results was achieved (see Figures 8.5 and 8.6), with some overestimation of the maximum bending moments (loads above 70 kN) for static loading and underestimation of maximum bending moments (loads above 60 kN) for cyclic loading. However, it should be borne in mind that repeated trial-and-error adjustments would have been necessary to obtain these results, since the p - y method is, in effect, merely an elaborate curve-fitting strategy.

Poulos (1982) used the modified boundary element method in his analysis. He assumed that the soil modulus varied linearly with depth ($m = 40$ kPa/m) and applied 100 cycles of symmetric two-way loading. For static loading, Poulos predicted much lower maximum bending moments than the measured results (Figure 8.5), and for the cyclic loading, he underestimated the maximum bending moments by 10% for loads above 60 kN (Figure 8.6).

Fixed-head pile

The fixed-head pile test is conducted at an eccentricity of 0.32 m, giving different bending moments at the mudline and at the load point. The comparisons with results were carried out at the load point where the restraining moments are maximum.

The predictions given by Matlock using the p - y method are shown in Figures 8.7 and 8.8, for static and cyclic analyses, respectively. For both static and cyclic analyses, Matlock predicted much lower maximum restraining moments than the measured values at the load point.

Poulos predictions for static loading, depicted in Figure 8.7, gave an overestimation of the maximum restraining moments at low load levels and an underestimation at higher load levels. For cyclic loading (Figure 8.8), he underestimated the maximum restraining moments.

8.4.2.3 Current analysis

The soil data used for the analyses are described in Section 8.4.2.1.

Free-head piles

For static analyses, APILEC gives excellent predictions of the measured maximum bending moments as shown in Figure 8.5. The differences between predicted and measured results are less than 2% for the full range of load levels. For cyclic analyses, the predictions by APILEC for ten cycles, depicted in Figure 8.6, gives a very good prediction (differences less than 1%) of maximum bending moment at a low load of 35 kN. An underestimation of the maximum bending moments by 11 and 24% at loads of 53 kN and 60 kN respectively, were observed. This is due to the insufficient number of cycles the pile is subjected to in the analyses. Increasing the number of cycles to fifty, Figure 8.9 shows that APILEC gives a very close prediction (differences less than 1%) of the measured maximum bending moment at a load of 60 kN. In addition, APILEC produces similar bending moment distributions along the pile length, with accurate predictions on the position at which the maximum bending moments occur.

Fixed-head piles

For the fixed-head piles, APILEC overestimates the maximum restraining moments for both static and cyclic analyses, as shown in Figures 8.7 and 8.8. This suggests that the strength properties of clay used in these analyses needed to be adjusted. Hence, it was decided to increase the c and m values to 10 kPa/m and 5 MPa/m ($m/c = 500$), respectively, to reduce the predicted maximum bending moments. This might be justified by possible variations in soil properties. With these modifications, APILEC still overestimated (by an average of 15%) the maximum restraining moments for both static (loads below 100 kN) and cyclic loadings (loads below 80 kN); see Figures 8.10 and 8.11. However, better estimates were achieved for higher load levels.

In comparison with the measured bending moment distribution along the pile length (at a load of 89 kN) depicted in Figure 8.12, APILEC closely estimates the negative moment distributions at the tenth cycle. The positive moment distributions and the depth at which the maximum positive moment occurs are underestimated. However, this is not the main concern, as a good prediction of the maximum restraining moment for fixed-head piles is of prime importance.

8.4.2.4 Discussion

The current analysis employed the soft clay model for its prediction (based on the fact that the soil is described as soft clay), rather than using constant shear strength of 14 kPa (suggested by experimental tests). However, its predictions indicated give good estimates of the actual pile responses for both static and cyclic loadings. Some adjustments of the soil strength properties are required to give good predictions for fixed-head piles. This may be justified by variations in soil properties for different locations at which the free-head and fixed-head piles were tested.

The p - y method employed by Matlock, gave better predictions for free-head piles than for fixed-head piles. This may imply that different p - y methods may be needed to deal with different pile-head fixity conditions.

APILEC gave good predictions of the measured pile responses by using only ten cycles. However, if better predictions are desired (especially for high load levels), further cycling (say up to fifty cycles) may be required (Figure 8.9).

APILEC is capable of giving better predictions for the cyclic pile-load tests, for free-head and fixed-head pile conditions, than other methods of analyses proposed by Matlock (1970) and Poulos (1982); see Figures 8.5, 8.6, 8.10 and 8.11. The predictions have shown that cyclic loading increases the maximum bending moments and that the increase depends on the magnitude of the loading and the number of cycles. They also show that the position at which the maximum bending moment occurs moves down the pile depth with an increasing number of cycles.

8.5 Field tests reported by Reese *et al.*

A series of field tests have been reported by Reese *et al.* (1975) on static and cyclic laterally loaded piles embedded in stiff overconsolidated marine clay. The hollow piles were

driven open-ended and tested under free-head conditions; the test set up can be seen in Figure 8.13. The details of the pile are:

Embedded length of pile (L)	= 14.95 m
Outer diameter of the pile (D)	= 0.64 m (top 7 m), 0.61 m
Inner diameter of the pile	= 0.59 m

For the cyclic loading tests, the load was applied in increments until the pile had stabilised at a particular maximum displacement or until 100 cycles of loading had been applied.

8.5.1 Soil conditions

The soil is described as stiff overconsolidated marine clay. The undrained shear strength (C_u) of the clay is of the order of 192 kPa, at the top 6 to 7.5 m. The soil descriptions are shown in Figure 8.14.

For the current analysis, a stiff clay model with constant E_s and C_u was adopted. The details of the soil parameters are:

Buoyant soil unit weight (γ)	= 10 kN/m ³
Lateral earth pressure coefficient (K_l)	= 1.0
Adhesion factor (α)	= 0.5
Undrained shear strength (C_u)	= 190 kPa
Soil Young's modulus (E_s)	= 190 MPa
Backsliding factor (β)	= 0
Residual/peak shear strength ratio (R_s)	= 0.3
Shear degradation rate factor (C_s)	= 0.2 mm ⁻¹
Residual/peak bearing strength ratio (R_b)	= 0.01
Bearing degradation rate factor (C_b)	= 100

The above R_s and C_s values are chosen from Figures 4.16a and 4.26a, respectively, based on an average liquid limit of 70% (top 10 m in Figure 8.14). From the bending moment distributions reported by Reese *et al.*, it has been shown that the soil resistance near the surface to a depth of 3.5 m (approximately 6 pile diameters) is extremely low, in fact, it is virtually zero. This indicates that the soil has undergone severe degradation with cycling. Reese *et al.* revealed that they were surprised at the severe deterioration of the soil resistance

as reflected in their derived p - y curves. Hamilton and Dunnavant (1993) reviewed the tests reported by Reese *et al.* and commented that the extreme degradation may be due to the fact that the tests were conducted in a soil that was deposited in a salt water environment but was inundated during the tests using fresh water. In view of the observations and comments, R_b is taken as a very low value of 0.01 and a rapid rate of degradation C_b of 100 is assumed.

The eccentricity of loading (e) is taken as 0.35 m, based on the bending moment measured at the ground surface. The equivalent pile Young's modulus (E_p) is determined from Appendix 8.1, giving E_p as 55 GPa.

8.5.2 Predictions by previous workers

Reese *et al.* used the p - y method (described in Section 1.3.2) to predict the pile responses under static and cyclic loadings; see Figures 8.15 to 8.18. For static loading, underestimation of less than 10% of the pile-head displacements at high load levels (above 500 kN) is observed in Figure 8.15. In comparison with the measured maximum bending moment responses, their predictions gave slight underestimation (approximately 5%) at high load levels (above 500 kN), as depicted in Figure 8.16. For cyclic loading, Reese *et al.* analyses show very good predictions (differences less than 5%) of the pile responses for both pile-head displacements and maximum bending moments, as illustrated in Figures 8.17 and 8.18.

Poulos (1982) used the modified boundary element method (described in Section 1.3.7) to validate the pile responses reported by Reese *et al.* After a series of static analyses, a reasonable fit to the static behaviour was obtained by the use of constant E_s value of 192 MPa. Poulos predictions under static loading, show a good estimate of the pile-head load-displacement responses at low load levels of up to 200 kN. However, at load levels above 500 kN, an overestimation of the pile-head displacements by approximately 20% was observed (Figure 8.15). In terms of pile-head load-maximum bending moment responses, Poulos underestimated the maximum bending moments as depicted in Figure 8.16. For cyclic loading, parameter value (e.g. the reference cyclic strain ϵ_{cr}) adjustments are necessary to give the pile-head displacement and maximum bending moment predictions shown in Figures 8.17 and 8.18. Poulos predictions for the pile-head displacements show a too soft response at high load levels above 400 kN, resulting in an overestimation of more than 40% as compared with

the measured displacements. An underestimation of the maximum bending moments at all load levels is observed in Figure 8.18.

Swane and Poulos (1985) used the bilinear-elasto-plastic analysis (described in Section 1.3.4) to predict the pile test responses reported by Reese *et al.* From their analyses of static pile responses, they assumed that E_s of the clay to be constant with a value of 53.4 MPa. Their predictions of pile-head displacements and maximum bending moments for the static analyses are shown in Figures 8.15 and 8.16. Good prediction of the pile-head displacements at low load levels was achieved. However, at higher load levels, the predicted pile responses are too stiff. For the maximum bending moment results, their predictions underestimated the measured values, with greater differences as the loading increases. For the cyclic analyses, Swane and Poulos predictions underestimated the pile-head displacements by an average of 15%, as illustrated in Figure 8.17. However, their predictions for the maximum bending moments are very good (Figure 8.18), with differences of less than 5% from the measured results.

8.5.3 Current analysis

The analyses are carried out using the soil data described in Section 8.5.1. For static analyses, APILEC predictions shown in Figures 8.15 and 8.16 (denoted as APILEC: S1), grossly underestimate the pile-head displacements and maximum bending moments. This suggests that the soil strength properties (described in Section 8.5.1) needed to be changed. From the undrained shear strength profile shown in Figure 8.14, a linear increase in undrained shear strength with depth is chosen (i.e. the soft clay model) with lower bound $c = 40$ kPa/m adopted; C_u at ground surface is assumed to be zero (water table is at the ground level). To give a good prediction of the measured pile-head load-displacement responses under static loading, a high rate of increase in soil Young's modulus with depth (m) of 190 MPa/m ($m/c = 4750$) was chosen. With these adjustments to the soil parameters, APILEC predictions depicted in Figures 8.15 and 8.16 (denoted as APILEC: S2), show that it gives very good estimates (differences less than 5%) of pile-head displacements and maximum bending moments for the entire load range.

For cyclic analyses, APILEC predictions on pile-head displacements were compared with the measured results; see Figure 8.17. At the tenth cycle, APILEC predictions are excellent (differences less than 1%) for loads up to 300 kN. With higher load levels, APILEC

predicts a stiffer response (about 10%). However, with further cycling to twenty cycles, APILEC gives a good estimate (differences of less than 5%) of the pile-head displacement at high load levels (above 300 kN). The maximum bending moment results depicted in Figure 8.18, show that APILEC gives excellent predictions (differences less than 1%) of the field results at low load levels of up to 150 kN, but an underestimation of less than 10% at load levels up to 445 kN is observed. In comparison with the measured bending moment distribution along the pile length at a load of 445 kN (Figure 8.19), APILEC (at cycle 20) has correctly predicted the bending moment distribution and accurately determined the pile depth at which the maximum bending moment occurs.

8.5.4 Discussion

The current analysis employed the stiff clay model initially (since the soil is described as stiff overconsolidated clay). However, the predicted pile response was far too stiff. Hence, it was decided to employ the soft clay model, which is supported by soil data and field observations (Figures 8.13 and 8.14). The use of m/c ratio of 4750 was required to give good predictions of the measured pile responses for both static and cyclic loadings.

From the experimental results depicted in Figures 8.15 to 8.19, it is clearly shown that pile-head displacements and bending moments increase with increasing load levels and with cycling. This behaviour is successfully predicted by APILEC. In addition, APILEC has shown that the depth at which the maximum bending moment occurs increases with cycling. Overall, APILEC has shown better agreement with the experimental results than methods proposed by Poulos and Swane (1985) and Poulos (1982), as observed in Figures 8.15 to 8.19. The p - y analysis was developed from the above experimental test results with various adjustments to best fit the measured pile responses, hence a slightly better agreement with measured results than APILEC was observed.

8.6 Field tests reported by Tassios and Levendis

Laterally loaded pile tests, both static and cyclic were reported by Tassios and Levendis (1974). One-way and two-way cyclic loading tests were conducted by jacking the Franki piles against each other until the specified load was attained; see Figure 8.20 for the test set up. The necessary details of the pile are:

Total length of pile = 10 m

Diameter of the pile (D) = 0.52 m
Eccentricity of loading (e) = 0.25 m

8.6.1 Soil conditions

The soil consists primarily of clay having an undrained shear strength (C_u) of 50 kPa (determined from triaxial tests). The unit weight and liquid limit of the soil, for the top 10 m are around 15 kN/m³ and 40%, respectively. Detail soil descriptions can be seen in Figure 8.21.

For the current analysis, a stiff clay model is assumed following the above soil descriptions. The values for the soil parameters are:

Soil unit weight (γ)	= 15 kN/m ³
Lateral earth pressure coefficient (K_r)	= 0.5
Adhesion factor (α)	= 0.5
Undrained shear strength (C_u)	= 50 kPa
Soil Young's modulus (E_s)	= 50 MPa
Backsliding factor (β)	= 0
Residual/peak shear strength ratio (R_s)	= 0.7
Shear degradation rate factor (C_s)	= 0.7 mm ⁻¹
Residual/peak bearing strength ratio (R_b)	= 0.5
Bearing degradation rate factor (C_b)	= 50

The above values for R_s and C_s are taken from Figure 4.16a and 4.26a, respectively, based on the average liquid limit of 40%. The R_b and C_b values (from Sections 4.7.1 and 4.8.1) are taken as 0.5 and 50, respectively, assuming 50% of bearing strength degradation and a medium rate of bearing strength degradation. The lateral earth pressure coefficient (K_r) is taken as 0.5 for bored piles, and the E_s/C_u ratio is taken as 1000. The pile Young's modulus (E_p) is taken as 25 GPa.

8.6.2 Field test observations

Static loading

Two static loading tests were performed at locations L1a and L1b, and the pile-head load-displacement responses are shown in Figure 8.22 (denoted as MEASURED: L1a and

L1b). It is clearly seen in Figure 8.22 that the pile-head responses at locations L1a and L1b are similar for loads up to 20 kN. However, with further loadings, say loads up to 80 kN, the pile at location L1a displays a much stiffer response than the pile at location L1b, with a reduction in pile-head displacement of approximately 40%. This suggests variations in soil properties.

One-way cyclic loading

For the one-way cyclic loading tests, the Piles D and G are jacked against each other at location L3a. Their responses at a load of 60 kN for fifteen cycles are depicted in Figure 8.23 (denoted as MEASURED: Pile D and Pile G). At the first cycle of the tests, which can be considered as the static loading, the pile-head displacement for Pile D is 10.3 mm and for Pile G is 9.4 mm (Figure 8.23). Compared with the static loading test results depicted in Figure 8.22, at a load of 60 kN, the maximum pile-head displacements at two different locations L1a and L1b are 4.0 mm and 5.5 mm, respectively. This demonstrates again the large differences in results of approximately 2 to 3 times when tested at different site locations, which may be due to variations in soil properties. It is also noted in Figure 8.23 that Pile G displacements are lower than Pile D. This may be due to the arrangement of the piles during testing as shown in Figure 8.20.

Two-way cyclic loading

The two-way cyclic loading tests were conducted at location L4a with three piles at a single location. The loading was applied by jacking the middle and the left or right pile against each other in any one loading direction. The pile-head displacement results recorded for the middle pile at a load of 60 kN, in terms of forward and backward displacements (denoted as MEASURED: Forward and Backward) are depicted in Figure 8.24.

The forward displacement for the load of 60 kN at cycle one, which can be considered as the pile-head displacement for the static loading, gives a displacement of 3.6 mm. This is lower than those measured for the static tests at locations L1a and L1b, and the initial cycle of the one-way cyclic loading tests at location L3a, based on the same load level. It is also noted that the forward (positive direction due to loading/reloading) and backward (negative direction due to unloading) displacements are not similar, with differences averaging about 40%. This may be due to the larger amount of soil yielding taking place in the unloading

stage, as compared with that of the loading/reloading stage. The differences between the forward and backward displacements, however, are usually small as can be seen in the test results reported by Tassios and Levendis at a load of 40 kN (Figure 1.1b).

8.6.3 Current analysis

Static loading

For the static loading, using the soil data described in Section 8.6.1, APILEC predicts a too stiff pile response as depicted in Figure 8.22 (denoted as APILEC: S1). As such, it is decided to reduce C_u value to 10 kPa with E_s assumed to be 25 MPa (in view of the above discussed probable variations in soil properties), to reduce the pile-head displacements. With these changes, APILEC predictions (denoted as APILEC: S2) lie between the two measured pile-head displacement results (Figure 8.22). Unfortunately, no bending moment results were measured by Tassios and Levendis, hence no further comparisons can be made.

One-way cyclic loading

For the one-way cyclic loading, APILEC uses $C_u = 10$ kPa and $E_s = 10$ MPa (other soil data are similar to those described in Section 8.6.1) to give good predictions of the measured pile-head displacements for the first cycle. However, with cycling to fifteen cycles, APILEC has underestimated the measured pile-head displacements after the second cycle as shown in Figure 8.23 (denoted as APILEC: C1). This suggests that the values for the soil strength degradation parameters will need to be increased. Since the rate of increase in pile-head displacements with cycling (i.e. rate of cyclic degradation) is high, it suggests a rapid rate of bearing strength degradation is required; R_b is taken as 0.2 and C_b as 100. This is based on the parametric studies reviewed in Sections 7.5.4 and 7.5.5 at high load levels. With these adjustments, APILEC predictions (denoted as APILEC: C2 in Figure 8.23) give higher pile-head displacements with cycling, but, they still underestimate the measured pile-head displacements after the third cycle. From the parametric studies (Section 7.5.5), a very fast rate of bearing strength degradation may be necessary to increase the rate of cyclic degradation. As such, C_b of 200 was considered. With this modification, APILEC (denoted as APILEC: C3 in Figure 8.23) gives very good predictions (average differences less than 5%) on the measured rate of cyclic degradation for the fifteen cycles, following closely the displacement trend of Pile D.

Two-way cyclic loading

From the field test observations described in Section 8.6.2 and the results depicted in Figure 8.24, $C_u = 10$ kPa and $E_s = 20$ MPa are taken for APILEC analysis in order to give a good prediction of pile-head displacements at cycle one. The other soil data described in Section 8.6.1 are used, except that R_b is now taken as 0.3 and C_b as 100. The predictions by APILEC depicted in Figure 8.24 (denoted as APILEC: C4 Forward and C4 Backward), show that it overestimated (average about 30%) the forward displacements, and underestimated (average about 20%) the backward displacements. Since the maximum pile-head displacements (ignoring the direction) is of main interest in the cyclic laterally loaded pile design, a very fast rate of bearing strength degradation with $C_b = 200$ was again adopted to increase the rate of cyclic degradation. With this change in C_b , APILEC predictions depicted in Figure 8.24 (denoted as APILEC: C5 Forward and C5 Backward), give excellent estimates (differences less than 2%) of the measured maximum pile-head displacements (i.e. backward displacements). However, APILEC overestimated the forward displacements by an average of around 50%; this is not particularly significant as a good match with the maximum pile-head displacements is of prime concern.

8.6.4 Discussion

The field test results, giving different pile-head displacements for static loading, one-way cyclic and two-way cyclic loadings (both at cycle one) under the same load level, clearly indicate the variations of soil properties at different locations. This suggests that having an average undrained shear strength for the entire test site is not sufficient for pile design purposes. Due to these factors, the C_u and E_s values for APILEC predictions have to be adjusted (E_s/C_u ratios ranging between 1000 to 2500 were used) to give good predictions of the measured pile-head displacements at the first cycle, before proceeding to the cyclic analyses. The analyses (APILEC) for one-way and two-way cyclic loadings have adopted a high C_b value of 200 to account for the fast rate of cyclic degradation observed in the field tests. This may be due to the rate of load application during the tests or the type of soils encountered, resulting in a very fast rate of strength degradation. Overall, APILEC has given good predictions of the measured pile responses for static loading, one-way and two-way cyclic loading tests.

8.7 Field tests reported by Hamilton and Dunnivant

Hamilton and Dunnivant (1993) and Long *et al.* (1993) gave detailed descriptions of pile-load tests carried out at Tilbrook Grange in Cambridgeshire, England. The test set up can be seen in Figure 8.25. The relevant pile details are:

Embedded length of pile (L)	= 29.4 m
Outer diameter of the pile (D)	= 0.76 m
Inner diameter of the pile	= 0.69 m
Eccentricity of loading (e)	= 0.6 m
Flexural rigidity ($E_p I_p$)	= 1136 MNm ²

The open-ended steel pipe pile was subjected to one-way cyclic loading by jacking the pile apart using a central steel strut. The ground surface elevation was arbitrarily set at 100 m for the test. A pit (elevation 98.4 m) of 1.6 m in depth was excavated around the pile to contain ponded water for a period of one month prior to the laterally loaded pile tests (Figure 8.25). This was to ensure that the testing area around both piles was submerged with water to simulate offshore conditions.

The tests conducted were displacement-controlled, in which the pile-head displacement was increased to a new, significantly higher level following around 100 cycles of loading at the previous displacement value. A total of nine displacement increments, comprising of one static and eight cyclic were used. The sequence of increments is outlined in Table 8.1.

8.7.1 Soil conditions

The soil strata in which the piles were embedded are known as Lowestoft Till and Oxford clay (Figure 8.26a). The Lowestoft Till is described as a very stiff to hard dark grey silty clay covering from ground surface to elevation 82.9 - 81.4 m. The clay is of intermediate plasticity with a liquid limit in the range of 35% to 45% and a plastic limit of about 15%. The effective unit weight of the soil has an average value of 11.5 kN/m³. The Oxford clay is described as hard dark grey fissured clay from level 82.9 m - 81.4 to level 60 m and beyond. The clay is of high to intermediate plasticity with liquid and plastic limit of about 55% and 20% respectively.

The undrained shear strength (C_u) profile for axial loaded pile analyses is given in Figure 8.26a. The upper portion of the shear strength profile was modified for the lateral load test after additional site investigation. Two supplementary borings, designated as Boring 207 and 208 were drilled and sampled to 8 m penetration at locations close to the test pile position. Unconsolidated undrained triaxial tests were performed on recovered samples. Figure 8.26b details the revised undrained shear strength profile of the soil for the upper 10 m.

For the current analysis, only the soil at level 98.4 to 90 m (less than ten pile diameters from the top) was taken into consideration to determine the appropriate undrained shear strength, and the effective unit weight of the soil. From the undrained shear strength results (Figure 8.26b), it suggests the use of the soft clay model, with C_u , (E_s) at the pit floor level taken as 150 kPa (75 MPa) . Other soil data used in the analysis are:

Buoyant soil unit weight (γ)	= 11.5 kN/m ³
Lateral earth pressure coefficient (K_r)	= 1.0
Adhesion factor (α)	= 0.5
Rate of increase in undrained shear strength (c)	= 50 kPa/m
Rate of increase in soil Young's modulus (m)	= 25 MPa/m
Backsliding factor (β)	= 0
Residual/peak shear strength ratio (R_s)	= 0.6
Shear degradation rate factor (C_s)	= 0.7 mm ⁻¹
Residual/peak bearing strength ratio (R_b)	= 0.5
Bearing degradation rate factor (C_b)	= 50

The soil strength-stiffness ratio (m/c) of 500 was used. The above R_s and C_s values are taken from Figure 4.16a and 4.26a, based on correlation with liquid limit of 35% to 45%. The above R_b and C_b values are taken, assuming 50% degradation in bearing strength and medium rate of bearing strength degradation (from Sections 4.7.1 and 4.8.1).

The pile-head displacement results indicated in Long *et al.* (1993) indicated that the lower portion (below the 90 m level) of the pile behaviour has virtually no influence on the upper part. The embedded pile length of twenty pile diameters was therefore assumed to economise on computational costs. The equivalent Young's modulus (E_p) of the pile was taken as 70 GPa (from Appendix 8.1).

8.7.2 Predictions by previous workers

The p - y methods established by Matlock (1970) and Reese *et al.* (1975) and a recent revised p - y method developed by Dunnavant and O'Neill (1989) were used to predict the pile responses. The above methods use $\varepsilon_{50} = 0.005$, typically assumed for design in the absence of field measurements for p - y methods. In addition, the p - y curves derived from the measured bending moment profiles of the piles, for the current pile-load tests described by Hamilton and Dunnavant (1993), known as the 'derived p - y ' method is used for predicting the pile responses.

Static analysis

The predictions using the above p - y methods for static loading are shown in Figure 8.27. The agreement between the measured pile-head load-displacement responses with those predicted using the derived p - y method is very good. This is because the derived p - y curves were extracted from the measured pile responses (together with some curve fitting techniques), and will naturally provide very good predictions. The predictions by Reese *et al.* at low displacement levels (less than 10 mm) are very good, but with further increases in the displacement levels, they predicted a very stiff pile response. Matlock predictions underestimated the pile-head load by 20% at low displacement levels and continue to give a soft response with the increase in displacements. Dunnavant and O'Neill predictions underestimated the pile-head load at low displacement levels, but give good estimates (differences less than 10%) at higher displacements.

Cyclic analysis

The comparisons with cyclic loading results using the above p - y methods are depicted in Figure 8.28. The derived p - y method provides the best predictions of the pile-head load-displacement results, with underestimation of pile-head load by 6% at displacement of 54 mm and overestimation at higher displacement levels. The method by Matlock predicted a too stiff pile response. Dunnavant and O'Neill gave good estimation of pile-head loads at low displacement levels, but overestimated the pile-head loads as the displacement levels increased. Reese *et al.* predicted a stiff pile response at low displacement levels (less than 25 mm), after which, they predicted a soft pile response; the pile-head load-displacement

response is essentially asymptotic after displacement of 25 mm. The method of analysis developed by Reese *et al.*, clearly leads to undue conservative design at high displacement or load levels.

Figure 8.29 shows the comparisons between the maximum bending moment-displacement responses with predictions obtained using the above p - y methods. As expected, the derived p - y method predictions give the best estimates of the maximum bending moments; overestimation of maximum bending moments at high displacement levels are observed. Other p - y methods (developed by Reese *et al.*, Dunnavant and O'Neill and Matlock) have grossly overestimated the maximum bending moments with increasing displacement levels, except the method by Reese *et al.*, which underestimated the measured maximum bending moments for displacement levels of more than 70 mm.

8.7.3 Current analysis

As APILEC is capable of analysing pile behaviour under displacement-controlled conditions, the controlled displacement is set according to the maximum value for each increment, outlined in Table 8.1. The minimum or residual displacements are all taken as zero, although this is different from the field test minimum values. However, this will have little effect on the overall pile behaviour. Furthermore, the maximum displacements of the pile corresponding to the maximum loadings and bending moments are the main concern in the analyses.

Static analysis

Static analyses were conducted using the soil data described in Section 8.7.1. APILEC predicted a very stiff pile response; see Figure 8.30 (denoted as APILEC: S1). As such m was lowered to $100c$, and the predictions (denoted as APILEC: S2) showed very good agreement (differences less than 5%) with the measured pile-head load-displacement responses at displacement levels above 50 mm. At displacement levels less than 40 mm, APILEC underestimated the pile-head loads by an average of 15% (Figure 8.30).

An examination on the bending moment distributions predicted by APILEC at displacement increment 9 (displacement of 104.5 mm), depicted in Figure 8.31, shows that the maximum bending moment is underestimated by approximately 20%. To have a more

accurate prediction of the maximum bending moment, the values for the soil strength parameters used in APILEC analyses, will need to be re-considered.

Figure 8.26b shows a significant reduction in the undrained shear strength of the soil after the additional site investigations from results of Borings 207 and 208 carried out close to the test pile location. As mentioned earlier, the soil in which the piles were embedded had been flooded with water for a month prior to the lateral load tests. This may imply that the soil at the pit floor level probably has a C_u value close to zero. Hence, a C_u value of zero at pit floor level with (lower bound) $c = 60$ kPa/m and $m = 90$ MPa/m ($m/c = 1500$) were chosen based on Figure 8.26b. With these changes in soil strength, APILEC predictions (denoted as APILEC: S3 in Figure 8.30) give close estimates (differences less than 1%) of the pile-head load-displacement responses at displacement levels of less than 15 mm. After which, the pile-head loads are overestimated with further increases in displacement levels. The bending moment distribution along the pile length depicted in Figure 8.31 (for displacement increment 9), shows that APILEC overestimated the maximum bending moments by around 20%.

From the above results, the value of m has to be reduced as the pile response is too stiff at large displacement levels. Taking $c = 60$ kPa/m and $m = 27$ MPa/m ($m/c = 450$), APILEC predictions (denoted as APILEC: S4 in Figure 8.30) show better predictions of the pile-head load-displacement responses as compared with previous predictions. A soft response of pile under displacement levels of less than 20 mm is observed, while a very good agreement (differences less than 5%) with pile responses at higher displacement levels (greater than 50 mm) are clearly seen. The predicted bending moment distributions along the pile length (Figure 8.31) gives very good estimates of the measured results, with the maximum bending moments correctly predicted (differences less than 2%). Further comparison with the measured bending moment distribution for displacement increment 8 (displacement at 54 mm), show that APILEC has again accurately predicted the bending moment distribution (Figure 8.31), at the same time giving excellent estimates (differences less than 2%) of the maximum bending moment. In addition, the depth at which the maximum bending moments occur for displacement increments 8 and 9 are accurately predicted.

In comparisons with other p - y methods (except derived p - y method) described in Section 8.6.2, APILEC analyses have shown to give better predictions of the pile-head load-displacement responses for the full range of displacement increments; see Figure 8.32.

Cyclic analysis

From the above evaluations, the use of $c = 60$ kPa/m and $m = 450c$ is justified in view of the possible variations in soil properties and the good predictions of the bending moment distributions and the pile-head load-displacement responses for static loading. These values are employed for APILEC cyclic analyses.

Using the strength degradation parameters described in Section 8.7.1, APILEC predictions for cycles 5 and 10 are depicted in Figure 8.33. Very good agreement (differences less than 5%) with measured pile-head load-displacement response is obtained at displacement levels greater than 30 mm (for the fifth cycle), and at displacement levels greater than 100 mm (for the tenth cycle). At displacement less than 20 mm, APILEC has underestimated the pile-head loads by approximately 15%.

APILEC predictions for maximum bending moments give a good agreement (average differences of 10%) with the measured results for the full range of displacement increments; see Figure 8.34. Slight underestimation of the maximum bending moments (average 5% for displacement levels greater than 30 mm) is observed at the fifth cycle. Increasing the number of cycles to ten, a lower maximum bending moment is predicted.

The measured bending moment distributions along the pile length at the first (static) and final cycles for displacement increments 8 and 9 are shown in Figures 8.35 and 8.36, respectively. They show that the maximum bending moment reduces and also the position at which it occurs, moves down the pile length, with the increasing number of cycles. Superimposed APILEC predictions for cycles 1, 5 and 10 to Figures 8.35 and 8.36, show good predictions of the measured responses. It is shown that APILEC correctly predicted the bending moment distributions and also gives good estimation of the maximum bending moments for both static and cyclic loadings. In addition, the position at which the maximum bending moment occurs is correctly predicted.

In comparisons with the predictions obtained via the p - y methods (except the derived p - y method), APILEC has certainly shown that its predictions for pile-head load-displacement (Figure 8.37) and maximum bending moment-displacement (Figure 8.38) responses are much better.

8.7.4 Discussion

The field results show significant reduction in the pile-head loads from the first cycle (static loading) to the end of the applied cycles (see Figure 8.33); this phenomenon is due to soil erosion, gap formation and soil strength degradation effects. The amount of reduction in pile-head loads increases with the increase in displacement levels. The same trend of pile response is clearly produced by APILEC, as illustrated in Figure 8.33.

Overall, the APILEC analysis gives better predictions of the measured results, than those using the established p - y methods (except the derived p - y method; reasons as explained earlier); see Figures 8.32, 8.37 and 8.38. This applies to both static and cyclic analyses.

APILEC predictions for cycles 5 and 10 can be taken as equivalent to the final cycle measured in the displacement-controlled pile-load tests.

The established p - y methods, in particular those developed by Matlock (1970) and Reese *et al.* (1975), are recommended by API RP 2A (1986) for the determination of static and cyclic pile responses in the offshore environment for soft clays and stiff clays, respectively. Given the significant errors in predicting the actual pile behaviour, the suitability of these methods must be in some doubt.

8.8 Discussion of results

Load cycles

The current analysis has shown good agreement with measured pile responses in most cases with cycling between 5 to 10 cycles. For low load levels, 5 to 10 cycles have proved to be sufficient to provide very good estimates, as the piles tend to stabilise, as evident in the many field results reported and in the parametric studies conducted in Chapter 7. For higher load levels, more cycles (say, up to 50 cycles) may be required in order to provide very good predictions (see Figures 8.4, 8.9, 8.17 and 8.18). However, this will greatly increase the computational cost.

Selection of soil parameters

From the comparisons with field test results, it has been shown that good predictions of pile responses for the static loading were vital before attempting to predict the pile responses for cyclic loading. As such, selection of strength parameters (i.e. C_u or c and E_s or m in Section 8.3) were critical in the analyses. This can be seen in the analyses carried out in Section 8.7.

For static analyses, it was shown that increasing the strength parameters reduced the pile-head displacements and maximum bending moments. For cyclic analyses, the strength degradation parameters were needed (R_s , C_s , R_b and C_b in Section 8.3) to obtain good predictions. These parameters increase the pile-head displacements, maximum bending moments and the rate of cyclic degradation.

Strength parameters

To achieve good predictions of pile response, the C_u values employed in the APILEC analysis were often different from those provided by the experimental tests. This may be a short-coming of APILEC analysis. However, in many cases, the C_u values provided may not be appropriate due to sampling disturbances, etc. Also, the C_u values may vary due to spatial variations of soil properties and soil disturbances during pile installations as suggested by the field data reported by Tassios and Levendis (1974). In view of this, many researchers have also adopted different C_u values from those suggested by experimental results.

For E_s determination, the values adopted by APILEC range between $450C_u$ to $4750C_u$. The $4750C_u$ was certainly much higher than that recommended in Section 8.3. In retrospect, it would have been more sensible (in this case) to have assumed a non-linear variation of strength with depth, allowing for both low stiffness at ground level and a rapid increase with depth. It was noted in the comparisons of field results, that many researchers had adopted a very wide range of E_s/C_u ratios.

Strength degradation parameters

The use of soil strength degradation parameters (R_s , C_s , R_b and C_b in Section 8.3) for cyclic analyses, had demonstrated their usefulness. The values adopted for these parameters were obtained from correlations with soil index properties and experimental results described in Chapter 4. This eliminates any empirical assumptions associated with them. However, it was sometimes necessary to adjust these parameters from the pile-load test results (e.g. from the rate of cyclic degradation), as shown in Figures 8.23 and 8.24. The effects of these parameters could also be seen in the parametric studies described in Chapter 7.

Backsliding factor

The backsliding factor (β) was not employed in the current analysis as there was no evidence for it in any of the five case histories reported. In the pile test results reported by Hamilton and Dunnavant (1993), APILEC predicted a soft response for loads below 1100 kN for both static and cyclic analyses. The use of β may perhaps be appropriate to reduce soil yielding, and thereby give a stiffer pile response at the low load levels.

p-y analysis

The *p-y* analyses only gave good agreements with the field results from which they were derived. These were observed in the tests of Matlock (1970), Reese *et al.* (1975), Dunnavant and O'Neill (1989) and Hamilton and Dunnavant (1993). However, if the *p-y* criteria established by Matlock, Reese *et al.* and Dunnavant and O'Neill were used to compare with the measured pile responses reported by Hamilton and Dunnavant, poor agreements were obtained as evident in Figures 8.32, 8.37 and 8.38. This illustrated that *p-y* analyses were not suitable for predicting the complex behaviour of laterally loaded piles using available soil data from other pile-load tests (reasons as explained in Section 1.3.2). Thus, the statement made by Davies and Budhu (1986) - "the *p-y* relationship has no basis in reality outside its role as an expedient empirical device to solve the present problem" appears to be confirmed.

8.9 Concluding remarks

From these comparisons with published field test results, the current analysis had proved useful in providing good predictions of measured pile responses. It had successfully predicted the phenomena observed in both the load-controlled and displacement-controlled cyclic pile-load tests. Overall, the current analysis had shown better predictions than other methods of analyses developed by Matlock (1970), Reese *et al.* (1975), Poulos (1982), Swane and Poulos (1985), and Dunnavant and O'Neill (1989). This is believed to be due to the fact that:

- It adopted the continuum approach, taking account the continuous nature of pile and soil interaction at the interface.
- It considered the three-dimensional nature of the cyclic laterally loaded pile problems, where the side, front and back face of the pile-soil interfaces are taken into account.

- The strength parameters (C_u or c and E_s or m) and strength degradation parameters (R_s , C_s , R_b and C_b), required for the analyses, involved few empirical assumptions.

Thus, given accurate values for the undrained shear strength and the soil index properties, applying the current analysis to cyclic laterally loaded piles can be done with a reasonable degree of confidence.

APPENDIX 8.1

Equivalent Pile Young's Modulus

APILEC is intended for the analysis of solid cylindrical piles (despite the fact that the internal representation assumes a square cross section). It can be applied to hollow piles or piles whose cross-section are not circular (e.g. H piles) by using an 'equivalent diameter' and 'equivalent Young's modulus'.

The essential sectional properties of the pile are its flexural rigidity and its projected width (in the plane normal to the loading). Let $E_p' I_p'$ be the flexural rigidity of the real pile and D' be its width. The equivalent diameter can be taken (with little error) as equal to the width of the real pile, i.e.

$$D = D' \quad (\text{A8.1-1})$$

The equivalent pile Young's modulus can be calculated as:

$$E_p = \frac{64 E_p' I_p'}{\pi D^4} \quad (\text{A8.1-2})$$

For a circular hollow or pipe pile, Equation (A8.1-2) is reduced to:

$$E_p = E_p' \left[1 - \left(\frac{d}{D} \right)^4 \right] \quad (\text{A8.1-3})$$

where d is the internal diameter of the pile.

For pipe piles, the equivalence is exact but for non-circular piles (e.g. H piles), some errors will arise from the shape effect but this should not be significant in practice, as suggested by Davies and Budhu (1986) and Budhu and Davies (1988).

Table 8.1 Displacement increment sequences for laterally loaded pile test at Tilbrook Grange.

Displacement Increment	No. of cycles	Displacement (mm)		Maximum force (MN)
		Minimum	Maximum	
1	1 (static)	0	4.3	0.29
2	100	2.4	4.1	0.28
3	100	2.9	6.2	0.37
4	100	3.9	9.3	0.47
5	100	4	15	0.61
6	100	4	24	0.74
7	120	5	37.2	1.05
8	120	7	54	1.23
9	136	30.8	104.5	1.83

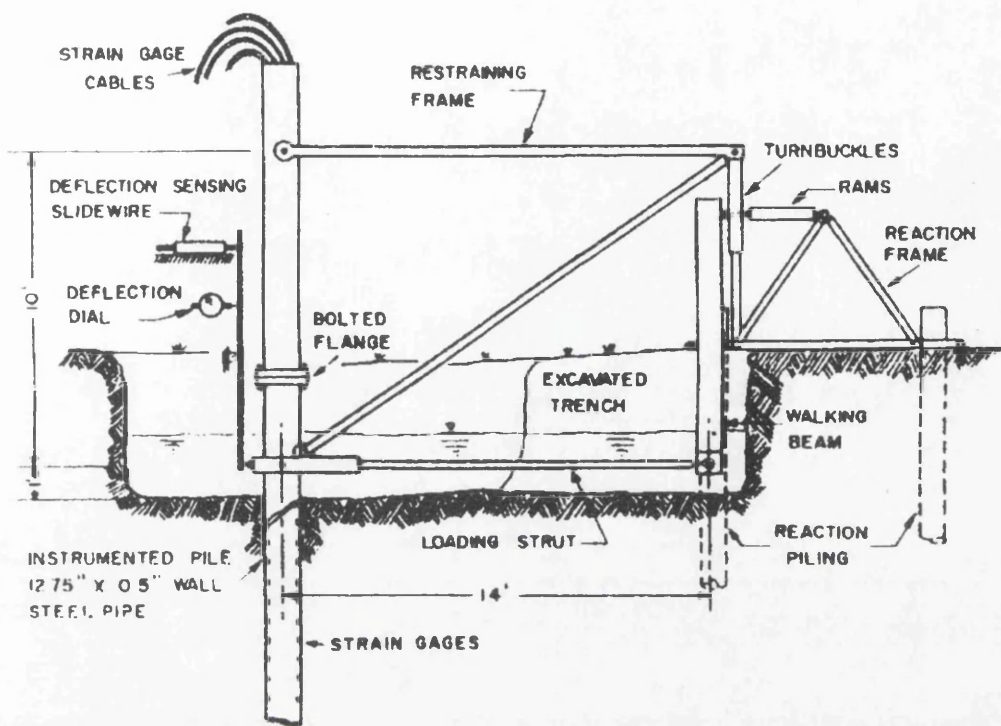


Figure 8.1 Arrangement of field tests at Sabine for fixed-head pile (Matlock, 1970).

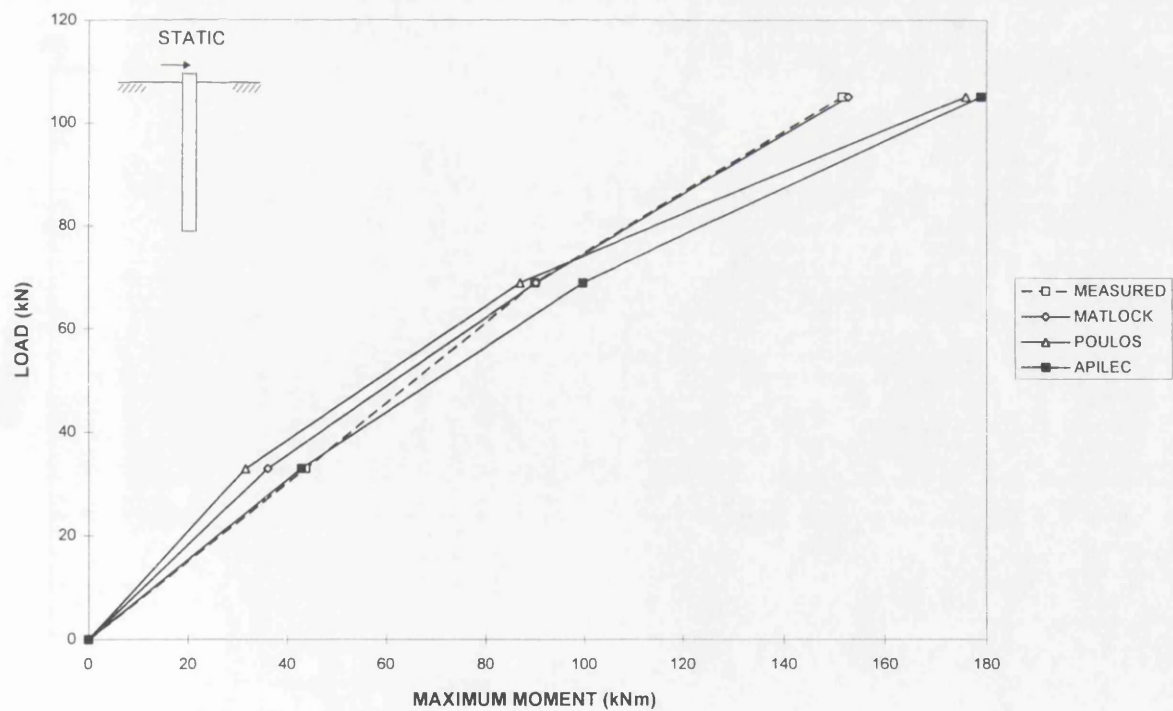


Figure 8.2 Comparisons with maximum bending moment data for static loading at Lake Austin. After Matlock (1970).

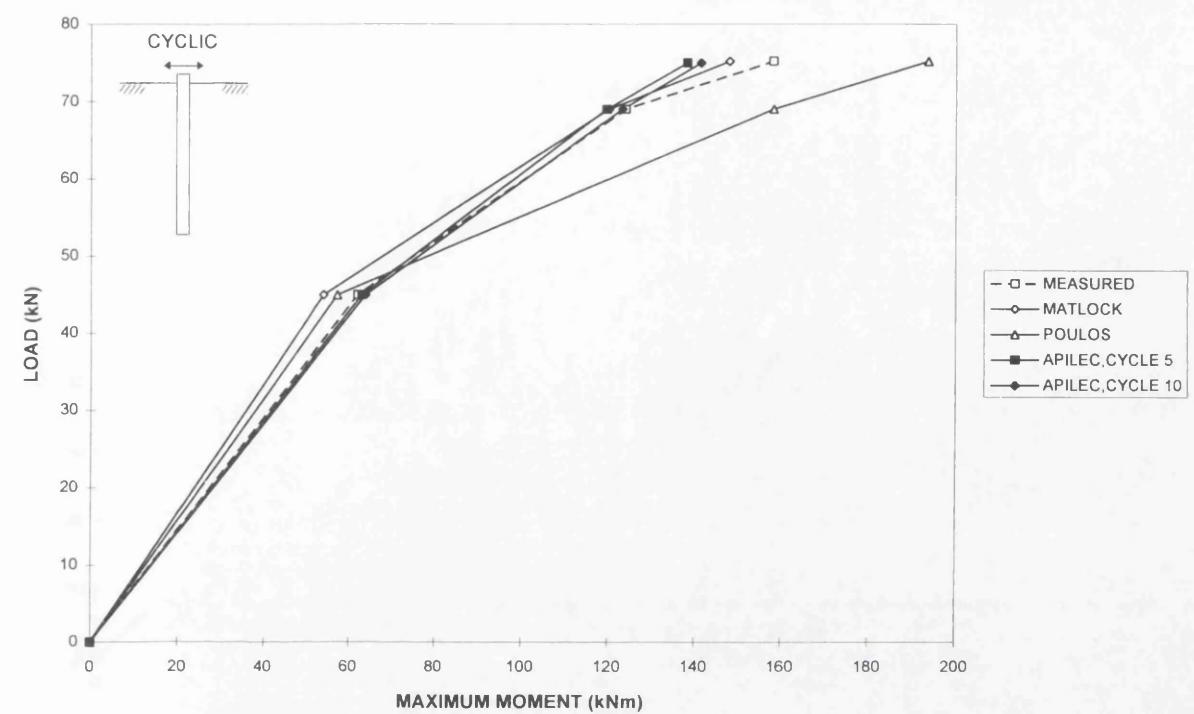


Figure 8.3 Comparisons with maximum bending moment data for cyclic loading at Lake Austin. After Matlock (1970).

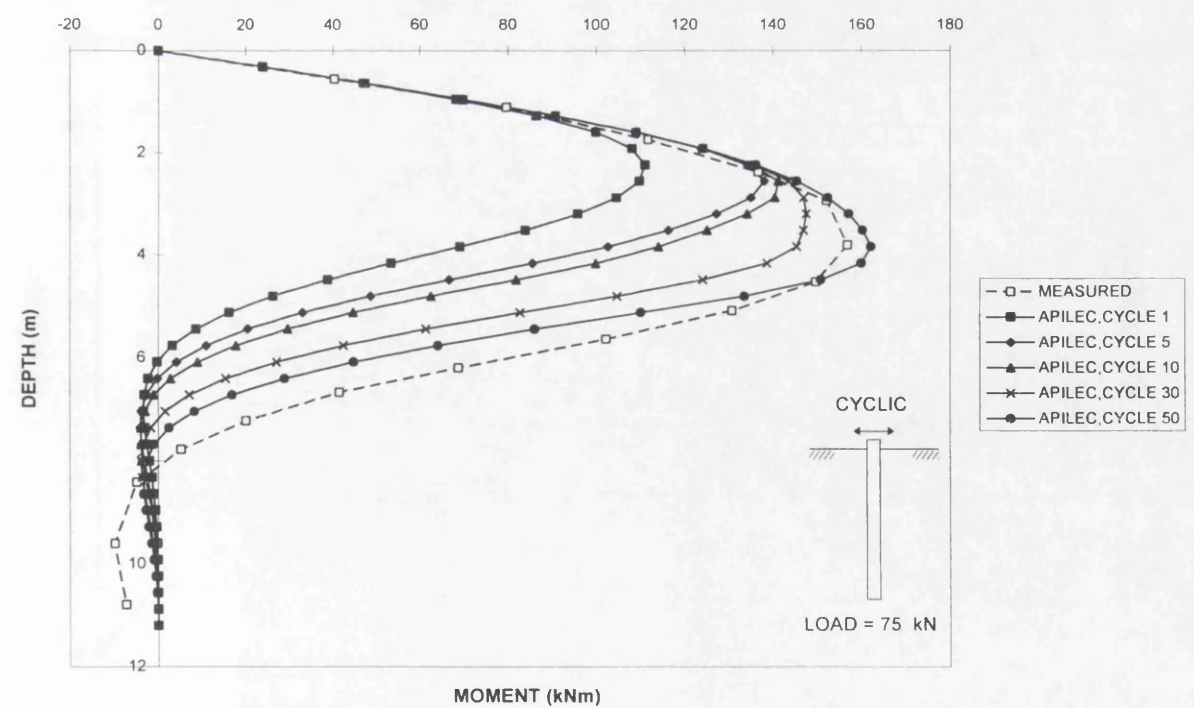


Figure 8.4 Comparisons with bending moment distributions for cyclic loading at Lake Austin. After Matlock (1970).

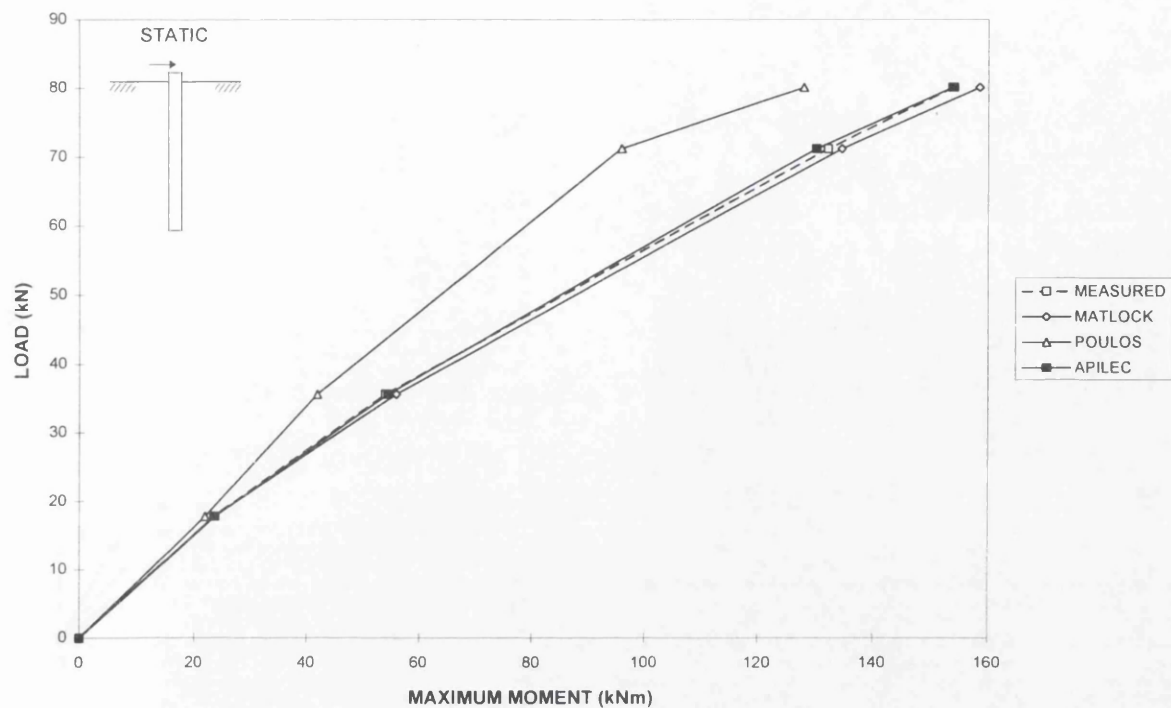


Figure 8.5 Comparisons with maximum bending moment data for static loading at Sabine with free-head pile. After Matlock (1970).

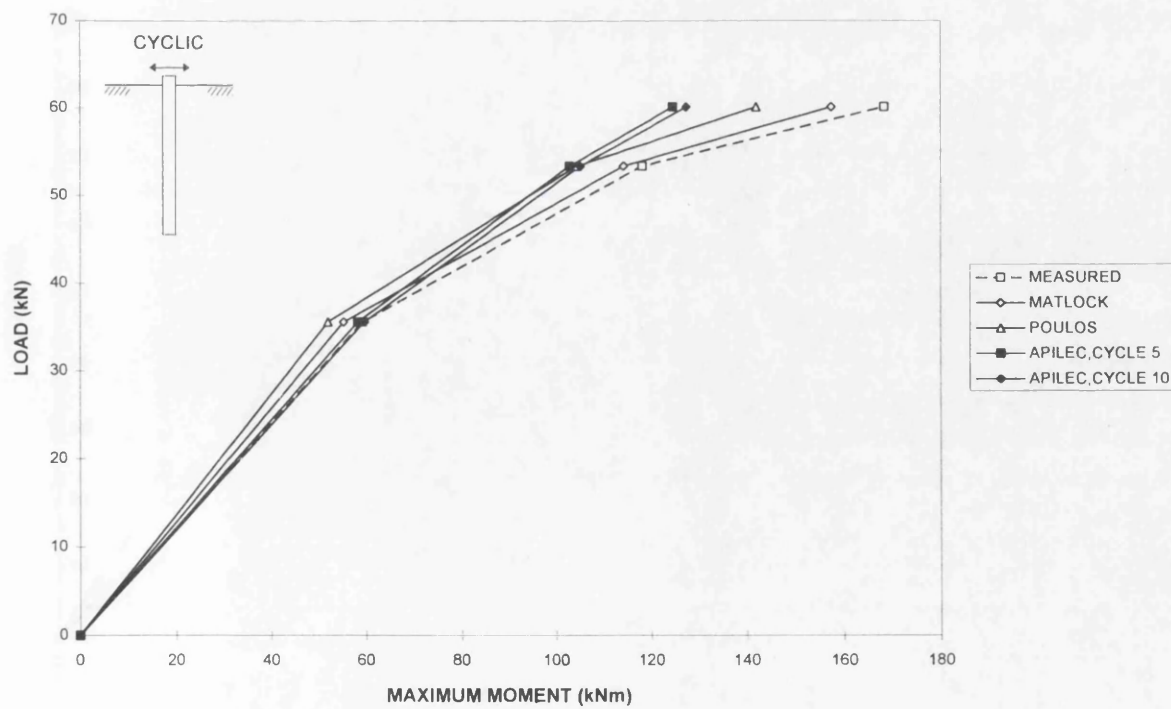


Figure 8.6 Comparisons with maximum bending moment data for cyclic loading at Sabine with free-head pile. After Matlock (1970).

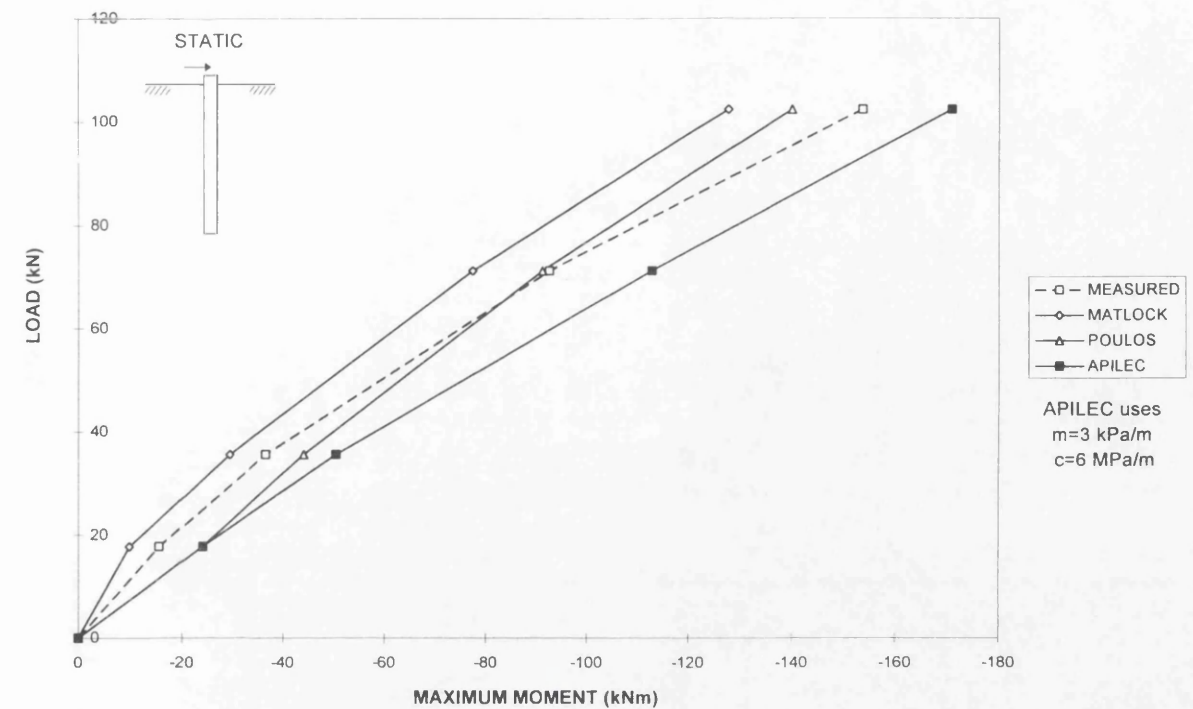


Figure 8.7 Comparisons with maximum restraining moment data for static loading at Sabine with fixed-head pile. After Matlock (1970).

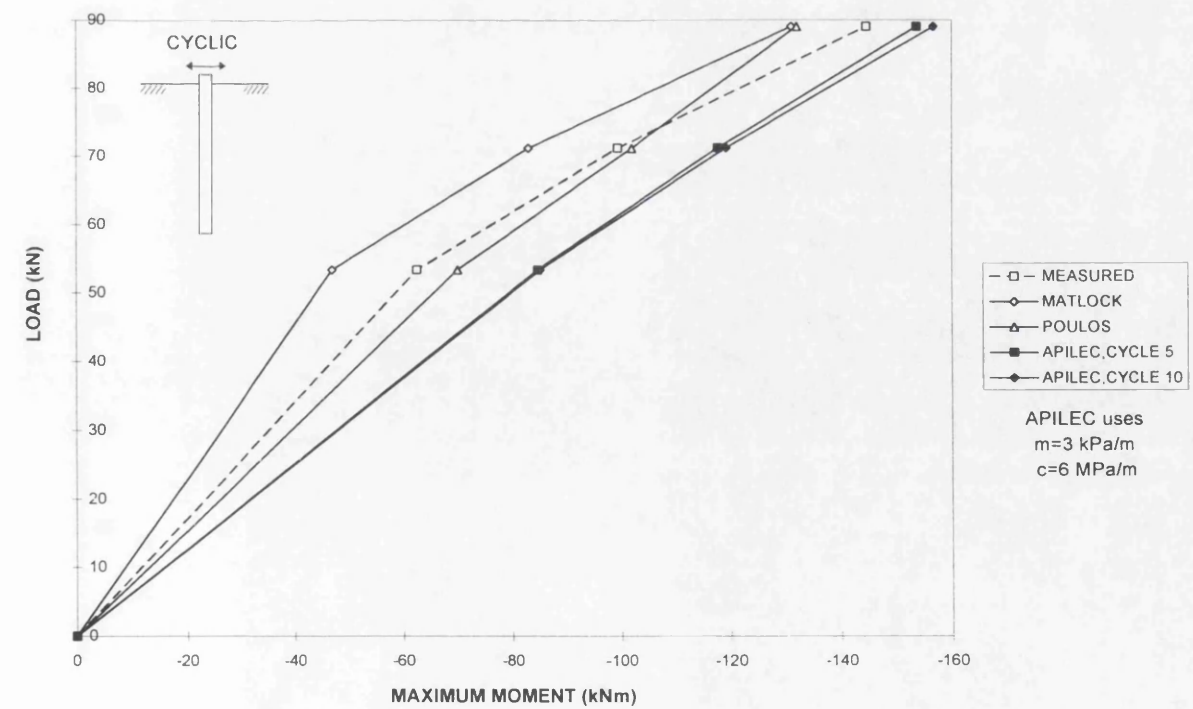


Figure 8.8 Comparisons with maximum restraining moment data for cyclic loading at Sabine with fixed-head pile. After Matlock (1970).

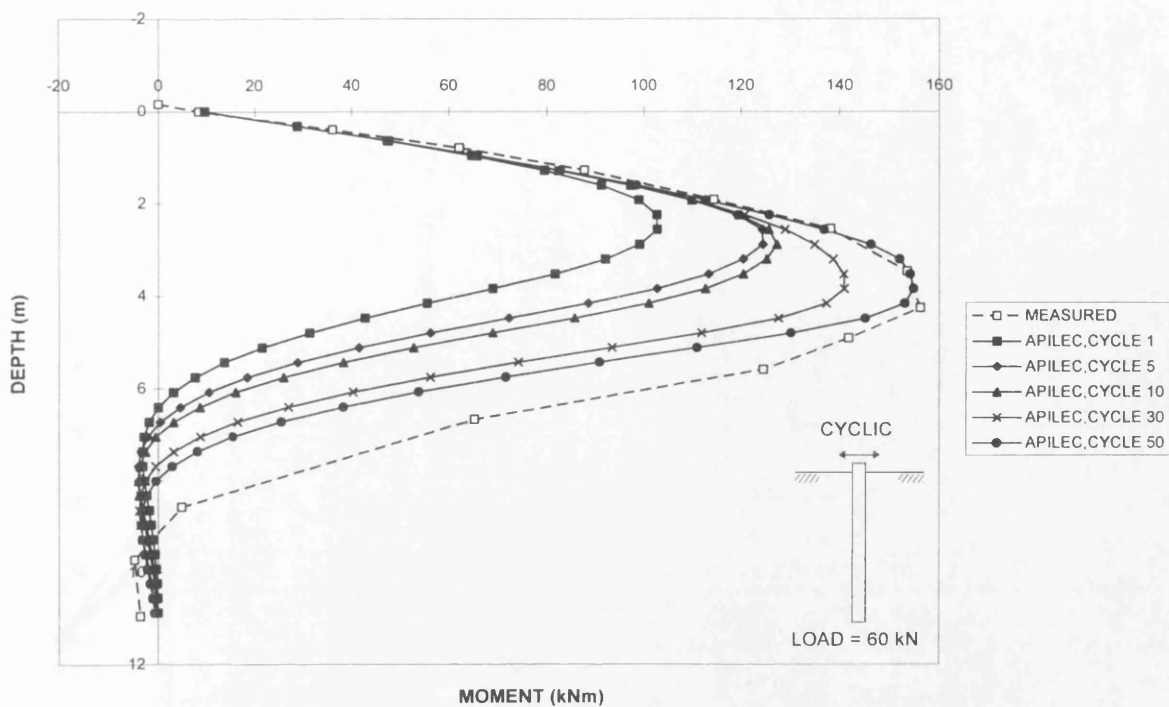


Figure 8.9 Comparisons with bending moment distributions for cyclic loading at Sabine with free-head pile. After Matlock (1970).

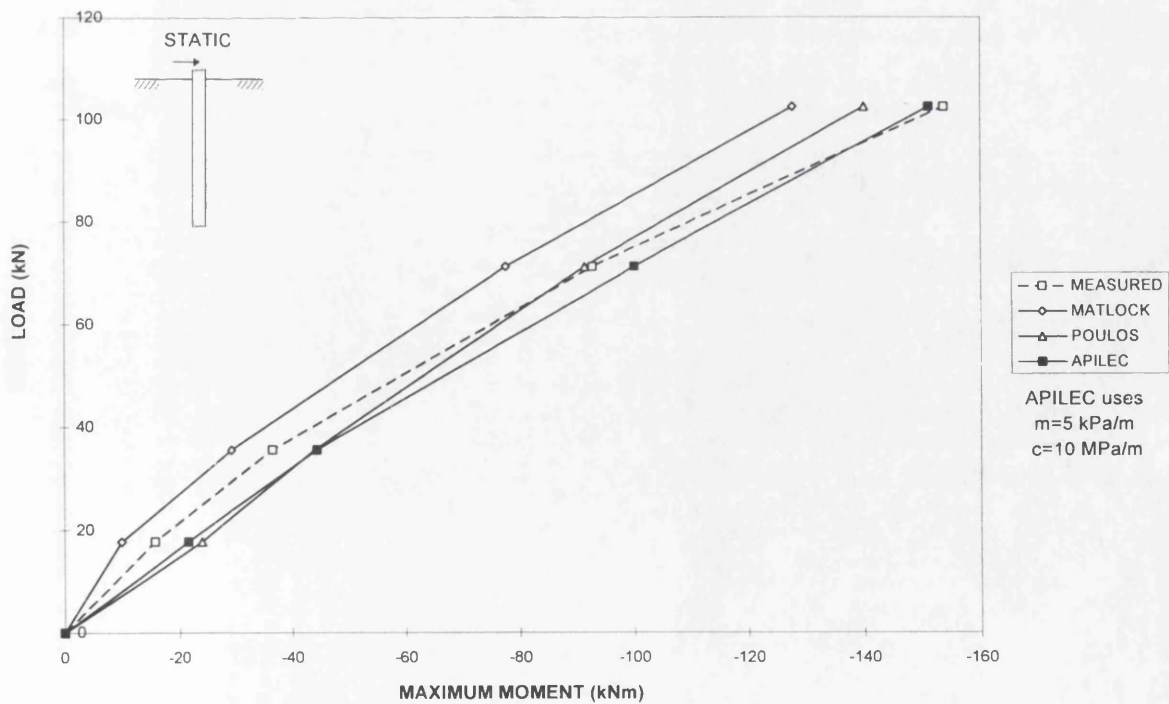


Figure 8.10 Comparisons with maximum restraining moment data for static loading at Sabine with fixed-head pile (with strength data modifications). After Matlock (1970).

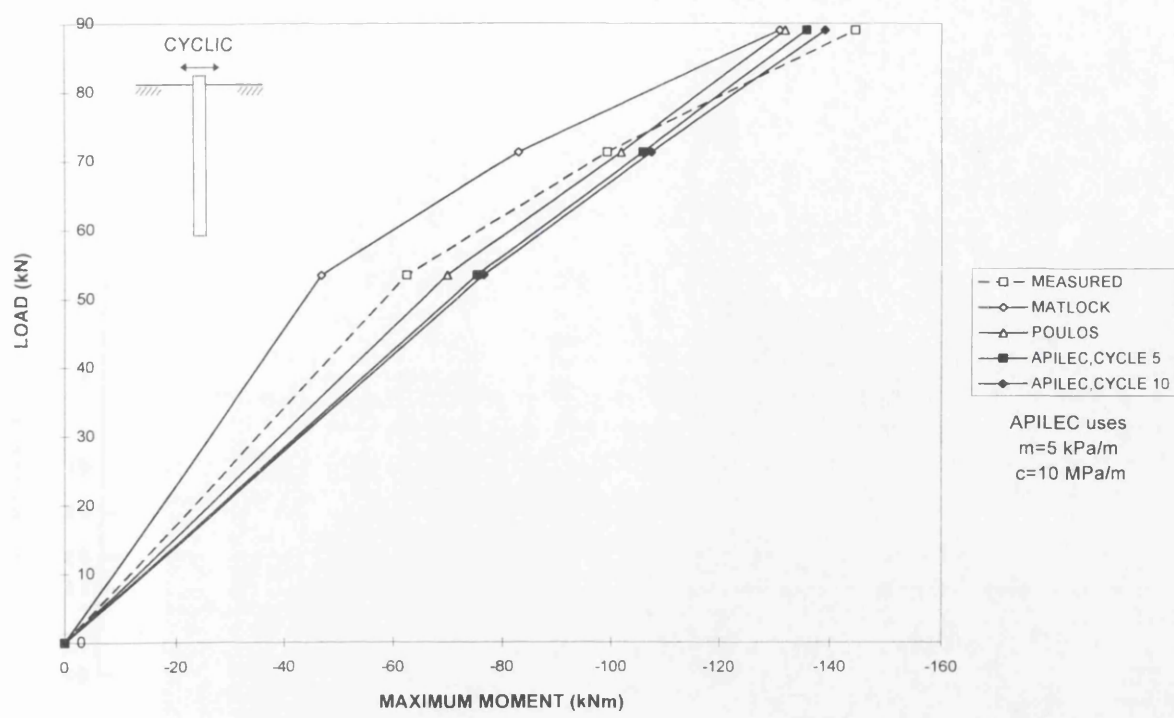


Figure 8.11 Comparisons with maximum restraining moment data for cyclic loading at Sabine with fixed-head pile (with strength data modifications). After Matlock (1970).

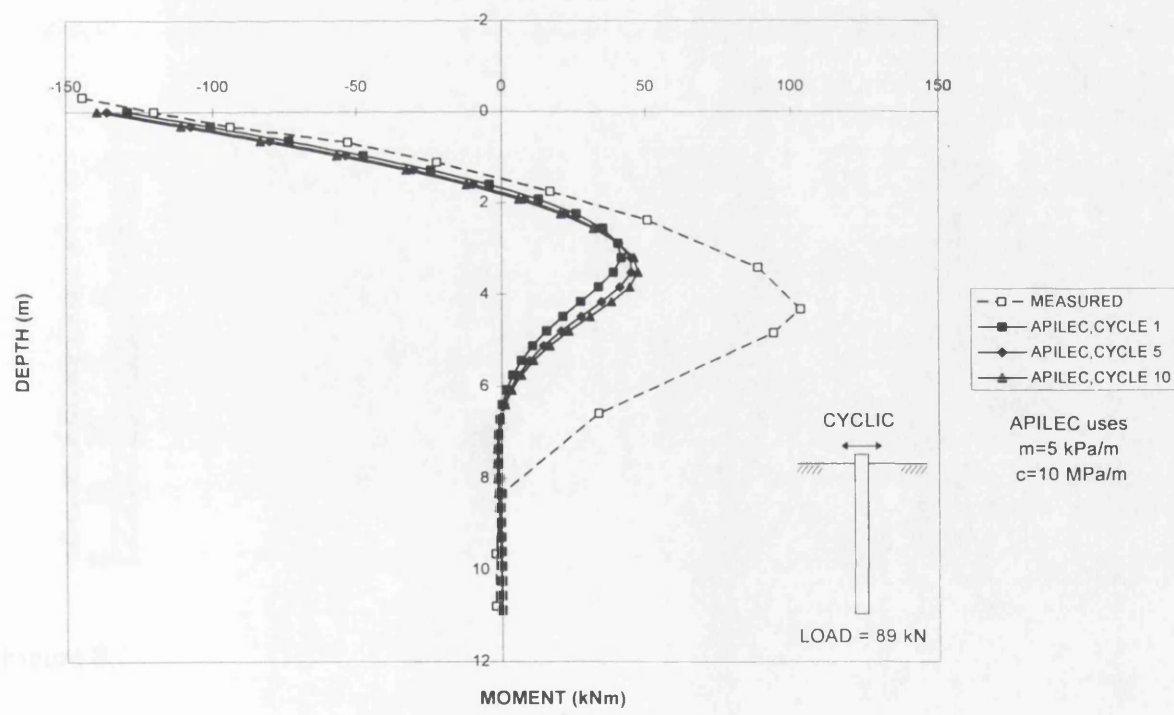


Figure 8.12 Comparisons with bending moment distributions for cyclic loading at Sabine with fixed-head pile (with strength data modifications). After Matlock (1970).

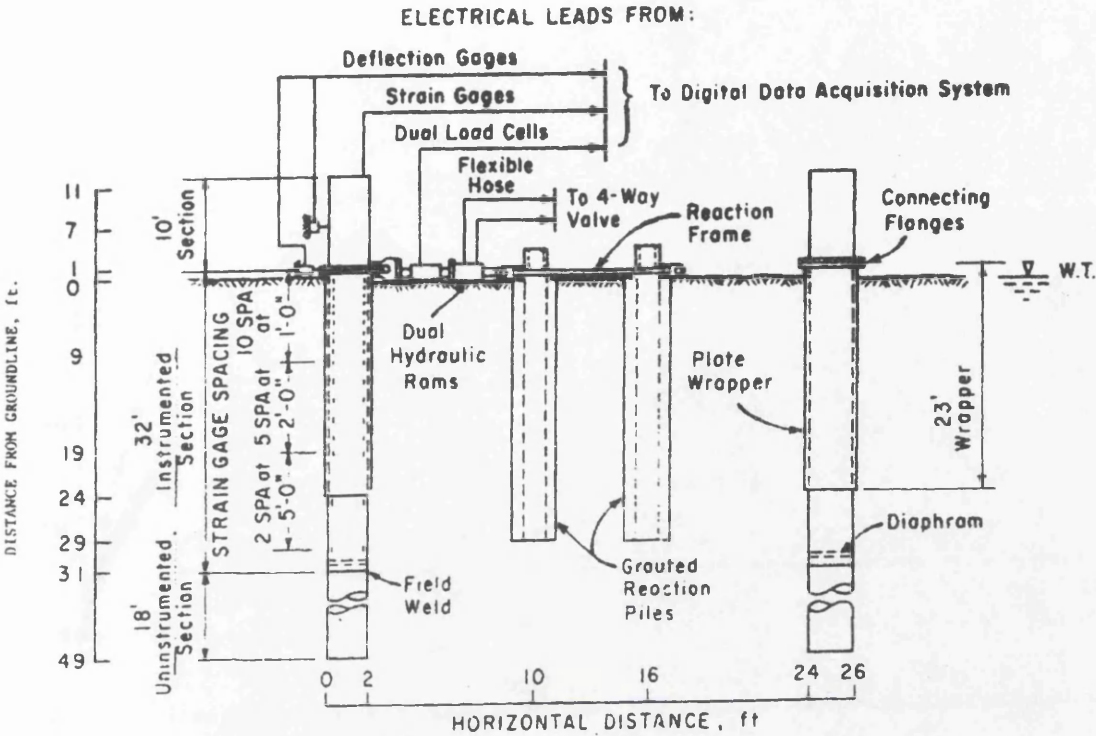


Figure 8.13 Pile test set up as described by Reese *et al.* (1975).

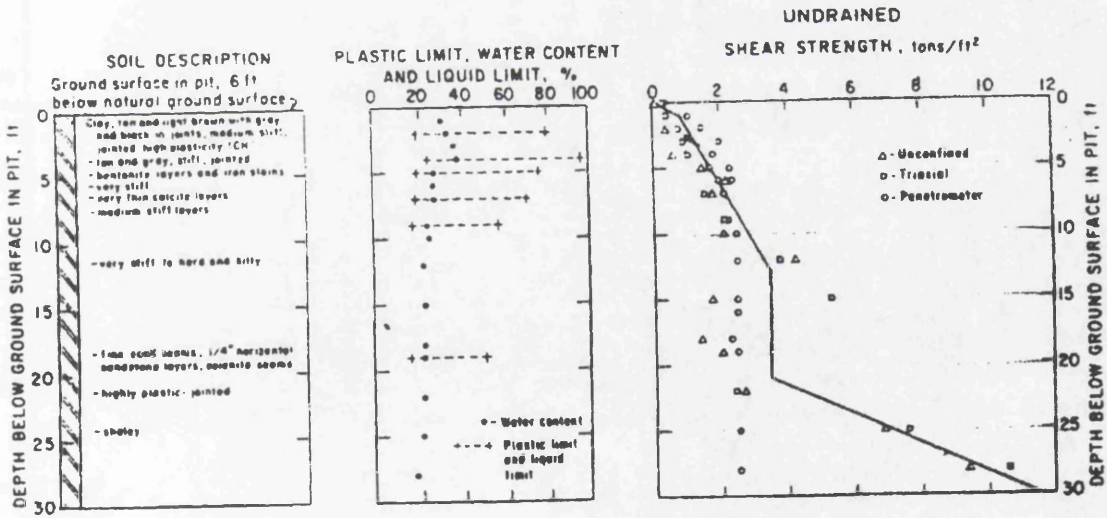


Figure 8.14 Soil profiles as described by Reese *et al.* (1975).

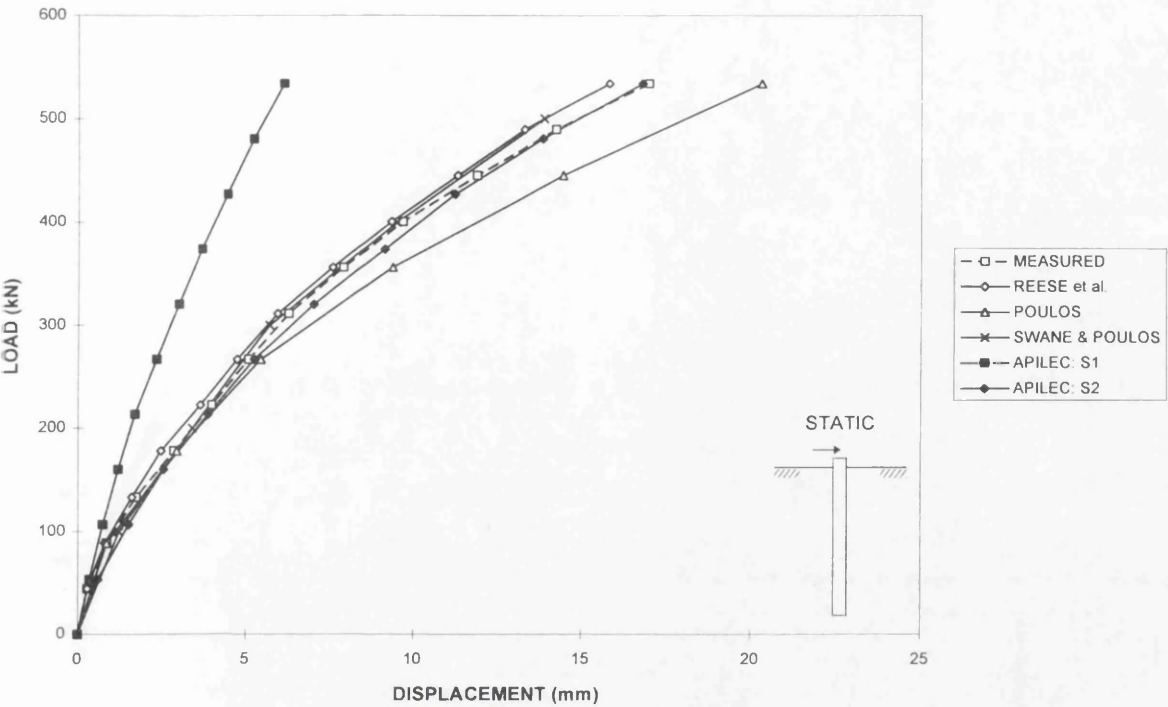


Figure 8.15 Comparisons with load-displacement responses for static loading. After Reese *et al.* (1975).

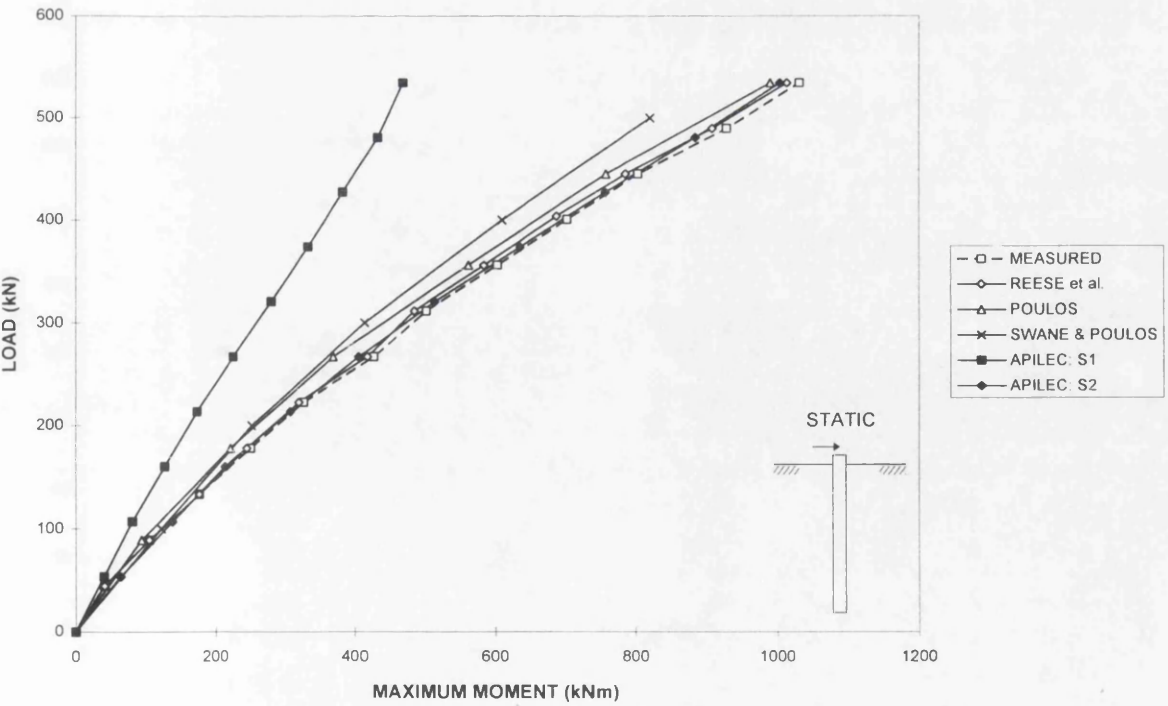


Figure 8.16 Comparisons with load-moment responses for static loading. After Reese *et al.* (1975).

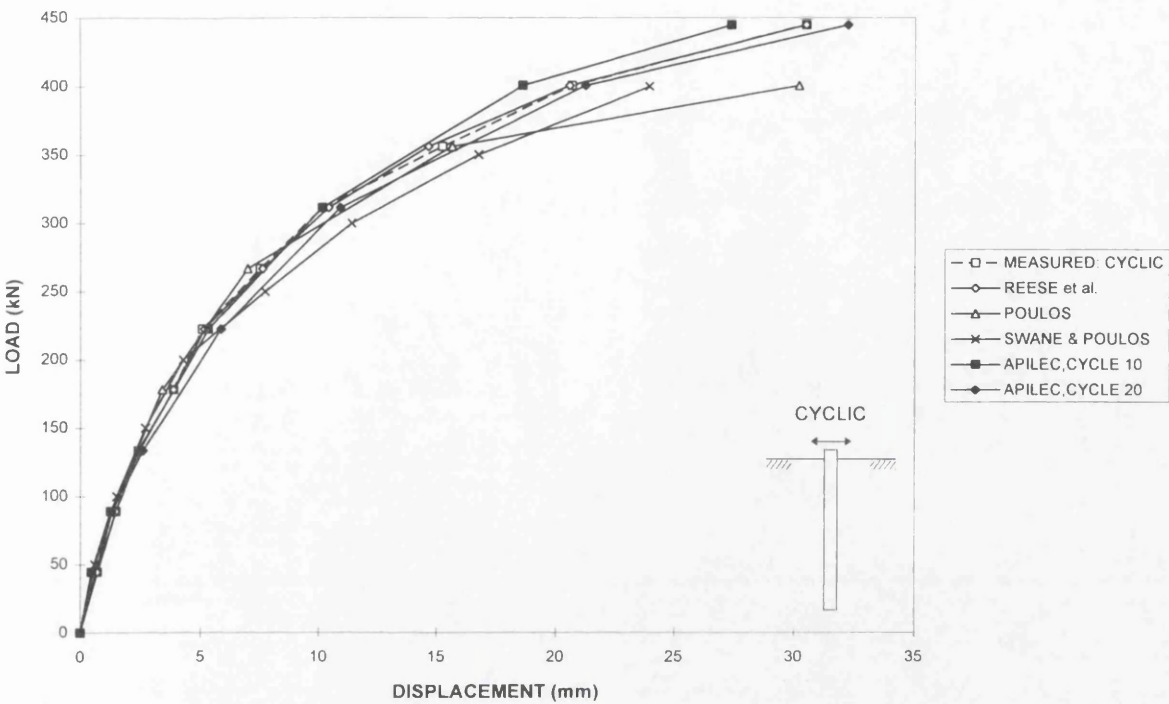


Figure 8.17 Comparisons with load-displacement responses for cyclic loading. After Reese *et al.* (1975).

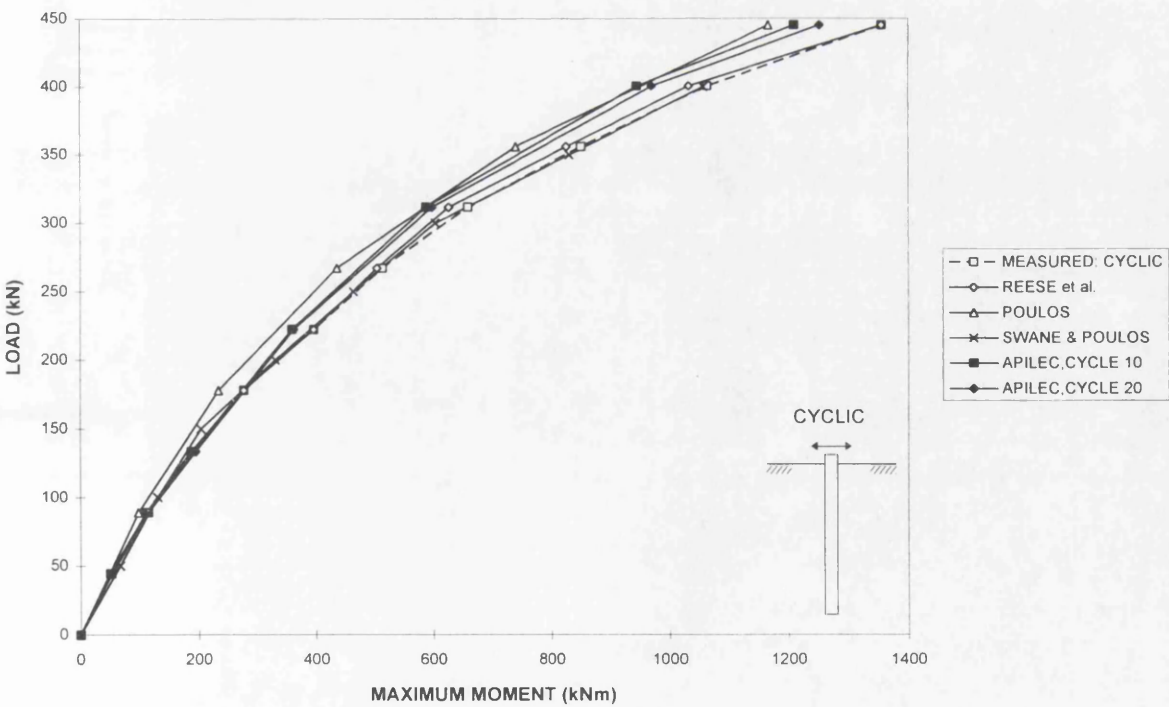


Figure 8.18 Comparisons with load-moment responses for cyclic loading. After Reese *et al.* (1975).

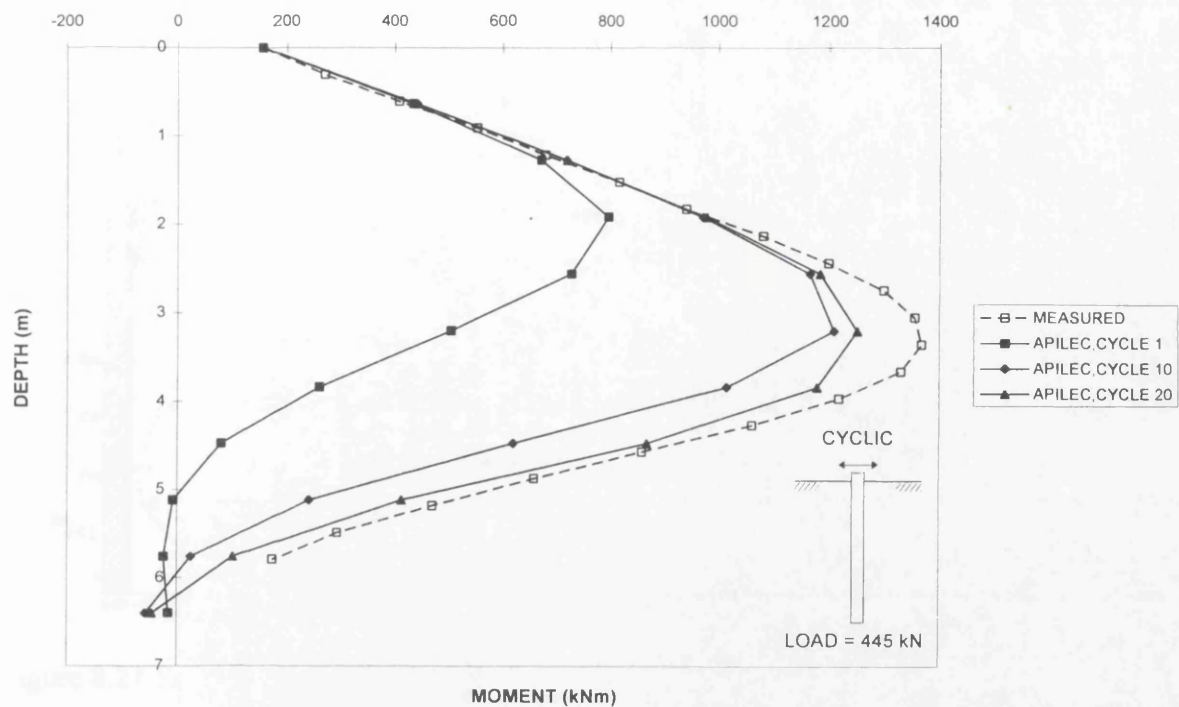


Figure 8.19 Comparisons with bending moment distributions for cyclic loading. After Reese *et al.* (1975).

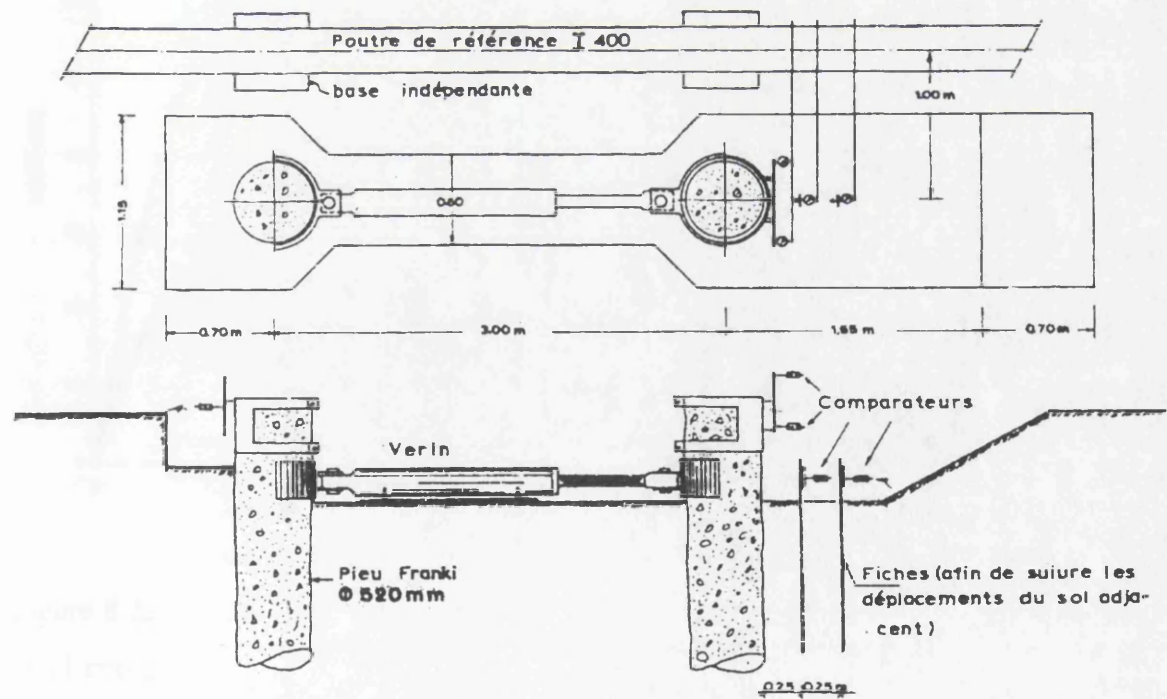


Figure 8.20 Pile test set up as described by Tassios and Levendis (1974).

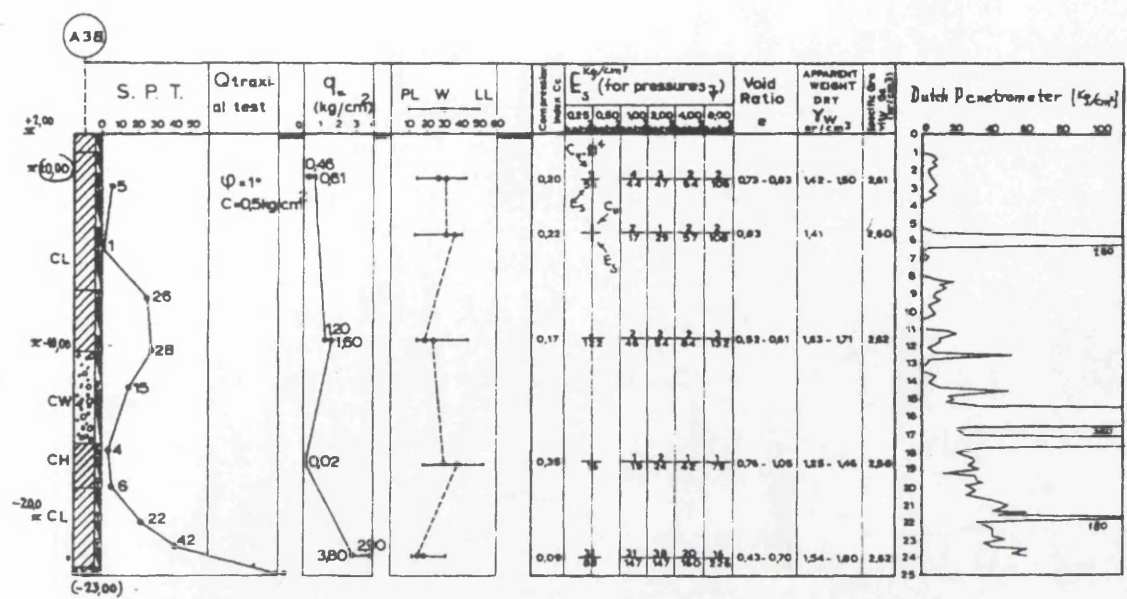


Figure 8.21 Soil profiles as described by Tassios and Levendis (1974).

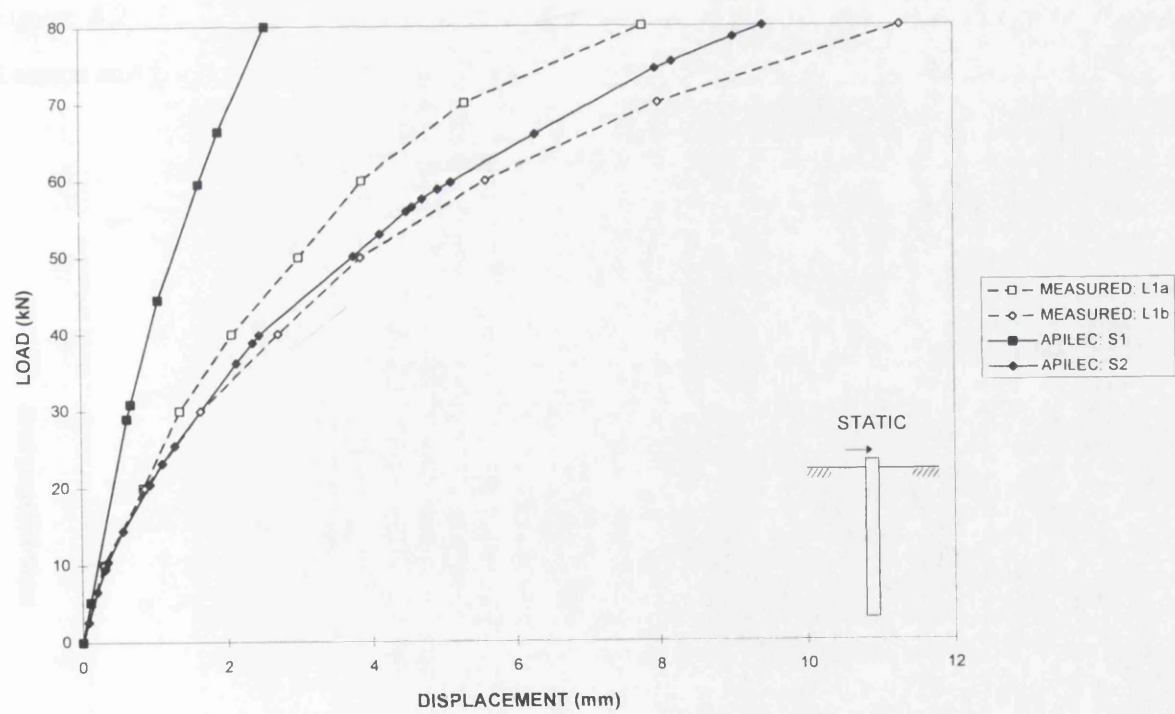


Figure 8.22 Comparisons with load-displacement responses for static loading. After Tassios and Levendis (1974).

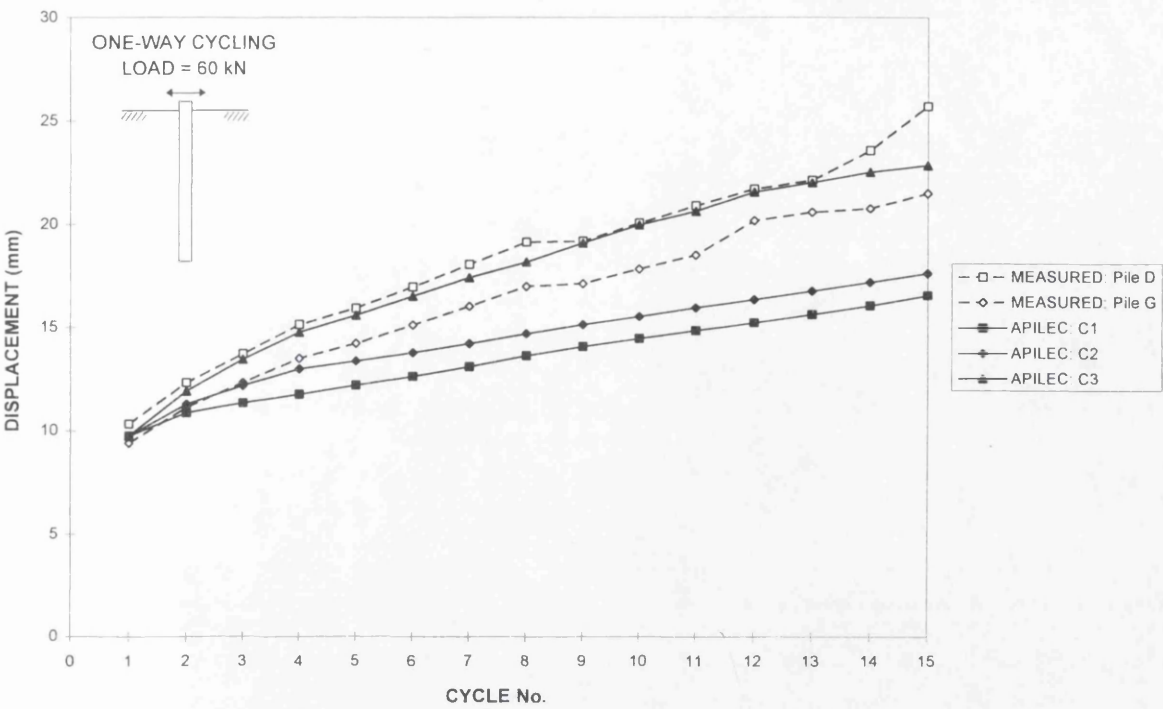


Figure 8.23 Comparisons with pile-head displacements for one-way cyclic loading. After Tassios and Levendis (1974).

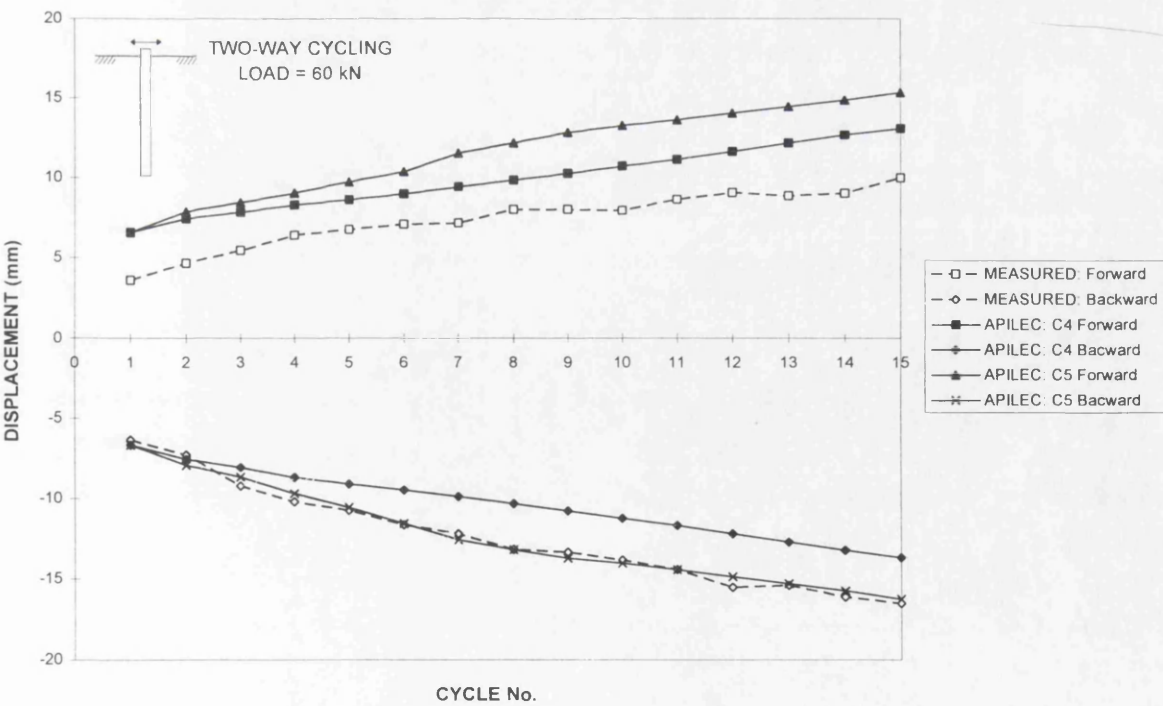


Figure 8.24 Comparisons with pile-head displacements for two-way cyclic loading. After Tassios and Levendis (1974).

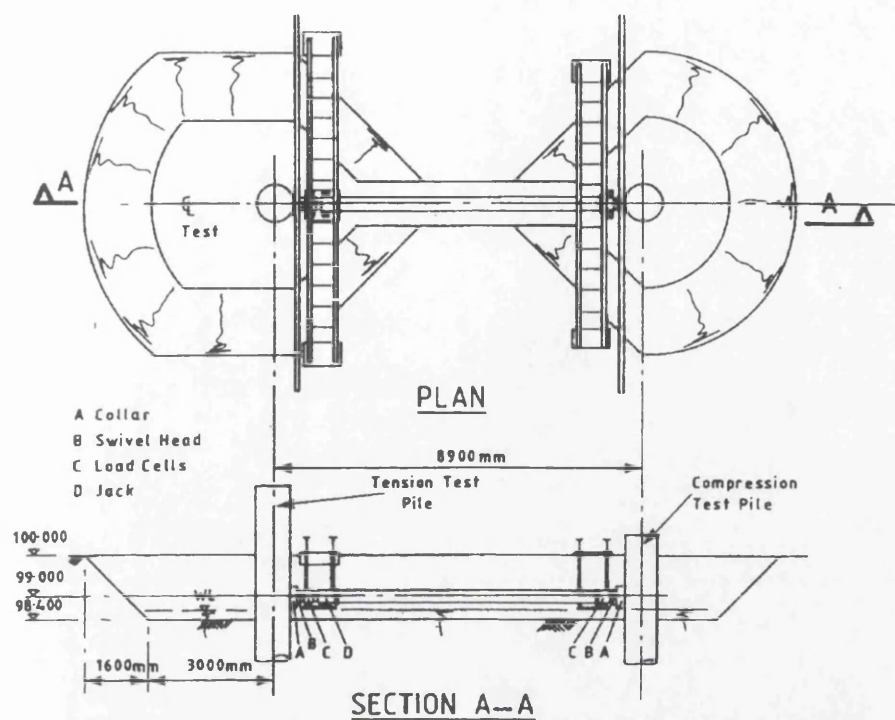


Figure 8.25 Pile test set up as described by Long *et al.* (1993).

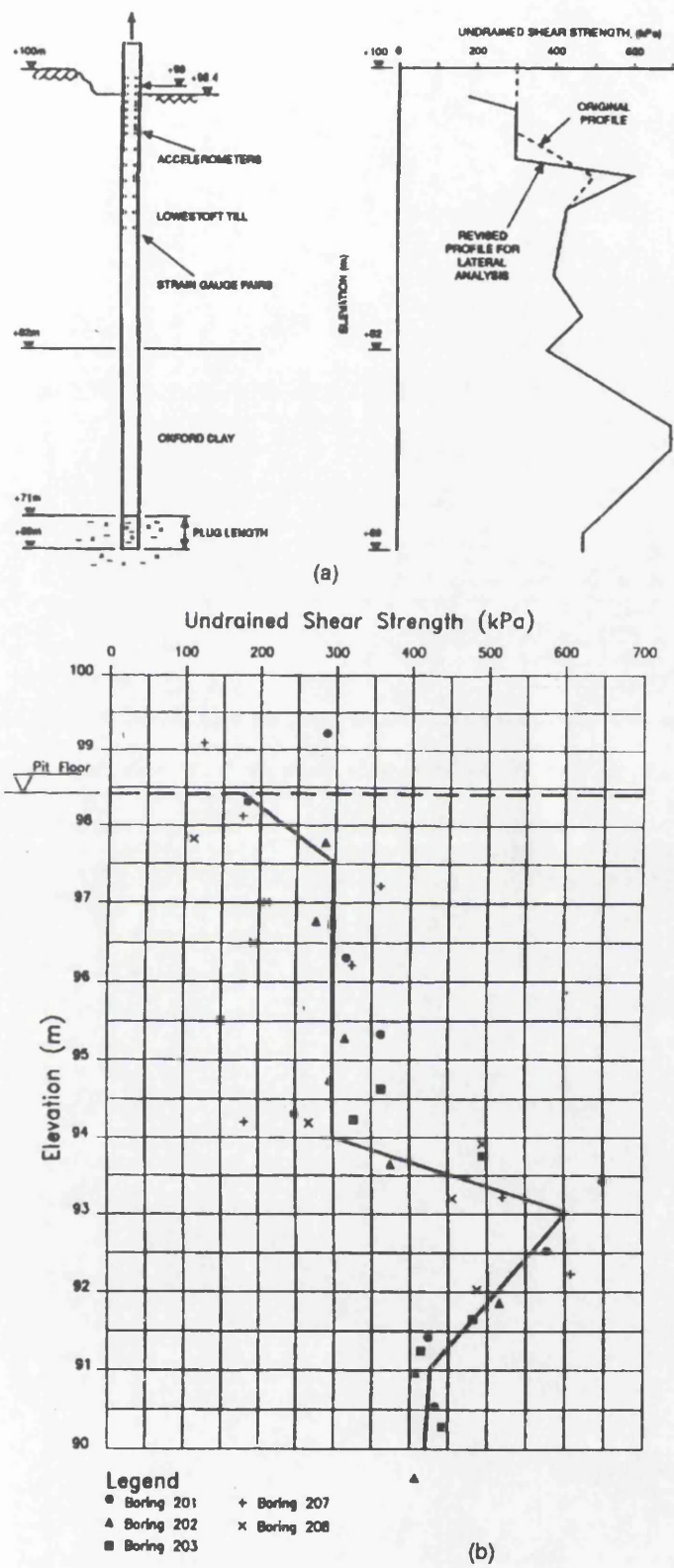


Figure 8.26 (a) Undrained shear strength profile for axial loaded pile analyses. (b) Detailed revised profile for undrained shear strength for laterally loaded pile analyses (Long *et al.*, 1993).

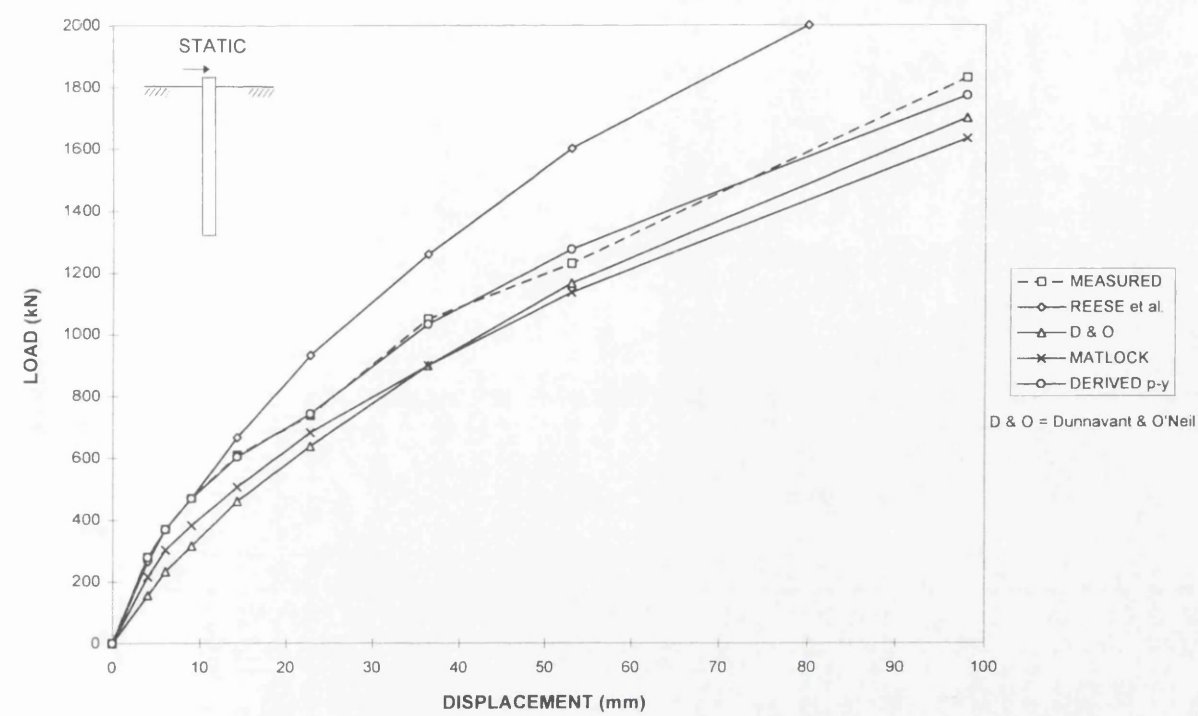


Figure 8.27 Comparisons with load-displacement responses for static loading using p - y methods. After Hamilton and Dunnavant (1993).

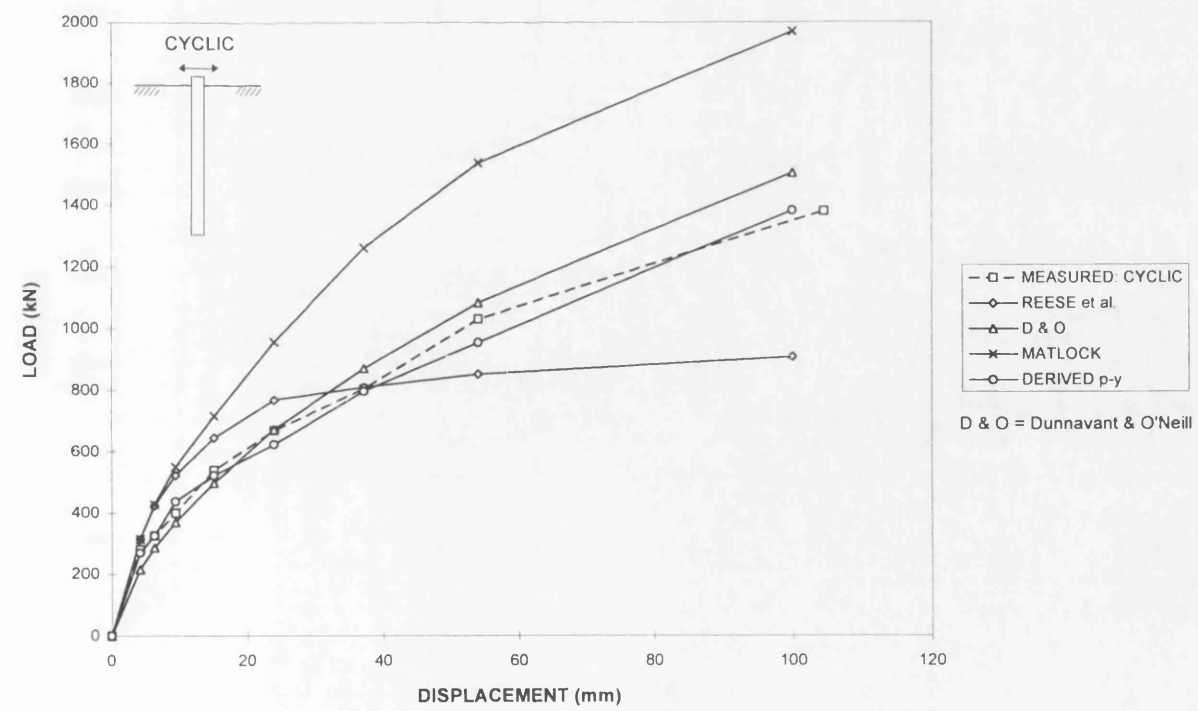


Figure 8.28 Comparisons with load-displacement responses for cyclic loading using p - y methods. After Hamilton and Dunnavant (1993).

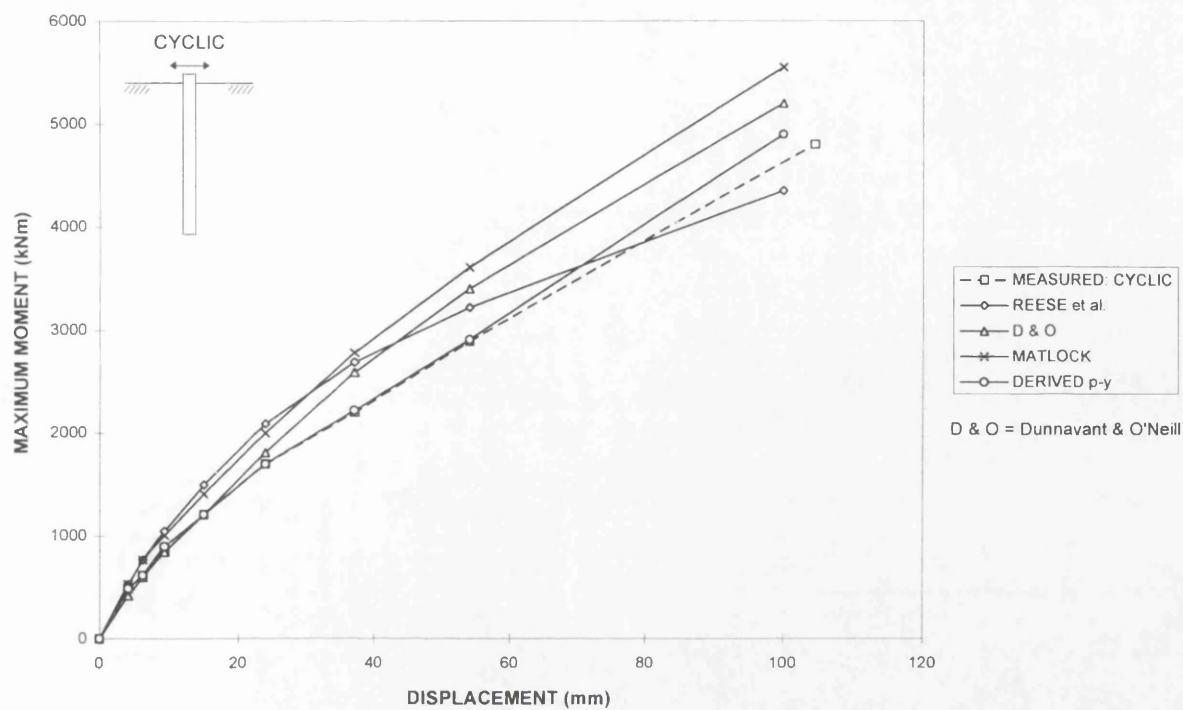


Figure 8.29 Comparisons with moment-displacement responses for cyclic loading using p - y methods. After Hamilton and Dunnavant (1993).

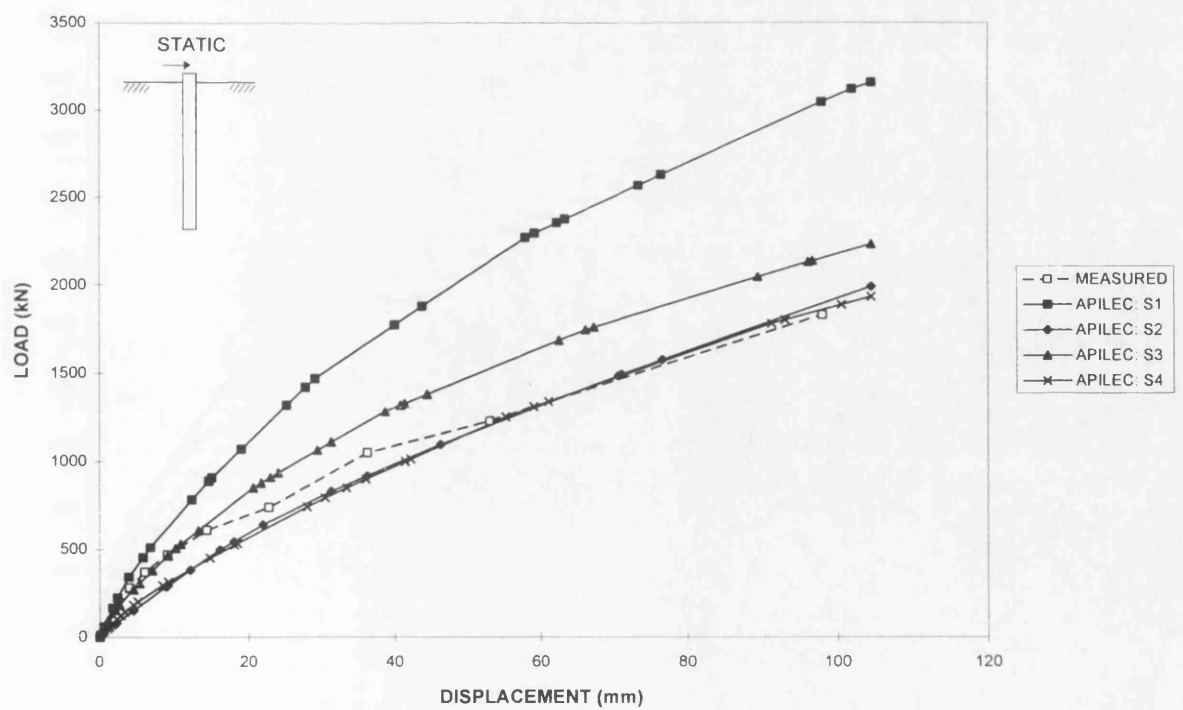


Figure 8.30 Comparisons with load-displacement responses for static loading using APILEC analysis. After Hamilton and Dunnavant (1993).

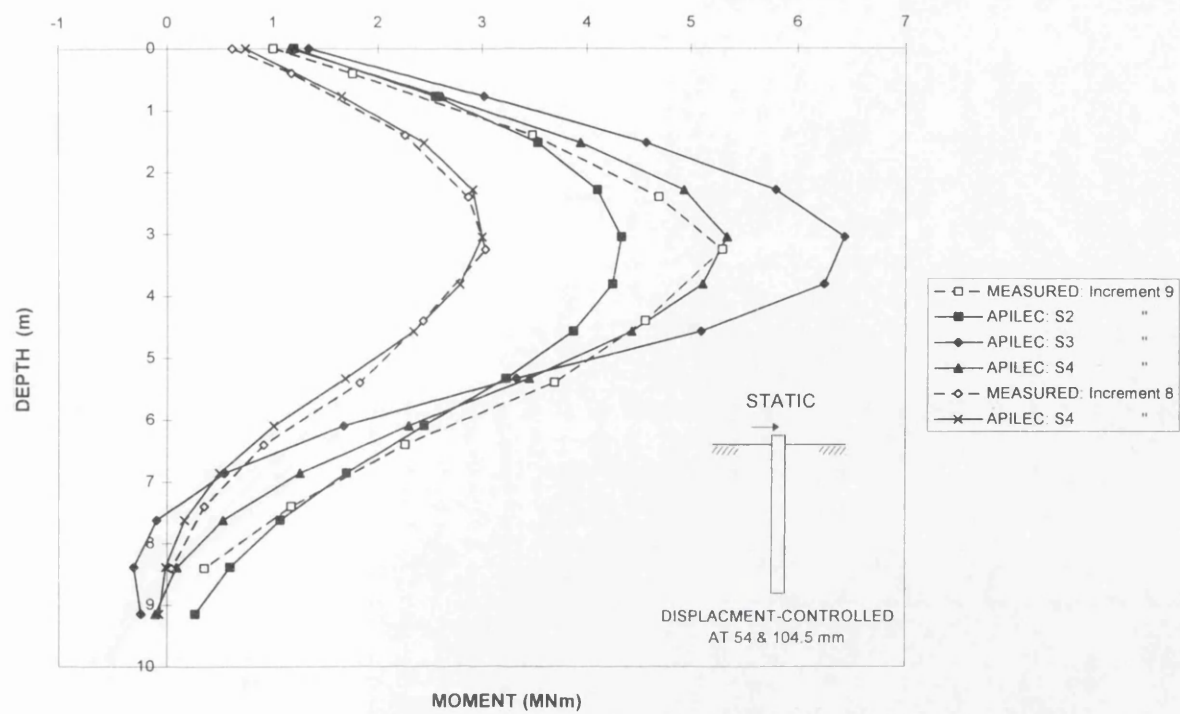


Figure 8.31 Comparisons with bending moment distributions for static loading. After Hamilton and Dunnivant (1993).

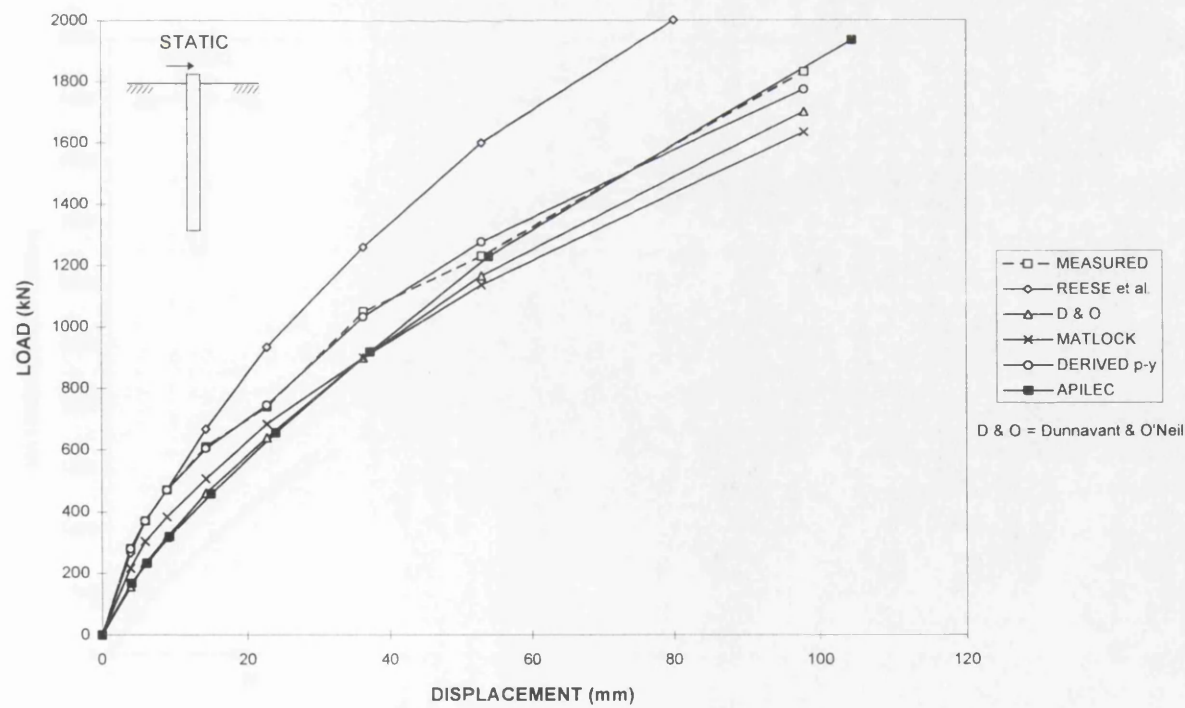


Figure 8.32 Comparisons with load-displacement responses for static loading using p - y methods and APILEC analysis. After Hamilton and Dunnivant (1993).

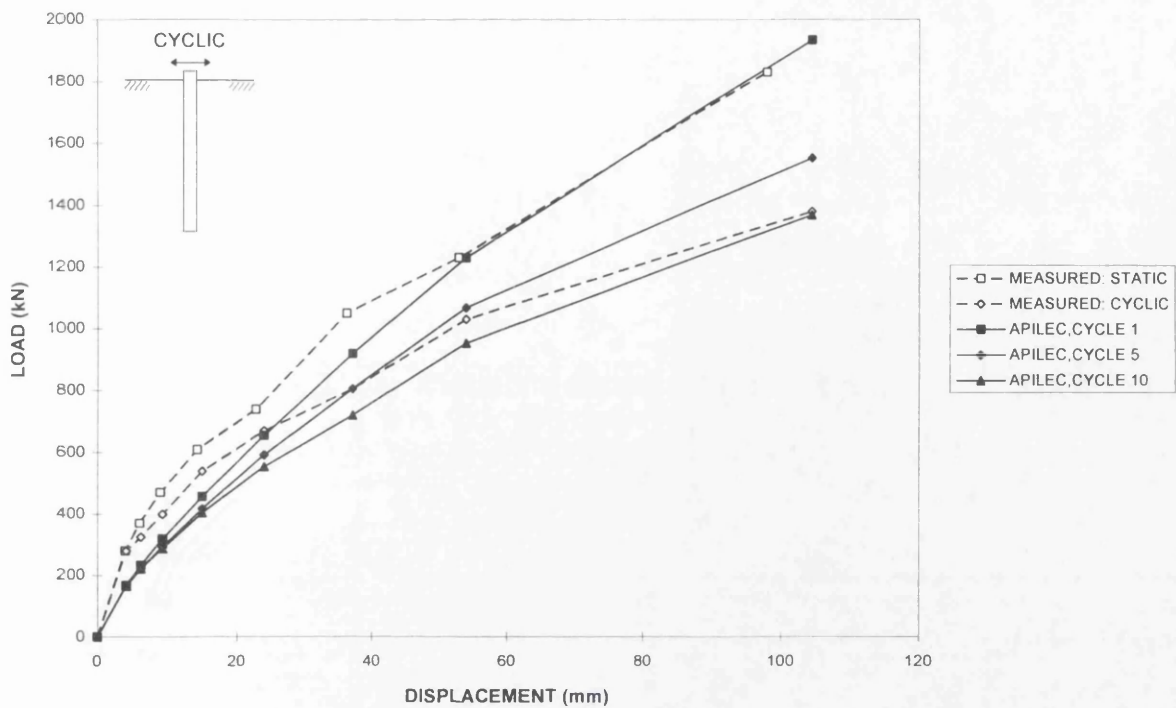


Figure 8.33 Comparisons with load-displacement responses for static and cyclic loadings using APILEC analysis. After Hamilton and Dunnivant (1993).

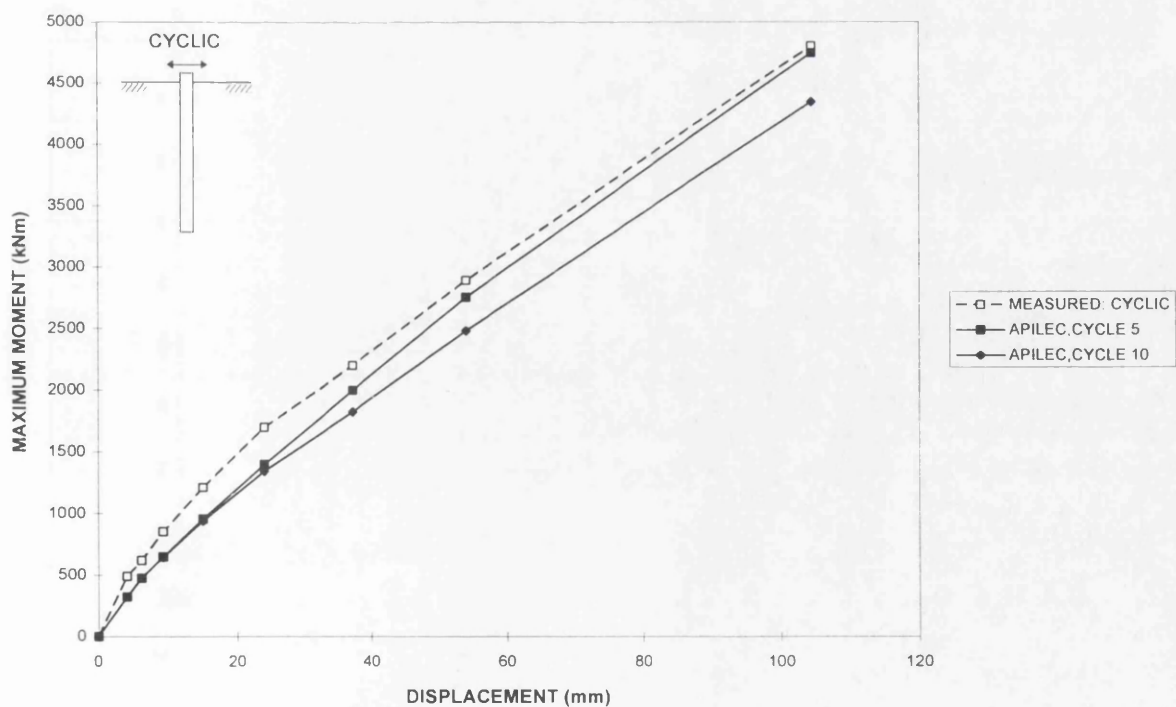


Figure 8.34 Comparisons with moment-displacement responses for cyclic loading using APILEC analysis. After Hamilton and Dunnivant (1993).

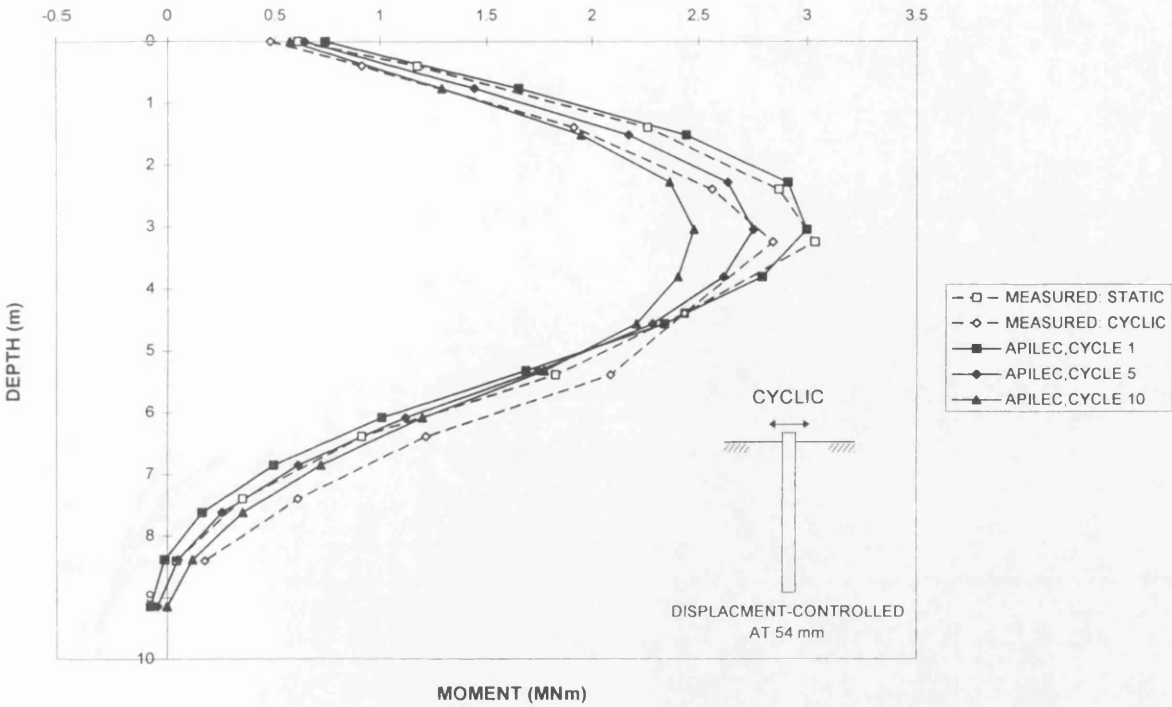


Figure 8.35 Comparisons with bending moment distributions for cyclic loading at displacement increment 8. After Hamilton and Dunnivant (1993).

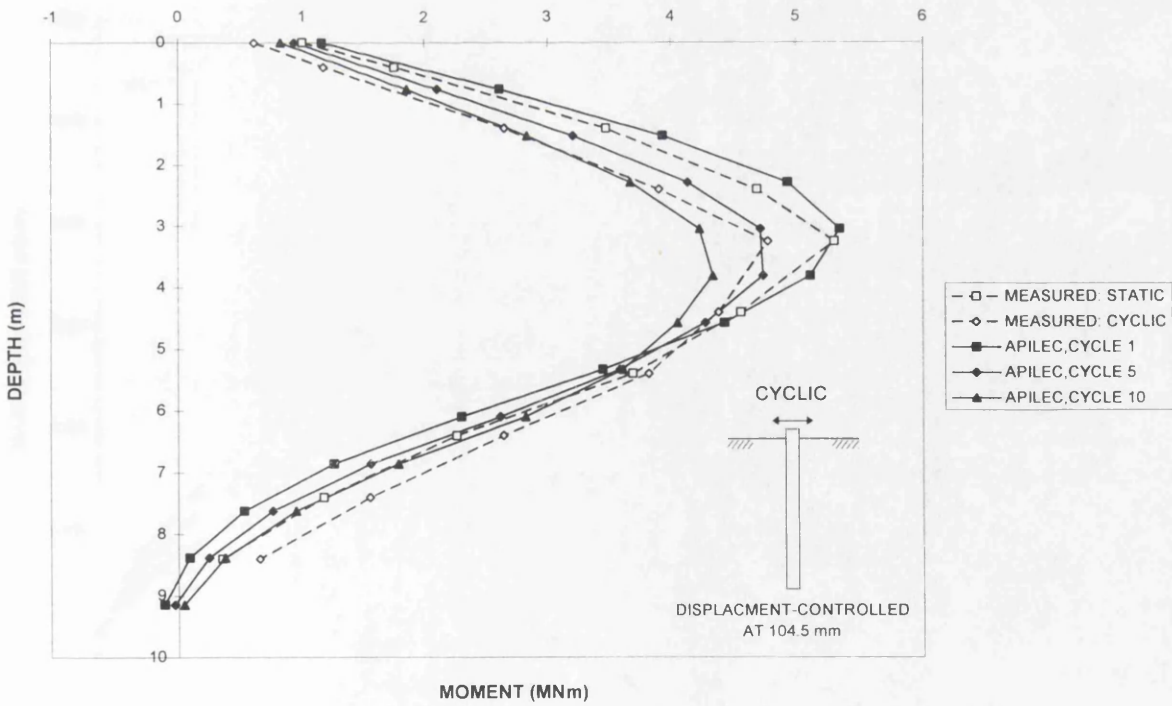


Figure 8.36 Comparisons with bending moment distributions for cyclic loading at displacement increment 9. After Hamilton and Dunnivant (1993).

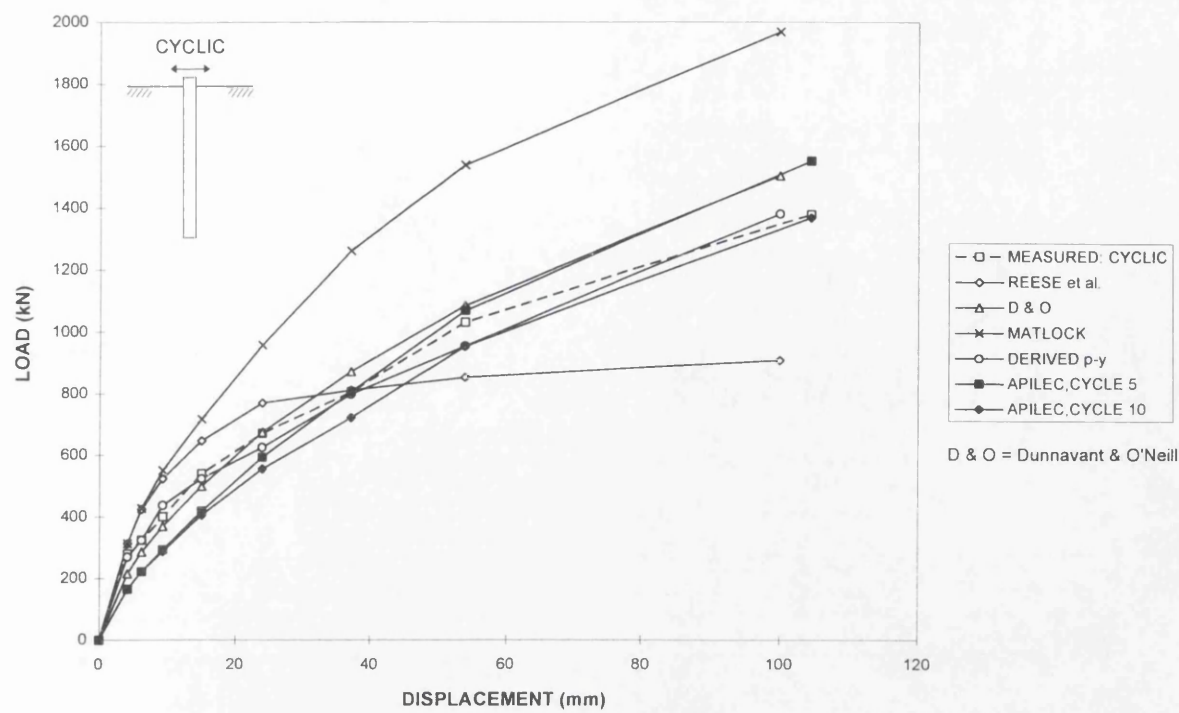


Figure 8.37 Comparisons with load-displacement responses for cyclic loading using p - y methods and APILEC analysis. After Hamilton and Dunnavant (1993).

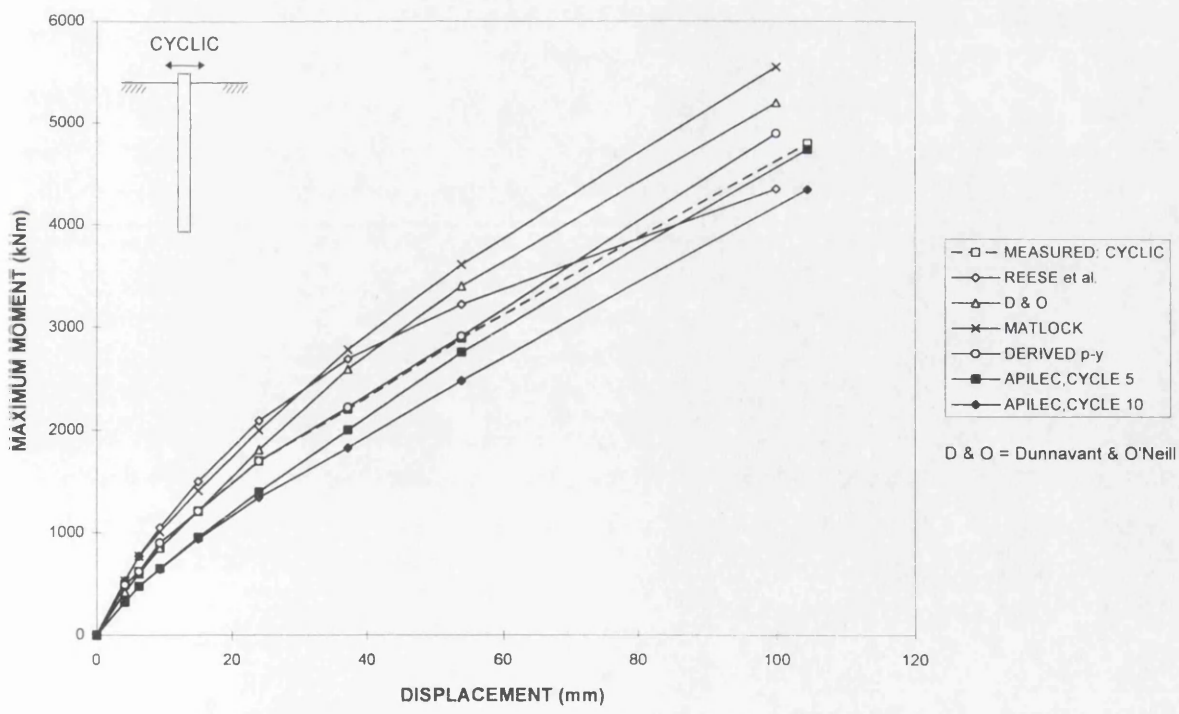


Figure 8.38 Comparisons with moment-displacement responses for cyclic loading using p - y methods and APILEC analysis. After Hamilton and Dunnavant (1993).

CHAPTER 9

Conclusions

9.1 Summary and general conclusions

9.2 Recommendations for future work

CHAPTER 9

Conclusions

9.1 Summary and general conclusions

The main objective of this project was to develop a rational method for analysing the behaviour of cyclic laterally loaded pile foundations, using a continuum approach, via the indirect boundary element method. This objective was achieved by the incorporation of a simple but realistic elasto-plastic soil model which allows for various phenomena observed in cyclic pile-load tests, including soil yielding, gap formation, backsliding and strength degradation.

The main conclusions of this work are as follows:

- (1) Due to the complicated nature of cyclic loading, advanced cyclic soil models may be required to simulate the salient features of soil subjected to cyclic loading. However, these models are complex and involve many ill-defined parameters. From this study, it appears that the 'bubble' model (Al-Tabbaa and Wood, 1989) offers a practical means of describing cyclic soil behaviour, except for strength reduction. This model was employed in the finite element analysis to give some insight into pile-soil interface behaviour.
- (2) The two-dimensional plane-strain finite element analyses of pile foundations subjected to cyclic loading were carried out by modelling the pile-soil system in plan section (Figure 3.7). From the analyses using the bubble model and Mohr-Coulomb model (for soil), the following observations were made:
 - ♦ It was shown that the soil at two pile diameters (or more) away from the pile face were not greatly influenced by the cyclic loading.
 - ♦ It was observed that the soil at the debonded interface (gap present) responded elastically.
 - ♦ The comparisons of results using the bubble model and the Mohr-Coulomb model (for soil), showed that the pile displacements for the former model were very much higher

than the latter model. This suggests that identifying suitable state and fundamental parameters for the bubble model is not straightforward.

(3) A detailed three-dimensional finite element analysis of cyclic laterally loaded pile problems would incur excessive computational cost and data preparation effort, which would be too tedious and cumbersome to contemplate. This is likely to be the reason why finite element analyses were not employed to predict the cyclic pile responses in the case histories examined in Chapter 8. The average time taken for the plane-strain analyses alone averaged more than an hour.

(4) The extension of the simple elastic-perfectly plastic soil model to incorporate strength degradation, was based on the detailed examinations of reported soil behaviour. The model parameters can be obtained from standard tests or by correlations with soil index properties, as presented in Chapter 4. The good agreement between predictions and experimental test results, indicated the applicability of these equations for cyclic analysis.

(5) A three-dimensional continuum approach, using incremental analysis, via the indirect boundary element method (Davies and Budhu, 1986; Budhu and Davies, 1988) was employed for the cyclic analysis. This approach is capable of analysing the three-dimensional pile-soil behaviour of cyclic laterally loaded piles without undue computational cost. The algorithm is able to account for one-way and two-way cyclic loadings, and load-controlled and displacement-controlled conditions. The algorithm takes into consideration the phenomena observed in the cyclic pile-load tests, such as soil yielding, gap formation, backsliding and strength degradation. The loading is applied incrementally, so that only one more soil element reaches the yield condition (or encountered gap closure), at the end of each increment. Unloading and reloading cycles are simply solved by reversing the direction of the traction and displacement increments. At the end of each increment, pile and soil tractions, pile displacements, bending moments, etc. are computed by updating these values from the data obtained from the previous increment.

(6) The algorithm has some useful features which may be of value in practice. Foremost amongst these is the generality of the algorithm which allows different pile-head fixity,

loading conditions, pile dimensions, etc., to be analysed. The soil model allows for many different soil conditions. In addition to their generality, the algorithm is very efficient. For example, for a pile subjected to ten cycles, the computational time for the analysis is less than five minutes, on an IBM-compatible 80486 DX2-66 computer. In addition, the data preparation and data entry effort for the current analysis is quite minimal.

(7) The current analysis gives good predictions of pile responses observed in the cyclic pile-load tests. Under load-controlled conditions, it predicts the increase in pile-head displacements and maximum bending moments with cycling. Under displacement-controlled conditions, it predicts a reduction in pile-head loads and maximum bending moments. In addition, the bending moment distributions along the pile length, and the position at which the maximum bending moment occurs (moving down the pile with cycling) can be predicted. The phenomena observed in cyclic pile-load tests, due to the increase in soil yielding, gap formation and strength degradation with cycling are accounted for in the current analysis.

(8) Finally, comparisons between the current analysis predictions and data from published case histories yields good agreement. This demonstrates the current analysis capabilities and usefulness. In comparison with other methods of analyses (e.g. p - y method), the current analysis gives better predictions of the measured pile responses. This lends some confidence in using the analysis in practice.

9.2 Recommendations for future work

The work described in this thesis, has demonstrated the usefulness of using an indirect boundary element method for analysing the complex behaviour of cyclic laterally loaded pile foundations embedded in cohesive soils. Further research in this field might include the following:

- 1.) Extending the current analysis to deal with pile foundations embedded in cohesionless soil (sand). This will involve thorough investigation on the behaviour of sand subjected to cyclic loading, followed by examination of the pile-soil interface interaction behaviour.
- 2.) Formulation of design rules and charts using the current analysis, to deal with cyclic laterally load pile problems commonly encountered in practice.

- 3.) Detailed study on the shakedown effects of cyclic laterally loaded pile foundations, followed by the examination of the feasibility of incorporating the shakedown theorems to the current analysis.

REFERENCES

- 1.) Agarwal, K.B. (1967). *The influence of size and orientation of sample on the undrained strength of London clay*. Ph.D. thesis, University of London.
- 2.) Al-Tabbaa, A. & O'Reilly, M. (1990). Some observations on the modified Cam-Clay 'bubble' model. *Proc. Int. Conf. on Numerical Methods in Eng.: Theory and Applications*. Swansea, Vol. 2, 779-786.
- 3.) Al-Tabbaa, A. & Wood, D. M. (1989). An experimentally based 'bubble' model for clay. *Proc. 3rd Int. Conf. on Numerical Methods in Geomech.*, Niagara Falls, Canada, 91-99.
- 4.) Al-Tabbaa, A. (1987). *The permeability and stress-strain response of speswhite kaolin*. Ph.D. thesis, Cambridge University.
- 5.) Andersen, K.H., Lacasse, S., Aas, P.M. & Andenaes (1982). Review of foundation design principle for offshore gravity platforms. *Norwegian Geotech. Institute*, Publication 143.
- 6.) Andersen, K.H. & Stenhamar, P. (1983). Static plate loading tests on overconsolidated clay. *Norwegian Geotech. Institute*, NR 145, 1-17.
- 7.) Andersen, K.H. (1976). Behaviour of clay subjected to undrained cyclic loading. *Proc. Int. Conf. on the Behaviour of Offshore Structures*. BOSS'76, Trondheim, Norway, Vol. 1, 392-403.
- 8.) Andersen, K.H., Pool, J.H., Brown, S.F. & Rosenbrand, W.F. (1980). Cyclic and static laboratory tests on Drammen clay. *J. Geotech. Eng. Div.*, ASCE, Vol. 106, No. 5, 499-529.
- 9.) Ansal, A.M. & Erken, A. (1989). Undrained behaviour of clay under cyclic shear stresses. *J. Geotech. Eng. Div.*, ASCE, Vol. 115, No. 7, 968-983.
- 10.) API RP 2A (1986). *Recommended practice for planning, designing and constructing fixed offshore platforms* (16th edn). American Petroleum Institute, Dallas, Texas.
- 11.) Aschenbrenner, T.B. & Olson, R.E. (1984). Prediction of settlement of single piles in clay. *Analysis and design of pile foundations*. J.R. Meyer (eds), ASCE, New York, 41-58.
- 12.) Atkinson, J.H. & Bransby, P.L. (1978). *The mechanics of soils. An introduction to critical state soil mechanics*. McGraw-Hill.

- 13.) Atkinson, J.H. & Farrar, D.M. (1985). Stress path tests to measure soil strength parameters for shallow slips. *Proc. of the 11th Int. Conf. of Soil Mech. and Fdns. Eng.*, San Francisco 2, 983-986.
- 14.) Banerjee, P.K. & Davies, T.G. (1978). The behaviour of axially and laterally loaded single piles embedded in non-homogeneous soils. *Géotechnique* 28, No. 3, 309-326.
- 15.) Banerjee, P.K. & Davies, T.G. (1980). Analysis of some reported case histories of laterally loaded pile groups. *Conf. Numerical Methods in Offshore Piling*, I.C.E., London, 101-108.
- 16.) Bhowmik, S.K. & Long, J.H. (1991). An analytical investigation of the behaviour of laterally loaded piles. *Geotech. Eng. Congress 1991*, Vol. 2, Geotech. Special Publication, No. 27, 1307-1318.
- 17.) Bijmagne, J.L., Berg, P., Zorn, N.F. & Dieterman, H.A. (1991). Laterally loaded single pile in soft soil. *HERON*, Vol. 36, No. 1, 1-77.
- 18.) Bishop, A.W., Green, G.E., Garga, V.K., Andersen, A. & Brown, J.D. (1971). A new ring shear apparatus and its application to the measurement of residual strength. *Géotechnique* 21, No. 4, 273-328.
- 19.) Bishop, A.W., Webb, D.L. & Lewin, P.I. (1965). Undisturbed samples of London clay from the Ashford Common shaft: strength-effective stress relationships. *Géotechnique* 15, No. 1, 1-31.
- 20.) Bjerrum, L. (1972). Embankments on soft ground. *Proc. Spec. Conf. Performance of Earth and Earth-supported Structures*, Purdue University II, ASCE, New York, 1-54.
- 21.) Broms, B.B. (1964). Lateral resistance of piles in cohesive soils. *J. Soil Mech. Fdns. Div.*, ASCE, Vol. 90, SM2, 27-63.
- 22.) Brown, D.A. & Shie, C.F. (1990). Three dimensional finite element model of laterally loaded piles. *Computers and Geotechnics*, 10, 59-79.
- 23.) Brown, D.A. & Shie, C.F. (1991). Some numerical experiments with a three dimensional finite element model of a laterally loaded pile. *Computers and Geotechnics*, 12, 149-162.
- 24.) Bucher, F. (1975). Die Restscherfestigkeit natürlicher Böden, ihre Einflussgrößen und Beziehungen als Ergebnis experimenteller Untersuchungen. Report No. 103, Zürich: Institutes für Grundbau und Bodenmechanik Eidgenössische Technische Hochschule.
- 25.) Budhu, M. & Davies, T.G. (1988). Analysis of laterally loaded piles in soft clays. *J. Geotech. Eng. Div.*, ASCE, Vol. 114, No. 1, 21-39.
- 26.) Burland, J.B., Rampello, S., Georgiannou, V.N. & Calabresi, G. (1996). A laboratory study of the strength of four stiff clays. *Géotechnique* 46, No. 3, 491-514.

- 27.) Burland, J.B. (1990). On the compressibility and shear strength of natural clays. *Géotechnique* 40, No. 3, 329-378.
- 28.) Butterfield, R. & Ghosh, N. (1980). A linear elastic interpretation of model tests on single piles and groups of piles in clay. *Int. Conf. on Numerical Methods in Offshore Piling*, ICE, 109-118.
- 29.) Calebresi, G. & Manfredini, G. (1973). Shear strength characteristics of the jointed clay of S. Barbara. *Géotechnique* 23, No. 2, 233-244.
- 30.) Chan, A.H.C. (1990). DIANA-SWANDYNE II user manual. University of Glasgow, U.K.
- 31.) Chen, L. & Poulos, H.G. (1993). Analysis of pile-soil interaction under lateral loading using infinite and finite elements. *Computers and Geotechnics*, 15, 189-220.
- 32.) Cooke, R.W., Price, G. & Tarr, K. (1979). Jacked piles in London clay: A study of load transfer and settlement under working conditions. *Géotechnique* Vol. 29, No. 2, 113-147.
- 33.) Coulomb, C.A. (1776). Essai sur une application des regles de maximis et minimis à quelques problems de statique, relatifs à l'architecture. *Mem. Acad. Roy. Pres. Divers, Sav.* 5, Vol. 7, Paris.
- 34.) D'Appolonia, D.J., Poulos, H.G. & Ladd, C.C. (1971). Initial settlement of structures on clay. *J. Soil Mech. Fdns. Div.*, ASCE, Vol. 97, SM 10, 1259-1376.
- 35.) Dafalias, Y.F. & Herrmann, L.R. (1980). A bounding surface soil plasticity model. *Int. Symp. on Soils under Cyclic and Transient Loading*, Swansea, U.K., Vol. 1, 335-345.
- 36.) Dafalias, Y.F. & Herrmann, L.R. (1982). Bounding surface formulation of soil plasticity. *Soil Mech. - Transient and Cyclic Loads*. Ed. G.N. Pande and O.C. Zienkiewicz, John Wiley & Sons Ltd, 253-282.
- 37.) Davies, T. G. & Budhu, M. (1986). Non-linear analysis of laterally loaded piles in heavily overconsolidated clays. *Géotechnique* 36, No. 4, 527-538.
- 38.) Davies, T.G. & Budhu, M. (1994). Program APILES. University of Glasgow, U.K.
- 39.) Desai, C.S. & Appel, G.C. (1976). 3-D analysis of laterally loaded structures. *Proc. 2nd Int. Conf. Numerical Methods in Geomech.*, Blacksburg, Vol. 1, 405-418.
- 40.) Dunnivant, T.W. & O'Neill, M.W. (1989). Experimental *p-y* model for submerged, stiff clay. *J. Geotech. Eng. Div.*, ASCE, Vol. 115, No. 1, 95-114.
- 41.) Faruque, M.O. & Desai, C.S. (1982). 3-D material and geometric nonlinear analysis of piles. *Proc. 2nd Int. Conf. on Numerical Methods in Offshore Piling*, University of Texas, 553-575.

- 42.) Finn, W.D.L., Lee, K.W. & Martin, G.R. (1977). An effective stress model for liquefaction. *J. Geotech. Eng. Div.*, ASCE, Vol. 103, No. 6, 517-533.
- 43.) Fleischer, S. (1972). Scherbruch- und Schergleitfestigkeit von Bindigen Erdstoffen. *Neue Bergbautechnik* 2, No. 2, 98-99. Freiburg: Mining Academy.
- 44.) Fleming, W.G.K., Weltman, A.J., Randolph, M.F. & Elson, W.K. (1985). *Piling engineering*. Surrey University Press.
- 45.) Golder, H.Q. & Leonard, M.W. (1954). Some tests on bored piles in London clay. *Géotechnique* 4, No. 1, 32-41.
- 46.) Grashuis, A.J., Dieterman, H.A. & Zorn, N.F. (1990). Calculation of cyclic response of laterally loaded piles. *Computers and Geotechnics*, 10, 287-305.
- 47.) Hamilton, J.M. & Dunnivant, T.W. (1993). Analysis of behaviour of the Tilbrook Grange lateral test pile. *Large-scale pile tests in clay* (eds J. Clarke), Thomas Telford, London, 454-468.
- 48.) Hashiguchi, K. (1985). Two and three surfaces model of plasticity. *Proc. 5th Conf. on Numerical Methods in Geomech.* Nagoya, 285-292.
- 49.) Head, K.H. (1988). *Manual of soil laboratory testing*. Vol. 2, Pentech Press, London.
- 50.) Hetenyi, M. (1946). *Beams on elastic foundations*. Ann Arbor, Mich., Univeristy of Mich, Press.
- 51.) Hettler, A. & Gudehus, G. (1980). Estimation of shakedown displacements in sand bodies with aid of model tests. *Int. Symp. on Soils under Cyclic and Transient Loading*, Swansea, Vol. 1, 3-8.
- 52.) Houston, W.N. & Herrmann, H.G. (1980). Undrained cyclic strength of marine soils. *J. Geotech. Eng. Div.*, ASCE, Vol. 106, No. 6, 691-712.
- 53.) Idriss, I.M., Dobry, R., Doyle E.H. & Singh, R.D. (1978b). Behaviour of soft clays under earthquake loading conditions. *Proc., Offshore Technology Conf.*, OTC 2671, Dallas, Texas, Vol. 3.
- 54.) Idriss, I.M., Dobry, R. & Singh, R.D. (1978a). Non-linear behaviour of soft clays during cyclic loading. *J. Geotech. Eng. Div.*, ASCE, Vol. 104, No. 12, 1427-1447.
- 55.) Idriss, I.M. & Seed, H.B. (1968). Seismic response of horizontal soil layers. *J. Soil Mech. Fdns. Div.*, ASCE, Vol. 94, No. SM4, 1003-1031.
- 56.) Ishihara, K., Yasuda, S. (1980). Cyclic strengths of undrained cohesive soils of Western Tokyo. *Int. Symp. on Soils under Cyclic and Transient Loading*, Swansea, U.K., Vol. 1, 57-66.

- 57.) Iwan, W.D. (1967). On a class of models for the yielding behaviour of continuous and composite systems. *J. Applied Mech.*, 34, 612-617.
- 58.) Kay, S., Griffiths, D.V. & Kolk, H. (1986). Application of pressuremeter testing to assess lateral pile response in clays. *ASTM Spec. Tech. Pub.* STP 950, 458-477.
- 59.) Kishida, H. & Nakai, S. (1977). Large deflections of single pile under horizontal load. Spec. Sess No. 10, *9th Int. Conf. of Soil Mech. and Fdns. Eng.*, Tokyo, 87-92.
- 60.) Kooijman, A.P. (1989a). Quasi three-dimensional model for laterally loaded piles. *Proc. 8th Int. Conf. Offshore Mech. Artic Eng.*, The Hague, 511-518.
- 61.) Kooijman, A.P. (1989b). Comparison of an elastoplastic quasi three-dimensional model for laterally loaded piles with field tests. *Proc. 3rd Int. Conf. on Numerical Methods in Geomech.*, Nigara Falls, Canada, 675-682.
- 62.) Kramer, S.L. (1996). *Geotechnical Earthquake Eng.*. Prentice Hall, Inc.
- 63.) Kuhlemeyer, R.L. (1979). Static and dynamic laterally loaded floating piles. *J. Geotech. Eng. Div.*, ASCE, Vol. 105, No. 2, 289-304.
- 64.) Lacasse, S., Berre, T. & Lefebvre, G. (1985). Block sampling of sensitive clays. *Proc. 11th Int. Conf. of Soil Mech. and Fdns. Eng.*, San Francisco, 2, 887-892.
- 65.) Larsson, R. (1980). Undrained shear strength in stability calculation of embankments and foundation on soft clays. *Canadian Geotech. Journal*, 17 (4), 591-602.
- 66.) Lee, K.L. & Focht, J.A. (1976). Strength of clay subjected to cyclic loading. *Marine Geotechnology*. Vol. 1, No. 3, 163-185.
- 67.) Lee, Y.P. (1995). *SWANDYNE: Example on plane strain cyclic loading using Al-Tabbaa/Wood model*. Ed. by Chan, A.H.C. University of Glasgow, U.K.
- 68.) Long, M.M., Lambson, M.D., Clarke, J. & Hamilton, J. (1993). Cyclic lateral loading of an instrumented pile in overconsolidated clay at Tilbrook Grange. *Large-scale pile tests in clay* (eds J. Clarke), Thomas Telford, London, 381-404.
- 69.) Lupini, J.F., Skinner, A.E. & Vaughan, P.R. (1981). The drained residual strength of cohesive soils. *Géotechnique* 31, No. 2, 181-213.
- 70.) Mahar, L.J. & O'Neill, M.W. (1983). *Geotechnical characterisation of desiccated clay*. ASCE 109(1), 56-71.
- 71.) Maksimovic, M. (1989a). Nonlinear failure envelope for soils. *J. Geotech. Eng. Div.*, ASCE, Vol. 115, No. 4, 581-586.
- 72.) Maksimovic, M. (1989b). On the residual shearing strength of clays. *Géotechnique* 39, No. 2, 347-351.

-
- 73.) Maksimovic, M. (1996). A family of nonlinear failure envelopes for non-cemented soils and rock discontinuities. *Electronic Journal of Geotech. Eng.*, Oct.
- 74.) Masing, G. (1926). Eigenspannungen und verfestigung beim messung. *Proc. of the Second Int. Congress of Applied Mechanics*.
- 75.) Matlock, H., Foo, S.H.C. & Bryant, L.M. (1978). Simulation of lateral pile behaviour under earthquake motion. *Spec. Conf. on Earthquake Eng.*, 600-619.
- 76.) Matlock, H. (1970). Correlations for design of laterally loaded piles in soft clay. *Proc. of the 2nd Offshore Technology Conf.*, OTC 1204, Houston Texas, Vol. 1, 577-594.
- 77.) Mersi, G., Cepeda-Diaz, A.F. (1986). Residual shear strength of clays and shales. *Géotechnique* 26, No. 2, 269-274.
- 78.) Mersi, G. (1975). Discussion: New design procedure for stability of soft clays. *J. Geotech. Eng. Div.*, ASCE, Vol. 101, No. 4, 409-412.
- 79.) Meyerhof, G.G. (1951). The ultimate bearing capacity of foundations. *Géotechnique*, 2, 301-332.
- 80.) Meyerhof, G.G., Brown, J.D. & Mouland, G.D. (1981). Prediction of friction pile capacity in a Till. *Proc. of the 10th Int. Conf. of Soil Mech. and Fdns. Eng.*, Stockholm, Sweden, 2, 777-780
- 81.) Mindlin, R.D. (1936). Force at a point in the interior of a semi-infinite solid. *Physics* 7, 195-202.
- 82.) Mróz, Z., Norris, V. A. & Zienkiewicz, O. C. (1978). An isotropic hardening model for soils and its application to cyclic loading. *Int. J. on Numerical and Analytical Methods in Geomech.* Vol. 2, 203-221.
- 83.) Mróz, Z., Norris, V.A. & Zienkiewicz, O.C. (1979). Application of an anisotropic hardening model in the analysis of elasto-plastic deformation of soils. *Géotechnique* 29, No. 1, 1-34.
- 84.) Mróz, Z., Norris, V.A. & Zienkiewicz, O.C. (1981). An anisotropic critical state model for soils subjected to cyclic loading. *Géotechnique* 31, No. 4, 451-469.
- 85.) Mróz, Z. (1967). On the description of anisotropic hardening. *J. Mech. Phys. Solids*, 15, 163-175.
- 86.) Oasys Limited, 1991. *Safe user manual*. London
- 87.) Ottaviani, M. & Marchetti, S. (1979). Observed and predicted test pile behaviour. *Int. J. for Numerical and Analytical Methods in Geomech.*, 3(2), 131-143.

-
- 88.) Petley, D.J. (1966). *The shear strength of soils at large strains*. Ph.D. thesis, University of London.
- 89.) Petley, D.J. (1969). Unpublished tests at Imperial College.
- 90.) Poulos, H.G. & Davis, E.H. (1980). *Pile foundation analysis and design*. John Wiley and Sons, New York.
- 91.) Poulos, H.G. (1971). Behaviour of laterally loaded piles: I - single piles. *J. Soil Mech. Fdns. Div.*, ASCE, Vol. 97, SM5, 711-731.
- 92.) Poulos, H.G. (1973). Load-deflection prediction for laterally loaded piles. *Aust. Geomech., Journal.*, Vol. G3, No. 1, 1-8.
- 93.) Poulos, H.G. (1982). Single pile response to cyclic lateral load. *J. Geotech. Eng. Div.*, ASCE, Vol. 108, No. 3, 355-375.
- 94.) Prévost, J.-H. & Griffiths, D.V. (1988). Parameter identification and implementation of a kinematic plasticity model for frictional soils. *Proc. of the Workshop on Constitutive Laws for the Analysis of Fill Retention Structures*, ed. Evgin, E. Dept. of Civil Eng., University of Ottawa, 285-358.
- 95.) Prévost, J.-H., (1977). Mathematical modelling of monotonic and cyclic undrained clay behaviour. *Int. J. for Numerical and Analytical Methods in Geomech.*, 1(2): 195-216.
- 96.) Pyke, R.M. (1979). Nonlinear soil models for irregular cyclic loadings. *J. Geotech. Eng. Div.*, ASCE, Vol. 105, No. 6, 715-726.
- 97.) Quek, S.T., Chow, Y.K. & Phoon, K.K. (1992). Further contributions to reliability-based pile-settlement analysis. *J. Geotech. Eng. Div.*, ASCE, Vol. 118, No. 5, 726-742.
- 98.) Rajashree, S.S. & Sundaravadivelu, R.S. (1996). Degradation model for one-way cyclic lateral load on piles in soft clay. *Computers and Geotechnics*, Vol. 19, No. 4, 289-300.
- 99.) Randolph, M.F. (1981). The response of flexible piles to lateral loading. *Géotechnique* 31, No. 2, 247-259.
- 100.) Rankine, W.J.M. (1857). On the stability of loose earth. *Phil. Trans. Roy. Soc.*, London, 147, Part 1, 9-27.
- 101.) Rao, S.N., Rao, K.M. & Prasad, Y.V.S.N. (1992). Behaviour of vertical piles under static and cyclic lateral load in marine clays. *Int. Offshore Polar Eng. Conf.*, San Francisco, USA, Vol. 1, 475-482.
- 102.) Rao, S.N. & Rao, K.M. (1993). Behaviour of rigid piles in marine clays under lateral cyclic loading. *Ocean Eng.*, Vol. 20, No. 3, 281-293.

- 103.) Reese, L.C., Cox, W.R. & Koop, F.D. (1975). Field testing and analysis of laterally loaded piles in stiff clay. *Proc. of the 7th Offshore Technology Conf.*, OTC 2312, Houston Texas, 671-690.
- 104.) Reese, L.C. & Desai, C.S. (1977). *Laterally loaded piles. Numerical Methods in Geotech. Eng.*, Ed. C.S. Desai and J.T. Christian, McGraw Hill, New York.
- 105.) Reese, L.C. & Matlock, H. (1956). Non-dimensional solutions for laterally-loaded piles with soil modulus assumed proportional to depth. *Proc. of the 8th Int. Conf. of Soil Mech. and Fdns. Eng.*, Austin, Texas, 1956, 63-94.
- 106.) Richart, F.E. (1975). Some effects of dynamics soil properties on soil-structure interaction. *J. Geotech. Eng. Div.*, ASCE, Vol. 101, No. 12, 1193-1240.
- 107.) Roscoe, K. H. & Burland, J. B. (1968). On the generalised stress-strain behaviour of 'wet' clay. *Eng. Plasticity*. Cambridge University Press.
- 108.) Roscoe, K. H. & Schofield, A. N. (1963). Mechanical behaviour of an idealised wet clay. *Proc. Conf. of Soils and Rocks*. British Geotechnical Society, London, 285-293.
- 109.) Ruiz, S. (1986). Uncertainty about p - y curves for piles in soft clays. *J. Geotech. Eng. Div.*, ASCE, Vol. 112, No. 6, 594-607.
- 110.) Sangrey, D.A., Castro, G., Poulos, S.J. & France, J.W. (1978). Cyclic loading of sands, silts and clays. *ASCE Spec. Conf. on Earthquake Eng. and Soil Dynamics*, 2: 836-851.
- 111.) Sangrey, D.A., Henkel, D.J. & Esrig, M.I. (1969). The effective stress response of a saturated clay soil to repeated loading. *Canadian Geotech. Journal*, 6 (3), 241-252.
- 112.) Sangrey, D.A. & France, J.W. (1980). Peak strength of clay soils after a repeated loading history. *Int. Symp. on Soils under Cyclic and Transient Loading*, Swansea, Vol. 1, 421-430.
- 113.) Simons, N.E. (1976). Normally consolidated and lightly overconsolidated cohesive material. *General report: Proc. Conf. Settlement of Structures*, University of Cambridge, U.K., 500-530.
- 114.) Skempton, A.W. & Hutchinson, J. (1969). Stability of natural slopes and embankment foundations. *Proc. 7th Int. Conf. of Soil Mech. and Fdns. Eng.*, Mexico, State-of-the-art, 291-340.
- 115.) Skempton, A.W. & Petley, D.J. (1967). The strength along structural discontinuities in stiff clay. *Proc. Geotech. Conf.*, Oslo 2, 29-46.
- 116.) Skempton, A.W. (1954). Discussion of the structure of inorganic soil. *Proc. ASCE, Soil Mech. and Fdns. Div.* 80, 19-22.

- 117.) Skempton, A.W. (1957). Discussion: The planning and design of the new Hong Kong airport. *Proc. ICE* 7, 305-307.
- 118.) Skempton, A.W. (1959). Cast in-situ bored piles in London clay. *Géotechnique* 9, No. 4, 153-173.
- 119.) Skempton, A.W. (1964). Long term stability of clay slopes. *Géotechnique* 14, No. 2, 77-101.
- 120.) Skempton, A.W. (1985). Residual strength of clays in landslides, folded strata and the laboratory. *Géotechnique* 35, No. 1, 3-18.
- 121.) Streeter, V.L., Wylie, E.B. & Richart, F.E., Jr. (1974). Soil motion computations by characteristics method. *J. Geotech. Eng. Div.*, ASCE, Vol. 100, No. 3, 247-263.
- 122.) Sullivan, W.R., Reese, L.C. & Fenske, C.W. (1980). Unified method for analysis of laterally loaded piles in clay. *Conf. on Numerical Methods in Offshore Piling*, I.C.E., London, 135-146.
- 123.) Swane, I.C. & Poulos, H.G. (1982). A theoretical study of the cyclic shakedown of laterally loaded piles. *Proc. 5th Int. Conf. Numerical Method Design in Geomech.*, Edmonton, 853-864.
- 124.) Swane, I.C. & Poulos, H.G. (1985). Shakedown analysis of a laterally loaded pile tested in stiff clay. *Institution of Engineers, Australia, Civil Eng. Transactions*, 275-280.
- 125.) Tassios, T., & Levendis, E. (1974). Efforts répétitifs horizontaux sur pieux verticaux. *Annales de L'Institut Technique du Batiment et des Travaux Publics*. March, No. 315, 45-71.
- 126.) Tomlinson, S.J. (1994). *Pile design and construction practice* (4th edn). E & FN Spon, London.
- 127.) Trak, B., LaRochelle, P., Tavenas, F., Leroueil, S. & Roy, M. (1980). A new approach to the stability analysis of embankments on sensitive clays. *Canadian Geotech. Journal*, 17 (4), 526-544.
- 128.) Tresca, H. (1868). Mémoire sur l'écoulement des corps solides, Mém. pres. par div. Savants 18, 733-799.
- 129.) Trochanis, A.M., Bielak, J. & Christiano, P. (1991). Three-dimensional nonlinear study of piles. *J. Geotech. Eng. Div.*, ASCE, Vol. 117, No. 3, 429-447.
- 130.) Vaughan, P.R., Hight, D.W., Sodha, V.G. & Walbancke, H.J. (1978). Factors controlling the stability of clay fills in Britain. clay fills, 203-217. London, ICE.
- 131.) Verrujit, A. & Kooijman, A.P. (1989). Laterally loaded piles in a layered elastic medium. *Géotechnique* 39, No. 1, 39-46.

- 132.) Voight, B. (1973). Correlation between Atterberg plasticity limits and residual shear strength of natural soils. *Géotechnique* 23, No. 2, 265-267.
- 133.) Ward, W.H., Marsland, A. & Samuels, S.G. (1965). Properties of the London clay at the Ashford Common shaft: in situ and undrained strength tests. *Géotechnique* 15, No. 4, 321-344.
- 134.) Webb, D.L. (1969). Residual strength in conventional triaxial tests. *Proc. 7th Int. Conf. of Soil Mech. and Fdns. Eng.*, Mexico City, 1, 433-441.
- 135.) Whitaker, T. (1970). *The design of piled foundations*. Pergamon Press, London.
- 136.) Wood, D.M. (1994). *Soil behaviour and critical state soil mechanics*. Cambridge University Press.
- 137.) Yegian, M. & Wright, S.G. (1973). Lateral soil resistance - displacement relationships for pile foundations in soft clays. *Offshore Technology Conf.*, OTC 1893, Vol. 2, 663-676.
- 138.) Grashuis, A.J. & Bijnagte, J.L. (1992). A model for cyclic pile-soil interaction, calculations and comparison with a full scale test. *Numerical Models in Geomech.*, Pande & Pietruszczak (eds). 301-308.
- 139.) Kanji, M.A. (1974). The relationship between drained friction angles and Atterberg limits of natural soils. *Géotechnique* 24, No. 4, 671-674.
- 140.) Kenney, T.C. (1967). The influence of mineralogical composition on the residual strength of natural clays. *Proc. of Oslo Geotech. Conf. on the Shear Strength Properties of Natural Soils and Rocks*, Vol 1, 123-129.
- 141.) O'Reilly, M. P. & Brown, S. F. (1991). Cyclic loading in geotechnical engineering. *Cyclic Loading of Soils: from theory to design*. M. P. O'Reilly & S. F. Brown (eds), Van Nostrand Reinhold, New York, 1-18.
- 142.) Seyček, J. (1978). Residual shear strength of soils. *Bull. Int. Ass. Eng. Geol.* 17, 73-75.

